frontiers | Research Topics

Substance and energy metabolism associated with neuroendocrine regulation in tumor cells

Edited by
Ruiqin Han, Xiaochen Yuan, Qingbin Wu,
Chenyu Sun and Peixin Dong

Published in
Frontiers in Endocrinology

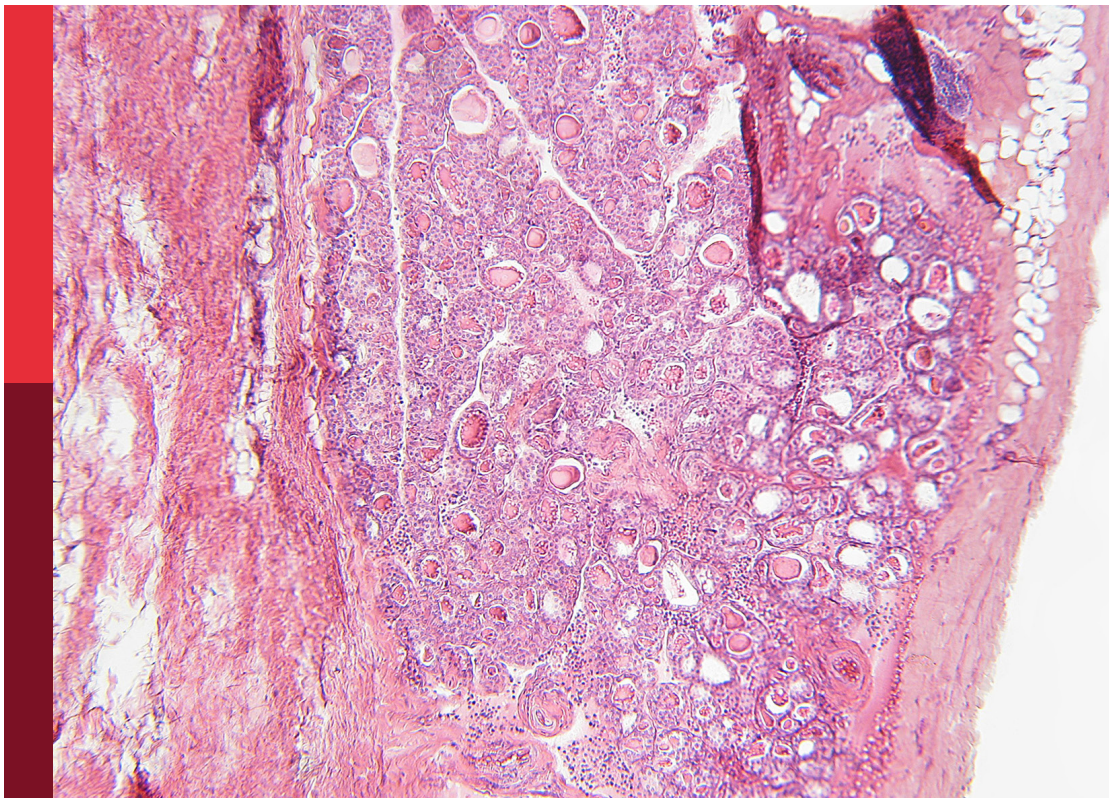

ISSN 1664-8714
ISBN 978-2-8325-3973-6
DOI 10.3389/978-2-8325-3973-6

About Frontiers

Frontiers is more than just an open access publisher of scholarly articles: it is a pioneering approach to the world of academia, radically improving the way scholarly research is managed. The grand vision of Frontiers is a world where all people have an equal opportunity to seek, share and generate knowledge. Frontiers provides immediate and permanent online open access to all its publications, but this alone is not enough to realize our grand goals.

Frontiers journal series

The Frontiers journal series is a multi-tier and interdisciplinary set of open-access, online journals, promising a paradigm shift from the current review, selection and dissemination processes in academic publishing. All Frontiers journals are driven by researchers for researchers; therefore, they constitute a service to the scholarly community. At the same time, the *Frontiers journal series* operates on a revolutionary invention, the tiered publishing system, initially addressing specific communities of scholars, and gradually climbing up to broader public understanding, thus serving the interests of the lay society, too.

Dedication to quality

Each Frontiers article is a landmark of the highest quality, thanks to genuinely collaborative interactions between authors and review editors, who include some of the world's best academicians. Research must be certified by peers before entering a stream of knowledge that may eventually reach the public - and shape society; therefore, Frontiers only applies the most rigorous and unbiased reviews. Frontiers revolutionizes research publishing by freely delivering the most outstanding research, evaluated with no bias from both the academic and social point of view. By applying the most advanced information technologies, Frontiers is catapulting scholarly publishing into a new generation.

What are Frontiers Research Topics?

Frontiers Research Topics are very popular trademarks of the *Frontiers journals series*: they are collections of at least ten articles, all centered on a particular subject. With their unique mix of varied contributions from Original Research to Review Articles, Frontiers Research Topics unify the most influential researchers, the latest key findings and historical advances in a hot research area.

Find out more on how to host your own Frontiers Research Topic or contribute to one as an author by contacting the Frontiers editorial office: frontiersin.org/about/contact

Substance and energy metabolism associated with neuroendocrine regulation in tumor cells

Topic editors

Ruiqin Han — State Key Laboratory of Medical Molecular Biology, Department of Biochemistry and Molecular Biology, Institute of Basic Medical Sciences, Chinese Academy of Medical Sciences, China

Xiaochen Yuan — Chinese Academy of Medical Sciences and Peking Union Medical College, China

Qingbin Wu — Chinese Academy of Medical Sciences and Peking Union Medical College, China

Chenyu Sun — AMITA Health, United States

Peixin Dong — Hokkaido University, Japan

Citation

Han, R., Yuan, X., Wu, Q., Sun, C., Dong, P., eds. (2023). *Substance and energy metabolism associated with neuroendocrine regulation in tumor cells*. Lausanne: Frontiers Media SA. doi: 10.3389/978-2-8325-3973-6

Table of contents

frontiers | Frontiers in Endocrinology

TYPE Original Research
PUBLISHED 15 March 2023
DOI 10.3389/fendo.2023.1144250

OPEN ACCESS

EDITED BY
Ruiqin Han,
Chinese Academy of Medical Sciences, China

REVIEWED BY
Jacques C. Mbongue,
Oakwood University, United States
Haijun Peng,
Hebei Chest Hospital, China
He Huang,
The Third Affiliated Hospital of Sun Yat-sen University, China

*CORRESPONDENCE
Haiming Zhang
hayming@126.com
Jiandong Guo
y215180041@zju.edu.cn
Jinxi Zhang
ice1998@sina.com

SPECIALTY SECTION
This article was submitted to Cancer Endocrinology, a section of the journal Frontiers in Endocrinology

RECEIVED 14 January 2023
ACCEPTED 17 February 2023
PUBLISHED 15 March 2023

CITATION
Li J, Cui Y, Jin X, Ruan H, He D, Che X, Gao J, Zhang H, Guo J and Zhang J (2023) Significance of pyroptosis-related gene in the diagnosis and classification of rheumatoid arthritis.
Front. Endocrinol. 14:1144250.
doi: 10.3389/fendo.2023.1144250

Significance of pyroptosis-related gene in the diagnosis and classification of rheumatoid arthritis

Jian Li[1], Yongfeng Cui[1], Xin Jin[1], Hongfeng Ruan[1,2], Dongan He[1], Xiaoqian Che[1], Jiawei Gao[1], Haiming Zhang[1*], Jiandong Guo[1*] and Jinxi Zhang[1*]

[1]Department of Orthopaedics, Hangzhou Ninth People's Hospital, Hangzhou, Zhejiang, China, [2]Department of Orthopaedics, The First Affiliated Hospital of Zhejiang University of Chinese Medicine, Hangzhou, China

Background: Rheumatoid arthritis (RA), a chronic autoimmune inflammatory disease, is often characterized by persistent morning stiffness, joint pain, and swelling. Early diagnosis and timely treatment of RA can effectively delay the progression of the condition and significantly reduce the incidence of disability. In the study, we explored the function of pyroptosis-related genes (PRGs) in the diagnosis and classification of rheumatoid arthritis based on Gene Expression Omnibus (GEO) datasets.

Method: We downloaded the GSE93272 dataset from the GEO database, which contains 35 healthy controls and 67 RA patients. Firstly, the GSE93272 was normalized by the R software "limma" package. Then, we screened PRGs by SVM-RFE, LASSO, and RF algorithms. To further investigate the prevalence of RA, we established a nomogram model. Besides, we grouped gene expression profiles into two clusters and explored their relationship with infiltrating immune cells. Finally, we analyzed the relationship between the two clusters and the cytokines.

Result: CHMP3, TP53, AIM2, NLRP1, and PLCG1 were identified as PRGs. The nomogram model revealed that decision-making based on established model might be beneficial for RA patients, and the predictive power of the nomogram model was significant. In addition, we identified two different pyroptosis patterns (pyroptosis clusters A and B) based on the 5 PRGs. We found that eosinophil, gamma delta T cell, macrophage, natural killer cell, regulatory T cell, type 17 T helper cell, and type 2 T helper cell were significant high expressed in cluster B. And, we identified gene clusters A and B based on 56 differentially expressed genes (DEGs) between pyroptosis cluster A and B. And we calculated the pyroptosis score for each sample to quantify the different patterns. The patients in pyroptosis cluster B or gene cluster B had higher pyroptosis scores than those in pyroptosis cluster A or gene cluster A.

Conclusion: In summary, PRGs play vital roles in the development and occurrence of RA. Our findings might provide novel views for the immunotherapy strategies with RA.

KEYWORDS

rheumatoid arthritis, pyroptosis, immunity, consensus clustering, bioinformatic analysis

1 Introduction

Rheumatoid arthritis (RA), a chronic autoimmune inflammatory disease, is often characterized by persistent morning stiffness, joint pain and swelling (1). RA affects approximately 1% of the world population and has become one of the most common causes of significant disability (2). Although the pathogenesis and etiology of RA have not been fully known, the interaction of environmental, genetic, and immunological factors has been shown to play an important role in the development of RA (3). Early diagnosis and timely treatment of RA can effectively delay the progression of the condition and significantly reduce the incidence of disability (4). Therefore, screening for diagnostic genes associated with RA, exploring their subtype classification, and elucidating the underlying pathogenesis of RA could be effective in preventing and treating RA, and might provide new approaches for clinical treatment of RA.

Pyroptosis, a novel inflammatory programmed cell death, is mediated by the caspase family and the GSDM protein family (5). Pyroptosis is characterized by cell swelling and cell membrane rupture, and the release of pro-inflammatory cytokines that eventually induce and aggravate the inflammatory response (6). Increasing studies conformed that pyroptosis might play a key role in the development of many immune diseases (7). In the arthritic mouse model, NLRP3$^{-/-}$ or Caspase-1$^{-/-}$ mice could alleviate symptoms of arthritis (8). Gsdme$^{-/-}$ mice have been demonstrated to reduce intestinal inflammation in the inducible colitis model (9). Besides, bronchial epithelial cell pyroptosis promotes airway inflammation in asthmatic mice (10). However, the role of pyroptosis-related genes (PRGs) in RA remains unclear.

In the research, we used bioinformatics methods to investigate the function of PRGs in the diagnosis and classification of rheumatoid arthritis form the Gene Expression Omnibus (GEO) datasets. Firstly, we identified differential expression of PRGs from the GSE93272 dataset. Then, we screened 5 PRGs associated with RA by support vector machine-recursive feature elimination (SVM-RFE), least absolute shrinkage and selection operator (LASSO) logistic regression and random forest (RF) algorithms, and established a nomogram model for predicting the prevalence of RA. In addition, we divided gene expression profiles into two clusters and explored their relationship with infiltrating immune cells. Finally, we further analyze the relationship between two clusters and cytokines. We found that the pyroptosis-related pattern could distinguish RA patients from normal people and provide new directions for the prevention and treatment of RA.

2 Materials and methods

2.1 Data acquisition and preprocessing

The microarray datasets were downloaded from the GEO database (https://www.ncbi.nlm.nih.gov/geo/) using "rheumatoid arthritis", "whole blood," and "Homo sapiens" as keywords. The inclusion criteria were as follows: the whole-genome expression profiling of whole blood of RA patients and healthy control samples was available in the datasets; every dataset contained a sample count of > 20; and all included samples were not treated with drugs. The microarray dataset GSE93272 from the GPL570 platform containing 35 healthy controls and 67 RA patients was downloaded from the GEO database (11).

2.2 Identification of differentially expressed PRGs

The GSE93272 cohort was normalized by the "limma" package of R software (12). Based on previous literatures (13–15), we acquired 52 PRGs. However, we did not find the expression data of GSDMA in GSE93272. Therefore, 51 PRGs were used for the following analysis. Then, we identified differentially expressed PRGs in RA and normal samples using the "limma" package. The p-value < 0.05 was considered a significant difference. Heatmap and boxplot were performed using the R packages "pheatmap" and "ggpubr" to visualize the differentially expressed PRGs.

2.3 Screening of PRGs for RA

Based on the differentially expressed PRGs, three feature selection algorithms, including SVM-RFE (16), LASSO logistic regression (17) and RF algorithm (18) were adapted to screen RA-related biomarkers, respectively. The SVM-RFE algorithm was performed by the R packages "e1071" and "caret" with five-fold cross-validation (19). The LASSO logistic regression was employed with the R package "glmnet" (20). The RF algorithm was analyzed by the R package "randomForest" (21). Then, the "venn" R package was used to select overlapping genes from the three algorithms as signature genes for further analysis.

2.4 Construction of a nomogram model

We constructed a nomogram model based on PRGs (CHMP3, TP53, AIM2, NLRP1, and PLCG1) to predict the occurrence of RA patients with the "rms" package in R (22). The calibration curve was used to assess the predictive performance of the nomogram model. Then, we further performed decision curve analysis (DCA) and clinical impact curve analysis (CICA) to estimate the clinical utility of the nomogram model (23).

2.5 Consensus clustering

Consensus clustering is an algorithm for identifying cluster each member and their number in datasets (24). We utilized the consensus clustering method to distinguish distinct pyroptosis-related clinical subtypes of RA and identify different PRGs patterns based on the significant differentially expressed PRGs with the package "ConsensusClusterPlus" in R (25). "Points" represents the score of the corresponding factor below and "Total Points" indicates the summation of all the scores of factors above.

2.6 Estimation of the pyroptosis gene signature

To quantify the pyroptosis patterns, we used principal component analysis (PCA) algorithms to calculate the pyroptosis score for each RA sample. The Principal Component 1 (PC1) and Principal Component 2 (PC2) were chosen as the signature scores. And pyroptosis scores for each RA patient were calculated using the following formula (26, 27): Pyroptosis Score = $\Sigma(PC1_i + PC2_i)$, where i is the expression of PRGs.

2.7 Estimation of immune cell infiltration for RA

The single-sample gene-set enrichment analysis (ssGSEA) was employed to measure the relative abundance of immune cells in RA samples *via* the R packages "limma", "GSVA", and "GSEABase" (28). And the gene set for marking each immune cell type was obtained from the study of Charoentong (29).

2.8 Functional and pathway enrichment analysis

To investigate the functional and molecular pathways of differentially expressed genes between pyroptosis gene clusters A and B, we performed GO, KEGG enrichment analyses by the "colorspace", "stringi" and "ggplot2" packages in R (30, 31). $P < 0.05$ was considered statistically significant.

2.9 Statistical analysis

The Kruskal-Wallis test was adopted to compare differences between normal samples and RA samples. The significant differences were identified with the p-value < 0.05. All statistical analysis were performed using the R version 4.0.3.

3 Results

3.1 The landscape of the differentially expressed PRGs

We analyzed the differential expression levels of 51 PRGs between RA patients and healthy controls using the "limma" R package (Supplementary Table 1). A heatmap and histogram were used to visualize the 23 differentially expressed PRGs. We found that BAX, CASP1, CASP3, CASP4, CASP5, CHMP2B, CHMP3, HMGB1, IL18, IL1A, AIM2, NLRC4, NOD2, TNF, and GZMA were overexpressed in RA patients compared to healthy controls (Figures 1A, B).

3.2 Identification of characteristic genes

To further screen the characteristic genes related to PRGs for RA, we utilized the LASSO logistic regression algorithm, the RF algorithm, and the SVM-RFE analysis for feature identification (Supplementary Table 2). Thirteen genes from differentially expressed PRGs were identified as biomarkers for RA using the LASSO logistic regression algorithm (Figure 1C). We used RF algorithm to detect nine key genes from differentially expressed PRGs as vital biomarkers (Figure 1D). Eight signature genes were identified from differentially expressed PRGs by the SVM-RFE analysis (Figure 1E). Finally, we overlapped three different algorithms analysis results and obtained 5 genes (CHMP3, TP53, AIM2, NLRP1, and PLCG1) that were significantly related to RA (Figure 1F).

3.3 Construction of the nomogram

To predict the prevalence of RA patients, we constructed a nomogram model based on the 5 PRGs (Figure 2A). As shown in Figure 2B, the calibration curve of the nomogram revealed accurate predictive ability. The DCA result revealed that decision-making based on established models may be beneficial for RA patients (Figure 2C). And the CICA result (Figure 2D) found that the predictive power of the nomogram model was significant.

3.4 Two distinct pyroptosis patterns

Based on the 5 PRGs, we identified two different pyroptosis patterns (cluster A and cluster B) using the consensus clustering method (Figure 3A and Supplementary Figure 1). There were 38 cases in cluster A and 29 cases in cluster B. We plotted the histogram to observe the differential expression levels of the 5 PRGs between the two clusters. TP53, NLRP1, and PLCG1 showed higher expression in pyroptosis gene cluster A than in pyroptosis gene cluster B, while AIM2 revealed the opposite results. And CHMP3 showed no differently expressed between the two patterns (Figure 3B). As shown in Figure 3C, the two pyroptosis patterns could be distinguished though the 5 significant PRGs with PCA analysis. Then, the differential immune cell infiltration between the two pyroptosis patterns was analyzed (Figure 3D). We found that eosinophil, gamma delta T cell, macrophage, natural killer cell, regulatory T cell, type 17 T helper cell, and type 2 T helper cell were significant high expressed in cluster B ($p < 0.05$). Besides, we calculated the abundance of immune cells in RA patients and evaluated the correlation between the 5 PRGs and immune cells (Figure 3E).

3.5 Function and pathway enrichment

A total of 56 differentially expressed genes (DEGs) were identified between the two pyroptosis patterns. To further explore the potential functional and molecular pathways of DEGs, we performed GO and KEGG enrichment analyses, and the results were shown through an enrichment circle diagram. In the GO enrichment analysis of differential expression PRGs, biological processes (BP) terms were correlated with defense response to virus (GO:0051607) and defense response to symbiont (GO:0140546); cellular components (CC) terms were related to tertiary granule (GO:0070820) and early endosome (GO:0005769); and molecular functions (MF) terms were associated

10.3389/fendo.2023.1144250

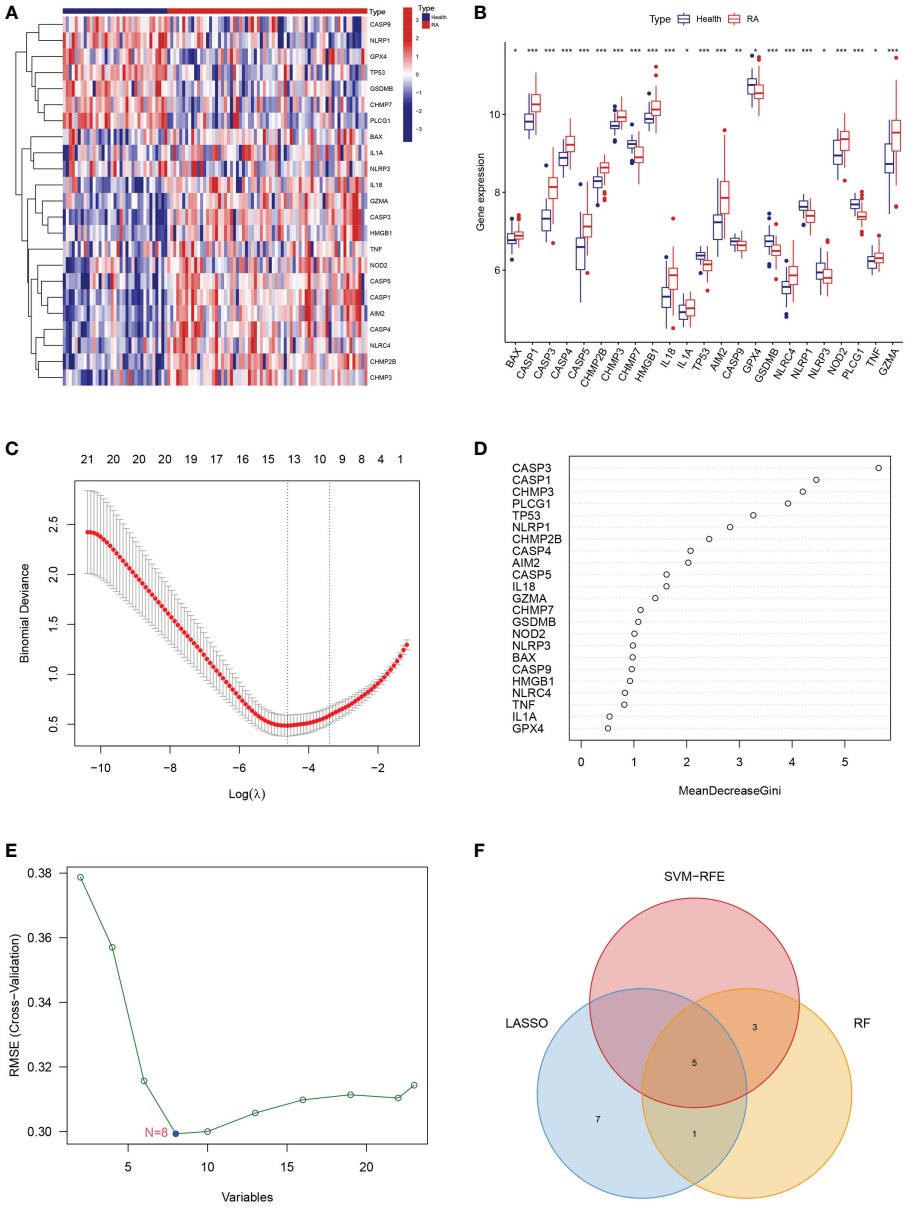

FIGURE 1
Landscape of the 23 PRGs. **(A)** Expression heatmap of the 23 PRGs in healthy control and RA patients. **(B)** Expression histogram of the 23 PRGs in healthy control and RA patients. **(C)** The PRGs screened using the LASSO logistic regression algorithm. **(D)** The hub genes identified *via* the RF algorithm. **(E)** The PRGs recognized using SVM-RFE algorithm. **(F)** Venn diagram showing the intersection among PRGs genes between the three algorithms. * means P < 0.05, ** means P < 0.01, *** means P < 0.001.

with double stranded RNA binding (GO:0003725) and pattern recognition receptor activity (GO:0038187) (Figure 4A; Supplementary Table 3). The results of KEGG enrichment analysis revealed that DEGs were significantly enriched in the NOD-like receptor signaling pathway and the NF-kappa B signaling pathway (Figure 4B; Supplementary Table 4).

3.6 Identification of two distinct gene patterns

To further verify the pyroptosis patterns, we classified the RA patients into different genetic subtypes and termed as gene cluster A and B based on the 56 DEGs by using the consensus clustering method (Figure 5A; Supplementary Figure 2). There were 37 cases in gene cluster A and 30 in gene cluster B. As shown in Figure 5B, the heatmap displayed the expression levels of the 56 DEGs in gene clusters A and B. In addition, we found that the differential expression levels of the 5 significant PRGs and immune cell infiltration between gene cluster A and B were consistent with those in the pyroptosis patterns (Figures 5C, D). The result again demonstrated the accuracy of dividing into distinct subtypes. Furthermore, we also compared the pyroptosis score between the two distinct pyroptosis patterns or DEGs patterns. The result revealed that the pyroptosis score in cluster B or gene cluster B

10.3389/fendo.2023.1144250

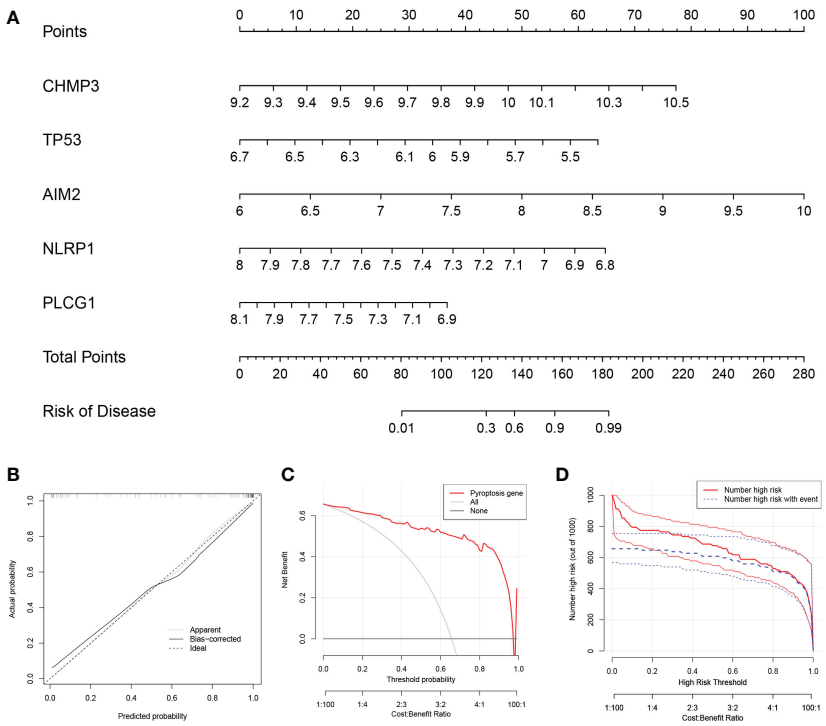

FIGURE 2
Construction of the nomogram model. **(A)** Construction of the nomogram model based on the 5 PRGs. **(B)** Predictive robustness of the nomogram model as revealed by the calibration curve. **(C)** Decisions based on the nomogram model may benefit RA patients. **(D)** Clinical impact of the nomogram model as assessed by the clinical impact curve.

was significantly higher than that in cluster A, or gene cluster A (Figure 6A). The relationship between pyroptosis patterns, pyroptosis gene patterns, and pyroptosis scores was visualized in a Sankey diagram (Figure 6B).

3.7 Identification of two distinct gene patterns

To further reveal the relationship between pyroptosis patterns and RA, we investigated the correlation between pyroptosis patterns and STAT1, CCR5, NLRP1, IL-15, and CXCL10. The results showed that the expression levels of STAT1, CCR5, NLRP1, IL-15, and CXCL10 were higher in pyroptosis gene cluster B or gene cluster B than in pyroptosis gene cluster A or gene cluster A, which suggested that pyroptosis gene cluster B or gene cluster B is highly linked to RA characterized by the immune response Figure 6C.

4 Discussion

RA is a chronic inflammatory disease characterized by persistent inflammatory synovitis and systemic inflammation. RA has attracted wide world attention in recent years due to its high disability rate (32). Currently, treatment strategies with biologics and disease-modifying anti-rheumatic drugs have led to significant improvement in the prognosis of RA patients, while a large proportion of RA patients still do not experience effective clinical relief. Studies showed that early diagnosis and positive treatment significantly improve the clinical prognosis of RA (33). Thus, there is an urgent need to identify RA-related diagnostic genes, further explore the molecular mechanisms of RA, and provide novel therapeutic strategies for the prevention and treatment of RA. Pyroptosis is a novel form of inflammatory programmed cell death that plays a vital role in the development of RA (34). Pyroptosis further exacerbates RA inflammation by releasing inflammatory cytokines like interleukin (IL)-1β and IL-18 (35). Besides, studies demonstrated that the serum concentrations of IL-1β (36) and IL-18 (37) were significantly higher in RA patients compared to healthy controls. In order to gain new knowledge for the diagnosis and management of RA, we further studied the connection between RA and pyroptosis by locating and screening PRGs in the serum of RA patients.

In this work, we used 51 PRGs to detect differential expression PRGs using differential expression analysis. We chose 5 candidate PRGs (CHMP3, TP53, AIM2, NLRP1, and PLCG1) from differential expression PRGs by applying RF, SVM-RFE, and LASSO methods in order to filter the 51 PRGs that were the most pertinent for RA. Then, we constructed a nomogram model based on the 5 PRGs to predict the occurrence of RA. In addition, we distinguished two different pyroptosis regulation patterns based on the 5 PRGs and explored the correlation between infiltrating immune cells and the 5 PRGs. A total of 56 DEGs were screened between the two pyroptosis patterns. We further investigated the GO and KEGG functional enrichment of 56 DEGs. Furthermore, we used the consensus clustering method to validate the pyroptosis

10.3389/fendo.2023.1144250

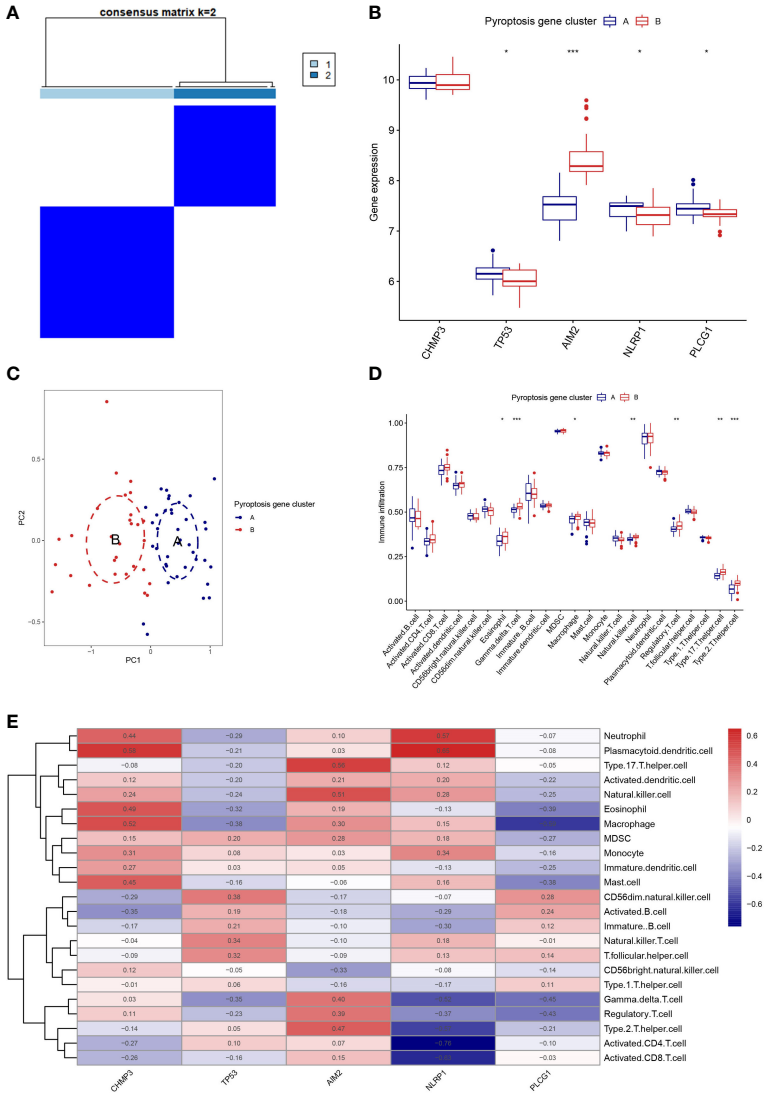

FIGURE 3
Consensus clustering of the 5 PRGs. **(A)** Consensus matrices of the 5 PRGs for k = 2. **(B)** Differential expression histogram of the 5 PRGs in gene cluster A and B. **(C)** PCA for the expression profiles of the 5 PRGs. **(D)** Differential immune cell infiltration between gene cluster A and B. **(E)** Correlation between infiltrating immune cells and the 5 PRGs. * means P < 0.05, ** means P < 0.01, *** means P < 0.001.

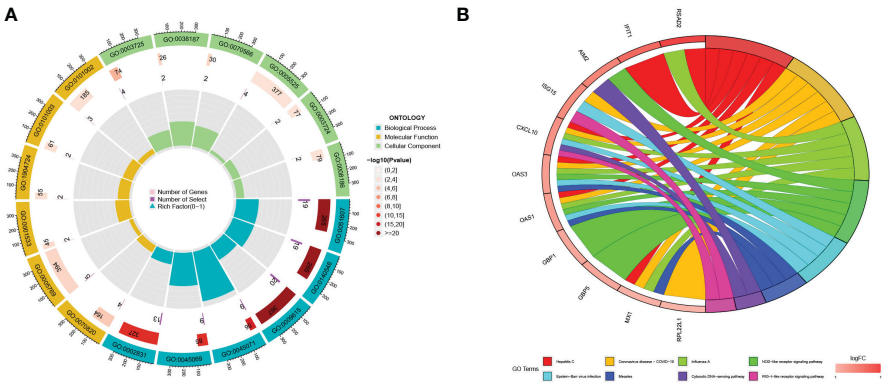

FIGURE 4
The functional enrichment analyses of DEGs. **(A)** The GO analyses results for DEGs; **(B)** The KEGG analysis results for DEGs.

10.3389/fendo.2023.1144250

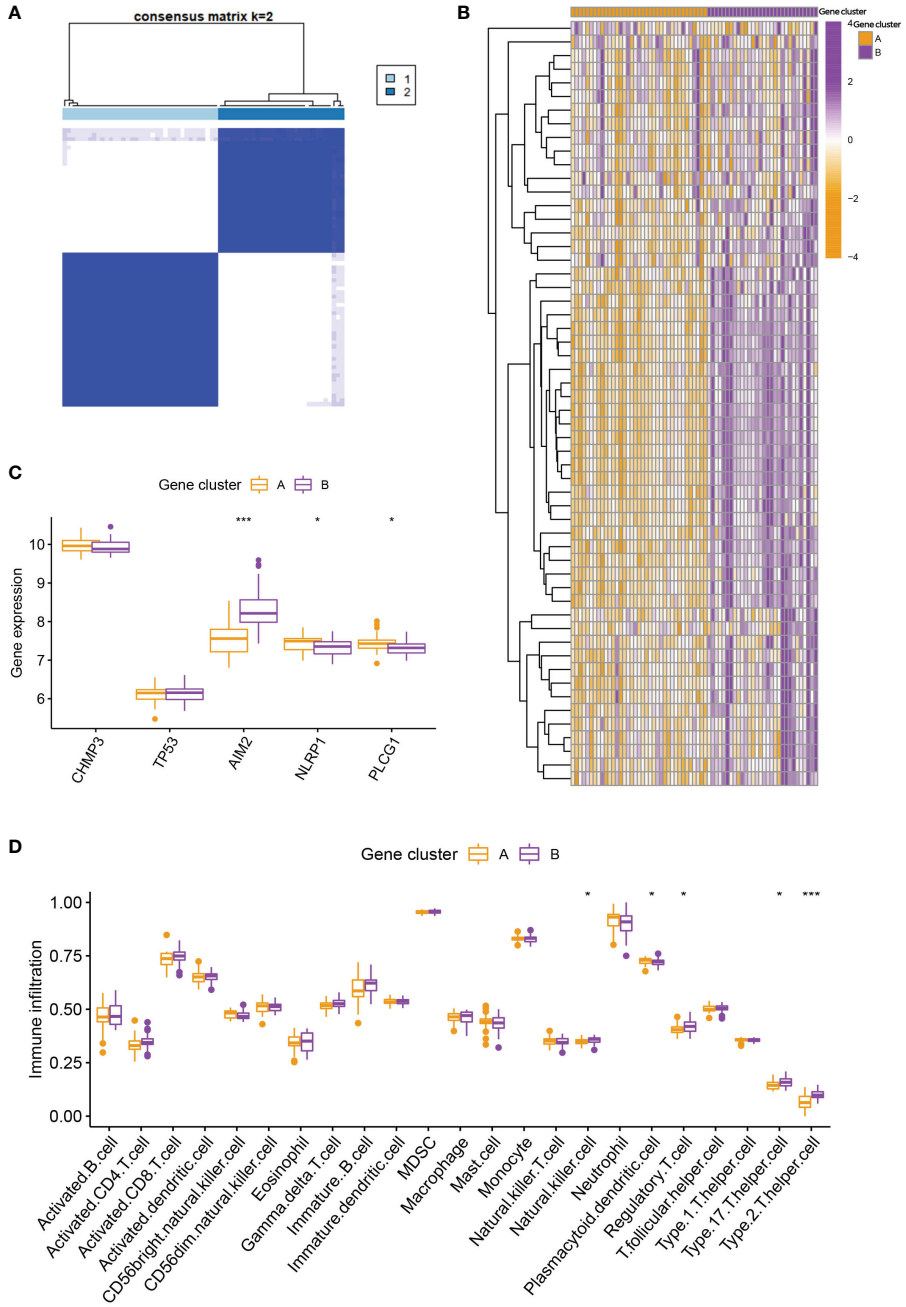

FIGURE 5
Consensus clustering of the DEGs. **(A)** Consensus matrices of the 56 DEGs for k = 2. **(B)** Expression heatmap of the 56 DEGs in gene cluster A and B. **(C)** Differential expression histogram of the 5 PRGs in gene cluster A and B. **(D)** Differential immune cell infiltration between gene cluster A and B. * means $P < 0.05$, *** means $P < 0.001$.

patterns based on 56 DEGs. We found that two distinct pyroptosis gene patterns were consistent with the grouping of pyroptosis patterns. During the progression of RA, cytokines have been involved in immune regulation, immune response, and inflammatory response (38). We also explore the relationship between inflammatory cytokines and the patterns of pyroptosis.

NOD-like receptor thermal protein domain associated protein 1 (NLRP1) is a member of the NLR family. NLRP1 has been found to be closely associated with the pathogenesis of RA (39). Activated NLRP1 promoted the release of inflammatory cytokines, such as IL-1β and IL-18 (40). Besides, a study showed that inhibition of NLRP1 activation effectively ameliorated joint inflammation and destruction in collagen-induced arthritis mice (41). Furthermore, the polymorphism of the NLRP1 gene was associated with the incidence of RA in the Han Chinese population (42). A member of the interferon-inducible HIN-200 protein family is absent in melanoma 2 (AIM2). AIM2 has emerged as a hub for research into the pyroptosis-specific pathophysiology of RA. AIM2 has been linked to the emergence of inflammatory illnesses and autoimmune arthritis, according to a research (43). AIM2 could format a

10.3389/fendo.2023.1144250

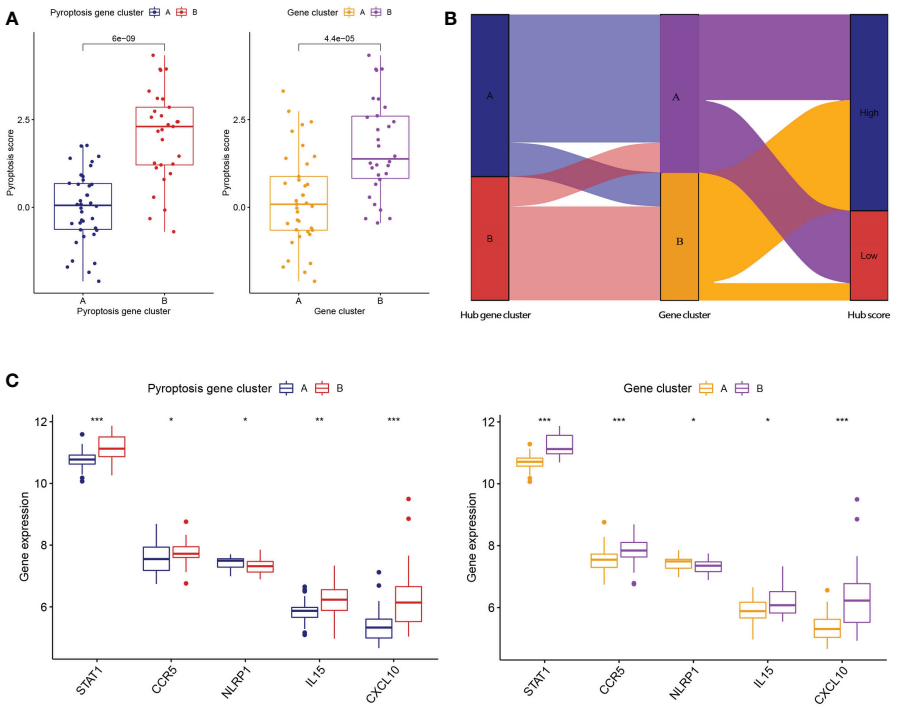

FIGURE 6
Role of pyroptosis patterns in distinguishing RA. **(A)** Differences in pyroptosis score between pyroptosis gene cluster A and B and differences in pyroptosis score between gene cluster A and B. **(B)** Sankey diagram showing the relationship between pyroptosis patterns, pyroptosis gene patterns, and pyroptosis scores. **(C)** Differential expression levels of STAT1, CCR5, NLRP1, IL-15, and CXCL10 between pyroptosis gene cluster A and B. **(C)** Differential expression levels of STAT1, CCR5, NLRP1, IL-15, and CXCL10 between gene cluster A and B. * means $P < 0.05$, ** means $P < 0.01$, *** means $P < 0.001$.

caspase-1-activating inflammasome, thereby controlling the proteolytic maturation of pro-inflammatory cytokines IL-1β and IL-18 (44). In addition, a meta-analysis revealed that AIM2 levels were highly expressed in peripheral blood mononuclear cells from RA patients (45). Recent study showed that the expression of AIM2 was higher in the RA synovium than in the OA. AIM2 siRNA could inhibit the proliferation of RA fibroblast-like synoviocytes (46).

PLCG1, also called phospholipase C, gamma 1, is involved in the receptor tyrosine kinase-(RTK-)-mediated signal transduction pathway (47). A study found that PRGPI might serve as a prognostic biomarker for pancreatic cancer patients (48). Besides, numerous studies have proven the involvement of PLCG1-mediated inflammatory response in the pathogenesis of osteoarthritis and lung cancer (49, 50). Charged multivesicular body protein 3 (CHMP3) is a subunit of ESCRT III involved in membrane remodeling (51). High CHMP3 expression in breast cancer patients predicts better survival outcomes (52). Moreover, immunohistochemistry revealed significant high expression of CHMP3 in tumor liver tissue (53). The P53 tumor suppressor gene (TP53), also known as the p53 gene, is a protein encoding a molecular weight of 53 kDa. TP53 was found to regulate important cellular functions, such as apoptosis, cell cycle regulation, DNA repair, and apoptosis (54). Besides, TP53 is an inflammatory suppressor associated with autoimmune diseases. Many studies have indicated that the TP53 mutation is closely related to the pathological changes of RA (55, 56). TP53 mutation was identified in synovium of RA patients (57). In the collagen-induced arthritis model, $p53^{-/-}$ mice showed increased severity of arthritis (58).

However, there are some limits to the study. Firstly, the lack of experimental verification of bioinformatics analysis results. We need to collect human serum samples to further validate our analysis results and elucidate their value as potential clinical biomarkers. Besides, due to the small number of available RA datasets in the GEO database and the limited sample size of this study, the analysis results may be biased. We will include more samples to further assess the reliability of the predicted signature genes.

5 Conclusion

In conclusion, our study first found PLCG1 and CHMP3 may be involved in the pathogenesis of RA. And pyroptosis pattern is involved in the progress of RA by bioinformatics analysis, which provides a novel prospective for the prevention and diagnosis of RA.

Data availability statement

The datasets presented in this study can be found in online repositories. The names of the repository/repositories and accession number(s) can be found in the article/Supplementary Material.

Author contributions

JZ, JGuo, and HZ contributed to the study design and critical revision of the manuscript. JL carried out the study and drafted the manuscript. JL, YC, XJ, DH, XC, HR, and JGuo analyzed the data. All authors read and approved the final manuscript.

Funding

This study was supported by grants from the Zhejiang Medical and Health Science and Technology Plan Project (2022504276), the Traditional Chinese Medicine of Zhejiang Province Science and Technology plan project (2023ZL128), and Health Science and Technology Program of Hangzhou (A20210086).

Conflict of interest

The authors declare that the research was conducted in the absence of any commercial or financial relationships that could be construed as a potential conflict of interest.

Publisher's note

All claims expressed in this article are solely those of the authors and do not necessarily represent those of their affiliated organizations, or those of the publisher, the editors and the reviewers. Any product that may be evaluated in this article, or claim that may be made by its manufacturer, is not guaranteed or endorsed by the publisher.

Supplementary material

The Supplementary Material for this article can be found online at: https://www.frontiersin.org/articles/10.3389/fendo.2023.1144250/full#supplementary-material

SUPPLEMENTARY FIGURE 1
Consensus clustering of the 5 PRGs in RA. (A-G) Consensus matrices of the 5 PRGs for k = 3–9.

SUPPLEMENTARY FIGURE 2
Consensus clustering of the 56 DEGs in RA. (A-G) Consensus matrices of the 56 DEGs for k = 3–9.

SUPPLEMENTARY TABLE 1
The list of 52 PRGs.

SUPPLEMENTARY TABLE 2
The details of PRG screened by the LASSO, RF, and SVM-RFE algorithms.

SUPPLEMENTARY TABLE 3
The details of GO analysis.

SUPPLEMENTARY TABLE 4
The details of KEGG analysis.

References

1. Ferreira-Silva M, Faria-Silva C, Viana BP, Fernandes E, Ramos FA, Corvo ML. Liposomal nanosystems in rheumatoid arthritis. *Pharmaceutics* (2021) 13(4):454. doi: 10.3390/pharmaceutics13040454

2. Firestein GS, McInnes IB. Immunopathogenesis of rheumatoid arthritis. *Immunity* (2017) 46:183–96. doi: 10.1016/j.immuni.2017.02.006

3. Ishikawa Y, Terao C. The impact of cigarette smoking on risk of rheumatoid arthritis: A narrative review. *Cells-basel* (2020) 9(2):475. doi: 10.3390/cells9020475

4. Aletaha D, Smolen JS. Diagnosis and management of rheumatoid arthritis: A review. *JAMA* (2018) 320:1360–72. doi: 10.1001/jama.2018.13103

5. Shi J, Gao W, Shao F. Pyroptosis: Gasdermin-mediated programmed necrotic cell death. *Trends Biochem Sci* (2017) 42(4):245–54. doi: 10.1016/j.tibs.2016.10.004

6. Tsuchiya K. Inflammasome-associated cell death: Pyroptosis, apoptosis, and physiological implications. *Microbiol Immunol* (2020) 64:252–69. doi: 10.1111/1348-0421.12771

7. Liang F, Zhang F, Zhang L, Wei W. The advances in pyroptosis initiated by inflammasome in inflammatory and immune diseases. *Inflammation Res* (2020) 69:159–66. doi: 10.1007/s00011-020-01315-3

8. Vande Walle L, Van Opdenbosch N, Jacques P, Fossoul A, Verheugen E, Vogel P, et al. Negative regulation of the NLRP3 inflammasome by A20 protects against arthritis. *Nature* (2014) 512:69–73. doi: 10.1038/nature13322

9. Tan G, Huang C, Chen J, Chen B, Zhi F. Gasdermin-e-mediated pyroptosis participates in the pathogenesis of crohn's disease by promoting intestinal inflammation. *Cell Rep* (2021) 35:109265. doi: 10.1016/j.celrep.2021.109265

10. Zhuang J, Cui H, Zhuang L, Zhai Z, Yang F, Luo G, et al. Bronchial epithelial pyroptosis promotes airway inflammation in a murine model of toluene diisocyanate-induced asthma. *Biomed pharmacother = Biomed pharmacother* (2020) 125:109925. doi: 10.1016/j.biopha.2020.109925

11. Tasaki S, Suzuki K, Kassai Y, Takeshita M, Murota A, Kondo Y, et al. Multi-omics monitoring of drug response in rheumatoid arthritis in pursuit of molecular remission. *Nat Commun* (2018) 9:2755. doi: 10.1038/s41467-018-05044-4

12. Gautier L, Cope L, Bolstad BM, Irizarry RA. Affy–analysis of affymetrix GeneChip data at the probe level. *Bioinformatics* (2004) 20:307–15. doi: 10.1093/bioinformatics/btg405

13. Xing Z, Liu Z, Fu X, Zhou S, Liu L, Dang Q, et al. Clinical significance and immune landscape of a pyroptosis-derived LncRNA signature for glioblastoma. *Front Cell Dev Biol* (2022) 10:805291. doi: 10.3389/fcell.2022.805291

14. Zeng R, Huang S, Qiu X, Zhuo Z, Wu H, Jiang L, et al. Predicting the prognosis of esophageal adenocarcinoma by a pyroptosis-related gene signature. *Front Pharmacol* (2021) 12:767187. doi: 10.3389/fphar.2021.767187

15. Ding J, He X, Luo W, Zhou W, Chen R, Cao G, et al. Development and validation of a pyroptosis-related signature for predicting prognosis in hepatocellular carcinoma. *Front Genet* (2022) 13:801419. doi: 10.3389/fgene.2022.801419

16. Tibshirani R. Least squares support vector machine classifiers. *J R Stat Society Ser B (Methodological)* (1996) 58:267–88. doi: 10.1111/j.2517-6161.1996.tb02080.x

17. Suykens JAK VJ. Regression shrinkage and selection via the lasso. *Neural Process Lett* (1999) 9:293–300. doi: 10.1023/A:1018628609742

18. Strobl C, Boulesteix AL, Zeileis A, Hothorn T. Bias in random forest variable importance measures: illustrations, sources and a solution. *BMC Bioinf* (2007) 8:25. doi: 10.1186/1471-2105-8-25

19. Huang ML, Hung YH, Lee WM, Li RK, Jiang BR. SVM-RFE based feature selection and taguchi parameters optimization for multiclass SVM classifier. *ScientificWorldJournal* (2014) 2014:795624. doi: 10.1155/2014/795624

20. Friedman J, Hastie T, Tibshirani R. Regularization paths for generalized linear models *via* coordinate descent. *J Stat Softw* (2010) 33:1–22.

21. Cutler A, Stevens JR. Random forests for microarrays. *Methods Enzymol* (2006) 411:422–32. doi: 10.1016/S0076-6879(06)11023-X

22. Iasonos A, Schrag D, Raj GV, Panageas KS. How to build and interpret a nomogram for cancer prognosis. *J Clin Oncol* (2008) 26:1364–70. doi: 10.1200/JCO.2007.12.9791

23. Vickers AJ, Elkin EB. Decision curve analysis: a novel method for evaluating prediction models. *Med Decis Making* (2006) 26:565–74. doi: 10.1177/0272989X06295361

24. Tanzhu G, Li N, Li Z, Zhou R, Shen L. Molecular subtypes and prognostic signature of pyroptosis-related lncRNAs in glioma patients. *Front Oncol* (2022) 12:779168. doi: 10.3389/fonc.2022.779168

25. Wilkerson MD, Hayes DN. ConsensusClusterPlus: a class discovery tool with confidence assessments and item tracking. *Bioinformatics* (2010) 26:1572–3. doi: 10.1093/bioinformatics/btq170

26. Meng J, Huang X, Qiu Y, Zheng X, Huang J, Wen Z, et al. Pyroptosis-related gene mediated modification patterns and immune cell infiltration landscapes in cutaneous melanoma to aid immunotherapy. *Aging (Albany NY)* (2021) 13:24379–401. doi: 10.18632/aging.203687

27. Wu J, Zhu Y, Luo M, Li L. Comprehensive analysis of pyroptosis-related genes and tumor microenvironment infiltration characterization in breast cancer. *Front Immunol* (2021) 12:748221. doi: 10.3389/fimmu.2021.748221

28. Hänzelmann S, Castelo R, Guinney J. GSVA: gene set variation analysis for microarray and RNA-seq data. *BMC Bioinf* (2013) 14:7. doi: 10.1186/1471-2105-14-7

29. Charoentong P, Finotello F, Angelova M, Mayer C, Efremova M, Rieder D, et al. Pan-cancer immunogenomic analyses reveal genotype-immunophenotype relationships and predictors of response to checkpoint blockade. *Cell Rep* (2017) 18:248–62. doi: 10.1016/j.celrep.2016.12.019

30. Yu G, Wang L, Han Y, He Q. clusterProfiler: an r package for comparing biological themes among gene clusters. *OMICS: A J Integr Biol* (2012) 16:284–7. doi: 10.1089/omi.2011.0118

31. Huang DW, Sherman BT, Lempicki RA. Bioinformatics enrichment tools: paths toward the comprehensive functional analysis of large gene lists. *Nucleic Acids Res* (2009) 37:1–13. doi: 10.1093/nar/gkn923

32. Bai L, Zhang Y, Wang P, Zhu X, Xiong JW, Cui L. Improved diagnosis of rheumatoid arthritis using an artificial neural network. *Sci Rep* (2022) 12:9810. doi: 10.1038/s41598-022-13750-9

33. Wu H, Wu H, He Y, Gan Z, Xu Z, Zhou M, et al. Synovitis in mice with inflammatory arthritis monitored with quantitative analysis of dynamic contrast-enhanced NIR fluorescence imaging using iRGD-targeted liposomes as fluorescence probes. *Int J Nanomed* (2018) 13:1841–50. doi: 10.2147/IJN.S155475

34. Kong R, Sun L, Li H, Wang D. The role of NLRP3 inflammasome in the pathogenesis of rheumatic disease. *Autoimmunity* (2022) 55:1–7. doi: 10.1080/08916934.2021.1995860

35. Zhao J, Jiang P, Guo S, Schrodi SJ, He D. Apoptosis, autophagy, NETosis, necroptosis, and pyroptosis mediated programmed cell death as targets for innovative therapy in rheumatoid arthritis. *Front Immunol* (2021) 12:809806. doi: 10.3389/fimmu.2021.809806

36. Verma I, Syngle A, Krishan P. Predictors of endothelial dysfunction and atherosclerosis in rheumatoid arthritis in Indian population. *Indian Heart J* (2017) 69:200–6. doi: 10.1016/j.ihj.2016.10.013

37. Min HK, Kim S, Lee JY, Kim KW, Lee SH, Kim HR. IL-18 binding protein suppresses IL-17-induced osteoclastogenesis and rectifies type 17 helper T cell/regulatory T cell imbalance in rheumatoid arthritis. *J Transl Med* (2021) 19:392. doi: 10.1186/s12967-021-03071-2

38. Guo Q, Mao X, Zhang Y, Meng S, Xi Y, Ding Y, et al. Guizhi-Shaoyao-Zhimu decoction attenuates rheumatoid arthritis partially by reversing inflammation-immune system imbalance. *J Transl Med* (2016) 14:165. doi: 10.1186/s12967-016-0921-x

39. Evavold CL, Kagan JC. How inflammasomes inform adaptive immunity. *J Mol Biol* (2018) 430:217–37. doi: 10.1016/j.jmb.2017.09.019

40. Addobbati C, Da Cruz H, Adelino JE, Melo Tavares Ramos AL, Fragoso TS, Domingues A, et al. Polymorphisms and expression of inflammasome genes are associated with the development and severity of rheumatoid arthritis in Brazilian patients. *Inflammation res: Off J Eur Histamine Res Soc* (2018) 67:255–64. doi: 10.1007/s00011-017-1119-2

41. Li F, Guo N, Ma Y, Ning B, Wang Y, Kou L. Inhibition of P2X4 suppresses joint inflammation and damage in collagen-induced arthritis. *Inflammation* (2014) 37:146–53. doi: 10.1007/s10753-013-9723-y

42. Sui J, Li H, Fang Y, Liu Y, Li M, Zhong B, et al. NLRP1 gene polymorphism influences gene transcription and is a risk factor for rheumatoid arthritis in han chinese. *Arthritis Rheum* (2012) 64:647–54. doi: 10.1002/art.33370

43. Man SM, Karki R, Kanneganti TD. AIM2 inflammasome in infection, cancer, and autoimmunity: Role in DNA sensing, inflammation, and innate immunity. *Eur J Immunol* (2016) 46:269–80. doi: 10.1002/eji.201545839

44. Baum R, Sharma S, Carpenter S, Li QZ, Busto P, Fitzgerald KA, et al. Cutting edge: AIM2 and endosomal TLRs differentially regulate arthritis and autoantibody production in DNase II-deficient mice. *J Immunol* (2015) 194:873–7. doi: 10.4049/jimmunol.1402573

45. Afroz S, Giddaluru J, Vishwakarma S, Naz S, Khan AA, Khan N. A comprehensive gene expression meta-analysis identifies novel immune signatures in rheumatoid arthritis patients. *Front Immunol* (2017) 8:74. doi: 10.3389/fimmu.2017.00074

46. Chen Y, Fujuan Q, Chen E, Yu B, Zuo F, Yuan Y, et al. Expression of AIM2 in rheumatoid arthritis and its role on fibroblast-like synoviocytes. *Mediat Inflamm* (2020) 2020:1693730. doi: 10.1155/2020/1693730

47. Zhang G, Yan Z. A new definition of pyroptosis-related gene markers to predict the prognosis of lung adenocarcinoma. *BioMed Res Int* (2021) 2021:8175003. doi: 10.1155/2021/8175003

48. Xie W, Li X, Yang C, Li J, Shen G, Chen H, et al. The pyroptosis-related gene prognostic index associated with tumor immune infiltration for pancreatic cancer. *Int J Mol Sci* (2022) 23(11):6178. doi: 10.3390/ijms23116178

49. Kim MS, Yang YM, Son A, Tian YS, Lee SI, Kang SW, et al. RANKL-mediated reactive oxygen species pathway that induces long lasting Ca2+ oscillations essential for osteoclastogenesis. *J Biol Chem* (2010) 285:6913–21. doi: 10.1074/jbc.M109.051557

50. Song W, Kim LC, Han W, Hou Y, Edwards DN, Wang S, et al. Phosphorylation of PLCgamma1 by EphA2 receptor tyrosine kinase promotes tumor growth in lung cancer. *Mol Cancer Res* (2020) 18:1735–43. doi: 10.1158/1541-7786.MCR-20-0075

51. Di Giaimo R, Penna E, Pizzella A, Cirillo R, Perrone-Capano C, Crispino M. Cross talk at the cytoskeleton-plasma membrane interface: Impact on neuronal morphology and functions. *Int J Mol Sci* (2020) 21(23):9133. doi: 10.3390/ijms21239133

52. Wang Z, Wang X. miR-122-5p promotes aggression and epithelial-mesenchymal transition in triple-negative breast cancer by suppressing charged multivesicular body protein 3 through mitogen-activated protein kinase signaling. *J Cell Physiol* (2020) 235:2825–35. doi: 10.1002/jcp.29188

53. Guo Y, Shang A, Wang S, Wang M. Multidimensional analysis of CHMP family members in hepatocellular carcinoma. *Int J Gen Med* (2022) 15:2877–94. doi: 10.2147/IJGM.S350228

54. Wang H, Wang X, Xu L, Zhang J. TP53 and TP53-associated genes are correlated with the prognosis of paediatric neuroblastoma. *BMC Genom Data* (2022) 23:41. doi: 10.1186/s12863-022-01059-5

55. Gansmo LB, Lie BA, Maehlen MT, Vatten L, Romundstad P, Hveem K, et al. Polymorphisms in the TP53-MDM2-MDM4-axis in patients with rheumatoid arthritis. *Gene* (2021) 793:145747. doi: 10.1016/j.gene.2021.145747

56. Kato S, Lippman SM, Flaherty KT, Kurzrock R. The conundrum of genetic "Drivers" in benign conditions. *J Natl Cancer Institute* (2016) 108(8):djw036. doi: 10.1093/jnci/djw036

57. Bolivar AM, Luthra R, Mehrotra M, Chen W, Barkoh BA, Hu P, et al. Targeted next-generation sequencing of endometrial cancer and matched circulating tumor DNA: identification of plasma-based, tumor-associated mutations in early stage patients. *Mod Pathol* (2019) 32:405–14. doi: 10.1038/s41379-018-0158-8

58. Yamanishi Y, Boyle DL, Pinkoski MJ, Mahboubi A, Lin T, Han Z, et al. Regulation of joint destruction and inflammation by p53 in collagen-induced arthritis. *Am J Pathol* (2002) 160:123–30. doi: 10.1016/S0002-9440(10)64356-8

frontiers | Frontiers in Endocrinology

TYPE Original Research
PUBLISHED 16 March 2023
DOI 10.3389/fendo.2023.1144258

OPEN ACCESS

EDITED BY
Ruiqin Han,
Chinese Academy of Medical Sciences, China

REVIEWED BY
Wenjian Hu,
Southwest Medical University, China
Wenyi Jin,
City University of Hong Kong, Hong Kong SAR, China
Junlin Shen,
China Medical University, China

*CORRESPONDENCE
Zhijiang Jin
408625796@qq.com
Zhongning Guan
18072720218@163.com
Feng Zhou
zf15158857895@163.com

†These authors have contributed equally to this work

SPECIALTY SECTION
This article was submitted to Cancer Endocrinology, a section of the journal Frontiers in Endocrinology

RECEIVED 14 January 2023
ACCEPTED 28 February 2023
PUBLISHED 16 March 2023

CITATION
Pan L, Yang F, Cao X, Zhao H, Li J, Zhang J, Guo J, Jin Z, Guan Z and Zhou F (2023) Identification of five hub immune genes and characterization of two immune subtypes of osteoarthritis. *Front. Endocrinol.* 14:1144258. doi: 10.3389/fendo.2023.1144258

Identification of five hub immune genes and characterization of two immune subtypes of osteoarthritis

Lifeng Pan[1†], Feng Yang[2†], Xianhua Cao[1], Hongchang Zhao[1], Jian Li[1], Jinxi Zhang[1], Jiandong Guo[1], Zhijiang Jin[1*], Zhongning Guan[1*] and Feng Zhou[1*]

[1]Department of Orthopaedics, Hangzhou Ninth People's Hospital, Hangzhou, Zhejiang, China, [2]Community Health Service Center, Hangzhou, Zhejiang, China

Background: Osteoarthritis (OA) is one of the most prevalent chronic diseases, leading to degeneration of joints, chronic pain, and disability in the elderly. Little is known about the role of immune-related genes (IRGs) and immune cells in OA.

Method: Hub IRGs of OA were identified by differential expression analysis and filtered by three machine learning strategies, including random forest (RF), least absolute shrinkage and selection operator (LASSO), and support vector machine (SVM). A diagnostic nomogram model was then constructed by using these hub IRGs, with receiver operating characteristic (ROC) curve, decision curve analysis (DCA), and clinical impact curve analysis (CICA) estimating its performance and clinical impact. Hierarchical clustering analysis was then conducted by setting the hub IRGs as input information. Differences in immune cell infiltration and activities of immune pathways were revealed between different immune subtypes.

Result: Five hub IRGs of OA were identified, including TNFSF11, SCD1, PGF, EDNRB, and IL1R1. Of them, TNFSF11 and SCD1 contributed the most to the diagnostic nomogram model with area under the curve (AUC) values of 0.904 and 0.864, respectively. Two immune subtypes were characterized. The immune over-activated subtype showed excessively activated cellular immunity with a higher proportion of activated B cells and activated CD8 T cells. The two phenotypes were also seen in two validation cohorts.

Conclusion: The present study comprehensively investigated the role of immune genes and immune cells in OA. Five hub IRGs and two immune subtypes were identified. These findings will provide novel insights into the diagnosis and treatment of OA.

KEYWORDS

osteoarthritis, immune microenvironment, diagnostic model, nomogram, machine learning

1 Introduction

Osteoarthritis (OA) is one of the most prevalent chronic diseases worldwide, leading to degeneration of joints, chronic pain, and disability in the elderly (1). Novel insights suggested that OA is a syndrome of joint destruction caused by different risk factors, and each of the factors could promote OA by instigating different mechanistic pathways (2). Typical processes involved in OA development contain mechanical (3), inflammatory (4), metabolic (5), and senescent (6) signaling pathways. Interestingly, synovitis is found in the majority of patients with OA. Moreover, the infiltration of T cells and activated macrophages in synovial tissue has a strong correlation with bone erosion and pain in OA patients (7). Little is known, however, about the osteo-immune microenvironment (OIME) of OA, and the role of immune-related genes has hardly been studied in this disease.

Hereby, we investigated the role of immune-related genes (IRGs) in OA from the aspects of OIME, disease classification, and diagnostic value. First, hub IRGs were identified by differential expression analysis and three strategies of feature selection, including random forest (RF), least absolute shrinkage and selection operator (LASSO), and support vector machine (SVM). Then, these hub IRGs were used to construct a diagnostic nomogram model with receiver operating characteristic (ROC) curve, decision curve analysis (DCA), and clinical impact curve analysis (CICA) estimating its diagnostic performance and clinical impact for OA. These hub IRGs were then subjected to hierarchical clustering analysis, and two immune subtypes of OA were characterized. The immune over-activated subtype showed a higher proportion of activated B-cell and activated CD8 T-cell infiltration, underlying an OIME with excessively activated cellular immunity for this group. Finally, two external cohorts of OA were utilized to validate the existence of the two immune subtypes of OA.

In all, the present study conducted a comprehensive analysis of the role of immune genes and immune cells in OA. An immune over-activated subtype of OA was identified, and a nomogram model was built for clinical practice. It was found that regulatory T-cell infiltration was positively correlated with TNFSF11 and IL1R1 and negatively correlated with EDNRB. These findings provided novel insights to understand the role of the osteo-immune microenvironment in the development of OA.

2 Materials and methods

2.1 Data collection and processing

The microarray datasets were downloaded from the Gene Expression Omnibus (GEO) database (https://www.ncbi.nlm.nih.gov/geo/) using "Osteoarthritis", "Tissue", and "Homo sapiens" as keywords. The microarray datasets GSE55235 and GSE55457 (doi: 10.1186/ar4526) and GSE82107 (doi: 10.1371/journal.pone.0167076) contained 27 healthy controls and 30 OA patients. A dataset of identified IRGs was acquired from the ImmPort database (http://www.immport.org).

We then performed log2 transformed for gene expression profiling and matched the probes to their gene symbols according to the annotation document of corresponding platforms. Finally, the gene matrix with row names as sample names and column names as gene symbols were obtained for subsequent analyses.

2.2 Identification of differentially expressed immune-related genes

These three datasets were merged and normalized by the "limma" package8 of R software (doi: 10.1093/nar/gkv007). The batch effect amid different arrays was eliminated by using the ComBat function of R (version 4.1.3) package sva9. We extracted the expression profiles of immune-related genes from this merged dataset. Then, we identified differentially expressed IRGs in OA and normal samples by the "limma" package. p-value <0.05 was considered a significant difference. Heatmap was generated using the R package "pheatmap" to visualize the differentially expressed IRGs.

2.3 Functional and pathway enrichment analyses

To investigate the functional and molecular pathways of differentially expressed IRGs, we performed Gene Ontology (GO) (8), Kyoto Encyclopedia of Genes and Genomes (KEGG) (9), and gene set enrichment analysis (GSEA) (10) enrichment analyses by the "colorspace", "stringi", and "ggplot2" packages in R (doi: 10.7717/peerj.11534). $p < 0.05$ was considered statistically significant.

2.4 Screening of OA-related biomarker characteristic genes

The protein–protein interaction (PPI) network was constructed to predict protein–protein interactions of differentially expressed IRGs using the Search Tool for the Retrieval of Interacting Genes database (STRING, http://www.stringdb.org). The gene with an interaction score >0.9 was retained, and Cytoscape software v3.6.0 is used to visualize the PPI network. Based on these IRGs, three feature selection algorithms including SVM–recursive feature elimination (SVM-RFE), LASSO logistic regression, and RF were adapted to screen OA-related biomarkers. The SVM-RFE algorithm was performed by R packages "e1071" and "caret" with fivefold cross-validation. The LASSO logistic regression was employed with the R package "glmnet" (11). The RF algorithm was analyzed by the "randomForest" package in R (https://CRAN.R-project.org/package=beeswarm). Then, the "venn" R package (12) (version 1.7) was used to select overlapping genes from the three algorithms as signature genes for further analysis.

2.5 Construction of a nomogram model

The ROC and area under the curve (AUC) were also calculated to evaluate the predictive effectiveness of the algorithm. We

constructed a nomogram model based on OA-related signature genes to predict the occurrence of OA patients with the "rms" package in R. The calibration curve was used to assess the predictive performance of the nomogram model. Then, we further performed DCA and CICA to estimate the clinical utility of the nomogram model.

2.6 Consensus clustering

Consensus clustering is an algorithm for identifying the cluster of each member and their number in datasets. We utilized the consensus clustering method to distinguish distinct immune-related clinical subtypes of OA and identify different IRG patterns based on the significant differentially expressed IRGs with the R package "ConsensusClusterPlus" (13). In the correlation between significant OA-related IRG expression and clinical features in subtypes of OA patients. "Points" represents the score of the corresponding factor below, and "Total Points" indicates the summation of all the scores of factors above.

2.7 Estimation of immune cell infiltration

The single-sample gene set enrichment analysis (ssGSEA) was employed to measure the relative abundance of immune cells in OA samples *via* the R packages "limma", "GSVA" (10), and "GSEABase". The gene set for marking each immune cell type was obtained from the study of Charoentong (14). We also conducted a correlation analysis of immune cells with OA-related genes.

2.8 Calculation of immune score

We used principal component analysis (PCA) algorithms to construct the signature of immune-related genes for OA samples (doi: 10.1038/nbt0308-303). Principal Component 1 (PC1) and Principal Component 2 (PC2) were chosen as the signature scores. Immune scores for each OA patient were calculated using the formula Immune Score = Σ(PC1i + PC2i), where i is the expression of immune-related genes. We calculated the relationship between different classifications and immune scores. We used limma and ggpubr packages to study the relationship between the different classifications and the expression level of notable molecules.

2.9 Statistics and software

Data processing and bioinformatics analyses were accomplished by R (version 4.1.3). Packages limma, ggplot2, rmda, clusterProfiler, ssGSEA, rsm, and glmnet were employed for analyses with proper citations. The Wilcoxon or Kruskal–Wallis test was applied for comparisons between two or more groups involved in this study. Pearson's and Spearman's rank correlation tests were adopted to estimate the statistical correlation of parametric or non-parametric variables. Two-sided $p < 0.05$ was considered a significant threshold for all statistical tests.

3 Results

3.1 Hub IRGs and their biological function in OA

Between the OA samples and the control samples, there was a significant difference in the expression of 2,483 IRGs (Figure 1A). As was to be predicted, enrichment of these genes was found in a number of processes related to bone production and resorption. These processes include MAPK, Osteoclast Differentiation, and Ras Signaling Pathways. In addition to this, the Th17 cell differentiation pathway was shown to be active in OA patients, which suggests the possible involvement of immune cells in the development of OA (Figures 1B, C).

3.2 Diagnostic value of the hub IRGs in OA

There were intense interactions amid these IRGs, and several genes seemed to be key regulators in OA, including VEGFA, EDN1, JUN, and MAPK8 (Figure 2A, Figure S1). Three machine learning strategies were then utilized for feature selection by inputting these IRGs and patients' diagnostic information (Figures 2B-D). Finally, 17, 11, and 21 core genes were authenticated by LASSO, SVM, and RF algorithms, respectively (Figure 2E). Of them, five intersected genes were submitted to the final diagnostic model, including PGF, TNFSF11, EDNRB, SDC1, and IL1R1 (Figure 2E).

In the end, TNFSF11 and SDC1 appeared to contribute the most in the diagnostic model to distinguish OA samples from control samples, suggesting that these two genes play an important role in the progression of OA (Figure S2). The AUC for TNFSF11 was 0.904 (0.806–0.979), and the AUC for SDC1 was 0.864 (0.744–0.959) (Figures S2D,E). The nomogram then quantified the contribution of each gene, and as a result, the patients' disease risk was quickly calculated by adding up the points from all five genes (Figure 2F). In the calibration curve, the nomogram's predicted disease risk and the actual disease condition were quite congruent with one another (Figure S3A). The subsequent DCA study demonstrated a significant internal advantage for this approach (Figure S3B). When the value of the threshold was greater than 0.6, the estimated number of patients came closer to matching the actual positive patient count (Figure S3C).

3.3 Characterization of the immune over-activated and immune-inhibited subtypes of OA

Two subtypes of OA were identified by executing hierarchical clustering analysis with the IRGs mentioned above (Figures 3A, C). Cluster A displayed higher expression of TNFSF11 and IL1R1, while Cluster B demonstrated an increased level of EDNRB

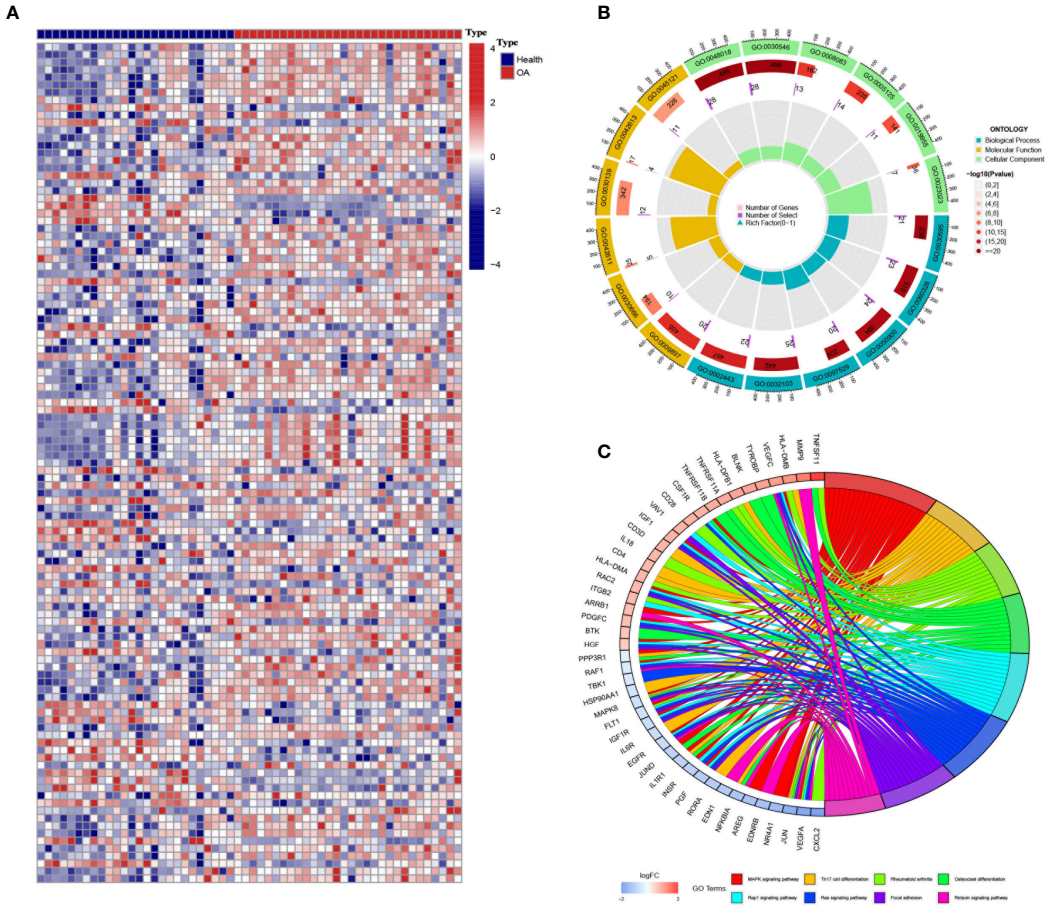

FIGURE 1
Differentially expressed immune genes in osteoarthritis (OA). **(A)** The heatmap shows the differentially expressed immune genes between OA and control samples (GSE55235). **(B, C)** Gene Ontology **(B)** and Kyoto Encyclopedia of Genes and Genomes **(C)** enrichment analyses revealed the biological function and downstream pathways of the differentially expressed immune genes.

(Figure 3B). Moreover, Cluster B was seen with increased infiltration of activated B cells and activated CD8 T cells and decreased infiltration of regulatory T cells, suggesting a microenvironment with excessively activated cellular immunity for this group (Figure 3D). On the contrary, Cluster A seemed to be the immune-inhibited subtype of OA with more infiltration of regulatory T cells. Correspondingly, TNFSF11 and IL1R1 were found positively correlated with the infiltration of regulatory T cells, partly accounting for its reduction in Cluster B (Figure 3E). In addition, Clusters A and B differed in many biological processes (Figure 3F) such as regulation of anatomical structure size (go:0090066), endoplasmic reticulum lumen (go:0005788), potassium channel activity (go:0005267), and heat generation (go:0031649).

3.4 External validation for the two immune subtypes in GSE55457 and GSE82107

Similar classifications were seen in two external validation cohorts: GSE55457 (N = 33) and GSE82107 (N = 17). The processes of clustering analyses for these two cohorts were illustrated in supplementary pictures (Figures S4, S5) with consensus matrix, CDF, and delta area determining the optimal number of clusters. Distinguishable two clusters were identified in GSE55457 with a group of genes upregulated in Cluster A (Figures 4A, B). Keeping consistent with the former results of the training cohort, TNFSF11, IL1R1, and regulatory T cells also showed a marked decrease in Cluster B (Figures 4C, D), implying a phenotype of immune over-activation with advanced bone absorption. In GSE55457, Cluster B was seen with an increased immune score in both the immune gene cluster and the gene cluster, supporting the immune-activated phenotype of this group. The Sankey diagram demonstrated the overlap of patients between the different clusters (Figures 5A, B). In parallel, Cluster B showed a distinct decline of TNFSF11 and GDF5, accompanied by significant ascending of FRZB and TRAPPC2 (Figures 5C, D).

4 Discussion

Non-infectious chronic inflammation, which occurs when inflammatory cells invade synovial tissue or synovial fluid, especially in the early stages of the illness, is the main clinical

10.3389/fendo.2023.1144258

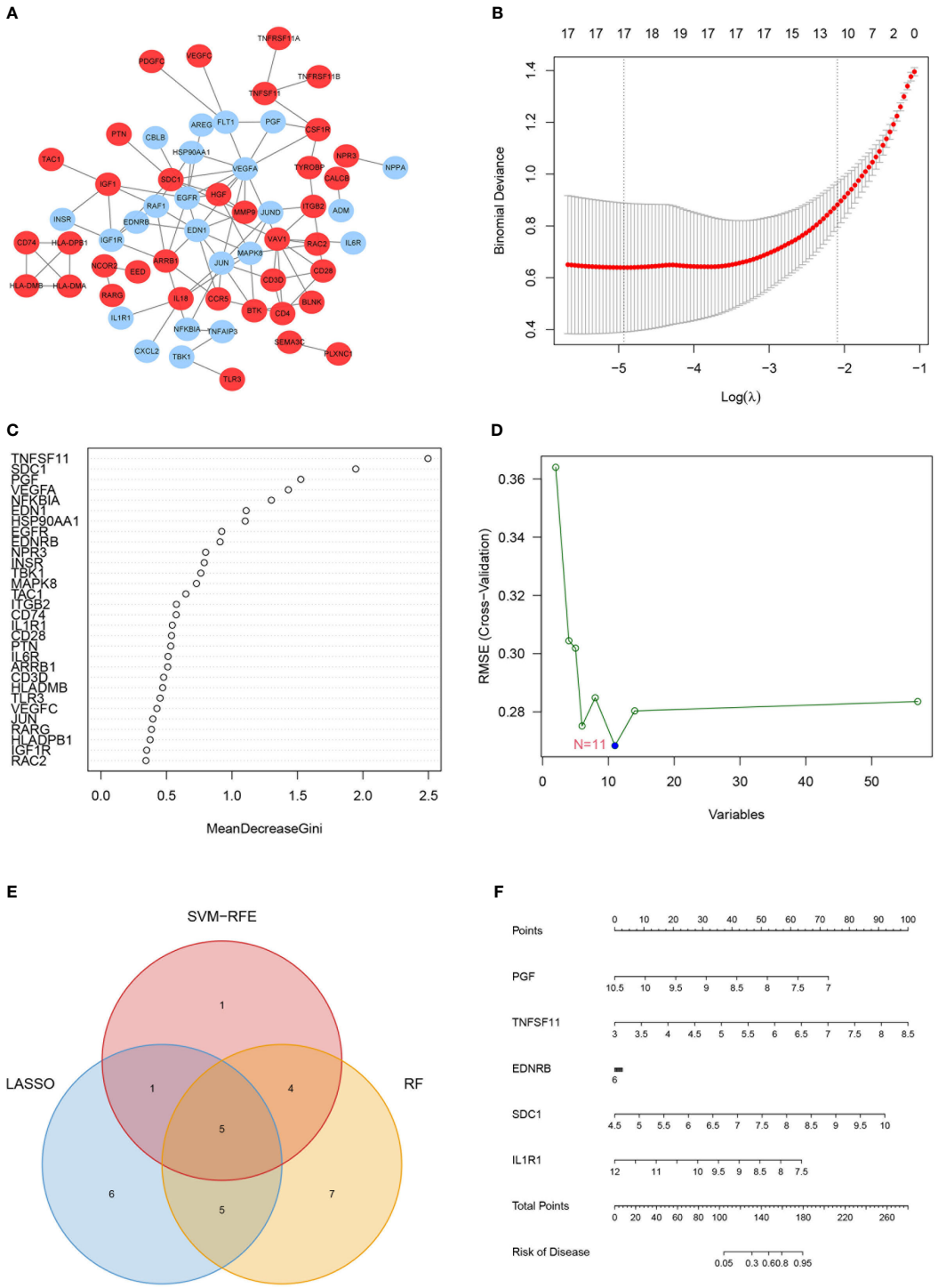

FIGURE 2
Hub immune-related genes (IRGs) and their diagnostic value. **(A)** Protein–protein interaction network of the IRGs. **(B–D)** Hub IRGs were filtered by three machine learning strategies of feature selection, including least absolute shrinkage and selection operator **(B)**, random forest **(C)**, and support vector machine **(D)**. **(E)** Five hub IRGs were identified by the three machine learning strategies. **(F)** The five-IRG-based nomogram model showed good diagnostic performance.

hallmark of OA (doi: 10.1053/joca.1998.0224, 10.1002/art.10768). Immunity plays a key role in the emergence and progression of OA.

The present study comprehensively investigated the role of immune genes and immune cells in OA, revealing the immune over-activated and immune-inhibited subtypes of OA. The former subtype showed higher infiltration of activated B cells and CD8 T cell, compared with lesser infiltration of regulatory T cells, underlying a microenvironment with excessive cellular immunity.

10.3389/fendo.2023.1144258

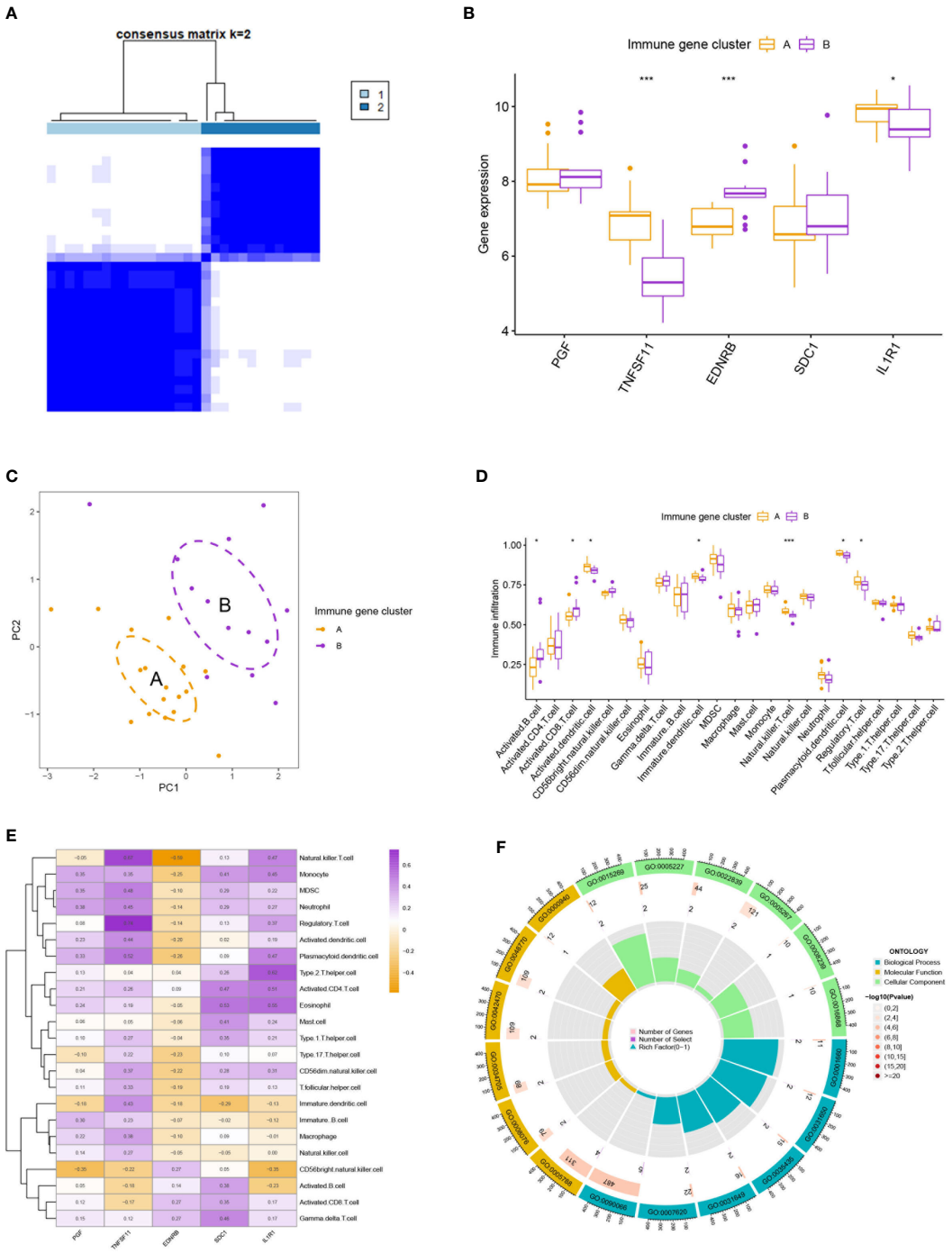

FIGURE 3
Clustering analysis and immune infiltration analysis. **(A)** Clustering analysis stratified patients into two subtypes. **(B, C)** The two immune subtypes differ in gene expression pattern **(B)** and geometrical distance **(C)**. **(D)** Immune subtype B showed higher infiltration of activated B cells and activated T cells than subtype **(A)**. **(E)** Correlation analysis between five hub immune genes and immune cells. **(F)** Gene Ontology enrichment analysis revealed the functional differences between the two immune subtypes. * means P < 0.05, *** means P < 0.001.

A nomogram model was also constructed by using five immune genes, showing rather good diagnostic performance. These findings will help understand the crosstalk between immune cells and bone tissue, providing novel insights for the diagnosis and treatment of OA.

First, five critical IRGs were identified in our study, including PGF, TNFSF11, EDNRB, SDC1, and IL1R1. It was shown that the presence of regulatory T cells was inversely connected with EDNRB and positively correlated with TNFSF11 and IL1R1. Of them, TNFSF11 contributed most significantly to the diagnosis of OA, followed by SCD1. Reportedly, TNFSF11 (TNF Superfamily Member 11) is a key factor responsible for osteoclast differentiation and activation, encoding RANKL, the ligand of osteoprotegerin (OPG) (15, 16), to regulate bone density.

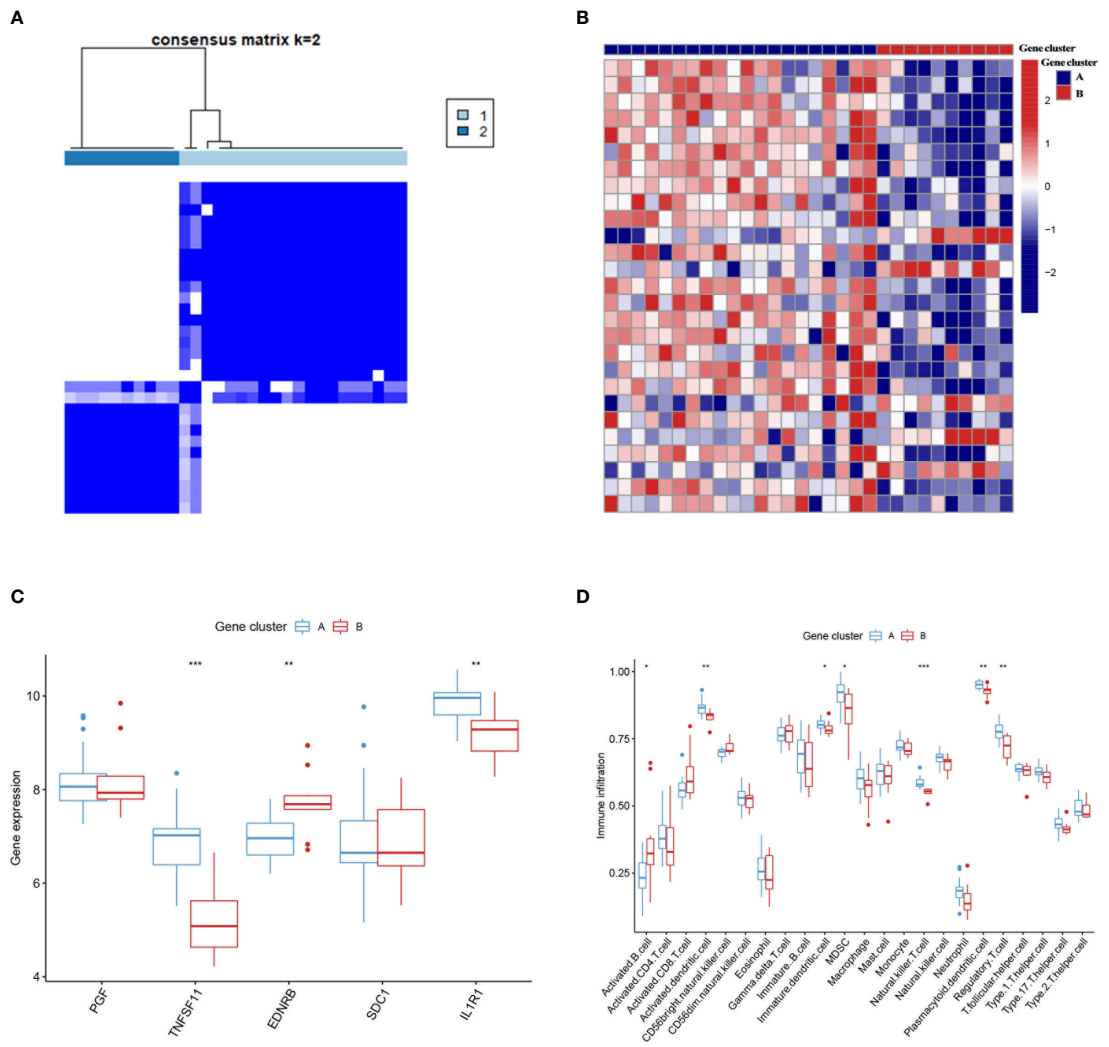

FIGURE 4
External validation for the two immune subtypes in GSE55457. **(A)** Two immune subtypes were found in GSE55457 by clustering analysis. **(B)** The heatmap showed the differentially expressed genes between the two subtypes. **(C, D)** The two immune subtypes differ in the pattern of immune gene expression **(C)** and immune cell infiltration **(D)**. Cluster B also displayed higher infiltration of activated B cells and T cells as the subtype B in GSE55235. * means P < 0.05, ** means P < 0.01, *** means P < 0.001.

Moreover, TNFSF11 has already been linked to a series of diseases with osteoproliferation or osteolysis, including osteopetrosis, dysosteosclerosis, Paget disease of bone 2, and familial expansile osteolysis (17). Therefore, it is reasonable to see the significant upregulation of TNFSF11 in osteoarthritis. Correspondingly, reducing TNFSF11 expression could relieve the progression of cartilage degradation in OA (18).

Meanwhile, TNFSF11 is key in the processes of lymph node development and production of activated B cells and T cells (19, 20). This is consistent with the results of our study: TNFSF11 was observed to be correlated with the infiltration of activated T cells, B cells, natural killer T cells, neutrophils, monocytes, etc. Similarly, elevated TNFSF11 was reported to induce a pro-inflammatory phenotype of OA (21), resulting in accelerated joint destruction and deteriorated clinical symptoms (22).

SCD1, stearoyl CoA desaturase 1, was found to promote the function of osteogenesis in bone marrow mesenchymal stem cells (23), and inhibition of SCD1 could prevent postmenopausal osteoporosis to some extent (24). Keeping consistent with these studies, we found that SCD1 also played a pivotal role in OA. SCD1 expression was positively correlated with the infiltration of monocyte, activated CD4 T cell, and gamma delta T cell, underlying an inflamed microenvironment. Potential mechanisms accounting for this correlation between SCD1 and immune imbalance are the activation of miR-203a/FOS and miR-1908/EXO1 signaling pathways by SCD1 (25).

The present study has several advantages. Comprehensive investigations were conducted on the role of immune genes and immune cells in OA. Several critical immune genes were identified, and a diagnostic nomogram was constructed with quite good performance. Immune over-activated and immune-inhibited subtypes of OA were revealed. The former subtype showed higher infiltration of activated B cells and CD8 T cells, underlying a microenvironment with excessive cellular immunity. These

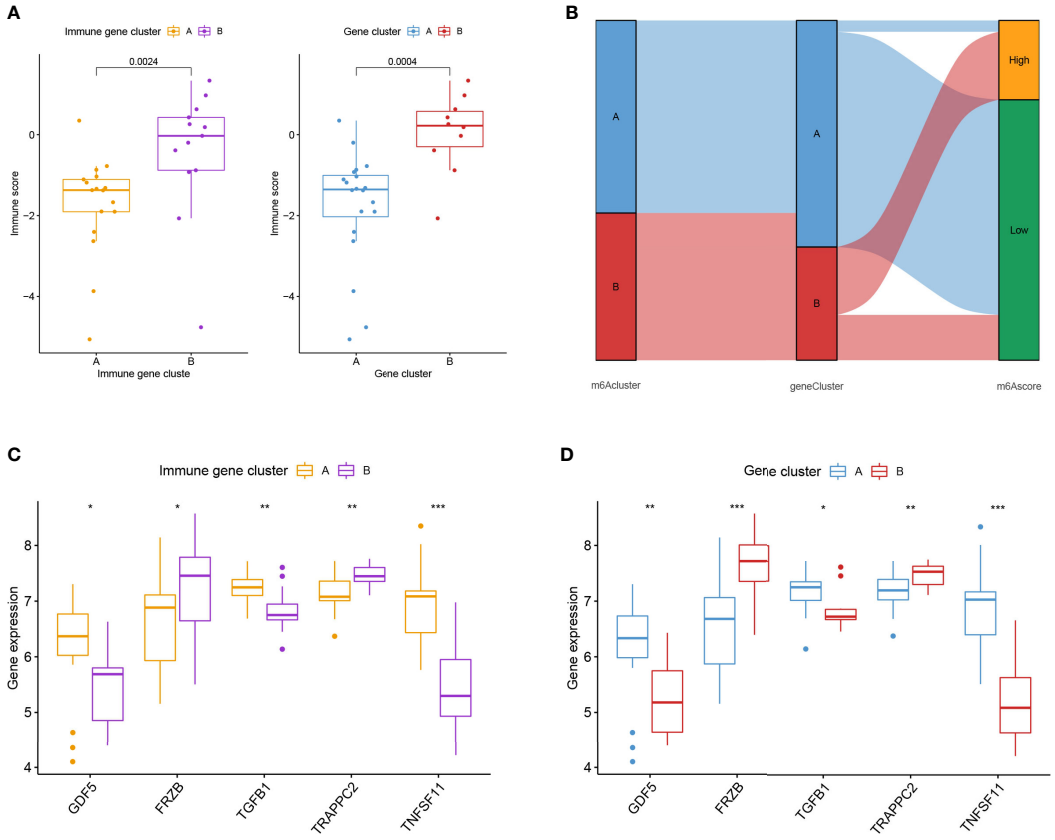

FIGURE 5
External validation for the two immune subtypes in GSE82107. **(A)** Boxplot showed the difference in immune score in the immune gene cluster and gene cluster in GSE82107. **(B)** The Sankey diagram showed the distribution of patients in different clusters. **(C, D)** Expression difference of five osteoarthritis-related genes in the immune gene cluster **(C)** and gene cluster **(D)**. * means P < 0.05, ** means P < 0.01, *** means P < 0.001.

findings will provide novel insights into the diagnosis and treatment of OA.

There were also some limitations to our study. First, it would be more convincing if there were some *in vitro* experiments. Second, the expression of TNFSF11, SCD1, and the two immune subtypes of OA could be tested in actual patient cohorts. Lastly, analysis of the pathways related to osteogenesis can be added to further explain the difference between the two immune subtypes of OA.

Data availability statement

The original contributions presented in the study are included in the article/Supplementary Material. Further inquiries can be directed to the corresponding authors.

Author contributions

FZ, ZG, and ZJ designed the study. LP, FY, XC, HZ, JL, JZ, and JG performed data analysis. LP and FY drafted the manuscript. FZ, ZG, and ZJ revised the manuscript. All authors read and approved the final manuscript.

Funding

This study was supported by grants from the Zhejiang Medical and Health Science and Technology Plan Project (2022504276), the Zhejiang Basic Public Welfare Research Project (LGF22H060032), and the Health Science and Technology Program of Hangzhou (A20210086).

Conflict of interest

The authors declare that the research was conducted in the absence of any commercial or financial relationships that could be construed as a potential conflict of interest.

Publisher's note

All claims expressed in this article are solely those of the authors and do not necessarily represent those of their affiliated organizations, or those of the publisher, the editors and the reviewers. Any product that may be evaluated in this article, or claim that may be made by its manufacturer, is not guaranteed or endorsed by the publisher.

Supplementary material

The Supplementary Material for this article can be found online at: https://www.frontiersin.org/articles/10.3389/fendo.2023.1144258/full#supplementary-material

References

1. Prieto-Alhambra D, Judge A, Javaid MK, Cooper C, Diez-Perez A, Arden NK. Incidence and risk factors for clinically diagnosed knee, hip and hand osteoarthritis: Influences of age, gender and osteoarthritis affecting other joints. *Ann Rheum Dis* (2014) 73(9):1659–64. doi: 10.1136/annrheumdis-2013-203355

2. Barnett R. Osteoarthritis. *Lancet* (2018) 391(10134):1985. doi: 10.1016/s0140-6736(18)31064-x

3. Scanzello CR. Role of low-grade inflammation in osteoarthritis. *Curr Opin Rheumatol* (2017) 29(1):79–85. doi: 10.1097/bor.0000000000000353

4. Bierma-Zeinstra SM, van Middelkoop M. Osteoarthritis: In search of phenotypes. *Nat Rev Rheumatol* (2017) 13(12):705–06. doi: 10.1038/nrrheum.2017.181

5. Courties A, Sellam J, Berenbaum F. Metabolic syndrome-associated osteoarthritis. *Curr Opin Rheumatol* (2017) 29(2):214–22. doi: 10.1097/bor.0000000000000373

6. Jeon OH, Kim C, Laberge RM, Demaria M, Rathod S, Vasserot AP, et al. Local clearance of senescent cells attenuates the development of post-traumatic osteoarthritis and creates a pro-regenerative environment. *Nat Med* (2017) 23(6):775–81. doi: 10.1038/nm.4324

7. Lopes EBP, Filiberti A, Husain SA, Humphrey MB. Immune contributions to osteoarthritis. *Curr Osteoporos Rep* (2017) 15(6):593–600. doi: 10.1007/s11914-017-0411-y

8. Ashburner M, Ball CA, Blake JA, Botstein D, Butler H, Cherry JM, et al. Gene ontology: Tool for the unification of biology. the gene ontology consortium. *Nat Genet* (2000) 25(1):25–9. doi: 10.1038/75556

9. Kanehisa M, Goto S. KEGG: kyoto encyclopedia of genes and genomes. *Nucleic Acids Res* (2000) 28(1):27–30. doi: 10.1093/nar/28.1.27

10. Hänzelmann S, Castelo R, Guinney J. GSVA: Gene set variation analysis for microarray and RNA-seq data. *BMC Bioinf* (2013) 14(7):7. doi: 10.1186/1471-2105-14-7

11. Lu X, Meng J, Zhu J, Zhou Y, Jiang L, Wang Y, et al. Prognosis stratification and personalized treatment in bladder cancer through a robust immune gene pair-based signature. *Clin Transl Med* (2021) 11(6). doi: 10.1002/ctm2.453

12. Chen H, Boutros PC. VennDiagram: A package for the generation of highly-customizable Venn and Euler diagrams in R. (2011) 12:35. doi: 10.1186/1471-2105-12-35

13. Wilkerson MD, Hayes DN. ConsensusClusterPlus: A class discovery tool with confidence assessments and item tracking. *Bioinformatics* (2010) 26(12):1572–3. doi: 10.1093/bioinformatics/btq170

14. Charoentong P, Finotello F, Angelova M, Mayer C, Efremova M, Rieder D, et al. Pan-cancer immunogenomic analyses reveal genotype-immunophenotype relationships and predictors of response to checkpoint blockade. *Cell Rep* (2017) 18 (1):248–62. doi: 10.1016/j.celrep.2016.12.019

15. Xiao L, Zhong M, Huang Y, Zhu J, Tang W, Li D, et al. Puerarin alleviates osteoporosis in the ovariectomy-induced mice by suppressing osteoclastogenesis *via* inhibition of TRAF6/ROS-dependent MAPK/NF-κB signaling pathways. *Aging (Albany NY)* (2020) 12(21):21706–29. doi: 10.18632/aging.103976

16. Udagawa N, Koide M, Nakamura M, Nakamichi Y, Yamashita T, Uehara S, et al. Osteoclast differentiation by RANKL and OPG signaling pathways. *J Bone Miner Metab* (2021) 39(1):19–26. doi: 10.1007/s00774-020-01162-6

17. Xue JY, Ikegawa S, Guo L. Genetic disorders associated with the RANKL/OPG/RANK pathway. *J Bone Miner Metab* (2021) 39(1):45–53. doi: 10.1007/s00774-020-01148-4

18. Li J, Jiang M, Yu Z, Xiong C, Pan J, Cai Z, et al. Artemisinin relieves osteoarthritis by activating mitochondrial autophagy through reducing TNFSF11 expression and inhibiting PI3K/AKT/mTOR signaling in cartilage. *Cell Mol Biol Lett* (2022) 27(1):62. doi: 10.1186/s11658-022-00365-1

19. Hess E, Duheron V, Decossas M, Lézot F, Berdal A, Chea S, et al. RANKL induces organized lymph node growth by stromal cell proliferation. *J Immunol* (2012) 188(3):1245–54. doi: 10.4049/jimmunol.1101513

20. Kawai T, Matsuyama T, Hosokawa Y, Makihira S, Seki M, Karimbux NY, et al. B and T lymphocytes are the primary sources of RANKL in the bone resorptive lesion of periodontal disease. *Am J Pathol* (2006) 169(3):987–98. doi: 10.2353/ajpath.2006.060180

21. Massicotte F, Lajeunesse D, Benderdour M, Pelletier JP, Hilal G, Duval N, et al. Can altered production of interleukin-1beta, interleukin-6, transforming growth factor-beta and prostaglandin E(2) by isolated human subchondral osteoblasts identify two subgroups of osteoarthritic patients. *Osteoarthritis Cartilage* (2002) 10(6):491–500. doi: 10.1053/joca.2002.0528

22. Tat SK, Pelletier JP, Lajeunesse D, Fahmi H, Duval N, Martel-Pelletier J. Differential modulation of RANKL isoforms by human osteoarthritic subchondral bone osteoblasts: influence of osteotropic factors. *Bone* (2008) 43(2):284–91. doi: 10.1016/j.bone.2008.04.006

23. Tao J, Shi J, Lu Y, Dou B, Zhou Z, Gao M, et al. Overexpression of stearoyl-CoA desaturase 1 in bone-marrow mesenchymal stem cells increases osteogenesis. *Panminerva Med* (2013) 55(3):283–9.

24. Lu L, Wang L, Wu J, Yang M, Chen B, Wang H, et al. DNMT3a promotes osteoblast differentiation and alleviates osteoporosis *via* the PPARγ/SCD1/GLUT1 axis. *Epigenomics* (2022) 14(12):777–92. doi: 10.2217/epi-2021-0391

25. Chen YS, Kang XR, Zhou ZH, Yang J, Xin Q, Ying CT, et al. MiR-1908/EXO1 and MiR-203a/FOS, regulated by scd1, are associated with fracture risk and bone health in postmenopausal diabetic women. *Aging (Albany NY)* (2020) 12(10):9549–84. doi: 10.18632/aging.103227

frontiers | Frontiers in Endocrinology

TYPE Original Research
PUBLISHED 21 March 2023
DOI 10.3389/fendo.2023.1155009

OPEN ACCESS

EDITED BY
Ruiqin Han,
Chinese Academy of Medical Sciences, China

REVIEWED BY
Xue Zhan,
Chongqing Medical University, China
Li Zhu,
Guizhou Medical University, China

*CORRESPONDENCE
Fengge Zhou
zfg1991125@163.com
Zhe Yang
sdslyyyz@sina.com

SPECIALTY SECTION
This article was submitted to Cancer Endocrinology, a section of the journal Frontiers in Endocrinology

RECEIVED 31 January 2023
ACCEPTED 09 March 2023
PUBLISHED 21 March 2023

CITATION
Nie Y, Yao G, Xu X, Liu Y, Yin K, Lai J, Li Q, Zhou F and Yang Z (2023) Single-cell mapping of N6-methyladenosine in esophageal squamous cell carcinoma and exploration of the risk model for immune infiltration.
Front. Endocrinol. 14:1155009.
doi: 10.3389/fendo.2023.1155009

Single-cell mapping of N6-methyladenosine in esophageal squamous cell carcinoma and exploration of the risk model for immune infiltration

Yuanliu Nie[1], Guangyue Yao[1], Xiaoying Xu[2], Yi Liu[3], Ke Yin[4], Jingjiang Lai[5], Qiang Li[6], Fengge Zhou[6]* and Zhe Yang[1,6]*

[1]Tumor Research and Therapy Center, Shandong Provincial Hospital, Shandong University, Jinan, Shandong, China, [2]Shandong First Medical University, College of Basic Medicine, Shandong First Medical University-Shandong Academy of Medical Sciences, Jinan, Shandong, China, [3]Department of Computer Science and Technology, Ocean University of China, Qingdao, China, [4]Department of Pathology, Shandong Provincial Hospital, Shandong University, Jinan, China, [5]Department of Oncology, Shandong Provincial Hospital Affiliated to Shandong First Medical University, Jinan, China, [6]Tumor Research and Therapy Center, Shandong Provincial Hospital Affiliated to Shandong First Medical University, Jinan, Shandong, China

Background: N6-methyladenosine (m6A) modification is the most common RNA modification, but its potential role in the development of esophageal cancer and its specific mechanisms still need to be further investigated.

Methods: Bulk RNA-seq of 174 patients with esophageal squamous carcinoma from the TCGA-ESCC cohort, GSE53625, and single-cell sequencing data from patients with esophageal squamous carcinoma from GSE188900 were included in this study. Single-cell analysis of scRNA-seq data from GSE188900 of 4 esophageal squamous carcinoma samples and calculation of PROGENy scores. Demonstrate the scoring of tumor-associated pathways for different cell populations. Cell Chat was calculated for cell populations. thereafter, m6A-related differential genes were sought and risk models were constructed to analyze the relevant biological functions and impact pathways of potential m6A genes and their impact on immune infiltration and tumor treatment sensitivity in ESCC was investigated.

Results: By umap downscaling analysis, ESCC single-cell data were labelled into clusters of seven immune cell classes. Cellchat analysis showed that the network interactions of four signaling pathways, MIF, AFF, FN1 and CD99, all showed different cell type interactions. The prognostic risk model constructed by screening for m6A-related differential genes was of significant value in the prognostic stratification of ESCC patients and had a significant impact on immune infiltration and chemotherapy sensitivity in ESCC patients.

Conclusion: In our study, we explored a blueprint for the distribution of single cells in ESCC based on m6A methylation and constructed a risk model for

10.3389/fendo.2023.1155009

immune infiltration analysis and tumor efficacy stratification in ESCC on this basis. This may provide important potential guidance for revealing the role of m6A in immune escape and treatment resistance in esophageal cancer.

KEYWORDS

N6-Methyladenosine, esophageal squamous cell carcinoma, single-gene sequencing, immune infiltration, bioinfomatics

Introduction

Esophageal cancer is a common malignancy worldwide, ranking seventh in incidence and sixth in mortality of all malignancies (1). Esophageal cancer is mainly classified into esophageal squamous cell carcinoma (ESCC) and esophageal Adenocarcinoma (EAC), with ESCC being the most common histological type of esophageal cancer. In Asian countries, squamous cell carcinoma of the esophagus, accounts for approximately 95% of esophageal cancers (2). Despite significant breakthroughs in the diagnosis and treatment of esophageal squamous carcinoma (3), the prognosis of patients with esophageal squamous carcinoma remains poor, with a 5-year survival rate of less than 15% (4), largely because its pathogenesis has not been fully elucidated. With the further analysis of tumor development mechanism, a variety of therapies based on new tumor immune and metabolic targets (immunotherapy and targeted therapy, etc.) have emerged to improve the efficacy, but the prognosis of esophageal cancer patients is still poor (5), therefore, in-depth study of the mechanisms related to the development of esophageal cancer and the search for new effective therapeutic targets are important means to improve the overall survival rate of esophageal cancer patients. At the same time, an in-depth understanding of tumor heterogeneity from a genetic perspective is more conducive to dissecting the intrinsic features of ESCC.

N6-methyladenosine, (m6A) modification is one of the most common RNA modifications (6). m6A methyltransferase-like 3 (METTL3) is the most important component of m6A methyltransferase (7). According to recent studies, m6A methylation has been associated with a variety of human cancers, including cervical, colorectal, ovarian and lung cancers (8–11). m6A methylation is closely involved in cancer cell proliferation, apoptosis, invasion and migration, autophagy and metabolism. as well as metabolism and other biological processes (12–16). However, its biological role and molecular mechanisms in the development of esophageal squamous carcinoma are relatively limited. The m6A methylation modification has an important regulatory role in the proliferation, migration and invasion of esophageal cancer cells, and is of great research value and clinical significance in predicting the prognosis and targeting therapy of esophageal cancer. However, the relationship between m6A methylation modification and esophageal cancer still needs to be further explored. Based on m6A-related genes, several previous studies have constructed riskscore that can stably predict the prognosis of patients with multiple cancer types, including ESCC (17, 18). But different from other studies, our study analyzed m6a-related genes from the perspective of single-cell mapping for the first time, and constructed a riskscore that stably predicts the prognosis of ESCC patients.

Therefore, we investigated the microscopic roles of the major pathways of m6A methylation and differential genes in esophageal carcinogenesis and invasive metastasis in ESCC patient tumors. Single cell sequencing and cell communication analysis were used to clarify the spatially specific major biological functions of the distribution of m6A methylation-related genes in tumor cells. Transcriptomics and single-cell sequencing revealed that subpopulations of tumor cells with differential expression of m6A methylation-related gene profiles were heterogeneously distributed within the lesion. m6A methylation differential expression correlated significantly with the immune infiltration status of EACC patients. This suggests that the aberrant distribution of m6A methylation may determine poor prognosis and immune tolerance in ESCC patients. To enrich the clinical scalability of the model, we assessed the specific relationship between m6A methylation-related genes and immune infiltration and constructed subgroups to assess their impact on drug sensitivity. These findings provide new insights into the spatial biology and immunological understanding of m6A methylation in ESCC, and make some breakthroughs for individualised treatment and new target development in ESCC.

Materials and methods

Data collection

All patient data in this study were obtained from online public databases, including the cancer genome atlas (tcga) and GEO DataSets. All patients included in the study had complete public gene expression data and clinical annotation. A bulk RNA-seq of 77 patients with esophageal squamous carcinoma from the tcga-ESCC cohort was included, while gene expression data containing samples of esophageal cancer tissue and normal esophageal tissue were downloaded from the gene expression omnibus (GEO) data (http://www.ncbi.nlm.nih.gov/geo/). GSE53625, a core data set of expression profiles, was used for validation. It includes bulk

RNA-seq from 174 patients with esophageal squamous carcinoma and single cell scRNA-seq data from GSE188900 from 4 patients with esophageal squamous carcinoma. The clinical data collected included age, gender, tumor stage and prognostic data. To ensure the availability and reliability of the data, strict inclusion and exclusion criteria were established for this study. Inclusion criteria: (1) primary squamous cell carcinoma of the esophagus confirmed by pathological sections; (2) patients with a prognostic follow-up of at least 30 days; (3) complete genomic expression level data included; and (4) clear reporting of pathological conditions and follow-up. Exclusion criteria: (1) other pathological types or secondary esophageal tumors; (2) concurrent primary tumors from other sites.

Collection of genes associated with epigenetic modifications of m6A and single-cell data processing

In this study, 21 m6A regulators were collected from the MSigDB database, including 8 writers (METTL3, METTL14, RBM15, RBM15B, WTAP, KIAA1429, CBLL1, ZC3H13), 2 erasers (ALKBH5, FTO) and 11 readers (YTHDC1, YTHDC2, YTHDF1, YTHDF2, YTHDF3, IGF2BP1, HNRNPA2B1, HNRNPC, FMR1, LRPPRC, ELAVL1). The original expression profile dataset (GSE188900) used for the analysis was filtered from the public database GEO database platform. The data set was 5 EACC tumor specimens, which were extracted from RNA and analyzed by expression profiling microarray, using the Illumina NextSeq detection platform. The raw data set was pre-processed with the Seurat R package to ensure quality control (QC) results. The number of genes detected in each cell (nFeature_RNA) and the total number of molecules detected within the cell (nCount_RNA) were calculated, and the number of genes detected per cell was proportional to the number of genes expressed (reads) obtained by sequencing. Cells were clustered based on the filtered principal components and visualized using uniform manifold approximation and projection (UMAP) dimensionality reduction techniques for cell classification. Tumour cell marker genes with adj. p value < 0.05 were screened. Cell marker genes were retrieved using the PanglaoDB database, and the genes corresponding to each class cluster were intersected to determine the class cluster in which the cells were located. Cell population grouping was performed by single cell sequencing data acquisition post-processing and downscaling analysis. This includes T cells, B cells, Mast cells, fibroblasts, myeloid and endothelial cells and the remaining cell types.

Analysis of protein interactions and cellular communication of m6A epigenetic modifications in ESCC at the single cell level

After pre-processing and downscaling analysis of single-cell scRNA-seq data from four patients with esophageal squamous carcinoma from GSE188900, PROGENy scores were calculated to demonstrate the scoring of tumor-associated pathways in different cell populations.PROGENy (Pathway RespOnsive GENes for activity inference) is an R package published in 2018. It is generally accepted that gene expression correlates with pathway signaling activity, and in previous pathway enrichment analyzes this has largely been used as a basis for assuming that the more genes highly expressed in a pathway, the more likely it is that the pathway is activated, however, the effect of post-translational modifications has been ignored. Based on this, PROGENy can use publicly available data from perturbation experiments to infer common core genes in the pathway response of human samples. This can be used to infer pathway activity from bulk RNAseq science. This fits in with our research aim to understand the m6A epigenetic gene pathway alterations in single cell samples from ESCC. Also, Cell Chat scores were calculated for different species of immune cells sequenced from single cells, demonstrating cellular communication for each cell population. Cellular communication analysis can help us understand cell-cell interactions and resolve intercellular communication networks. It will help us to unravel the interactions of various cell types during development, explore the immune microenvironment of tumors and uncover potential therapeutic targets for diseases. CellChat has built a cellular interaction database of 2021 ligand-receptor pairs that can be used to quantify intercellular communication networks from single cell transcriptome data, resolve the major input and output signals for each cell type, and suggest how each cell type and multiple signaling pathways work together. Based on the fact that the macrophage migration inhibitory factor (MIF) signaling pathway is the secretory signaling pathway with the highest probability of communication in ESCC cells, the cellular communication network of the 'MIF' pathway is demonstrated.

Gene enrichment and functional analysis of the m6A epigenetic pathway

The m6A signature (m6A epigenetic) was scored for gene set enrichment using the AddModuleScore function of the Seruat package, and was divided into two groups: m6A signature-high and m6A signature-low. It can be seen that most of the immune cells have a mixture of m6A signature-high and m6A signature-low groups. Further analysis was carried out in the Bulk transcriptome. The R package "LIMMA" (version 3.48.3) was used to compare the two groups. LMFIT and bayes functions were used to ensure accuracy. The R packages clusterProfiler, org.Hs.eg.db, DOSE, enrichment plot, and colourspace were used for gene enrichment and pathway functional analysis of DEGs and core genes. The clusterProfiler R package was used to perform gene ontologyGO) functional enrichment analysis and Kyoto encyclopedia of genes and genomes (KEGG) pathway enrichment analysis on the differential gene sets. The enrichment analysis is based on the principle of hypergeometric distribution, where GO is a comprehensive database describing gene function and can be divided into 3 parts: biological process (BP), cellular component (CC) and molecular function (MF). KEGG is a comprehensive

database that integrates genomic, chemical and systemic functional information. We want to analyze the key macroscopic associations of m6A epigenetically related genes and signaling pathways during development at the cellular component, molecular function and biological process levels. Enrichment pathways are all significant at p value < 0.05. In addition, we used the "Limma" package to find out the differential genes between the two groups based on the "Ebays" function, and performed a univariate Cox regression analysis on the differentially expressed genes (DEGs) based on the tinyarray package, with a p value < 0.01, and 29 genes were selected.

m6A epigenetic survival-related differential gene acquisition and prognostic model construction

To further visualise as well as quantify the potential impact of m6A epigenetic inheritance on the development of ESCC patients. We performed univariate Cox regression analysis on the 29 DEGs obtained in the previous step, and selected prognostic genes with p value < 0.05 as the screening criterion. The cohort GSE53625 of 174 patients with squamous esophageal cancer was also used for independent external validation. We divided ESCC patients into high-risk and low-risk groups by the median riskscore. Also, Kaplan-Meier (K-M) survival curves were plotted for the high- and low-risk groups. Combining common clinical parameters and riskscore to draw a nomogram for further clinical visualization and auxiliary application of the model.

Exploring the relationship between the role of m6A epigenetics in immune infiltration and the impact of treatment sensitivity in ESCC

Clarifying the immune infiltration of m6A epigenetics in the tumor microenvironment and the lymphocyte association is an important prerequisite for understanding its impact on treatment resistance in ESCC patients. To ensure predictive accuracy, we used ssGSEA and xCell algorithm (19) to assess the level of immune infiltration. Based on the expression matrix, xCell evaluates the composition and abundance of immune cells in mixed cells by combining the advantages of deconvolution methods and gene enrichment. Based on the expression matrix and the immune cell marker gene set, ssGSEA can calculate enrichment scores for individual samples and gene set pairs to determine the level of immune infiltration. ssGSEA is able to quantify the abundance of immune cells and stromal cells from transcriptomic data to assess the level of immunity one at a time. In addition, immune scores and tumor purity were calculated for each sample by the ESTIMATE algorithm.

In view of the above studies showing the close association of m6A epigenetics for immune infiltration in ESCC, it is considered that m6A may interfere with immune infiltration in ESCC by interfering with tumor immunity against chemotherapy. Further, we wanted to analyze whether the therapeutic susceptibility of ESCC patients to multiple chemotherapeutic agents is definitively associated with the m6A epigenetic pathway, in order to facilitate the clinical dissemination and application of the model in the future. Here, we used the Cancer Genome Project (CGP) database to predict the therapeutic susceptibility of chemotherapeutic agents using the R package "prophet". After initial analysis of the data, we used the Genomics of drug sensitivity in Cancer (GDSC) database to calculate drug sensitivity scores using the R package 'oncopredict' (20) and visualised the predicted images using multiple box plots.

Tissue acquisition and quantitative real-time PCR

Ten pairs of ESCC tissues and adjacent normal tissues were collected from Shandong Provincial Hospital of Shandong University and stored at -80°C for a long time. RNAiso Plus (Takara Bio, Japan) was used to extract total RNA from tissues, PrimeScript RT Master Mix (Takara Bio, Japan) was used for reverse transcription of cDNA, and TB green (Takara Bio, Japan) was used for RT-qPCR reaction. and normalized with GAPDH. All primer sequences are detailed in Supplementary Table 1.

Statistical analysis

Independent t-tests and Mann-Whitney U tests were used to compare two groups of variables with normal and non-normal distributions, respectively, and to determine statistical significance. One-way ANOVA (analysis of variance) and Krush-Wallis tests were used to compare differences between multiple sets of statistics. RT-qPCR data were compared using Student's t-test. All statistical analyzes were performed using R software for statistical analysis. Statistical significance was defined as a p value < 0.05.

Results

Preliminary visualization and distribution analysis of single-cell sequencing data from ESCC

First, single-cell analysis was performed on scRNA-seq data from four esophageal squamous carcinoma samples from GSE188900, downlinked into seven cell clusters. Preliminary in-expression normalization was performed and we classified the cells into coherent transcriptional clusters using a graph-based clustering approach. UMAP method downlink analysis was performed to group the cells into clusters. The main categories of immune cell clusters identified and annotated included:Tcell, B cell, Epithelial, Fibrobalst, Mast Cell, Endotheli and Myeloid (Figure 1A), and cells were annotated according to the source of the sample. Furthermore, single-cell sequencing data obtained from four ESCC patients were annotated for spatial distribution and classified primarily based primarily on differences in the taxonomic content of their immune cells and associated signaling pathway alterations. These were

10.3389/fendo.2023.1155009

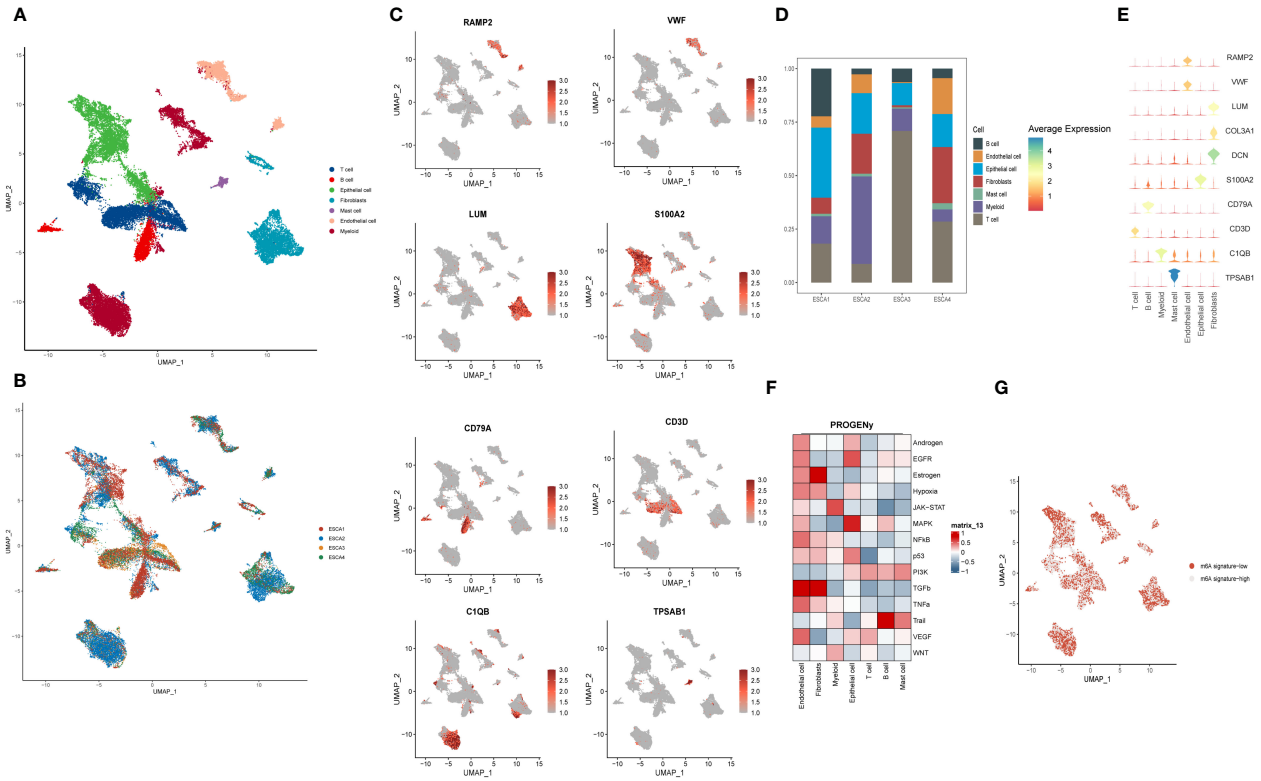

FIGURE 1
Spatial depiction of single-cell sequencing data and annotation of immune cell types and gene distribution in ESCC patients. **(A)** U-MAP plot showing the sample source of the single-cell data, with each colour representing one sample, including a total of 4 patients; **(B)** Representative 7 major immune cell types and distribution annotations in ESCC cells, including T cells, B cells, epithelial cells, fibroblasts, mast cells, endothelial cells and myeloid cells; **(C)** Single-cell sequencing obtained from 7 cell types in the major m6A gene cluster expression distribution maps, including RAMP2, VWF, S100A2, LUM, CD79A and CD3D. outlines the spatial distribution of expression of their major immune cell types. **(D)** Scale bar graphs further analyze the distribution of immune cell types in four different ESCC patients; **(E)** Bubble plots further visualize the major m6A epitopes obtained in **(B)** 7 major immune cell types and distribution annotated expression relationships; **(F)** Heat map showing the expression of tumor-associated pathway scores for different immune cell populations obtained by the PROGENy method; **(G)** Single-cell sequencing visualization of m6A signature for gene set enrichment scoring, divided into m6A signature-high and m6A signature-low groups.

ESCA1, ESCA2, ESCA3 and ESCA4, respectively (Figure 1B). The images yielded that ESCA1 and ESCA2 patients were labelled with more single cell sequencing data and expressed higher content. In contrast, for ESCA3 and ESCA4 patients, relatively low levels of single cell expression were annotated. Cells were annotated by clusters and clusters were classified into seven main categories. By combining the cellular distribution of the multi-locus single cell transcriptome profiles, we found that the annotated expression of endothelial cells was high, mainly in ESCA1, ESCA2 and ESCA3 patients, located throughout the top right side of the image. myeloid cells were mostly distributed in the ESCA3 patient population, located in the lower part of the image. Fibroblasts are mainly annotated in ESCA2 patients and are located in the lower left of the image. B cells and Mast cells received relatively few cellular annotations.

We wanted to gain further insight into the genetic correlation between the expression of m6 epigenetic-related genes in single-cell data and their distribution in different sequencing groups. We first analyzed the expression distribution of 8 immune cell-specific marker genes in 7 types of immune cells (Figure 1C). RAMP2 and VWF were highly expressed in endothelial cells; Epithelial mainly expressed S100A2, fibroblasts expressed LUM, CD79A and CD3D were expressed in B cells and T cells respectively, and C1QB was mainly located in Myeloid cells. tPSAB1 gene was less expressed. In Figure 1D, we applied a scale bar chart to further analyze the distribution of immune cell types in four different ESCC patients. In ESCA1 patients, Epithelial cells were found to be more expressed in about 30% of the patients, in addition to mainly T cells and B cells. For all four patients, Mast cells were relatively less expressed, which is similar to our perception of the distribution of immune space. For ESCA2, Myeoloid cells were the main component, with Epithelial cells and fibroblasts dominating the distribution. In contrast, ESCA3 is dominated by T cells. For ESCA4, the distribution of the content of the various types of immune cells was more uniform. In Figure 1E, we further visualised the distribution of the main m6A epigenetic immune cell types obtained in Figure 1B through bubble plots. Further, we used PROGENy to show the tumor-related pathway scores of the different cell populations (Figure 1F). Endothelial cells were highly positively correlated with the expression of various tumor cell pathways, the most active of which was the TGFb pathway, considering that they may be mainly related to ESCC invasion and

metastasis. Fibroblasts mainly expressed Estrogen and TGFb pathways. The tumor pathways of Epithelial cells are mainly enriched in EGFR and MAPK, and the significant enrichment of these two 'star pathways' may suggest a significant role of Epithelial cells in the development of ESCC. For T cells, all tumor pathways were not significantly enriched. In contrast, B cells showed a significant positive correlation with Trail pathway expression. In addition, the m6A signature was scored for gene set enrichment by function into two groups: m6A signature-high and m6A signature-low. It was concluded in Figure 1G that the majority of immune cells were present in a mixture of m6A signature-high and m6A signature-low groups, suggesting the need for further quantitative studies for analysis.

Further, we studied single cell sequencing data and interactions between different immune cells from ESCC patients through cellular communication. CellChat score is an open source R package (http://github.com/sqjin/CellChat) that allows the use of scRNA-seq data to infer, visualize and analyze intercellular communication. As shown in Figure S1A, T cells and B cells interact primarily with Epithelial cells. Epithelial cells send signals that are primarily associated with T cells. Fibroblasts are more closely associated with T cells and Epithelial cells. Mast cells send signals focused on T cells. Endothelial cells and Myeloid cells interacted mainly with T cells. In addition, we calculated the interaction of four signaling pathway networks, MIF, AFF, FN1 and CD99, as shown in Figure S1B. In the MIF signaling pathway network, T cells and B cells were the main signal sourcing as well as signal receivers, suggesting their main immune regulatory role in the MIF network. For the APP signaling network, Endothelial cells are the main source of signaling, targeting a wide range of immune cells. Similarly, in FN1, the major signaling pathway for fibrosis, fibroblasts play a more dominant role, sending signals targeting a variety of immune cell types. In contrast, for the CD99 signaling pathway network, the interaction of signaling pathways across cell types is more complex and there is no key cell type that is more deterministic.

Gene enrichment and pathway functional analysis of m6A epigenetic inheritance

To clarify the specific implications and potential biological functions of the macroscopic role of m6A epigenetics in the development of ESCC, we used GSEA, KEGG and GO analysis to enrich for markers and pathway functions. In the GSEA analysis (Figure 2A), signaling pathways were mainly enriched in cytoplasmic translation, cell-substrate junction, postsynaptic specialization, and focal adhesion. In the GO analysis (Figure 2B), the main m6A epigenetic pathways were expressed in the structural constituent of Oxidative phosphorylation, Proteasome, ribosome, Protein processing in endoplasmic reticulum, etc. In the KEGG pathways of m6A epigenetics in ESCC patients were mainly enriched in structural constituent of ribosome, cytoplasmic translation, secretory granule lumen, cadherin binding, etc (Figure 2C).

Acquisition of survival-associated differential genes for m6A epigenetic inheritance and construction and validation of prognostic models

Subsequently, to further clarify the direct association of m6A epigenetically related genes with survival in ESCC patients directly, We obtained m6A-signature differential genes and screened out the prognostic genes among them. Using the TCGA-ESCC cohort, nine out of 29 genes were selected based on Lasso regression to build a prognostic model. The specific process of LASSO regression and the coefficient selection process are shown in Figures 3A, B. The risk genes screened included BST2, COL6A2, CTSL, HNRNPA3, MAP3K8, MYC, PSMA4, RBM8A, TPT1. and riskscore were constructed by linearly multiplying the screened risk genes by linear multiplication to distinguish the low-risk group from the high-risk group by the median of the riskscore to build to clarify the stratification of the constructed riskscore on the prognosis of ESCC patients, we analyzed the survival status of different m6A epigenetic subgroups using K-M curves. A significant difference in survival prognosis between patients with high as well as low expression of m6A epigenetic markers can be seen in Figure 3C. In addition, bubble and scatter plots were used to further visualise the survival prognosis of the different riskscore patients, as shown in Figure 3D. Further, we also depicted the distribution of expression of nine risk genes in the m6A epigenetic low- and high-risk groups of the patient population (Figure 3E). The results showed that, except for RBM8A, TPT1 and HNRNPA3, all m6A epigenetically inherited genes were highly expressed in the low-risk group, suggesting that they were the main protective genes. In Figure 3F, we analyzed the expression correlations of the nine risk genes constituting the riskscore, and the results showed that the expression among RBM8A, MYC, and TPT1 genes possessed a high positive correlation. The expression of HNRNPA3, PSMA4, MAP3K8, BST2, CTSL and COL6A2 were more closely associated with each other.

In the 174 patients with esophageal squamous carcinoma in cohort GSE53625, we further performed independent external validation of the constructed m6A epigenetic riskscore. In Figure 4A, we performed survival analysis and survival curve validation in the independent validation group. The results show that our constructed riskscore is able to significantly differentiate the survival status of ESCC patients, with patients with high m6A riskscore having a significantly lower prognostic survival status than those in the low-risk group. We also applied scatter plots and dotted line plots to depict the distribution of m6A riskscore among patients in the low- and high-risk groups, as shown in Figure 4B. This suggests that the riskscore we constructed has significant prognostic stratification predictive power in both patient groups with ESCC. In more depth, we wanted to understand the distribution of the m6A epigenetic gene. In Figure 4C it is shown that RB8MA and HNRNPA3 are located on chromosomes 1 and 2, respectively, and that MYC, CTSL and MAP3K8 are expressed on chromosomes 8, 9 and 10. tPT1 and PSMA4 are distributed on chromosomes 14 and 15. bst2 and COL6A2 are distributed

10.3389/fendo.2023.1155009

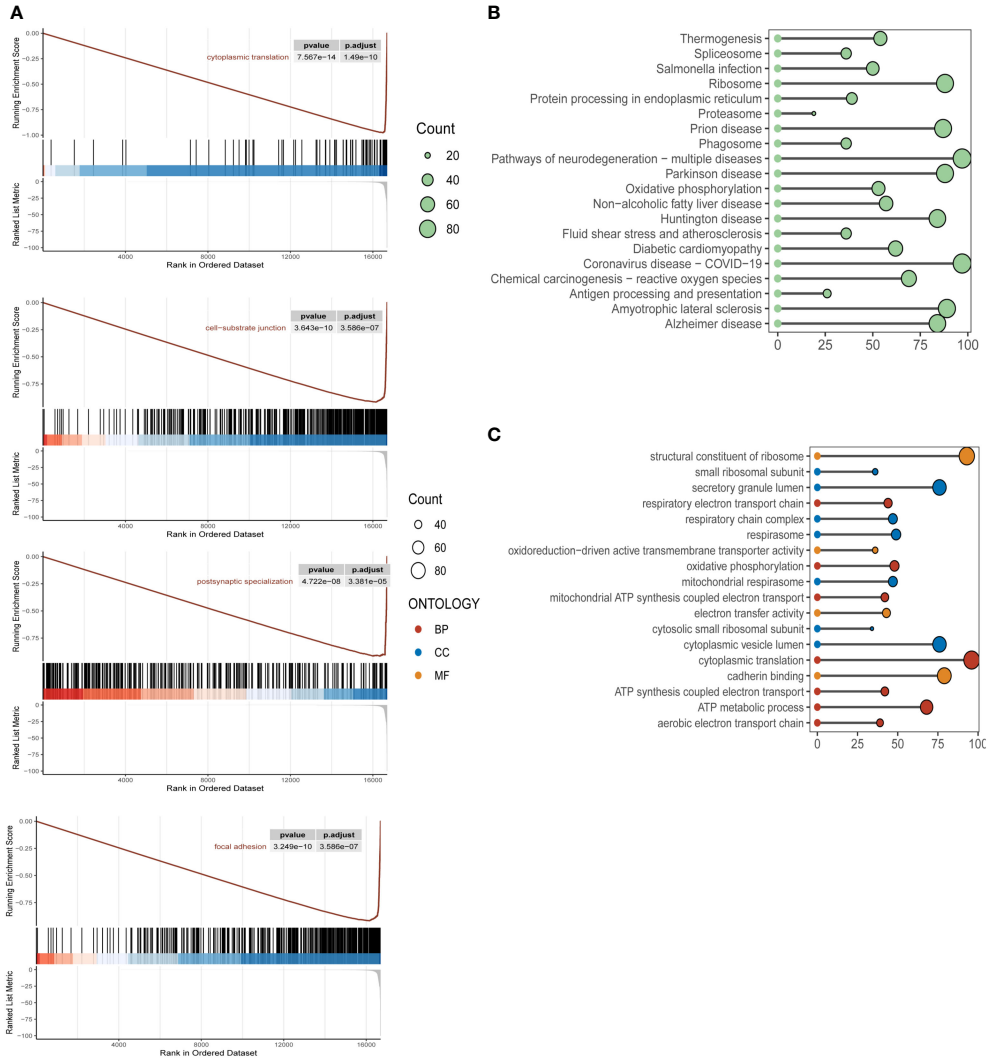

FIGURE 2
Biological functional enrichment analysis of m6A epigenetic in ESCC single cell data **(A)**. KEGG enrichment pathway analysis of m6A epigenetic-related genes in ESCC patients, mainly enriched in the functional features of cytoplasmic translation, cell-substrate junction, postsynaptic specialization, focal adhesion **(B)**. GSEA pathway analysis of m6A epigenetically related genes in ESCC patients; **(C)** GO pathway analysis of m6A epigenetically related genes in ESCC patients.

on chromosomes 19 and 22, respectively. The results showed that the genomic localization of m6A-related genes was scattered and did not show obvious clustering. In order to further facilitate the clinical use of riskscore and to combine the decision-making features of integrated clinical multifaceted analysis and judgment. We constructed a Nomogram for model visualization based on m6A epigenetic and other clinicopathological factors (Figure 4D). The Nomogram, consisting of age, Stage, Gender, and riskscore, significantly predicted the prognosis of ESCC patients in a stratified manner. In addition, we also preliminarily explored the correlation of m6A epigenetic score with the expression of immune-related signalling pathways and signalling molecules. In addition, we performed correlation analysis on riskscore and immune modulator analysis. The results showed that CD80, HAVCR2, ICOS, IL10, TNFRSF4 and multiple immune-related pathway proteins were significantly positively correlated with the expression of riskscore (Figure 4E). This tentatively revealed a potential association between m6A epigenetics and tumor immune infiltration.

Assessment of the role of m6A epigenetics in immune infiltration in ESCC

To further determine the direct association of lysosomal pathway-related risk genes with the specificity of immune infiltration and immune cell secretion in ESCC, we calculated immune infiltration scores using two methods, ssGSEA and xCell, visualized by box plot, heat map and scatter plot, respectively. The results of immune infiltration analyzed by the ssGSEA method were first analyzed. In Figure 5A, we analyzed the differential expression of multiple immune cells and immune-related proteins in the m6A

10.3389/fendo.2023.1155009

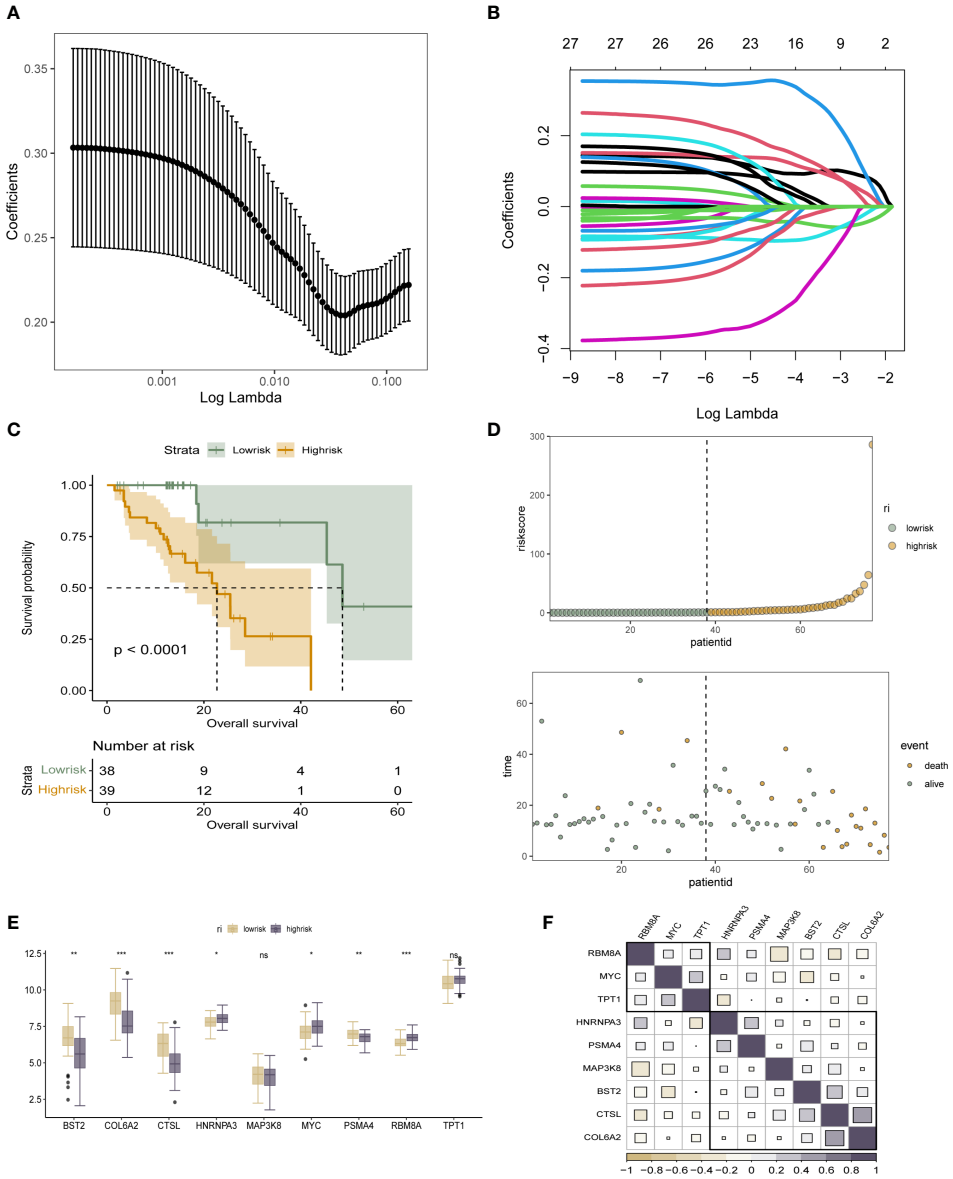

FIGURE 3
Acquisition of survival-associated differential genes for m6A epigenetic inheritance and prognostic model construction **(A, B)**. LASSO regression process for screening survival-related prognostic genes from 29 m6A epigenetically related differential genes; **(C)**. K-M analysis reveals the prognostic stratification ability of the constructed m6A epigenetically related riskscore for patients in the high-risk and low-risk groups, respectively; **(D)**. Dotted line and scatter plots reveal the different riskscore of survival time and survival status of ESCC patients, from left to right representing the high and low variation of riskscore, respectively, and scatter colours representing survival and death status; **(E)**. Box line plot revealing the expression distribution of 10 risk genes in the low- and high-risk groups of the 6A epigenetic patient population; **(F)**. Expression correlation plot of the 10 risk genes constituting the riskscore. * means <0.05, ** means <0.01, *** means <0.001, ns means >0.05.

high-risk and low-risk groups, and presented them in the form of box plots. We noted that the expression of activated CD8T cells, MDSC, gama delta T cells, activated dendritic cells, NK T cells, macrophages and Monocyte were significantly different between the different subgroups, and the expression levels of these immune cells were significantly higher in patients in the m6A epigenetic low-risk group than in those in the high-risk group. This suggests that m6A may have a potential impact on tumor development, mainly by affecting the expression of immune cells and their immune function. Further, we analyzed the expression correlation between several of the previously proposed cell types and the riskscore. The specific characteristics of the associations were analyzed by means of linear correlation plots, as shown in Figure 5B. The results showed that multiple immune cells were negatively correlated in expression with increased riskscore, p value < 0.05. In Figure 5C, we further clarified the expression correlation of multiple immune cells and immune infiltration levels with specific each gene in the m6A risk model using correlation heat map analysis. Here we found that COL6A2, BST2, TPT1, and MAP3K8 were predominantly positively correlated with high expression of immune cells. In

10.3389/fendo.2023.1155009

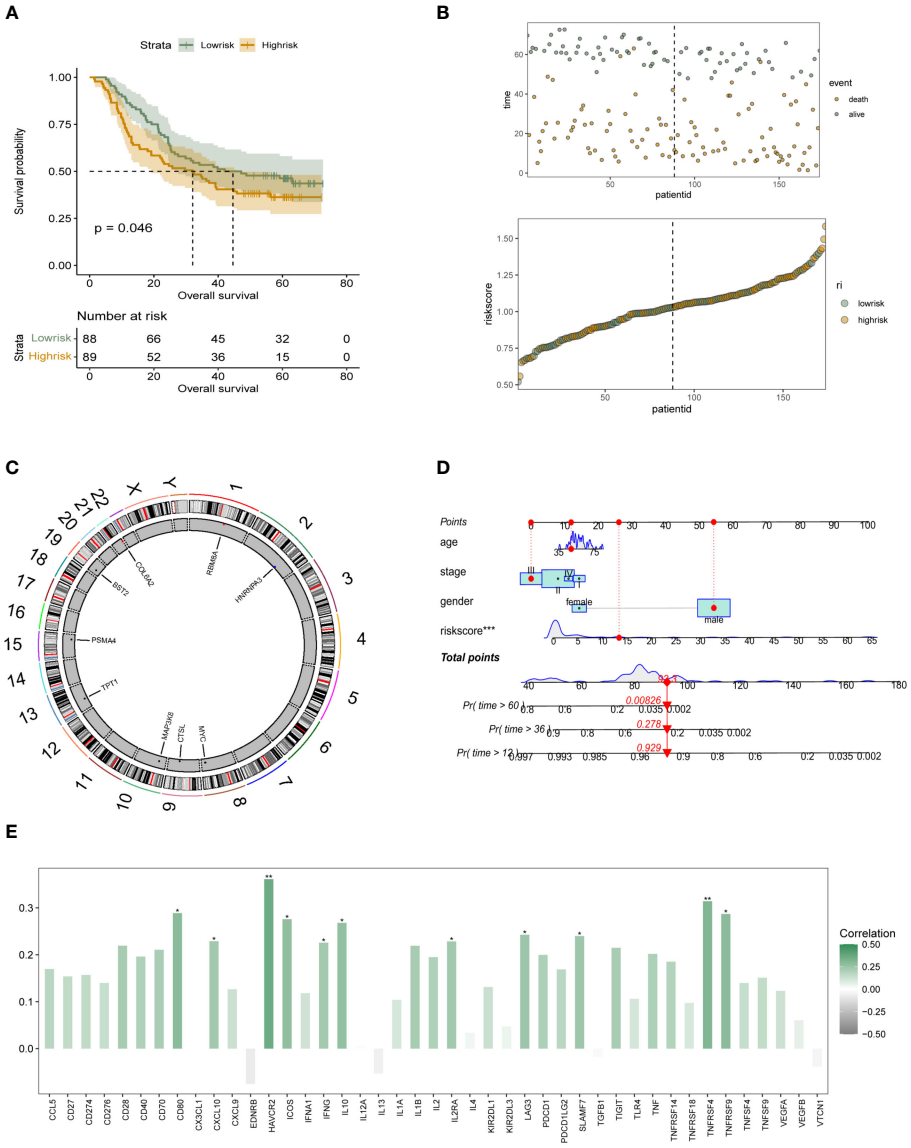

FIGURE 4
Independent validation and initial immune-related characterization of the survival risk model for m6A epigenetics **(A)** K-M analysis in GEO's independent validation database reveals the prognostic stratification ability of the constructed m6A epigenetic-associated riskscore for patients in the high-risk and low-risk groups, respectively; **(B)** Dotted line and scatter plots reveal the survival time and survival status of ESCC patients with different riskscore, from left to right, representing the riskscore of high and low variation, and the scatter colours represent survival and death status; **(C)** Chromosomal expression location map of m6A genes constituting the risk model; **(D)** Nomogram based on m6A riskscore reveals the prognostic stratification score of ESCC patients; **(E)** Bar graphs initially show the potential association between m6A epigenetic and tumor immune infiltration-related proteins. * means <0.05, ** means <0.01, *** means <0.001.

contrast, for the other genes that make up the m6A epistatic risk model, including CTSL, PSMA4, MYC, HNRNPA3, and RB8MA, there was a negative correlation with the majority of differentially expressed immune cells. In addition, we further clarified and multi-methodologically confirmed this differential expression relationship using the xCell method (Figure S2A-S2C). The results likewise showed that the m6A epigenetic-based riskscore was significantly correlated with multiple immune cell types, with ESCC patients with higher riskscore having lower expression levels of their major immune cells, with this difference being reflected mainly in NKT, CD4+ naive T cells, M1 macrophages, aDC, and macrophages.

Assessing the role of m6A epigenetics in ESCC treatment sensitivity

As a result of the immune infiltration analysis described above and the multi-method functional evaluation of different immune cell types, we have been able to understand the specific patterns of association between the m6A methylation risk model and tumor immunity and prognosis in ESCC patients. Several clinical trials have shown that current ESCC immunotherapy is less effective, and to explore whether m6A could be helpful in this pathway in ESCC, specific associations between the therapeutic sensitivity of various

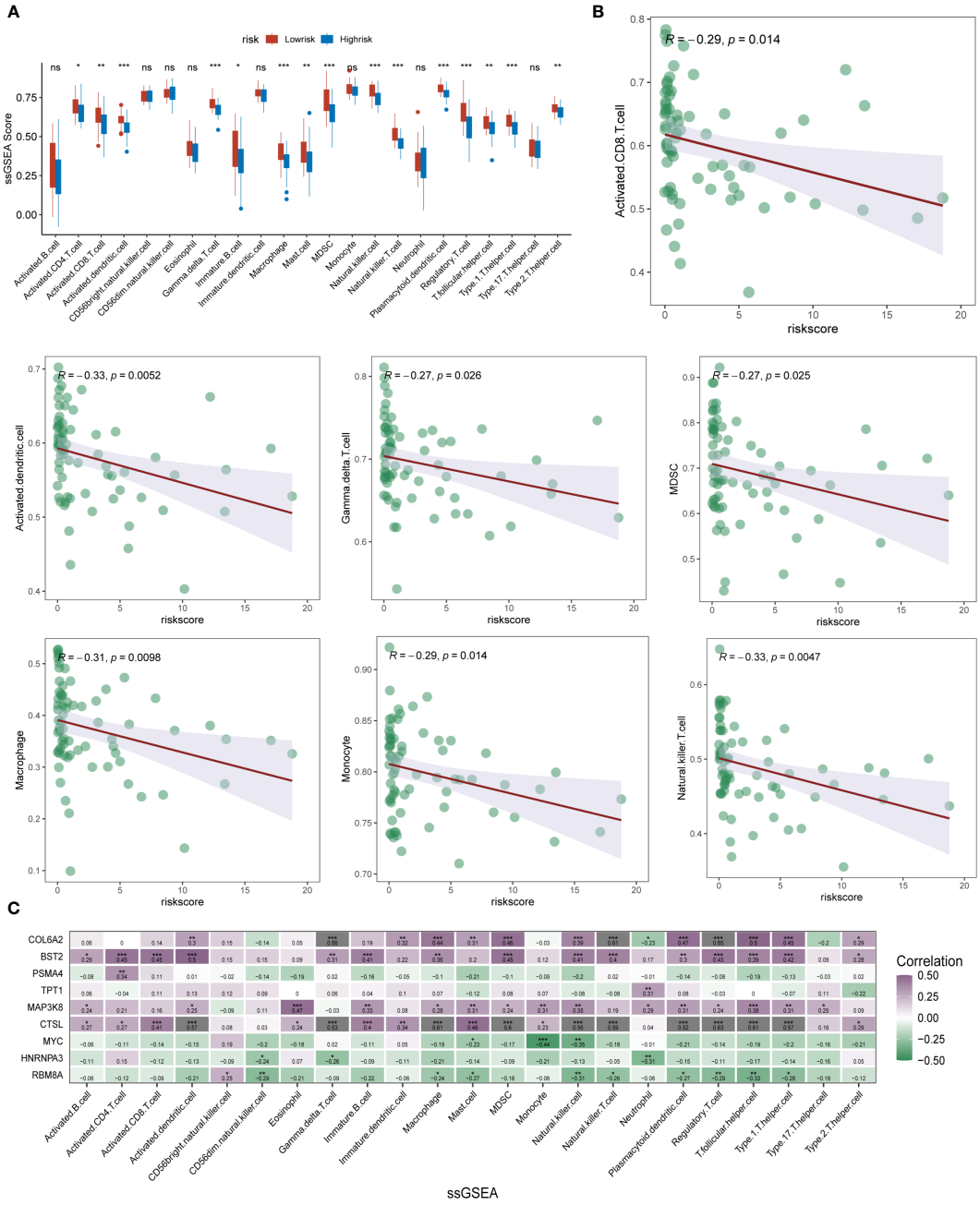

FIGURE 5
ssGSEA analysis of immune infiltration and cell expression annotation in ESCC patients. **(A)** Box plot format analyzing the differential expression of multiple immune cells and immune-related proteins in the m6A high-risk and low-risk groups. The expression of several types of immune cells, including activated CD8 T cells, MDSC, gama delta T cells, activated dendritic cells, NK T cells, macrophages, and Monocyte, differed significantly between subgroups, and the m6A epistasis The expression levels of these immune cell types were significantly higher in the low-risk group than in the high-risk group; **(B)** Linear correlation plots assessed the expression correlations between multiple immune cell types and the riskscore; **(C)** Correlational heat map analysis further clarified the correlation between multiple immune cells and immune infiltration levels and the expression of each specific gene in the m6A risk model (shades of colour indicate the level of correlation, purple indicates positive correlation, blue indicates negative correlation). * means <0.05, ** means <0.01, *** means <0.001, ns means >0.05.

oncology therapies and the riskscore subgroup were assessed. Sensitivity scores for drugs in the GDSC database were calculated based on the R package "oncoppredict". As shown in Figure 6A, for chemotherapeutic agents such as AZD8186_1918, patients in the low-risk group of the m6A riskscore had significantly lower treatment sensitivity than those in the high-risk group. In contrast, for chemotherapeutic agents such as GSK269962A_1192, Acetalax_1804, Bl-2536_1086, JQ1_2172 and PF-4708671_1129, patients in the m6A low-risk group had higher therapeutic sensitivity, which may be related to the close m6A epigenetic in tumor immune infiltration and regulation of multiple immune cells association. In Figure 6B, we used correlation heat map analysis to

10.3389/fendo.2023.1155009

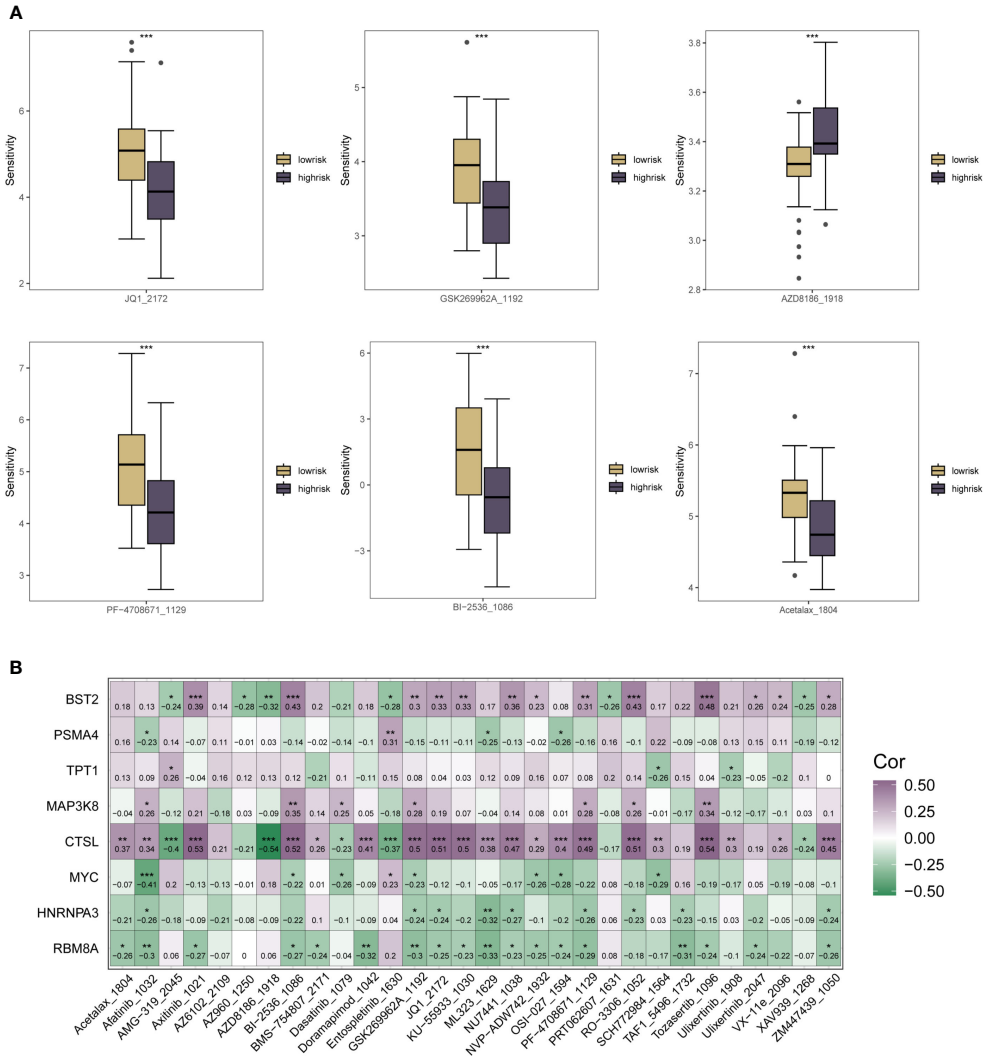

FIGURE 6
Correlation analysis of the riskscore expression of m6A in ESCC patients with the sensitivity scores of drugs in the GDSC database. **(A)** Box plots of specific expression associations between treatment sensitivity and riskscore groupings for multiple oncology therapies. Chemotherapeutic agents include AZD8186_1918, SK269962A_1192, Acetalax_1804, Bl-2536_1086, JQ1_2172, PF-4708671_1129; **(B)** Correlation heat map analysis further clarifies the therapeutic sensitivity of multiple chemotherapeutic agents with specific each gene in the m6A risk model for expression correlation. * means <0.05, ** means <0.01, *** means <0.001.

further clarify the correlation between the therapeutic sensitivity of multiple chemotherapeutic agents and the expression of each specific gene in the m6A risk model. Here we found that CTSL, BST2, PSMA4, TPT1 and MAP3K8 were predominantly positively correlated with the therapeutic sensitivity of multiple chemotherapeutic agents. In contrast, for the other genes that make up the m6A epistatic risk model, including COL6A2, MYC, HNRNPA3, and RB8MA, there was a resistance correlation with the majority of chemotherapeutic drug treatment effects.

Expression verification of risk genes

In order to further explore the expression of risk genes in ESCC tissues, we verified the expression of risk genes in ESCC tissues and adjacent normal tissues using RT-qPCR. The results showed that, except for TPT1, there was no difference in expression between cancer and paracancerous tissues, and the expression of the other 8 risk genes in ESCC tissues was significantly higher than that in paracancerous normal tissues (Figures 7A–I).

Discussions

In recent years, although the incidence and mortality rates of esophageal cancer have been significantly reduced, the overall survival rate of esophageal cancer patients after surgery is still low and the prognosis is poor. The study of the molecular biology of esophageal cancer development can provide new targeted therapeutic strategies for the precise treatment of esophageal cancer and improve the prognosis and overall survival time of patients, and is therefore a hot research topic in the field of

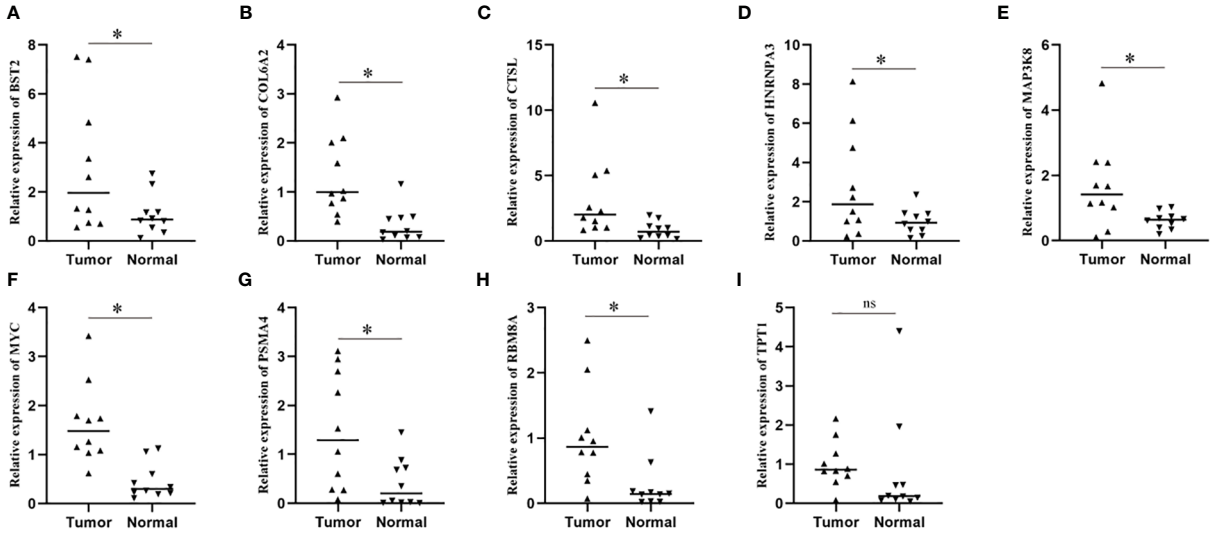

FIGURE 7
Expression levels of model genes in a real-world cohort. **(A–I)** qPCR assay was used to detect the transcription levels of model genes in tissue samples. * means <0.05.

esophageal cancer (21, 22). m6A methylated modification, as one of the most common RNA modifications, can regulate gene expression at the post-transcriptional level, and in recent years its related enzymes or proteins have also been investigated for their role in the development of esophageal cancer. In recent years, the function of its related enzymes or proteins in the development of esophageal carcinoma has also been widely investigated. Studies (23) have shown that m6A methylation-modified binding protein is specifically highly expressed in a variety of tumors and that its upregulated expression promotes tumor proliferation, migration and invasion. However, the mechanism of its role in esophageal cancer remains unclear. In this study, we investigated the specific mechanism of m6A epigenetic development in esophageal cancer and clarified the immune cell distribution of m6A-related genes in ESCC tumor microenvironment by single cell sequencing analysis. Meanwhile, m6A differential genes were selected to construct a risk model to achieve a sensitive stratification of ESCC patients' prognosis. The association of m6A epigenetics with immune infiltration and abnormal expression of immune cells was also investigated by various methods. Finally, the specific impact of differential m6A expression in esophageal cancer in ESCC on tumor chemotherapy resistance was analyzed.

Related studies have found that m6A, as the most abundant epigenomic modification in eukaryotic cells, plays an important role in tumorigenesis and progression (24). Studies have shown that among hundreds of known RNA modifications, m6 A methylation modification is the most common internal modification in messenger RNA (mRNA), affecting RNA shearing, translation, stability and epigenetic effects of certain non-coding RNAs. In mammalian cells, there are on average one to two m6 A methylation sites per 1,000 nucleotides (25). m6 A methylation regulators have been shown to be aberrantly expressed in a variety of tumors and play an important role in the regulation of malignant biological behaviours such as cell proliferation, invasion and metastasis (26), and are involved in the development and progression of various cancers such as leukaemia, glioblastoma, lung cancer and liver cancer (27). In this paper, we explored and described the composition and mode of action of m6 A modification regulators, their biological functions in the disease progression of esophageal cancer, as well as the prognostic value and potential clinical applications of m6 A methylation modification in esophageal cancer, providing some entry angles for in-depth exploration of the mechanism of esophageal cancer development and the search for esophageal cancer biomarkers and therapeutic targets. In our study, we used the ESCC single-cell mapping to perform enrichment scoring according to m6a-related genes, and divided them into m6a signature-high and m6a signature-low. And the differential genes among different m6a features were analyzed. We performed further pathway and biological function enrichment analysis of the screened DEGs. The results revealed that m6A was mainly associated with cytoplasmic translation, cell-substrate junction, Thermogenesis, structural constituent of ribosome. This suggests that m6A may influence the development of ESCC and cell mutation through chromosome structural composition pathway and cellular structural reorganization, providing a new way to investigate the specific mechanism of m6A in ESCC. In addition, the study also found a specific association between differential m6A expression and tumor immune infiltration and abnormal expression of immune cells, suggesting that m6A interferes with tumor immune pathways to influence treatment resistance in ESCC.

This study also has some limitations. Firstly, as a retrospective analysis, there are limitations in terms of data acquisition. Secondly, the study design was biased in terms of variable selection. Information on important molecular factors such as HER2/neu overexpression was not included in the data analysis (28, 29). These factors have been shown to be associated with the prognosis of patients with ESCC. Also, the database does not contain complete

treatment records, such as information on the choice of chemotherapy regimen or targeted therapy (30). Furthermore, some factors of laboratory tests, such as tumor markers, are important for survival of cancer patients (31) and the authors do not have sufficient knowledge of these factors. These advances will be incorporated into these important factors to improve the prognostic value of future m6A-related esophageal cancer studies.

In our study, a blueprint for the single-cell distribution of ESCC based on m6A methylation was explored, and on this basis risk models were constructed for immune infiltration analysis and tumor efficacy stratification in ESCC. m6A methylation plays a close role in tumor developmental invasion, but there is a lack of relevant studies reported in ESCC. Therefore, this may play an important potential guide to reveal the role played by m6A for immune escape and treatment resistance in esophageal cancer.

Data availability statement

The datasets presented in this study can be found in online repositories. The names of the repository/repositories and accession number(s) can be found in the article/Supplementary Material.

Ethics statement

Studies involving human subjects were reviewed and approved by the Ethics Committee of Shandong Provincial Hospital of Shandong University. Patients/participants provided written informed consent to participate in this study.

Author contributions

Manuscript writing: YN; Review and correct: FZ, ZY; data collection: GY. All authors contributed to the article and approved the submitted version.

Funding

This study is supported by Beijing Xisike Clinical Oncology Research Foundation [grant number Y-2019AZMS-0522]; the Natural Science Foundation of Shandong Province [grant number ZR2020MH229] and the Xisike - 2019 Qilu Oncology Research Fund Project [grant number Y-QL2019-0149].

Acknowledgments

We sincerely appreciate all members who participated in data collection and analysis.

Conflict of interest

The authors declare that the research was conducted in the absence of any commercial or financial relationships that could be construed as a potential conflict of interest.

Publisher's note

Supplementary material

The Supplementary Material for this article can be found online at: https://www.frontiersin.org/articles/10.3389/fendo.2023.1155009/full#supplementary-material

References

1. Sung H, Ferlay J, Siegel RL, Laversanne M, Soerjomataram I, Jemal A, et al. Global cancer statistics 2020: GLOBOCAN estimates of incidence and mortality worldwide for 36 cancers in 185 countries. *CA: Cancer J Clin* (2021) 71(3):209–49. doi: 10.3322/caac.21660

2. Yang Y, Hong P, Xu WW, He Q, Li B. Advances in targeted therapy for esophageal cancer. *Signal Transduct Targeted Ther* (2020) 5(1):229. doi: 10.1038/s41392-020-00323-3

3. Zhang Z, Leng Z, Fang K, Sun M, Li Z, Kang L, et al. Global research trend of esophageal squamous cell carcinoma from 2012 to 2022: A bibliometric analysis. *Front Oncol* (2022) 12:977935. doi: 10.3389/fonc.2022.977935

4. Ji Z, Bao S, Li L, Wang D, Shi M, Liu X. Hypoxia-inducible factor-2α promotes EMT in esophageal squamous cell carcinoma through the notch pathway. *Adv Clin Exp Med Off Organ Wroclaw Med Univ* (2022) 31(7):795–805. doi: 10.17219/acem/147270

5. Cui J, Wen Q, Tan X, Chen Z, Liu G. A genomic-clinicopathologic nomogram predicts survival for patients with laryngeal squamous cell carcinoma. *Dis Markers* (2019) 2019:5980567. doi: 10.1155/2019/5980567

6. Chen M, Wong C. The emerging roles of N6-methyladenosine (m6A) deregulation in liver carcinogenesis. *Mol Cancer* (2020) 19(1):44. doi: 10.1186/s12943-020-01172-y

7. Cui L, Ma R, Cai J, Guo C, Chen Z, Yao L, et al. RNA Modifications: importance in immune cell biology and related diseases. *Signal Transduct Targeted Ther* (2022) 7(1):334. doi: 10.1038/s41392-022-01175-9

8. Li R, Song Y, Chen X, Chu M, Wang Z, Zhu X. METTL3 increases cisplatin chemosensitivity of cervical cancer cells *via* downregulation of the activity of RAGE. *Mol Ther Oncolytics* (2021) 22:245–55. doi: 10.1016/j.omto.2021.05.013

9. Zeng C, Huang W, Li Y, Weng H. Roles of METTL3 in cancer: mechanisms and therapeutic targeting. *J Hematol Oncol* (2020) 13(1):117. doi: 10.1186/s13045-020-00951-w

10. Bi X, Lv X, Liu D, Guo H, Yao G, Wang L, et al. METTL3-mediated maturation of miR-126-5p promotes ovarian cancer progression *via* PTEN-mediated PI3K/Akt/mTOR pathway. *Cancer Gene Ther* (2021) 28(3-4):335–49. doi: 10.1038/s41417-020-00222-3

11. Gao F, Wang Q, Zhang C, Zhang C, Qu T, Zhang J, et al. RNA Methyltransferase METTL3 induces intrinsic resistance to gefitinib by combining with MET to regulate PI3K/AKT pathway in lung adenocarcinoma. *J Cell Mol Med* (2021) 25(5):2418–25. doi: 10.1111/jcmm.16114

12. Fu Y, Dominissini D, Rechavi G, He C. Gene expression regulation mediated through reversible m^6A RNA methylation. *Nat Rev Genet* (2014) 15(5):293–306. doi: 10.1038/nrg3724

13. An Y, Duan H. The role of m6A RNA methylation in cancer metabolism. *Mol Cancer* (2022) 21(1):14. doi: 10.1186/s12943-022-01500-4

14. Ma S, Chen C, Ji X, Liu J, Zhou Q, Wang G, et al. The interplay between m6A RNA methylation and noncoding RNA in cancer. *J Hematol Oncol* (2019) 12(1):121. doi: 10.1186/s13045-019-0805-7

15. Yin H, Zhang X, Yang P, Zhang X, Peng Y, Li D, et al. RNA m6A methylation orchestrates cancer growth and metastasis *via* macrophage reprogramming. *Nat Commun* (2021) 12(1):1394. doi: 10.1038/s41467-021-21514-8

16. Yang B, Wang J, Tan Y, Yuan R, Chen Z, Zou C. RNA Methylation and cancer treatment. *Pharmacol Res* (2021) 174:105937. doi: 10.1016/j.phrs.2021.105937

17. Shang Q, Kong W, Huang W, Xiao X, Hu W, Yang Y, et al. Identification of m6a-related signature genes in esophageal squamous cell carcinoma by machine learning method. *Front Genet* (2023) 14:1079795. doi: 10.3389/fgene.2023.1079795

18. Ye F, Hu Y, Gao J, Liang Y, Liu Y, Ou Y, et al. Radiogenomics map reveals the landscape of m6A methylation modification pattern in bladder cancer. *Front Immunol* (2021) 12:722642. doi: 10.3389/fimmu.2021.722642

19. Aran D, Hu Z, Butte AJ. xCell: digitally portraying the tissue cellular heterogeneity landscape. *Genome Biol* (2017) 18(1):220. doi: 10.1186/s13059-017-1349-1

20. Maeser D, Gruener RF, Huang RS. oncoPredict: An r package for predicting in vivo or cancer patient drug response and biomarkers from cell line screening data. *Brief Bioinform* (2021) 22(6):bbab260. doi: 10.1093/bib/bbab260

21. Zhu J, Ma S, Chen R, Xie S, Liu Z, Li X, et al. Biological correlates before esophageal cancer screening and after diagnosis. *Sci REP-UK* (2021) 11(1):17015. doi: 10.1038/s41598-021-96548-5

22. Hirata H, Niida A, Kakiuchi N, Uchi R, Sugimachi K, Masuda T, et al. The evolving genomic landscape of esophageal squamous cell carcinoma under chemoradiotherapy. *Cancer Res* (2021) 81(19):4926–38. doi: 10.1158/0008-5472.CAN-21-0653

23. Fang R, Chen X, Zhang S, Shi H, Ye Y, Shi H, et al. EGFR/SRC/ERK-stabilized YTHDF2 promotes cholesterol dysregulation and invasive growth of glioblastoma. *Nat Commun* (2021) 12(1):177. doi: 10.1038/s41467-020-20379-7

24. Shi H, Wei J, He C. Where, when, and how: Context-dependent functions of RNA methylation writers, readers, and erasers. *Mol Cell* (2019) 74(4):640–50. doi: 10.1016/j.molcel.2019.04.025

25. Liu J, Harada BT, He C. Regulation of gene expression by N(6)-methyladenosine in cancer. *Trends Cell Biol* (2019) 29(6):487–99. doi: 10.1016/j.tcb.2019.02.008

26. Zhao W, Qi X, Liu L, Ma S, Liu J, Wu J. Epigenetic regulation of m(6)A modifications in human cancer. *Mol Ther Nucleic Acids* (2020) 19:405–12. doi: 10.1016/j.omtn.2019.11.022

27. Muthusamy S. m(6)A mRNA methylation: A pleiotropic regulator of cancer. *GENE* (2020) 736:144415. doi: 10.1016/j.gene.2020.144415

28. Maruyama T, Mimura K, Sato E, Watanabe M, Mizukami Y, Kawaguchi Y, et al. Inverse correlation of HER2 with MHC class I expression on oesophageal squamous cell carcinoma. *Brit J Cancer* (2010) 103:552–9. doi: 10.1038/sj.bjc.6605772

29. Jia Y, Tian C, Wang H, Yu F, Lv W, Duan Y, et al. Long non-coding RNA NORAD/miR-224-3p/MTDH axis contributes to CDDP resistance of esophageal squamous cell carcinoma by promoting nuclear accumulation of β-catenin. *Mol Cancer* (2021) 20:162. doi: 10.1186/s12943-021-01455-y

30. Li K, Lin Y, Luo Y, Xiong X, Wang L, Durante K, et al. A signature of saliva-derived exosomal small RNAs as predicting biomarker for esophageal carcinoma: A multicenter prospective study. *Mol Cancer* (2022) 21:21. doi: 10.1186/s12943-022-01499-8

31. Salem ME, Puccini A, Xiu J, Raghavan D, Lenz H, Korn WM, et al. Comparative molecular analyses of esophageal squamous cell carcinoma, esophageal adenocarcinoma, and gastric adenocarcinoma. *Oncologist* (2018) 23:1319–27. doi: 10.1634/theoncologist.2018-0143

frontiers | Frontiers in Endocrinology

TYPE Original Research
PUBLISHED 22 March 2023
DOI 10.3389/fendo.2023.1154410

OPEN ACCESS

EDITED BY
Ruiqin Han,
Chinese Academy of Medical Sciences, China

REVIEWED BY
Jie Ren,
Dalian Medical University, China
Biao Zhang,
Dalian Medical University, China
Jian Liu,
Qingpu Branch of Zhongshan Hospital Affiliated To Fudan University, China

*CORRESPONDENCE
Wei Wang
wangwei15261883958@163.com
Hong Liu
Lh029@163.com
Jiaheng Xie
xiejiaheng@njmu.edu.cn

†These authors have contributed equally to this work and share the first authorship

SPECIALTY SECTION
This article was submitted to Cancer Endocrinology, a section of the journal Frontiers in Endocrinology

RECEIVED 30 January 2023
ACCEPTED 09 March 2023
PUBLISHED 22 March 2023

CITATION
Zhang P, Pei S, Gong Z, Ren Q, Xie J, Liu H and Wang W (2023) The integrated single-cell analysis developed a lactate metabolism-driven signature to improve outcomes and immunotherapy in lung adenocarcinoma.
Front. Endocrinol. 14:1154410.
doi: 10.3389/fendo.2023.1154410

The integrated single-cell analysis developed a lactate metabolism-driven signature to improve outcomes and immunotherapy in lung adenocarcinoma

Pengpeng Zhang[1†], Shengbin Pei[2†], Zeitian Gong[1†], Qianhe Ren[1†], Jiaheng Xie[3*], Hong Liu[4*] and Wei Wang[1*]

[1]Department of Thoracic Surgery, The First Affiliated Hospital of Nanjing Medical University, Nanjing, China, [2]Department of Breast Surgery, The First Affiliated Hospital of Nanjing Medical University, Nanjing, China, [3]Department of Burns and Plastic Surgery, The First Affiliated Hospital of Nanjing Medical University, Nanjing, China, [4]Department of Thoracic Surgery, The Second Hospital of Nanjing, Nanjing, China

Background: It has been suggested that lactate metabolism (LM) is crucial for the development of cancer. Using integrated single-cell RNA sequencing (scRNA-seq) analysis, we built predictive models based on LM-related genes (LMRGs) to propose novel targets for the treatment of LUAD patients.

Methods: The most significant genes for LM were identified through the use of the AUCell algorithm and correlation analysis in conjunction with scRNA-seq analysis. To build risk models with superior predictive performance, cox- and lasso-regression were utilized, and these models were validated on multiple external independent datasets. We then explored the differences in the tumor microenvironment (TME), immunotherapy, mutation landscape, and enriched pathways between different risk groups. Finally, cell experiments were conducted to verify the impact of AHSA1 in LUAD.

Results: A total of 590 genes that regulate LM were identified for subsequent analysis. Using cox- and lasso-regression, we constructed a 5-gene signature that can predict the prognosis of patients with LUAD. Notably, we observed differences in TME, immune cell infiltration levels, immune checkpoint levels, and mutation landscapes between different risk groups, which could have important implications for the clinical treatment of LUAD patients.

Conclusion: Based on LMRGs, we constructed a prognostic model that can predict the efficacy of immunotherapy and provide a new direction for treating LUAD.

KEYWORDS

lung adenocarcinoma, lactate, signature, prognosis, immunotherapy

1 Introduction

Lung cancer (LC) is a highly prevalent malignant tumor and the leading cause of cancer-specific deaths worldwide, resulting in over 350 deaths per day in 2022 (1). In the past decade, significant improvements have been made in the science of non-small cell lung cancer (NSCLC), which occupies almost 80% of all LC cases. LUAD is the most common histological subtype of NSCLC. In terms of disease prevention, the wide application of low-dose chest computed tomography has achieved the goal of early detection, greatly reducing all-cause mortality (2, 3). The treatment of LC has also evolved with the generation of several lines of tyrosine kinase inhibitors (TKIs) and immune checkpoint inhibitors (ICIs). Despite that, the 5-year overall survival rate remains poor, ranging from 68% in patients with stage IB to less than 10% in patients with stage IV (4). Thus, it is imperative to explore novel molecular markers for LUAD to improve prognosis.

Since the Warburg effect was proposed in the 1920s, there has been ample evidence that lactic acid plays a critical role in malignant cell proliferation (5). As we know, glucose is the main energy source of tumor cell metabolism. While, due to abnormal metabolic activities, cancer cells desire an excessive quantity of nutrients and oxygen. Based on the Warburg effect, tumor energy metabolism is inclined to anaerobic glycolysis rather than oxidative phosphorylation, even under an aerobic state, which leads to a hypoxic tumor microenvironment (TME) (6). Lactate, the byproduct of glycolysis, is found concentrated in tumor tissue 5-20 times higher than in normal tissue (7). An increased concentration of lactate in the TME is correlated with rapid tumor growth, metastasis, and resurgence, also creating an immunosuppressive TME favorable for a cancer cell to gain immune escape potential (8). Tumor cells may produce lactate and transfer it to surrounding cancer cells, immune cells, and stromal cells, resulting in metabolic reprogramming (9). Thus, lactate plays the role of a mediator between intrinsic metabolism and immunosuppression. Recent studies have identified a number of lactate-metabolizing enzymes that are dysregulated in LUAD, including lactate dehydrogenase A (LDHA), monocarboxylate transporters (MCTs), and lactate oxidase (LOX). Targeting these enzymes with small molecule inhibitors has shown promise as a therapeutic strategy for LUAD (10). Reducing the concentration of lactate by blocking the production pathway of lactate or the transport of lactate has proven to be a promising therapeutic strategy, especially for drug-resistant malignant tumors (11). Although the LMRGs have been proven to perform a critical function in the progression of LUAD in recent years (12, 13), comprehensive analyses of the relationship between LMRGs and the diagnosis, risk stratification, and prognosis of LUAD are urgently needed.

Hence, in the present study, we aimed to screen out the LMRGs in LUAD and elaborate on the role of LMRGs in the TME and prognosis of LUAD. Then, we will establish a signature capable of predicting the prognosis of patients with LUAD on basis of LMRGs. Our research may improve the existing lactate-dependent therapeutic schedule, providing novel insights into prognostic biomarkers and therapeutic targets for LUAD.

2 Materials and methods

2.1 Data acquisition

In this study, LUAD scRNA-seq data were obtained from the GSE150938 database (https://www.ncbi.nlm.nih.gov/geo/), which consisted of 12 LUAD samples. The training cohort comprised LUAD RNA expression patterns and relevant clinical information from The Cancer Genome Atlas (TCGA) database (https://portal.gdc.cancer.gov/). Additionally, the validation set was obtained from the GSE29016, GSE30219, GSE31210, and GSE42127 GEO expression profiles. To facilitate data comparability, all expression data were converted to transcripts per million (TPM) format. The "sva" R package was used to eliminate the batch effect, and all data were transformed to log2 before analysis. A total of 247 lactate-related metabolic genes (LMRGs) with correlation values greater than 15 were selected from the GeneCards database (https://www.genecards.org/) for further analysis.

2.2 scRNA-seq data processing and cell annotation

We validated the scRNA-seq data using the "Seurat" R program. Screening criteria included expressing genes in at least three cells, expressing 200-7000 genes in each cell, and expressing no more than 10% of mitochondrial genes. Finally, 46,286 appropriate cells were identified. The top 3000 highly variable genes were screened using the "FindVariableFeatures" program. The canonical correlation analysis (CCA) function "findintegrationanchors" was used to reduce batch effects that might interfere with downstream analysis. We utilized the "IntegrateData" and "ScaleData" methods to appropriately integrate and expand the data. Anchor points were discovered using principal component analysis (PCA) dimensionality reduction. To locate relevant clusters, the first 20 PC were tested using the t-distribution random neighborhood embedding (t-SNE) technique. We obtained 20 cell clusters by using the "FindNeighbors" and "FindClusters" functions (resolution = 0.8). We assessed cell cycle heterogeneity along cell clusters using cell cycle markers from the "seurat" package. The "CellCycleScoring" program was used to generate cell cycle scores based on the expression of G2/M and S-phase markers. The "FindAllMarkers" program was used to identify differentially expressed genes (DEGs) for each cluster. To select which genes were employed as markers for each cluster, we used a cut-off threshold and modified $P< 0.01$ and log2 (foldchange) > 0.25 criterion. Cell types were meticulously defined using common marker genes for each cluster. The "AUCell" R program, which analyzes the activity state of gene sets, was used to assign LM activity ratings to each cell. The cells were separated into high- and low-LM-AUC groups based on the median AUC score, and visualization was done with the "ggplot2" R program. We next performed differential analyses to discover DEGs in high- and low-LM-AUC groups, and 440 DEGs were selected for further investigation. Furthermore, we used correlation analysis to look at

the genes most connected with LM activity, with the top 150 most associated genes being included for future study. The DEGs and genes discovered through association analysis were the ones that had the greatest effect on LM activity (590 genes in total).

2.3 Construction and validation of the risk scoring

We used univariate analysis on the 590 genes that regulated LM activity to find genes that significantly related with patient survival ($P< 0.01$). Following that, LASSO and multivariate regression analysis were used to further screen for genes and risk coefficients that were highly linked with prognosis. Based on the coefficients revealed by the multivariate analysis, each LUAD patient was assigned a risk score. Patients from the TCGA-LUAD were separated into high- and low-risk groups based on their median risk score. Meanwhile, survival curves were plotted using the Kaplan-Meier technique for prognostic reasons, and log-rank tests were used to establish statistical significance. The prediction model's effectiveness was evaluated using receiver operating characteristic (ROC) curves; an AUC value of >0.65 indicated outstanding performance. The signature's prediction capacity was verified in nine distinct GEO datasets using survival analysis and AUC. PCA analysis was used to show the distribution of patients in different risk groups. A similar method was used to validation cohorts.

2.4 Nomogram construction

We created a nomogram that used the risk score, age, and pathological stage as independent prognostic criteria to compute the probability of OS at 1-, 3-, and 5- years (14). The receiver operating characteristic (ROC) curve, calibration curve, and concordance index curve were also utilized to evaluate the prediction accuracy of the nomogram. The prognostic significance of risk score clinical characteristics was assessed using stratified analysis (age, pathological T, N stage, and clinical stage).

2.5 Mutation landscape

The TCGA database was used to generate gene mutation profiles from LUAD patients, and the "ComplexHeatmap" R package was used to visualize the mutation landscape and immune infiltration scores (15). According to the median risk score and tumor mutational load, TCGA-LUAD patients were separated into four groups (H-TMB+high-risk, H-TMB+low-risk, L-TMB+high-risk, and L-TMB+low-risk), and their survival disparities were compared.

2.6 Assessment of immune infiltration

The timer 2.0 database was used to download data from seven different methods that were utilized to determine the degree of immune infiltration in TCGA-LUAD patients. A heatmap graphic was used to show differences in immune infiltration across various risk categories. The "estimate" R program was used to quantify the stromal and immune cell abundance and tumor purity in malignant tumor tissues based on the expression patterns (16). A higher score indicates that there is a greater percentage of TME components.

2.7 Immunotherapy comparisons

Immune checkpoints are a group of molecules that are expressed on immunological cells that control the amount of immune activation. They are critical in controlling excessive immunological activation. We evaluated the levels of expression of well-known immune checkpoint genes in both groups (ICGs). Correlations between ICGs expression, model genes, and risk scores were investigated further. The Immunophenoscores (IPS) for LUAD were obtained from the Cancer Immunome Atlas (TCIA) database (17).

2.8 Enrichment analysis

The GSVA used the MSigDB signature gene sets "h.all.v7.5.1.symbols.gmt" (https://www.gseamsigdb.org/gsea/msigdb/index.jsp). The GSEABase program was then used to analyze the activity of each gene set in each sample. GSEA was used to identify which signaling pathways and biological activities were enriched in the high- and low-risk groups. ssGSEA was used to determine the enrichment scores of infiltrating immune cells and immunological function.

2.9 The Role of AHSA1 in LUAD

Using the timer database, researchers investigated the expression of AHSA1 in pan-cancer. Patients were divided into two groups based on AHSA1 expression to study changes in survival: both high- and low- expression.

2.10 Cell lines culture

The Cell Resource Center at Shanghai Life Sciences Institute provided BEAS-2B, A549, and H1299 human LUAD cell lines. These cells were cultured in F12K or RPMI-1640 (Gibco BRL, USA) with 10% FBS, 1% streptomycin, and penicillin (Gibco, Invitrogen, Waltham, MA, USA). Cells were grown at 37°C, 5% CO2, and 95% humidity.

2.11 Cell transfection

SIRNAs knocked down AHSA1 (siRNAs). Supplementary Table S1 included AHSA1 siRNA sequences. In a 6-well plate, cells were plated at 50% confluence and infected with negative

control (NC) and knockdown (siAHSA1). All transfections used Lipofectamine 3000 (Invitrogen, USA).

2.12 Extraction of RNA and Real-Time PCR (RT-PCR)

Cell lines were TRIzol-extracted for total RNA (15596018, Thermo). Using PrimeScriptTMRT, cDNA was made (R232-01, Vazyme). SYBR Green Master Mix (Q111-02, Vazyme) was used for real-time polymerase chain reaction (RT-PCR), and each mRNA was standardized to GAPDH. Expression levels were counted using 2−-Ct. Supplementary Table S1 lists all primer sequences from Beijing-based Tsingke Biotech.

2.13 Colony formation

We transfected $1x10^3$ cells into each well of a 6-well dish and cultured them for 14 days. The cells were fixed in 4% paraformaldehyde for 15 minutes and then stained with Crystal violet (Solarbio, China).

2.14 EdU

After the cells adhered to the side of the 96-well plate, the experiment was performed. Then, the manufacturer's 5-Ethynyl-2'-deoxyuridine (EdU) test was carried out (Ribobio, China). Cells that were actively dividing were tallied using an inverted microscope.

2.15 Wound-healing assay

A cell incubator was used to grow transfected cells in 6-well plates to 95% confluence. Each cultured well was scraped along a single straight line using a sterile 20-L plastic pipette tip, and the scrapings and any loose cells or debris were rinsed away twice with phosphate-buffered saline. Taking pictures of the scratches at 0h and 48h, we next used the Image J program to quantify the breadth of the wounds.

2.16 Transwell assay

The transwell test was used to examine the invading and migrating cells. Incubation of treated A549 and H1299 cells ($2x10^5$ per well) in 24-well plates began after 12 hours. The cells' invading and migrating abilities were measured by precoating the top of the plate with matrigel solution (BD Biosciences, USA) or leaving it untreated. The cells on the top surface were removed, while the remaining cells on the bottom were fixed in 4% paraformaldehyde and stained with 0.1% crystal violet (Solarbio, China).

2.17 Statistical analysis

Data and statistics were processed in R (version 4.1.3). The experimental data were analyzed using Graphpad and Image J (1.8.0) (version 9.4.0). Kaplan-Meier curves and a log-rank test were used to evaluate the differences in survival times between the two groups (18). The "survminer" R program was used to generate all survival curves. Cox and lasso regression analysis were used to assess risk factors. For visualization, we utilized "ggplot2" program, and for analysis, the R package "survival" was used to calculate both OS and risk scores. It was made using "Pheatmap", an online heatmap generator. Significant quantitative differences for normally distributed variables were identified using a two-tailed t-test or a one-way analysis of variance. For non-normally distributed data, the significance of any differences was determined using either the Wilcoxon test or the Kruskal-Wallis test. All statistical testing was performed in R. If the number is less than 0.05, it is considered to be statistically significant.

3 Results

3.1 Analysis process of scRNA-seq

Figure 1 depicted the flowchart for the study. A total of 46286 high-quality cells were deemed suitable for future study. The expression characteristics of each sample were shown in Supplementary Figure S1A. There was a statistically significant positive connection between sequencing depth and total intracellular sequences (R=0.94, Supplementary Figure S1B). The PCA reduction plot indicated no discernible differences in cell cycles (Supplementary Figure S1C). The study included 12 samples, and the cell distribution within each sample was mostly identical, indicating that there was no discernible batch impact between samples, which might be useful for future research (Supplementary Figure S1D). Following that, the dimensionality reduction methods, namely t-SNE, classified all cells into 22 clusters (Figure 2A). Bubble plots depicted the typical marker genes (19) of various cell types as well as the connection of distinct groups (Figure 2B). In Figure 2C, an t-SNE plot was used to depict the distribution of each cell population. Each cell's LM activity was evaluated. AUC values were higher in cells that expressed more LMRGs, which were mostly orange-colored myeloid cells (Figure 2D). Based on the AUC score median values, all cells were assigned an AUC score for the LMRGs and divided into high- and low-LM-AUC groups (Figure 2E). Correlation study revealed that the genes most closely associated with LM activity (Figure 2F). The single-cell study yielded the 590 genes most linked with LM activity.

3.2 Construction and validation of the risk scoring

We eliminated the batch effect from the GEO-obtained data for improved data consistency, and Figures 3A, B displayed the PCA

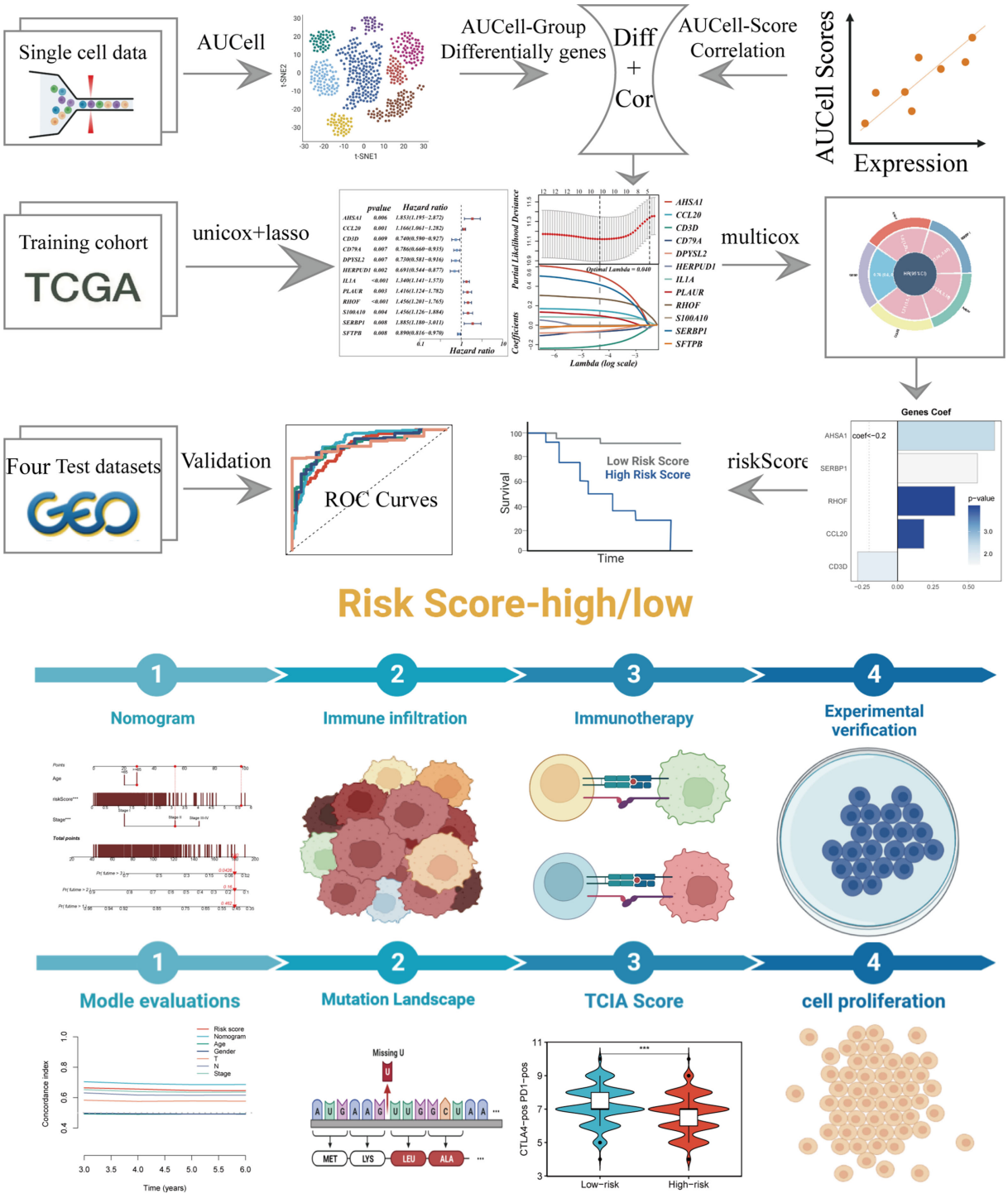

FIGURE 1
The workflow of the present study.

plots before and after the batch effect was removed from the TCGA data, respectively. Following that, TCGA was separated into 6:4 training and validation sets, and univariate COX analysis was done, with the findings indicated by a forest plot (Figure 3C, P< 0.01), before lasso (Figure 3D) and multivariate COX regression analysis were used to create the risk model consisting of 5 genes. Figure 3E displayed the coefficients associated with each model gene from which the risk score was computed. The following was the formula:

$$risk\ \ score = \sum_{n=i}^{k}(Coef_i \mathrm{Exp}i)$$

The coefficient and expression of each model gene were represented by Coefi and Expi, respectively, and the risk score for each sample

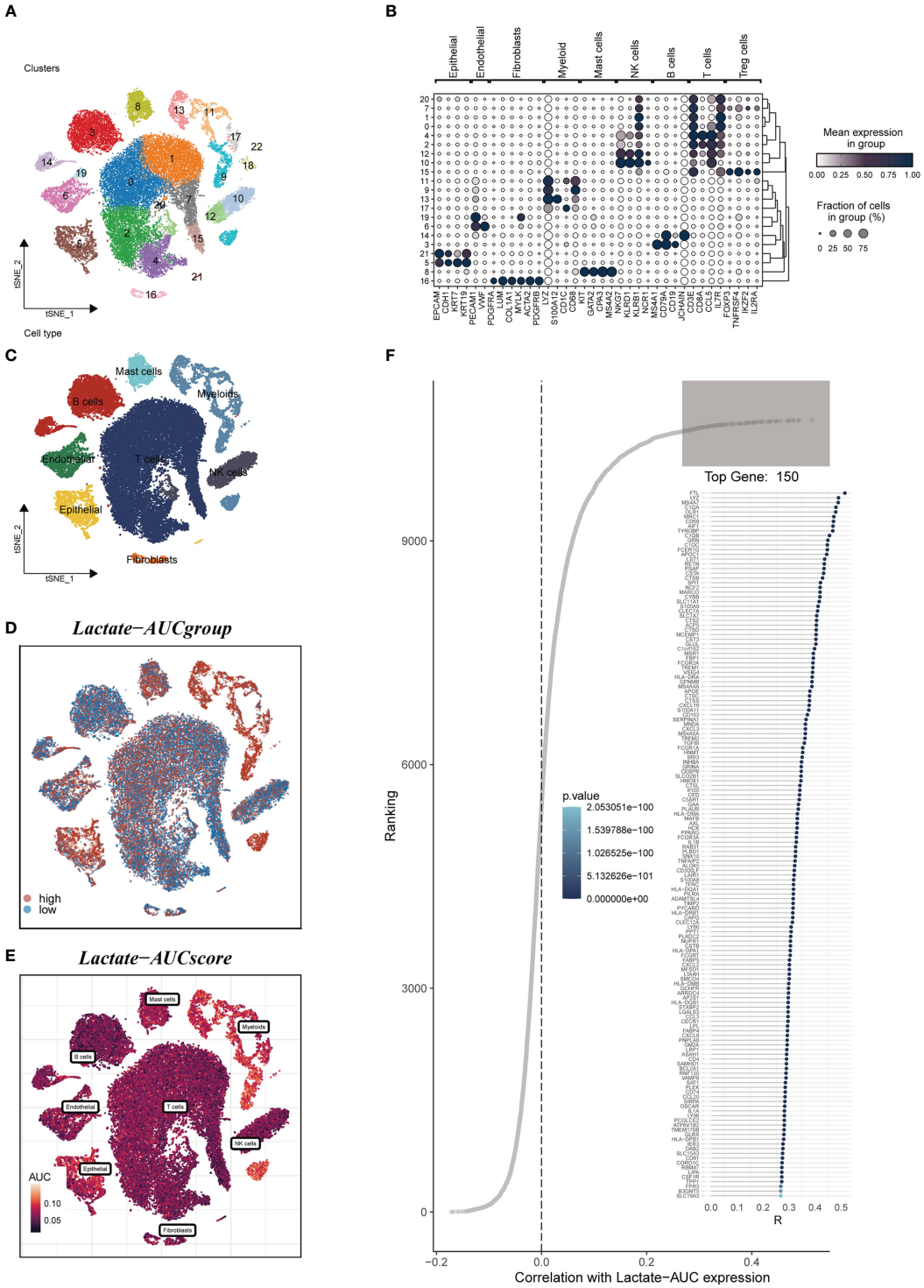

FIGURE 2
Annotation of single-cell data. **(A)** The t-SNE plot showed that all the cells in 22 clusters. **(B)** A bubble plot exhibited typical marker genes for each cell cluster. **(C)** The t-SNE map indicates that LUAD samples can be annotated as 8 cell types in the TME (different colors represent different cell types). **(D, E)** AUCell score and groups of LM activity in each cell. **(F)** Correlation analysis between LM-AUCell score and genes.

was determined using the above method. The circle diagram depicted the predictive HR value of five model genes, and it was obvious that AHSA1, SERBP1, RHOF, and CCL20 are at high risk. CD3D, on the other hand, had been demonstrated to be a low-risk gene (Figure 3F).

3.3 Survival analysis and model evaluation

Based on median risk values, patients were split into high- and low-risk groups, and a survival analysis revealed a substantial OS difference for TCGA-LUAD patients (train set, test set, and all set,

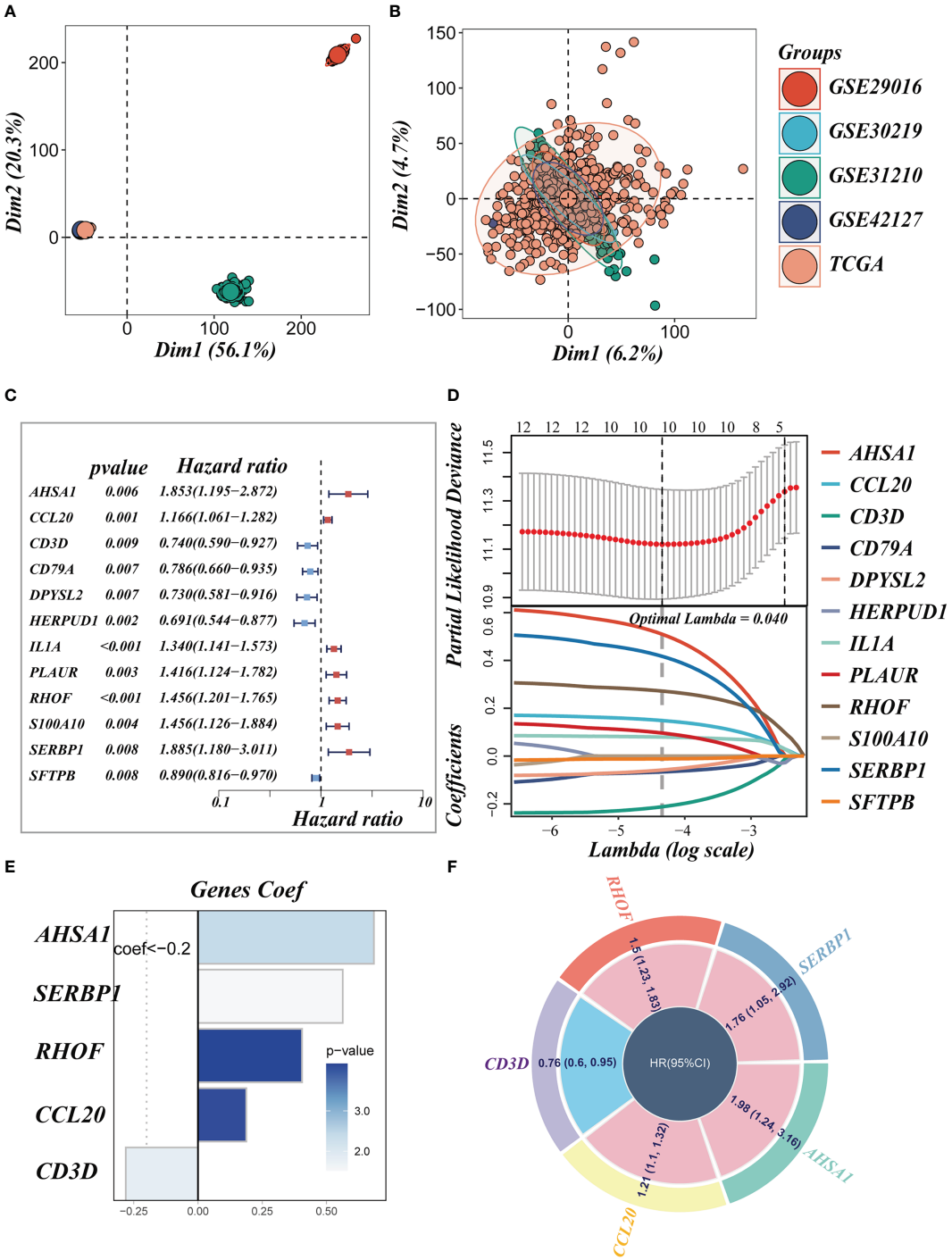

FIGURE 3
Construction of the signature. **(A, B)** PCA plots before and after removal of batch effects for 5 datasets. **(C)** A forest plot presents prognostic associated LMRGs. **(D)** Eleven prognostic LMRGs were included in the LASSO regression analysis to screen the most important model genes. **(E, F)** Coefficients for model genes as well as HR values for model genes.

Figures 4A–C). Similarly, four GEO datasets also had statistically significant survival differences (P< 0.05; Figures 4G–I; 5A). According to the expression levels of the model genes, PCA analysis was performed on all the samples from TCGA and GEO, and the results showed that the samples of the high- and low- risk groups could be clearly distributed into two clusters Figures 4D–F, J–L and Figure 5B. ROC analysis measured the discrimination of this signature, with 1-, 3-, 5-,7-, and10-year AUCs of 0.0.734, 0.721, 0.695, 0.710, and 0.682 in TCGA-train set; 0.711, 0.707, 0.602, 0.615, and 0.597 in TCGA-test set; 0.724, 0.719, 0.647, 0.658, and

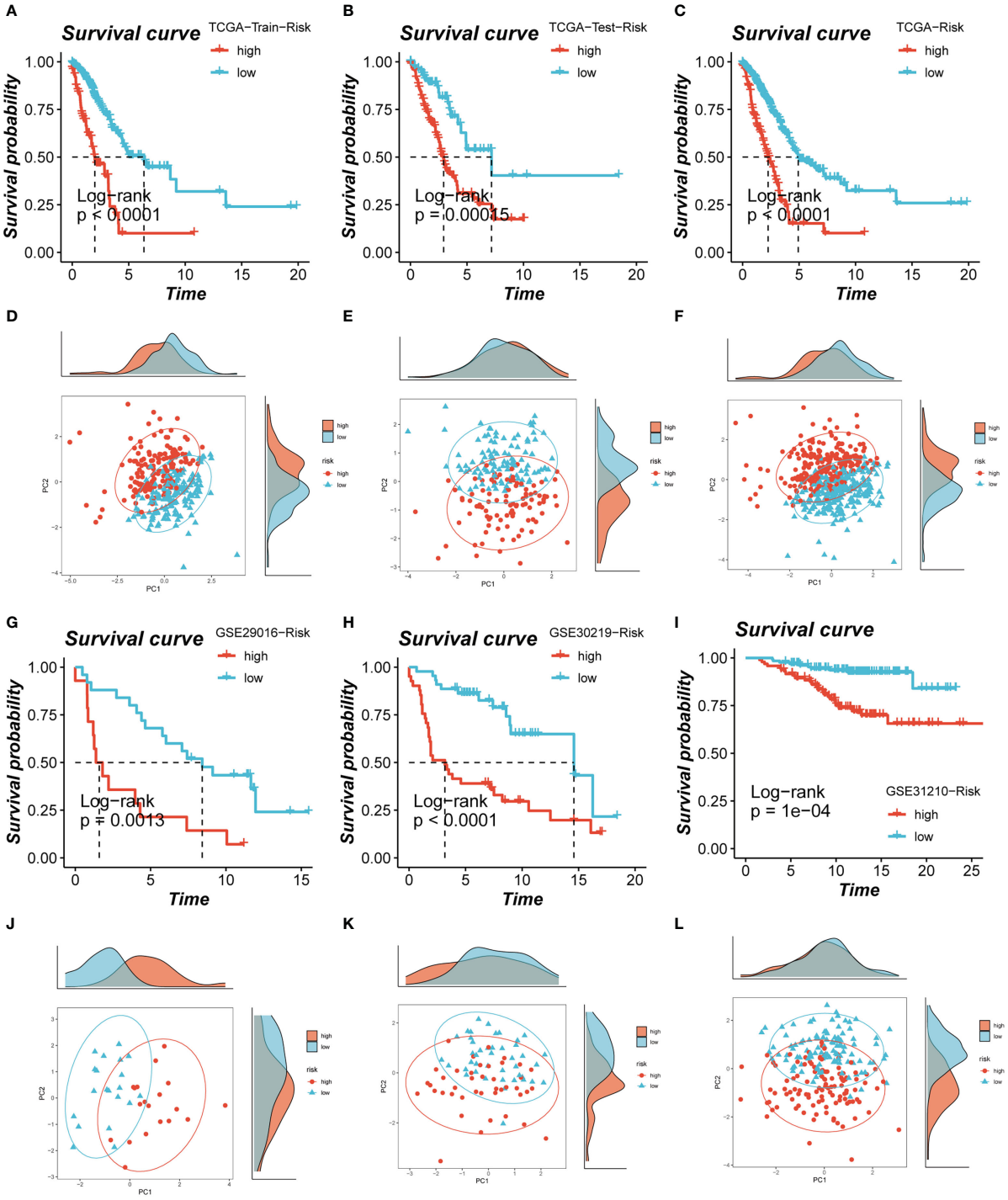

FIGURE 4
Assessment of risk models. **(A-C)** Kaplan-Meier survival analysis of signatures in the TCGA (train, test, and all set) datasets. **(D-F)** The PCA analysis was used to evaluate the distribution of the samples in the TCGA (train, test, and all set) datasets. **(G-I)** Kaplan-Meier survival analysis of signatures in the GEO (GSE29016, GSE30219, and GSE31210) datasets. **(J-L)** PCA analysis showed the distribution of samples in the GEO (GSE29016, GSE30219, and GSE31210) cohorts.

0.632 in TCGA-all set; 0.626, 0.728, 0.687, 0.616, and 0.607 in GSE29016; 0.690, 0.715, 0.737, 0.709, and 0.654 in GSE30219; 0.725, 0.645, 0.650, and 0.666 in GSE31210 (LUAD-patients on survival less than 1 year were lacking); and 0.764, 0.608, 0.596, 0.576, and 0.6606 in GSE42127 (Figures 5C-I).

3.4 Construction and validation of nomogram

A heatmap was constructed to highlight the correlations between model genes and clinical characteristics. Some clinical

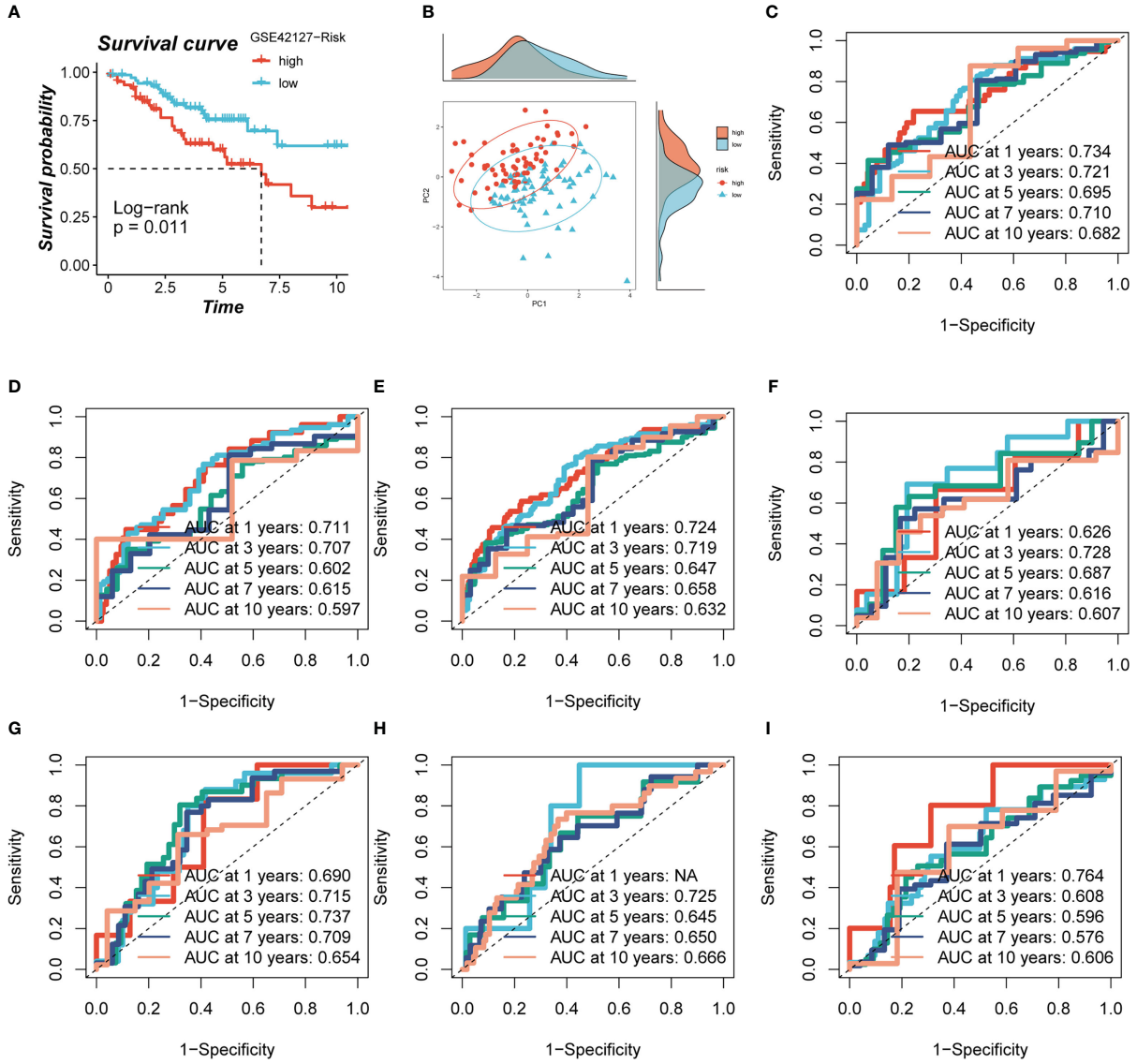

FIGURE 5
Evaluation of model. **(A, B)** Survival analysis revealed the survival significance of high and low risk scores in the GSE42127 cohort, and the sample distribution of high and low risk groups was shown in the PCA plot. **(C-I)** The ROC curve showed the survival accuracy of the model in TCGA (train, test, and all set) and GEO (GSE29016, GSE30219, GSE31210 and GSE42127) cohorts.

factors (T stage, N stage, clinical stage, and survival status) differed significantly between the high- and low-risk groups (P< 0.05, Supplementary Figure S2A). The prevalence of different phases across groups was then compared and shown as a percentage bar plot. We observed that the high-risk group had worse T stage, N stage, and clinical stage (Figures 6A-D). Based on the TCGA-LUAD dataset, a predictive nomogram comprising risk score and clinicopathological parameters (age and clinical stage) was built to better predict prognosis (Figure 6E). Survival statuses at 1, 2, and 3 years were used as clinical outcome measures. The calibration plot revealed that this signature had outstanding prediction ability for 1-, 2-, and 3-year survival rates (Figure 6F). The C-index curves revealed that the nomogram outperforms the risk score and any other clinical measure in predicting prognosis (Figure 6G). The predictive ability of the nomogram score, risk score, and other clinical characteristics was also evaluated using ROC analysis. The AUC value of the nomogram score over one, three, five, and seven years was 0.760, 0.7749, 0.711, and 0.734, which were greater than risk scores and other clinical indicators (Figures 6H–K).

3.5 Mutational landscape

This was especially true for personalized cancer therapy, where mutations in certain genes play a crucial role. We studied the somatic mutation profiles of various risk categories. Statistics indicated that the high-risk group had a higher mutation frequency for the top 20 high-frequency mutated genes (Figure 7A), which included TP53, TTN, and CSMD3. Figure 7B indicated a significant difference in TMB between the high- and

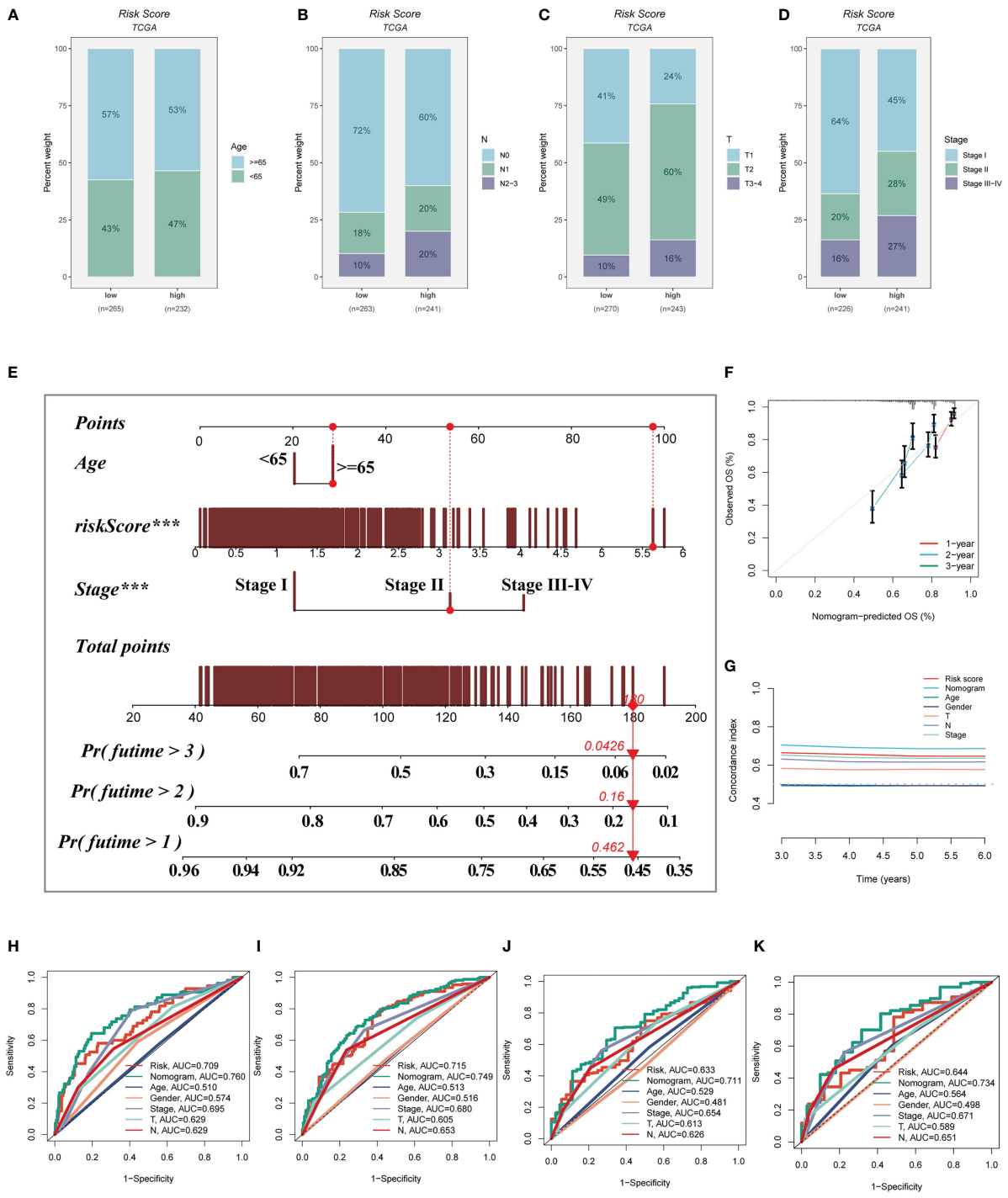

FIGURE 6
Building a more accurate nomogram. **(A-D)** The proportion of clinical characters (age, N stage, T stage, and clinical stage) in different risk groups. **(E)** Nomogram was constructed by combining clinical features with risk score. **(F)** The calibration plots test consistency between the actual OS rates and the predicted survival rates, with the 45°line representing the best prediction. **(G)** The C-index curves were used to evaluate the predictive performance of different clinical characteristics, nomogram scores and risk scores. **(H-K)** ROC curves for 1, 3, 5, and 7 years showed AUC values for various clinical factors, risk scores, and nomogram scores.

low-risk groups, with greater TMB in the high-risk group. Spearman correlation analysis was utilized to study the association between risk score and TMB, and a significant positive correlation was obtained (R = 0.12, P< 0.001, Figure 7C). We then divided patients into four groups (H-TMB+high-risk, H-TMB+low-risk, L-TMB+high-risk, and L-TMB+low-risk) based on median TMB values and median risk values; the results showed that LUAD patients with H-TMB+low-risk had the best prognosis, and LUAD patients with L-TMB+high-risk had the worst prognosis (Figure 7D).

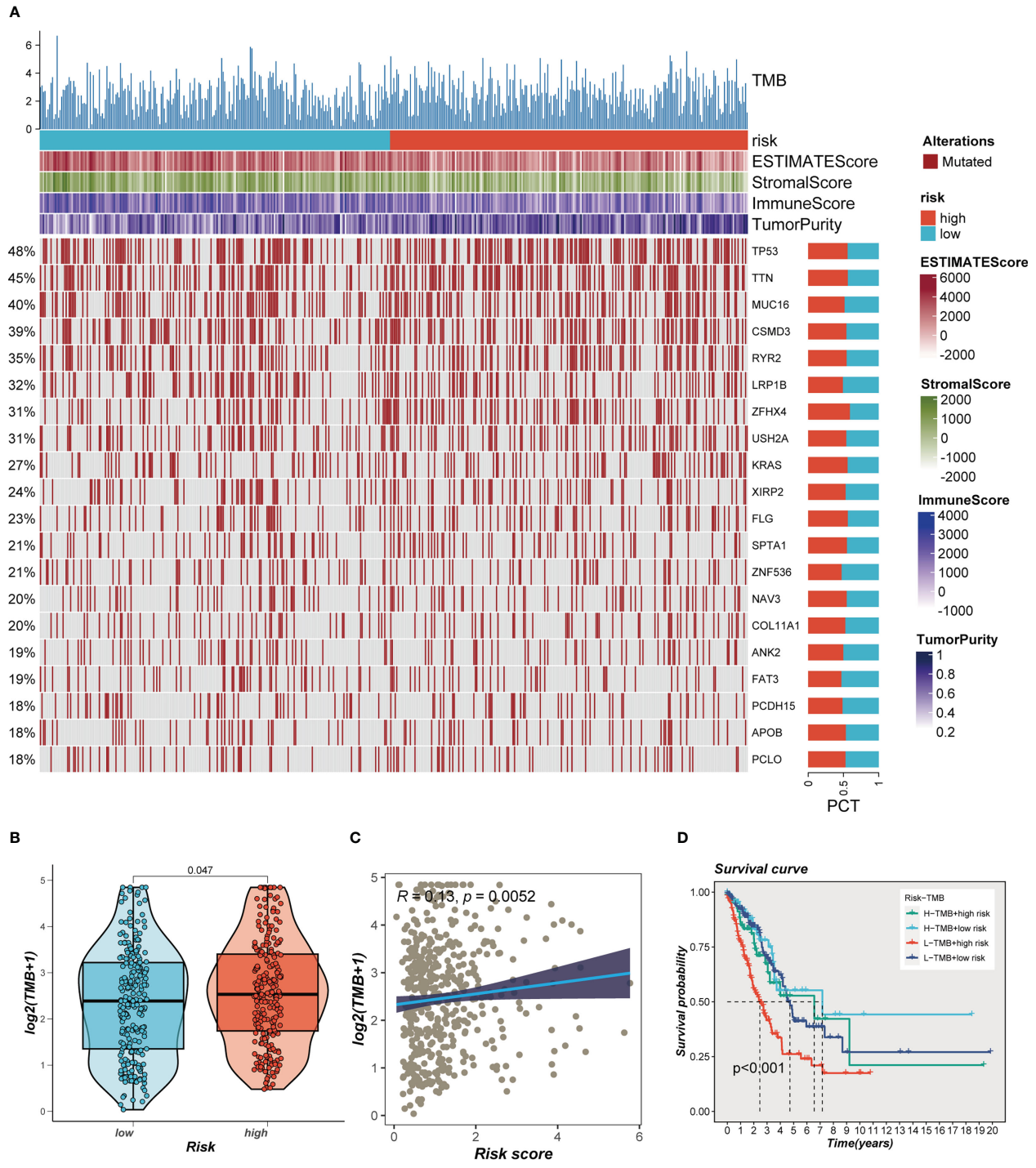

FIGURE 7
Landscape of LUAD sample mutation profiles. **(A)** Mutation landscape of the top 20 genes with mutation frequency in differential risk subgroups. **(B)** Comparison of tumor mutation burden (TMB) between different risk groups. **(C)** Correlation analysis between risk score and TMB. **(D)** Survival differences for four different subgroups (H-TMB+high-risk, H-TMB+low-risk, L-TMB+high-risk, and L-TMB+low-risk).

3.6 Differences in the immune microenvironment and immunotherapy response

Seven separate algorithms indicated that tumors at low risk had greater immune cell infiltration, such as T cells, B cells, NK cells, and activated Mast cells as illustrated in Figure 8A. The ESTIMATE approach was used to analyze the amount of immune infiltration in the various risk groups, and Figure 8B similarly confirmed the prior study, with the low-risk group having greater stromal, immunological, and ESTIMATE scores than the other groups (stromal score combined with immune score). Spearman

correlation analysis was utilized to evaluate the link between risk score and the score of immune infiltration. The risk scores were favorably connected with stromal (R = -0.22, FDR< 0.001), immune (R = -0.28, FDR< 0.001), and ESTIMATE (R = -0.27, FDR< 0.001) scores, and negatively correlated with tumor purity (R = -0.28, FDR< 0.001, Figure 8C). The risk score was correlated with the degree of immune cell infiltration and the quantity of each component in the TME, according to the data. Depending on the degree of immune infiltration, disease progression and immunotherapeutic efficacy may differ. Given the above results, we investigated whether the prognostic model might predict LUAD patients' reaction to ICIs. First, we examined the relation between risk score and commonly identified immunotherapy biomarkers in the TCGA-LUAD cohort. It demonstrated that practically all ICGs, including as PD-1, TIGIT, and CTLA4, were all substantially expressed in the high-risk group (Figure 9A). The correlations between modeling genes, risk scores, and ICGs were further analyzed and shown in the bubble plot (Figure 9B), with blue representing negative correlations and orange representing positive correlations, with bigger bubbles and deeper hues suggesting a

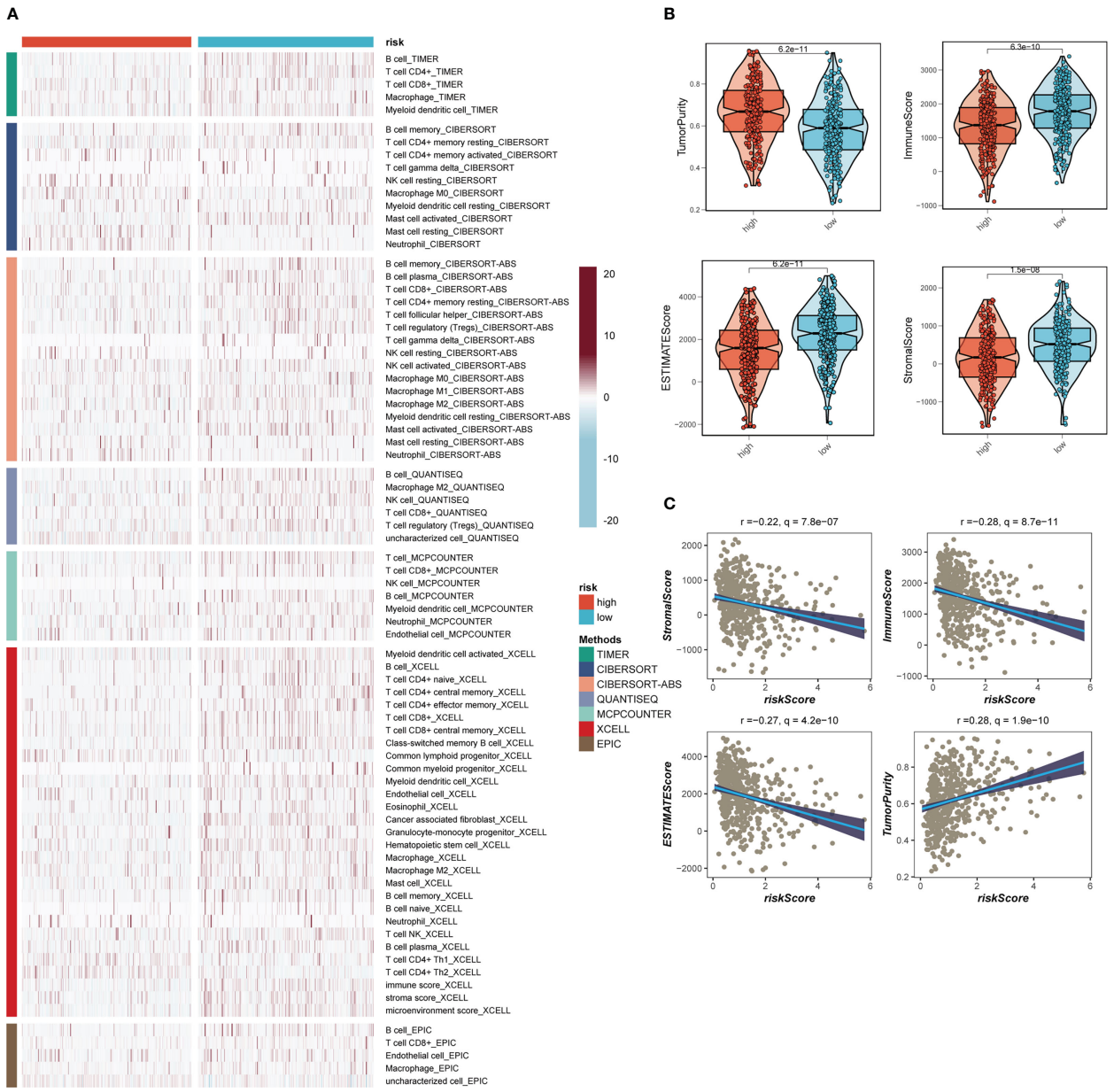

FIGURE 8
Analysis of immune infiltration. **(A)** Seven algorithms assess differences in immune infiltration status between different risk groups. **(B)** The violin plot demonstrated the difference in Stromal Score, Immune Score, ESTIMATE Score, and tumor purity calculated using the ESTIMATE algorithm between the two risk subgroups. **(C)** The correlations in Stromal Score, Immune Score, ESTIMATE Score, and tumor purity calculated using the ESTIMATE algorithm between the two risk subgroups.

10.3389/fendo.2023.1154410

stronger link. The IPS can help you locate persons who possibly benefit from immunotherapy. It was hypothesized that tumor samples from these individuals would have a positive immune response to PD-1/PD-L1 or CTLA4 inhibitors, or both (Figures 9C-F). Patients in the group with the lowest risk had much higher IPS scores, indicating that they would benefit the most from this kind of immunotherapy.

3.7 Functional enrichment analysis

In order to investigate the underlying process that may lead to a poor prognosis for high-risk LUAD patients, an analysis of hallmark pathway gene profiles was conducted, revealing distinct characteristics between high- and low-risk groups. A direct comparison between the Risk-High and Risk-Low groups showed

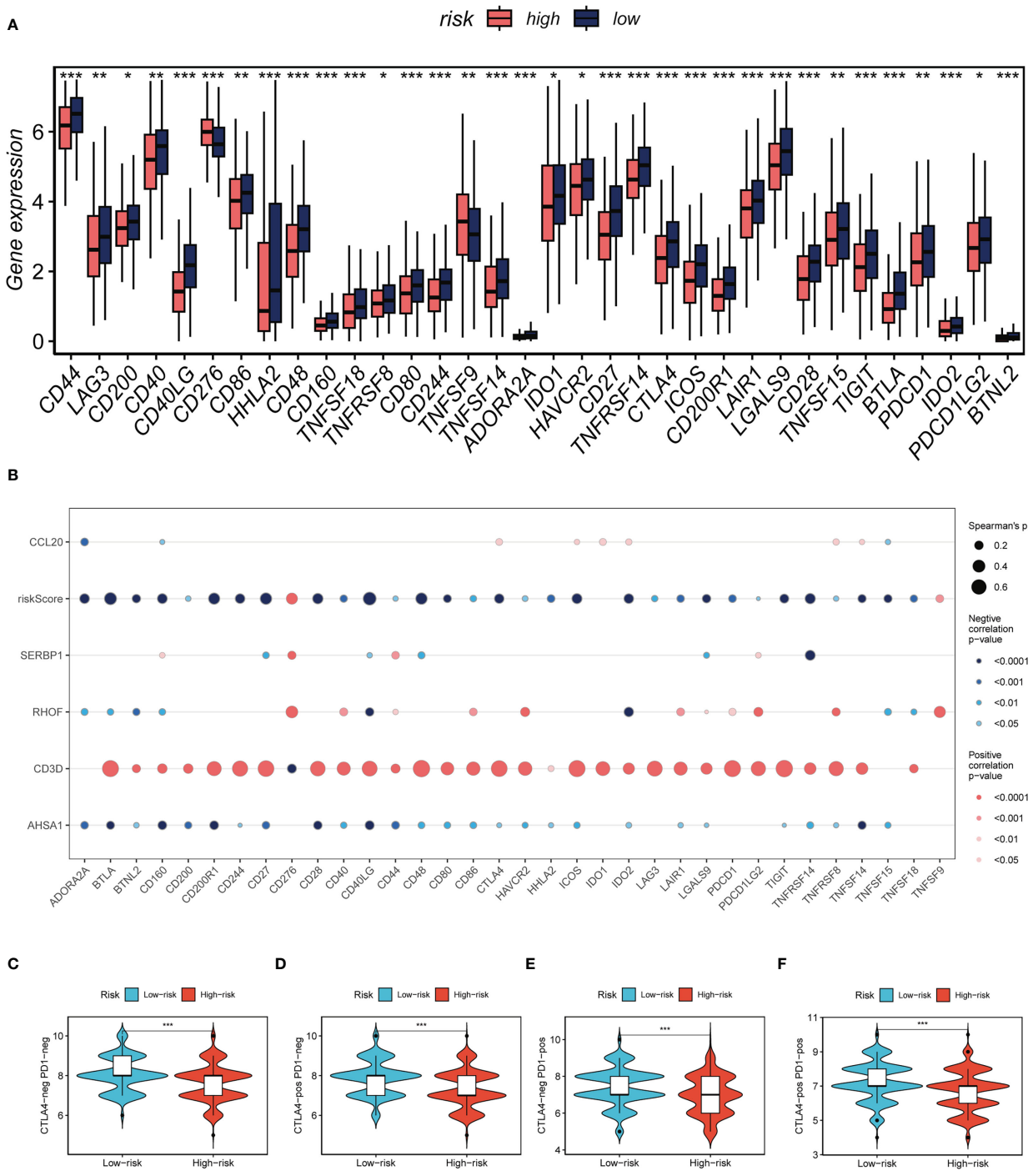

FIGURE 9
Immune checkpoint and TCIA analysis. **(A)** A box plot showed that differences in immune checkpoint gene expression between high- and low-risk groups. **(B)** Correlation between model genes and immune checkpoint. **(C-F)** The low-risk group has significantly greater IPS, IPS-CTLA4-neg-PD-1-neg, IPS-CTLA4-pos-PD-1-neg, IPS-CTLA4-neg-PD-1-pos, and IPS-CTLA4-pos-PD-1-pos. Note: *$P< 0.05$, **$P< 0.01$, ***$P< 0.001$.

that the top five enriched signatures in the high-risk group were MYC target v1, MYC target v2, mTORC1 signaling, G2M checkpoint, and Glycolysis (Figure 10A). GSEA enrichment analysis also indicated that the high-risk group had significantly enriched Cell Cycle (NES = 1.93, p< 0.001) and DNA Replication (NES = 1.78, p = 0.000) (Figure 10B). The ssGSEA algorithm was employed to examine differences in immune status across distinct risk groups. Low-risk LUAD patients showed increased infiltration of various immune cells, including Active dendritic cells (aDCs), B cells, CD8+ T cells, Dendritic cells (DCs), Immature dendritic cells (iDCs), Mast cells, neutrophils, T helper cell, Tumor-infiltrating lymphocytes (TILs), and Regulatory T cells (Treg), in their tumor microenvironment (TME). Furthermore, almost all immune-related pathways were significantly expressed in the low-risk group (Figures 10C, D).

3.8 Experimental verification

A pan-cancer study of AHSA1 expression levels demonstrated that AHSA1 was substantially expressed in LUAD compared to normal tissue (Figure 11A). Figures 11B, C demonstrated that AHSA1 was substantially expressed in tumor groups and that patients with high AHSA1 expression in the TCGA database had a worse prognosis. In accordance with our earlier findings, AHSA1 was expressed at a greater level in LUAD cell lines (Figure 11D). Then, five days after transfection, we quantified the amount of AHSA1 expression in A549 and H1299 cell lines by qRT-PCR to determine the efficiency of siRNA-mediated AHSA1 knockdown (Figure 11E). According to research on clonal formation, AHSA1 knockdown inhibits the capacity of LUAD cells to produce clones (Figure 11F). Then, EdU tests were conducted to investigate whether knockdown of AHSA1 affected the proliferative capacity of LUAD cells. Lower AHSA1 expression decreased the proliferation of A549 and H1299 cells relative to the control group (Figure 12A), indicating that AHSA1 may play a role in the proliferation of LUAD cell lines. According to these results, AHSA1 knockdown inhibited the proliferation of LUAD cells. The investigation on wound healing demonstrated that AHSA1 knockdown dramatically decreased LUAD cell migration and invasion (Figure 12B). The trans-well experiment demonstrated that LUAD cells transfected with si- AHSA1 exhibited a reduced capacity for migration and invasion, which was consistent with the wound healing assay outcomes (Figure 12C). All experimental investigations demonstrated that AHSA1 was a tumor-promoting oncogene in tumor development and progression and acted as a pro-oncogenic regulator in LUAD.

4 Discussion

LC remains one of the most prevalent malignant tumors and the greatest contributor to cancer-specific death worldwide. Despite significant improvements have been made in diagnostic techniques and treatment schedules of NSCLC, the 5-year overall survival rate remains poor. At present, lactic acid, the byproduct of glycolysis, was repeatedly confirmed could promote malignant cell proliferation and induce immunosuppressive microenvironment. It acts as a mediator between intrinsic metabolism and immunosuppression. In recent years, researchers found that reducing the concentration of lactate might be a promising therapeutic strategy. Hence, lactate-related genes have the potential to act as novel molecular biomarkers and therapeutic targets. In the present study, we explored an original diagnostic signature and prognostic scoring system based on LRMGs, bringing prospect for reversing immune resistance and improving prognosis of patients. Numerous groundbreaking research demonstrated the potential of the lactic acid-induced immunosuppressive milieu and its role in the promotion of tumors. As far as we are aware, LUAD does not have a lactate-related prognostic grading system.

We conducted scRNA-seq on 12 LUAD samples in this study and identified eight distinct cell types. LM activity was evaluated using the LM gene set obtained from the GeneCards database, and myeloid and epithelial cells were found to exhibit the highest levels of LM activity, suggesting that LM may play a role in regulating these cells and influencing carcinogenesis and development. Key genes that regulate LM activity were then investigated, and prognostic models were constructed using Cox and lasso regression. The high-risk group was found to have a worse prognosis, and a signature derived from this analysis demonstrated good accuracy and stable performance across four public GEO datasets. We also integrated clinical information to develop a nomogram, which showed better performance in predicting survival than risk scores and other clinical characteristics. While previous studies have suggested a link between genetic modifications and the generation of neoantigens and potential immunotherapeutic advantages (20), our findings showed that patients in the low-risk group had fewer TMB, while patients in the high-risk group had more mutations in high-frequency genes. We further categorized the patients into four groups based on TMB and risk status, and the H-TMB+low-risk group had the best prognosis, providing potential clinical implications for prognostic assessment.

The immune microenvironment is composed of a variety of cellular components including extracellular matrix, epithelial cells, blood vessels and tumor-infiltrating lymphocytes, which may accelerate tumor destruction, enhance tumor invasiveness, and improve antitherapeutic response (21). To further understand how TME effects tumor prognosis, we examined immune cell infiltration in high- and low-risk LUAD patients. Seven algorithms were used to quantify immune cell infiltration in various risk categories, and the results revealed that tumors in the low-risk group had more immune cell infiltration. The ESTIMATE approach also revealed that low-risk samples had more immune cell infiltration, and the risk score was inversely connected to the stromal, immune, and ESTIMATE scores (FDR< 0.001). Furthermore, we discovered that the majority of the known ICGs were expressed at a greater level in the low-risk group, and the

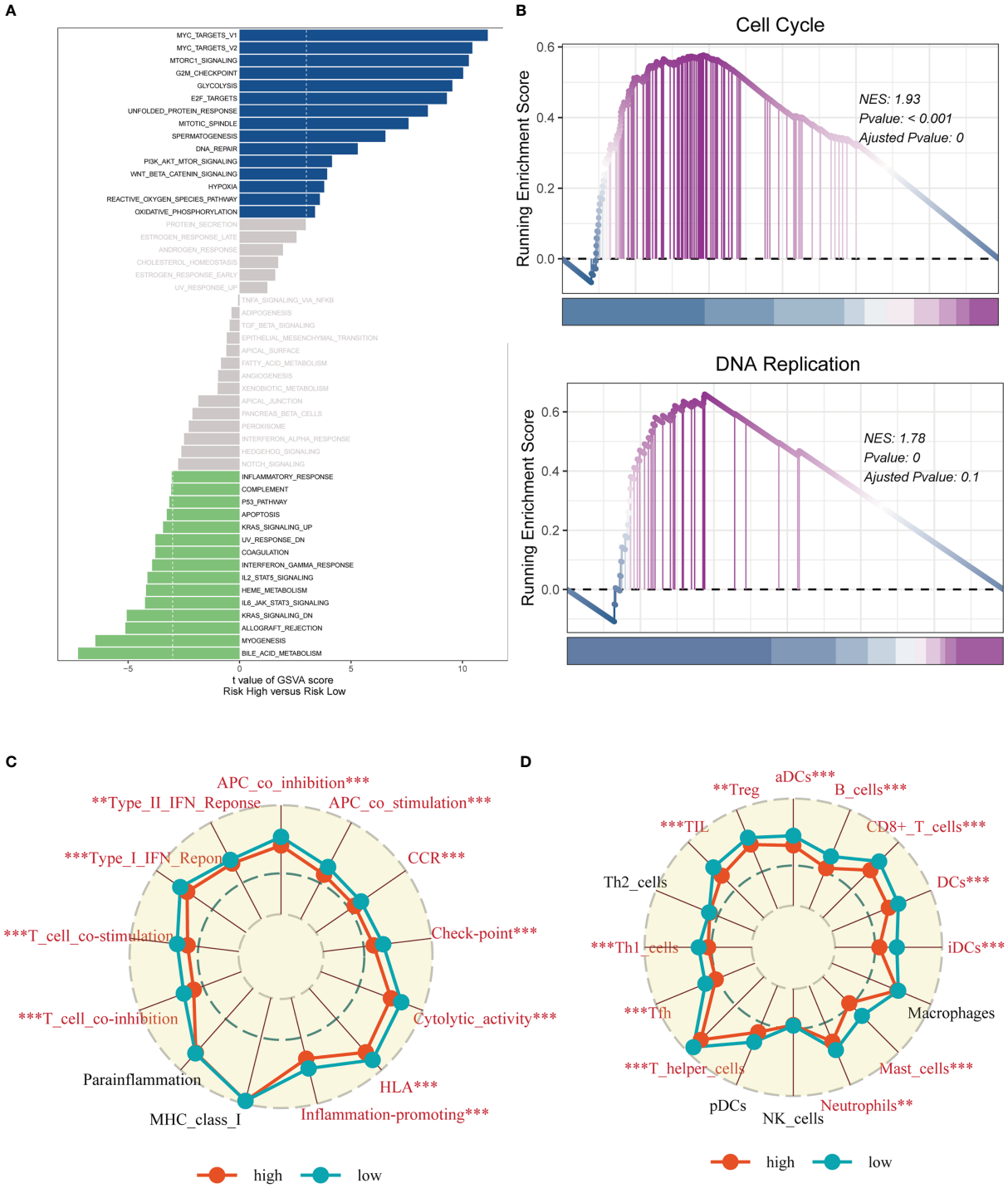

FIGURE 10
Enrichment analysis. **(A)** GSVA analysis revealed pathways enriched in the 50 hallmark gene sets for the high- and low- risk groups. **(B)** GSEA showed pathway differences between high- and low-risk groups. **(C, D)** The ssGSEA algorithm was employed to quantify the immune cell infiltration and immune function between the high-risk and low-risk groups. Note: $^{**}P < 0.01$, $^{***}P < 0.001$.

correlation analysis revealed that the risk scores were strongly negatively linked with the majority of the immunological checkpoint genes. TCIA was utilized to investigate the effects of PD-1 and CTLA-4 treatment in order to better understand the variations in immunotherapy effectiveness among risk groups. Because their IPS score was substantially higher than that of the high-risk group, the findings suggested that LUAD patients in the low-risk group would benefit more from immunotherapy.

GSEA results show that Cell Cycle and DNA Replication were mainly enriched in the high-risk group. Tumor is a kind of disease in which cell cycle regulation mechanism is destroyed. In the whole monitoring system of cell cycle progression, cell cycle detection sites

10.3389/fendo.2023.1154410

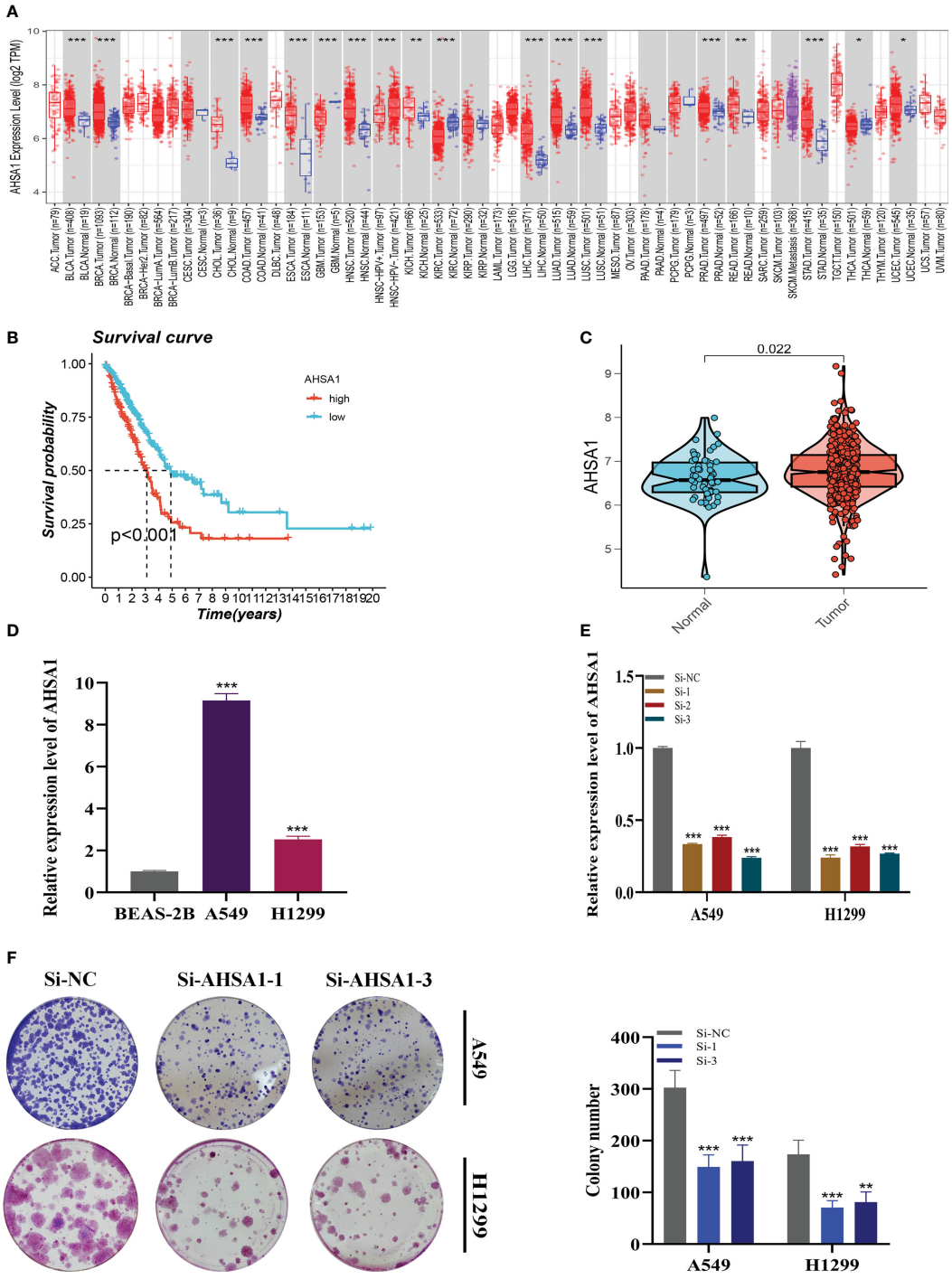

FIGURE 11
Cell Experiment. **(A)** The expression of AHSA1 in pan-cancer tissues was analyzed using the TIMER database. **(B)** Prognosis was evaluated by performing survival analysis on the effect of AHSA1 expression. **(C)** TCGA database analysis revealed a difference in AHSA1 expression between normal samples and tumor samples. **(D)** To assess AHSA1 expression, qRT-PCR was performed on both normal cells and LUAD cell lines. **(E)** The level of AHSA1 expression was evaluated 5 days after transfection using qRT-PCR, and significant reduction in AHSA1 expression (P< 0.001) was observed with siRNA sequences. **(F)** The number of colonies was significantly reduced in cells with reduced AHSA1 expression compared to the NC group, as shown by the colony formation assay. Note: *P < 0.05, **P < 0.01, ***P < 0.001.

play a core role function. DNA replication is an important part of the cell cycle, dysregulation of which is also one of the significant factors leading to tumorigenesis and tumor proliferation. Currently, cell cycle checkpoint kinase inhibitors are utilized therapeutically and are successful in LC. These inhibitors induce cell death and cell cycle arrest, therefore reversing the acquired drug resistance induced by cell cycle disorder (22).

Interestingly, in TCGA database, AHSA1 was highly expressed in tumor groups, and LUAD patients with high-expression AHSA1 had poor prognosis. In order to understand the underlying

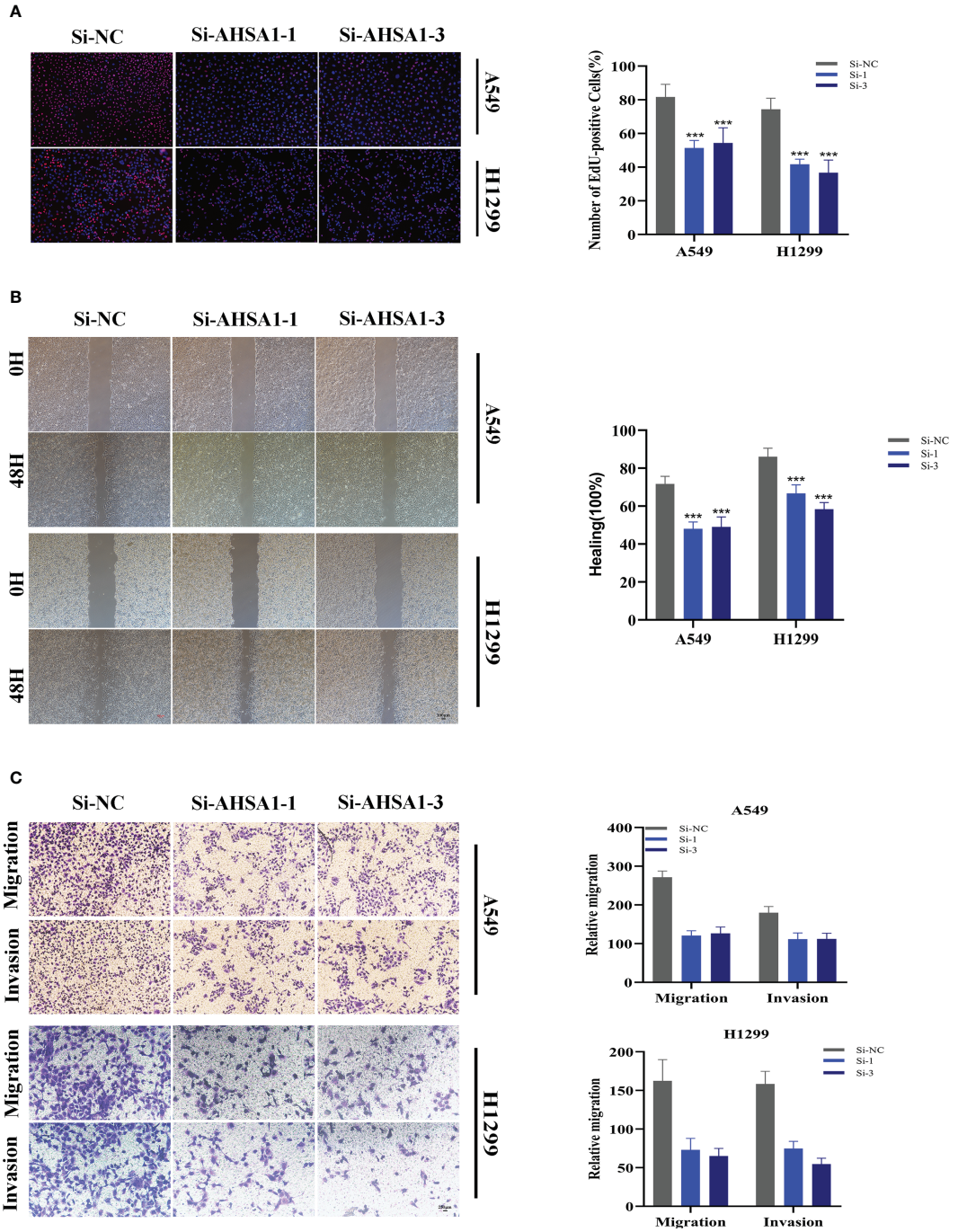

FIGURE 12
Related experiments for AHSA1. **(A)** EdU staining assay indicated that downregulation of AHSA1 expression repressed cell proliferation in LUAD cell lines. **(B)** Scratch-wound healing assay depicted that a significantly slower wound healing rate was observed in cells with a decreased expression of AHSA1. **(C)** Transwell assay showed that downregulation of AHSA1 expression inhibited the migration and invasion capacity of LUAD cells. To demonstrate the accuracy and reproducibility of the results, all experiments were repeated in two LUAD (A549, H1299) cell lines and all data were presented as the means ± SD of three independent experiments. Note: ***$P < 0.001$.

mechanism, we conducted a series of experiments. According to the results, knocking down AHSA1 significantly decreased cell invasion, migration, and proliferation in LUAD cell lines.

The current research has certain problems. To begin, this signature was built utilizing publicly accessible datasets. Large-scale prospective clinical investigations are required to verify the prognostic potential. In conclusion, we constructed an LM-related signature, which can predict the prognosis and immunotherapy of LUAD patients, and our findings can provide help for the clinical treatment of LUAD.

Data availability statement

The datasets presented in this study can be found in online repositories. The names of the repository/repositories and accession number(s) can be found in the article/Supplementary Material.

Author contributions

PZ, SP, ZG, and QR contributed conception and design of the study. JX, HL and WW collected the data. PZ and SP performed the statistical analysis. PZ, SP, and ZG wrote the first draft of the manuscript. JX, HL, and WW gave the final approval of the version to be submitted. All authors contributed to the article and approved the submitted version.

Acknowledgments

We are very grateful for data provided by databases such as TCGA, GEO. Thanks to reviewers and editors for their sincere comments.

Conflict of interest

The authors declare that the research was conducted in the absence of any commercial or financial relationships that could be construed as a potential conflict of interest.

Publisher's note

Supplementary material

The Supplementary Material for this article can be found online at: https://www.frontiersin.org/articles/10.3389/fendo.2023.1154410/full#supplementary-material

References

1. Siegel RL, Miller KD, Fuchs HE, Jemal A. Cancer statistics, 2022. *CA Cancer J Clin* (2022) 72(1):7–33. doi: 10.3322/caac.21708

2. National Lung Screening Trial Research T, Aberle DR, Adams AM, Berg CD, Black WC, Clapp JD, et al. Reduced lung-cancer mortality with low-dose computed tomographic screening. *N Engl J Med* (2011) 365(5):395–409. doi: 10.1056/NEJMoa1102873

3. National Lung Screening Trial Research T, Aberle DR, Berg CD, Black WC, Church TR, Fagerstrom RM, et al. The national lung screening trial: Overview and study design. *Radiology* (2011) 258(1):243–53. doi: 10.1148/radiol.10091808

4. Goldstraw P, Chansky K, Crowley J, Rami-Porta R, Asamura H, Eberhardt WE, et al. The iaslc lung cancer staging project: Proposals for revision of the tnm stage groupings in the forthcoming (Eighth) edition of the tnm classification for lung cancer. *J Thorac Oncol* (2016) 11(1):39–51. doi: 10.1016/j.jtho.2015.09.009

5. Warburg O, Wind F, Negelein E. The metabolism of tumors in the body. *J Gen Physiol* (1927) 8(6):519–30. doi: 10.1085/jgp.8.6.519

6. Gatenby RA, Gillies RJ. Why do cancers have high aerobic glycolysis? *Nat Rev Cancer* (2004) 4(11):891–9. doi: 10.1038/nrc1478

7. Walenta S, Mueller-Klieser WF. Lactate: Mirror and motor of tumor malignancy. *Semin Radiat Oncol* (2004) 14(3):267–74. doi: 10.1016/j.semradonc.2004.04.004

8. Somarribas Patterson LF, Vardhana SA. Metabolic regulation of the cancer-immunity cycle. *Trends Immunol* (2021) 42(11):975–93. doi: 10.1016/j.it.2021.09.002

9. Hayes C, Donohoe CL, Davern M, Donlon NE. The oncogenic and clinical implications of lactate induced immunosuppression in the tumour microenvironment. *Cancer Lett* (2021) 500:75–86. doi: 10.1016/j.canlet.2020.12.021

10. Ishikawa M, Iwasa S, Nagashima K, Aoki M, Imazeki H, Hirano H, et al. Retrospective comparison of nab-paclitaxel plus ramucirumab and paclitaxel plus ramucirumab as second-line treatment for advanced gastric cancer focusing on peritoneal metastasis. *Investigational New Drugs* (2020) 38(2):533–40. doi: 10.1007/s10637-019-00822-3

11. Ying M, You D, Zhu X, Cai L, Zeng S, Hu X. Lactate and glutamine support nadph generation in cancer cells under glucose deprived conditions. *Redox Biol* (2021) 46:102065. doi: 10.1016/j.redox.2021.102065

12. Zhu HE, Li T, Shi S, Chen DX, Chen W, Chen H. Esco2 promotes lung adenocarcinoma progression by regulating Hnrnpa1 acetylation. *J Exp Clin Cancer Res* (2021) 40(1):64. doi: 10.1186/s13046-021-01858-1

13. Li X, Zhang Z, Zhang Y, Cao Y, Wei H, Wu Z. Upregulation of lactate-inducible snail protein suppresses oncogene-mediated senescence through P16 (Ink4a) inactivation. *J Exp Clin Cancer Res* (2018) 37(1):39. doi: 10.1186/s13046-018-0701-y

14. Ma Y, Yuan Q, He S, Mao X, Zheng S, Chen C. Characterizing the prognostic and therapeutic value of necroptosis in sarcoma based on necroptosis subtypes. *Front Genet* (2022) 13:980209. doi: 10.3389/fgene.2022.980209

15. Miao Y, Yuan Q, Wang C, Feng X, Ren J, Wang C. Comprehensive characterization of rna-binding proteins in colon adenocarcinoma identifies a novel prognostic signature for predicting clinical outcomes and immunotherapy responses based on machine learning. *Comb Chem High Throughput Screen* (2022) 26 (1):163–82. doi: 10.2174/1386207325666220404125228

16. Yoshihara K, Shahmoradgoli M, Martínez E, Vegesna R, Kim H, Torres-Garcia W, et al. Inferring tumour purity and stromal and immune cell admixture from expression data. *Nat Commun* (2013) 4:2612. doi: 10.1038/ncomms3612

17. Van Allen E, Miao D, Schilling B, Shukla S, Blank C, Zimmer L, et al. Genomic correlates of response to Ctla-4 blockade in metastatic melanoma. *Science (New York, NY)* (2015) 350(6283): 207–11. doi: 10.1126/science.aad0095

18. Chen X, Yuan Q, Liu J, Xia S, Shi X, Su Y, et al. *In vivo*comprehensive characterization of extracellular matrix-related genes in paad identified a novel prognostic panel related to clinical outcomes and immune microenvironment: A silico analysis with and vitro validation. *Front Immunol* (2022) 13:985911. doi: 10.3389/fimmu.2022.985911

19. Lambrechts D, Wauters E, Boeckx B, Aibar S, Nittner D, Burton O, et al. Phenotype molding of stromal cells in the lung tumor microenvironment. *Nat Med* (2018) 24(8):1277–89. doi: 10.1038/s41591-018-0096-5

20. Anagnostou V, Smith KN, Forde PM, Niknafs N, Bhattacharya R, White J, et al. Evolution of neoantigen landscape during immune checkpoint blockade in non-small cell lung cancer. *Cancer Discov* (2016) 7(3):264–76. doi: 10.1158/2159-8290.Cd-16-0828

21. Swartz M, Iida N, Roberts E, Sangaletti S, Wong M, Yull F, et al. Tumor microenvironment complexity: Emerging roles in cancer therapy. *Cancer Res* (2012) 72 (10):2473–80. doi: 10.1158/0008-5472.Can-12-0122.

22. Gaillard H, García-Muse T, Aguilera A. Replication stress and cancer. *Nat Rev Cancer* (2015) 15(5):276–89. doi: 10.1038/nrc3916

frontiers | Frontiers in Endocrinology

TYPE Original Research
PUBLISHED 23 March 2023
DOI 10.3389/fendo.2023.1163046

OPEN ACCESS

EDITED BY
Peixin Dong,
Hokkaido University, Japan

REVIEWED BY
Xinpei Deng,
Sun Yat-sen University Cancer Center (SYSUCC), China
Shousen Wang,
Xiamen University, China
Chenfei Jia,
Cangzhou Central Hospital, China

*CORRESPONDENCE
Jian Tang
tangjian@njmu.edu.cn
Gang Yao
yaogang2005@hotmail.com
Zhijia Xia
Zhijia.Xia@med.uni-muenchen.de

†These authors have contributed equally to this work and share first authorship

SPECIALTY SECTION
This article was submitted to Cancer Endocrinology, a section of the journal Frontiers in Endocrinology

RECEIVED 10 February 2023
ACCEPTED 13 March 2023
PUBLISHED 23 March 2023

CITATION
Liu J, Zhang P, Yang F, Jiang K, Sun S, Xia Z, Yao G and Tang J (2023) Integrating single-cell analysis and machine learning to create glycosylation-based gene signature for prognostic prediction of uveal melanoma.
Front. Endocrinol. 14:1163046.
doi: 10.3389/fendo.2023.1163046

Integrating single-cell analysis and machine learning to create glycosylation-based gene signature for prognostic prediction of uveal melanoma

Jianlan Liu[1†], Pengpeng Zhang[2†], Fang Yang[3†], Keyu Jiang[1†], Shiyi Sun[1], Zhijia Xia[4*], Gang Yao[1*] and Jian Tang[1*]

[1]Department of Plastic and Burns Surgery, The First Affiliated Hospital of Nanjing Medical University, Nanjing, China, [2]Department of Thoracic Surgery, The First Affiliated Hospital of Nanjing Medical University, Nanjing, China, [3]Department of Ophthalmology, Charité – Universitätsmedizin Berlin, Campus Virchow-Klinikum, Berlin, Germany, [4]Department of General, Visceral, and Transplant Surgery, Ludwig-Maximilians-University Munich, Munich, Germany

Background: Increasing evidence suggests a correlation between glycosylation and the onset of cancer. However, the clinical relevance of glycosylation-related genes (GRGs) in uveal melanoma (UM) is yet to be fully understood. This study aimed to shed light on the impact of GRGs on UM prognosis.

Methods: To identify the most influential genes in UM, we employed the AUCell and WGCNA algorithms. The GRGs signature was established by integrating bulk RNA-seq and scRNA-seq data. UM patients were separated into two groups based on their risk scores, the GCNS_low and GCNS_high groups, and the differences in clinicopathological correlation, functional enrichment, immune response, mutational burden, and immunotherapy between the two groups were examined. The role of the critical gene AUP1 in UM was validated through *in vitro* and *in vivo* experiments.

Results: The GRGs signature was comprised of AUP1, HNMT, PARP8, ARC, ALG5, AKAP13, and ISG20. The GCNS was a significant prognostic factor for UM, and high GCNS correlated with poorer outcomes. Patients with high GCNS displayed heightened immune-related characteristics, such as immune cell infiltration and immune scores. *In vitro* experiments showed that the knockdown of AUP1 led to a drastic reduction in the viability, proliferation, and invasion capability of UM cells.

Conclusion: Our gene signature provides an independent predictor of UM patient survival and represents a starting point for further investigation of GRGs in UM. It offers a novel perspective on the clinical diagnosis and treatment of UM.

KEYWORDS

glycosylation, uveal melanoma, immunotherapy, machine learning, AUP1

1 Introduction

Uveal melanoma (UM), the most common type of intraocular cancer in adults, originates from melanocytes in the uvea, which includes the iris, ciliary body, and choroid (1). UM accounts for 3% to 5% of all melanoma and 79% to 81% of ocular melanoma (2). The global average incidence of UM ranges from 0.002‰ to 0.008‰, with significant geographic and ethnic disparities (3). Around 50% of UM patients experience hematogenous metastasis, with the liver being the primary and most common site of metastasis (4, 5). Several studies have been conducted to prevent metastasis in UM, high-dose interferon is the only adjuvant therapy shown to improve recurrence-free survival time and control the primary UM. However, there has been no significant improvement in overall survival (OS) or metastasis-free survival in any of these studies (1).

Patients with metastatic UM have a median survival time of 6 to 12 months, and their prognosis heavily depends on liver metastasis and disease progression in the liver (6). Despite the numerous studies by scholars exploring various immunotherapies, such as immune checkpoint inhibitors (ICI), cancer vaccines, and T-cell passaged cell therapy (7, 8), the effects of immunotherapy for UM have been disappointing (9). Given the limited therapeutic options for UM, it is crucial to investigate its underlying pathophysiological pathways and develop a reliable prognostic prediction model for UM patients.

Glycosylation is a biological process that occurs through the action of various glycosyltransferases (GTs) and glycosidases (10, 11). This modification changes the protein's conformation and structure, which in turn affects its functional activity (12). The regulation of glycosylation is controlled by glycogenes, which are genes that encode for glycosidases and sulfotransferases. An abnormal expression or regulation of these genes is linked to tumor progression and is considered a hallmark of cancer (13, 14). A translational study showed that the expression levels of 210 GTs genes could differentiate between six types of cancer, including breast cancer and ovarian cancer. Moreover, glycosylation has the potential to act as a prognostic indicator, as a signature of glycosylation-related genes (GRGs) was shown to predict clinical outcomes in ovarian cancer patients (15). Other post-translational regulatory mechanisms, such as ubiquitination (16), phosphorylation (17) and epigenetic modifications (18) have also been reported as potential biomarkers in UM prognostic models. However, despite being one of the most crucial post-transcriptional alterations among the 300 protein modifications, few studies have explored the relationship between GRGs signature and the tumor microenvironment (TME) of UM.

To address this gap, we leveraged bulk RNA-seq and scRNA-seq data to establish the GRGs signature in UM and divided UM patients into GCNS_low and GCNS_high groups using a selected cut-off value. Our analysis revealed a significant difference in prognosis between the two groups. The results were validated using the GSE84976 dataset from the Gene Expression Omnibus (GEO) database. Furthermore, we examined the utility of the GRGs signature in the TME, tumor mutational burden (TMB), immunotherapy response, and drug sensitivity. Lastly, we explored the impact of inhibiting AUP1 expression on UM cell proliferation and migration *in vitro*. Our study provides novel insights into the role of glycosylation in UM and holds promise for improved patient stratification and targeted therapy development.

2 Materials and methods

2.1 Data acquisition

The scRNA-seq data of UM was obtained from the GEO (https://www.ncbi.nlm.nih.gov/geo/), which comprised 59,915 tumor and non-tumorous cells from eight primary and three metastatic samples (accession number: GSE139829). The RNA expression profiles, gene mutations, and relevant clinical information of UM were extracted from The Cancer Genome Atlas (TCGA) database (https://tcgadata.nci.nih.gov/), with a sample size of 80 and served as the training dataset. The FPKM format of the TCGA-UM was transformed into the TPM format. Additionally, the expression profiles of GSE84976 were obtained from the GEO database and used as the validation set. Before any further analysis, all transcriptome data were log2-transformed. The "sva" package adjusted for batch effects between TCGA-UM and GSE84976. The GeneCards database (https://www.genecards.org/) was consulted to obtain GRGs, and a total of 110 GRGs with a relevance score greater than 1.0 were selected for further analysis. To assess the prognostic utility of the risk score in ICI therapy, we utilized the IMvigor 210 Core Biologies database of patients with advanced urothelial cancer undergoing anti-PD-L1 immunotherapy, which was analyzed using the R program (19).

2.2 Data processing and annotation

We employed the "seurat" and "singleR" R packages to perform quality control on scRNA-seq data (20). To ensure the data's accuracy, we eliminated genes expressed in less than three single cells, cells with less than 200 or more than 7,000 genes, and cells with more than 10% mitochondrial genes. Out of the total, 30,934 cells were selected for further analysis. These cells underwent scaling after normalization through a linear regression model that utilized the log-normalization method. Using the "FindVariableFeatures" function, we identified the top 3,000 hypervariable genes. To remove batch effects that may affect downstream analysis, we utilized the "FindIntegrationAnchors" function of the canonical correlation analysis (CCA) method. We integrated and scaled the data using the "IntegrateData" and "ScaleData" functions, determined the anchor points by principal component analysis (PCA), and evaluated the top 20 PCs using the t-distributed stochastic neighbor embedding (t-SNE) algorithm to discover significant clusters. We used the "FindNeighbors" and "FindClusters" functions (resolution

=0.8) to obtain 24 cell clusters, which were visualized as a t-SNE diagram. The "FindAllMarkers" function in the "seurat" package was applied to identify the differentially expressed genes (DEGs) in each cluster. The "singleR" package annotated cell types based on the cluster's canonical marker genes, which were later manually validated against published literature (21).

2.3 AUCcell

The "AUCell" R package was utilized to determine the active status of gene sets in scRNA-data by assigning glycosylation activity scores to each cell lineage (22). The gene expression rankings of each cell were calculated based on the AUC value of selected GRGs to assess the fraction of highly expressed gene sets. Cells with larger AUC values had higher gene expression levels. The "AUCell_exploreThresholds" function was used to identify cells actively involved in glycosylation gene sets. These cells were then grouped into high and low G-AUC categories using AUC score cutoff values and visualized in a t-SNE embedding with the help of the "ggplot2" R package. A gene set variation analysis (GSVA) was conducted to uncover enriched biological pathways among the high and low G-AUC subgroups. The results were represented in a bar chart, displaying all the significantly different pathways.

2.4 Gene set enrichment analysis (GSEA)

This study determined the absolute enrichment fraction of a specified gene set in every sample by applying ssGSEA. To assign glycosylation enrichment values to each participant in the TCGA-UM cohort, we employed ssGSEA. Based on their glycosylation enrichment scores, participants were divided into two groups, high-GSN and low-GSN, for further investigation.

2.5 Weighted gene co-expression network analysis (WGCNA)

The systems biological method WGCNA was applied to the gene co-expression network of TCGA-UM (23). The following outlines the steps are taken: exclusion of genes with missing values using the "goodSamplesGenes" function, grouping of tumor samples, deletion of outliers, and establishment of a cut line of 100. The optimal soft threshold for adjacency calculation was determined using graphical methods. An adjacency matrix was generated from the expression matrix to determine the genetic interconnectedness of the network. The topological overlap matrix (TOM) was then constructed from the adjacency matrix. Hierarchical clustering was performed using an average linkage approach and the differences in TOM. The hierarchical clustering tree was dynamically pruned to identify similar modules with high correlation coefficients ($r > 0.25$). Pearson's correlation test was applied to examine the relationship between eigengenes and clinical characteristics. The modules containing genes with the most significant correlations to clinical traits, such as glycosylation score, survival status, and survival time were selected for further investigation.

2.6 Construction of the risk scoring

A venn diagram analysis was conducted to pinpoint the intersection between the DEGs and the target genes in WGCNA. This was followed by a univariate analysis of the overlapping genes to select those that showed a statistically significant correlation with patients' OS ($P < 0.01$). The least absolute shrinkage and selection operator (LASSO) analysis was then employed to narrow down further the list of genes and risk coefficients strongly linked to prognosis, creating a risk model using the "glmnet" package. Based on the coefficients obtained from the LASSO analysis, a risk score was assigned to each UM patient. The patients in the TCGA-UM dataset were divided into two groups, GCNS_low and GCNS_high, using the median risk score as the cutoff. The Kaplan–Meier (K-M) method was utilized to generate prognostic survival curves. The performance of the predictive model was evaluated employing receiver operating characteristic (ROC) curves, with a good performance defined as an area under the curve (AUC) value of > 0.8. The accuracy of the signature in predicting outcomes was demonstrated by using survival analysis and AUC value in an independent dataset (GSE84976). PCA was carried out to reduce dimensionality and visualize the differences between the two risk groups. The same analysis was performed on the GSE84976 cohort.

2.7 Assessment of the prognostic model's independence and validity

A nomogram combining GCNS, age, gender, and the pathological stage was developed to estimate the 1-, 2-, and 3-year OS probability (24). The accuracy of the nomogram was assessed through ROC curves and calibration curves. The net benefit of the nomogram and individual clinical features was also evaluated through decision curve analysis (DCA). Subgroup analysis was performed to determine the prognostic value of the GCNS among subpopulations defined by specific clinical characteristics, including age, gender and clinical stage.

2.8 Assessment of the relationship between prognostic models and tumor immunity and its impact on immunotherapy

We analyzed the immune infiltration level of UM patients in the TCGA database using data from the TIMER 2.0 database, which comprises seven evaluation methods. We then conducted a ssGSEA analysis of genes in the prognostic model with the "GSEABase" package to determine immune-related properties. The "estimate" R package facilitated the calculation of the relative proportions of

stromal cells, immune cells, tumor cells and their comparison across different GCNS categories. A higher score indicates a greater presence of components in the TME. Furthermore, several immune cell-expressed molecules serve as immunological checkpoints that regulate the level of immune activation and prevent excessive immunological activation (25). We compared the expression levels of both groups of well-known immune checkpoint genes (ICGs) extracted from the literature. To assess their potential in predicting immunotherapy response, tumor immune dysfunction and exclusion (TIDE) was applied. Finally, we evaluated the IMvigor210 cohort to confirm the ability of the GCNS model to predict immunotherapy outcomes.

2.9 Mutational landscape and drug sensitivity

From the TCGA database, gene mutation profiles of UM patients were obtained, and the "maftools" software was used to display them. The GCNS and the comprehensive gene mutation files were combined. GCNS_low and GCNS_high groups' signaling pathways were compared using GSEA, and the essential active pathways in the GCNS_high group were identified. To establish the half-maximal inhibitory concentrations (IC50) of common chemotherapeutic drugs, we also used the R package "pRRophetic," which allowed us to look into the relationship between the GCNS and drug sensitivity (26). Wilcoxon signed-rank tests compared the IC50 values between the two GCNS groups.

2.10 Cell culture and transfection

The Cell Resource Center at Shanghai Life Sciences Institute provided the human uveal melanoma cells (MuM-2B, OCM-1) used in this study. The cells were cultured in DMEM (Dulbecco's Modified Eagle's Medium) (Gibco, USA) with 1% penicillin/streptomycin and 10% fetal bovine serum (FBS) (Gibco, USA) in a humid incubator (37°C and 5% CO_2). Cells were sown in six-well plates and cultured at 37°C to 80% confluence before transfecting. Ribobio created the si-AUP1 and si-NC (control) (Ribobio, Guangzhou, China). Then, following the manufacturer's instructions, they were transfected into MuM-2B and OCM-1 cells using Lipofectamine 3000 (Invitrogen, Carlsbad, CA, USA). After the transfection had been going on for 48 h, more research was done. AUP1 siRNA sequences were given in Supplementary Table S1.

2.11 Real time-polymerase chain reaction (RT-PCR)

Using TRIzol reagent (15596018, Thermo, Waltham, MA, USA), total RNA was extracted from MuM-2B and OCM-1 cells, and RNA purity and concentrations were measured using the manufacturer's recommendations. When creating cDNA using the PrimeScriptTM RT reagent Kit (R232-01, Vazyme, Nanjing, China), the following settings were made: 15 min at 37°C, then 5 s at 85°C, and finally storage at -20°C. The PCR procedure was performed using a 10 µL volume in 40 cycles of 95°C for 10 s and 60°C for 30 s. Three times each operation was carried out. GAPDH was used as a reference standard, and the relative gene expression was analyzed using the $2^{-\Delta\Delta Ct}$ technique. Tsingke Biotech company created specific primers (Tsingke, Beijing, China). In Supplementary Table S1, used primers were supported.

2.12 Cell proliferation

CCK-8 was used to determine how AUP1 affected the ability of UM cells to proliferate. UM cells were grown in triplicate in 96-well microplates with a cell density of 5,000 per well. Following transfection, the cells were treated at 37°C for 2 h with 10 µL of CCK-8 solution (A311-01, vazyme, Nanjing, China) mixed with 90 µL of complete media in each well at 0, 24, 48, 72, or 96 h. Finally, the absorbance of each well was measured at 450 nm using a microplate reader. The EdU test was used as an additional technique to quantify cell proliferation using the EdU proliferation detection kit (Ribobio, Guangzhou, China). In a nutshell, EdU was applied to MuM-2B and OCM-1 cells (2×10^5 cells per well) for 2 h before they were stained with DAPI (Thermo Fisher Scientific, USA). A fluorescent microscope (Olympus, Japan) was used to take pictures of the EdU-positive cells, which were then processed in ImageJ.

2.13 Transwell migration

The Transwell migration test was used to detect cell migration in a 24-well transwell plate with 8 m-pore membrane filters. In a nutshell, 10% FBS was added to the media in the bottom chamber, and 2×10^5 cells in serum-free medium were coated on the top chamber. After a 48-hour incubation period, the cells that had migrated to the chamber's bottom were bathed in 4% methanol for 10 minutes before being stained for 15 min with 0.1% crystal violet (Solarbio, Beijing, China). The images were taken using a microscope's eyepiece, and the number of migrating cells was counted using ImageJ software.

2.14 Wound-healing assay

The wound healing experiment reflects the MuM-2B and OCM-1 cells' migratory patterns. 80% confluence was obtained by the transfected cells after they had been cultured in a six-well plate and incubated at 37°C. A sterile 200 µL pipette tip left a liner scrape in cell monolayers. The medium was changed to one without serum following two PBS washes to remove cell debris. Under an inverted microscope, the distance that cells traveled into the wound surface was gauged at 0 h and 48 h (Olympus, Japan). Lastly, we examined the wound region using ImageJ software. Data were shown as the rate of relative cell migration.

2.15 Animal models

All animal studies were authorized by the Nanjing Medical University Animal Experiment Ethics Committee. Null BALB/c mice that were five weeks old were utilized as the xenotransplantation model. MuM-2B cells that were stably transfected with AUP1 and control cells were implanted into mice's left and right groins to conduct tumorigenic studies. The tumor volume was calculated every five days. The tumor from the xenograft was removed and weighed 25 days after injection.

2.16 Statistical analysis

R software, namely version 4.2.0, was used to conduct our analyses. Student t-tests or one- or two-way ANOVAs with Bonferroni's multiple comparison *post hoc* tests were used to determine statistical significance in GraphPad Prism 8 (La Jolla, CA, USA). Three times each operation was carried out. The mean and standard deviation (SD) of the data were shown. With a p-value of 0.05, the result was considered statistically significant.

3 Results

3.1 scRNA profiling of uveal melanoma

Figure 1 shows the process used in this investigation. 28,981 cells were deleted after quality screening using the aforementioned standards. The eleven samples included in the investigation had no observable batch effects since the distribution of cells within each piece was pretty uniform (Figure 2A). Then, using the t-SNE approach, all cells were divided into 24 more specific clusters depending on all levels of gene expression (Figure 2B). We used differential expression analysis to find DEGs—cluster marker genes—for several clusters. These clusters were recognized as known cell lineages using "singleR" package annotation and previously reported marker genes (Figure 2C). An image of the expression of

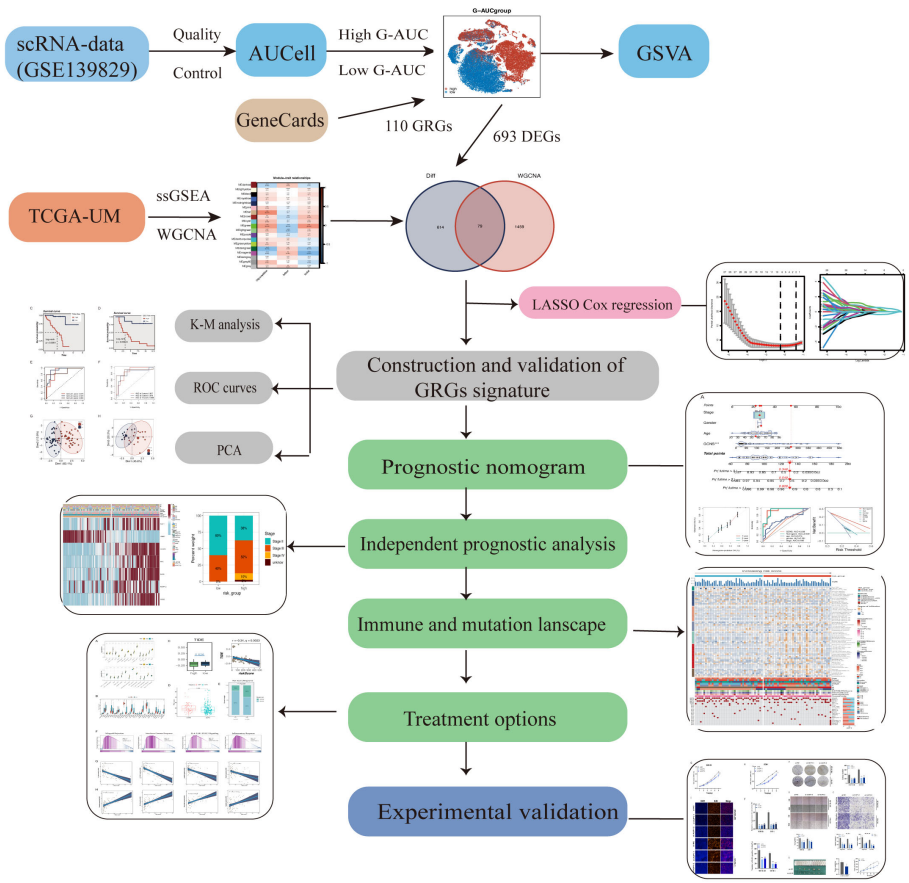

FIGURE 1
The technical roadmap of this study.

10.3389/fendo.2023.1163046

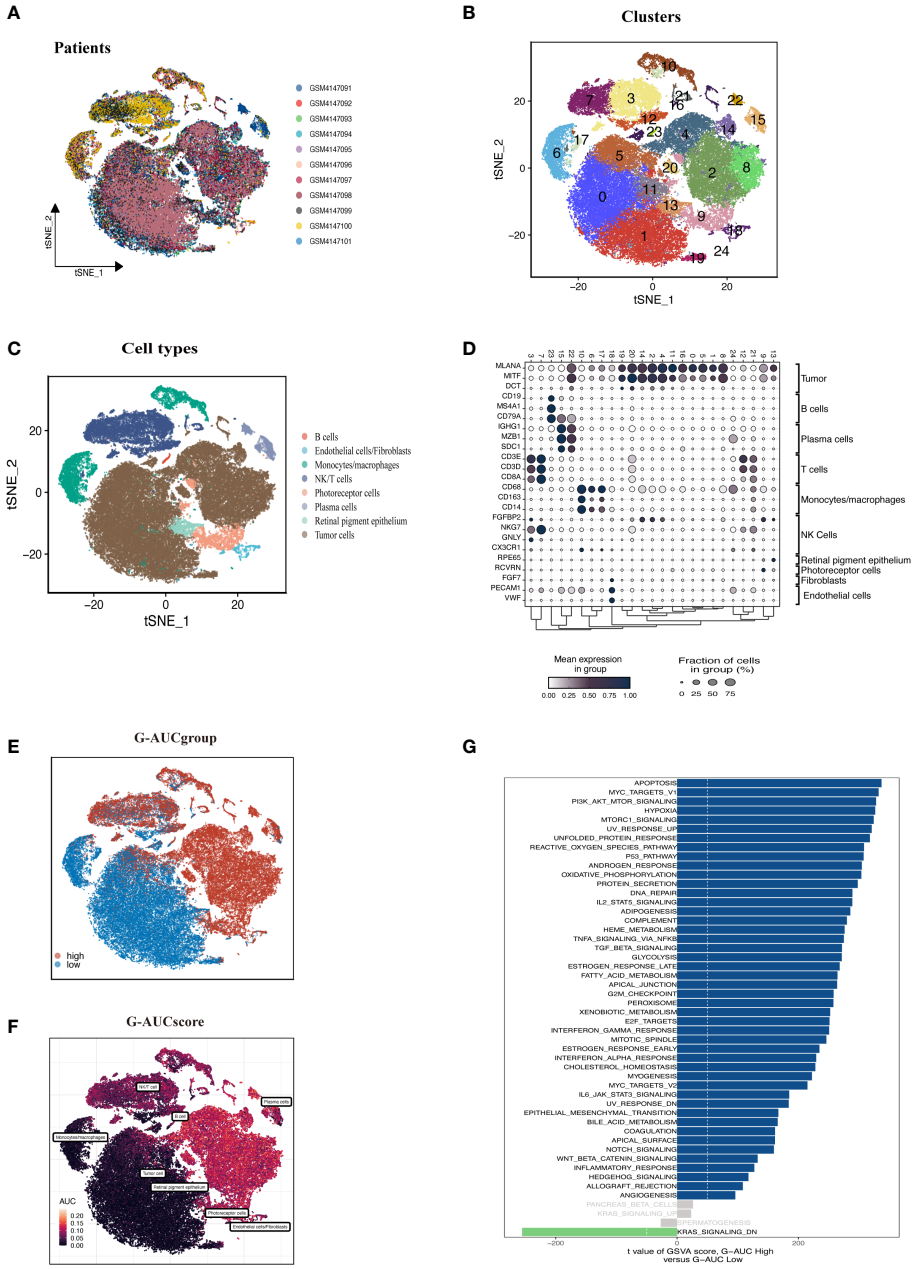

FIGURE 2
Overview of the single-cell landscape of UM tumor samples of GSE139829. **(A)** The t-SNE plot shows the integration of 11 samples. Cells were evenly distributed among all samples, suggesting no significant batch effects among the UM clusters. **(B)** After quality control and standardization, all cells in 11 samples revealed 24 cell clusters marker with unique colors. **(C)** The cells were annotated into eight categories of cell types according to the composition of the marker genes, namely B cells, endothelial cells, monocytes/macrophages, NK/T cells, photoreceptor cells, plasma cells, retinal pigment epithelium, and tumor cells. **(D)** Dot plot of cell type marker genes. Cell-specific marker genes were selected according to previous studies. The color of the dots represents the average expression, and the size represents the average percentage of cells expressing the desired gene. **(E)** Visualization of the percentage of GRGs in each cell *via* the AUCell package. The cells were divided into high and low groups, namely high G-AUC and low G-AUC subgroups. **(F)** t-SNE plots of the AUC score in all clusters. B cells and plasma cells express more GRGs and exhibit higher AUC values. **(G)** GSVA analysis revealed significant enrichment pathways between the high G-AUC and low G-AUC groups; blue represents the enrichment pathway in the high G-AUC group, and the green represents the pathway involved in the low G-AUC group.

cell type-specific marker genes is shown in Figure 2D. There are eight kinds of cells, including tumor cells, monocytes/macrophages, and endothelial cells/fibroblasts. We could examine the GRGs expression patterns by measuring each cell line's GRGs activity using the "AUCell" package (Figure 2E). The AUC values were higher in cells that expressed more genes, and in this study, most of these cells were orange-colored B cells and plasma cells (Figure 2F). According to the AUC score threshold values, all cells were given an AUC score for the associated GRGs, and they were then split into two groups (high and low G-AUC subgroups). To understand the

likely biological processes behind these variations, we conducted differential and functional analyses. According to GSVA data, we discovered apoptosis, MYC targets V1, and the PI3K/AKT/mTOR signaling pathway were particularly prevalent in the high G-AUC subgroups (Figure 2G).

3.2 WGCNA

Each TCGA-UM sample received a glycosylation score from ssGSEA, as shown in Figure 3A. Patients were split into high-GSN and low-GSN groups depending on the median glycosylation score. The survival analysis discriminated between the high-GSN and low-GSN groups. Glycosylation may be a risk factor for UM since we discovered that patients in the high-GSN group had increased mortality ($P < 0.001$). WGCNA was utilized to narrow the possible GRGs strongly associated with UM prognosis (Figure 3B). 19 non-gray modules were produced with these settings (soft domain value = 7, minimum number of modules = 100, deepSplit = 3, similarity threshold = 0.25) (Figures 3C, D). The relationships between phenotypic traits and each module's expression were evaluated. The DEGs and MEgreen module's 79 overlapping genes were then chosen to be examined in the subsequent phases (Figure 3E).

3.3 Establishment of GRGs signature for prognosis prediction

We sought to create a GRGs prognostic signature based on the previously mentioned 79 intersected genes to investigate further the connection between GRGs and the prognosis of UM patients. When we initially used the TCGA-UM cohort as our training set for univariate Cox analysis, we discovered 63 genes to be substantially ($P < 0.01$) linked with the OS of UM patients. Next, the prognostic model was created using LASSO Cox regression analysis (Figures 4A, B). Finally, seven GRGs (AUP1, HNMT, PARP8, ARC, ALG5, AKAP13, and ISG20) were filtered out with optimal regularization settings. Patients in the TCGA cohort were divided into GCNS_high and GCNS_low groups based on their median risk ratings. According to K-M analysis, individuals in the GCNS_high group served a lower survival time than those in the GCNS_low group ($P < 0.001$) (Figure 4C). We also assessed the connection between GCNS and OS in GSE84976 to demonstrate the predictive

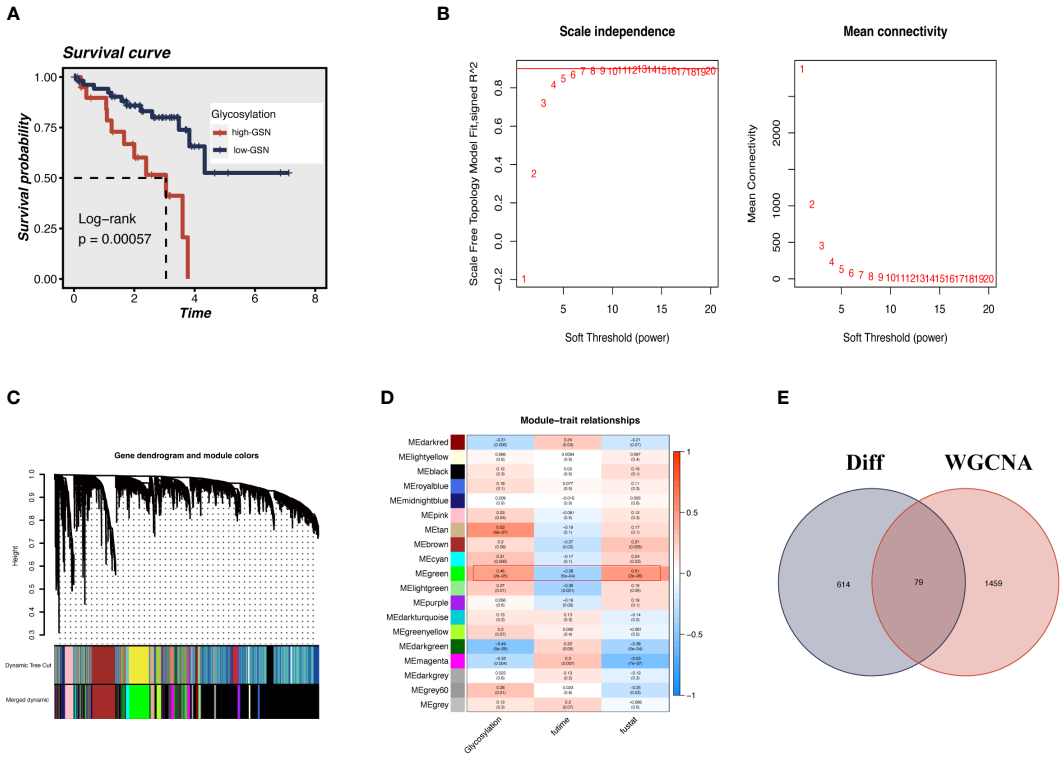

FIGURE 3
ssGSEA and WGCNA. **(A)** The glycosylation score for each UM patient in the TCGA database was calculated. UM patients in the high-GSN group had worse outcomes (P<0.001), suggesting that glycosylation is a risk factor for UM. **(B)** We applied WGCNA to construct the gene co-expression networks of UM patients. The distribution and trends of scale-free topological model fit, mean connectivity and soft threshold. **(C)** The clustering of genes among different modules by the dynamic tree cut and merged dynamic method. **(D)** Heatmap shows the average correlations among module eigengenes and clinical features. The correlation coefficient and p-value (in parentheses) are shown. The MEgreen module is closely related to glycosylation and survival time, marked with red frames. **(E)** The Venn diagram shows the intersection of the DEGs identified between high G-AUC and low G-AUC groups and MEgreen module genes obtained from WGCNA.

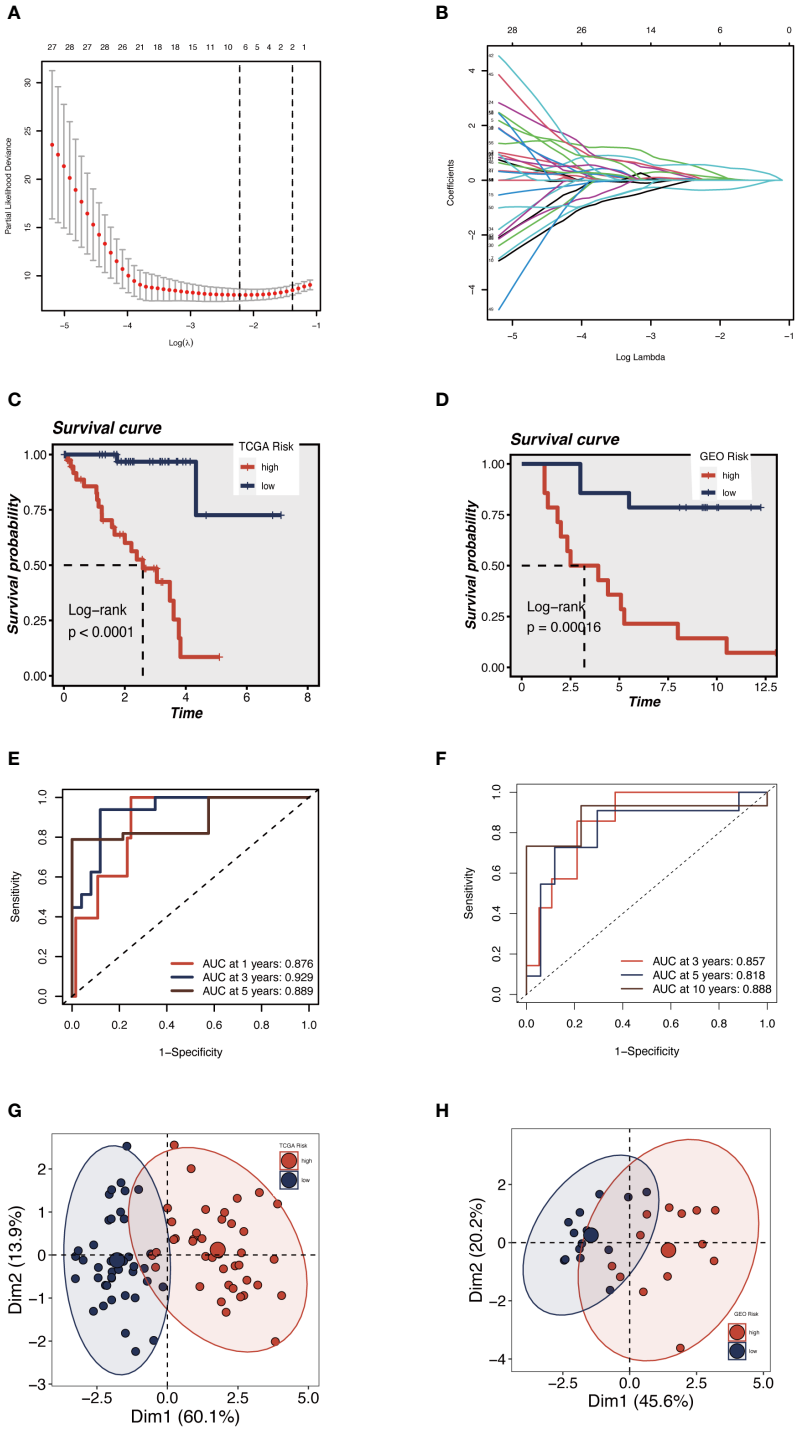

FIGURE 4
Construction and validation of the 5 GRGs model in TCGA-UM cohort and GSE84976. **(A)** 10-fold cross-validation for tuning parameter selection in the LASSO model. **(B)** The Y-axis shows LASSO coefficients and the X-axis is –log (lambda). Dotted vertical lines represent the minimum and one standard error values of lambda. Differences in OS in different risk subgroups in TCGA-UM cohort **(C)** and GSE84976 cohort **(D)** were assessed using the log-rank test. Compared to low-risk UM patients, a shorter OS is found in high-risk UM patients. **(E)** Time-dependent ROC curve depicting the predictive accuracy of the risk model for OS at 1-, 3- and 5-year in the training set (AUC = 0.876, 0.929, and 0.889, respectively). **(F)** The AUC value of the risk score for predicting 3-, 5- and 10-year survival in the validation cohort (GSE84976) were 0.857, 0.818 and 0.888, respectively. The PCA demonstrates that the model can distinguish patients into GCNS_high and GCNS_low groups well in the training set **(G)** and validation set **(H)**.

power of GCNS. Using the same technique, we assigned each patient a GCNS and divided them into two groups. The two groups showed a clear difference in survival analyses, with the GCNS_high groups showing a worse prognosis than the GCNS_low groups, which is consistent with earlier findings (Figure 4D). The training cohort's AUC at 1, 3, and 5 years was 0.876, 0.929, and 0.889, respectively, showing that our model was incredibly influential in predicting UM patients' prognosis (Figure 4E). In the validation set, similar outcomes were attained. Additionally, ROC analysis revealed that the AUC of the model value varied between 0.81 and 0.88, demonstrating the outstanding predictive accuracy of our GCNS model (Figure 4F). PCA well-distinguished patients in the various GCNS groups, showing that the model can stratify risk subtypes in both the training and validation cohorts (Figures 4G, H).

3.4 Development and validation of prognostic nomogram

An integrated GCNS and clinical parameters prognostic nomogram was created to forecast the prognosis of UM patients. Clinical results at 1, 2, and 3 years were used to calculate the patients' survival rates (Figure 5A). The calibration plot demonstrated that the GRGs signature offered exact estimates of UM patients' OS (Figure 5B). The nomogram has more extraordinary predictive ability than any clinical trait, as shown by the ROC curve's AUC of 0.939. (Figure 5C). DCA plots showed that adding clinical variables to GCNS might increase the precision of survival prediction (Figure 5E). The clinical stage and survival status showed a favorable link to a heatmap of clinical variables and prognostic indicators of GRGs. However, other clinical characteristics did not vary statistically (Figure 5D). A percentage bar plot was used to compare the distributions of certain stages among the groups. According to our research, stage II patients make up the majority of patients in the GCNS_low group, whereas stage III patients are in the GCNS_high group (Figure 5F). UM patients were divided into subgroups based on unique clinical characteristics, and the GCNS's ability to predict outcomes was evaluated in each group. Additionally, we saw that patients with GCNS_high consistently had reduced survival chances in all categories, which suggests that the prognostic model applies to all situations.

3.5 Tumor microenvironment components

Given the significant differences in OS amongst GCNS subgroups, we anticipated that the immune milieu would be critical in tumor formation and clinical outcomes. Therefore, we looked for distinctive immunological characteristics in the TCGA-UM patients. Figure 6 illustrates how patients with GCNS_high exhibited higher immune cell infiltration, including M2 macrophage cells and B cells. According to the estimating methodology, patients with high GCNS had significantly higher immune scores, stromal scores, and estimate scores (stromal score plus immune score) than those with low GCNS. According to the data, a relationship exists between GCNS and the amount of immune cell infiltration and TME components. Various rates of disease onset and immunotherapeutic efficacy may result from different immune infiltration levels. We assessed somatic mutation profiles of UM patients based on GCNS in light of the intrinsic link between genetic mutation and tailored treatment for cancer patients. The top three mutant genes were GNAQ, GNA11, and SF3B1, as shown in Figure 6. Combining the mutational gene distributions with GCNS, we found the most prevalent mutation in GCNS_low patients in GNAQ, whereas the most frequent mutation in GCNS_high patients was in GNA11. This discrepancy may help to explain why these groups respond to immunotherapy so differently.

3.6 Immunotherapy and chemotherapy response prediction

To support these findings, we used ssGSEA to compare the immune cell makeup of two GCNS groups (Figure 7A). Those with high GCNS had significantly more partial innate immune cells (like macrophages and DC cells) and adaptive immunity cells (like B cells and T cells) than patients with low GCNS. The GCNS_high subgroup also had higher enrichment scores for functions created linked to the immune system. These results imply that immunological glycosylation-related characterization is more prevalent in the GCNS_high group. We looked at the possibility of this prognostic model to forecast UM patients' responses to ICI therapy. We examined the relationship between the TCGA-UM cohort's GCNS and the most common immunotherapeutic targets. Nearly all ICGs showed noticeably greater expression in the GCNS_high group, including PDCD1 (PD-1), CD274 (PD-L1), CTLA4 and LAG3 (Figure 7B). As shown in Figure 7C, the immunotherapy responses in the GCNS groups were contrasted. One of the key characteristics of cancer that depends on the tumor's ability to survive in the human body is immune system evasion. TIDE is a valuable biomarker for predicting the response to immunotherapy in patients with diverse malignancies, particularly those treated with ICI. This evaluation measures the immune escape capability of tumors (27). In patients taking anti-PD-1 and anti-CTLA-4 therapy, the poorer the ICI response, the higher the tumor TIDE score. We found that patients with high GCNS had significantly lower TIDE scores and a negative association between GCNS and TIDE values ($P < 0.001$, $|r| > 1$).

The risk of a tumor immune escape increased as the TIDE value increased. However, the effectiveness of immunotherapy has decreased. We could infer from this that those with high GCNS are better candidates for immunotherapy. Subsequently, we evaluated the ability of our model to predict the efficacy of immunotherapy using the IMvigor210 cohort to confirm the validity of this discovery. The number of patients receiving anti-PD-1 therapy who saw an objective and partial response increased as the risk score rose (Figures 7D, E). According to our findings, patients in the GCNS_high group had a higher chance of benefiting

10.3389/fendo.2023.1163046

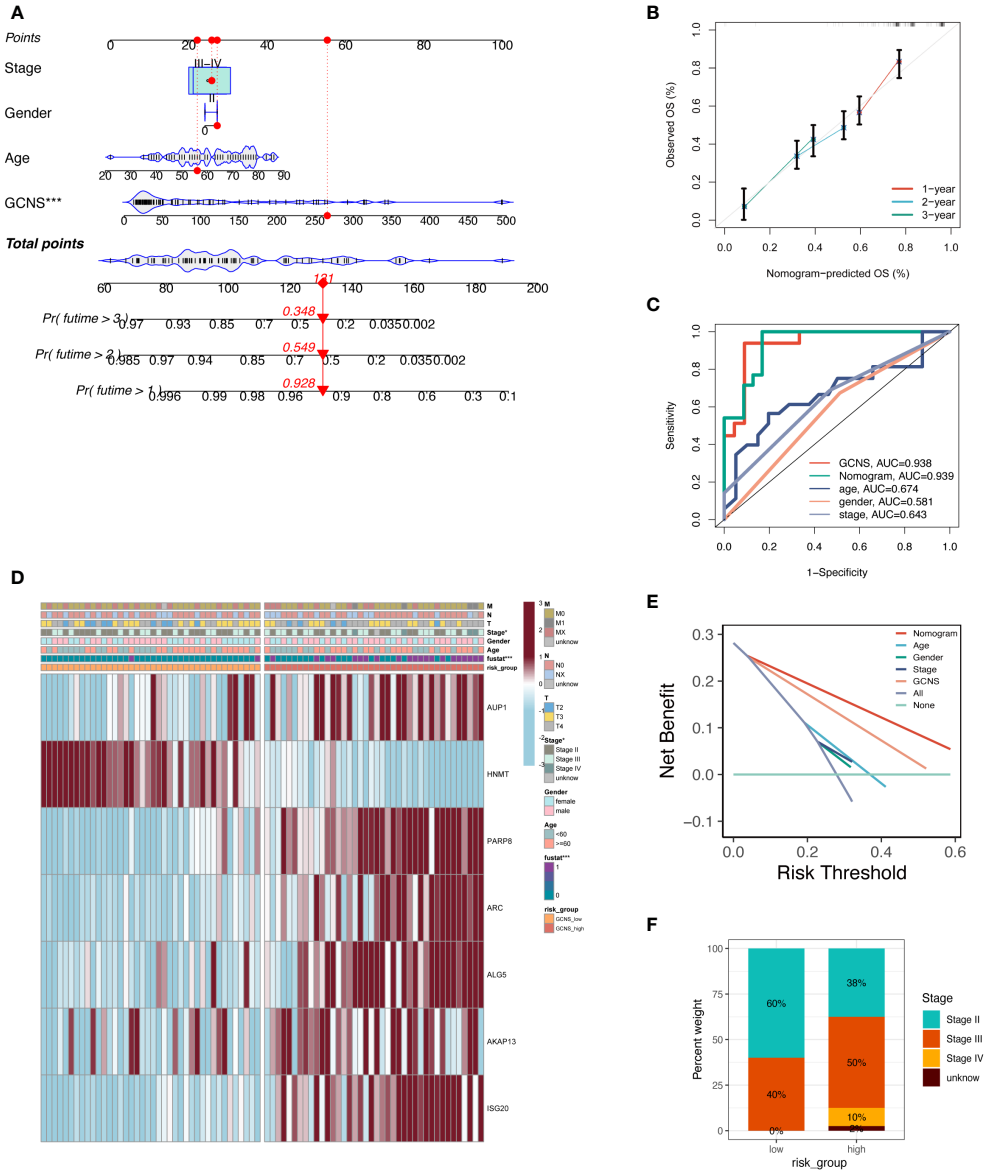

FIGURE 5
Development and evaluation of prognostic nomogram integrating GCNS and conventional clinical traits. **(A)** A nomogram was generated to evaluate the 1, 2, and 3-year survival rates of UM patients based on the TCGA cohort. The red line shows an example of how to predict the prognosis. **(B)** The calibration curve depicted the consistency between nomogram predicted 1-, 2-, and 3-year survival rates of patients and actual survival rates. **(C)** The AUC value predicted by the nomogram for patient prognosis remains about 0.939, which is significantly higher than other clinical features. **(D)** Differences in clinicopathologic features and expression levels of GRGs between the GCNS_high and GCNS_low subtypes. **(E)** DCA curve was drawn to compare the clinical efficacy of the nomogram based on the threshold probability. The upper lines indicate more net benefit. **(F)** UM stage III and IV patients accounted for the largest proportion in the GCNS_high group and increased significantly compared to the GCNS_low group.

from immunotherapy. The GCNS may be a biomarker to pinpoint the right patient population for immunotherapy.

To examine the differences in route enrichment between the GCNS_high and GCNS_low groups, GSEA was used. We discovered that allograft rejection, IL-6/JAK/STAT3 signaling, and the inflammatory response were enriched in the GCNS_high group, suggesting that GCNS_high patients are intimately connected to immune regulation-related and inflammatory pathways (Figure 7F). In order to broaden the practical application of the prognostic model, we forecast how susceptible patients in the GCNS_high and GCNS_low groups would be to chemotherapeutic drugs. Lapatinib, foretinib, LY317615 and 17-AAG all had lower IC50 values in the GCNS_high group, indicating that GCNS_high patients respond better to these medications (Figure 7G). There was a strikingly negative correlation between drug sensitivity and GCNS for cytarabine, SN-38, PD-0332991 and cisplatin, suggesting that these drugs may be more effective in treating GCNS_low people identified by our model (Figure 7H).

10.3389/fendo.2023.1163046

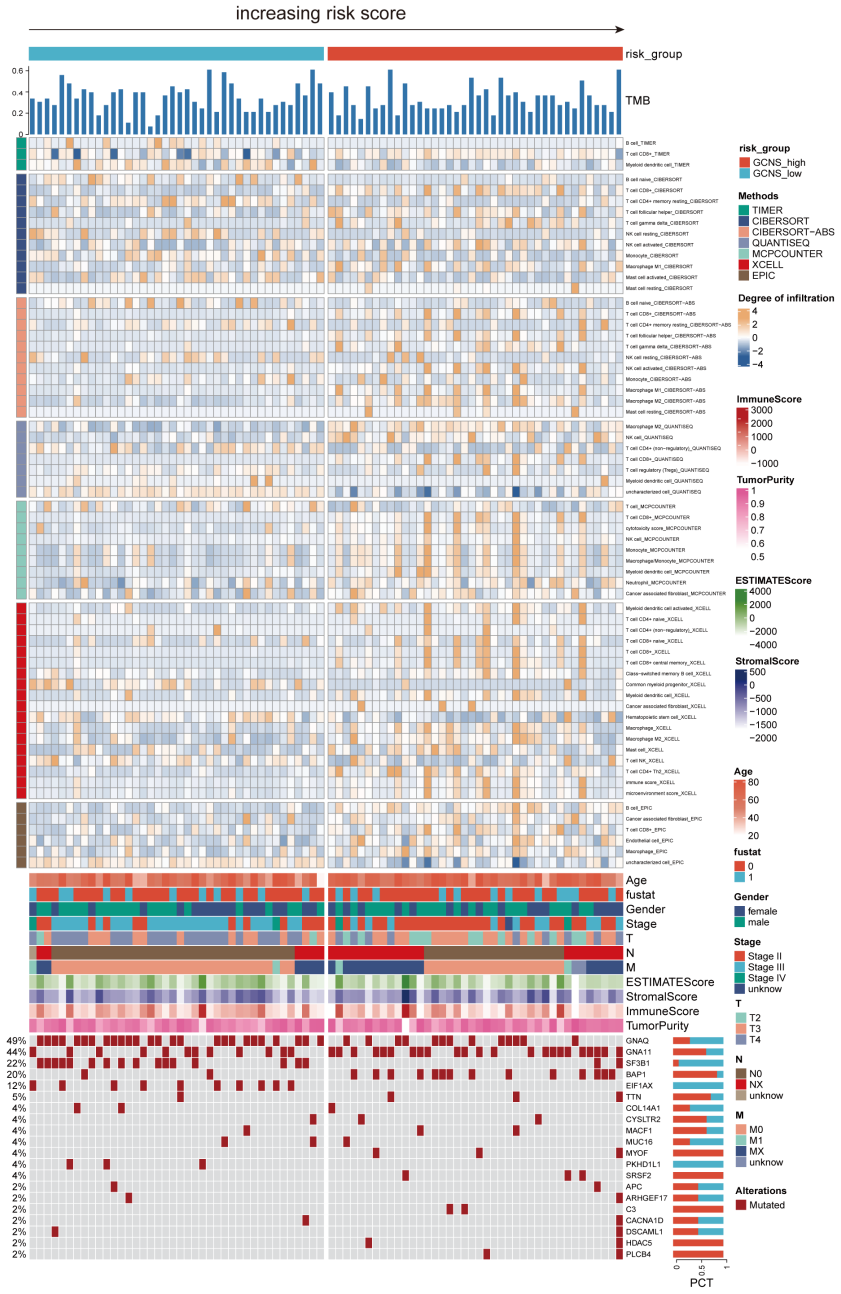

FIGURE 6
The landscape of immune and stromal cell infiltrations in the GCNS_high and GCNS_low groups. The heatmap shows the normalized scores of immune and stromal cell infiltrations according to the evidence from the TIMER database. The Wilcoxon Test compared the two groups' statistical differences in immune cell infiltration. For the GCNS_high group, blue-gray represents cells with lower infiltration, while yellow represents cells with higher infiltration. The GCNS_high group tended to have higher levels of immune cell infiltration. The TMB calculated by package "maftools" was also displayed. Patient's clinical features and gene mutation patterns were also illustrated as an annotation.

3.7 AUP1 promoted the proliferation, migration, and invasion abilities of UM cells

Using univariate and multivariate Cox analysis, the predictive value of AUP1 was contrasted with that of other clinicopathological factors. Forest plots showed that AUP1 had the highest HR among the clinical features, suggesting that AUP1 constituted a separate risk factor for predicting the prognosis of UM patients (Figures 8A, B). Patients with high AUP1 expression had a significantly poorer prognosis than those with low AUP1 expression (Figure 8C). In light of these results, AUP1 was chosen for further *in vitro* testing to confirm its role in UM. GO analysis showed that high AUP1 expression groups were mainly focused on immunoglobulin production, immunoglobulin complex and antigen binding, suggesting the expression of AUP1 was related to immune regulation and metabolism (Figure 8D). According to GSEA, high-AUP1 groups were significantly enriched in allograft rejection, IL6/JAK/STATA3 signaling and inflammatory response

10.3389/fendo.2023.1163046

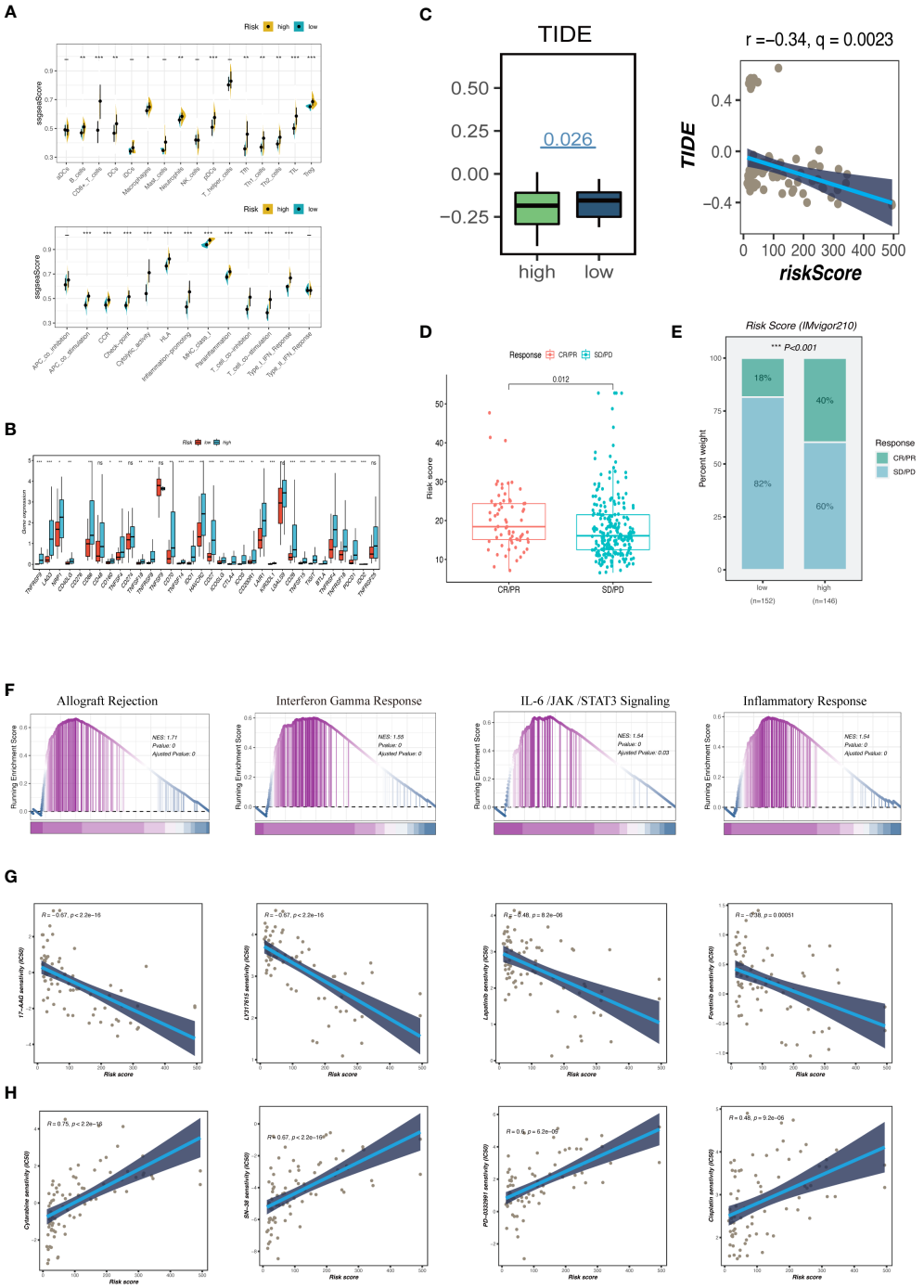

FIGURE 7
Analysis of immune infiltration, immunotherapy and enrichment pathways. **(A)** The differences of tumor-infiltrating of 16 cell types and the score of immune pathways between the GCNS groups by ssGSEA. Between-group differences were evaluated using the Wilcoxon test. The black dots represent the median values, and asterisks indicate significance. **(B)** The differences in expression levels of ICGs between the GCNS_high and GCNS_low subtypes. The lines inside the boxes represent the median values, and the lines outside indicate the 95% confidence interval. **(C)** Prediction of response to immunotherapy. TIDE score was low in the GCNS_high group. Pearson correlation analysis showed a negative correlation between GCNS and TIDE. **(D)** Comparing risk scores in groups with different anti-PD-L1 treatment response statuses in the IMvigor210 cohort. R represents complete response (CR)/partial response (PR); NR represents progressive disease (PD)/stable disease (SD). **(E)** The comparison of the proportion of non-responders and responders to anti-PD-L1 immunotherapy between the two GCNS groups in the IMvigor210 cohort. **(F)** GSEA showed that allograft rejection, IL-6/JAK/STAT3 signaling, and inflammatory response pathways related to immune regulation were activated in the GCNS _high group. **(G, H)** Comparison of the IC50 values of chemotherapy agents in the two GCNS groups. The predicted IC50 values of 17-AAG, LY317615, lapatinib and foretinib were generally lower in the GCNS_high group, whereas cytarabine, SN-38, PD-0332991 and cisplatin had a lower IC50 in the GCNS_low group. *P < 0.05; **P < 0.01; ***P < 0.001.

10.3389/fendo.2023.1163046

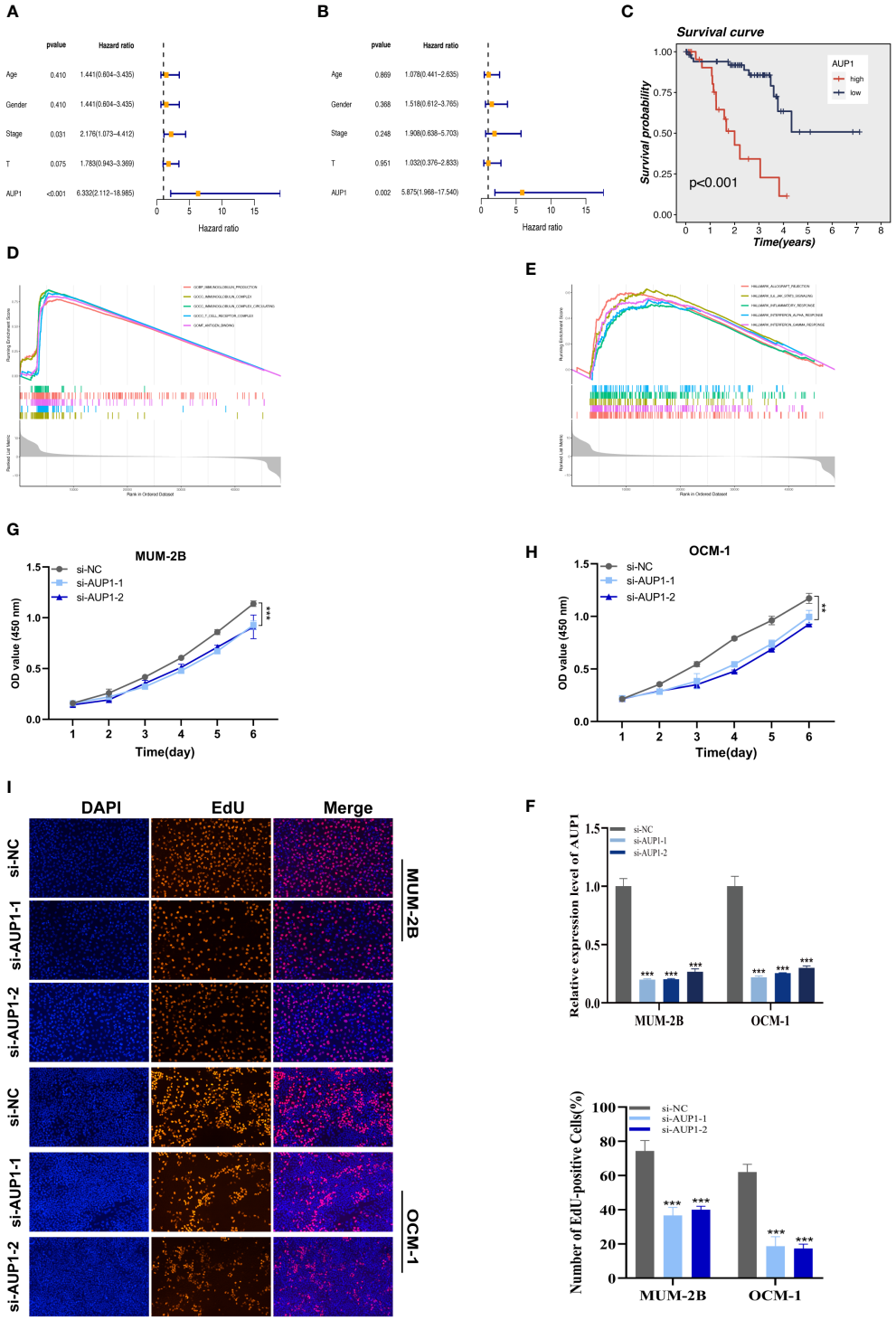

FIGURE 8
The results of univariate **(A)** and multivariate **(B)** Cox regression indicated that the AUP1 was an independent prognostic factor for OS in UM patients. **(C)** Survival analysis of AUP1 in TCGA database. High expression of AUP1 is associated with a poor prognosis of UM. **(D)**. GO analysis of AUP1 high expression group. **(E)** GSEA enrichment plots represented enriched biological pathways in high AUP1 groups. **(F)** The role of the critical gene AUP1 in uveal melanoma cell lines was verified in vitro. Both siRNAs significantly down-regulated AUP1 expression in MuM-2B and OCM-1 cell lines. **(G, H)** The CCK-8 assay showing the proliferation ability of MuM-2B and OCM-1 cells decreased significantly after silencing AUP1. **(I)** EdU staining assay indicated that downregulation of AUP1 expression repressed MuM-2B and OCM-1 cell proliferation. **P < 0.01; ***P < 0.001.

signaling pathways (Figure 8E). The AUP1 knockdown system was created in MuM-2B and OCM-1 cells (Figure 8F). The CCK-8 and EdU assays revealed that AUP1 silencing decreased the proliferation rate of UM cells (Figures 8G–I). Clonal formation experiments simultaneously showed that the MuM-2B and OCM-1 cell lines' capacity to form colonies was significantly diminished (Figure 9A). Additionally, the transwell test and wound healing experiment revealed a lower tendency for UM cell migration and invasiveness following the reduction of AUP1 compared those transfected with si-NC (Figures 9B, C). Comparing AUP1 knockdown to controls, tumor growth, size, and weight were all reduced (Figure 9D). These results suggest that AUP1 was involved in regulating pro-oncogenic processes in UM.

4 Discussion

About 50% of patients with UM die from metastatic UM, the leading cause of mortality in this population (28). Due to the unique characteristics of the ocular anatomy, systemic medication administration in UM patients is frequently suboptimal (29). Because of this, researchers in the UM area are motivated to

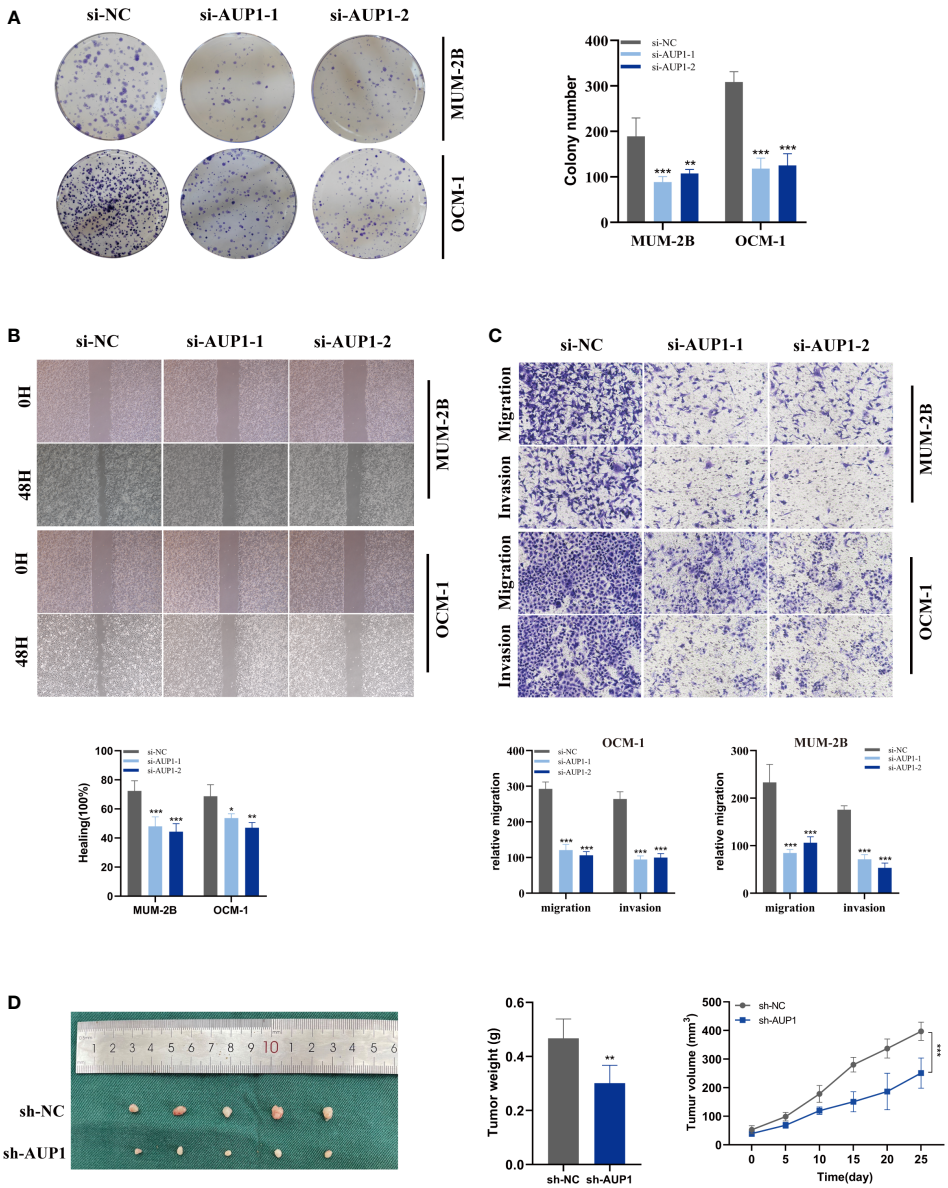

FIGURE 9
Related experiments for AUP1. **(A)** Colony formation assays revealed that the ability of the MuM-2B and OCM-1 cell lines to produce colonies was considerably reduced following AUP1 knockdown. **(B, C)** AUP1 knockdown dramatically reduced the migration and invasion capacity of MuM-2B and OCM-1 cell lines in the wound healing and transwell experiment. **(D)** Experiments using naked mice. AUP1 knockdown decreased tumor growth, and tumor volume and weight were lower in the knockdown group than in the control group. All tests were performed in two UM cell lines (MuM-2B and OCM-1) to verify the accuracy and reproducibility of the results. *P < 0.05; **P < 0.01; ***P < 0.001.

provide more accurate approaches for identifying and managing metastatic illness. A more profound comprehension of the complex ecology of UM is necessary to define the therapy goals for UM patients.

Over 60 years ago (30), the first report of glycosylation variations connected to oncogenic transformation appeared. The disruption of crucial functions within cancer cells and the TME by various types of glycoconjugates is thought to contribute to the growth and spread of cancer (31). Several physiopathological processes may be controlled through glycosylation, which incorporates a number of enzymes, organelles, and other elements to produce post-translational alterations linked to carbohydrates (11). Due to glycosylation's susceptibility, even minor pathogenic alterations or metabolic stress can cause it to malfunction, creating abnormal glycochains and glycoproteins (14). Understanding the causes and consequences of glycosylation changes linked to tumor illness will offer priceless insights into tumor development (11). The complete picture of glycosylation in UM could be more intricate. Therefore, more studies must be done.

Single-cell sequencing technology has made it possible to examine the diverse tumor environment and extract gene expression from UM tumor cells at the individual cell level, essential for identifying the treatment targets for UM patients (32, 33). In this study, using bulk RNA-seq and scRNA data, we built a GCNS model for UM patients and examined the expression patterns of the GRGs. We first identified numerous cell subpopulations inside UM and discovered that the activity of GRGs differed throughout cell lineages, focusing on increased glycosylation activity in B cells and plasma cells. The high G-AUC subgroup was strongly enriched in apoptosis, MYC targets V1, and PI3K/AKT/mTOR signaling pathways, all of which deserve in-depth research in the future, according to GSVA algorithm.

Next, using LASSO algorithm on the TCGA dataset, a prognostic model based on seven OS-related GRGs was created and validated using GSE84976. UM patients were classified into GCNS_high and GCNS_low groups, with those in the GCNS_high group displaying a worse prognosis independent of clinical parameters. We investigated the underlying mechanism after the prognostic signature showed a robust predictive capacity for prognosis in both the training and validation groups. As anticipated, there were differences in the levels of immune infiltration, TMB and immunotherapy response between the GCNS_high and GCNS_low groups, which may cause the heterogeneity of UM tumors.

A growing number of studies have shown that TME is intimately connected to carcinogenesis and can, to some degree, predict tumor prognosis and the effectiveness of immunotherapy. The immune system is suppressed, and lymphatic circulation is restricted in the eye, which eventually causes the CD8+ T cell population to decline (34, 35). High levels of M2-type macrophages and $CD8^+$ T cells are found in the UM immune milieu in the GCNS_high group. $CD8^+$ T cells emerge as a critical player in the tumor immunosurveillance system, indicating a bad prognosis for UM patients. The two G subunit genes, GNAQ and GNA11, which are mutually exclusive, frequently have to activate mutations in UM (36). Notably, the GNAQ mutation was more widespread in the GCNS_low group, whereas the GNA11 mutation was more prevalent in the GCNS_high group. Mutations in GNAQ and GNA11 activate pathways that might serve as a foundation for using MEK or Akt inhibitors in clinical settings (37, 38), thus providing a reference for optimizing targeted therapy in UM patients.

Tumor immunotherapy has quickly advanced, and it is now becoming clear that its primary goals are to stop tumor cells from evading the immune system, boost the body's immunological reaction to tumor cells, and cause immune-received tumor cells to die (39, 40). James P Allison and Tasuku Honjo disclosed numerous immunological checkpoints' immunosuppressive modes and created ICI based on this to block PD-L1/PD-1/CTLA4 (41, 42). ICI in clinical trials have significantly improved cancer treatment in some cancer types, including melanoma. Contrary to previous study's findings, we concluded that immunotherapy would be successful for those in the GCNS_high group using the TIDE algorithm and data from the IMvigor210 cohort. To obtain exact and individualized treatment, we propose giving each UM patient a risk score based on a prognostic model, ascertaining whether they fall into the GCNS_high or GCNS_low group, and treating UM patients in the GCNS_high group with immunotherapy. Rather than PD-1 and CTLA4, the critical sign of failure in UM is the suppressive immunological checkpoint of LAG3 (43). This partially explains why anti-PD-1 and anti-CTLA4 treatments are ineffective. LAG3 is highly expressed in tumor-infiltrating lymphocytes in UM, as Triozzi et al. discovered in 2014 (44). There are several clinical studies evaluating the therapeutic effectiveness of LAG3 inhibitors in treating various malignancies, one of which (NCT02519322) uses relatlimab to treat advanced UM (45).

Clarifying the function of modeling genes in controlling glycosylation in UM is necessary to offer new treatment options for malignancy. Our analysis of seven modeled genes showed that AUP1 had the greatest HR value. A subsequent survival study showed elevated AUP1 expression levels were significantly associated with a poorer clinical outcome in UM patients. Of note, suppressing AUP1 expression significantly inhibited the proliferation and invasiveness of UM cells. Based on the studies, AUP1 is a prospective clinical biomarker for UM. Meisler first recognized and defined AUP1, which contains 410 amino acids and is found on human chromosome 2p13 in a conserved linkage region (46). AUP1 has an "ancient conserved area" in proteins from unrelated organisms (47). Due to its age and high level of sequence conservation, the protein encoded by AUP1 is essential for cell biology (48). However, the function of AUP1 in UM has yet to be determined. The AUP1 high and low expression groups were compared using GSEA to determine which biochemical pathways were significantly enriched in either group. The results of GSEA identified 5 AUP1-associated enriched pathways, and the IL-6/JAK/STAT3 signaling pathway was part of the activated signaling pathway. To our knowledge, the IL-6/JAK/STAT3 signaling pathway is aberrantly hyperactivated in individuals with chronic inflammatory diseases, hematopoietic malignancies and solid tumors (49). Several cell types within the TME release IL-6, activating JAK/STAT3 signaling in both tumor cells and immune cells infiltrating the tumor, promoting tumor-cell

proliferation, survival, invasiveness and metastasis (49). Consequently, we speculated that AUP1 is involved in the IL6/JAK/STAT3 signaling pathway to drive the proliferation, invasion and migration of UM cells. However, the crosstalk and mechanism of the above bioinformatics prediction need verification with well-designed experiments.

Despite the favorable results, the research nevertheless contained several flaws. Since UM had a significant degree of heterogeneity and our signature was built and validated using cohorts in relatively small sample sizes, it is crucial to confirm the GCNS propensity for prognostication in a big multicenter cohort before applying the model in clinical practice. Additionally, we were only concerned with how AUP1 silencing affected UM cell proliferation, invasion, and migration. The description of the potential relationship between the expression of AUP1 and the prognosis for UM. More research is still needed to determine how AUP1 contributes to the development and progression of UM tumors through glycosylation alteration. The predictive biomarker potential of our risk model creates fresh treatment options for UM.

Data availability statement

The original contributions presented in the study are included in the article/Supplementary Material. Further inquiries can be directed to the corresponding authors.

Ethics statement

The animal study was reviewed and approved by The Nanjing Medical University Animal Experiment Ethics Committee.

Author contributions

JL, PZ, and FY contributed conception and design of the study; KJ, SS, and ZX collected the data; JL, PZ, and KJ performed the statistical analysis; JL, PZ, FY, and KJ wrote the first draft of the manuscript; JL, GY, and JT revised the manuscript; JT provided technical and material support; GY and JT gave the final approval of the version to be submitted. All authors contributed to the article and approved the submitted version.

Acknowledgments

We are very grateful for data provided by databases such as TCGA, GeneCards, and GEO. Thanks to reviewers and editors for their sincere comments.

Conflict of interest

The authors declare that the research was conducted in the absence of any commercial or financial relationships that could be construed as a potential conflict of interest.

Publisher's note

Supplementary material

The Supplementary Material for this article can be found online at: https://www.frontiersin.org/articles/10.3389/fendo.2023.1163046/full#supplementary-material

References

1. Chattopadhyay C, Kim DW, Gombos DS, Oba J, Qin Y, Williams MD, et al. Uveal melanoma: From diagnosis to treatment and the science in between. *Cancer* (2016) 122(15):2299–312. doi: 10.1002/cncr.29727

2. Singh AD, Turell ME, Topham AK. Uveal melanoma: Trends in incidence, treatment, and survival. *Ophthalmology* (2011) 118(9):1881–5. doi: 10.1016/j.ophtha.2011.01.040

3. Kaliki S, Shields CL. Uveal melanoma: Relatively rare but deadly cancer. *Eye (Lond)* (2017) 31(2):241–57. doi: 10.1038/eye.2016.275

4. Bustamante P, Piquet L, Landreville S, Burnier JV. Uveal melanoma pathobiology: Metastasis to the liver. *Semin Cancer Biol* (2021) 71:65–85. doi: 10.1016/j.semcancer.2020.05.003

5. Kujala E, Mäkitie T, Kivelä T. Very long-term prognosis of patients with malignant uveal melanoma. *Invest Ophthalmol Vis Sci* (2003) 44(11):4651–9. doi: 10.1167/iovs.03-0538

6. Ortega MA, Fraile-Martínez O, García-Honduvilla N, Coca S, Álvarez-Mon M, Buján J, et al. Update on uveal melanoma: Translational research from biology to clinical practice (Review). *Int J Oncol* (2020) 57(6):1262–79. doi: 10.3892/ijo.2020.5140

7. Igarashi Y, Sasada T. Cancer vaccines: Toward the next breakthrough in cancer immunotherapy. *J Immunol Res* (2020) 2020:5825401. doi: 10.1155/2020/5825401

8. Kennedy LB, Salama AKS. A review of cancer immunotherapy toxicity. *CA Cancer J Clin* (2020) 70(2):86–104. doi: 10.3322/caac.21596

9. Fu Y, Xiao W, Mao Y. Recent advances and challenges in uveal melanoma immunotherapy. *Cancers (Basel)* (2022) 14(13):3094. doi: 10.3390/cancers14133094

10. Moremen KW, Tiemeyer M, Nairn AV. Vertebrate protein glycosylation: Diversity, synthesis and function. *Nat Rev Mol Cell Biol* (2012) 13(7):448–62. doi: 10.1038/nrm3383

11. Stowell SR, Ju T, Cummings RD. Protein glycosylation in cancer. *Annu Rev Pathol* (2015) 10:473–510. doi: 10.1146/annurev-pathol-012414-040438

12. Helenius A, Aebi M. Intracellular functions of n-linked glycans. *Science* (2001) 291(5512):2364–9. doi: 10.1126/science.291.5512.2364

13. Mereiter S, Balmaña M, Campos D, Gomes J, Reis CA. Glycosylation in the era of cancer-targeted therapy: Where are we heading? *Cancer Cell* (2019) 36(1):6–16. doi: 10.1016/j.ccell.2019.06.006

14. Silsirivanit A. Glycosylation markers in cancer. *Adv Clin Chem* (2019) 89:189–213. doi: 10.1016/bs.acc.2018.12.005

15. Zhao C, Xiong K, Zhao F, Adam A, Li X. Glycosylation-related genes predict the prognosis and immune fraction of ovarian cancer patients based on weighted gene coexpression network analysis (Wgcna) and machine learning. *Oxid Med Cell Longev* (2022) 2022:3665617. doi: 10.1155/2022/3665617

16. Zhao CX, Zeng CM, Wang K, He QJ, Yang B, Zhou FF, et al. Ubiquitin-proteasome system-targeted therapy for uveal melanoma: What is the evidence? *Acta Pharmacol Sin* (2021) 42(2):179–88. doi: 10.1038/s41401-020-0441-3

17. Li J, Liu X, Wang W, Li C, Li X. Msk1 promotes cell proliferation and metastasis in uveal melanoma by phosphorylating creb. *Arch Med Sci* (2020) 16(5):1176–88. doi: 10.5114/aoms.2019.85810

18. Chokhachi Baradaran P, Kozovska Z, Furdova A, Smolkova B. Targeting epigenetic modifications in uveal melanoma. *Int J Mol Sci* (2020) 21(15):5314. doi: 10.3390/ijms21155314

19. Wang L, Sfakianos JP, Beaumont KG, Akturk G, Horowitz A, Sebra RP, et al. Myeloid cell-associated resistance to pd-1/Pd-L1 blockade in urothelial cancer revealed through bulk and single-cell rna sequencing. *Clin Cancer Res* (2021) 27(15):4287–300. doi: 10.1158/1078-0432.Ccr-20-4574

20. Zhang P, Pei S, Gong Z, Feng Y, Zhang X, Yang F, et al. By integrating single-cell rna-seq and bulk rna-seq in sphingolipid metabolism, cacybp was identified as a potential therapeutic target in lung adenocarcinoma. *Front Immunol* (2023) 14:1115272. doi: 10.3389/fimmu.2023.1115272

21. Durante MA, Rodriguez DA, Kurtenbach S, Kuznetsov JN, Sanchez MI, Decatur CL, et al. Single-cell analysis reveals new evolutionary complexity in uveal melanoma. *Nat Commun* (2020) 11(1):496. doi: 10.1038/s41467-019-14256-1

22. Aibar S, González-Blas CB, Moerman T, Huynh-Thu VA, Imrichova H, Hulselmans G, et al. Scenic: Single-cell regulatory network inference and clustering. *Nat Methods* (2017) 14(11):1083–6. doi: 10.1038/nmeth.4463

23. Langfelder P, Horvath S. Wgcna: An r package for weighted correlation network analysis. *BMC Bioinf* (2008) 9:559. doi: 10.1186/1471-2105-9-559

24. Zhao J, Li D, Xie S, Deng X, Wen X, Li J, et al. Nomogram for predicting prognosis of patients with metastatic melanoma after immunotherapy: A Chinese population-based analysis. *Front Immunol* (2022) 13:1083840. doi: 10.3389/fimmu.2022.1083840

25. Alemohammad H, Najafzadeh B, Asadzadeh Z, Baghbanzadeh A, Ghorbaninezhad F, Najafzadeh A, et al. The importance of immune checkpoints in immune monitoring: A future paradigm shift in the treatment of cancer. *BioMed Pharmacother* (2022) 146:112516. doi: 10.1016/j.biopha.2021.112516

26. Chi H, Xie X, Yan Y, Peng G, Strohmer DF, Lai G, et al. Natural killer cell-related prognosis signature characterizes immune landscape and predicts prognosis of hnscc. *Front Immunol* (2022) 13:1018685. doi: 10.3389/fimmu.2022.1018685

27. Jiang P, Gu S, Pan D, Fu J, Sahu A, Hu X, et al. Signatures of T cell dysfunction and exclusion predict cancer immunotherapy response. *Nat Med* (2018) 24(10):1550–8. doi: 10.1038/s41591-018-0136-1

28. Beasley AB, Chen FK, Isaacs TW, Gray ES. Future perspectives of uveal melanoma blood based biomarkers. *Br J Cancer* (2022) 126(11):1511–28. doi: 10.1038/s41416-022-01723-8

29. Niederkorn JY. Immune escape mechanisms of intraocular tumors. *Prog Retin Eye Res* (2009) 28(5):329–47. doi: 10.1016/j.preteyeres.2009.06.002

30. Pinho SS, Reis CA. Glycosylation in cancer: Mechanisms and clinical implications. *Nat Rev Cancer* (2015) 15(9):540–55. doi: 10.1038/nrc3982

31. Oliveira-Ferrer L, Legler K, Milde-Langosch K. Role of protein glycosylation in cancer metastasis. *Semin Cancer Biol* (2017) 44:141–52. doi: 10.1016/j.semcancer.2017.03.002

32. Hedlund E, Deng Q. Single-cell rna sequencing: Technical advancements and biological applications. *Mol Aspects Med* (2018) 59:36–46. doi: 10.1016/j.mam.2017.07.003

33. Zou Y, Ye F, Kong Y, Hu X, Deng X, Xie J, et al. The single-cell landscape of intratumoral heterogeneity and the immunosuppressive microenvironment in liver and brain metastases of breast cancer. *Adv Sci (Weinh)* (2023) 10(5):e2203699. doi: 10.1002/advs.202203699

34. Keino H, Horie S, Sugita S. Immune privilege and eye-derived T-regulatory cells. *J Immunol Res* (2018) 2018:1679197. doi: 10.1155/2018/1679197

35. Tao T, Liu Y, Zhang J, Huang L, Tao Y. Dynamic observation: Immune-privileged microenvironment limited the effectiveness of immunotherapy in an intraocular metastasis mouse model. *Ophthalmic Res* (2022) 65(5):584–94. doi: 10.1159/000524485

36. Zhang ED, Zhang M, Li G, Zhang CL, Li Z, Zang G, et al. Mutation spectrum in gnaq and Gna11 in Chinese uveal melanoma. *Precis Clin Med* (2019) 2(4):213–20. doi: 10.1093/pcmedi/pbz021

37. Khan S, Patel SP, Shoushtari AN, Ambrosini G, Cremers S, Lee S, et al. Intermittent mek inhibition for the treatment of metastatic uveal melanoma. *Front Oncol* (2022) 12:975643. doi: 10.3389/fonc.2022.975643

38. Croce M, Ferrini S, Pfeffer U, Gangemi R. Targeted therapy of uveal melanoma: Recent failures and new perspectives. *Cancers (Basel)* (2019) 11(6):846. doi: 10.3390/cancers11060846

39. Zhang Y, Zhang Z. The history and advances in cancer immunotherapy: Understanding the characteristics of tumor-infiltrating immune cells and their therapeutic implications. *Cell Mol Immunol* (2020) 17(8):807–21. doi: 10.1038/s41423-020-0488-6

40. Zheng S, Liang JY, Tang Y, Xie J, Zou Y, Yang A, et al. Dissecting the role of cancer-associated fibroblast-derived biglycan as a potential therapeutic target in immunotherapy resistance: A tumor bulk and single-cell transcriptomic study. *Clin Transl Med* (2023) 13(2):e1189. doi: 10.1002/ctm2.1189

41. Sharma P, Siddiqui BA, Anandhan S, Yadav SS, Subudhi SK, Gao J, et al. The next decade of immune checkpoint therapy. *Cancer Discovery* (2021) 11(4):838–57. doi: 10.1158/2159-8290.Cd-20-1680

42. Iwai Y, Hamanishi J, Chamoto K, Honjo T. Cancer immunotherapies targeting the pd-1 signaling pathway. *J BioMed Sci* (2017) 24(1):26. doi: 10.1186/s12929-017-0329-9

43. Souri Z, Wierenga APA, Kroes WGM, van der Velden PA, Verdijk RM, Eikmans M, et al. Lag3 and its ligands show increased expression in high-risk uveal melanoma. *Cancers (Basel)* (2021) 13(17):4445. doi: 10.3390/cancers13174445

44. Triozzi PL, Schoenfield L, Plesec T, Saunthararajah Y, Tubbs RR, Singh AD. Molecular profiling of primary uveal melanomas with tumor-infiltrating lymphocytes. *Oncoimmunology* (2019) 8(10):e947169. doi: 10.4161/21624011.2014.947169

45. Amaria RN, Postow M, Burton EM, Tezlaff MT, Ross MI, Torres-Cabala C, et al. Neoadjuvant relatlimab and nivolumab in resectable melanoma. *Nature* (2022) 611(7934):155–60. doi: 10.1038/s41586-022-05368-8

46. Jang W, Weber JS, Bashir R, Bushby K, Meisler MH. Aup1, a novel gene on mouse chromosome 6 and human chromosome 2p13. *Genomics* (1996) 36(2):366–8. doi: 10.1006/geno.1996.0477

47. Jo Y, Hartman IZ, DeBose-Boyd RA. Ancient ubiquitous protein-1 mediates sterol-induced ubiquitination of 3-Hydroxy-3-Methylglutaryl coa reductase in lipid droplet-associated endoplasmic reticulum membranes. *Mol Biol Cell* (2013) 24(3):169–83. doi: 10.1091/mbc.E12-07-0564

48. Chen C, Zhao W, Lu X, Ma Y, Zhang P, Wang Z, et al. Aup1 regulates lipid metabolism and induces lipid accumulation to accelerate the progression of renal clear cell carcinoma. *Cancer Sci* (2022) 113(8):2600–15. doi: 10.1111/cas.15445

49. Johnson DE, O'Keefe RA, Grandis JR. Targeting the il-6/Jak/Stat3 signalling axis in cancer. *Nat Rev Clin Oncol* (2018) 15(4):234–48. doi: 10.1038/nrclinonc.2018.8

frontiers | Frontiers in Endocrinology

TYPE Original Research
PUBLISHED 24 March 2023
DOI 10.3389/fendo.2023.1153562

OPEN ACCESS

EDITED BY
Ruiqin Han,
Chinese Academy of Medical Sciences, China

REVIEWED BY
Xianzhou Jiang,
Qilu Hospital, Shandong University, China
Junqiao Lv,
Shanxi Medical University, China

*CORRESPONDENCE
Jingzhi Wang
wangjzjs@163.com

SPECIALTY SECTION
This article was submitted to Cancer Endocrinology, a section of the journal Frontiers in Endocrinology

RECEIVED 29 January 2023
ACCEPTED 14 March 2023
PUBLISHED 24 March 2023

CITATION
Xu X and Wang J (2023) Prognostic prediction and multidimensional dissections of a macrophages M0-related gene signature in liver cancer. *Front. Endocrinol.* 14:1153562. doi: 10.3389/fendo.2023.1153562

Prognostic prediction and multidimensional dissections of a macrophages M0-related gene signature in liver cancer

Xiaoming Xu[1] and Jingzhi Wang[2]*

[1]Department of Gastroenterology, Jining First People's Hospital, Jining, China, [2]Department of Radiotherapy Oncology, The Affiliated Yancheng First Hospital of Nanjing University Medical School, The First People's Hospital of Yancheng, Yancheng, China

Background: Liver hepatocellular carcinoma (LIHC) is the seventh most commonly diagnosed malignancy and the third leading cause of all cancer death worldwide. The undifferentiated macrophages M0 can be induced into polarized M1 and M2 to exert opposite effects in tumor microenvironment. However, the prognostic value of macrophages M0 phenotype remains obscure in LIHC.

Methods: The transcriptome data of LIHC was obtained from TCGA database and ICGC database. 365 LIHC samples from TCGA database and 231 LIHC samples from ICGC database were finally included. Macrophages M0-related genes (MRGs) were screened by Pearson correlation analysis and univariate Cox regression analysis based on the infiltration level of Macrophages M0. LASSO regression analysis was employed to construct a prognostic signature based on MRGs, and risk scores were accordingly calculated. Then we investigated the MRGs-based prognostic signature with respects to prognostic value, clinical significance, strengthened pathways, immune infiltration, gene mutation and drug sensitivity. Furthermore, the expression pattern of MRGs in the tumor microenvironment were also detected in LIHC.

Results: A ten-MRG signature was developed and clarified as independent prognostic predictors in LIHC. The risk score-based nomogram showed favorable capability in survival prediction. Several substance metabolism activities like fatty acid/amino acid metabolism were strengthened in low-risk group. Low risk group was deciphered to harbor TTN mutation-driven tumorigenesis, while TP53 mutation was dominant in high-risk group. We also ascertained that the infiltration levels of immune cells and expressions of immune checkpoints are significantly influenced by the risk score. Besides, we implied that patients in low-risk group may be more sensitive to several anti-cancer drugs. What's more important, single-cell analysis verified the expression of MRGs in the tumor microenvironment of LIHC.

Conclusion: Multidimensional evaluations verified the clinical utility of the macrophages M0-related gene signature to predict prognosis, assist risk decision and guide treatment strategy for patients with LIHC.

KEYWORDS

liver cancer, macrophages M0, prognostic signature, immune infiltration, immunotherapy, single-cell analysis

1 Introduction

According to GLOBOCAN statistics 2020, liver cancer is reported to be the seventh most commonly diagnosed malignancy, with over 900,000 new cases per year, while it is the third leading cause of all cancer death (8.3%), which induces a huge disease burden worldwide (1). Liver hepatocellular carcinoma (LIHC) and intrahepatic cholangiocarcinoma (ICC) are the two major histopathological subtypes of liver cancer in clinics, accounting for over 90% of cases (1). Currently, surgical resection is still the primary therapy strategy for liver cancer, and other treatments, including interventional therapy, chemo/radiotherapy, molecular targeted therapy, and immunotherapy are considered supplementary methods. With the development of comprehensive treatment, the prognosis of patients with liver cancer has been partially prolonged (2, 3). However, the whole prognosis of liver cancer remains unsatisfactory on account of concealed early symptoms, local recurrence, and distant metastasis (4). TNM stage is the traditional method to assess the prognosis of patients, whereas it has particular limitations, for it can only analyze the clinical outcome at a macro level. In the era of precision medicine, it is prevalent to process prognostic evaluation utilizing a comprehensive molecular signature, especially in cancer studies. Therefore, the identification of a reliable gene signature to predict the prognosis of patients with liver cancer may contribute to clinical management and risk decision, rendering possible priority for survival improvement.

Tumor microenvironment (TME) is a sophisticated ecosystem that ameliorates tumor growth by promoting angiogenesis and supporting immunosuppression (5). Notably, the interactive mechanisms between cancer cells and diverse immune infiltrating cells have been increasingly focused, in an attempt to exploit novel anticancer strategies. The facts suggest that immune infiltrating cells may exert tumor-promoting effects by driving chronic inflammation and blinding host immune surveillance (5). Commonly, danger-associated molecular patterns (DAMPs) and pathogen-associated molecular patterns (PAMPs) as stimuli to stir tissue homeostasis can be identified by pattern recognition receptors on the surface of innate immune cells like neutrophils, macrophages, dendritic cells, and NK cells, thereby subsequently inflaming the TME (6, 7). However, the inflammation remains unlocked and becomes chronic in TME, which significantly benefits cancer cells (8). Multiple factors gradually remodel the ECM toward more tumor-friendly (8, 9). Macrophages, have been determined to propel tumor progression by enhancing angiogenesis, invasion, and metastasis *in vivo* according to their functional status induced by the TME (10). It is believed that the diversity of macrophages can be employed by cancer cells to contribute to progression utilizing EGF stimulation, for instance (10). Considering the pivotal roles of macrophages in cancer development, previous studies managed to establish favorable prognostic models utilizing macrophages-related genes (MRGs) in several malignancies (11–13). However, the prognostic value of MRGs in liver cancer remains obscure.

Liver cancer cells express PDL1 to inhibit the activity of cytotoxic T cells, so as to evade immune surveillance and infinitely proliferate. Immunocheckpoint inhibitors can reverse the inhibition of liver cancer cells on cytotoxic T cells, rendering cytotoxic T cells active to kill cancer cells (14). At present, immunotherapy for LIHC presents a multi-plan situation. The combination of the anti-PDL1 antibody atezolizumab and the anti-angiogenesis antibody bevacizumab is getting standard in first-line therapy. The anti-PD1 antibody nivolumab and pembrolizumab can also be sequentially applied after tyrosine kinase inhibitor (TKI) in several conditions (15). The current bottlenecks for immunotherapy of LIHC are the exploitation of novel predictive tools to assess therapeutic efficacy and conducting clinical trials to widen the applicable patients, as well as discovering more effective dosage regimens (16).

In this present study, we managed to develop and validate a prognostic signature based on MRGs, through which better risk decisions may be achieved in clinics. Distinct subgroups were also classified based on MRGs. Investigations of the gene signature concerning clinical subgroup, functional characterization, immune infiltration, immune checkpoint expression, and mutation landscape were organized. We also provided implications of drug agents *via* IC50 drug sensitivity analysis. Moreover, single-cell analysis determined the expression pattern of MRGs in the TME of LIHC. The workflow of the present study is summarized in Figure 1.

2 Materials and methods

2.1 Data acquisition and preprocessing

RNA-sequencing data and clinical information of liver hepatocellular carcinoma (LIHC) samples were downloaded from the TCGA database (http://cancergenome.nih.gov) and the ICGC

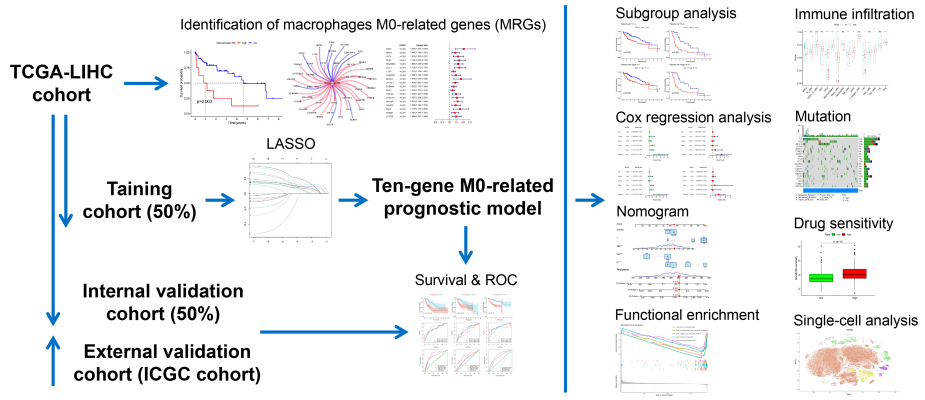

FIGURE 1
Workflow of the present study.

database (https://dcc.icgc.org). Samples without complete survival information were excluded. We thus finally enrolled 365 LIHC samples from TCGA database and 231 LIHC samples from ICGC database.

2.2 Identification of M0-related genes

Above all, we quantified the infiltration levels of 22 immune cells of each TCGA-LIHC sample by the CIBERSORT algorithm. Then the survival difference between the low infiltration group and the high infiltration group of a specific immune cell was investigated. Pearson correlation analysis was used to identify the genes (MRGs) significantly correlated with macrophages M0. Genes with $|r| > 0.4$ and $P < 0.001$ were considered significantly relevant. We next processed Gene Ontology (GO)/Kyoto Encyclopedia of Genes and Genomes (KEGG) functional enrichment analyses of MRGs based on cluster Profiler and org.Hs.eg.db R packages. Univariate analysis was conducted to further filter MRGs that harbor significant prognostic importance.

2.3 Consensus clustering of LIHC based on M0-related genes

Consensus clustering was employed to testify the consistency of selected MRGs by means of dissecting different LIHC subtypes in TCGA cohort. We compared the MRGs expressions and infiltration levels of immune cells between LIHC subtypes. Survival differences between the subtypes were also determined.

2.4 Construction and validation of the prognostic signature based on M0-related genes

TCGA cohort was randomly divided into the training cohort (50%) and internal validation cohort (50%) respectively, while the ICGC cohort was used as the external validation cohort. LASSO regression analysis was employed to construct a prognostic signature based on MRGs in the training cohort. Risk score = $\Sigma(C_i{*}E_i)$, i represented a certain MRG, C represented the coefficient of MRG and E represented the expression level of MRG. The low-risk group and high-risk group were evenly divided according to the median cut-off value of the risk score. Principal component analysis (PCA) was utilized to check out the discrimination between the high-risk group and the low-risk group. We also compared the survival difference between the low-risk group and the high-risk group *via* survminer and survival R packages. The predictive capability of the prognostic signature was tested by receiver operating characteristic (ROC) curves *via* the timeROC R package. Corresponding analyses were also performed in the internal validation cohort and the ICGC cohort.

2.5 Clinical attachment of the prognostic signature and establishment of nomogram

We applied the prognostic signature in several clinical subgroups to further determine its clinical prognostic utility. Next, univariate and multivariate Cox regression analyses were conducted to decipher independent prognostic predictors for LIHC from several clinicopathological parameters and risk score in both the TCGA cohort and the ICGC cohort. We subsequently developed a nomogram to predict overall survival (OS) utilizing several clinicopathological factors. The predictive accuracy of the nomogram was verified by calibration curves.

2.6 Functional strengthens of the two risk groups

The differentially expressed genes (DEGs) between the low-risk group and the high-risk group were identified with the DEGseq R package. Genes with $|\text{Log}_2\text{FC}| > 1$ and $P < 0.05$ were considered DEGs. Gene Set Enrichment Analysis (GSEA) was performed to

determine the significantly enriched functional characterizations in the two risk groups, respectively.

2.7 Differences of immune infiltration and immune checkpoint expression between the two risk groups

We compared the activity of several immune activities between the low-risk group and the high-risk group utilizing single sample gene set enrichment analysis (ssGSEA), as well as the infiltration levels of various immune cells. Moreover, we investigated the expression pattern of 40 immune checkpoints between the two risk groups to ascertain the potential value of the prognostic signature in immunotherapy.

2.8 Mutation landscapes of the two risk groups

The mutation landscapes of the low-risk group and the high-risk group were obtained *via* the maftools R package, respectively. The top twenty most frequently altered genes in the two risk groups were displayed respectively. The difference in tumor mutation burden (TMB) between the low-risk group and the high-risk group was checked out. Besides, low TMB group and high TMB group were divided according to the median cut-off value of TMB. Survival differences between patients in the low-TMB group and the high-TMB group with or without combination of risk groups were further uncovered.

2.9 Drug sensitivity analysis

With the pRRophetic R package, we processed broad drug screening based on the GDSC database (https://www.sanger.ac.uk/tool/gdsc-genomics-drug-sensitivity-cancer/) to ascertain the drug agents that the two risk groups may sensitively respond to.

2.10 Single-cell RNA-sequencing data analysis

About 110992 high-quality cells were filtered and obtained from the LIHC_GSE189903 dataset. The expression pattern of the MRGs were visualized by the Seurat R package based on the single-cell profile of LIHC_GSE189903.

2.11 Statistical analysis

Bioinformatic analyses were all conducted by R 4.0.3. The comparison of the K-M survival curve was achieved by Cox regression analysis. Differences in expression levels between groups were compared by the Wilcoxon rank sum test. Pearson correlation was taken for correlation analysis. $P < 0.05$ was deemed statistically significant. "*" indicates $P < 0.05$, "**" indicates $P < 0.01$ and "***" indicates $P < 0.001$ throughout this study.

3 Results

3.1 Macrophages M0 abundance extremely correlated with the prognosis of LIHC

The infiltration levels of 22 immune cells of each TCGA-LIHC sample were qualified (Figure 2A). We found that the survival difference between high- and low macrophages M0 infiltration groups is the most significant according to its polarized *P*-value ($P = 0.003$) among the 22 immune infiltrating cells (Figures 2B–F). Patients with higher infiltration levels of macrophages M0 suffered from poorer outcomes. A total of 31 MRGs were identified to be

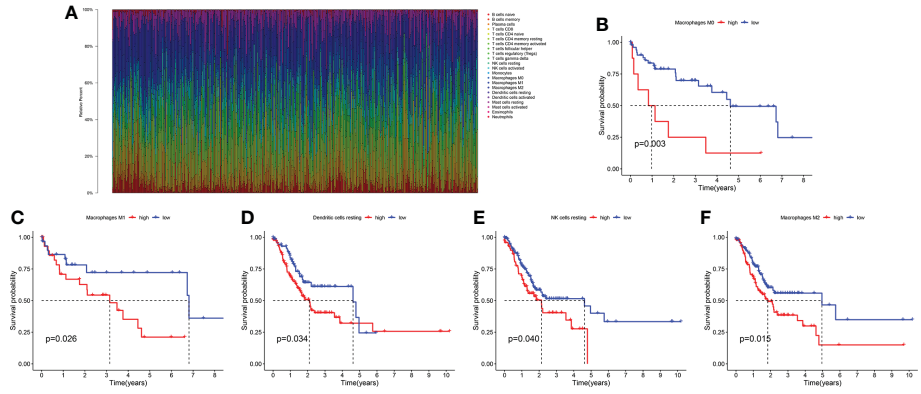

FIGURE 2
The survival significance of 22 immune infiltrating cells in LIHC. **(A)** Quantification of the infiltration levels of 22 immune cells in the TCGA cohort. **(B)** The survival significance of macrophages M0. **(C)** The survival significance of macrophages M1. **(D)** The survival significance of dendritic cells resting. **(E)** The survival significance of NK cells resting. **(F)** The survival significance of macrophages M2.

significantly correlated with macrophages M0 in LIHC, among which ten genes showed positive correlation and the other 21 genes showed negative correlation (Figure 3A). Most MRGs positively correlated with each other (Figure 3B). GO/KEGG functional enrichment analyses indicated that these MRGs are enriched in the external side of the plasma membrane, phagosome, lysosome, apoptosis, protein export, and chemical carcinogenesis-oxidative oxygen species, etc. (Figures 3C, D). Univariate Cox regression analysis further determined 19 MRGs significantly correlated with the prognosis of LIHC ($P < 0.001$) (Figure 3E).

3.2 Two subtypes were divided based on M0-related genes in LIHC

We divided TCGA-LIHC samples into subtype 1 and subtype 2 based on 19 MRGs (Figures 4A–C). The 19 MRGs were all differentially expressed between the two subtypes (Figure 4D). Subtype 1 with higher infiltration levels of macrophages M0 harbored a worse prognosis than subtype 2 ($P < 0.001$) (Figures 4E, F).

3.3 A ten-gene signature was constructed and validated for prognosis prediction in LIHC

A ten-gene signature was generated by LASSO regression analysis in the training cohort (Figures 5A, B). Risk score = 0.1308 * RBFA exp. + 0.0489 * IRAK1 exp. + 0.0882 * KIAA0930 exp. + 0.0936 * CCT3 exp. + 0.0735 * CTSV exp. + 0.1284 * FKBP9P1 exp. + 0.1209 * LPCAT1 exp. + 0.0873 * TUBA4A exp. + 0.058 * SNHG4 exp. + 0.075 * ING5 exp. The expression pattern of the ten MRGs between the low-risk group and the high-risk group was visualized (Figure 5C). The distribution of patients with risk scores in different risk groups was displayed (Figure 5D). PCA further verified the distinct demarcation between the low-risk group and the high-risk group (Figure 5E). Corresponding investigations were performed in the internal validation cohort (Figures 5F–H).

The survival differences between the low-risk group and the high-risk group in the training cohort, internal validation cohort and ICGC cohort were all well distinguished (Figures 6A, D, G). In the training cohort, the AUCs at 1-, 3- and 5-year were 0.779, 0.718, and 0.722 (Figure 6B). In the internal validation cohort, the AUCs at 1-, 3- and 5-year were 0.744, 0.685, and 0.624 (Figure 6E). In the ICGC cohort, the AUCs at 1-, 3- and 5-year were 0.760, 0.819, and 0.772 (Figure 6H). Furthermore, we found that the prediction capability of the prognostic signature is better than any other clinical characteristics, for its general AUCs were 0.792, 0.748, and 0.766 in the three cohorts respectively (Figures 6C, F, I).

3.4 The risk score was identified as an independent prognostic predictor for LIHC

Firstly, we applied the prognostic signature in eight clinical subgroups (Figures 7A–H). Results confirmed the broad applicability of the prognostic signature in all types of patients with LIHC. Distributions of several clinical parameters between the low-risk group and the high-risk group were also demonstrated (Figure 7I). We next identified risk score as an independent prognostic predictor for LIHC in both the TCGA cohort and the ICGC cohort by Cox regression analyses, which verified the strong prognostic value of the prognostic signature ($P < 0.001$) (Figures 7J–M).

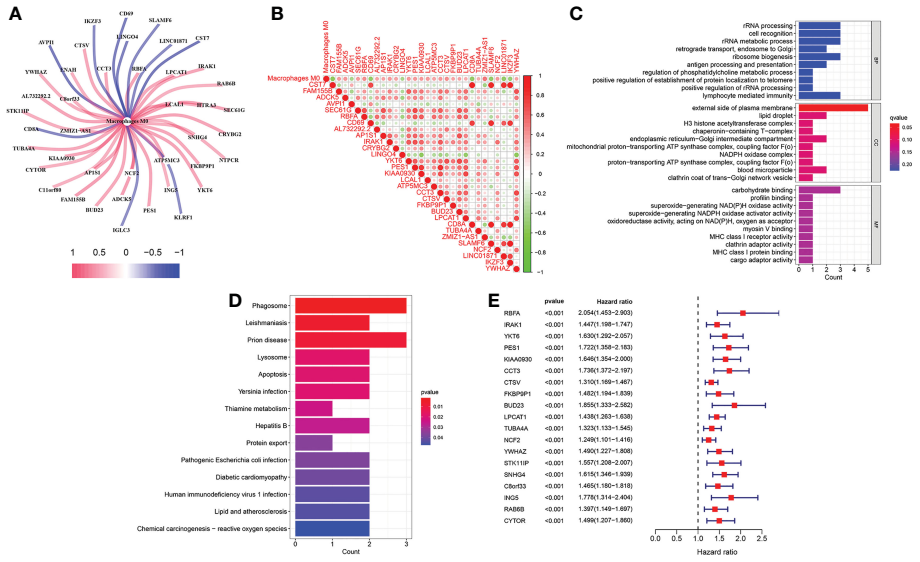

FIGURE 3
Identification of M0-related genes. **(A)** Correlations between MRGs and macrophages M0. **(B)** Correlations within the 31 MRGs. **(C)** GO functional enrichment analysis of the MRGs. **(D)** KEGG functional enrichment analysis of the MRGs. **(E)** Univariate Cox regression analysis of the MRGs.

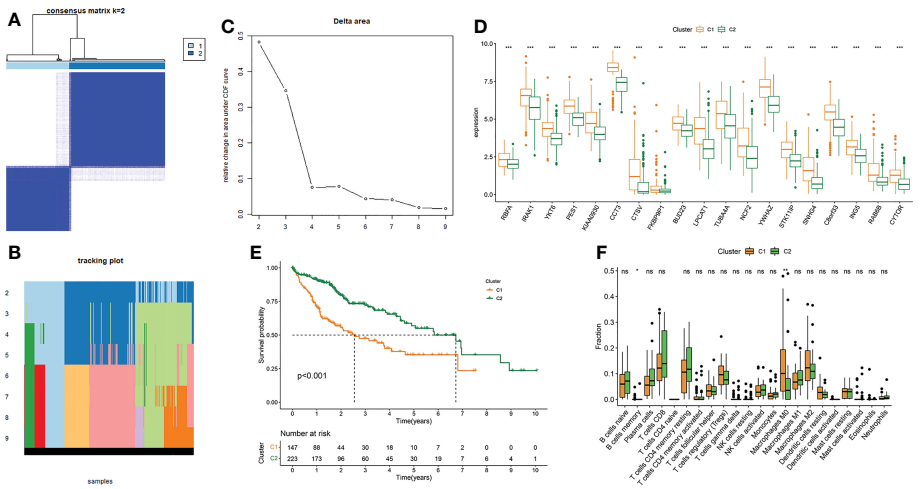

FIGURE 4
Consensus clustering of LIHC based on MRGs. **(A–C)** Consensus clustering. **(D)** Differential expressions of the 19 MRGs between subtype 1 and subtype 2. **(E)** Survival difference between subtype 1 and subtype 2. **(F)** Differences in 22 immune cells' infiltration levels between subtype 1 and subtype 2. **P*-value < 0.05, ***P*-value < 0.01 and ****P*-value < 0.001, ns, represents non-significant.

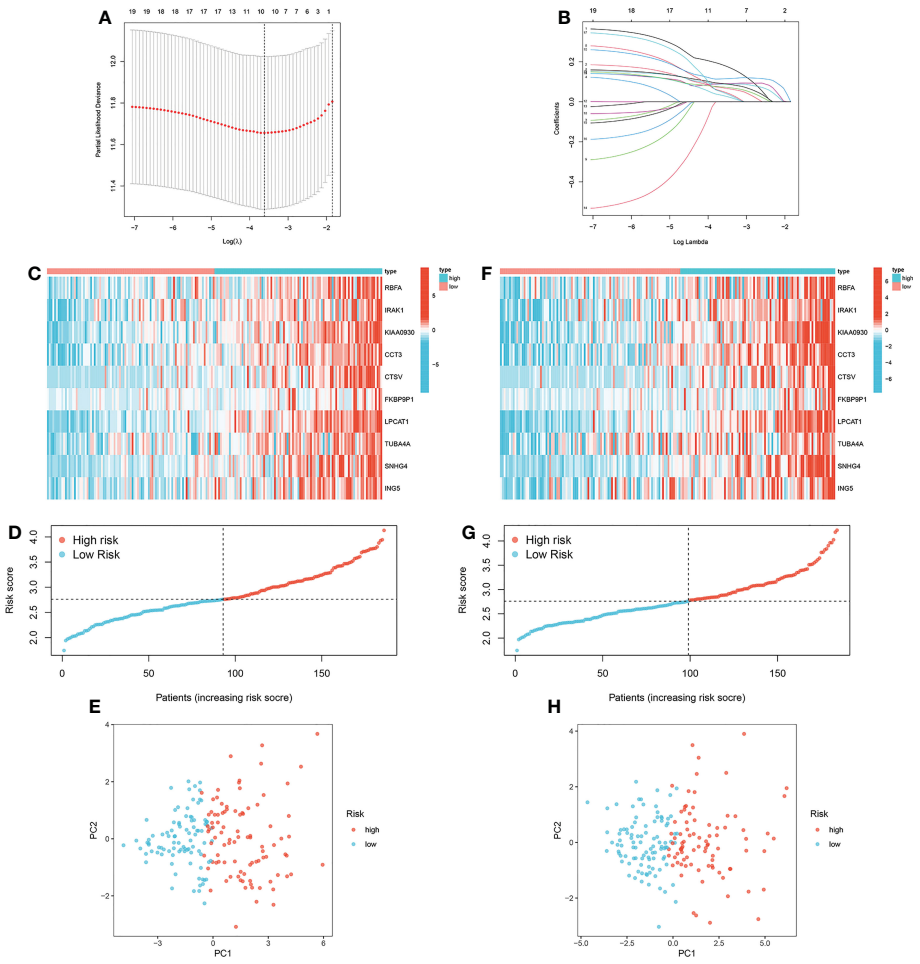

FIGURE 5
Construction of the prognostic signature based on MRGs. **(A, B)** LASSO regression analysis in the training cohort. **(C)** Expression pattern of the ten MRGs between the low-risk group and the high-risk group in the training cohort. **(D)** Distribution of patients with risk scores in different risk groups in the training cohort. **(E)** Principal component analysis in the training cohort. **(F)** Expression pattern of the ten MRGs between the low-risk group and the high-risk group in the internal validation cohort. **(G)** Distribution of patients with risk scores in different risk groups in the internal validation cohort. **(H)** Principal component analysis in the internal validation cohort.

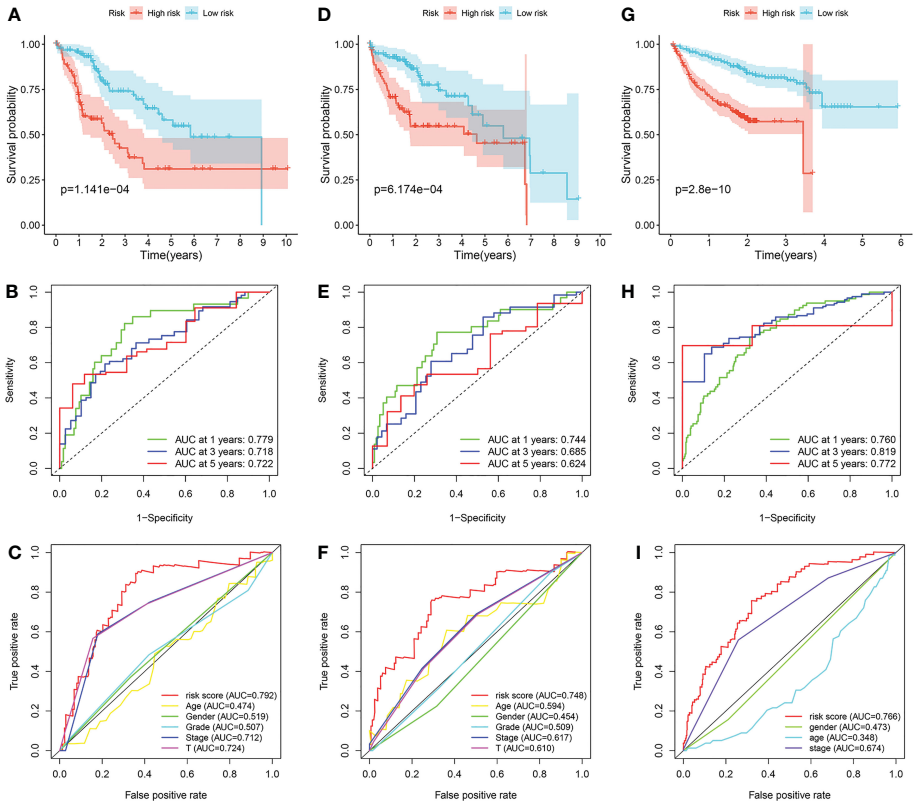

FIGURE 6
Validation of the prognostic signature. **(A–C)** Application of the prognostic signature in the training cohort. **(D–F)** Application of the prognostic signature in the internal validation cohort. **(G–I)** Application of the prognostic signature in the ICGC cohort.

3.5 The risk score-based nomogram showed favorable prediction capability

A nomogram was further developed based on several clinicopathological factors and risk score for OS prediction in the training cohort (Figure 8A). Calibration curves were employed to examine the predictive accuracy, which was close to the ideal line, suggesting excellent predictive efficacy of the nomogram in the ICGC cohort, training cohort, and internal validation cohort (Figures 8B–D).

3.6 Substance metabolism activities were strengthened in low-risk group

Above all, the DEGs between the low-risk group and the high-risk group were ascertained. The DEGs in different risk groups were submitted to GSEA functional enrichment analysis, respectively. The biological activities that are significantly enriched in the high-risk group were positive regulation of cell activation, regulation of lymphocyte activation, external encapsulating structure, immunoglobulin complex, signaling receptor regulator activity, cell adhesion molecules cams, cytokine-cytokine receptor interaction, ECM receptor interaction, hematopoietic cell lineage, and neuroactive ligand receptor interaction (Figures 9A, B). The biological activities that are significantly enriched in the low-risk group were xenobiotic catabolic process, microbody lumen, arachidonic acid monooxygenase activity, aromatase activity, oxidoreductase activity acting on paired donors with incorporation, fatty acid metabolism, glycine serine and threonine metabolism, primary bile acid biosynthesis, retinol metabolism, and tryptophan metabolism (Figures 9C, D). It appeared to be that the substance metabolism activities are significantly strengthened in the low-risk group.

3.7 The risk score correlated with higher immune infiltration and immune checkpoint expression

The ssGSEA results suggested that high risk score is significantly correlated with more active immune activities and higher infiltration levels of immune cells like APC co-stimulation, CCR, checkpoint, HLA, Para inflammation, MHC class I, aDCs, iDCs, macrophages, pDCs, Tfh, Th2 and Tregs (Figures 10A, B). We also determined that high risk score significantly correlates with multiple immune checkpoints, including LAG3, CTLA4, and PD1 (Figure 10C).

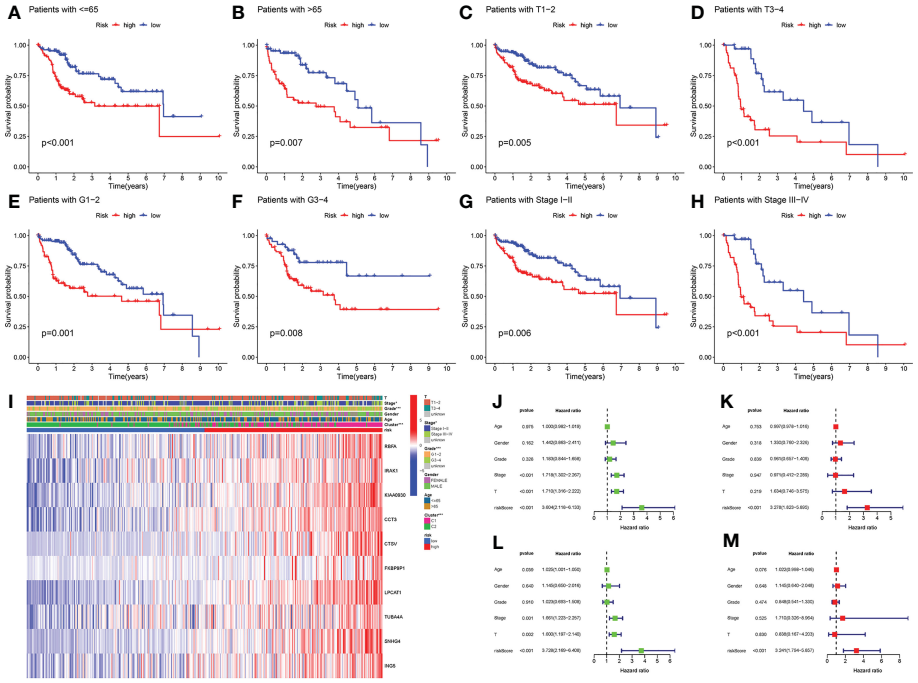

FIGURE 7
Clinical analyses of the prognostic signature. **(A)** LIHC patients with ≤ 65. **(B)** LIHC patients with > 65. **(C)** LIHC patients with T1-T2. **(D)** LIHC patients with T3-T4. **(E)** LIHC patients with G1-G2. **(F)** LIHC patients with G3-G4. **(G)** LIHC patients with stage I-II. **(H)** LIHC patients with stage III-IV. **(I)** Distributions of clinicopathological parameters between the low-risk group and the high-risk group. **(J)** Univariate Cox regression analysis of risk score in TCGA cohort. **(K)** Multivariate Cox regression analysis of risk score in TCGA cohort. **(L)** Univariate Cox regression analyses of risk score in ICGC cohort. **(M)** Multivariate Cox regression analysis of risk score in ICGC cohort. *P-value < 0.05, ***P-value < 0.001.

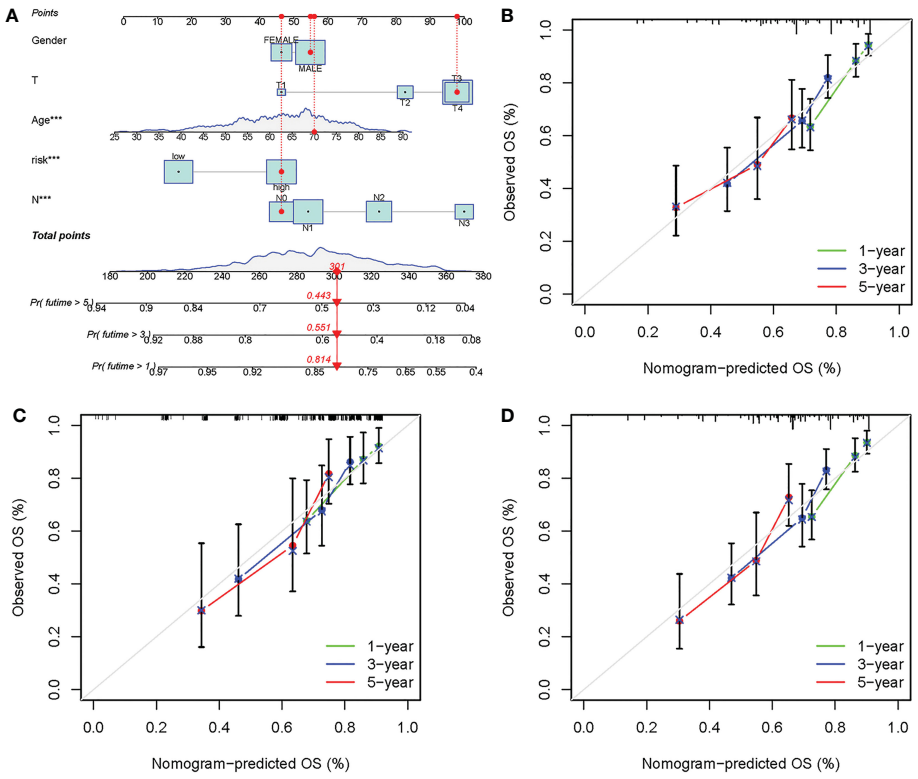

FIGURE 8
Development of a prognostic nomogram based on the risk score. **(A)** Development of the nomogram based on clinicopathological parameters and risk score in the training cohort. Calibration curves at 1-, 3- and 5-year in the **(B)** ICGC cohort, **(C)** training cohort, and **(D)** internal validation cohort. ***P-value < 0.001.

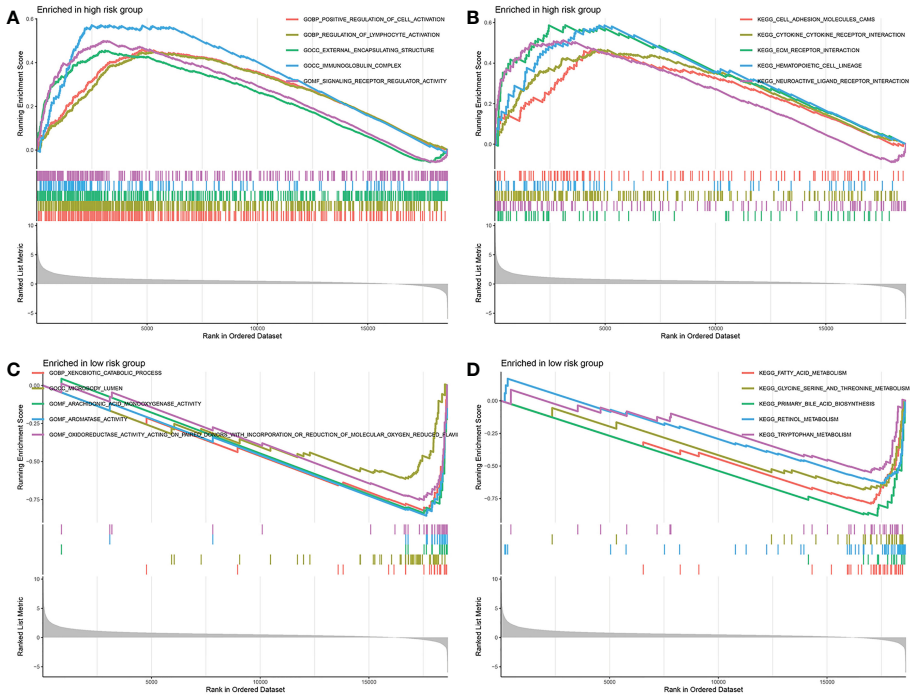

FIGURE 9
Gene set enrichment analysis. **(A, B)** Biological activities enriched in the high-risk group. **(C, D)** Biological activities enriched in the low-risk group.

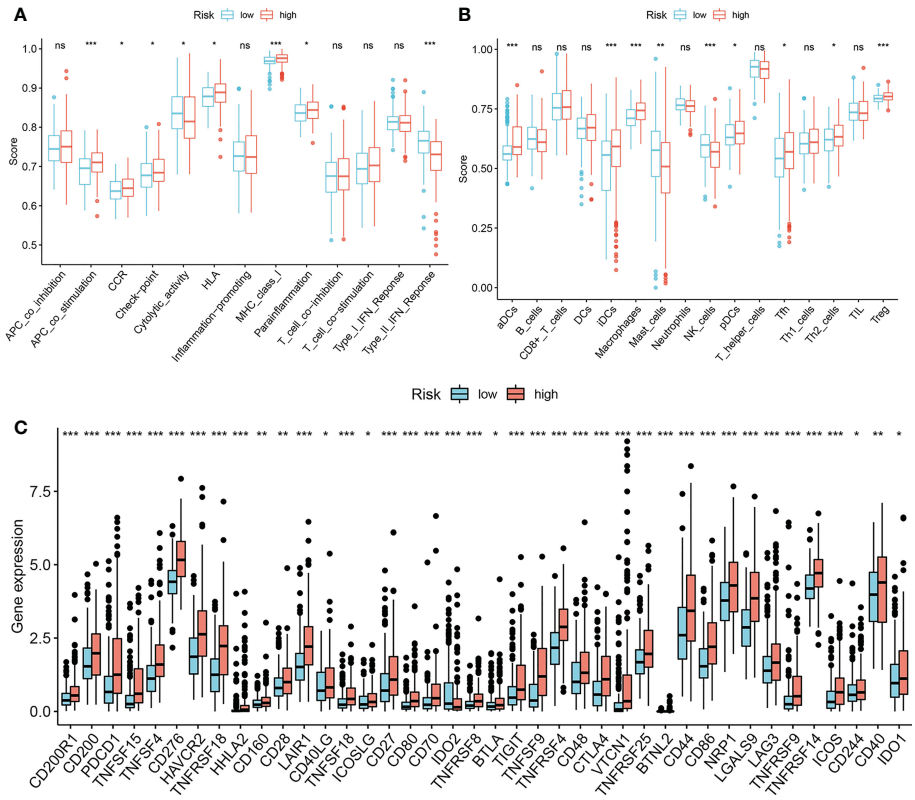

FIGURE 10
Associations between prognostic signature and immune infiltrating cells/immune checkpoints. **(A, B)** single sample Gene Set Enrichment Analysis. **(C)** Expression pattern of 40 immune checkpoints between the low-risk group and the high-risk group. *P-value < 0.05, **P-value < 0.01 and ***P-value < 0.001, ns, represents non-significant.

3.8 Distinct mutation characteristics in low-risk group and high-risk group

We displayed the top 20 most frequently altered genes in the low-risk group and the high-risk group, respectively (Figures 11A, B). TTN (21%) and TP53 (36%) were deciphered to be the most frequently altered genes in the low-risk group and the high-risk group, respectively, and the most common mutation type was observed to be missense mutation. We also compared the TMB difference between the two risk groups, which turned out to be not statistically significant ($P = 0.055$) (Figure 11C). Patients with high TMB harbor poorer clinical outcomes than those with low TMB ($P = 0.031$) (Figure 11D). Survival analysis combining risk score and TMB revealed that patients carrying low TMB and low risk score have the best prognosis, while patients taking high TMB and high-risk score suffered from the worst prognosis ($P < 0.001$) (Figure 11E).

3.9 Patients in low-risk group were potentially sensitive to several drug agents

Drug sensitivity analysis with IC50 indicated that patients in the low-risk group may more sensitively respond to fludarabine, axitinib, cytarabine, sorafenib, and oxaliplatin ($P < 0.001$) (Figure 12).

3.10 Single-cell analysis of the M0-related genes

To further understand the expression pattern of MRGs in the tumor microenvironment (TME) of LIHC, we processed investigations based on single-cell profiles. It was found that the expression levels of RBFA, KIAA0930, CCT3, and TUBA4A were detected in various cell types in the TME (Figure 13). RBFA was detected in hepatocytes and megakaryocyte-erythroid progenitor cells. KIAA0930 was detected in monocytes. CCT3 was detected in B cells, endothelial cells, epithelial cells, hepatocytes, megakaryocyte-erythroid progenitor cells, monocytes, T cells, and tissue stem cells. TUBA4A was detected in B cells, epithelial cells, hepatocytes, and megakaryocyte-erythroid progenitor cells.

4 Discussion

Though progress has been made in achieving better survival probability for patients with LIHC, the general prognosis remains unsatisfactory on account of local recurrence and distant metastasis (2, 3). It is getting prevalent to exploit models for prognosis prediction and risk stratification currently. It is worth mentioning that Zhang et al. (17) first report a macrophages M0-related gene model to predict the survival of patients with LIHC. However, our present prognostic signature has several following distinctions and advantages. Firstly, genes that are negatively or positively correlated with macrophages M0 were both included for subsequent analysis. Secondly, we constructed the prognostic signature with ten MRGs, which renders it more robust. What's more important, the predictive capability of our prognostic signature was stronger, we have higher AUC values in both the training cohort and the validation cohort, which indicated the priority of the present signature to be applied in clinics. In addition, the risk score showed the highest predictive value compared with other traditional clinicopathological features, suggesting the potential advantage of the present signature in aiding practical decision-making. We also applied the prognostic signature in the training cohort, internal validation cohort, and external validation cohort sequentially. Thus, the applicability is verified more rigorously.

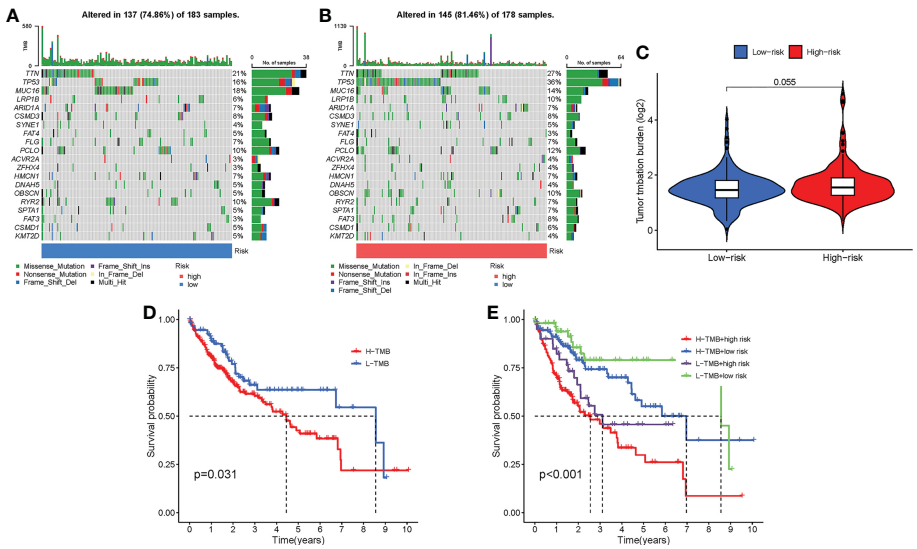

FIGURE 11
Mutation differences between the low-risk group and the high-risk group. **(A)** Mutation landscape in the low-risk group. **(B)** Mutation landscape in the high-risk group. **(C)** Differences in TMB between the two risk groups. **(D)** Survival analysis between patients with low TMB and patients with high TMB. **(E)** Survival analysis combining risk score and TMB.

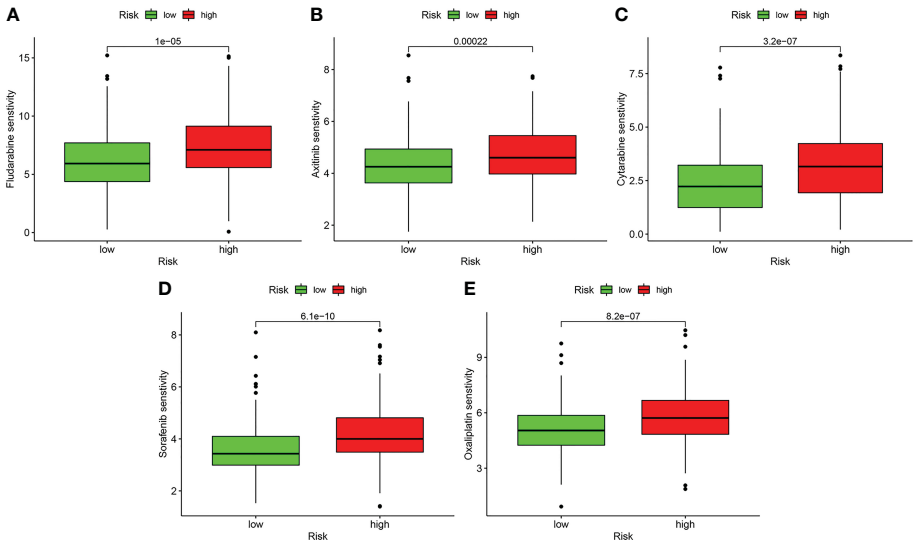

FIGURE 12
Drug sensitivity analysis. **(A)** Fludarabine. **(B)** Axitinib. **(C)** Cytarabine. **(D)** Sorafenib. **(E)** Oxaliplatin.

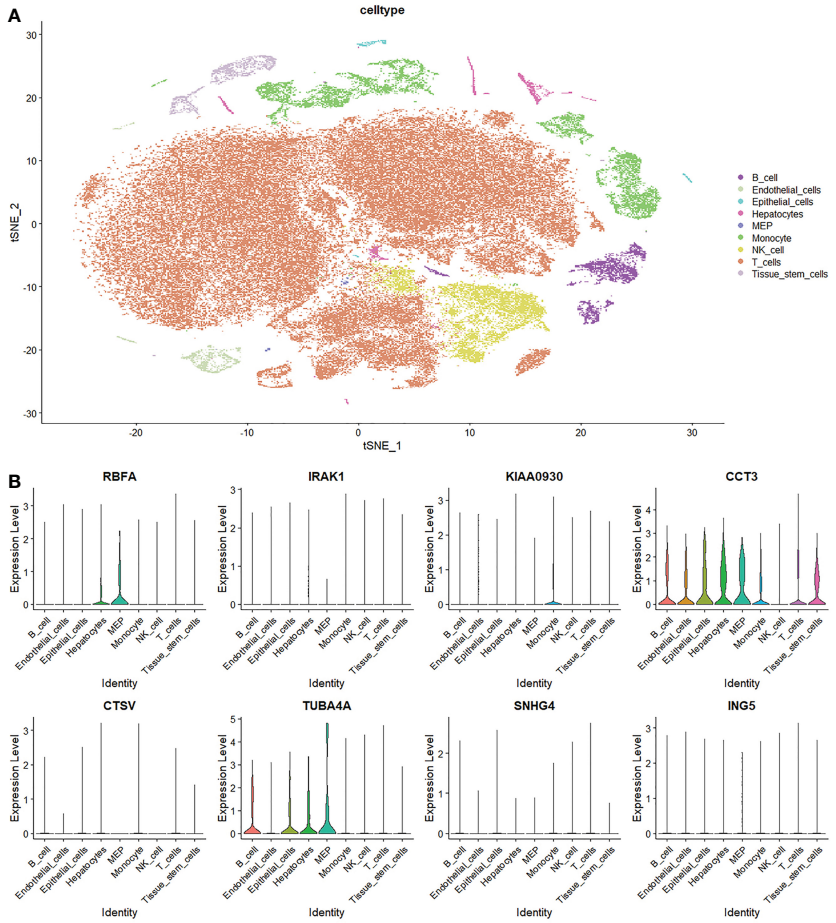

FIGURE 13
Single-cell analysis of macrophages M0-related genes. **(A)** Annotation of cell subclusters in the tumor microenvironment of LIHC. **(B)** Expression pattern of MRGs in the tumor microenvironment.

Subgroup analysis further confirmed the broad applicability of the prognostic signature in all types of patients with LIHC. In addition, the expression pattern of several MRGs in the TME was detected by single-cell analysis. Thus, the macrophages M0-related prognostic signature constructed in the present study may be more clinically practical.

The ten-MRG prognostic signature revealed favorable predictive capability for patients with LIHC, which was more accurate than other clinicopathological factors like grade, T stage, clinical stage, etc. In addition, the risk score was deciphered as an independent prognostic predictor for patients with LIHC, indicating the strong predictive power of the macrophages M0-related gene signature. Macrophages M0 are the undifferentiated cell type that can be potentially induced to polarized cell types, M1 or M2, according to corresponding signals and microenvironment. Macrophages M1 are inflammation-promoting macrophages that secret inflammatory factors, which are caused by lipopolysaccharide (LPS) with or without Th1 cytokines (IFN-γ, GM-CSF, etc.). In contrast, macrophages M2 are induced by Th2 cytokines (IL-4, IL-13, etc.) to exert anti-inflammatory and immune-modulatory effects *via* producing anti-inflammatory factors (18, 19). The regulatory role of macrophages M0 in LIHC remains incompletely demonstrated. We noticed that the ten MRGs presented in this study are all risk factors for the prognosis of LIHC. To this extent, our study lies in the primary demonstration of the association between macrophages M0 phenotype and the prognosis of LIHC. However, more experimental evidence is required to strengthen our implication.

Another significance of the present study revealed that several metabolic activities (fatty acid metabolism, bile acid biosynthesis, retinol metabolism, and amino acid metabolism) are significantly upregulated in low-risk group with better prognosis and relatively low macrophages infiltration. Aberrant substance metabolism or metabolic reprogramming is commonly observed in malignancies whereby tumor cells positively respond to metabolic stress caused by glucose deficiency and hypoxia microenvironment (20). The liver is the largest organ that physiologically undertakes the degradation of metabolites and the synthesis of pivotal substances like urea and albumin (21). Thus, the metabolic stress would even be increased during hepatocarcinogenesis. The processing of glucose, fatty acid, amino acid, and glutamine is generally enhanced in liver cancer cells (22). On the other hand, the liver also functions as an immune organ orchestrated by antigen-presenting cells and lymphocytes wandering around the hepatic sinusoids (23). Thus, in the double settings, liver-resident immunocytes attach great importance to metabolic dysregulation in liver diseases. For instance, the switch between polarized macrophages (from M2 to M1) determined the transformation of the inflammatory microenvironment in the progression of obesity (24). But the complex regulatory network behind is largely unexplored, especially that relevant to macrophages. Macrophages in the TME are also named tumor-associated macrophages (TAMs), which are versatile in carcinogenesis (25). A study regarding the TAMs-LIHC interaction ascertained that TAMs could propel the migration of cancer cells by means of stimulating cellular fatty acid oxidation *via* secreting IL-1β (26). Thus, based on our findings, it is suggested that the TAMs may potentially contribute to aberrant substance metabolism like fatty acid oxidation to affect the malignant phenotypes of liver cancer cells. More experimental analyses are necessary to further explore the association between TAMs and metabolic dysregulation in LIHC.

Immunotherapy, as a promising anti-cancer strategy, has somewhat improved the survival probability of patients with LIHC. Massive tumor-infiltrating immune cells resident in the hepatic sinusoids are potential to be activated by stimulation of immune checkpoint blockade (27–29). Investigation of immune checkpoint expression pattern indicated that key immune checkpoints like PD1 and CTLA4 are significantly upregulated in the high-risk group. Thus, immune checkpoint blockade may better benefit patients in the high-risk group, where lies the value of the M0-related prognostic signature in guiding immunotherapy of patients with LIHC. Excessive gene mutations are one of the triggers for tumorigenesis, especially the tumor suppressor genes (30). TTN and TP53 were determined to be the dominant carcinogenesis-driven genes in the low-risk group and the high-risk group respectively, suggesting the possibility of targeting the two dominant genes for prognosis improvement in different risk groups. Several drug agents were also implied by the M0-related prognostic signature to guide the clinical treatment strategy for patients in low-risk group. For instance, the multi-kinase inhibitor sorafenib is originally suitable for patients with unresectable LIHC. Thus, our findings may serve as a clinical reference to apply sorafenib to patients with low risk score. Additionally, the other four drug agents (fludarabine, axitinib, cytarabine, and oxaliplatin) lack the indication in LIHC. Our findings may imply that clinical trials can be conducted to explore the clinical benefits of applying these old drugs in LIHC.

Single-cell transcriptome data is sequenced from annotated cells with high quality, which renders it more precise than common bulk RNA-sequencing data. Thus, it is widely applied to dissect the TME to further understand the intertumoral heterogeneity (31–33). In the present study, we detected the expression pattern of MRGs in the TME based on single-cell analysis. Results revealed that T cells are the most abundant immune infiltrating cells in the TME. Besides, the active expression of two MRGs, CCT3, and TUBA4A, was determined in multiple immunocytes and stromal cells in the TME. Zheng et al. (31) identified 11 T cell subclusters in the TME based on single-cell technology and clinical LIHC samples. They found that the exhausted CD8+ T cells and Tregs were predominant and potentially clonally expanded in the TME. Other studies also indicated the association between exhausted CD8+ T cells infiltration and unfavorable clinical outcomes in LIHC (34, 35). Thus, positive activation of exhausted CD8+ T cells may help to reverse the poor prognosis. In addition, the interaction between TAMs and T cells may be potentially mediated by the two MRGs, CCT3 and TUBA4A, in LIHC, which requires further investigation.

However, there are certain limitations in the present study. Firstly, specimens from actual clinical patients are needed to get precise verification of the expression of the MRGs. Secondly, a prospective study with a large LIHC cohort from multiple centers will make the M0-related prognostic signature and corresponding results more convincing. Thirdly, more experimental studies are required to further unfold the obscure regulatory axes and functional characterizations of the MRGs in LIHC.

5 Conclusions

In this present study, a ten-gene prognostic signature was constructed and validated based on macrophages M0-related genes in LIHC. Substance metabolism, like fatty acid metabolism, was significantly strengthened in the low-risk group, which may potentially result from TAMs modulation. Multi-dimensional investigations verified the clinical utility of the prognostic signature. Furthermore, single-cell analysis dissected the active expression of MRGs in the TME of LIHC. Taken together, this macrophages M0-related gene signature may provide new insights into prognostic prediction, risk decision, and clinical treatment strategy for patients with LIHC.

Data availability statement

The original contributions presented in the study are included in the article/Supplementary Material. Further inquiries can be directed to the corresponding author.

Author contributions

XX and JW designed the study. XX collected and analyzed the data. XX drafted the initial manuscript. JW reviewed and edited the article. All authors approved the final manuscript. All authors contributed to the article and approved the submitted version.

Conflict of interest

The authors declare that the research was conducted in the absence of any commercial or financial relationships that could be construed as a potential conflict of interest.

Publisher's note

All claims expressed in this article are solely those of the authors and do not necessarily represent those of their affiliated organizations, or those of the publisher, the editors and the reviewers. Any product that may be evaluated in this article, or claim that may be made by its manufacturer, is not guaranteed or endorsed by the publisher.

References

1. Sung H, Ferlay J, Siegel RL, Laversanne M, Soerjomataram I, Jemal A, et al. Global cancer statistics 2020: GLOBOCAN estimates of incidence and mortality worldwide for 36 cancers in 185 countries. *CA Cancer J Clin* (2021) 71(3):209–49. doi: 10.3322/caac.21660

2. Lee DH, Kim D, Park YH, Yoon J, Kim JS. Long-term surgical outcomes in patients with hepatocellular carcinoma undergoing laparoscopic vs. open liver resection: A retrospective and propensity score-matched study. *Asian J Surg* (2021) 44(1):206–12. doi: 10.1016/j.asjsur.2020.05.028

3. Orcutt ST, Anaya DA. Liver resection and surgical strategies for management of primary liver cancer. *Cancer Control* (2018) 25(1):1073274817744621. doi: 10.1177/1073274817744621

4. Forner A, Reig M, Bruix J. Hepatocellular carcinoma. *Lancet* (2018) 391 (10127):1301–14. doi: 10.1016/S0140-6736(18)30010-2

5. Pitt JM, Marabelle A, Eggermont A, Soria JC, Kroemer G, Zitvogel L. Targeting the tumor microenvironment: removing obstruction to anticancer immune responses and immunotherapy. *Ann Oncol* (2016) 27(8):1482–92. doi: 10.1093/annonc/mdw168

6. Woo SR, Corrales L, Gajewski TF. Innate immune recognition of cancer. *Annu Rev Immunol* (2015) 33:445–74. doi: 10.1146/annurev-immunol-032414-112043

7. Sun L, Wang X, Saredy J, Yuan Z, Yang X, Wang H. Innate-adaptive immunity interplay and redox regulation in immune response. *Redox Biol* (2020) 37:101759. doi: 10.1016/j.redox.2020.101759

8. Coussens LM, Zitvogel L, Palucka AK. Neutralizing tumor-promoting chronic inflammation: a magic bullet? *Science* (2013) 339(6117):286–91. doi: 10.1126/science.1232227

9. Kessenbrock K, Plaks V, Werb Z. Matrix metalloproteinases: regulators of the tumor microenvironment. *Cell* (2010) 141(1):52–67. doi: 10.1016/j.cell.2010.03.015

10. Joyce JA, Pollard JW. Microenvironmental regulation of metastasis. *Nat Rev Cancer* (2009) 9(4):239–52. doi: 10.1038/nrc2618

11. Yang Z, Zi Q, Xu K, Wang C, Chi Q. Development of a macrophages-related 4-gene signature and nomogram for the overall survival prediction of hepatocellular carcinoma based on WGCNA and LASSO algorithm. *Int Immunopharmacol* (2021) 90:107238. doi: 10.1016/j.intimp.2020.107238

12. Xu Q, Chen S, Hu Y, Huang W. Clinical M2 macrophages-related genes to aid therapy in pancreatic ductal adenocarcinoma. *Cancer Cell Int* (2021) 21(1):582. doi: 10.1186/s12935-021-02289-w

13. Wang LJ, Xue Y, Lou Y. Tumor-associated macrophages related signature in glioma. *Aging (Albany NY)* (2022) 14(6):2720–35. doi: 10.18632/aging.203968

14. Llovet JM, Castet F, Heikenwalder M, Maini MK, Mazzaferro V, Pinato DJ, et al. Immunotherapies for hepatocellular carcinoma. *Nat Rev Clin Oncol* (2022) 19(3):151–72. doi: 10.1038/s41571-021-00573-2

15. Sperandio RC, Pestana RC, Miyamura BV, Kaseb AO. Hepatocellular carcinoma immunotherapy. *Annu Rev Med* (2022) 73:267–78. doi: 10.1146/annurev-med-042220-021121

16. Sangro B, Sarobe P, Hervás-Stubbs S, Melero I. Advances in immunotherapy for hepatocellular carcinoma. *Nat Rev Gastroenterol Hepatol* (2021) 18(8):525–43. doi: 10.1038/s41575-021-00438-0

17. Zhang Y, Zou J, Chen R. An M0 macrophage-related prognostic model for hepatocellular carcinoma. *BMC Cancer* (2022) 22(1):791. doi: 10.1186/s12885-022-09872-y

18. De Santis M, Locati M, Selmi C. The elegance of a macrophage. *Cell Mol Immunol* (2018) 15(3):196–8. doi: 10.1038/cmi.2017.64

19. Shapouri-Moghaddam A, Mohammadian S, Vazini H, Taghadosi M, Esmaeili SA, Mardani F, et al. Macrophage plasticity, polarization, and function in health and disease. *J Cell Physiol* (2018) 233(9):6425–40. doi: 10.1002/jcp.26429

20. Kroemer G, Pouyssegur J. Tumor cell metabolism: cancer's achilles' heel. *Cancer Cell* (2008) 13(6):472–82. doi: 10.1016/j.ccr.2008.05.005

21. Trefts E, Gannon M, Wasserman DH. The liver. *Curr Biol* (2017) 27(21):R1147–51. doi: 10.1016/j.cub.2017.09.019

22. Du D, Liu C, Qin M, Zhang X, Xi T, Yuan S, et al. Metabolic dysregulation and emerging therapeutical targets for hepatocellular carcinoma. *Acta Pharm Sin B* (2022) 12(2):558–80. doi: 10.1016/j.apsb.2021.09.019

23. Racanelli V, Rehermann B. The liver as an immunological organ. *Hepatology* (2006) 43(2 Suppl 1):S54–62. doi: 10.1002/hep.21060

24. Chatzigeorgiou A, Chavakis T. Immune cells and metabolism. *Handb Exp Pharmacol* (2016) 233:221–49. doi: 10.1007/164_2015_8

25. Locati M, Curtale G, Mantovani A. Diversity, mechanisms, and significance of macrophage plasticity. *Annu Rev Pathol* (2020) 15:123–47. doi: 10.1146/annurev-pathmechdis-012418-012718

26. Zhang Q, Wang H, Mao C, Sun M, Dominah G, Chen L, et al. Fatty acid oxidation contributes to IL-1β secretion in M2 macrophages and promotes macrophage-mediated tumor cell migration. *Mol Immunol* (2018) 94:27–35. doi: 10.1016/j.molimm.2017.12.011

27. He X, Xu C. Immune checkpoint signaling and cancer immunotherapy. *Cell Res* (2020) 30(8):660–9. doi: 10.1038/s41422-020-0343-4

28. Makarova-Rusher OV, Medina-Echeverz J, Duffy AG, Greten TF. The yin and yang of evasion and immune activation in HCC. *J Hepatol* (2015) 62(6):1420–9. doi: 10.1016/j.jhep.2015.02.038

29. Owusu Sekyere S, Schlevogt B, Mettke F, Kabbani M, Deterding K, Wirth TC, et al. HCC immune surveillance and antiviral therapy of hepatitis c virus infection. *Liver Cancer* (2019) 8(1):41–65. doi: 10.1159/000490360

30. Vogelstein B, Papadopoulos N, Velculescu VE, Zhou S, Diaz LAJr, Kinzler KW. Cancer genome landscapes. *Science* (2013) 339(6127):1546–58. doi: 10.1126/science.1235122

31. Zheng C, Zheng L, Yoo JK, Guo H, Zhang Y, Guo X, et al. Landscape of infiltrating T cells in liver cancer revealed by single-cell sequencing. *Cell* (2017) 169 (7):1342–1356.e16. doi: 10.1016/j.cell.2017.05.035

32. Sun Y, Wu L, Zhong Y, Zhou K, Hou Y, Wang Z, et al. Single-cell landscape of the ecosystem in early-relapse hepatocellular carcinoma. *Cell* (2021) 184(2):404–421.e16. doi: 10.1016/j.cell.2020.11.041

33. Zhang Q, He Y, Luo N, Patel SJ, Han Y, Gao R, et al. Landscape and dynamics of single immune cells in hepatocellular carcinoma. *Cell* (2019) 179(4):829–845.e20. doi: 10.1016/j.cell.2019.10.003

34. Ma J, Zheng B, Goswami S, Meng L, Zhang D, Cao C, et al. PD1Hi CD8+ T cells correlate with exhausted signature and poor clinical outcome in hepatocellular carcinoma. *J Immunother Cancer* (2019) 7(1):331. doi: 10.1186/s40425-019-0814-7

35. Barsch M, Salié H, Schlaak AE, Zhang Z, Hess M, Mayer LS, et al. T-Cell exhaustion and residency dynamics inform clinical outcomes in hepatocellular carcinoma. *J Hepatol* (2022) 77(2):397–409. doi: 10.1016/j.jhep.2022.02.032

frontiers | Frontiers in Endocrinology

TYPE Original Research
PUBLISHED 27 March 2023
DOI 10.3389/fendo.2023.1142014

OPEN ACCESS

EDITED BY
Ruiqin Han,
Chinese Academy of Medical Sciences, China

REVIEWED BY
Santosh Chokkakula,
Chungbuk National University, Republic of Korea
Mubashir Ayaz Ahmed,
AMITA Health St. Joseph Hospital, United States
Balaji Pathakumari,
Mayo Clinic, United States

*CORRESPONDENCE
Jun Lyu
lyujun2020@jnu.edu.cn
Liehua Deng
Liehuadeng@126.com

†These authors have contributed equally to this work

‡These authors have contributed equally to this work and share first authorship

SPECIALTY SECTION
This article was submitted to Cancer Endocrinology, a section of the journal Frontiers in Endocrinology

RECEIVED 11 January 2023
ACCEPTED 02 March 2023
PUBLISHED 27 March 2023

CITATION
Chong S, Huang L, Yu H, Huang H, Ming W-k, Ip CC, Mu H-H, Li K, Zhang X, Lyu J and Deng L (2023) Crafting a prognostic nomogram for the overall survival rate of cutaneous verrucous carcinoma using the surveillance, epidemiology, and end results database. *Front. Endocrinol.* 14:1142014. doi: 10.3389/fendo.2023.1142014

Crafting a prognostic nomogram for the overall survival rate of cutaneous verrucous carcinoma using the surveillance, epidemiology, and end results database

Siomui Chong[1‡], Liying Huang[2‡], Hai Yu[1], Hui Huang[1], Wai-kit Ming[3], Cheong Cheong Ip[1,4], Hsin-Hua Mu[5], Kexin Li[6], Xiaoxi Zhang[1], Jun Lyu[2,7*†] and Liehua Deng[1,6*†]

[1]Department of Dermatology, The First Affiliated Hospital of Jinan University and Jinan University Institute of Dermatology, Guangzhou, China, [2]Department of Clinical Research, The First Affiliated Hospital of Jinan University, Guangzhou, China, [3]Department of Infectious Diseases and Public Health, Jockey Club College of Veterinary Medicine and Life Sciences, City University of Hong Kong, Hong Kong, Hong Kong SAR, China, [4]Department of Dermatology, University Hospital Macau, Macau, Macau SAR, China, [5]General Surgery Breast Medical Center, Taipei Medical University Hospital, Taipei, China, [6]Department of Dermatology, The Fifth Affiliated Hospital of Jinan University, He Yuan, China, [7]Guangdong Provincial Key Laboratory of Traditional Chinese Medicine Informatization (2021B1212040007), Guangzhou, China

Background: The aim of this study was to establish and verify a predictive nomogram for patients with cutaneous verrucous carcinoma (CVC) who will eventually survive and to determine the accuracy of the nomogram relative to the conventional American Joint Committee on Cancer (AJCC) staging system.

Methods: Assessments were performed on 1125 patients with CVC between 2004 and 2015, and the results of those examinations were recorded in the Surveillance, Epidemiology, and End Results (SEER) database. Patients were randomly divided at a ratio of 7:3 into the training (n = 787) and validation (n = 338) cohorts. Predictors were identified using stepwise regression analysis in the COX regression model for create a nomogram to predict overall survival of CVC patients at 3-, 5-, and 8-years post-diagnosis. We compared the performance of our model with that of the AJCC prognosis model using several evaluation metrics, including C-index, NRI, IDI, AUC, calibration plots, and DCAs.

Results: Multivariate risk factors including sex, age at diagnosis, marital status, AJCC stage, radiation status, and surgery status were employed to determine the overall survival (OS) rate (P<0.05). The C-index nomogram performed better than the AJCC staging system variable for both the training (0.737 versus 0.582) and validation cohorts (0.735 versus 0.573), which AUC (> 0.7) revealed that the nomogram exhibited significant discriminative ability. The statistically significant NRI and IDI values at 3-, 5-, and 8-year predictions for overall survival (OS) in the validation cohort (55.72%, 63.71%, and 78.23%, respectively and 13.65%, 20.52%, and 23.73%, respectively) demonstrate that the established nomogram outperforms the AJCC staging system (P < 0.01) in predicting OS for patients

with cutaneous verrucous carcinoma (CVC). The calibration plots indicate good performance of the nomogram, while decision curve analyses (DCAs) show that the predictive model could have a favorable clinical impact.

Conclusion: This study constructed and validated a nomogram for predicting the prognosis of patients with CVC in the SEER database and assessed it using several variables. This nomogram model can assist clinical staff in making more-accurate predictions than the AJCC staging method about the 3-, 5-, and 8-year OS probabilities of patients with CVC.

KEYWORDS

cutaneous verrucous carcinoma, nomograms, SEER, prognosis, overall survival (OS)

Introduction

Ackerman discovered the uncommon and unique form of low-grade squamous cell carcinoma known as cutaneous verrucous carcinoma (CVC) in 1948 (1). This cancer develops slowly, is mostly exogenously, and keratoacanthoma-like tumors may appear anywhere on the surface of the skin. However, it appears most frequently on the plantar surface of the foot, anogenital area, and mouth. CVC is uncommon and has been found to occur on the face, maxillary antrum, and buttocks (2–4). Factors induced by chemical carcinogens, trauma, chronic irritability, and human papillomavirus are a few of the causes that have been linked to the development of CVC (5). Only a few instances of CVC have been documented to have metastasized to the local lymph nodes which cannot be attributed to skin metastases that have insufficient supporting documentation (6–9).

The incidence of CVC appears to be increasing rapidly, and it is now the second most common kind of skin cancer (10, 11). In the US, CVC constitutes 20% of skin cancers, corresponding to 1 million cases and contributing to up to 9000 predicted fatalities per year (12). Surgery is still the main treatment intervention. Radiotherapy and chemotherapy are adjuvant treatments, but for primary low-risk patients, the recurrence rate is 8–10% (13, 14).

The American Joint Commission on Cancer (AJCC) Staging Manual includes CVC, and is a significant tool for advising patients, selecting their best treatment, and categorizing them for clinical studies. However, there are a few important limitations in the AJCC staging system for CVC regarding factors that might not be assessed similarly across centers, such as differentiation grading. Another disadvantage is that no independent evaluation of histologic investigations has been performed, and hence risk factors are assumed to be missing if they are not reported. Some pathologic characteristics, such as the tumor depth in millimeters, are not recorded consistently and may impact some instances of AJCC staging. Furthermore, certain AJCC stages of CVC fall short of exact prognostic classification when outcome metrics differ (15–17).

Nomograms have emerged as a valuable predictive tool in the field of oncology in recent years (18). Compared to conventional evaluation methods, nomograms provide a more accurate and easily interpretable means of estimating the probability of a particular clinical outcome in an individual patient. This method has the potential to enhance the precision of prognostic assessments and facilitate more informed clinical decision-making (19). Nomograms have been widely utilized in the prognostication of various kind of malignancies (20–22), such as liver cancer, lung cancer, and breast cancer, their application in predicting clinical outcomes of patients with CVC remains inadequate. Presently, no predictive models have been established that can precisely prognosticate the overall survival (OS) of patients with CVC. Therefore, we have decided to investigate the survival rate of CVC utilizing Surveillance, Epidemiology, and End Results (SEER) data to aid clinicians and patients in determining appropriate treatment options.

The aim of this study was to establish a comprehensive nomogram for CVC patients using the Surveillance, Epidemiology, and End Results (SEER) database, which incorporates essential clinical and pathological features, demographic variables, treatment modalities, and other relevant characteristics. Consequently, the novel nomogram provides clinicians with more accurate and personalized patient survival predictions, superior to AJCC staging system in clinical efficacy. This is may have the potential to enhance population health by promoting improved quality of life and extending lifespan among patients.

Materials and methods

Patient source and extraction

We obtained patient data from the Surveillance, Epidemiology, and End Results (SEER) database, which includes 18 cancer registries and is publicly available at www.seer.cancer.gov. We used SEER*Stat version 8.3.6 software to retrieve and analyze the data. Additional access to the SEER Plus database was requested in compliance with ethical and legal standards. We reviewed information from the public SEER database, a cancer database that covers approximately 28% of Americans (23), and extracted

data on CVC patients from this database (24). Subsequently, the proceeded as follows: the major CVC locations were chosen using the codes "C00.0 to C63.2." All CVC-related ICD-O-3(third revision of the International Classification) histology and behavior codes (8051/3: Verrucous carcinoma, NOS) were included.

Predictor selection

This study aimed to identify prognostic factors for cancer overall survival on CVC patients who were diagnosed between 2004-2015 and staged according to the sixth edition of the American Joint Committee on Cancer (AJCC) staging system which published in 2004. The various demographic and clinical variables screened as CVC prognostic factor that were age, sex, race, marital status, AJCC stage, surgery, radiation, cause-specific death, vital status, chemotherapy, tumor size, combined summary stage, and income. However, due to significant multicollinearity among these factors, we only used the AJCC staging system in the analysis. The outcome predicting variable was cancer overall survival. It is important to note that patient-informed permission was not necessary, as the SEER database used in this study did not include any personally identifying information.

Data selection criteria

A retrospective analysis was conducted using the SEER database, where 2889 patients with CVC between 2004-2015 were initially selected, based on the criteria mentioned previously. After a careful screening process, 1125 patients were finally selected, whereas 1764 patients were excluded due to unknown tumor size, race, or marital status, as well as unknown AJCC stage or an age exceeding 100 years old, which criteria were exclusion. The data selection procedure is depicted in Figure 1.

Nomogram contruction and Cox regression analysis

In order to construct, 70% of patients were randomly allocated to the training cohort (n = 787) and 30% to the validation cohort (n = 338). We applied with univariate Cox regression to identify relevant prognostic factors, subsequent to multivariate Cox regression to determine independent risk factors in the training set. Hazard ratios (HR) and 95% confidence intervals (CI) were simultaneously recorded during this analysis. The nomogram was constructed based on a Cox regression model to identify significant variables for determining the 3-, 5-, and 8-year OS rates in patients with CVC.

Through the allocation of weights to each variable, multiple lines are created, with each variable corresponding to a specific point. Through the cumulative sum of points assigned to all variables, an overall score is obtained, which can be used to predict survival rates at different points in time.

Nomogram verification and clinical applicability

A range of validation method were utilized to ensure the accuracy and reliability of the constructed nomogram in current study. The following describes the content and methods of evaluation applied in this study. These validation method was included the following texts

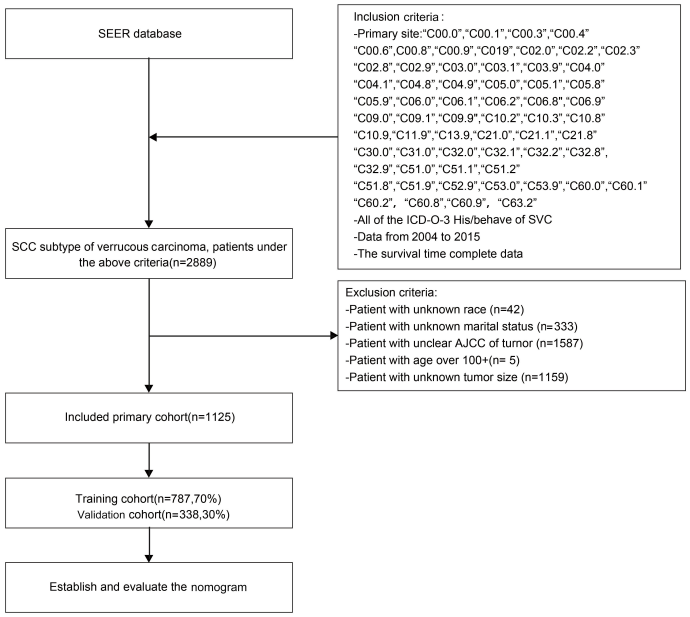

FIGURE 1
Flow chat of research selection. SEER, Surveillance, Epidemiology, and End Result Program; ICD-0-3, International Classification of Disease for Oncology, Third Edition.

mention:the calibration and discrimination of the nomogram were evaluated using bootstrapping with 500 resamples. Comparisons were conducted using net reclassification index (NRI) and integrated discrimination improvement (IDI), which are relatively new markers. This method made the comparisons more thorough and accurate. The concordance index (C-index) and the area under the time-dependent receiver operating characteristic curve (AUC) were employed as assessment tools to assess the potential for differentiation in the new model (25). The accuracy of the survival probability estimations made using the nomogram were evaluated using calibration plots. We further constructed judgment curves in order to assess the potential use of the nomogram in clinical contexts (26).

Decision curve analysis (DCA) is a novel method to assess the clinical utility of a model by determining the net benefit at different risk thresholds. DCA was employed for evaluating new nomogram of clinical potential application. The threshold probability and net benefit of the model were plotted on the abscissa and ordinate, respectively. A higher DCA curve for a model indicates greater clinical utility, as it reflects a higher net benefit at a given risk threshold (27).

Statistical analysis

The software packages R (version 4.2.2; http://www.Rproject.org) and SPSS (version 25.0, SPSS, Chicago, Illinois, USA) were utilized for all statistical analyses of the data. In this analysis of 1125 patients, the log-rank test was used in R software to ensure that noticeable differences did not occur between the two cohorts. The continuous variable of age was quantified as median(25^{th}-75^{th}percentile) and did not follow a normal distribution. Percentages were used to express categorical variables.

The potential prognostic factors were identified using univariate Cox regression, and the relevant variables were included in the multivariate analysis. Then, a Cox regression model was selected using the stepwise regression method. A two-tailed test probability value of $p < 0.05$ was selected as the criterion for significance.

Result

Patient characteristics

This study comprised of 1125 patients with CVC, who were stratified into a training cohort (N=787) and a validation cohort (N=338). The clinicopathological and demographic characteristics of the two cohorts were summarized in Table 1 using SPSS, and no statistically significant differences were found between the groups. The median ages at the CVC diagnosis were in 67 years (interquartile range (IQR), = 56–99 years) and 65 years (IQR = 54– 98 years) in the training and validation cohorts, respectively. Most of the patients in the training and validation cohorts were white (84.0% and 85.2%, respectively), married (52.2% and 51.2%), and male (59.2% and 59.8%). The AJCC cancer staging was in an early stage, predominately at stage I (49.3% and 50.9%), and local invasion predominated in both the training and validation cohorts (76.1% and 75.2%). Most patients accepted surgical resection

TABLE 1 Patient characteristics and socio-demographic.

Variable	Training group	Validation Group
Number of patient n(%)	787(70)	338(30)
Diagnosis of age	67(56-99)	65(54-98)
Race n(%)		
White	661(84.0)	288(85.2)
Black	78(9.9)	27(8.0)
Others	48(6.1)	23(6.8)
Sex n(%)		
Male	466(59.2)	202(59.8)
Female	321(40.8)	136(40.2)
Married status n(%)		
Married	411(52.2)	173(51.2)
Single	153(19.4)	67(19.8)
Divorced/Separated/Widowed	223(28.4)	98(29.0)
AJCC staging n(%)		
I	389(49.3)	172(50.9)
II	240(30.5)	100(29.6)

(Continued)

10.3389/fendo.2023.1142014

TABLE 1 Continued

Variable	Training group	Validation Group
III	99(12.6)	37(10.9)
IV	59(7.5)	29(8.6)
Combined Summary Stage n(%)		
Local	599(76.1)	254(75.2)
Regional metastasis	148(18.8)	66(19.5)
Distant metastasis	40(5.1)	18(5.3)
Surgery n(%)		
Yes	707(89.8)	300(88.8)
No/Unknown	80(10.2)	38(11.2)
Radiation n(%)		
Yes	161(20.5)	72(21.3)
No/Unknown	626(79.5)	266(78.7)
Chemotherapy n(%)		
Yes	67(8.5)	32(9.5)
No/Unknown	720(91.5)	306(90.5)
Income(US dollor) n(%)		
<$35,000, $35, 000-44,999	75(9.5)	38(11.2)
$45,000-$59,999	193(24.5)	78(23.1)
$60,000-74,999	332(42.2)	141(41.7)
$75,000+	187(23.8)	81(24.0)

treatment (89.8% and 88.8% in the training and validation cohorts, respectively) but refused radiotherapy (79.5% and 78.7%) and chemotherapy (91.5% and 90.5%). Upper-middle-income class families suffering from CVC in this study comprised about 42.2% and 41.7%, respectively.

Variable screening

The significant variables in the univariate Cox regression analyses were age at diagnosis, AJCC stage, marital status, radiation status, sex, combined summary stage, tumor size, and surgery status, which were further assessed using multivariate Cox stepwise regression analysis($P<0.05$). The following factors were significant after multivariate analysis, which results list in Table 2: age at diagnosis (HR = 1.059, 95%CI =1.050-1.067, $p < 0.001$), female (versus male: HR = 0.813, 95%CI =0.669-0.988,$p = 0.037$), divorced/widowed/separated (versus single: HR = 1.356, 95%CI =1.013-1.814,$p = 0.040$), AJCC stage II (combined summary stage versus AJCC stage I: HR = 1.224, 95%CI =1.001-1.496,$p = 0.04$), AJCC stage III (vs AJCC stage I: HR = 1.404, 95%CI =1.087-1.814,$p = 0.010$), AJCC stage IV (versus AJCC stage I: HR = 1.888, 95%CI =1.396-2.553,$p < 0.001$), without surgery (versus surgery: HR = 2.025, 95%CI =1.538-2.665, $p < 0.01$).

Nomogram for OS prognosis

A nomogram was constructed using chosen variables with their HRs, which comprised all the significant independent variables for forecasting the OS rates at 3, 5, and 8 years in the training cohort. Figure 2 shows that age had the greatest effect on the prognosis according to the nomogram, followed by AJCC stage, marital status, race, sex, and combine summary stage(Sums). Each nomogram variable was given a score on a points system. After adding the scores for all variables, a line is drawn vertically downward to obtain the total score that indicates the OS probabilities at 3, 5, and 8 years.

Evaluation of the OS nomogram

The C-indexes of the OS nomogram were 0.737 and 0.735, in the training and validation cohorts, respectively, compared with 0.582 and 0.573 for AJCC staging. Our model demonstrates superior discriminatory performance and prognostic ability compared to AJCC staging, as evidenced by its C-index values exceeding 0.7 and surpassing those of AJCC staging.

The AUC values for OS at 3, 5, and 8 years were 0.767, 0.789, and 0.789, respectively, in the training cohort, and 0.757, 0.773, and 0.792 in the validation cohort. The AUC was > 0.7 for the prediction

TABLE 2 Selected variables by multivariable Cox regression analysis.

	Multivariable analysis		
Variable	HR	95% CI	P-value
Diagnosis of age	1.059	1.050-1.067	<0.001
Sex			
Male	Reference		
Female	0.813	0.669-0.988	0.037
Marital status			
Single	Reference		
Married	0.814	0.621-1.067	0.137
Divorced/widowed/Separate	1.356	1,013-1.814	0.040
AJCC			
I	Reference		
II	1.224	1.001-1.496	0.04
III	1.404	1.087-1.814	0.010
IV	1.888	1.396-2.553	<0.001
Radiation			
Yes	Reference		
No/Unknown	0.843	0.668-1.063	0.149
Surgery			
Yes	Reference		
No/Unknown	2.025	1.538-2.665	<0.001

AJCC, American Joint Committee on Cancer; HR, hazard ratio, CI, confidence interval.

of OS at 3, 5, and 8 years in both the training and validation cohorts (Figure 3), indicating favorable discrimination by the nomogram. The model demonstrated excellent discriminative capacity through its accurate predictions of the OS probabilities at 3, 5, and 8 years, which were made possible by highly precise predictive models of both set (Figure 3).

For the 3-, 5-, and 8-year OS probabilities, the NRI values were 68.08% (95% confidence interval [CI] = 0.559–0.867), 77.56% (95% CI = 0.677–0.945), and 79.34% (95% CI = 0.699–0.960), respectively, in the training cohort, and 55.72% (95% CI = 0.226–0.829), 63.71% (95% CI = 0.363–0.876), and 78.23% (95% CI = 0.561–0.964) in the validation cohort. The corresponding IDI values

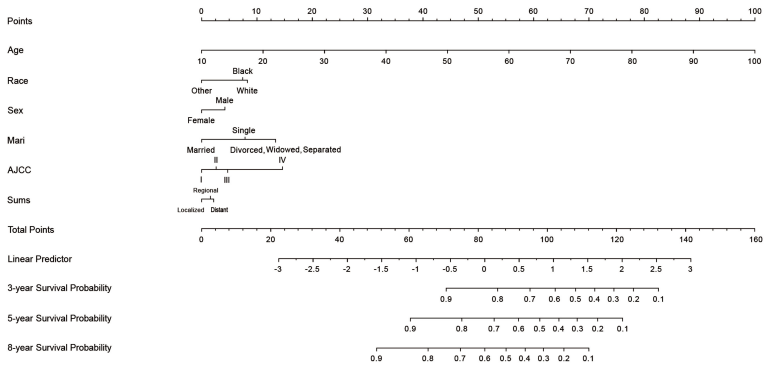

FIGURE 2
Nomogram for predicting 3-, 5-, and 8-years cutaneous verrucous carcinoma overall survival of probability. The value of each of variable was given a score on the point scale axis. A total score could be easily calculated by adding each single score and, by projecting the total score to the lower total point scale, we were able to estimate the probability of CVC. Sums, combined summary of stage; Mari, marital status; AJCC, American Joint Committee on Cancer.

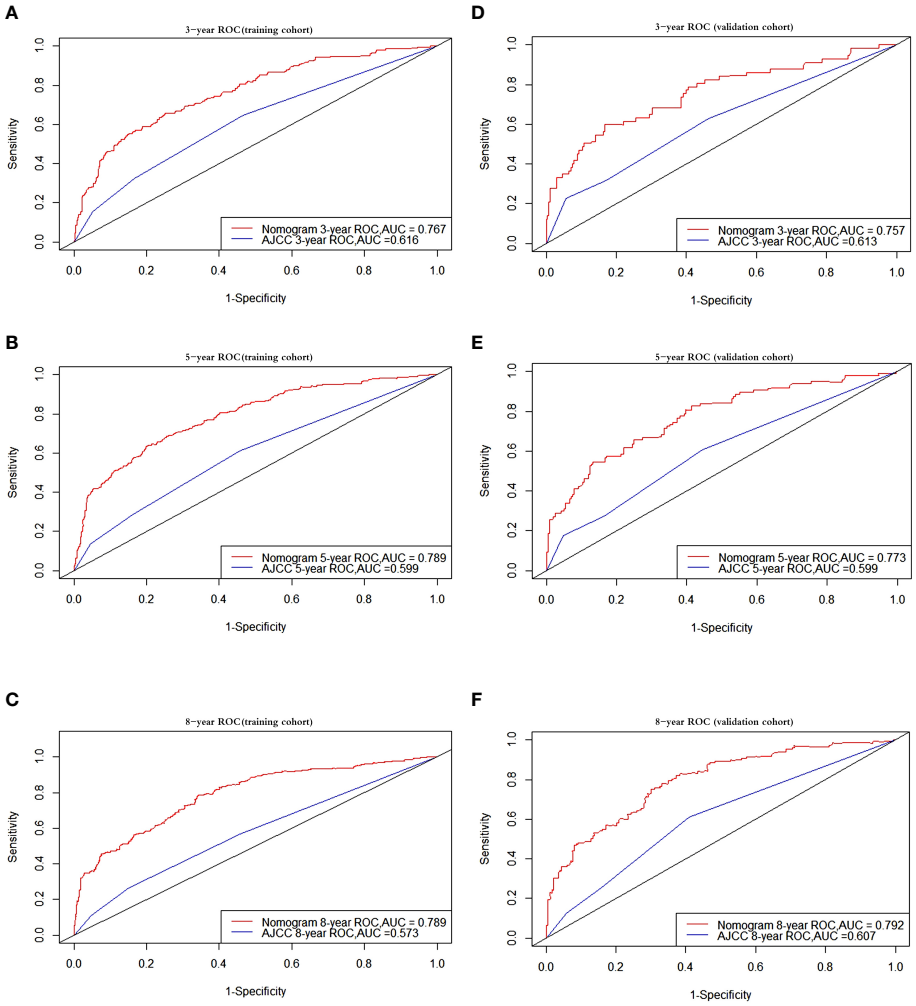

FIGURE 3
Receiver operating characteristic curves. ROC curve analyses to evaluate the performance of the new model compared to the traditional AJCC model. The area under the curve (AUC) metric was used to predict the overall survival probability with 3-, 5-, and 8-years OS probability in the training and validation cohorts. The results of the training cohort represent in **(A–C)** while **(D–F)** represent the results of validation cohort. OS, overall survival.

were 15.48%, 20.23%, 23.66%, 13.65%, 20.52%, and 23.73% (p = 0.001), respectively. When compared with the AJCC staging system, the new model performed much better in every circumstance in which the IDI and NRI values were higher than zero. These results indicating that the nomogram predicted prognosis with greater accuracy than the AJCC staging.

The calibration plot was used to test whether the model effectively differentiated between actual and expected values. The calibration curves of the nomogram showed high consistency between the predicted and observed survival probabilities in both the training and validation cohorts. In summary, the calibration plot of the OS nomogram demonstrated that the expected 3-, 5-, and 8-year survival probabilities for the training and validation cohorts closely matched the survival probabilities calculated using the actual data (Figure 4), indicating that the model had considerable discriminative and calibrating abilities. This proves that the model exhibited a high level of calibration.

Ultimately, A decision-curve analysis (DCA) was conducted to assess the clinical validity of the new model, and satisfactory results were obtained for curves calculated at 3, 5, and 8 years in the training and validation cohorts (Figure 5). In the comparison between the clinical benefits of the nomogram and those of the AJCC staging, the DCA curves demonstrated that the nomogram outperformed the AJCC staging in predicting the 3-, 5-, and 8-year overall survival rates. This was evidenced by the fact that the nomogram provided more net benefits than the AJCC staging for nearly all threshold probabilities in both the training and validation cohorts.

Discussion

With a lifetime prevalence of 7–11% in the USA, CVC is the second-most prevalent nonmelanoma skin cancer among white people (28). However, there are insufficient data for forecasting

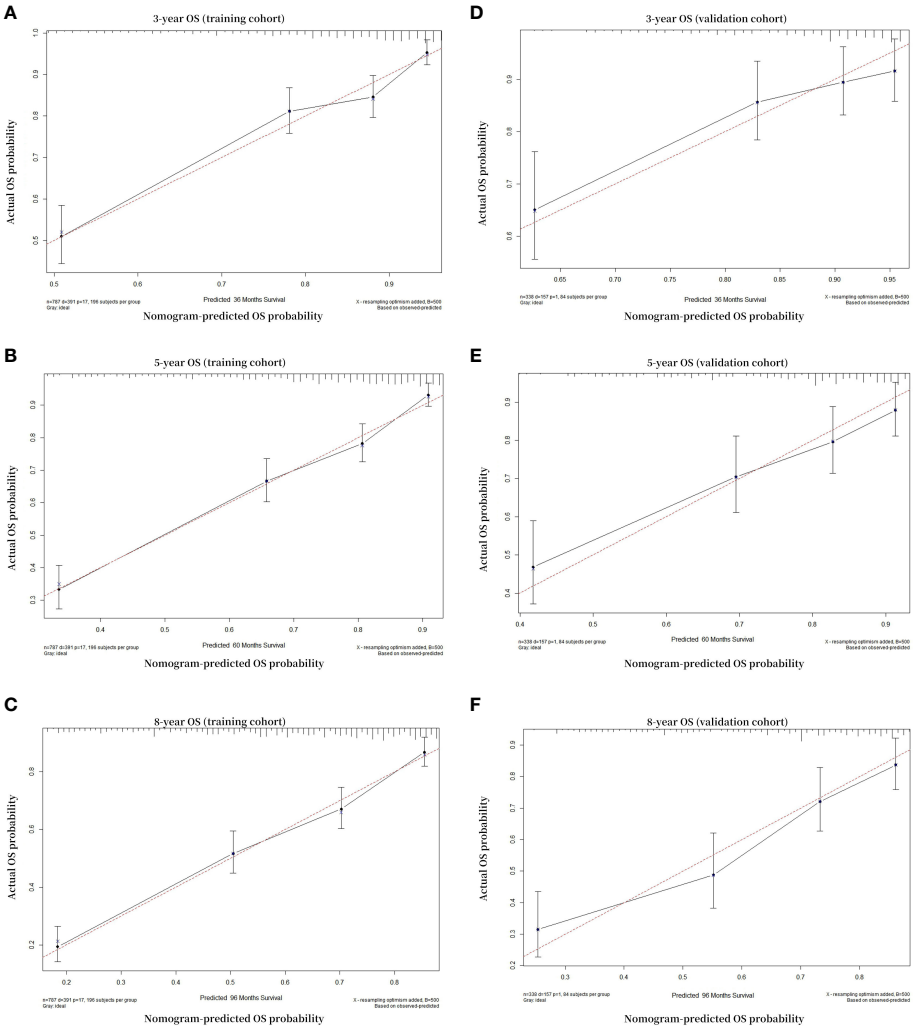

FIGURE 4
Calibration curves. Calibration curves for 3-, 5-, and 8-year OS depict the calibration of each model in terms of agreement between the predicted probabilities and observed outcomes of the training cohort **(A–C)** and validation cohort **(D–F)**. The solid black line indicates the ideal reference line where predicted probabilities would match the observed survival rates. The black dots are calculated by bootstrapping (resample: 500) and represent the performance of the nomogram. The closer the solid black line is to the dash red line, the more accurately the model predicts survival. OS, overall survival.

the OS in patients with CVC, and so our investigation addressed this aforementioned lack of research.

This study effectively used case data from the SEER database to construct a unique and simple prediction nomogram for patients with CVC. The 3-, 5-, and 8-year OS probabilities of patients with CVC can be estimated using this nomogram. In both internal and external evaluation, our nomogram showed satisfactory accuracy and discrimination. Nomograms can be used to identify and categorize participants in clinical trials to produce personalized prognostics. It is important for both the physician and the patient to properly interpret the probability of the 3-, 5-, or 8-year recurrence for the patient (29). We can examine two patients with CVC before AJCC stage IV as an illustration: a 60-year-old married white male known as patient 1 had a localized invasive tumor, while patient 2 was an 88-year-old black single female who had a distant metastasis tumor. The outcomes produced by the new nomogram were distinct: the 3-, 5-, and 8-year OS rate predictions for patient 1 were 80%, 68%, and 55%, respectively, and those for patient 2 were 28%, 12%, and 0%. We can identify patients with various prognoses using this nomogram, allowing for more-customized treatment and follow-up plans for this uncommon malignancy. The present results are consistent with several nomograms having been developed for other types of cancer that are more accurate than the current AJCC staging system (30).

Our study found that the average age at which CVC was diagnosed was 67 years, with males comprising the majority (>50%) of cases in both cohorts (Table 1). Multivariate analysis identified age as a significant risk factor for overall survival (OS), with older patients experiencing lower survival rates. Meanwhile, our model found that the nomogram score increased as the AJCC stage progressed, meaning that a higher AJCC stage was also linked to negative effects on patient survival (31). Females fared better than

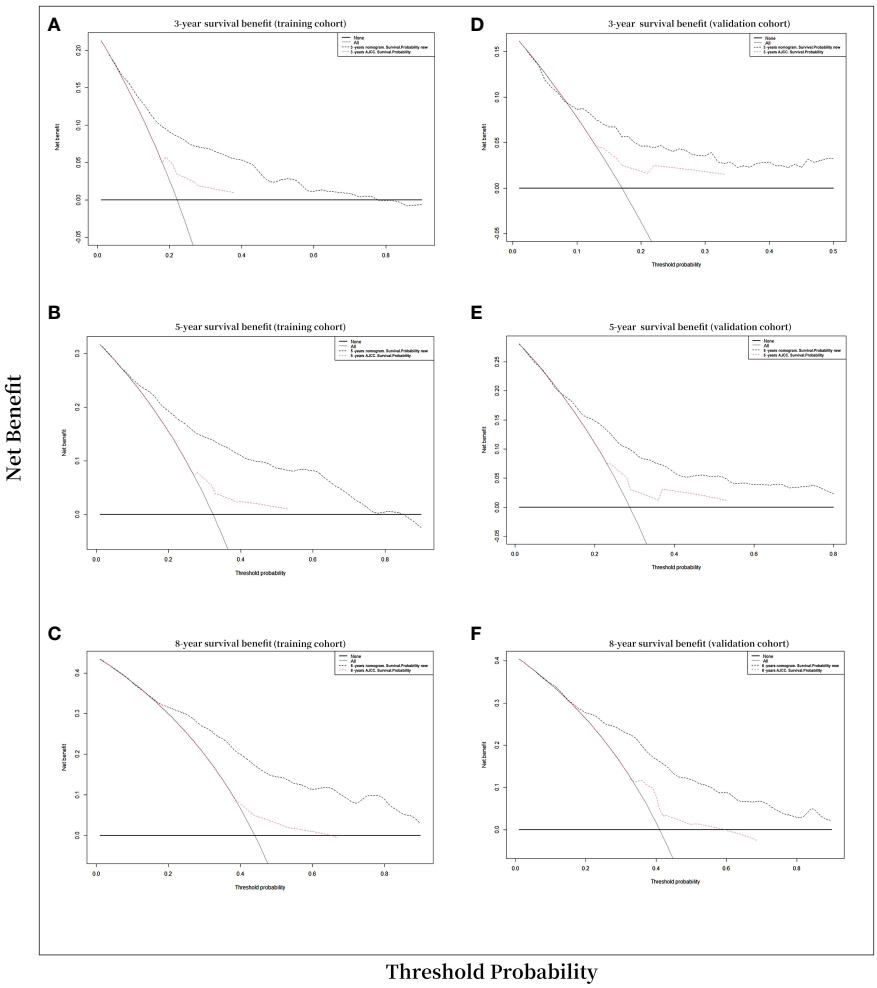

FIGURE 5
Decision curve analysis curves. Decision curve analysis of the nomogram for prediction of 3-, 5-, and 8-years overall survival probability with CVC patients. **(A)** 3-year survival benefit in the training cohort. **(B)** 5-year survival benefit in the training cohort. **(C)** 8-year survival benefit in the training cohort. **(D)** 3-year survival benefit in the validation cohort. **(E)** 5-year survival benefits in the validation cohort. **(F)** 8-year survival benefit in the validation cohort.

males in our study, and there were significant variations in OS related to sex, meaning that it is an important prognostic factor (Table 2). The healthy male and middle-aged population tendency may be related to alcohol use and health which has been documented.

It was particularly interestingly that this study found that having experienced divorce is a risk factor for the OS (HR = 1.356, $p < 0.05$) in CVC. A previous study found that divorced patients with cancer had worse outcomes than married patients (32), which may be related to a sudden interruption or loss of health insurance, reduction in social support, or financial instability, and raises the possibility that a patient may have worse outcomes after receiving cancer treatment (33). According to Hanske et al., the lower cancer screening rate among single people may be responsible for their higher risk of adverse outcomes (34). It can be speculated that unmarried or divorced patients undergo cancer screening less frequently, which could have an impact on their OS rate and cause more-advanced stages among this population. Previous research has found that supportive partnerships may have positive impacts on the behavior of a partner to obtain medical care (35).

Clinically, an CVC tumor lesion is defined by progression to a large, necrotic, and infected state with local aggressive metastasis, with results that are comparable to those of our study. Although uncommon, metastases to nearby lymph nodes and other distant regions are possible. Metastatic CVC has a fatal prognosis; our nomogram indicated that distant tumors in CVC increases negative outcomes for the survival rate, with a few large studies indicating mortality rates of 70% (36). This is an indication that the difficulty of treating metastatic CVC will depend on the affected areas and the degree of metastasis. Biologic aggression is well-documented and indicated by an increased frequency of numerous tumors, risk of local recurrence, regional and distant metastases, and higher mortality (37).

Our investigation found that patients who underwent surgery had an improved prognosis (Table 2). The outcome gives us a hint about CVC management: detecting tumors at an earlier stage is

preferable since localized illness is frequently treatable with an appropriate surgical excision with sufficient margins (38), which may improve the survival probability and the prognosis of the patient. This might also facilitate a reduction in the frequency of local recurrences (39). Our study also found that receiving radiation as a monotherapy for CVC had no predominant effectiveness, while not receiving radiation was not a significant factor (Table 2). Although radiation therapy can shrink the tumor size, the patient who only receives radiation therapy may experience anaplastic transformation of their tumor that could eventually metastasize to the organ or the lymph node, which has been demonstrated in previous studies of skin cancer (6, 40). Radiation therapy can reduce the tumor size, but even with surgery, death might not be avoided.

A nomogram for OS has been constructed based on an assessment of the relevant prognostic indicators, and the nomogram was compared with the standard AJCC model by employing an internal validation cohort and a training cohort. The C-index and AUC were utilized to assess the discrimination abilities of the two approaches, and we discovered that both of these were superior for the monogram compared with the AJCC staging system in both the training and validation cohorts (Figure 3). An increase in AUC is not always immediately apparent when a brand-new metric is added to a model, and so a comparison needs to be performed to determine whether the predictive ability of the model has improved. Instead, the NRI is often used to compare the predictive capabilities of models, whereas the IDI may be used to indicate overall model progress (41, 42). According to the NRI of the nomogram model, the proportion of participants with correctly classified 3-, 5-, and 8-year survival probabilities increased after the new index was added by 68.08%, 77.56%, and 79.34% in the training cohort, respectively, and by 55.72%, 63.71%, and 78.23% in the validation cohort ($p < 0.001$). The IDI values indicated that the new model outperformed the AJCC staging system in terms of the probabilities of 3-, 5-, and 8-year survival by 15.48%, 20.23%, and 23.66% in the training cohort, respectively, and by 13.65%, 20.52%, and 23.73% in the validation cohort.

In order to establish the accuracy of our nomogram, the calibration curves and C-indexes were checked using both the training and validation cohorts. When subjected to internal and external validation, the C-indexes for the 3-, 5-, and 8-year OS models were 0.737 and 0.735, respectively. Both internal and external verification methodologies indicated that the C-index of the OS model exceeded 0.7. Excellent performance of the nomogram was also demonstrated by the calibration curves being highly consistent with the 45-degree ideal lines. These outcomes demonstrated that in both the training and verification cohorts, our nomogram had good calibration and discrimination performance (43) (Figure 4).

Decision-curve analysis (DCA) was employed to assess the clinical net benefit of the prediction models (44). The results of the study showed that the OS model had a beneficial impact on both the training and validation cohorts, as revealed by the 3-, 5-, and 8-year DCA curves, which demonstrated good performance (Figure 5). According to Vickers and Elkin (45), they have introduced DCAs to estimate the clinical utility of prediction models by determining the threshold probability, which is the probability at which the harm of a false-positive intervention exceeds the harm of a false-negative non-intervention, and subsequently derive the net benefit. In our current study, DCAs curve demonstrated significant net benefits for both the training and validation cohort. For example, in the validation cohort, assuming timely intervention for CVC patients with a 20% risk of mortality, every 6 and 15 of 100 individuals would benefit from the intervention at 3 and 5 years, respectively. The net benefits of clinical intervention were considered good when the threshold probability was greater than 0.4 at 3-,5-,8-year OS model (Figure 5).

While our study had important strengths, there were also a few limitations. First, because of the retrospective design of extracting data from the SEER database, selection and information biases were unavoidable. Second, therapy information in the SEER database is not all-inclusive; for example, no information was available on the type of surgical techniques utilized or some crucial clinical pathologic characteristics associated with prognoses, such as vascular invasion and the surgical margin. Third, the SEER database information lacks some laboratory tests results for important prognostic indicators, such as tumor and immunohistochemical analyses markers of p53, Rb gene, and HMB-45. Fourth, the projected values of the nomogram are only intended to serve as a general reference for doctors and will not always provide a correct prognosis. Future prospective studies will be conducted to test the nomogram to account for these limitations.

Conclusion

This study is the first to utilize the SEER database to construct a comprehensive CVC nomogram based on an analysis of various variables. One intriguing finding was that divorce was a risk factor that harms the prognosis. Our nomogram may be useful as a tool to assist clinical staff in determining more-precise forecasts of the 3-, 5-, and 8-year OS rates of patients with CVC compared with using the AJCC staging system.

Data availability statement

The original contributions presented in the study are included in the article/supplementary material. Further inquiries can be directed to the corresponding authors.

Ethics statement

Ethical approval was not provided for this study on human participants because public database. Written informed consent to participate in this study was provided by the participants' legal guardian/next of kin.

Author contributions

SC and LH designed the study. JL and LD reviewed and edited the article. HY, HH, W-KM, CI, revised the article critically. H-HM, KL, XZ reviewed and edited the article. All authors approved the final manuscript.

Funding

This work was supported by Guangdong Provincial Key Laboratory of Traditional Chinese Medicine Informatization (2021B1212040007).

Conflict of interest

The authors declare that the research was conducted in the absence of any commercial or financial relationships that could be construed as a potential conflict of interest.

Publisher's note

References

1. Ackerman LV. Verrucous carcinoma of the oral cavity. *Surgery.* (1948) 23 (4):670–8.

2. Klima M, Kurtis B, Jordan PHJr. Verrucous carcinoma of skin. *J cutaneous pathology.* (1980) 7(2):88–98. doi: 10.1111/j.1600-0560.1980.tb01187.x

3. Agrawal R, Martin FW. Unusual presentation of verrucous carcinoma of maxillary antrum. *J otolaryngology.* (1992) 21(5):371–2.

4. Nguyen KQ, McMarlin SL. Verrucous carcinoma of the face. *Arch Dermatol* (1984) 120(3):383–5. doi: 10.1001/archderm.1984.01650390105024

5. Hurt MA, Weedon D. Weedon's skin pathology. In: *Dermatology practical & conceptual, 3rd ed*, vol. 2. . London: Churchill Livingstone Elsevier2012 (2010).

6. Kao GF, Graham JH, Helwig EB. Carcinoma cuniculatum (verrucous carcinoma of the skin): a clinicopathologic study of 46 cases with ultrastructural observations. *Cancer.* (1982) 49(11):2395–403. doi: 10.1002/1097-0142(19820601)49:11<2395::AID-CNCR2820491129>3.0.CO;2-3

7. Owen WR, Wolfe ID, Burnett JW, Bruce WG. Epithelioma cuniculatum. *South Med J* (1978) 71(4):477–9. doi: 10.1097/00007611-197804000-00040

8. McKee PH, Wilkinson JD, Corbett MF, Davey A, Sauven P, Black MM. Carcinoma cuniculatum: a cast metastasizing to skin and lymph nodes. *Clin Exp Dermatol* (1981) 6(6):613–8. doi: 10.1111/j.1365-2230.1981.tb02365.x

9. Snider L, Demuth RJ. Plantar squamous cell carcinoma. *Cutis.* (1976) 18 (2):195–7.

10. Motley R, Kersey P, Lawrence C. Multiprofessional guidelines for the management of the patient with primary cutaneous squamous cell carcinoma. *Br J Dermatol* (2002) 146(1):18–25. doi: 10.1046/j.0007-0963.2001.04615.x

11. Bernstein SC, Lim KK, Brodland DG, Heidelberg KA. The many faces of squamous cell carcinoma. *Dermatologic Surg Off Publ Am Soc Dermatologic Surg* (1996) 22(3):243–54. doi: 10.1111/j.1524-4725.1996.tb00315.x

12. Waldman A, Schmults C. Cutaneous squamous cell carcinoma. *Hematology/oncology Clinics North America.* (2019) 33(1):1–12. doi: 10.1016/j.hoc.2018.08.001

13. Rowe DE, Carroll RJ, Day CLJr. Prognostic factors for local recurrence, metastasis, and survival rates in squamous cell carcinoma of the skin, ear, and lip. implications for treatment modality selection. *J Am Acad Dermatol* (1992) 26(6):976–90. doi: 10.1016/0190-9622(92)70144-5

14. Koch BB, Trask DK, Hoffman HT, Karnell LH, Robinson RA, Zhen W, et al. National survey of head and neck verrucous carcinoma: patterns of presentation, care, and outcome. *Cancer.* (2001) 92(1):110–20. doi: 10.1002/1097-0142(20010701)92:1<110::AID-CNCR1298>3.0.CO;2-K

15. Metchnikoff C, Mully T, Singer JP, Golden JA, Arron ST. The 7th edition AJCC staging system for cutaneous squamous cell carcinoma accurately predicts risk of recurrence for heart and lung transplant recipients. *J Am Acad Dermatol* (2012) 67 (5):829–35. doi: 10.1016/j.jaad.2012.01.010

16. Ruiz ES, Karia PS, Besaw R, Schmults CD. Performance of the American joint committee on cancer staging manual, 8th edition vs the Brigham and women's hospital tumor classification system for cutaneous squamous cell carcinoma. *JAMA Dermatol* (2019) 155(7):819–25. doi: 10.1001/jamadermatol.2019.0032

17. Farasat S, Yu SS, Neel VA, Nehal KS, Lardaro T, Mihm MC, et al. A new American joint committee on cancer staging system for cutaneous squamous cell carcinoma: creation and rationale for inclusion of tumor (T) characteristics. *J Am Acad Dermatol* (2011) 64(6):1051–9. doi: 10.1016/j.jaad.2010.08.033

18. Balachandran VP, Gonen M, Smith JJ, DeMatteo RP. Nomograms in oncology: more than meets the eye. *Lancet Oncol* (2015) 16(4):e173–80. doi: 10.1016/S1470-2045(14)71116-7

19. Lv J, Liu YY, Jia YT, He JL, Dai GY, Guo P, et al. A nomogram model for predicting prognosis of obstructive colorectal cancer. *World J Surg Oncol* (2021) 19 (1):337. doi: 10.1186/s12957-021-02445-6

20. van den Hoven I, van Klaveren D, Verheuvel NC, van la Parra RFD, Voogd AC, de Roos WK, et al. Predicting the extent of nodal involvement for node positive breast cancer patients: Development and validation of a novel tool. *J Surg Oncol* (2019) 120 (4):578–86. doi: 10.1002/jso.25644

21. Zhang Y, Zheng D, Xie J, Li Y, Wang Y, Li C, et al. Development and validation of web-based nomograms to precisely predict conditional risk of site-specific recurrence for patients with completely resected non-small cell lung cancer: A multiinstitutional study. *Chest.* (2018) 154(3):501–11. doi: 10.1016/j.chest.2018.04.040

22. Hu T, Wang S, Huang L, Wang J, Shi D, Li Y, et al. A clinical-radiomics nomogram for the preoperative prediction of lung metastasis in colorectal cancer patients with indeterminate pulmonary nodules. *Eur radiology.* (2019) 29(1):439–49. doi: 10.1007/s00330-018-5539-3

23. Yang J, Li Y, Liu Q, Li L, Feng A, Wang T, et al. Brief introduction of medical database and data mining technology in big data era. *J Evid Based Med* (2020) 13(1):57–69. doi: 10.1111/jebm.12373

24. Wu WT, Li YJ, Feng AZ, Li L, Huang T, Xu AD, et al. Data mining in clinical big data: the frequently used databases, steps, and methodological models. *Military Med Res* (2021) 8(1):44. doi: 10.1186/s40779-021-00338-z

25. Miller DL, Weinstock MA. Nonmelanoma skin cancer in the united states: incidence. *J Am Acad Dermatol* (1994) 30(5 Pt 1):774–8. doi: 10.1016/S0190-9622(08)81509-5

26. Leening MJ, Steyerberg EW, Van Calster B, D'Agostino RBSr., Pencina MJ. Net reclassification improvement and integrated discrimination improvement require calibrated models: relevance from a marker and model perspective. *Stat Med* (2014) 33(19):3415–8. doi: 10.1002/sim.6133

27. Vickers AJ, Cronin AM, Elkin EB, Gonen M. Extensions to decision curve analysis, a novel method for evaluating diagnostic tests, prediction models and molecular markers. *BMC Med Inf decision making.* (2008) 8:53. doi: 10.1186/1472-6947-8-53

28. Callegaro D, Miceli R, Bonvalot S, Ferguson P, Strauss DC, Levy A, et al. Development and external validation of two nomograms to predict overall survival and occurrence of distant metastases in adults after surgical resection of localised soft-tissue sarcomas of the extremities: a retrospective analysis. *Lancet Oncol* (2016) 17(5):671–80. doi: 10.1016/S1470-2045(16)00010-3

29. Iasonos A, Schrag D, Raj GV, Panageas KS. How to build and interpret a nomogram for cancer prognosis. *J Clin Oncol Off J Am Soc Clin Oncol* (2008) 26 (8):1364–70. doi: 10.1200/JCO.2007.12.9791

30. Fisher SB, Chiang YJ, Feig BW, Cormier JN, Hunt KK, Torres KE, et al. Comparative performance of the 7th and 8th editions of the American joint committee on cancer staging systems for soft tissue sarcoma of the trunk and extremities. *Ann Surg Oncol* (2018) 25(5):1126–32. doi: 10.1245/s10434-018-6378-9

31. Edge SB, Compton CC. The American joint committee on cancer: the 7th edition of the AJCC cancer staging manual and the future of TNM. *Ann Surg Oncol* (2010) 17(6):1471–4. doi: 10.1245/s10434-010-0985-4

32. Dinh KT, Aizer AA, Muralidhar V, Mahal BA, Chen YW, Beard CJ, et al. Increased vulnerability to poorer cancer-specific outcomes following recent divorce. *Am J Med* (2018) 131(5):517–23. doi: 10.1016/j.amjmed.2017.11.039

33. Dupre ME, Beck AN, Meadows SO. Marital trajectories and mortality among US adults. *Am J Epidemiol* (2009) 170(5):546–55. doi: 10.1093/aje/kwp194

34. Hanske J, Meyer CP, Sammon JD, Choueiri TK, Menon M, Lipsitz SR, et al. The influence of marital status on the use of breast, cervical, and colorectal cancer screening. *Prev Med* (2016) 89:140–5. doi: 10.1016/j.ypmed.2016.05.017

35. Ding W, Ruan G, Lin Y, Zhu J, Tu C, Li Z. Dynamic changes in marital status and survival in women with breast cancer: a population-based study. *Sci Rep* (2021) 11 (1):5421. doi: 10.1038/s41598-021-84996-y

36. Burton KA, Ashack KA, Khachemoune A. Cutaneous squamous cell carcinoma: A review of high-risk and metastatic disease. *Am J Clin Dermatol* (2016) 17(5):491–508. doi: 10.1007/s40257-016-0207-3

37. Cassarino DS, Derienzo DP, Barr RJ. Cutaneous squamous cell carcinoma: a comprehensive clinicopathologic classification–part two. *J cutaneous pathology.* (2006) 33(4):261–79. doi: 10.1111/j.0303-6987.2006.00516.x

38. Mohs FE, Sahl WJ. Chemosurgery for verrucous carcinoma. *J dermatologic Surg Oncol* (1979) 5(4):302–6. doi: 10.1111/j.1524-4725.1979.tb00663.x

39. Alonso JE, Kuan EC, Arshi A, St John MA. A population-based analysis of verrucous carcinoma of the oral cavity. *Laryngoscope.* (2018) 128(2):393–7. doi: 10.1002/lary.26745

40. Proffitt SD, Spooner TR, Kosek JC. Origin of undifferentiated neoplasm from verrucous epidermal carcinoma of oral cavity following irradiation. *Cancer.* (1970) 26 (2):389–93. doi: 10.1002/1097-0142(197008)26:2<389::AID-CNCR2820260220>3.0.CO;2-4

41. Su Y, Leung J, Hans D, Lamy O, Kwok T. The added value of trabecular bone score to FRAX® to predict major osteoporotic fractures for clinical use in Chinese older people: the mr. OS and ms. OS cohort study in Hong Kong. *Osteoporosis Int J established as result cooperation between Eur Foundation Osteoporosis Natl Osteoporosis Foundation USA* (2017) 28(1):111–7. doi: 10.1007/s00198-016-3741-1

42. Chambless LE, Cummiskey CP, Cui G. Several methods to assess improvement in risk prediction models: extension to survival analysis. *Stat Med* (2011) 30(1):22–38. doi: 10.1002/sim.4026

43. Wang F, Zhang H, Wen J, Zhou J, Liu Y, Cheng B, et al. Nomograms forecasting long-term overall and cancer-specific survival of patients with oral squamous cell carcinoma. *Cancer Med* (2018) 7(4):943–52. doi: 10.1002/cam4.1216

44. Ma K, Dong B, Wang L, Zhao C, Fu Z, Che C, et al. Nomograms for predicting overall survival and cancer-specific survival in patients with surgically resected intrahepatic cholangiocarcinoma. *Cancer Manage Res* (2019) 11:6907–29. doi: 10.2147/CMAR.S212149

45. Vickers AJ, Elkin EB. Decision curve analysis: a novel method for evaluating prediction models. *Med decision making an Int J Soc Med Decision Making.* (2006) 26 (6):565–74. doi: 10.1177/0272989X06295361

frontiers | Frontiers in Endocrinology

TYPE Review
PUBLISHED 27 March 2023
DOI 10.3389/fendo.2023.1126271

OPEN ACCESS

EDITED BY
Ruiqin Han,
Chinese Academy of Medical Sciences, China

REVIEWED BY
Zhao-Wei Sun,
Academy of Military Medical Sciences, China
Shunbang Yu,
Tsinghua University, China
Pi-Xian Gong,
Harbin Institute of Technology, China

*CORRESPONDENCE
Hongru Zhang
zhr5001@vip.163.com
Xin Gu
290418@njucm.edu.cn
Yihuang Gu
gyh5196411@163.com

†These authors have contributed equally to this work

SPECIALTY SECTION
This article was submitted to Cancer Endocrinology, a section of the journal Frontiers in Endocrinology

RECEIVED 17 December 2022
ACCEPTED 07 February 2023
PUBLISHED 27 March 2023

CITATION
Liu Y, Gu R, Gao M, Wei Y, Shi Y, Wang X, Gu Y, Gu X and Zhang H (2023) Emerging role of substance and energy metabolism associated with neuroendocrine regulation in tumor cells.
Front. Endocrinol. 14:1126271.
doi: 10.3389/fendo.2023.1126271

Emerging role of substance and energy metabolism associated with neuroendocrine regulation in tumor cells

Yingying Liu[1,2†], Renjun Gu[2†], Murong Gao[3†], Yangwa Wei[4], Yu Shi[5], Xu Wang[6], Yihuang Gu[7,8*], Xin Gu[2*] and Hongru Zhang[2*]

[1]Institute for Immunology and School of Medicine, Tsinghua University, Beijing, China, [2]School of Chinese Medicine and School of Integrated Chinese and Western Medicine, Nanjing University of Chinese Medicine, Nanjing, China, [3]Beijing Rehabilitation Hospital Affiliated to Capital Medical University, Beijing, China, [4]Department of Hepatobiliary Surgery, Hainan Provincial People's Hospital, Haikou, China, [5]Shanghai East Hospital, Tongji University School of Medicine, Shanghai, China, [6]School of Basic Medical Sciences, Fujian Medical University, Fuzhou, China, [7]School of Acupuncture and Tuina, School of Regimen and Rehabilitation, Nanjing University of Chinese Medicine, Nanjing, China, [8]The Second Hospital of Nanjing, Nanjing, China

Cancer is the second most common cause of mortality in the world. One of the unresolved difficult pathological mechanism issues in malignant tumors is the imbalance of substance and energy metabolism of tumor cells. Cells maintain life through energy metabolism, and normal cells provide energy through mitochondrial oxidative phosphorylation to generate ATP, while tumor cells demonstrate different energy metabolism. Neuroendocrine control is crucial for tumor cells' consumption of nutrients and energy. As a result, better combinatorial therapeutic approaches will be made possible by knowing the neuroendocrine regulating mechanism of how the neuroendocrine system can fuel cellular metabolism. Here, the basics of metabolic remodeling in tumor cells for nutrients and metabolites are presented, showing how the neuroendocrine system regulates substance and energy metabolic pathways to satisfy tumor cell proliferation and survival requirements. In this context, targeting neuroendocrine regulatory pathways in tumor cell metabolism can beneficially enhance or temper tumor cell metabolism and serve as promising alternatives to available treatments.

KEYWORDS

substance, energy, metabolism, neuroendocrine regulation, tumor cells

1 Introduction

Cancer is a disease that seriously threatens people's life and health and is one of the leading causes of death each year, despite tremendous advances in detection and treatment in recent decades. According to statistics, there were about 23.6 million new cases of cancer worldwide and about 10 million people died from cancer in 2019 (1). Since 2000, the

number of cancer cases and deaths as well as the crude incidence and mortality of cancer in China have gradually increased (2). Cancer is a heavy burden for both the patients themselves and the whole of society. At present, the global situation is still not optimistic. Therefore, it is crucial to find new regulated pathways of tumor cell death and investigate their therapeutic potential.

In the study of cancer biology, cancer metabolism represents one of the most important research directions. The synthesis, release, conversion, and utilization of energy in the whole metabolism are summarized under the term energy metabolism. Glucose is primarily converted to energy by cells. The primary energy source of normal cells is the aerobic oxidation of glucose, whereas the energy metabolism of tumor cells differs significantly from that of normal cells. The ability to reconfigure their metabolic network gives cancer cells the ability to adapt and ensure survival in the face of significant environmental change. During the 1920s, Warburg observed that the rate of glycolysis in tumor cells was significantly increased in tumor cells compared with normal cells. This phenomenon was later termed the Warburg effect, also known as aerobic glycolysis, which occurs in tumor cells even in the presence of sufficient oxygen (3). Despite its low production efficiency, glycolysis can rapidly produce ATP for tumor cells and also produce a variety of macromolecules to meet the material and energy requirements of tumor cells that proliferate rapidly. Although oxidative phosphorylation in mitochondria is an effective method for energy production, tumor cells prefer glycolysis as their method for energy production. Different tumor cells produce ATP in varying proportions from glycolysis and oxidative phosphorylation. In 2011, reprogramming of energy metabolism was named as one of the ten most important features of tumors (4). Reprogramming of energy metabolism not only provides energy and biomacromolecules for tumor cell growth and proliferation, but also supports tumor cell survival under stress conditions.

Surprisingly, a growing body of research has shown that neuroendocrine systems regulate a variety of molecular dynamics in substance and energy metabolism in tumors. To control numerous elements of energy intake, consumption, digestion, and absorption, the central nervous system (CNS) interacts with a number of peripheral organs and tissues (5). For example, food-induced changes in gastrointestinal tract tension can directly trigger vagal afferents, or indirectly activate taste receptors through chemical stimuli and trigger the production of gastrointestinal peptides (5). The released peptides, including ghrelin, gastric leptin, cholecystokinin, and peptide YY, or appetite-stimulating substances such as glucagon-like peptide 1 increase the feeling of satiety (5). Through circuits between the brainstem and hypothalamus, nutrient levels in the blood influence food intake (5). The circuits of homeostatic energy metabolism are called hypothalamic circuits (6). Neuropeptide Y (NPY) and dopamine pathways associated with sensory inputs of food such as smell and taste, and influenced by physiological states such as hunger and satiety, regulate food intake in the hypothalamus and extrahypothalamic nuclei (7, 8). In addition to food intake, the hypothalamic circuit controls other elements of energy homeostasis, such as fat metabolism (9), adipose tissue distribution (10), glucose metabolism (11), and insulin sensitivity (12). Energy expenditure, glucose and fat metabolism, and feeding behavior have been shown to change under stress (13). However, the neurobiology underlying these processes is constantly changing to meet the demands of energy supply in tumors. This review aims to highlight the molecular interface that neuroendocrine dynamics represent as an important general physiological condition for modulating tumor substance and energy metabolism and clinically determining cancer progression, and to provide a reference for basic research and clinical treatment of tumors by targeting neuroendocrine molecules.

2 Energy metabolism in tumor cell

Energy metabolism is one of the fundamental features of an organism's life activities. Energy is needed for the growth and reproduction of cells. One of the reasons cancer why is so damaging to the body and so difficult to overcome is because of its ability to alter metabolic pathways, and give tumor cells a greater competitive advantage. Energy in cancer cells is provided mainly by adenosine triphosphate (ATP), with most of the ATP in the cells being generated by the breakdown of glucose, and a small amount by the breakdown of glutamine and fatty acid metabolism.

2.1 Glucose metabolism

In normal cells, the energy required for cellular metabolism is converted mainly from glycogen and other substances into 6-phosphate-glucose, and then enters the mitochondria *via* the glycolysis pathway, where it undergoes the tricarboxylic acid (TCA) cycle and oxidative phosphorylation, providing 70% of the energy required for its own metabolism. Glycolysis can only provide a small portion of the energy, which is about 20-30% of the metabolism of normal cells. The Warburg effect describes that how cancer cells tend to absorb glucose and convert it predominantly to lactate, even in the presence of oxygen, and refers to the abnormal glucose metabolism in cancer cells (Figure 1). The Warburg effect assumes that glycolysis is the main energy supply pathway for tumor cells, and that tumor cells rely on glycolysis for energy supply even when sufficient oxygen is available. Studies have shown that tumor cells transport extracellular glucose into the cell *via* glucose transporters distributed on the cell membrane and catabolize it to generate ATP using glycolytic enzymes such as hexokinase, phosphoglucose isomerase, and the product of the multistep metabolism of pyruvate. In the hypoxic region of the tumor, a large amount of lactate is formed from pyruvate by lactate dehydrogenase. Lactate is released to the outside of the cell through the only carboxyl transporter in the cell membrane and accumulates locally, creating an acidic environment for tumor growth. This microenvironment promotes tumor cell invasion into surrounding tissues (14). At the same time, researchers found that tumor cells in the oxygenated area could take up the lactic acid produced by cells in the hypoxic area and synthesize glucose through gluconeogenesis, which can be used by

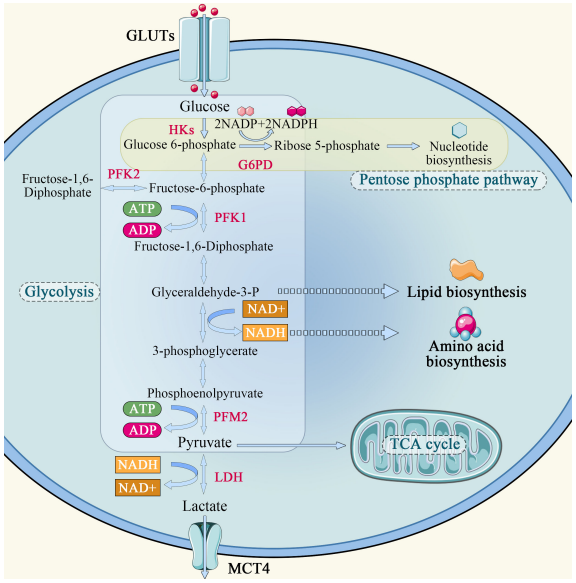

FIGURE 1
Schematic diagram of glucose metabolism in tumor cell.

tumor cells in the hypoxic area to realize energy cycle (14). Lactic acid can also enter the bloodstream, reach the liver *via* gluconeogenesis, and eventually generate liver glycogen or blood glucose, resulting in a lactic acid cycle (15). In the oxygenated tumor oxygen region, tumor cells also have the same energy me of the TCA cycle as normal cells, i.e, the metabolite pyruvate enters the mitochondria through oxidative decarboxylation to form acetyl-CoA *via* transporters, and is oxidatively metabolized in the TCA cycle.

Aerobic glycolysis is a unique metabolic mode of tumor cells. The aerobic glucose metabolic pathway is actually a low-productivity metabolic pathway. One molecule of glucose is degraded to pyruvate *via* the glycolytic pathway, generating 2 molecules of ATP, whereas complete oxidation by oxidative phosphorylation in mitochondria generates 32 to 33 molecules of ATP. Tumor cells require a large amount of energy to proliferate rapidly, but they choose glycolysis, which is less productive. However, there is no obvious defect in the mitochondria of tumor cells. It has been found that mitochondria maintain complete functions in tumor cells, and the tumorigenic function of cancer cell lines *in vitro* and *in vivo* is reduced when mitochondrial DNA is specifically knocked down (4, 16).

Why do some tumor cells still prefer the less efficient pathway of glycolysis as their primary energy source, even though mitochondria are so efficient? First, the cytoplasm produces ATP 100 times faster than mitochondria, meaning the yield is low but the rate is high. As long as glucose supply is sufficient, the ATP produced by glycolysis per unit time is higher than that of oxidative phosphorylation (17). Second, the increase in glycolysis leads to the accumulation of metabolic intermediates that can generate the demand for tumor cell proliferation through other reactions. Finally, the massive accumulation of pyruvate during glycolysis generates lactate under the action of lactate dehydrogenase A (LDHA), which is transported outside the cell by monocarboxylic acid transporter 4 (MCT4), creating an acidic environment outside the cell that promotes tumor cell growth, invasion and metastasis.

In addition, tumor cells adapt to different survival conditions by altering their metabolism, a process known as metabolic plasticity. When using chemotherapeutic agents that target the proliferation phase of tumor cells, cancer stem cells (CSCs) can circumvent the killing effects of chemotherapeutic agents by regulating their own metabolic processes to keep them in a "resting state" with low energy metabolism. At the same time, CSCs also promote the metabolism of the pentose phosphate pathway and increase their own antioxidant capacity to adapt to different tumor microenvironments (TMEs) (18). Elgendy et al (19) also demonstrated through intermittent diet and drug administration that tumor cells have metabolic plasticity that can switch between glycolysis and oxidative phosphorylation to adapt to different survival challenges. Adenosine-activated protein kinase (AMPK) and HIF-1 are two important regulators of oxidative phosphorylation and glycolysis. To explain the Warburg effect in tumor metabolism, Sotgia et al (20) proposed that cancer-associated fibroblasts in the vicinity of the tumor are "induced" by cancer cells to switch energy metabolism to aerobic glycolysis and that these interstitial cells are "induced" by cancer cells. Metabolites of fibers can provide metabolic substrates for epithelial cancer cells as an energy source. In this model, interstitial cell glycolysis produces L-lactate and ketone bodies that provide raw materials for mitochondrial metabolism, and their transport to epithelial tumor cells with oxidative properties drives mitochondrial oxidative phosphorylation. This metabolic mode is also referred to as the "reverse Warburg effect" because mesenchymal cells, rather than tumor cells, take over aerobic glycolysis. At the same time, this also shows that tumor and tumor stromal cells belong to the same metabolic symbiosis.

2.2 Glutamine metabolism

Glutamine is the most abundant non-essential amino acid in human blood under normal conditions and accounts for about 50% of the free amino acids in the human body (21). In stressful situations, the body must supply glutamine to meet the demand, and glutamine is absorbed by the body and classified as a conditional non-essential amino acid. Under normal conditions, glutamine is synthesized and stored primarily in skeletal muscle, and some is also synthesized in adipose tissue, lung and liver, with skeletal muscle having the highest glutamine synthase activity. Glutamine taken up and stored by skeletal muscle is gradually released into the bloodstream and delivered to all parts of the body. The proliferation of lymphocytes and macrophages stimulated by antigens, and the renewal and maintenance of the intestinal mucosa require large amounts of glutamine. Therefore, the intestine and immune cells are important consumption organs for glutamine.

Glutamine metabolism is another characteristic of tumor cells (22) (Figure 2). Glutamate is synthesized from glutamate and ammonia under the catalysis of glutamine synthase (GS).

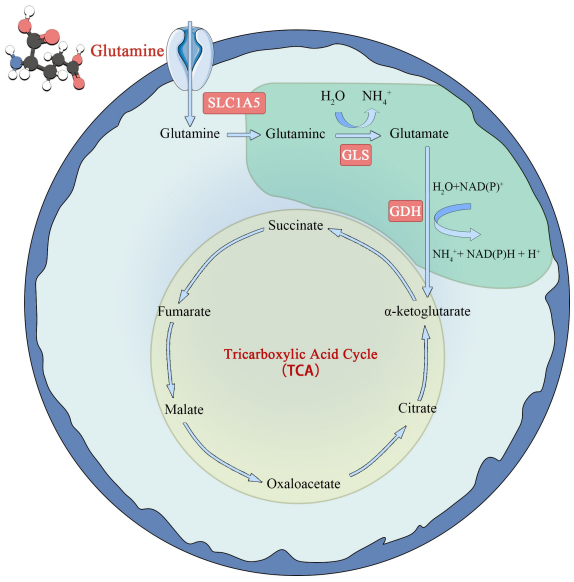

FIGURE 2
Schematic diagram of glutamine metabolism in tumor cell.

However, in tumor cells or rapidly proliferating cells, the *de novo* synthesis of glutamine cannot meet the demand of cellular energy metabolism for glutamine, so it is converted to a conditionally essential amino acid. Glutamine enters the cell *via* the amino acid transporters SLClA5 and SLC7A5/SLC3A2, and is deaminated into glutamate in the mitochondria by glutaminase (GLS). Glutamate is formed under the action of glutamate dehydrogenase (GDH) or amino acid transaminase. Ketoglutarate (KG) is fed back into the TCA cycle and provides energy to cells through oxidative phosphorylation. The study found that tumor cells take up more glutamine and less glucose than immune cells in the TME. At the same time, it was observed that glutamine uptake and metabolism can significantly inhibit glucose metabolism. The specific mechanism is not clear (23), but it indicates that glutamine metabolism is very important for tumor cells. However, in later studies, glutamines was found to be an energy source only in some tumor cells and not in all tumor cells (24).

2.3 Fatty acid metabolism

In recent years, researchers have paid more attention to fatty acid metabolism in tumor cells because fatty acids are not only the main components of membrane formation, but also a source of energy supply and secondary messengers of signal transduction in rapidly proliferating tumor cells (25). In a state of energy stress, fatty acids in mitochondria produce acetyl-CoA through iodine oxidation, accompanied by the production of NADH and FADH, thereby supporting the cell's biosynthetic pathway and producing ATP. In addition, phosphatidylinositol 3-kinase (PI3K) regulates several important signaling pathways. PI3K-AKT signaling pathway promotes glucose uptake and glycolysis by activating glucose transporter 1 (GLUT1) and hexokinase. PI3K-AKT signaling pathway can also enhance glutamine replenishment and lipid remodeling by activating glutamate pyruvate transaminase (26).

3 Neuroendocrine system

The endocrine/neuroendocrine system includes the endocrine organs like the pineal gland, adrenal gland, pituitary gland, thyroid gland, and parathyroid gland, as well as clusters of endocrine cells such as the pancreatic islets of Langerhans, bronchial neuroepithelial bodies, scattered epithelial endocrine cells (such as gastrointestinal endocrine cells), and neurons (27). In the literature, the terms "endocrine" and "neuroendocrine" are frequently used interchangeably, particularly when discussing neoplasms derived from these cells. In this review, we use the condensed classification system of the sympathetic nervous system (SNS) and hypothalamic–pituitary–adrenal (HPA) gland axis as the neuroendocrine system. The various distinct cell types composing this system produce and secrete a wide variety of amino acids, including glycine, glutamate, acetylcholine (ACh), and gamma-aminobutyric acid (GABA); biogenic amines including the neurotransmitters epinephrine (E) and norepinephrine (NE), and serotonin; neuropeptides including neuropeptide Y (NPY), vasoactive intestinal polypeptide (VIP), calcitonin gene-related peptide (CGRP), neurotensin, brainstem, and many others; steroid hormones including adrenocorticotropic hormone, growth hormone, hydrocortisone, and many others. The HPA axis is activated at the molecular level by the production of corticotrophin- releasing hormone and arginine vasopressin, both of which induce the release of adrenocorticotropin from the anterior pituitary gland as a crucial part of the hormonal response to dangerous stimuli. The following generation of glucocorticoids mediates the final output of the system (28, 29). Epinephrine and norepinephrine are produced by the sympathetic division of the SNS and the adrenal medulla, signaling physiological changes in response to a dangerous scenario (28, 29), which act either locally (paracrine function) or systemically *via* the vascular system (Table 1). Neuroendocrine regulation is the crucial element of the adaptive systems of organisms to regain homeostasis following environmental and psychosocial stresses. Both the SNS and HPA axis have been shown to modulate the substance and energy metabolism (28, 49), and other specific molecular processes implicated in these dynamics are also thought to influence the formation of tumors.

4 Crosstalk between neuroendocrine regulation and tumor cell metabolism

Specific responses (inhibitory or excitatory) are displayed by specialized subsets of brainstem and hypothalamus neurons in response to variations in extracellular glucose concentrations (50). For proper control of systemic physiology, these two brain areas must work in close collaboration (51, 52). The lateral, arcuate, and ventromedial hypothalamic nuclei were identified to include hypothalamic glucose-sensing neurons in the 1960s (53); in contrast, the nucleus of the solitary tract, region postrema, and dorsal motor

TABLE 1 Neuroendocrine mediators.

Neuroendocrine system	Neuroendocrine mediators	Reference
Amino acids	Glycine	(30)
	Glutamate	(31)
	Acetylcholine (Ach)	(32)
	Gamma-aminobutyric acid (GABA)	(33)
	Epinephrine (NE) and norepinephrine (E)	(34, 35)
	Serotonin	(36)
	Neuropeptide including neuropeptide Y (NPY)	(37)
Biogenic amines	Vasoactive intestinal polypeptide (VIP)	(38)
	Calcitonin gene related peptide (CGRP)	(39)
	Neurotensin	(40)
	Taurine	(41)
	6-alanine	(42)
	Hypocretin/Orexin (HO)	(43)
	Prooplomelanocortin (POMC)	(44)
Steroid hormones	Adreno corticotropic hormone	(45)
	Growth hormone	(46)
	Hydrocortisone	(47)
	Melanin-Concentrating Hormone (MCH)	(48)

nucleus of the vagus was revealed to contain brainstem glucose-sensing neurons. Importantly, these neurons release mediators, which are essential for maintaining physiological homeostasis, controlling sleep-wake cycles, regulating food patterns, and other functions that are disturbed in cancer (Figure 3). Therefore, understanding the role of neurotransmitters play in the development of cancer provides a foundation for a suggested connection between psychosocial and physiological factors (54, 55). The functionality of migration of tumor cells has also been revealed to be significantly influenced by neurotransmitters and hormones (56). The section that follows will go through the impact of numerous traditional neurotransmitters and neuropeptides on the material and energy metabolism of tumors.

The hypothalamus and brainstem contain several neuroendocrine mediators that are sensitive to variations in extracellular glucose levels. These neuroendocrine mediators regulate a wide range of behavioral and physiological processes, including hepatic gluconeogenesis, energy balance, sleep/wake phases, eating behavior, and stress tolerance. Therefore, the effects of cancer-related alterations in glucose on central neuronal activity and subsequent physiology/behavior are anticipated to be extensive. Understanding and modifying these circuits may offer a unique strategy for treating co-morbidities linked with cancer, such as disturbed sleep, exhaustion, cachexia/anorexia, depression, and anxiety.

4.1 Epinephrine and norepinephrine

The catecholamines epinephrine (adrenaline) and norepinephrine (noradrenaline) are the best-known and most studied neurotransmitters, formed from the amino acid tyrosine and released mainly by sympathetic nerves and the adrenal medulla. The interactions between epinephrine and norepinephrine and the

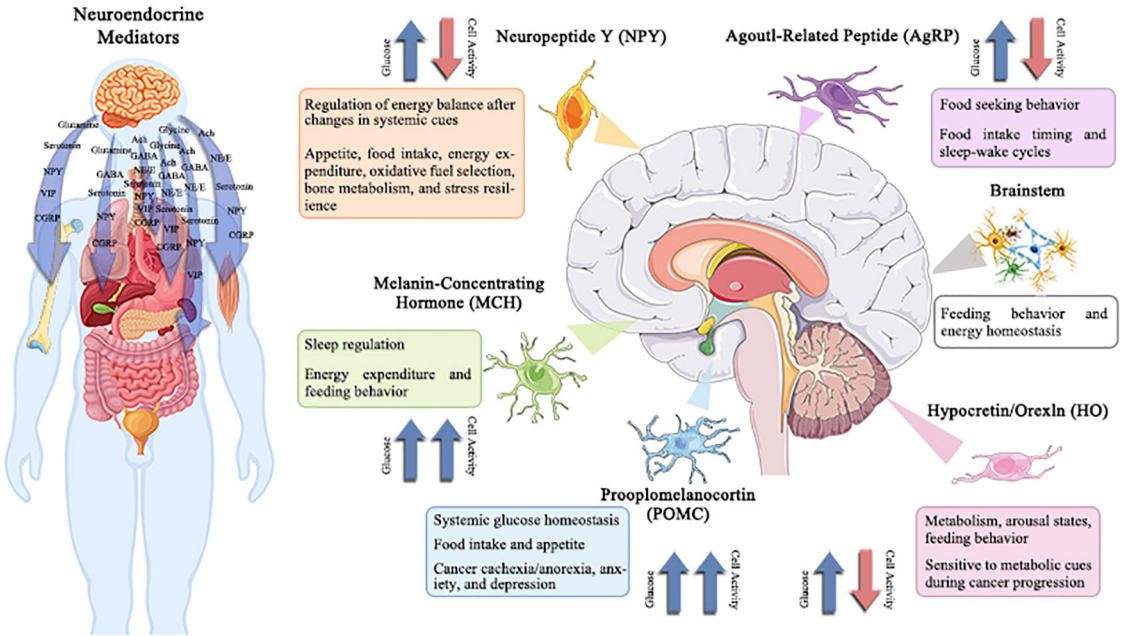

FIGURE 3
Potentially changed glucose-sensitive neuroendocrine mediator in the context of cancer-induced hyperglycemia.

alpha (α)- and beta (β)-adrenergic receptors (ARs), which are G-protein-coupled 7-transmembrane receptors widely distributed in most tissues of mammals, mediate their actions. Epinephrine and norepinephrine, serve as stress hormones to respond to external stress or danger to the sympathetic and adrenal nervous systems (57, 58). Norepinephrine, in particular, plays a crucial role as a neurotransmitter in the brain and at the output of the sympathetic nervous system, which includes the network of peripheral nerves that controls the body's organs. It was reported that there is a gender difference in responses to epinephrine. In men, but not in women, the release of free fatty acids (FFA) from lower body adipose tissue increased in response to epinephrine, whereas in both sexes the release of palmitate increased in the upper body. These results support some *in vitro* research and suggest that the differences in body fat distribution between males and females may be influenced by catecholamine activity (59). Furthermore, the biological properties of malignant tumors, such as cancer cell proliferation, invasion, metastasis, angiogenesis, resistance to apoptosis, and stromal compartments in the tumor microenvironment, are strongly influenced by epinephrine and norepinephrine (60). Isoproterenol, an α-adrenergic agonist, can imitate the tumor growth and angiogenesis brought on by prolonged stress, while propranolol, an α-adrenergic antagonist, can prevent this (61). Importantly, epinephrine and norepinephrine have been considered to be one of the main regulators in the metabolism of tumor cells. In breast cancer survivors, epinephrine, cortisol, and lactate responses appeared to be attenuated compared with controls, while glucose and responses showed larger magnitude changes. The adrenergic system regulates energy balance in part by promoting thermogenesis and the release of lipids from brown or white adipose tissues (62, 63), and human fat cells are equipped with adrenergic receptors (adrenoceptors) β_1 (ADRB1), β_2 (ADRB2) and β_3 (ADRB3). Beta-adrenergic genes have already been linked to a variety of cancers, including their interactions with environmental or other risk factors (64–67). Adrenoceptor polymorphisms and the dopamine beta-hydroxylase enzyme, which produces norepinephrine, can modify insulin resistance and change glucose signaling (68–71), which may have an impact on the Warburg effect. Norepinephrine can activate the metabolism of endothelial cells to block oxidative phosphorylation and activate an angiogenic switch that promotes the growth of cancer (72, 73). In pancreatic cancer, catecholamines promote neurotrophins to be secret by β-ARs, which in turn raises norepinephrine levels and aids tumor growth (74). Chronic stress-induced epinephrine promotes the development of breast cancer stem-like traits by rewiring the metabolism in a lactate dehydrogenase A (LDHA) dependent manner (75). Catecholamines norepinephrine and epinephrine have been demonstrated to play a role in metabolic reprogramming and epithelial-to-mesenchymal transition in liver and colorectal cancers (76, 77). PCK1 regulates glucose metabolism and neuroendocrine differentiation through the activation of LIF/ZBTB46 signaling in castration-resistant prostate cancer (78). Together, these and other numerous studies provide compelling evidence that epinephrine and norepinephrine play an important role in the metabolism of substances and energy, which promotes the growth and spread of tumors in multiple of cancer types (Figure 4).

Epinephrine (EPI) and norepinephrine (NE) interact with environmentally-regulated factors like obesity, hypertension, unhealthy dietary components, physical inactivity, substance abuse, and mental or emotional stress to promote the Warburg

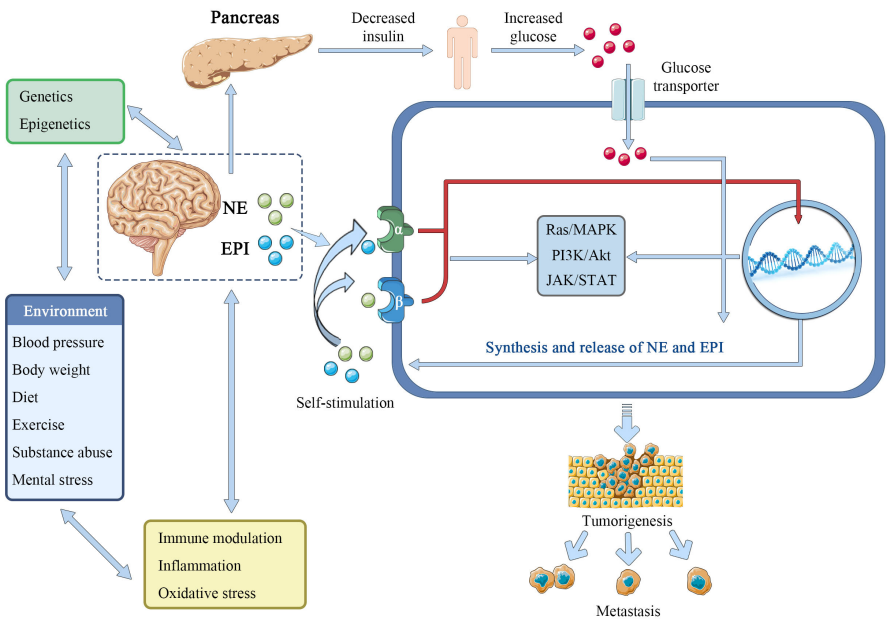

FIGURE 4
Epinephrine and norepinephrine contribute to tumorigenesis.

effect by facilitating glucose. These interactions are in addition to the direct interaction of elevated central catecholamine release or peripheral sympathetic-adrenomedullary signaling with epigenetic and genetic risk factors including mutagenesis, and perhaps by increasing insulin resistance. Additionally, it is suggested in this research that many cancer cells produce and release catecholamine molecules to autocrinely activate their own α-ARs and β-ARs. To encourage cancer and metastasis, EPI and NE may potentially interact with oxidative stress, systemic inflammation, and immunological function.

4.2 Gamma-aminobutyric acid (γ-GABA)

γ-GABA is the adult mammalian brain's major inhibitory neurotransmitter for CNS. The ionotropic $GABA_A$ and $GABA_C$ receptors as well as the metabotropic $GABA_B$ receptor are three distinct types of GABA (A, B, and C) receptors. Numerous tumor tissues have been found to contain GABA receptors, which control the migration and proliferation of tumor cells (79, 80). The GABAergic system and the growth of tumors appear to be closely associated, according to recent research using human cancer cell lines, animal models, and human tissues. In general, stimulation of GABA receptors slows migration (81) and suppresses tumor cell proliferation (82). These findings imply that the GABAergic system contributes significantly to cell pathology, and it is possible that GABA plays a substantial role in the prognosis of cancer patients. Some cancers has been shown to have higher GABA levels, such as breast cancer (80), ovarian cancer (80), gliomas (83), gastric cancer (84), colon cancer (85), and prostate cancer (86). Typically, GABA inhibits cancer cell growth through the $GABA_B$ receptor, but stimulates cancer cell growth through the $GABA_A$ receptor pathway (87). The GABAergic system and the growth of tumors appear to be closely related, according to recent research using human cancer cell lines, animal models, and human tissues. Recently, it was demonstrated that two independent 13C-labeled substrates, [1,6-13C2] glucose and [2-13C] acetate, which are metabolized in neurons and glia differently, may be used to evaluate the TCA cycle and neurotransmitter cycle fluxes of glutamatergic and GABAergic neurons *in vivo* separately (88). Using this technique in adult rats under halothane anesthesia, it was found that cortical glutamatergic and GABAergic neurons contribute 80% and 20%, respectively, of neuronal glucose oxidation and neuronal/glial cycling (88). The γ-GABA abnormality is present in many diseases and can be served as potential target. It was reported that abnormalities in Glu/GABA-Gln are present in rat dyskinetic syndrome, and the amino acid neurotransmitter imbalance was improved by "Tiapride," which also increased the expression of GS and EAAT2 protein, decreased Glu levels, increased γ-GABA levels, and increased γ-GABA levels (89). Additionally, treatment with 10 mM γ-GABA considerably slowed down the loss of malate and titratable acidity and increased the levels of succinate and oxalate. Fruit treated with GABA had higher cytosolic activities of nicotinamide adenine dinucleotide-dependent malate dehydrogenase (cyNAD-MDH) and phosphoenolpyruvate carboxylase (PEPC) than control fruit, whereas administration of 10 mM GABA significantly reduced the loss of malate and titratable acidity and raised the concentrations of succinate and oxalate. GABA-treated fruit had larger cytosolic activities of nicotinamide adenine dinucleotide-dependent malate dehydrogenase (cyNAD-MDH) and phosphoenolpyruvate carboxylase (PEPC) than control fruit, although cyNADP-ME and phosphoenolpyruvate carboxykinase activities were lower. Notably, GABA administration drastically decreased ethylene production while also downregulating the expression of MdACS, MdACO, and MdERF. GABA therapy also boosted the accumulation of GABA and improved the function of the GABA shunt (89). The $GABA_A$ receptor agonist muscimol promotes gastric cancer cell growth by triggering mitogen-activated protein kinases (MAPK). Similar to this, GABA promotes the formation of pancreatic cancer by increasing intracellular Ca^{2+} levels and the MAPK/ERK cascade by overexpressing GABRP, a subunit of $GABA_A$ (90). Contrarily, activation of $GABA_B$ receptors successfully prevents DNA synthesis and cell migration by inhibiting isoproterenol-induced cAMP, p-CREB, cAMP response element-luciferase activity, and ERK1/2 phosphorylation (91). The GABA or $GABA_B$ agonist baclofen has been demonstrated to promote Epidermal growth factor receptor (EGFR) transactivation, which has been connected to the propensity of prostate cancer cells to invade (92). According to these findings, various GABA activation-induced effects on cancer development and migration may vary on the kind of cancer or GABA receptor. Contrary to the mechanism described above, our most recent research showed that the $GABA_A$ receptor subunit promotes the growth of pancreatic cancer by altering KCNN4-mediated Ca^{2+} in a GABA-independent manner (93). Besides, it is intriguing that GABA is present in the tumor microenvironment, which suggests that it may be able to control inflammation by concentrating on immune cells that have invaded the tumor (93). In summary, these advances remind that nutrition has evidently metabolic consequences that may change the incidence and progression of cancer, reinforcing the metabolic cancer model.

4.3 Glutamate

In brain tissue, glutamate is widely distributed and has the highest concentration all amino acids. Over the past 50 years, numerous studies have been conducted on the functions of glutamate in the brain, revealing a wealth of information about glutamate. Early research by Krebs indicated that glutamate has an important metabolic function in the brain (94). Waelsch and colleagues made the first observation about the complicated compartmentation of glutamate metabolism in the brain (95). Neurotransmission in both cell types has the highest energetic cost, which increases with cortical activity. Interpretation of functional imaging results is significantly influenced by the contribution of GABAergic neurons and inhibition to cortical energy metabolism (88). Using NAD or NADP as cofactors, glutamate dehydrogenase (GDH) catalyzes the oxidative deamination of glutamate to α-ketoglutarate. GDH is found in primarily in astrocytes in the mammalian brain, where it is likely

involved in the metabolism of the transmitter glutamate. Thus, while GTP primarily controls housekeeping GDH, the availability of ADP or L-leucine has a significant impact on GDH activity in neural tissue. GDH specific to neural tissue is likely to be activated under circumstances that promote hydrolysis of ATP to ADP (e.g., during intense glutamatergic transmission), increasing glutamate flux through this pathway (96). In synaptosomes and cultured neurons that do not produce GDH, the rate of oxidative glutamine metabolism was significantly lowered when glucose was restricted. In contrast, the absence of GDH expression had no impact on glutamine metabolism when glucose was present. In brain mitochondria from GDH KO mice, respiration powered by glutamate was significantly lower, and synaptosomes were unable to increase their respiration in response to increased energy demand. The importance of GDH for neurons, especially during times of high energy demand, is highlighted by its role in the metabolism of glutamine and the capacity for respiration. This may be due to the significant allosteric activation of GDH by ADP (97). Using 13C, astroglia plays a role in energy metabolism of human brain. The primary pathway for the neurotransmitter glutamate repletion has been identified, and nuclear magnetic resonance spectroscopy has been used to study astrocytic oxidative metabolism (98). The pathophysiology of hyperammonemia and hepatic encephalopathy appears to be heavily influenced by abnormalities in glutamate metabolism and glutamatergic neurotransmission. The pathogenesis of hepatic encephalopathy and other hyperammonemia conditions involves an abnormality in astroglial glutamate uptake caused by ammonia (99). Additionally, in the absence of *ad hoc* activity-related metabolic restrictions, the glutamate-glutamine cycle does not control the relative energy requirements of neurons and astrocytes, and as a result, their intake of glucose and the exchange of lactate (100). Glutamate-induced Ca^{2+} loads cause mitochondria to sequester Ca^{2+}, which then uncouples respiration and results in metabolic acidosis. The acidification brought on by glutamate is a sign of metabolic stress and may suggest that mitochondria are crucial in the process of glutamate-induced neuronal death (101).

4.4 Dopamine

Dopamine served as a minor intermediary in the synthesis of noradrenaline in 1957. Today, it is a significant neurotransmitter in the brain. It was reported that dopamine plays a key role in modulating learning and motivation. Excitatory and inhibitory synaptic transmission are altered by dopamine. While the nature of neuromodulation of inhibitory transmission is still under discussion, it appears that activation of the dopamine 1 (D1) receptor specifically promotes N-methyl-D-aspartic acid receptor (NMDA) but not α-amino-3-hydroxy-5-methyl-4-isoxazole-propionicaci (AMPA) synaptic transmission in the cortex and striatum. Because of their dependence on voltage, NMDA currents are less active when the postsynaptic cell is not firing than they are when it is depolarized. Large networks of pyramidal neurons may be induced to enter bistable states resembling working memory, according to experimental and theoretical data (102). The capacity of the striatum to store dopamine as assessed by L-[^{18}F]-fluorodopa uptake was normal, but dopamine (D2) receptor binding was decreased in huntington's disease compared with normal subjects (103). In addition, glutathione is a critical neuroprotectant for midbrain neurons in conditions when energy metabolism is compromised and show that an oxidative challenge occurs during suppression of energy metabolism by malonate (104). Parkinson's disease (PD) neurons had damaged PI3K/Akt, mTOR, eIF4/p70S6K, and Hif-1 pathways, which are part of a network regulating energy metabolism and cell survival in response to growth factors, oxidative stress, and nutrient deprivation. The primary hubs of this network, which is important for longevity and may be a target for therapeutic intervention along with the stimulation of mitochondrial biogenesis, are PI3K/Akt and mTOR signaling (105). Recently, a distinct metabolomic profile linked to parkin dysfunction and demonstrate the value of combining metabolomics with an iPSC-derived dopaminergic neuronal model of parkinson's disease to gain fresh understanding of the pathogenesis of the disease (105). The striatum and prefrontal cortex of the spontaneously hypertensive rat model of attention deficit hyperactivity disorder (ADHD) show impaired energy metabolism and disturbed dopamine and glutamate signaling (106). Several metabolic abnormalities, including insulin resistance, abdominal obesity, dyslipidemia, and hypertension, make up the metabolic syndrome. Its pathogenesis may be influenced by faulty dopamine D2 receptor (D2R) signaling, according to earlier studies. D2R activation simultaneously improves various metabolic traits in obese women (107). The failure of dopamine and glutamate's connection in controlling energy metabolism results in neuronal death (108). Midbrain dopaminergic cells with Lesch-Nyhan disease have limited developmental potential and impaired energy metabolism (109). Catecholamine toxicity may result from interactions with the mitochondrial electron transport system as well as from the induction of an oxidative stress state, and this was further supported by the fact that ADP was able to reverse the dose-dependent inhibition of NADH dehydrogenase activity caused by dopamine (110).

4.5 Serotonin

Serotonin (5-hydroxytryptamine [5-HT]) is a monoamine that has a variety of effects on the peripheral organs as well as the CNS. In the brain, 5-HT is a neurotransmitter that regulates mood, sleep, behavior, appetite, and other functions (111). Serotonin is also an important regulator of the inputs to the energy balance, including energy intake and energy expenditure. Serotonin in the CNS plays a complex and intricate role in appetite and subsequent nutrient intake (112). Receptor agonists for the treatment of obesity have been approved due to serotonin's inhibition of appetite (113). The rate-limiting enzyme tryptophan hydroxylase (TPH) transforms the amino acid tryptophan into 5-hydroxtryptophan (5-HTP), which is then converted to 5-HT by aromatic acid decarboxylase. TPH2 is expressed in the CNS and peripheral neuronal tissues, whereas TPH1 is present in peripheral nonneuronal tissues. These two

isoforms of TPH were discovered to be expressed in a mutually exclusive pattern in the early 2000s (114). Since 2010, scientists have become more aware of how peripheral serotonin controls systemic energy metabolism. The enterochromaffin cells of the gut produce the majority of the 5-HT present in the body. However, 5-HT is also generated by many metabolic organs and has been shown to have biological effects that are endocrine, paracrine, and autocrine in nature. 5-HT promotes proliferation and mass enlargement of pancreatic β-cells. 5-HT encourages lipogenesis and prevents adaptive thermogenesis in adipose tissues. 5-HT activates hepatic stellate cells and causes lipogenesis and gluconeogenesis in the liver (115). It was reported that dairy cows in late lactation treated with 5-HTP had improved energy metabolism, reduced urinary calcium loss, and increased milk calcium secretion. To ascertain any advantages for post-partum calcium and glucose metabolism, additional research should focus on the effects of increased serotonin during the transition period. Chronic acetyl-l-carnitine administration reduced the conversion of glucose to lactate, elevated energy metabolite levels, and changed the levels of monoamine neurotransmitters in the mouse brain (116). Recent genetic studies suggest that leptin signaling physiological processes, most notably leptin's control over appetite and the accumulation of bone mass, are primarily involved in the inhibition of serotonin synthesis and released by brainstem neurons (117). Collectively, 5-HT plays an emerging role in regulating metabolism in cancer cells.

4.6 Neuropeptides

Neuropeptide Y (NPY) is one of the most prevalent neuropeptides in the brain, with 36 amino acids (118, 119). In order to regulate hunger and energy balance, agouti-related protein neurons (AgRP) in the CNS emit NPY, which was first identified as a powerful neuropeptide that stimulates appetite (120–122). The central regulatory effects of NPY on circadian rhythm, the cardiovascular system, stress, and anxiety were gradually demonstrated as this peptide's role in the body's regulation of these processes became better understood (123). Mammals have five different types of NPY receptors (Y1, Y2, Y4, Y5, and Y6), which are found throughout the CNS (124, 125) and linked to various stages of oncogenesis, allowing NPY to exercise its biological effects. When Y2-R is activated, it appears to encourage angiogenesis, whereas Y1-R appears to be involved in the regulation of cancer cell growth. Furthermore, a thorough investigation of the NPY receptor revealed that it is expressed in peripheral tissues such as adipose tissue, the pancreas, and bone (126, 127). As a result, the peripheral effect of NPY has drawn a lot of attention. For instance, activating the NPY receptor in the pancreas can lower hyperglycemia and β-cell apoptosis (128). Adipocyte proliferation and adipogenesis are promoted by NPY in adipose tissue (127). This suggests that in addition to being secreted in the brain by peripheral tissues, NPY also plays significant regulatory roles in the endocrine system (129, 130). In addition to these conventional functions, neuropeptides have been shown to promote tumor growth (131, 132). Numerous neuropeptides, including SP and NPY (133) have been thoroughly investigated in malignancies. Neuropeptide receptors are often GPCRs, which is a superfamily of receptors. For instance, the neurokinin-1 (NK-1) receptor, which is connected to the Gq family of G proteins, is primarily responsible for the pharmacological activity of SP. Upon activation, the NK-1 receptor produces the second messenger's inositol 1,4,5-triphosphate (IP3) and diacylglycerol (DAG) (134). Through its effects on energy homeostasis, the NPY system has complex and significant implications for the development of cancer. Botox particularly, but not only, suppresses NPY in cancer using *in vitro* models and tissues from a prior human chemical denervation investigation. NPY nerve quantification is an independent predictor of prostate cancer-specific mortality. Last but not least, radiation-induced apoptosis is reduced when prostate cancer cells are cocultured with dorsal root ganglia/nerves, and NPY-positive nerves are increased in the prostates of patients who failed radiation therapy, suggesting that NPY nerves may be involved in radiation therapy resistance (135). In summary, understanding the role of NPY in whole-body energy balance could provide insight on mechanisms underlying the pathogenesis of cancer.

5 Therapeutic implications of the interaction between energy metabolism and neuroendocrine regulation

In the past ten years, numerous advancements have been made to reprogram the highly dynamic and heterogeneous energy metabolism of cancer cells. Cancer was first recognized as a disease with altered metabolism one hundred years ago. Migration, invasion, and metastasis are significantly influenced by metabolic alterations in the tumor cell. Despite a lengthy study history, the intricate connections between tumor metabolism, tumor development, and immunosuppression continue to be fascinating fields of study. For the creation of anti-cancer medications, modifications in tumor cell metabolism, such as increased glycolysis, glutaminolysis, and fatty acid metabolism, constitute appealing targets (136). Targeting the metabolism of tumor cells, however, is a strategy that can indirectly affect stromal components like fibroblasts or immune cells in addition to directly killing tumor cells.

In many distinct forms of human malignancies, the neurotransmitters variably control a wide range of activities of cancer cells, endothelial cells, and immune cells. The increasing involvement of the neurotransmitter system in tumor biology and the tumor microenvironment is now better understood, creating new potential for the development of cancer-targeted treatments. Many traditional neurotransmitter-related medications, including β-AR antagonists, serotonin receptor antagonists, AChR antagonists, and DR agonists, may have clinical consequences in the treatment of cancer and be interesting candidates for combination drug therapy. Further research should be done on surgical or chemical denervation and targeting neurotrophic signaling to avoid neoneurogenesis as a cancer treatment option.

It is interesting to note that recent research suggests that a number of neurotransmitters, including 5-HT, dopamine, NE, and histamine, may act as substrates for protein posttranslational modification, such as the well-known crotonylation of histones (137). Selective serotonin reuptake inhibitors (SSRIs) or other small compounds that act on biogenic amines or transglutaminase may therefore prove to be a cutting-edge treatment for cancer. However, additional research is necessary to solidify the use of these medications in the arsenal of cancer therapy and to prevent side effects.

Notably, several neurotransmitters and their analogs, antagonists, and agonists for their receptors have therapeutic benefits and are used as medications for various illnesses, including cancer. Around 2008, a team of French physicians published a paper suggesting the use of propranolol, which inhibits β-ARs (i.e., receptors that EPI and NE activate), to reduce or eradicate benign tumors known as infantile hemangiomas in newborns (138). Since then, numerous academic publications have been written about this subject, and therapeutically, propranolol has taken the place of other treatments for malignancies (139). Meanwhile, studies using *in vitro* preparations, *in vivo* rodent models, and retrospective epidemiological studies of human subjects have suggested that propranolol is therapeutic in a variety of cancer types (counteracting both tumorigenesis and metastasis, including when combined with other pharmacological agents) (140, 141). According to a recent, well-known retrospective study, women with ovarian cancer who used non-selective beta-blockers (like propranolol) had a median overall survival of 94.9 months, compared with 42 months for non-users (142). Propranolol guards against disease recurrence in people with thick cutaneous melanoma, according to a prospective human subjects study (143). Numerous preclinical and clinical studies suggest that propranolol may have therapeutic benefits for angiosarcoma, poor prognosis or refractory cancer (144, 145). Additionally, propranolol is the subject of numerous ongoing clinical trials for a range of different neoplasms. Prazosin (which blocks the alpha1 adrenoceptor) and other medications other than propranolol that also block adrenoceptors are therapeutic in rat models, and additional research has suggested that NE itself promotes cancer (146, 147). In addition, to modify tumorigenesis and metastasis, the molecules serotonin, acetylcholine, and melatonin may act centrally or interact with the sympathetic-adrenomedullary system in the periphery (148, 149). Propranolol, a non-selective beta-adrenoceptor (beta1 and beta2) blocking medication, is being studied more and more for its potential to prevent or treat a variety of human cancers (150). However, in a specific situation, cancer cells need not produce their own NE/EPI or release it in an autocrine manner in order to be responsive to propranolol treatment, as this medication or those in its family (carvedilol, nebivolol) may lower blood sugar by altering pancreatic insulin release or improving insulin sensitivity (151). Propranolol and related beta-blockers, including in breast cancer cells, may enhance glycemic control through modulation of GLUT4 glucose transporter expression and hexokinase-2 (152, 153). In this case, propranolol might also inhibit beta-adrenoceptors on the cancer cell's extracellular surfaces, which would be responding to NE/EPI from non-autocrine sources like the adrenal glands. Additionally, propranolol (or related medications) can still inhibit beta-adrenoceptors on the surface of cancer cells, dampening intracellular molecular pathways linked to cancer, even in the absence of the Warburg effect in cancer cells. Additionally, propranolol or closely related medications may still be able to lower blood sugar levels *via* the pancreas or improve insulin sensitivity even in cases where cancer cells exhibit the Warburg effect but lack adrenoceptors.

Differences between normal and mutant oncogenic enzymes and cancer cells' addiction to nutrients to support uncontrolled cell growth programs imposed by cancer genes are the therapeutic windows for addressing cancer cell metabolism. Therefore, the intricate regulatory networks involving cancer genes and metabolic pathways must be identified for particular cancer types in order for somatic genetic changes in tumors to strategically direct the targeting of cancer cell metabolism. It is hoped that during the next ten years, new medicines will emerge from the fundamental sciences of metabolism, with the increase in knowledge and interest in cancer metabolism.

6 Concluding remarks

Cancer cells develop the capacity to remodel their metabolic network, enabling them to adjust and maintain their survival in the face of drastic environmental changes. The rate of glycolysis in tumor cells was significantly increased in tumor cells compared to normal cells, which was termed the Warburg effect, also known as aerobic glycolysis, which occurs in tumor cells even in the presence of sufficient oxygen. Glutamine metabolism is another characteristic of tumor cells. In addition, fatty acids are not only the main components of membrane construction, but also a source of energy supply and secondary messengers of signal transduction in rapidly proliferating tumor cells. Neuroendocrine control is crucial for tumor cells' consumption of nutrients and energy. There is a crosstalk between neuroendocrine regulation and tumor cell metabolism. Numerous traditional neurotransmitters and neuropeptides including epinephrine and norepinephrine, γ-GABA, glutamate, dopamine, serotonin and neuropeptides have an impact on the material and energy metabolism of tumors. As a result of understanding the neuroendocrine regulatory mechanism of how the neuroendocrine system can fuel cellular metabolism, better combinatorial treatment methods will be possible. Innovative anti-cancer medicines may be based on research on tumor metabolism and neuroendocrine influences on tumors. The creation of medications that directly affect the altered tumor metabolism at the neuroendocrine level may prove to be a ground-breaking oncology treatment. These novel understandings of key catabolic pathways in cancer provide a focus for further research in this field and may aid in the development of effective therapeutic strategies.

Author contributions

YG guided the proof of the manuscript, and offer the financial support for the project leading to this publication. All authors contributed to the article and approved the submitted version.

Funding

This work was supported by 2021-2023 science and technology development program. Item category: Clinical research and eduction (sub-class of project) The National Natural Science Foundation of China (81904092) Jiangsu Province Traditional Chinese Medicine Science and Technology Development Plan-Youth Talent Project (QN202206).

Conflict of interest

The authors declare that the research was conducted in the absence of any commercial or financial relationships that could be construed as a potential conflict of interest.

The reviewer [SY] declared a shared affiliation with the author [YL], to the handling editor at the time of the review.

Publisher's note

References

1. Kocarnik JM, Compton K, Dean FE, Fu W, Gaw BL, Harvey JD, et al. Cancer incidence, mortality, years of life lost, years lived with disability, and disability-adjusted life years for 29 cancer groups from 2010 to 2019: A systematic analysis for the global burden of disease study 2019. *JAMA Oncol* (2022) 8(3):420–44. doi: 10.1001/jamaoncol.2021.6987

2. Siegel RL, Miller KD, Fuchs HE, Jemal A. Cancer statistics, 2022. *CA: Cancer J Clin* (2022) 72(1):7–33. doi: 10.3322/caac.21708

3. Warburg O. On the origin of cancer cells. *Science* (1956) 123(3191):309–14. doi: 10.1126/science.123.3191.309

4. Hanahan D, Weinberg RA. Hallmarks of cancer: The next generation. *Cell* (2011) 144(5):646–74. doi: 10.1016/j.cell.2011.02.013

5. DeLellis RA. The neuroendocrine system and its tumors: An overview. *Am J Clin Pathol* (2001) 115(Suppl):S5–16. doi: 10.1309/7GR5-L7YW-3G78-LDJ6

6. Yeo GS, Heisler LK. Unraveling the brain regulation of appetite: Lessons from genetics[J]. *Nat Neurosci* (2012) 15(10):1343–9. doi: 10.1038/nn.3211

7. Broberger C, Hokfelt T. Hypothalamic and vagal neuropeptide circuitries regulating food intake. *Physiol Behav* (2001) 74(4-5):669–82. doi: 10.1016/S0031-9384(01)00611-4

8. Baskerville TA, Douglas AJ. Dopamine and oxytocin interactions underlying behaviors: Potential contributions to behavioral disorders. *CNS Neurosci Ther* (2010) 16(3):e92–123. doi: 10.1111/j.1755-5949.2010.00154.x

9. Dieguez C, Vazquez MJ, Romero A, López M, Nogueiras R. Hypothalamic control of lipid metabolism: focus on leptin, ghrelin and melanocortins. *Neuroendocrinology* (2011) 94(1):1–11. doi: 10.1159/000328122

10. Stefanidis A, Wiedmann NM, Adler ES, Oldfield BJ. Hypothalamic control of adipose tissue. *Best Pract Res Clin Endocrinol Metab* (2014) 28(5):685–701. doi: 10.1016/j.beem.2014.08.001

11. Thorens B. Sensing of glucose in the brain. *Handb Exp Pharmacol* (2012) 209):277–94. doi: 10.1007/978-3-642-24716-3_12

12. Timper K, Bruning JC. Hypothalamic circuits regulating appetite and energy homeostasis: Pathways to obesity. *Dis Model Mech* (2017) 10(6):679–89. doi: 10.1242/dmm.026609

13. Yau YH, Potenza MN. Stress and eating behaviors. *Minerva Endocrinol* (2013) 38(3):255–67.

14. Kianercy A, Veltri R, Pienta KJ. Critical transitions in a game theoretic model of tumour metabolism. *Interface Focus* (2014) 4(4):20140014. doi: 10.1098/rsfs.2014.0014

15. Whitaker-Menezes D, Martinez-Outschoorn UE, Lin Z, Ertel A, Flomenberg N, Witkiewicz AK, et al. Evidence for a stromal-epithelial "lactate shuttle" in human tumors: MCT4 is a marker of oxidative stress in cancer-associated fibroblasts. *Cell Cycle (Georgetown Tex.)* (2011) 10(11):1772–83. doi: 10.4161/cc.10.11.15659

16. Tan AS, Baty JW, Dong LF, Bezawork-Geleta A, Endaya B, Goodwin J, et al. Mitochondrial genome acquisition restores respiratory function and tumorigenic potential of cancer cells without mitochondrial DNA. *Cell Metab* (2015) 21(1):81–94. doi: 10.1016/j.cmet.2014.12.003

17. Vaupel P, Schmidberger H, Mayer A. The warburg effect: essential part of metabolic reprogramming and central contributor to cancer progression. *Int J Radiat Biol* (2019) 95(7):912–9. doi: 10.1080/09553002.2019.1589653

18. Chen K, Zhang C, Ling S, et al. The metabolic flexibility of quiescent CSC: Implications for chemotherapy resistance. *Cell Death Dis* (2021) 12(9):835. doi: 10.1038/s41419-021-04116-6

19. Elgendy M, Cirò M, Hosseini A, Weiszmann J, Mazzarella L, Ferrari E, et al. Combination of hypoglycemia and metformin impairs tumor metabolic plasticity and growth by modulating the PP2A-GSK3β-MCL-1 axis. *Cancer Cell* (2019) 35(5):798–815.e795. doi: 10.1016/j.ccell.2019.03.007

20. Sotgia F, Martinez-Outschoorn UE, Pavlides S, Howell A, Pestell RG, Lisanti MP, et al. Understanding the warburg effect and the prognostic value of stromal caveolin-1 as a marker of a lethal tumor microenvironment. *Breast Cancer Res BCR* (2011) 13(4):213. doi: 10.1186/bcr2892

21. Zong WX, Rabinowitz JD, White E. Mitochondria and cancer. *Mol Cell* (2016) 61(5):667–76. doi: 10.1016/j.molcel.2016.02.011

22. DeBerardinis RJ, Cheng T. Q's next: The diverse functions of glutamine in metabolism, cell biology and cancer. *Oncogene* (2010) 29(3):313–24. doi: 10.1038/onc.2009.358

23. Reinfeld BI, Madden MZ, Wolf MM, Chytil A, Bader JE, Patterson AR, et al. Cell-programmed nutrient partitioning in the tumour microenvironment. *Nature* (2021) 593(7858):282–8. doi: 10.1038/s41586-021-03442-1

24. Sandulache VC, Ow TJ, Pickering CR, Frederick MJ, Zhou G, Fokt I, et al. Glucose, not glutamine, is the dominant energy source required for proliferation and survival of head and neck squamous carcinoma cells. *Cancer* (2011) 117(13):2926–38. doi: 10.1002/cncr.25868

25. Koundouros N, Poulogiannis G. Reprogramming of fatty acid metabolism in cancer. *Br J Cancer* (2020) 122(1):4–22. doi: 10.1038/s41416-019-0650-z

26. Gao P, Tchernyshyov I, Chang TC, Lee YS, Kita K, Ochi T, et al. C-myc suppression of miR-23a/b enhances mitochondrial glutaminase expression and glutamine metabolism. *Nature* (2009) 458(7239):762–5. doi: 10.1038/nature07823

27. Erlandson RA, Nesland JM. Tumors of the endocrine/neuroendocrine system: An overview. *Ultrastruct Pathol* (1994) 18(1-2):149–70. doi: 10.3109/01913129409016286

28. Antoni MH, Lutgendorf SK, Cole SW, Dhabhar FS, Sephton SE., McDonald PG, et al. The influence of bio-behavioural factors on tumour biology: pathways and mechanisms. *Nat Rev Cancer* (2006) 6(3):240–8. doi: 10.1038/nrc1820

29. Irwin MR, Cole SW. Reciprocal regulation of the neural and innate immune systems. *Nat Rev Immunol* (2011) 11(9):625–32. doi: 10.1038/nri3042

30. Hall JC. Glycine. *JPEN J Parenter Enteral Nutr* (1998) 22(6):393–8. doi: 10.1177/014860719822006393

31. Watkins JC, Jane DE. The glutamate story. *Br J Pharmacol* (2006) 147(Suppl 1):S100–108. doi: 10.1038/sj.bjp.0706444

32. Brownlow S, Webster R, Croxen R, et al. Acetylcholine receptor delta subunit mutations underlie a fast-channel myasthenic syndrome and arthrogryposis multiplex congenita[J]. *J Clin Invest* (2001) 108(1):125–30. doi: 10.1172/JCI200112935

33. Elliott KA, Hobbiger F. Gamma aminobutyric acid; circulatory and respiratory effects in different species; re-investigation of the anti-strychnine action in mice[J]. *J Physiol* (1959) 146(1):70–84. doi: 10.1113/jphysiol.1959.sp006178

34. Dalal R, Grujic D. Epinephrine. In: *StatPearls*. Treasure Island (FL (2022) The physiological society.

35. Silverberg AB, Shah SD, Haymond MW, et al. Norepinephrine: hormone and neurotransmitter in man. *Am J Physiol* (1978) 234(3):E252–256. doi: 10.1152/ajpendo.1978.234.3.E252

36. Mohammad-Zadeh LF, Moses L, Gwaltney-Brant SM. Serotonin: A review. *J Vet Pharmacol Ther* (2008) 31(3):187–99. doi: 10.1111/j.1365-2885.2008.00944.x

37. Groneberg DA, Folkerts G, Peiser C, Neuropeptide Y. (NPY). *Pulm Pharmacol Ther* (2004) 17(4):173–80. doi: 10.1016/j.pupt.2004.04.003

38. Said SI. Vasoactive intestinal polypeptide (VIP): Current status. *Peptides* (1984) 5(2):143–50. doi: 10.1016/0196-9781(84)90197-9

39. Russo AF. Calcitonin gene-related peptide (CGRP): A new target for migraine. *Annu Rev Pharmacol Toxicol* (2015) 55:533–52. doi: 10.1146/annurev-pharmtox-010814-124701

40. Vincent JP, Mazella J, Kitabgi P. Neurotensin and neurotensin receptors. *Trends Pharmacol Sci* (1999) 20(7):302–9. doi: 10.1016/S0165-6147(99)01357-7

41. Huxtable RJ. Taurine in the central nervous system and the mammalian actions of taurine. *Prog Neurobiol* (1989) 32(6):471–533. doi: 10.1016/0301-0082(89)90019-1

42. Williams M, Risley EA, Totaro JA. Interactions of taurine and beta-alanine with central nervous system neurotransmitter receptors. *Life Sci* (1980) 26(7):557–60. doi: 10.1016/0024-3205(80)90319-7

43. Li SB, de Lecea L. The hypocretin (orexin) system: From a neural circuitry perspective. *Neuropharmacology* (2020) 167:107993. doi: 10.1016/j.neuropharm.2020.107993

44. Bardin CW. Pro-opiomelanocortin peptides in reproductive physiology. *Hosp Pract (Off Ed)* (1988) 23(4):109–12. 117-121, 124 passim. doi: 10.1080/21548331.1988.11703456

45. Schlesinger N. Overview of the management of acute gout and the role of adrenocorticotropic hormone. *Drugs* (2008) 68(4):407–15. doi: 10.2165/00003495-200868040-00002

46. Levi-Montalcini R, Angeletti PU. Nerve growth factor. *Physiol Rev* (1968) 48 (3):534–69. doi: 10.1152/physrev.1968.48.3.534

47. Derendorf H, Mollmann H, Barth J, et al. Pharmacokinetics and oral bioavailability of hydrocortisone. *J Clin Pharmacol* (1991) 31(5):473–6. doi: 10.1002/j.1552-4604.1991.tb01906.x

48. Diniz GB, Bittencourt JC. The melanin-concentrating hormone (MCH) system: A tale of two peptides. *Front Neurosci* (2019) 13:1280. doi: 10.3389/fnins.2019.01280

49. Cole SW, Sood AK. Molecular pathways: Beta-adrenergic signaling in cancer. *Clin Cancer Res an Off J Am Assoc Cancer Res* (2012) 18(5):1201–6. doi: 10.1158/1078-0432.CCR-11-0641

50. Burdakov D, Luckman SM, Verkhratsky A. Glucose-sensing neurons of the hypothalamus. *Philos Trans R Soc Lond B Biol Sci* (2005) 360(1464):2227–35. doi: 10.1098/rstb.2005.1763

51. D'Agostino G, Lyons DJ, Cristiano C, Burke LK, Madara JC, Campbell JN, et al. Appetite controlled by a cholecystokinin nucleus of the solitary tract to hypothalamus neurocircuit. *Elife* (2016) 5:e12225. doi: 10.7554/eLife.12225

52. Liu J, Conde K, Zhang P, Lilascharoen V, Xu Z, Lim BK, et al. Enhanced AMPA receptor trafficking mediates the anorexigenic effect of endogenous glucagon-like peptide-1 in the paraventricular hypothalamus. *Neuron* (2017) 96(4):897–909.e895. doi: 10.1016/j.neuron.2017.09.042

53. Anand BK, Chhina GS, Sharma KN, Dua S, Singh B. Activity of single neurons in the hypothalamic feeding centers: Effect of glucose. *Am J Physiol* (1964) 207:1146–54. doi: 10.1152/ajplegacy.1964.207.5.1146

54. Entschladen F, Drell T, Lang K, Joseph J, Zaenker K S. Tumour-cell migration, invasion, and metastasis: navigation by neurotransmitters. *Lancet Oncol* (2004) 5 (4):254–8. doi: 10.1016/S1470-2045(04)01431-7

55. Heffner KL, Loving TJ, Robles TF, Kiecolt-Glaser J K. Examining psychosocial factors related to cancer incidence and progression: iIn search of the silver lining. *Brain Behav Immun* (2003) 17(Suppl 1):S109–111. doi: 10.1016/S0889-1591(02)00076-4

56. Entschladen F, Lang K, Drell TL, Joseph J, Zaenker KS, et al. Neurotransmitters are regulators for the migration of tumor cells and leukocytes. *Cancer Immunol Immunother* (2002) 51(9):467–82. doi: 10.1007/s00262-002-0300-8

57. Jezova D, Jurankova E, Mosnarova A, Kriska M, Skultétyová I. Neuroendocrine response during stress with relation to gender differences. *Acta Neurobiol Exp (Wars)* (1996) 56(3):779–85.

58. Everest P. Stress and bacteria: Microbial endocrinology. *Gut* (2007) 56(8):1037–8. doi: 10.1136/gut.2006.117150

59. Jensen MD, Cryer PE, Johnson CM, Murray MJ. Effects of epinephrine on regional free fatty acid and energy metabolism in men and women. *Am J Physiol* (1996) 270(2 Pt 1):E259–264. doi: 10.1152/ajpendo.1996.270.2.E259

60. Sood AK, Armaiz-Pena GN, Halder J, Murray MJ. Adrenergic modulation of focal adhesion kinase protects human ovarian cancer cells from anoikis. *J Clin Invest* (2010) 120(5):1515–23. doi: 10.1172/JCI40802

61. Thaker PH, Han LY, Kamat AA, Arevalo JM, Takahashi R, Lu C, et al. Chronic stress promotes tumor growth and angiogenesis in a mouse model of ovarian carcinoma. *Nat Med* (2006) 12(8):939–44. doi: 10.1038/nm1447

62. Lafontan M, Berlan M. Fat cell adrenergic receptors and the control of white and brown fat cell function. *J Lipid Res* (1993) 34(7):1057–91. doi: 10.1016/S0022-2275(20)37695-1

63. Arch JR, Kaumann AJ. Beta 3 and atypical beta-adrenoceptors. *Medicinal Res Rev* (1993) 13(6):663–729. doi: 10.1002/med.2610130604

64. Huang XE, Hamajima N, Saito T, Matsuo K, Mizutani M, Iwata H, et al. Possible association of beta2- and beta3-adrenergic receptor gene polymorphisms with susceptibility to breast cancer. *Breast Cancer Res BCR* (2001) 3(4):264–9. doi: 10.1186/bcr304

65. Takezaki T, Hamajima N, Matsuo K, Tanaka R, Hirai T, Kato T, et al. Association of polymorphisms in the beta-2 and beta-3 adrenoceptor genes with risk of colorectal cancer in Japanese. *Int J Clin Oncol* (2001) 6(3):117–22. doi: 10.1007/PL00012092

66. Çırakoğlu A, Fejzullahu A, Benli E, Yuce A, Ayyıldız A, Aynacıoğlu AŞ, et al. Association between the Trp64Arg polymorphism of the ADRB3 gene and overactive bladder. *Neurourology urodynamics* (2021) 40(7):1780–5. doi: 10.1002/nau.24742

67. He RH, He YJ, Tang YJ, Zhou HH, McLeod HL, Liu J, et al. The potential anticancer effect of beta-blockers and the genetic variations involved in the interindividual difference. *Pharmacogenomics* (2016) 17(1):74–9. doi: 10.2217/pgs.15.152

68. Walston J, Lowe A, Silver K, Yang Y, Bodkin NL, Hansen BC, et al. The beta3-adrenergic receptor in the obesity and diabetes prone rhesus monkey is very similar to human and contains arginine at codon 64. *Gene* (1997) 188(2):207–13. doi: 10.1016/S0378-1119(96)00796-2

69. Kasznicki J, Blasiak J, Majsterek I, Przybyłowska K, Drzewoski J. The Trp64Arg beta3-adrenergic receptor amino-acid variant is not associated with overweight and type 2 diabetes mellitus in polish population. *Exp Clin Endocrinol Diabetes Off journal German Soc Endocrinol [and] German Diabetes Assoc* (2005) 113(10):593–7. doi: 10.1055/s-2005-872840

70. Masuo K, Katsuya T, Fu Y, Rakugi H, Ogihara T, Tuck ML, et al. Beta2-adrenoceptor polymorphisms relate to insulin resistance and sympathetic overactivity as early markers of metabolic disease in nonobese, normotensive individuals. *Am J hypertension* (2005) 18(7):1009–14. doi: 10.1016/j.amjhyper.2005.01.006

71. Abe M, Wu Z, Yamamoto M, Jin JJ, Tabara Y, Mogi M, et al. Association of dopamine beta-hydroxylase polymorphism with hypertension through interaction with fasting plasma glucose in Japanese. *Hypertension Res Off J Japanese Soc Hypertension* (2005) 28(3):215–21. doi: 10.1291/hypres.28.215

72. Zahalka AH, Arnal-Estapé A, Maryanovich M, et al. Adrenergic nerves activate an angio-metabolic switch in prostate cancer. *Science* (2017) 358(6361):321–6. doi: 10.1126/science.aah5072

73. Hondermarck H, Jobling P. The sympathetic nervous system drives tumor angiogenesis. *Trends Cancer* (2018) 4(2):93–4. doi: 10.1016/j.trecan.2017.11.008

74. Renz BW, Takahashi R, Tanaka T, Macchini M, Hayakawa Y, Dantes Z, et al. beta2 adrenergic-neurotrophin feedforward loop promotes pancreatic cancer. *Cancer Cell* (2018) 33(1):75–90 e77. doi: 10.1016/j.ccell.2017.11.007

75. Cui B, Luo Y, Tian P, Peng F, Lu J, Yang Y, et al. Stress-induced epinephrine enhances lactate dehydrogenase a and promotes breast cancer stem-like cells. *J Clin Invest* (2019) 129(3):1030–46. doi: 10.1172/JCI121685

76. Huan HB, Wen XD, Chen XJ, Wu L, Wu L L, Zhang L, et al. Sympathetic nervous system promotes hepatocarcinogenesis by modulating inflammation through activation of alpha1-adrenergic receptors of kupffer cells. *Brain Behav Immun* (2017) 59:118–34. doi: 10.1016/j.bbi.2016.08.016

77. Albo D, Akay CL, Marshall CL, Wilks JA, Verstovsek G, Liu H, et al. Neurogenesis in colorectal cancer is a marker of aggressive tumor behavior and poor outcomes. *Cancer* (2011) 117(21):4834–45. doi: 10.1002/cncr.26117

78. Wen YC, Liu CL, Yeh HL, Chen WH, Jiang KC, Tram VTN, et al. PCK1 regulates neuroendocrine differentiation in a positive feedback loop of LIF/ZBTB46 signalling in castration-resistant prostate cancer. *Br J Cancer* (2022) 126(5):778–90. doi: 10.1038/s41416-021-01631-3

79. Kanbara K, Otsuki Y, Watanabe M, Yokoe S, Mori Y, Asahi M, et al. GABAB receptor regulates proliferation in the high-grade chondrosarcoma cell line OUMS-27 *via* apoptotic pathways. *BMC Cancer* (2018) 18(1):263. doi: 10.1186/s12885-018-4149-4

80. Sung HY, Yang SD, Ju W, Ju W, Ahn JH. Aberrant epigenetic regulation of GABRP associates with aggressive phenotype of ovarian cancer. *Exp Mol Med* (2017) 49 (5):e335. doi: 10.1038/emm.2017.62

81. Ortega A. A new role for GABA: Inhibition of tumor cell migration. *Trends Pharmacol Sci* (2003) 24(4):151–4. doi: 10.1016/S0165-6147(03)00052-X

82. Watanabe M, Maemura K, Oki K, Shiraishi N, Shibayama Y, Katsu K, et al. Gamma-aminobutyric acid (GABA) and cell proliferation: Focus on cancer cells. *Histol Histopathol* (2006) 21(10):1135–41. doi: 10.14670/HH-21.1135

83. Hujber Z, Horvath G, Petovari G, Krencz I, Dankó T, Mészáros K, et al. GABA, glutamine, glutamate oxidation and succinic semialdehyde dehydrogenase expression in human gliomas. *J Exp Clin Cancer Res* (2018) 37(1):271. doi: 10.1186/s13046-018-0946-5

84. Maemura K, Shiraishi N, Sakagami K, Kawakami K, Inoue T, Murano M, et al. Proliferative effects of gamma-aminobutyric acid on the gastric cancer cell line are

associated with extracellular signal-regulated kinase 1/2 activation. *J Gastroenterol Hepatol* (2009) 24(4):688–96. doi: 10.1111/j.1440-1746.2008.05687.x

85. Maemura K, Yamauchi H, Hayasaki H, Kanbara K, Tamayama T, Hirata I, et al. Gamma-amino-butyric acid immunoreactivity in intramucosal colonic tumors. *J Gastroenterol Hepatol* (2003) 18(9):1089–94. doi: 10.1046/j.1440-1746.2003.03131.x

86. Azuma H, Inamoto T, Sakamoto T, Kiyama S, Ubai T, Shinohara Y, et al. Gamma-aminobutyric acid as a promoting factor of cancer metastasis; induction of matrix metalloproteinase production is potentially its underlying mechanism. *Cancer Res* (2003) 63(23):8090–6.

87. Zhang X, Du Z, Liu J, et al. Gamma-aminobutyric acid receptors affect the progression and migration of tumor cells. *J Recept Signal Transduct Res* (2014) 34 (6):431–9. doi: 10.3109/10799893.2013.856918

88. Patel AB, de Graaf RA, Mason GF, Rothman DL, Shulman RG, Behar KL, et al. The contribution of GABA to glutamate/glutamine cycling and energy metabolism in the rat cortex *in vivo*. *Proc Natl Acad Sci United States America* (2005) 102(15):5588–93. doi: 10.1073/pnas.0501703102

89. Hao J, Jiang K, Zhang X, Wu M, Ma B, et al. "Glu/GABA-gln" metabolic loop abnormalities in iminodipropionitrile (IDPN)-induced dyskinetic syndrome. *Neurological Sci Off J Ital Neurological Soc Ital Soc Clin Neurophysiol* (2021) 42 (11):4697–706. doi: 10.1007/s10072-021-05570-y

90. Takehara A, Hosokawa M, Eguchi H, Ohigashi H, Ishikawa O, Nakamura Y, et al. Gamma-aminobutyric acid (GABA) stimulates pancreatic cancer growth through overexpressing GABAA receptor pi subunit. *Cancer Res* (2007) 67(20):9704–12. doi: 10.1158/0008-5472.CAN-07-2099

91. Schuller HM. Neurotransmission and cancer: Implications for prevention and therapy. *Anticancer Drugs* (2008) 19(7):655–71. doi: 10.1097/CAD.0b013e3283025b58

92. Xia S, He C, Zhu Y, Wang S, Li H, Zhang Z, et al. GABA(B)R-induced EGFR transactivation promotes migration of human prostate cancer cells. *Mol Pharmacol* (2017) 92(3):265–77. doi: 10.1124/mol.116.107854

93. Jiang SH, Zhu LL, Zhang M, Li RK, Yang Q, Yan JY, et al. GABRP regulates chemokine signalling, macrophage recruitment and tumour progression in pancreatic cancer through tuning KCNN4-mediated Ca(2+) signalling in a GABA-independent manner. *Gut* (2019) 68(11):1994–2006. doi: 10.1136/gutjnl-2018-317479

94. Krebs HA. Metabolism of amino-acids: The synthesis of glutamine from glutamic acid and ammonia, and the enzymic hydrolysis of glutamine in animal tissues. *Biochem J* (1935) 29(8):1951–69. doi: 10.1042/bj0291951

95. . *AMINO ACID AND PROTEIN METABOLISM-VI CEREBRAL COMPARTMENTS OF GLUTAMIC ACID METABOLISM.*

96. Plaitakis A, Zaganas I. Regulation of human glutamate dehydrogenases: implications for glutamate, ammonia and energy metabolism in brain. *J Neurosci Res* (2001) 66(5):899–908. doi: 10.1002/jnr.10054

97. Hohnholt MC, Andersen VH, Andersen JV, Christensen SK, Karaca M, et al. Glutamate dehydrogenase is essential to sustain neuronal oxidative energy metabolism during stimulation. *J Cereb Blood Flow Metab Off J Int Soc Cereb Blood Flow Metab* (2018) 38(10):1754–68. doi: 10.1177/0271678X17714680

98. Lebon V, Petersen KF, Cline GW, Shen J, Mason GF, Dufour S, et al. Astroglial contribution to brain energy metabolism in humans revealed by 13C nuclear magnetic resonance spectroscopy: Elucidation of the dominant pathway for neurotransmitter glutamate repletion and measurement of astrocytic oxidative metabolism. *J Neurosci* (2002) 22(5):1523–31. doi: 10.1523/JNEUROSCI.22-05-01523.2002

99. Norenberg MD, Huo Z, Neary JT, Roig-Cantesano A. The glial glutamate transporter in hyperammonemia and hepatic encephalopathy: Relation to energy metabolism and glutamatergic neurotransmission. *Glia* (1997) 21(1):124–33. doi: 10.1002/(SICI)1098-1136(199709)21:1<124::AID-GLIA14>3.0.CO;2-U

100. Massucci FA, DiNuzzo M, Giove F, Maraviglia B, Castillo IP, Marinari E, et al. Energy metabolism and glutamate-glutamine cycle in the brain: A stoichiometric modeling perspective. *BMC Syst Biol* (2013) 7:103. doi: 10.1186/1752-0509-7-103

101. Wang GJ, Randall RD, Thayer SA. Glutamate-induced intracellular acidification of cultured hippocampal neurons demonstrates altered energy metabolism resulting from Ca2+ loads. *J Neurophysiol* (1994) 72(6):2563–9. doi: 10.1152/jn.1994.72.6.2563

102. Lisman JE, Fellous JM, Wang XJ. A role for NMDA-receptor channels in working memory. *Nat Neurosci* (1998) 1(4):273–5. doi: 10.1038/1086

103. Leenders KL, Frackowiak RS, Quinn N, Marsden CD. Brain energy metabolism and dopaminergic function in huntington's disease measured *in vivo* using positron emission tomography. *Mov Disord* (1986) 1(1):69–77. doi: 10.1002/mds.870010110

104. Zeevalk GD, Bernard LP, Nicklas WJ. Role of oxidative stress and the glutathione system in loss of dopamine neurons due to impairment of energy metabolism. *J Neurochem* (1998) 70(4):1421–30. doi: 10.1046/j.1471-4159.1998.70041421.x

105. Elstner M, Morris CM, Heim K, Bender A, Mehta D, Jaros E, et al. Expression analysis of dopaminergic neurons in parkinson's disease and aging links transcriptional dysregulation of energy metabolism to cell death. *Acta Neuropathol* (2011) 122(1):75–86. doi: 10.1007/s00401-011-0828-9

106. Dimatelis JJ, Hsieh JH, Sterley TL, Marais L, Womersley JS, Vlok M, et al. Impaired energy metabolism and disturbed dopamine and glutamate signalling in the striatum and prefrontal cortex of the spontaneously hypertensive rat model of attention-deficit hyperactivity disorder. *J Mol Neurosci* (2015) 56(3):696–707. doi: 10.1007/s12031-015-0491-z

107. Kok P, Roelfsema F, Frölich M, van Pelt J, Stokkel MP, Meinders AE, et al. Activation of dopamine D2 receptors simultaneously ameliorates various metabolic features of obese women. *Am J Physiol Endocrinol Metab* (2006) 291(5):E1038–1043. doi: 10.1152/ajpendo.00567.2005

108. Calabresi P, Pisani A, Centonze D, Bernar. Synaptic plasticity and physiological interactions between dopamine and glutamate in the striatum. *Neurosci Biobehav Rev* (1997) 21(4):519–23. doi: 10.1016/S0149-7634(96)00029-2

109. Bell S, McCarty V, Peng H, Hettige N, Antonyan L, Crapper L, et al. Lesch-nyhan disease causes impaired energy metabolism and reduced developmental potential in midbrain dopaminergic cells. *Stem Cell Rep* (2021) 16(7):1749–62. doi: 10.1016/j.stemcr.2021.06.003

110. Ben-Shachar D, Zuk R, Glinka Y. Dopamine neurotoxicity: inhibition of mitochondrial respiration. *J Neurochem* (1995) 64(2):718–23. doi: 10.1046/j.1471-4159.1995.64020718.x

111. Tecott LH, Sun LM, Akana SF, Strack AM, Lowenstein DH, Dallman , et al. Eating disorder and epilepsy in mice lacking 5-HT2c serotonin receptors. *Nature* (1995) 374(6522):542–6. doi: 10.1038/374542a0

112. Tecott LH. Serotonin and the orchestration of energy balance. *Cell Metab* (2007) 6(5):352–61. doi: 10.1016/j.cmet.2007.09.012

113. Smith SR, Weissman NJ, Anderson CM, Sanchez M, Chuang E, Stubbe S, et al. Multicenter, placebo-controlled trial of lorcaserin for weight management. *New Engl J Med* (2010) 363(3):245–56. doi: 10.1056/NEJMoa0909809

114. Walther DJ, Peter JU, Bashammakh S, Hörtnagl H, Voits M, Fink H, et al. Synthesis of serotonin by a second tryptophan hydroxylase isoform. *Science* (2003) 299 (5603):76. doi: 10.1126/science.1078197

115. Moon JH, Oh CM, Kim H. Serotonin in the regulation of systemic energy metabolism. *J Diabetes Investig* (2022) 13(10):1639–45. doi: 10.1111/jdi.13879

116. Smeland OB, Meisingset TW, Borges K, Sonnewald U. Chronic acetyl-l-carnitine alters brain energy metabolism and increases noradrenaline and serotonin content in healthy mice. *Neurochem Int* (2012) 61(1):100–7. doi: 10.1016/j.neuint.2012.04.008

117. Oury F, Karsenty G. Towards a serotonin-dependent leptin roadmap in the brain. *Trends Endocrinol Metab* (2011) 22(9):382–7. doi: 10.1016/j.tem.2011.04.006

118. Hofmann S, Bellmann-Sickert K, Beck-Sickinger AG. Chemical modification of neuropeptide y for human Y1 receptor targeting in health and disease. *Biol Chem* (2019) 400(3):299–311. doi: 10.1515/hsz-2018-0364

119. Kawakami Y. [Neuropeptide y]. *Nihon Rinsho* (2005) 63(Suppl 8):421–4. doi: 10.1002/cne.24090

120. Cedernaes J, Huang W, Ramsey KM, Waldeck N, Cheng L, Marcheva B, et al. Transcriptional basis for rhythmic control of hunger and metabolism within the AgRP neuron. *Cell Metab* (2019) 29(5):1078–1091.e1075. doi: 10.1016/j.cmet.2019.01.023

121. Ip CK, Zhang L, Farzi A, Qi Y, Clarke I, Reed F, et al. Amygdala NPY circuits promote the development of accelerated obesity under chronic stress conditions. *Cell Metab* (2019) 30(1):111–128 e116. doi: 10.1016/j.cmet.2019.04.001

122. Krashes MJ, Shah BP, Madara JC, Olson DP, Strochlic DE, Garfield AS, et al. An excitatory paraventricular nucleus to AgRP neuron circuit that drives hunger. *Nature* (2014) 507(7491):238–42. doi: 10.1038/nature12956

123. Lee DY, Hong SH, Kim B, Lee DS, Yu K, Lee KS, et al. Neuropeptide y mitigates ER stress-induced neuronal cell death by activating the PI3K-XBP1 pathway. *Eur J Cell Biol* (2018) 97(5):339–48. doi: 10.1016/j.ejcb.2018.04.003

124. Fetissov SO, Kopp J, Hokfelt T. Distribution of NPY receptors in the hypothalamus. *Neuropeptides* (2004) 38(4):175–88. doi: 10.1016/j.npep.2004.05.009

125. Huang L, Tan HY, Fogarty MJ, Andrews ZB, Veldhuis JD, Herzog H, et al. Actions of NPY, and its Y1 and Y2 receptors on pulsatile growth hormone secretion during the fed and fasted state. *J Neurosci* (2014) 34(49):16309–19. doi: 10.1523/JNEUROSCI.4622-13.2014

126. Park MH, Lee JK, Kim N, Min WK, Lee JE, Kim KT, et al. Neuropeptide y induces hematopoietic Stem/Progenitor cell mobilization by regulating matrix metalloproteinase-9 activity through Y1 receptor in osteoblasts. *Stem Cells* (2016) 34 (8):2145–56. doi: 10.1002/stem.2383

127. Shin MK, Choi B, Kim EY, Park JE, Hwang ES, Lee H, et al. Elevated pentraxin 3 in obese adipose tissue promotes adipogenic differentiation by activating neuropeptide y signaling. *Front Immunol* (2018) 9:1790. doi: 10.3389/fimmu.2018.01790

128. Franklin ZJ, Tsakmaki A, Fonseca Pedro P, King AJ, Huang GC, Amjad S, et al. Islet neuropeptide y receptors are functionally conserved and novel targets for the preservation of beta-cell mass. *Diabetes Obes Metab* (2018) 20(3):599–609. doi: 10.1111/dom.13119

129. Khan D, Vasu S, Moffett RC, Irwin N, Flatt PR. Influence of neuropeptide y and pancreatic polypeptide on islet function and beta-cell survival. *Biochim Biophys Acta Gen Subj* (2017) 1861(4):749–58. doi: 10.1016/j.bbagen.2017.01.005

130. Loh K, Herzog H, Shi YC. Regulation of energy homeostasis by the NPY system. *Trends Endocrinol Metab* (2015) 26(3):125–35. doi: 10.1016/j.tem.2015.01.003

131. Sommerfeldt DW, Rubin CT. Biology of bone and how it orchestrates the form and function of the skeleton. *Eur Spine J Off Publ Eur Spine Society Eur Spinal*

Deformity Society Eur Section Cervical Spine Res Soc (2001) 10(Suppl 2):S86–95. doi: 10.1007/s005860100283

132. You JS, Ji HI, Chang KJ, Yoo MC, Yang HI, Jeong IK, et al. Serum osteopontin concentration is decreased by exercise-induced fat loss but is not correlated with body fat percentage in obese humans[J]. *Mol Med Rep* (2013) 8(2):579–84. doi: 10.3892/mmr.2013.1522

133. Israel DI, Nove J, Kerns KM, Kaufman RJ, Rosen V, Cox KA, et al. Heterodimeric bone morphogenetic proteins show enhanced activity in vitro and *in vivo*. *Growth factors (Chur Switzerland)* (1996) 13(3-4):291–300. doi: 10.3109/08977199609003229

134. Muñoz M, Rosso M, Coveñas R. The NK-1 receptor: A new target in cancer therapy. *Curr Drug Targets* (2011) 12(6):909–21. doi: 10.2174/138945011795528796

135. Ding Y, Lee M, Gao Y, Bu P, Coarfa C, Miles B, et al. Neuropeptide y nerve paracrine regulation of prostate cancer oncogenesis and therapy resistance. *Prostate* (2021) 81(1):58–71. doi: 10.1002/pros.24081

136. Tennant DA, Duran RV, Gottlieb E. Targeting metabolic transformation for cancer therapy. *Nat Rev Cancer* (2010) 10(4):267–77. doi: 10.1038/nrc2817

137. Anastas JN, Shi Y. Histone serotonylation: Can the brain have "Happy" Chromatin?[J]. *Mol Cell* (2019) 74(3):418–20. doi: 10.1016/j.molcel.2019.04.017

138. Leaute-Labreze C, Dumas de la Roque E, Hubiche T, Boralevi F, Thambo JB, Taïeb A, et al. Propranolol for severe hemangiomas of infancy. *New Engl J Med* (2008) 358(24):2649–51. doi: 10.1056/NEJMc0708819

139. Polites SF, Watanabe M, Crafton T, Jenkins TM, Alvarez-Allende CR, Hammill AM, et al. Surgical resection of infantile hemangiomas following medical treatment with propranolol versus corticosteroids. *J Pediatr Surg* (2019) 54(4):740–3. doi: 10.1016/j.jpedsurg.2018.08.001

140. Fitzgerald PJ. Beta blockers, norepinephrine, and cancer: an epidemiological viewpoint. *Clin Epidemiol* (2012) 4:151–6. doi: 10.2147/CLEP.S33695

141. Akbar S, Alsharidah MS. Are beta blockers new potential anticancer agents? *Asian Pac J Cancer Prev* (2014) 15(22):9567–74. doi: 10.7314/APJCP.2014.15.22.9567

142. Watkins JL, Thaker PH, Nick AM, Ramondetta LM, Kumar S, Urbauer DL, et al. Clinical impact of selective and nonselective beta-blockers on survival in patients with ovarian cancer. *Cancer* (2015) 121(19):3444–51. doi: 10.1002/cncr.29392

143. De Giorgi V, Grazzini M, Benemei S, et al. Propranolol for off-label treatment of patients with melanoma: Results from a cohort study. *JAMA Oncol* (2018) 4(2): e172908. doi: 10.1001/jamaoncol.2017.2908

144. Stiles JM, Amaya C, Rains S, Diaz D, Pham R, Battiste J, et al. Targeting of beta adrenergic receptors results in therapeutic efficacy against models of hemangioendothelioma and angiosarcoma. *PloS One* (2013) 8(3):e60021. doi: 10.1371/journal.pone.0060021

145. Banavali S, Pasquier E, Andre N. Targeted therapy with propranolol and metronomic chemotherapy combination: sustained complete response of a relapsing metastatic angiosarcoma. *Ecancermedicalscience* (2015) 9:499. doi: 10.3332/ecancer.2015.499

146. Krizanova O, Babula P, Pacak K. Stress, catecholaminergic system and cancer. *Stress* (2016) 19(4):419–28. doi: 10.1080/10253890.2016.1203415

147. Barbieri A, Bimonte S, Palma G, Luciano A, Rea D, Giudice A, et al. The stress hormone norepinephrine increases migration of prostate cancer cells *in vitro* and *in vivo*. *Int J Oncol* (2015) 47(2):527–34. doi: 10.3892/ijo.2015.3038

148. Chan HL, Chiu WC, Chen VC, Huang KY, Wang TN, Lee Y, et al. SSRIs associated with decreased risk of hepatocellular carcinoma: A population-based case-control study. *Psychooncology* (2018) 27(1):187–92. doi: 10.1002/pon.4493

149. Chuffa LGA, Reiter RJ, Lupi LA. Melatonin as a promising agent to treat ovarian cancer: molecular mechanisms. *Carcinogenesis* (2017) 38(10):945–52. doi: 10.1093/carcin/bgx054

150. Galvan DC, Ayyappan AP, Bryan BA. Regression of primary cardiac angiosarcoma and metastatic nodules following propranolol as a single agent treatment. *Oncoscience* (2018) 5(9-10):264–8. doi: 10.18632/oncoscience.472

151. Nguyen LV, Ta QV, Dang TB, Nguyen PH, Nguyen T, Pham TVH, et al. Carvedilol improves glucose tolerance and insulin sensitivity in treatment of adrenergic overdrive in high fat diet-induced obesity in mice. *PloS One* (2019) 14(11):e0224674. doi: 10.1371/journal.pone.0224674

152. Kang F, Ma W, Ma X, Shao Y, Yang W, Chen X, et al. Propranolol inhibits glucose metabolism and 18F-FDG uptake of breast cancer through posttranscriptional downregulation of hexokinase-2. *J Nucl Med* (2014) 55(3):439–45. doi: 10.2967/jnumed.113.121327

153. Zanquetta MM, Nascimento ME, Mori RC, D'Agord Schaan B, Young ME, Machado UF, et al. Participation of beta-adrenergic activity in modulation of GLUT4 expression during fasting and refeeding in rats. *Metabolism* (2006) 55(11):1538–45. doi: 10.1016/j.metabol.2006.06.026

frontiers | Frontiers in Endocrinology

TYPE Original Research
PUBLISHED 05 April 2023
DOI 10.3389/fendo.2023.1138457

OPEN ACCESS

EDITED BY
Ruiqin Han,
Chinese Academy of Medical Sciences, China

REVIEWED BY
Jiahao Ma,
Xinxiang University, China
Yushun Gao,
Chinese Academy of Medical Sciences and Peking Union Medical College, China

*CORRESPONDENCE
Xia Gao
gaoxiaxinwai@163.com

SPECIALTY SECTION
This article was submitted to Cancer Endocrinology, a section of the journal Frontiers in Endocrinology

RECEIVED 05 January 2023
ACCEPTED 10 March 2023
PUBLISHED 05 April 2023

CITATION
Wei J, Wu X, Wang S, Liu S and Gao X (2023) Spatial heterogeneity and Immune infiltration of cellular lysosomal pathways reveals a new blueprint for tumor heterogeneity in esophageal cancer. *Front. Endocrinol.* 14:1138457. doi: 10.3389/fendo.2023.1138457

Spatial heterogeneity and Immune infiltration of cellular lysosomal pathways reveals a new blueprint for tumor heterogeneity in esophageal cancer

Jinxing Wei[1], XiaoMing Wu[1], Shuohao Wang[2], Siqing Liu[3] and Xia Gao[1]*

[1]Henan Provincial Chest Hospital, Zhengzhou University, Zhengzhou, China, [2]Department of Broad Discipline of Computing, The Hong Kong Polytechnic University, Hung Hom, Kowloon, Hong Kong SAR, China, [3]The Second Clinical Medical College, Tianjin Medical University, Heping, Tianjin, China

Background: Esophageal squamous cell carcinoma (ESCC) is a common Malignant tumor of digestive tract which have a potential association with lysosomal pathway. The purpose of this study was to explore the correlation between lysosome pathway and immune infiltration of ESCC.

Methods: The cell type annotation of ESCC patients and the distribution of their gene markers were analyzed by single cell data. They were also grouped according to the expression of lysosomal pathways. Gene set variation analysis (GSVA) enriched pathway scoring, Cellchat cell communication was performed to demonstrate the tumour-associated pathway scores and interactions of different cell populations. Relevant differential genes were screened, prognostic risk markers were constructed and direct associations of lysosomal pathway-related gene risk scores with immune infiltration and tumour treatment drug sensitivity were assessed by algorithms. In cellular experiments, qPCR and flow cytometry were used to assess the role of the lysosomal pathway gene-MT1X on tumour cell development.

Results: ESCC single cell data were annotated into 7 Cluster clusters by t-sne downscaling analysis. Cellchat analysis revealed that the "MIF" cellular communication network is the main communication mode of the lysosomal pathway in ESCC cells. The lysosomal pathway genetic risk model was found to be significantly different from ESCC prognosis in both the training and validation groups. The lysosome pathway gene risk model was associated with treatment resistance in ESCC patients using oncopredict R package. The correlation between the expression of lysosomal-DEG and tumour immune infiltration and immune cell types by the MCPcounter method. Cellular assays showed that the lysosomal pathway gene MT1X was less expressed in oesophageal cancer cells than in normal oesophageal epithelial cells. Knockdown of MT1X significantly promoted the growth rate of oesophageal cancer cells.

Conclusion: Based on the single cell sequencing technology and transcriptomic analysis, we confirmed that there is a close association between the lysosomal pathway and the immune infiltration and treatment sensitivity of ESCC, which may be a potential target for a new direction of ESCC therapy.

KEYWORDS

lysosomes, esophageal squamous cell carcinoma, cellular autophagy, single-gene sequencing, immune infiltration

Introduction

Esophageal cancer is one of the more aggressive malignancies (1). Epidemiological studies (2, 3) have shown that esophageal squamous cell carcinoma (ESCC) accounts for about 90% of esophageal cancers and esophageal adeno-carcinoma (EAC) accounts for only 10%. ESCC is therefore the main type of oesophageal cancer and has a high morbidity and mortality rate among patients with oesophageal cancer, with a 5-year survival rate of less than 20% (4). The poor prognosis is associated with difficulties in early diagnosis, frequent metastases and reduced therapeutic sensitivity (5). Therefore, there is an urgent need to develop new diagnostic, therapeutic and prognostic assessment strategies to improve the overall survival of EC patients. At the same time, further in-depth studies on the altered immune infiltration microenvironment and molecular pathway amount in esophageal cancer, combined with information on tumour heterogeneity, are needed to dissect the intrinsic features of ESCC from a molecular perspective (6–8). It is an important factor to promote the development of new clinical ESCC therapies and innovative esophageal cancer treatment strategies.

Autophagy is a process by which self-damaged organelles and proteins are separated in autophagic vacuoles (AVs) and transported to lysosomes for catabolism (9). The nucleation of AVs is mediated by the mammalian target of rapamycin complex 1 (mTORC1) and adenosine monophosphate activated protein kinase (AMPK); the extension and maturation of AVs is regulated by autophagy related gene (ATG) and phosphoinositide 3-kinase (PI3Ks) (10). Recent studies have shown that autophagy regulates tumour cell growth both as a promoter and an inhibitor, and that targeting autophagy may influence the efficacy of anti-tumour therapy (11, 12). However, the important functions of autophagy and lysosomal pathways in the development of ESCC have not yet been reported and systematically summarized (13). As esophageal cancer is a tumour type with high tumour antigenicity and cross-over effects of immunotherapy, we suggest that the lysosomal pathway and cellular autophagy have important potential in the exploration of new therapies and assessment of immune infiltration in ESCC.

Herein, we investigated the specific roles of lysosomal-related pathways and cellular autophagy in the development of oesophageal carcinogenesis and invasive metastasis in tumour samples from ESCC patients, and further determined the spatial specificity of the distribution of related genes and cellular pathways in ESCC cells by means of single-cell sequencing and spatial transcriptomic analysis. The results showed that subpopulations of tumour cells with different lysosomal pathway-associated gene profiles appeared heterogeneously distributed between and within tumour foci. This suggests that aberrant distribution of the lysosomal pathway may determine poor prognosis and immune tolerance in ESCC patients. In addition, we assessed the specific relationship between the lysosomal pathway and related genes and immune infiltration in ESCC, and constructed subgroups to assess their impact on drug sensitivity. These findings provide new insights into the spatial characteristics, complex ecosystem and biological behaviour of ESCC clones, and provide new insights into individualized treatment of ESCC.

Materials and methods

Methods

Data acquisition

The GEO public gene expression data and full clinical annotation were searched, and this study included bulk RNA-seq from patients in the GSE53624 cohort (including 117 oesophageal squamous carcinomas), GSE53622 cohort (including 60 oesophageal squamous carcinomas), and single-cell scRNA-seq data from five patients with oesophageal squamous carcinomas in the GSE188900 cohort for further analysis. The RNA-Seq data were corrected for batch effects using the R package "sva" (version 3.44.0). Each included patient contained complete matching clinical data such as age, gender, tumour stage, TNM stage, survival status, etc. The inclusion and exclusion criteria for this study were as follows. Inclusion criteria: (1) follow-up time of at least 30 d; (2) primary oesophageal tumour; (3) inclusion of data related to mRNA, lncRNA and miRNA gene expression levels; (4) complete personal basic information, pathological information and follow-up information of the patient. Exclusion criteria: (1) secondary oesophageal tumours; (2) concurrent primary tumours from other sites.

Lysosome-related pathway gene acquisition and single-cell data pre-processing

Lysosomal-related pathways were included in this study from the MSigDB database: including CCDC115, CLN3, DPP7, GBA,

LAMP2, LAPTM4B, LDLR, LRP1, LRP2, MARCHF2, MFSD8, MGAT3, TMEM106B, TMEM199, TPP1, VPS13A, and VPS35, a total of 17 genes. The expression of lysosomal pathway-related genes was collected and analysed in the GSE53624 cohort and the GSE188900 cohort, respectively. Single-cell analysis of the scRNA-seq data from GSE188900 was performed on five oesophageal squamous carcinoma samples. t-distributed stochastic neighbor embedding (t-SNE) is a machine learning algorithm for dimensionality reduction, which is very suitable for visualizing high-dimensional data down to two-dimension or three-dimension. The AUCell R package was used to determine the lysosomal pathway activity of each cell line in seven cell populations, which were divided into two groups, Lysosome-high and Lysosome-low, according to the median AUC score. Cell population grouping was performed by post-processing of single cell sequencing data acquisition and downscaling analysis. This included Fibroblasts, Myeloid and Endothelial cell groups as well as the remaining cell types. GSVA enrichment pathway scores were collected and calculated for both Lysosome-high and Lysosome-low groups using 50 Hallmark datasets.

Cellular communication and tumour-associated pathway analysis of single-cell sequencing data from ESCC samples

After pre-processing and downscaling analysis of single cell scRNA-seq data from five patients with esophageal squamous carcinoma from GSE188900, CellChat scores were calculated for the seven cell populations of the downscaled subgroups, demonstrating the cellular communication of each cell population, as well as the relationship between the Lysosome-high group dominated by Fibroblasts, Myeloid and CellChat constructed a database of cellular interactions containing 2021 ligand-receptor pairs. CellChat can be used to quantify intercellular communication networks from single cell transcriptomic data, to resolve the major input and output signals of each cell type, and to suggest how each cell type and multiple signalling pathways operate in concert. The Macrophage migration inhibitory factor (MIF) signalling pathway is the secretory signalling pathway with the highest probability of communication in ESCC cells, and we demonstrate the cellular communication network of the “MIF” pathway. We also calculated PROGENy scores to show the scores of tumour-associated pathways in different cell populations.

Gene enrichment analysis for differential genes in lysosome-associated pathways

The R package “LIMMA” (version 3.48.3) was applied to compare the Lysosome-high and Lysosome-low groups. LMFIT and EBayes functions were used to ensure accuracy. Differentially expressed genes (DEGs) were screened with adjusted P values < 0.05 and absolute values of logFC > 0.585. GO functional enrichment analysis and KEGG metabolic pathway enrichment analysis were performed on DEGs and core genes using the R packages clusterProfiler, org.Hs.eg.db, DOSE, enrichplot, colourspace, etc. GO enrichment analysis can annotate genes with significant differences at three levels: cellular component, molecular function and biological process. The cellular component describes the location of the differential gene, such as the cytoplasm, nucleus or mitochondria. Molecular function describes the function of the differential gene at the molecular biological level. Biological processes mainly describe the biological processes in which the differential genes participate, such as regulation of cell proliferation, cell development and cell migration. The present study can summarise the large number of differential genes at the cellular component, molecular function and biological process levels, reflecting the macroscopic association of ESCC with the lysosomal pathway.

Acquisition of survival-related genes from lysosomal pathways and construction of prognostic models

The differentially expressed genes (DEGs) obtained in the previous step were subjected to univariate Cox regression analysis based on the tinyarray package, with p-value < 0.05 as the screening criterion, and a total of 117 genes were selected. The GSE53624 cohort was used as a training cohort to select genes with prognostic significance from the 117 genes and construct a prognostic model based on Randomforest random forest. After calculating the median for the risk score, this median was distinguished between the High-risk and Low-risk groups by using Kaplan-lysosome pathway-related genes to intervene in the possible mechanisms of ESCC survival. For having significant prognostic differences. And independent external validation was performed by applying the cohort GSE53622 of 60 patients with esophageal squamous carcinoma.

Scoring of immune infiltration levels and evaluation of treatment sensitivity for markers of lysosomal-related pathways

To further clarify the relevance of lysosomal pathway-related genes to immune infiltration and ESCC drug resistance. We assessed the level of immune infiltration by 3 algorithms, Cibersort, ssGSEA and MCP-Counter. Based on the expression matrix, Cibersort used a deconvolution algorithm to assess the composition and abundance of immune cells in mixed cells. Based on the expression matrix and the immune cell Marker gene set, ssGSEA calculates enrichment scores for single samples and gene set pairs to determine the level of immune infiltration. ssGSEA uses transcriptomic data to quantify the abundance of immune cells and stromal cells. The TIDE algorithm predicts tumour response to immunotherapy, correlating expression matrices and T cell dysfunction in tumours with high Cytotoxic T lymphocyte (CTL) expression, predicting high correlation in patients with no response to immunotherapy. In CTL low expression tumours, the expression matrix and T-cell rejection characteristics of tumour patients were correlated to predict highly relevant patients as non-responders to

immunotherapy. In addition, immune scores and tumour purity were calculated for each sample by the ESTIMATE algorithm.

In addition, we tested the therapeutic sensitivity of lysosomal-related pathway markers to a variety of chemotherapeutic agents to further explore the clinical reality of the association between the lysosomal pathway and ESCC drug resistance. The R package "pRRophetic" was used to predict drug sensitivity based on the Cancer Genome Project (CGP) database. Similarly, drug sensitivity scores were calculated by the R package "oncoPredict" based on the Genomics of Drug Sensitivity in Cancer (GDSC) database.

Cell culture and flow cytometry validation

Human oesophageal cancer cells Eca-109 and normal oesophageal epithelial cells HET-1A were purchased from Shanghai Cell Bank, Chinese Academy of Sciences; RPMI-1640 was purchased from Gibco; fetal bovine serum was purchased from Thermo Fisher. The frozen Eca-109 cells and HET-1A cells were recovered and inoculated into RPMI-1640 medium containing 10% fetal bovine serum and incubated at 37°C in a 5% CO2 incubator. Differences in the expression of lysosome-related genes between ESCC cells and normal cells were measured and analysed. Independent control groups were set up to construct cell lines with knockdown MT1X gene and two replicate groups were set up. The cells were collected, centrifuged at 400 × g for 5 min, the supernatant was discarded, washed twice with pre-chilled PBS, added with pre-chilled 75% ethanol and fixed in a refrigerator at -20°C for more than 24 h. The cells were centrifuged at 700 × g for 5 min, and the supernatant was discarded. The cells were incubated for 10 min at 4°C, protected from light. The cell cycle was measured on a flow cytometer. The cells were transfected 1 day prior to transfection at a final concentration of 100 nmol/L. After 8 h of transfection, the cells were replaced with complete culture medium. After 48 h of transfection, total RNA was extracted and cDNA was synthesized by MMLV reverse transcriptase, and the interference efficiency was measured by real-time quantitative PCR using β-actin as internal reference. The cycling conditions for MT1X and β-actin were as follows: 95°C for 5 min, 95°C for 10 s, 61°C for 15 s and 85°C for 5 s. A total of 30 cycles were performed. The MT1X gene value was divided by the β-actin gene value to calculate the expression of the sample.

Results

Initial visualization and distribution analysis of single-cell sequencing of ESCC cells

By collecting single-cell scRNA-seq data from the GSE188900 cohort of five patients with esophageal squamous carcinoma, we mapped a comprehensive multi-locus single-cell transcriptome profile of ESCC. After expression normalization, cells were subsequently classified into coherent transcriptional clusters (Clusters) using a graph-based clustering approach. The cells were divided into Clusters by t-sne descending analysis. We annotated the cells in clusters and grouped the Clusters into seven main categories, namely: Tcell.B cell, Epithelial cell, Fibroblasts, Mast cell, Endothelial cell and Myeloid (Figure 1A), and annotated the cells according to their sample origin. The distribution of cells shows that the different types of immune cells have distinctly different subspatial locations in the ESCC cells. The Fibroblasts are mainly located on the upper side of the ESCC, with Myeloid and T-cells in close proximity; the B-cells and Endothelial cells are located closer together, mainly on the left side of the axis; the Mast cells and Endothelial cells are mainly located in the The other main distribution area of Mast cells and Endothelial cells is located in the lower right corner of the axis. We can further see that Endothelial cells, T cells and B cells are the main cell types annotated in the ESCC single cell sequencing. Immediately afterwards, we annotated the cells according to their sample origin. As seen in Figure 1B, the spatial distribution of the samples from the five ESCC patients is also characteristic: Patient 1, Patient 2 and Patient 5 samples yielded more cell annotations, occupying 70-80% of the entire space. The annotation information obtained for Patient 2's sample was mainly located in the upper half of the space, while Patient 4's annotation information was more sporadic and less obtained. Having obtained the spatial distribution characteristics of ESCC immune cell types, we wanted to further understand the association of immune cell types with lysosomal pathway-related genes and the positions occupied in the grouping (Figure 1C). In Myeloid cells, LYZ and C1QB genes were highly expressed; in Endothelial cells, RAMP2 and VWF were highly expressed; in Mast cells, TPSAB1 and CPA3 were associated; and in B cells, CD79A was consistently expressed. The expression of T cells and Epithelial cells was less consistent with CD79A. In Figure 1D, we further visualise the cell type representation of several patients by means of cascading bar charts. Patient 1 and patient 2 had a relatively similar distribution of cells, with Myeloid cells and T cells predominating. In contrast, for the overall five patients, all basically showed a higher annotation of Myeloid cells, T cells, Fibroblasts and a lower content of other cell types. We mapped t-SNE based on specific expressed genes in different types of clusters and found typical genetic markers used to identify cell types, the results of which are shown in Figure 1E. In Endothelial cells, RAMP2 and VWF possessed high expression; LUM was distributed in Fibroblasts cells; S1002 was distributed in Epithelial cells, while C1QB and CAP3 were located in Myeloid and Mast cells, respectively.

Cell grouping and the exploration of signaling pathways

Immediately afterwards, to assess the correlation between specific immune cell types and the lysosomal pathway in ESCC patients, we applied the AUCell R package to determine the lysosomal pathway activity of each cell line (Figure 2A). The groups were divided into Lysosome-high and Lysosome-low according to the median AUC score value. It can be seen that Fibroblasts, Myeloid and Endothelial cells are predominantly in the Lysosome-high group and the remaining cells are predominantly in

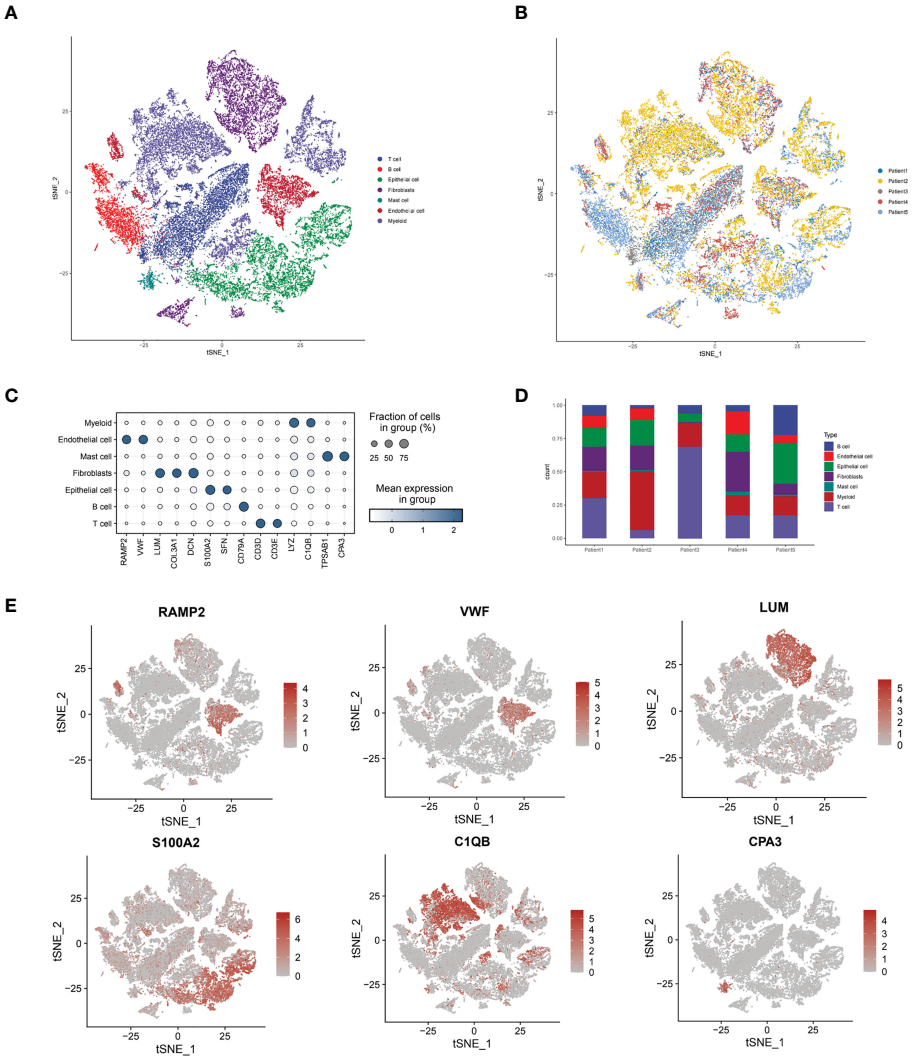

FIGURE 1
Sample immune cell type analysis and lysosomal pathway gene distribution by single cell sequencing of ESCC cells. **(A)** t-SNE diagram showing the distribution of 7 major cell types in ESCC cells: Tcell.B cell,Epithelial cell, Fibroblasts, Mast cell, Endothelial cell and Myeloid; **(B)** t-SNE diagram showing the source of the cell samples, each colour indicates one sample, a total of 5 patients are included; **(C)** bubble diagram of the major genes and groups expressed in the 7 cell types obtained from single cell sequencing, the results show that in Myeloid cells, LYZ and C1QB genes are highly expressed; in Endothelial cells, RAMP2 and VWF have high expression. LYZ and C1QB genes are highly expressed; in Endothelial cells, RAMP2 and VWF possess high expression; **(D)** Cascade bar graphs further visualize the specific type number share of the 7 immune cell types in ESCC patients, with Myeloid cells, T cells, Fibroblasts more annotated and other cell types less abundant; **(E)** t SNE plots show the expression of typical marker genes for the different cell types.

the Lysosome-low group. This suggests that several ESCC metabolic pathways and cellular synthesis processes, namely fibrosis, endothelial formation, and myeloid neoblast processes, may be closely related to the lysosomal pathway of ESCC, pending our further study in the future. In Figure 2B, GSVA enrichment pathway scores were calculated for both Lysosome-high and Lysosome-low groups using 50 Hallmark data sets. For GSVA pathway enrichment analysis, the average gene expression for each cell type was used as input data using the GSVA package. Results show. In Fibroblasts cells, ANGIOGENESIS, EPITHELIAL_MESENCHYMAL_TRANSITION, MYOGENESIS and Notch were predominantly expressed; in Endothelial cells, WNT_BETA_CATENIN and TGF_beta expression; Mast cells were associated with IL6_JAK_STAT3_SIGNALING and TNFα; Epithelial cells were mainly associated with E2F_targets and MYC_TARGETS_V1 and MYC_TARGETS_V2; while T cells and B cells lacked significant pathway correlation. Further, we calculated PROGENy scores to demonstrate the scores of tumour-associated pathways for different cell populations (Figure 2C). As can be seen, Endothelial cells are associated with a variety of tumour pathways, including Androgen, EGFR, Estrogen, Hypoxia, JAK-STAT, MAPK, NFKB and TGFb. Fibroblasts are highly correlated with Estrogen pathway expression. cells were significantly associated with MAPK and EGF pathways. For other cell types, there was less agreement with tumour-related pathways. In Figure 2D, the cellular communication of each cell population is shown by calculating the CellChat score, an open source R package (http://github.com/sqjin/CellChat) that can use scRNA-seq data to infer,

10.3389/fendo.2023.1138457

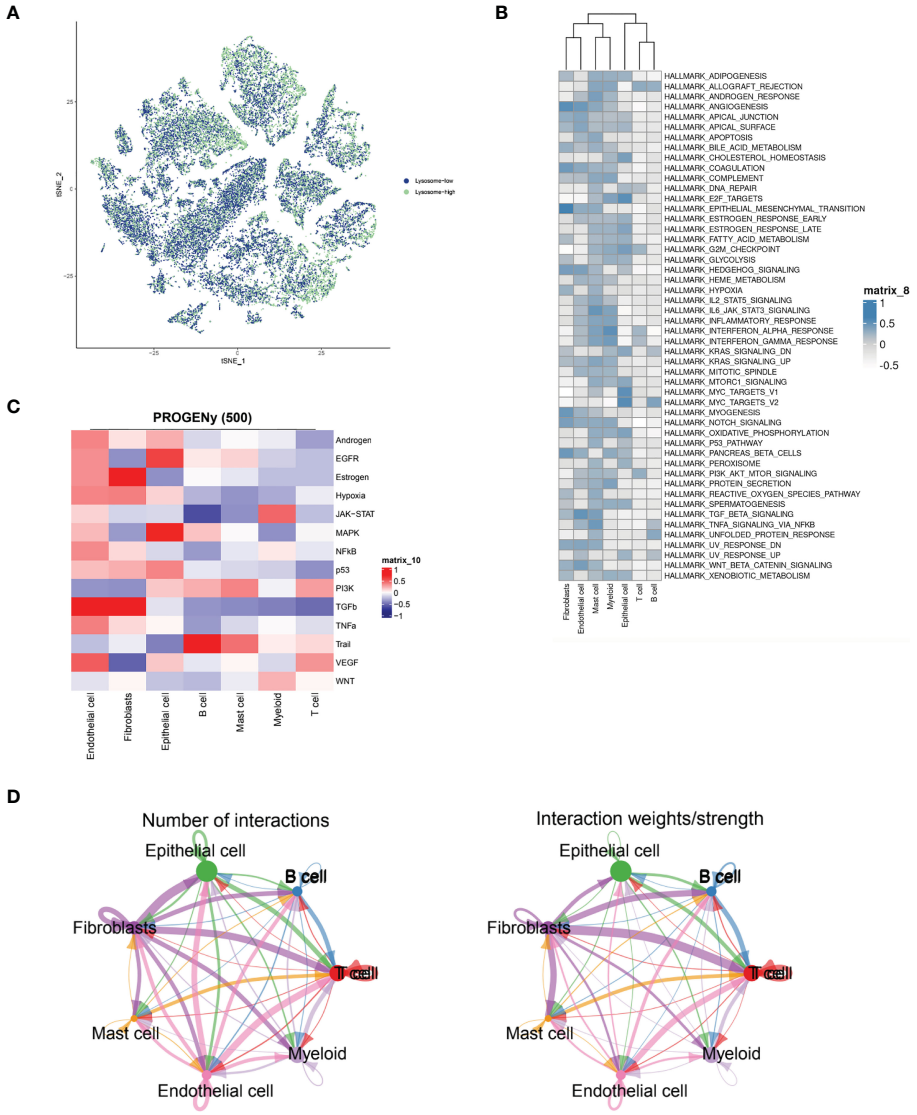

FIGURE 2
ESCC immune cell types interacting with lysosomal pathway and GSVA enrichment analysis. **(A)** t-SNE plots showing the expression of lysosomal pathway-related genes in seven major cell types in ESCC cells, divided into two groups, lysosome-high and lysosome-low, based on colour; **(B)** GSVA enrichment pathway scores were calculated for the Lysosome-high and Lysosome-low groups using 50 Hallmark data sets; **(C)** Calculation of PROGENy scores will obtain heat maps showing the scores of tumour-associated pathways for different cell populations; **(D)** Circle interaction plots showing the number and weight analysis of ineraction of Fibroblasts cells with the remaining several immune cells.

visualise and analyse intercellular communication. For cell types with high lysosomes, Fibroblasts had more interactions with Epithelial cells and T cells; while communication between Fibroblasts and Epithelial cells, T cells, B cells and Mast cells was highly weighted in the overall ESCC cell tumour expression composition.

The communication networks and interactions analysis between cells based on ESCC single-cell sequencing data

In Figure 3A, we delve further into the interactions of immune cell types obtained from single cell sequencing data from ESCC patients. As seen in the images, T cells interacted more uniformly with all types of cells, while B cells sent more signals to T cells. Epithelial cells interacted more with T cells and B cells. Fibroblasts, as the main cell type that sends signals, send more signals to T cells, B cells and EPITHELIAL cells, while Mast cells, Endothelial cells and Myeloid cells have more interactions with T cells. This suggests that T cells may function as the primary recipient of intercellular communication signals in ESCC patients. Immediately afterwards, we further quantitatively visualized the major intercellular links as well as mediating cytokines of several lysosomal-high cells by means of bubble plots. In Figure 3B, we found that Fibroblasts interaction with Myeloid is mainly mediated by APP-CD74, interaction with Endothelial *via* CD99 and CD74, transmission of MastCell

10.3389/fendo.2023.1138457

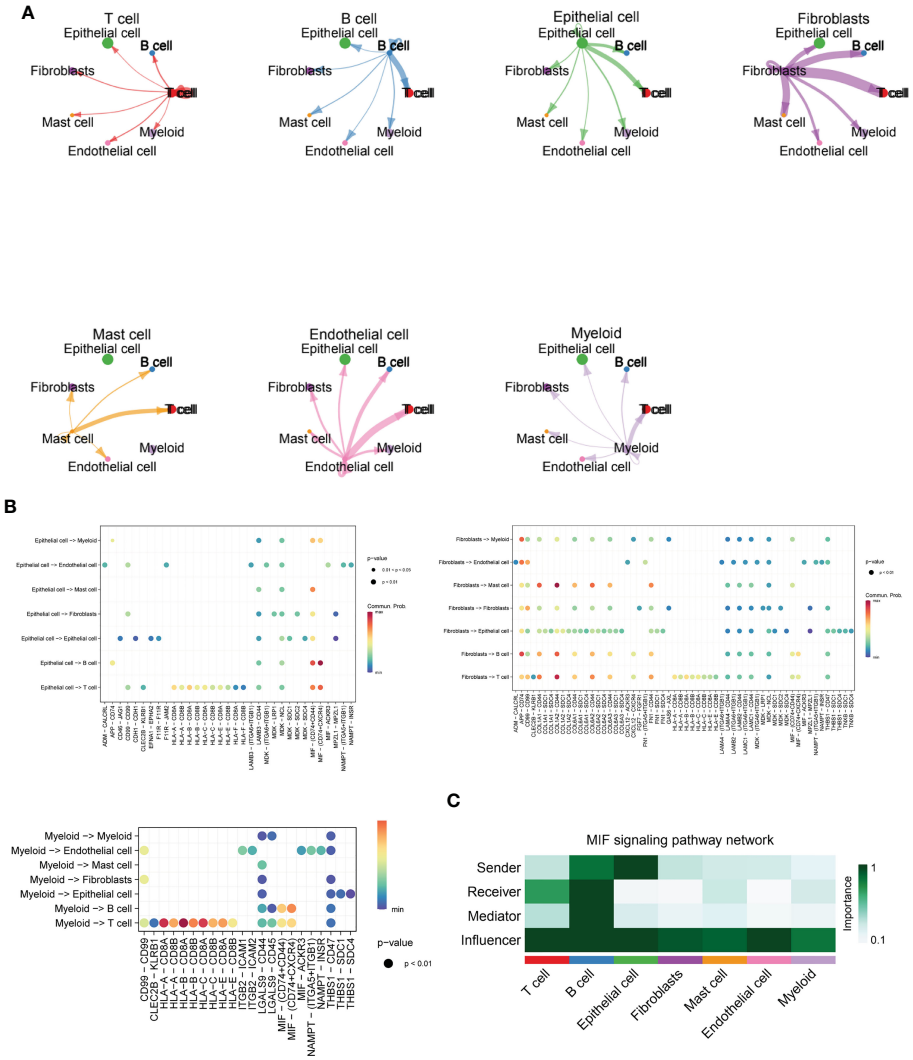

FIGURE 3
Cellchat and MIF signalling communication between immune cell types in ESCC. **(A)** Cross-correlation map of immune cell types obtained from single-cell sequencing data of ESCC patients, including T cells, B cells, Fibroblasts, Mast cells, Endothelial cells, and Myeloid cells; **(B)** Bubble plots further quantitatively visualize the major intercellular links of several lysosomal-high cells as well as mediating cytokines, including Fibroblasts, Myeloid, and Epithelial cells.**(C)**. Heat map demonstrating the prominence of each cell subpopulation as a major sender, receiver, mediator and influencer at the centre of the MIF secretory signalling communication network. B cells and EPITHELIAL cells play the role of major MIF signal senders. B cells are also important Receivers and Mediators, while throughout the MIF signalling pathway, T cells, B cells as well as Epithelial cells played a major Influencer role in the overall MIF signalling pathway.

signals *via* COL1A1 - CD44, COL6A2 - CD44, and FN1 - CD44, and their communication with B and T cells For Epithelial cells, there is more interaction and signalling to T and B cells, mediated by the MIF - (CD74+CD44) and MIF - (CD74+CXCR4) pathways. Myeloid cells, on the other hand, interact less efficiently with a variety of cell types and also mediate their immune effects by signalling to T and B cells. -A - CD8B, HLA-B - CD8A, HLA-B - CD8B, HLA-C - CD8A, HLA-C - CD8B, and HLA-E - CD8A. This shows that multiple cellular pathways can mediate the interaction of Myeloid with T cells. Subsequently, in Figure 3C, we show by heat map the significant extent to which each cell subpopulation plays a major role as a central sender, receiver, mediator and influencer of the MIF secretory signalling communication network. b cells and EPITHELIAL cells play the role of major MIF signalling senders. b cells are also important Receiver and Mediator, while throughout the MIF In the signalling pathway, T cells, B cells and Epithelial cells play the role of major Influencer. this parallels our knowledge of the tumour immune system, where T cells and B cells play the role of major signal receivers and enforcers.

Lysosomal pathway-related transcriptomic risk model construction and functional linkage analysis for ESCC

The R package "LIMMA" (version 3.48.3) was applied to compare the Lysosome-high and Lysosome-low groups. LMFIT and EBayes

functions were used to ensure accuracy. Differentially expressed genes (DEGs) were screened for adjusted P values < 0.05 and absolute values of logFC > 0.585. statistically significant lysosome-DEGs were thus obtained. and subjected to GO analysis and KEGG analysis. As shown in Figure 4A, the DEGs associated with lysosomal expression were mainly enriched in signaling receptor activator activity, receptor ligand activity, extracellular matrix structural constituent -peptidase regulator activity, glycosaminoglycan binding,endopeptidase regulator activity,peptidase inhibitor activity,endopeptidase inhibitor activity, heparinbinding-collagenbinding, regulation of hydrolase activity and negative regulation of proteolysis -negative regulation of peptidase activity. Further, we performed KEGG functional analysis to understand the importance of lysosomal-DEG in cell development, pathway expression and growth and development through multiple perspectives, as shown in Figure 4B. The results indicate that the lysosomal DEG-related pathway is mainly associated with ommunition and coagulation cascades that Staphylococcus aureus infection, Viral protein interaction with cytokine and cytokine receptor, the Lysosome, ECM-receptor interaction, IL-17 signaling pathway, Chemokine signaling pathway Amoebiasis, Proteoglycans in cancer, pathway, Pertussis, Malaria, and Cytokine-cytokine receptor interaction were related. After obtaining the relevant functional characteristics of lysosomal DEG, we selected four genes of prognostic significance from 117 genes according to the Randomforest random forest algorithm and constructed prognostic models, namely SCPEP1, DUSP2, C10orf10, and MT1X. decision tree simulations for the random forest analysis of lysosomal DEG are shown in Figure 4C shows. The weights occupied by the expression of different genes in the lysosomal-DEG prognostic model were further quantified in the form of dotted line plots, as seen in Figure 4D. MT1X

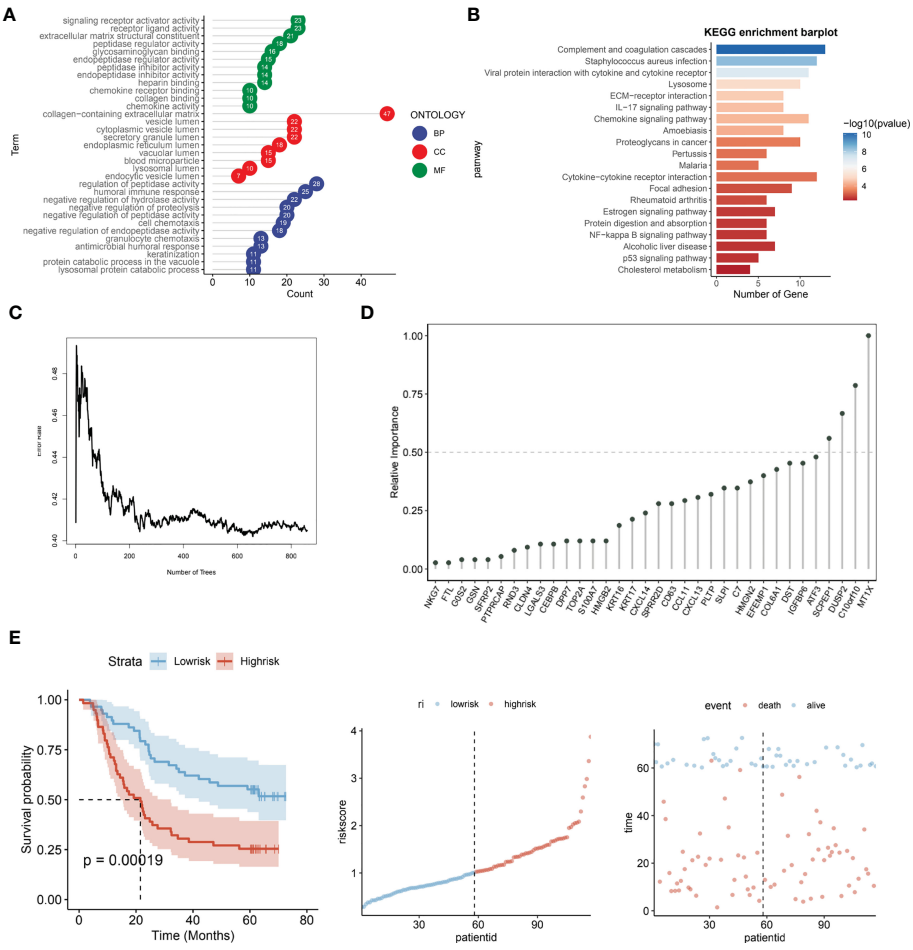

FIGURE 4
Prognostic risk modeling and functional enrichment analysis of lysosomal pathway-related transcriptomics in ESCC. **(A)** GO analysis revealed that DEG associated with lysosomal expression was mainly enriched in signaling receptor activator activity,receptor ligand activity,extracellular matrix structural constituent -peptidase regulator activity,glycosaminoglycan binding,endopeptidase regulator activity; **(B)** KEGG enrichment barplot showed that lysosomal DEG-related pathways were mainly enriched in omplement and coagulation cascades, Staphylococcus aureus infection, Viral protein interaction with cytokine and cytokine receptor enriched in; **(C)** Transcriptomic risk model construction for lysosomal-DEG by decision trees constructed from random forest; **(D)** Histogram analysis of the relative importance of lysosomal-DEG models in the final transcriptomic prognostic risk model, with MT1X possessing the highest prognostic-related importance; **(E)** Assessment of the predictive power of the constructed lysosomal pathway-related transcriptomic prognostic risk models, from left to right. Kaplan-Meire curves for the lysosome-associated prognostic risk model, distribution of risk scores, and scatter plots of prognostic survival times for patients with different risk scores.

was the main lysosomal-DEG gene that determined the difference in prognosis of ESCC patients, with a relative importance close to 1.0. while the relative importance of all three genes, SCPEP1, DUSP2, and C10orf10, was also higher than 0.50, significantly higher than the other lysosomal-DEG genes. In Figure 4E, we further analyzed the prognostic predictive power of the constructed lysosomal pathway-associated transcriptomic risk model. The results showed that the model exhibited good survival prediction performance in the GSE53624 cohort. Differentiating the High-risk and Low-risk groups by the median risk score, the two groups had significant prognostic differences. Patients in the Low-risk group in the lysosomal-DEG-related prognostic risk model had significantly better prognostic survival than those in the High-risk group ($p<0.0001$), while patients in the High-risk group had a significantly shorter prognostic survival time than those in the Low-risk group and were visualised in the scatter plot. This suggests a close association between lysosomal pathway-related genes and ESCC survival, perhaps related to the underlying functional characteristics of the lysosomal pathway and the specific mechanisms of immune tolerance to tumours.

Immuno-infiltration analysis of a lysosomal pathway-associated transcriptomic risk model for ESCC

We further evaluated the prognostic ROC curves of the lysosomal pathway-associated prognostic risk model (Figure 5A) with AUC values of 0.70, 0.72 and 0.70 for the 1-year, 3-year and 5-year cohorts, respectively, indicating that our constructed lysosomal risk model has good prognostic performance. In the GSE53622 cohort, we further evaluated and analysed the prognostic performance of the constructed risk model in an independent validation cohort of ESCC. In Figure 5B, the Kaplan-Meier curve in the validation cohort also achieved excellent prognostic prediction performance at $P<0.0001$. We also analysed the correlation of the expression of the four lysosomal-DEGs constituting the risk model by correlation heat map (Figure 5C). The results showed that SCPEP1 had a high correlation with C10orf10, suggesting that these two genes may play a similar role in the development of the lysosomal pathway. In contrast, there was a significant association between the expression of DUSP2 and MT1X. Further, we calculated the correlation and significant association between the expression of lysosomal-DEG and tumour immune infiltration and immune cell types by the MCPcounter method (Figure 5D). In Figure S1D, we showed that all types of immune cells and immune infiltrate types were highly expressed in the risk scores associated with the lysosomal pathway in ESCC patients. The expression of activated dendritic cells and activated CD4 T cells showed a high correlation with the tumour-related risk score (Figure 5E), with a negative correlation between the expression of activated dendritic cells and the risk score ($p<0.001$) and a positive correlation between the expression of activated CD4 T cells and the lysosomal pathway-related risk score ($p<0.05$), with a significant linear relationship. This suggests that the lysosomal pathway has a significant positive value for immune infiltration and development of tumour resistance in T cells as well as in dendritic cells. In Figure 5F, we further assessed the enrichment of immune cells and immune infiltrative pathways between the low-risk and high-risk groups by GSEA analysis. Among them, the expression of Neutrophill, lmmature.dendritic as well as Th1 T cells was significantly higher in the low-risk group than in the high-risk group. In contrast, the expression of NK T cells as well as Activated.dendritic.cells was significantly higher in the high-risk group than in the low-risk group. Further, our Pearson correlation in Figure 5G reveals the correlation between the expression of different immune cells, immune pathways. Activated CD4 T cells had a higher expression correlation with activated CD8 T cells, and activated CD8 also had a higher expression correlation with MDSK and Th1T cells. The rest of the immune cells were also more or less correlated with each other.

To further determine the specific direct association of lysosomal pathway-related risk genes with immune infiltration and immune cell secretion in ESCC, we calculated immune infiltration scores by three methods: ssGSEA, MCPcounter, and the xCell algorithm, which were visualized with box plots, heat maps, and scatter plots, respectively. Figure S1A shows the immune cell scores between the low-risk and high-risk groups calculated with the xCell method. The expression of CD4 Memory T cells, Macrophages, and Marcophages M1 was higher in the low-risk group than in the high-risk group; while Basophils, CLP, Epithelial, and HSC cells were less expressed in the low-risk group than in the high-risk group. In Figure S1B, we also applied box plot depictions to compare immune pathway scores between ESCC lysosome-associated low-risk and high-risk groups, with MEP, Monocytes, Neurons, smooth muscle, and Th2 cells being higher in the low-risk group than in the high-risk group; and Myocytes and Pericytes being more expressed in the high-risk group than in the low-risk group. In addition, we also compared the linear correlation between several immune cell types with significantly different expression and their respective risk scores, and the results are shown in Figure S1C. The results showed that Neutrophils, CD4 memory T cells and Macrophages M1 expression were linearly and negatively correlated with risk scores ($p<0.05$). In contrast, Epithelial cells as well as Myocytes corresponded to a linear positive correlation with risk score, suggesting a differential role of different cell types in the lysosomal pathway contributing to the development of ESCC ($p<0.05$). In addition, we analysed the interaction of genes constituting the lysosomal pathway risk model with immune infiltrating cells and pathways by correlation heat map (Figure S1D). the MT1X gene was mainly negatively correlated with Adipocyts, B-cellsdun, Class-switched memory T cells, HSC, Neurons expression ($p<0.05$), with CD8 naive T cells, MSC, NK Cells, and NKT expression. c10orf10 gene was significantly positively correlated with aDC, CD4 memory T cells, CD8 T cells, CD8 Tcm, macrophages, macrophage M1 type, and macrophage M2 type. The DUSP2 gene was significantly associated with the expression of CD4 Tem, Adipocytes, Epithelial and macrophages. For the SCPEP1 gene, there was a high correlation with macrophages and smooth muscle cells.

We also applied the MCP method to calculate the immune infiltration scores of patients in the low-risk versus high-risk groups of the lysosomal pathway and visualized them using box line plots

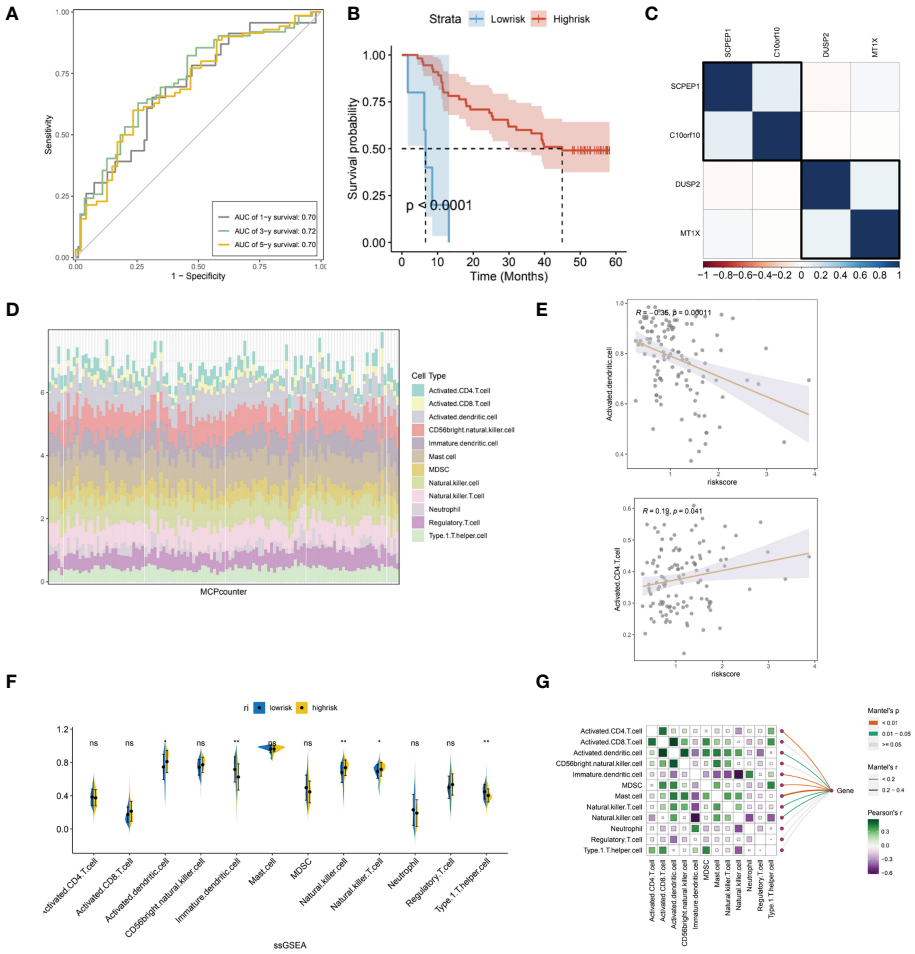

FIGURE 5
Independent validation of the lysosomal pathway-associated risk model and preliminary analysis of immune infiltration. **(A)** Prognostic prediction ROC curves for the lysosomal pathway-associated prognostic risk model ,with AUC values of 0.70, 0. 72 and 0.70 for 1-year, 3-year and 5-year, respectively; **(B)** Kaplan-Meier curves for the prognostic risk model in the GSE53622 independent validation cohort, p<0.0001. **(C)** Heat map revealing the expression correlation of the four lysosomal-DEGs that comprise the lysosomal pathway risk model, with SCPEP1 possessing a high expression correlation with C10orf10 and a significant association between DUSP2 and MT1X expression; **(D)** MCPcounter calculated histograms analyzing the potential immune cell constitutive types of risksocre; **(E)** in addition, we analysed the correlation between the expression of activated dendritic cells as well as activated CD4 T cells and risk scores; **(F)** ssGSEA analysis, revealing the enriched expression of immune cells and immune infiltration pathways between the low and high risk groups. Among them, the expression of Neutrophill, Immature.dendritic and Th1 T cells was significantly higher in the low-risk group than in the high-risk group. In contrast, the expression of NK T cells as well as Activated.dendritic.cells was significantly higher in the high-risk group than in the low-risk group; **(G)** Heat map reveals the correlation between the expression of different immune cells and immune pathways using Pearson correlation. * means <0.05,** means <0.01, ns means >0.05.

(Figure S2A). Fibroblasts expression was lower in the low-risk group than in the high-risk group, while B lineage expression was higher in the low-risk group than in the high-risk group. The expression of B lineage, T cells, Neutropilis, Monocytic Lineage, Myeloid dendritic and Endothelial cells all showed a linear correlation with the risk score. The expression of B lineage, T cells, Neutropilis, Monocytic Lineage, Myeloid dendritic and Endothelial cells were linearly and negatively correlated with the corresponding risk scores, the same as those calculated by our XCell method (Figures S2B, S2C). In Figure S2D we used Pearson's correlation to reveal the correlation between the expression of different immune cells and immune pathways in the MCPcpunter method, where T cells showed a high correlation with CD8 T cells, B lineage, Monocytic lineage and Meyloid dendritic cells, while Monocytic Lineage showed a high correlation with Monocytic Lineage was highly correlated with the expression of Endothelial cells and B lineage. Similarly, we also analysed the interaction of genes constituting a risk model for the lysosomal pathway with immune infiltrating cells and pathways by correlation heat map (Figure S2E). MT1X gene was mainly negatively correlated with B lineage and Cytotoxic lymphocytes expression (p<0.05), and with Endothelial and Monocytic lymphocytes expression. The C10orf10 gene was significantly positively correlated with aDC, CD4 memory T cells, CD8 T cells, CD8 Tcm, macrophages, macrophage M1 type, and macrophage M2 type. In contrast, the DUSP2 gene was significantly associated with the expression of CD4 Tem,

Adipocytes, Epithelial and macrophages. For the SCPEP1 gene, there was a high correlation with macrophages and smooth muscle cells.

Analysis of the role of ESCC lysosomal pathway risk models on tumour treatment sensitivity

Through the previously constructed risk model and the relationship between immune infiltration, we have explored in depth the significant association between lysosomal pathway genes and tumour immunity and tumour cellular pathways with poorer prognosis in ESCC patients. Considering the current poor immunotherapeutic effect of ESCC and the strong immunogenicity of the tumour, we further investigated whether the lysosomal pathway gene risk model is associated with treatment resistance in ESCC patients We further investigated whether the lysosomal pathway gene risk model was associated with treatment resistance in ESCC patients. A sensitivity score was calculated for drugs in the GDSC database based on the R package "oncoPredict". MT1X was associated with the therapeutic susceptibility of AGI-5198_5913, Cyclophosphamide, ML323, Rapamycin, Venetoclax. AZD8186, GSDK591, SB505124 was significantly associated with treatment efficacy. expression of DUSP2 in ESCC patients was associated with treatment efficacy of GSK2578215, I-BRD9, ML-323. For SCPEP1, treatment with Fulvetrant, MK-1775, Venetoclax_1909 was highly correlated with it (Figure 6A). In Figures 6B, C, we applied box-line plots to analyse the potential correlation between several key chemotherapeutic agents used for ESCC treatment and the

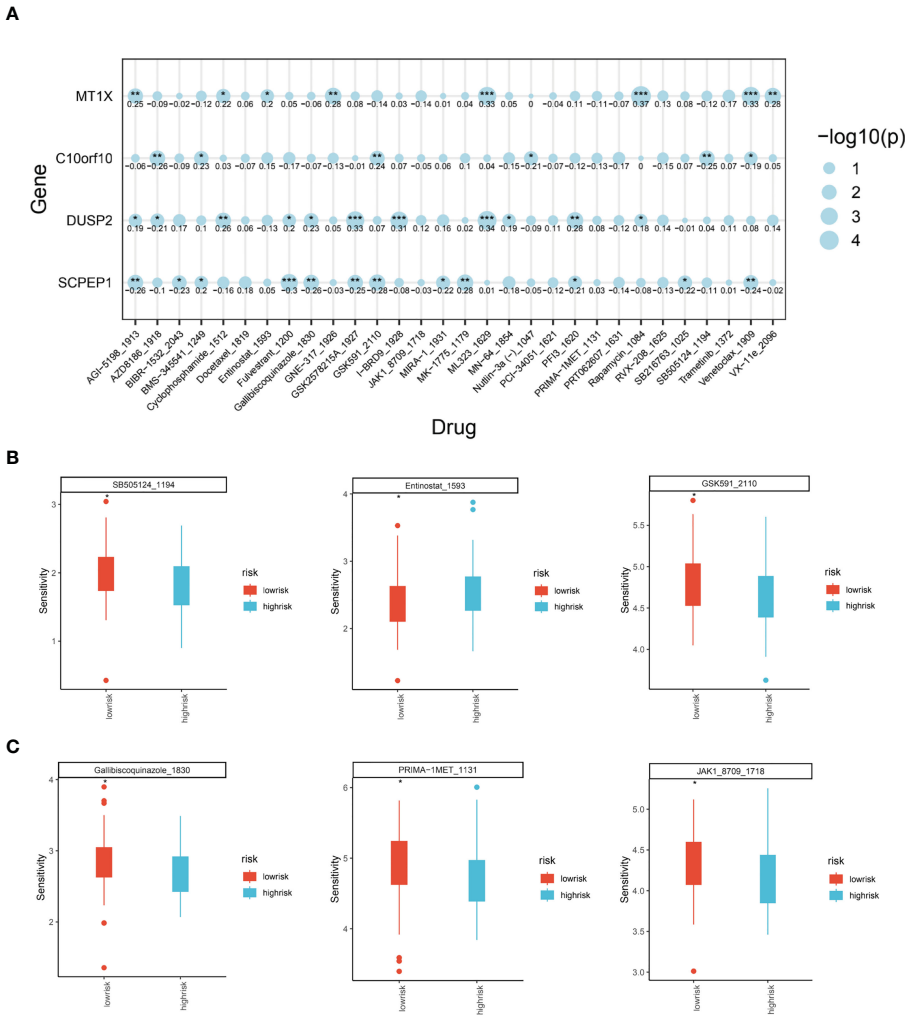

FIGURE 6
Analysis of the role of ESCC lysosomal pathway risk models on tumor treatment sensitivity. **(A)** Bubble diagram showing the association of four key genes constituting the lysosomal pathway risk model with the therapeutic sensitivity of multiple chemotherapeutic agents: MT1X was associated with AGI-5198_5913, Cyclophosphamide, ML323, Rapamycin, Venetoclax. expression of C10orf10 was significantly associated with AZD8186, GSDK591, SB505124. GSDK591, SB505124 were significantly associated. for DUSP2, it was associated with GSK2578215, I-BRD9, ML-323. For SCPEP1, treatment with Fulvetrant, MK-1775, Venetoclax_1909 had a high correlation with it. **(B)** Box plot of treatment sensitivity between low and high risk groups for lysosomal risk scores for several chemotherapeutic agents, SB505124_1194, Entinostat_1593, GSK591_2110; **(C)** Gallibiscoquinazole_1830, PRIMA-1MET_1131, JAK1_8709_ 1718 Box line plot of treatment sensitivity of these chemotherapeutic agents between low risk and high risk groups for lysosomal risk scores. * means <0.05,** means <0.01,*** means <0.001.

distribution of lysosomal pathway risk models. The results show that for several chemotherapeutic agents, SB505124_1194, GSK591_2110, Gallibiscoquinazole_1830, PRIMA-1MET_1131 and JAK1_8709_1718, the treatment sensitivity of patients in the low-risk group of the lysosomal pathway is significantly higher than that of the high-risk group of the lysosomal pathway; while for Entinostat_1593, its therapeutic sensitivity increased with higher lysosomal-risk score, which depends on further studies to confirm.

Cellular validation of MT1X, a key lysosomal pathway gene, on ESCC invasion and physiological reproduction

Following the above single-cell sequencing and transcriptomic studies and bioinformatic validation, we have initially demonstrated that a risk model consisting of four lysosomal pathway-related genes is strongly associated with immune infiltration and chemo-sensitivity in ESCC. Therefore, we wanted to further validate this organic association experimentally. Here, we selected the MT1X gene, which has the highest weight in the risk model, and performed corresponding knockdown and suppression experiments in oesophageal cancer cells and normal cells to assess its effect on the development of ESCC. First, we analysed the number and significance relationships of several constitutive genes in the lysosomal pathway risk model in different carcinomas (Figure 7A). The results showed that the SCPEP1 gene was highly expressed in BRCA, KIRC and THCA tumour types, and the DUSP2 gene was more expressed in KICH, LIHC and BRCA. In contrast, for the MT1X gene, his expression was more significant in BRCA, while for ESCC, its expression level was more limited. To explore the role played by MT1X, the most critical gene in the lysosomal pathway, in ESCC, we further analysed the expression of MT1X in different tumour types using box-line plots in Figure 7B. The results showed that MT1X gene expression was weaker in tumour cells than in paraneoplastic tissues in most tumour types, except CESC, GBM, UCEC and LUSC. Further, we analysed the expression of MT1X in tumour and normal tissues in ESCC in Figure 7C, which showed that MT1X expression was significantly higher in normal tissues than in tumour tissues. MT1X expression was determined by flow cytometry in esophageal cancer cells ECA-109 as well as in normal esophageal epithelial cells HET-1A (Figure 7D), again in agreement with the above results, i.e. the expression of MT1X was lower in esophageal cancer cells. Correspondingly, to clarify the role of key genes of the lysosomal pathway in the development of ESCC. We knocked down MT1X gene expression in ECA-109 cells, and the success of the knockdown is shown in the qPCR results in Figure 7E, where MT1X gene expression was significantly lower in both knockdown cell groups. In Figure 7F, we analysed the cell cycle distribution for tumour cells as well as for ECA-109 cells after MT1X knockdown using flow cytometry. The results show that when the MT1X gene was further knocked down in the esophageal cancer cells, the number and proportion of tumour cells in the S and G2+M phases of the cell cycle increased. This suggests that the proliferation and growth of esophageal cancer cells were significantly promoted after knocking down the MT1X gene. It is suggested that the MT1X gene in the lysosomal pathway may be associated with the proliferation and growth of tumour cells.

Discussions

As a common malignant tumour of the digestive system, oesophageal cancer still has a poor overall survival rate and a poor prognosis, although its incidence and mortality rate have been significantly reduced in recent years (14, 15). The lysosomal pathway, as an important underlying mechanism in tumour cell metabolism, invasion, metastasis and development, is inevitably associated with poor immunotherapy outcomes and poor prognosis in ESCC patients (16, 17). The autophagic lysosome system is a cellular degradation system that plays an important role in the regulation of proteins, lipids and cell homeostasis. Therefore, the autophagic lysosome system can play key functions in a variety of diseases, including cancer, immune and inflammation-related diseases, etc (18). It has been found that lysosomes regulate the growth and proliferation of tumor cells by activating the growth factor signaling pathway through tyrosine kinase receptors on the membrane. the uncontrolled proliferation of tumor cells often requires more nutrients to maintain cell metabolism. Lysosomes can degrade proteins inside and outside cells through autophagy and pinocytosis, and provide a large amount of amino acids to cells (19). Therefore, the relationship between lysosomes and cancer is inextricably linked. LAMP1 is the main protein component located on the lysosome membrane. Immunohistochemical staining of ESCC patients indicated that LAMP1 expression level was significantly different between TNM stage and tumor histological differentiation degree. This also indicates that lysosomes are closely related to the occurrence and development of ESCC (20). The study of the lysosome pathway related to the development of ESCC and immune infiltration is of great significance and has a guiding role in the development of new targeted therapy strategies for ESCC.

In this study, we identified genes related to the lysosomal pathway based on the GEO database, and systematically identified the relevant biological pathways and pharmacological sensitivities of these genes. Single-cell sequencing was used to analyse the close association between lysosomal pathway-related genes and the gene distribution of oesophageal cancer. Pathway enrichment analysis revealed that lysosomal DEGs were significantly associated with various elements of tumour progression, such as metabolism, cellular processes and biological systems. We found that the ECM-receptor interaction pathway was enriched. Extracellular matrix (ECM) is an important component of the tumor microenvironment. It has various functions, including mechanical support and regulation of the microenvironment. In the process of tumorigenesis, the interaction between cancer cells and tumor microenvironment (TME) often leads to the stiffness of ECM, thus causing further tumor deterioration (21). Thus, ECM plays an important role in tumor progression. Cytokines are the key proteins of signaling in the tumor microenvironment (TME) and have pleiotropy. It can be divided into interleukin, interferon, tumor necrosis factor, hematopoietic factor, growth factor, chemokine

10.3389/fendo.2023.1138457

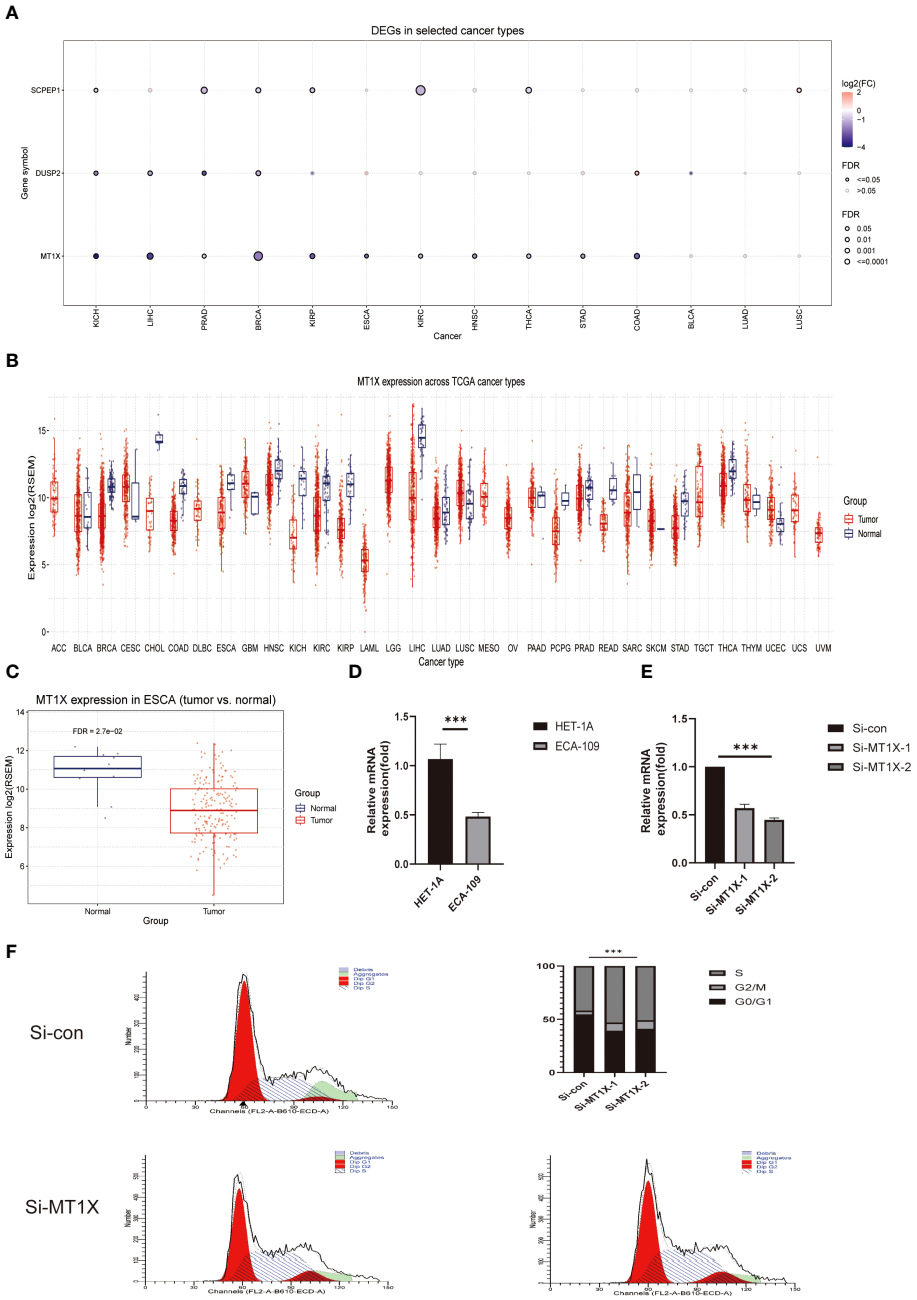

FIGURE 7
Cellular experimental validation of the role of MT1X, a key gene of the lysosomal pathway, in the growth and invasion of ESCC. **(A)** Box plot analysis reveals the number and significance of the four constitutive genes of the lysosomal pathway risk model in different tumours; **(B)** Box plot analysis of MT1X expression in different tumour types and paraneoplastic tissues, showing that MT1X gene expression was weaker in most tumour types than in paraneoplastic tissues, except for CESC, GBM, UCEC and LUSC **(C)** Box plot analysis of MT1X expression in tumour and normal tissues in ESCC, showing that MT1X expression in normal tissues was significantly higher than that in tumour tissues; **(D)** Cellular assays demonstrating the role of MT1X in the expression and growth invasion of oesophageal cancer cells: qPCR analysis of MT1X expression in ECA-109 and HET-1A cell lines; **(E)** qPCR analysis of MT1X expression in ECA-109 and HET-1A cell lines. qPCR confirmed the successful knockdown of MT1X in ECA-109 cells in two replicate sets; **(F)** Flow cytometry analysis of the cell growth cycle percentage of ECA-109 cell lines before and after MT1X knockdown. *** means <0.001.

receptor interaction and so on. Cytokine-cytokine receptor interaction plays an important role in the occurrence and development of tumor. Interferon and TGF-β can directly or indirectly inhibit tumor cell growth, TNF and various chemokines play a role by promoting angiogenesis, and IL-18 can activate NF-κB signal, induce cancer cell proliferation and invasion, and prevent cell apoptosis (22). All the mechanisms mentioned above indicate the close relationship between cytokines and tumors. In addition, IL-17 signaling pathway was also enriched. According to the study of Chen et al., IL-17 can promote the recruitment and activation of neutrophils in esophageal squamous cell carcinoma, thus playing a role in anti-tumor immunity (23). Meanwhile, IL-17 is also a kind of cytokine, which indicates that lysosome-DEGs is closely related to cytokines. The lysosomal pathway prognostic risk model is a

significant predictor of prognosis in ESCC patients. It also highly influences the immune infiltration and chemosensitivity of ESCC patients. On this basis, we further confirmed the microscopic role of the lysosomal pathway in the invasion and metastasis of esophageal cancer by knocking down the lysosomal pathway gene - MT1X in cellular assays. This suggests that the lysosomal pathway and its related genes play an important role in the development of ESCC and drug resistance, and the study of the organic interaction between esophageal cancer-lysosomal pathway-immune infiltration may become a breakthrough for further exploration of esophageal cancer.

The common treatment option for oesophageal cancer is surgical resection followed by chemotherapy and radiotherapy, but patients are more prone to develop resistance, which affects the therapeutic effect. The lysosomal pathway promotes the establishment of drug resistance in cancer cells (18). Currently, the commonly used clinical inhibitors of the lysosomal pathway are chloroquine and its derivative chloroquine, an antimalarial drug that prevents lysosomal acidification and prevents lysosomal pathway vesicles from being cleared (19). Clinical studies (20, 21) have demonstrated the therapeutic potential of chloroquine and its derivative hydroxychloroquine, alone or in combination with other drugs, to improve the efficacy of radiotherapy in patients with melanoma, colorectal cancer, myeloma and renal cell carcinoma by inhibiting the lysosomal pathway. However, no studies have been conducted using these lysosomal pathway inhibitors in patients with ESCC. The lysosomal pathway plays an important and complex regulatory role in the development and progression of oesophageal cancer and can influence its therapeutic outcome. Although the lysosomal pathway has been shown to play a protective role in the conversion of BE to EAC, further *in vivo* models need to be developed to investigate the regulatory mechanisms of the lysosomal pathway. When considering the use of lysosomal pathway inhibitors in the treatment of oesophageal cancer, it is critical to understand whether the cell body and the underlying lysosomal pathway levels are being disrupted. It is important to accurately determine whether a patient's lysosomal pathway is activated or deactivated, and to combine this with factors such as whether they are receiving radiotherapy. In addition, due to the complexity of lysosomal pathway regulation in tumours, how to judge the level of basal autophagy and assess the role played by autophagy still requires further development of new assay systems to achieve specific regulation of lysosomal pathway levels and better guide clinical treatment. This study attempts to make some breakthroughs in this field and to identify important genes related to the lysosomal pathway. On the basis of this, risk models will be constructed and direct associations between them and immune infiltration will also be investigated. This may advance the process of lysosomal targeting and therapeutic resistance research in ESCC.

This study also has some limitations. Firstly, as a retrospective analysis, the data obtained were mostly from public databases, and although we have performed a preliminary validation through cellular experiments, there is a need for rich mechanistic studies in the future. As for the key genes that were previously screened, we were able to find downstream molecules through mass spectrometry and proteomics analysis. It was verified by molecular biology experiments. In addition, we can further verify this *in vivo* using knockout mice. Secondly, the study set lacks important molecular and clinical data on ESCC patients, and these pathological factors, which are more relevant to clinical treatment decisions, may also be associated with lysosomal pathway actions. Also, the GEO database lacks complete treatment records, such as chemotherapy regimen selection or targeted therapy information. We can use clinical samples from our hospital to further explore the correlation between lysosome pathway molecules and cancer through immunohistochemical and clinical data analysis, as well as immunotherapy analysis. It is hoped that future studies will include more molecular pathology and clinical information, and that basic research will be used to analyse the interaction between MT1X and ESCC targets in depth, in order to more fully explore the close association between the lysosomal pathway and ESCC. We can further explore this with prospective studies.

Herein, based on single cell sequencing and transcriptomic analysis, we investigated the microscopic role of the lysosomal pathway and related genes in the development of ESCC, and confirmed that there is a close association between the lysosomal pathway and the immune infiltration and immune pathway of ESCC. The preliminary validation was performed by cellular assay. This suggests that studying the interaction between the lysosomal pathway and immune infiltration and immune cells may be a potential target to promote new directions in the treatment of ESCC.

Data availability statement

Publicly available datasets were analyzed in this study. This data can be found here: MSigDB database (GSE53624, GSE188900).

Author contributions

JW was responsible for the main article conception, data collection and processing. XG was responsible for full-text operation, testing the validity of articles. The rest were responsible for assisting the above two to improve the content of the article.

Acknowledgments

We sincerely appreciate all members who participated in data collection and analysis.

Conflict of interest

The authors declare that the research was conducted in the absence of any commercial or financial relationships that could be construed as a potential conflict of interest.

Publisher's note

All claims expressed in this article are solely those of the authors and do not necessarily represent those of their affiliated organizations, or those of the publisher, the editors and the reviewers. Any product that may be evaluated in this article, or claim that may be made by its manufacturer, is not guaranteed or endorsed by the publisher.

Supplementary material

The Supplementary Material for this article can be found online at: https://www.frontiersin.org/articles/10.3389/fendo.2023.1138457/full#supplementary-material

References

1. Ferlay J, Soerjomataram I, Dikshit R, Eser S, Mathers C, Rebelo M, et al. Cancer incidence and mortality worldwide: Sources, methods and major patterns in GLOBOCAN 2012. *Int J Cancer* (2015) 136(5):E359–86. doi: 10.1002/ijc.29210

2. Abnet CC, Arnold M, Wei W. Epidemiology of esophageal squamous cell carcinoma. *Gastroenterology* (2018) 154(2):360–73. doi: 10.1053/j.gastro.2017.08.023

3. Cook MB, Chow W, Devesa SS. Oesophageal cancer incidence in the united states by race, sex, and histologic type, 1977-2005. *Brit J Cancer* (2009) 101(5):855–9. doi: 10.1038/sj.bjc.6605246

4. DiSiena M, Perelman A, Birk J, Rezaizadeh H. Esophageal cancer: An updated review. *South Med J* (2021) 114(3):161–8. doi: 10.14423/SMJ.0000000000001226

5. Reichenbach ZW, Murray MG, Saxena R, Farkas D, Karassik EG, Klochkova A, et al. Clinical and translational advances in esophageal squamous cell carcinoma. *Adv Cancer Res* (2019) 144:95–135. doi: 10.1016/bs.acr.2019.05.004

6. Sun J, Shen L, Shah MA, Enzinger P, Adenis A, Doi T, et al. Pembrolizumab plus chemotherapy versus chemotherapy alone for first-line treatment of advanced oesophageal cancer (KEYNOTE-590): A randomised, placebo-controlled, phase 3 study. *Lancet* (2021) 759–71. doi: 10.1016/S0140-6736(21)01234-4

7. Lu Z, Wang J, Shu Y, Liu L, Kong L, Yang L, et al. Sintilimab versus placebo in combination with chemotherapy as first line treatment for locally advanced or metastatic oesophageal squamous cell carcinoma (ORIENT-15): Multicentre, randomised, double blind, phase 3 trial. *BMJ* (2022) e68714. doi: 10.1136/bmj-2021-068714

8. Mei D, Zhu Y, Zhang L, Wei W. The role of CTHRC1 in regulation of multiple signaling and tumor progression and metastasis. *Mediat Inflammation* (2020) 2020:9578701. doi: 10.1155/2020/9578701

9. Xie Y, Kang R, Sun X, Zhong M, Huang J, Klionsky DJ, et al. Posttranslational modification of autophagy-related proteins in macroautophagy. *Autophagy* (2015) 11 (1):28–45. doi: 10.4161/15548627.2014.984267

10. Viry E, Paggetti J, Baginska J, Mgrditchian T, Berchem G, Moussay E, et al. Autophagy: An adaptive metabolic response to stress shaping the antitumor immunity. *Biochem Pharmacol* (2014) 92(1):31–42. doi: 10.1016/j.bcp.2014.07.006

11. Khan T, Relitti N, Brindisi M, Magnano S, Zisterer D, Gemma S, et al. Autophagy modulators for the treatment of oral and esophageal squamous cell carcinomas. *Med Res Rev* (2020) 40(3):1002–60. doi: 10.1002/med.21646

12. Zhang L, Gao Y, Zhang X, Guo M, Yang J, Cui H, et al. TSTA3 facilitates esophageal squamous cell carcinoma progression through regulating fucosylation of LAMP2 and ERBB2. *Theranostics* (2020) 10(24):11339–58. doi: 10.7150/thno.48225

13. Shao C, Zhou X, Zheng X, Huang Q. Ganoderic acid d induces synergistic autophagic cell death except for apoptosis in ESCC cells. *J Ethnopharmacol* (2020) 262:113213. doi: 10.1016/j.jep.2020.113213

14. Jia Y, Tian C, Wang H, Yu F, Lv W, Duan Y, et al. Long non-coding RNA NORAD/miR-224-3p/MTDH axis contributes to CDDP resistance of esophageal squamous cell carcinoma by promoting nuclear accumulation of β-catenin. *Mol Cancer* (2021) 20(1):162. doi: 10.1186/s12943-021-01455-y

15. Sun Y, Zhou Y, Xia J, Wen M, Wang X, Zhang J, et al. Abnormally high HIP1 expression is associated with metastatic behaviors and poor prognosis in ESCC. *Oncol Lett* (2021) 21(2):79. doi: 10.3892/ol.2020.12340

16. Huang F, Ma G, Zhou X, Zhu X, Yu X, Ding F, et al. Depletion of LAMP3 enhances PKA-mediated VASP phosphorylation to suppress invasion and metastasis in esophageal squamous cell carcinoma. *Cancer Lett* (2020) 479:100–11. doi: 10.1016/j.canlet.2020.03.014

17. Zheng K, Ma J, Wang Y, He Z, Deng K. Sulforaphane inhibits autophagy and induces exosome-mediated paracrine senescence *via* regulating mTOR/TFE3. *Mol Nutr Food Res* (2020) 64(14):e1901231. doi: 10.1002/mnfr.201901231

18. Hall TM, Tétreault M, Hamilton KE, Whelan KA. Autophagy as a cytoprotective mechanism in esophageal squamous cell carcinoma. *Curr Opin Pharmacol* (2018) 41:12–9. doi: 10.1016/j.coph.2018.04.003

19. Levy JMM, Towers CG, Thorburn A. Targeting autophagy in cancer. *Nat Rev Cancer* (2017) 17(9):528–42. doi: 10.1038/nrc.2017.53

20. Li W, Li S, Li Y, Lin X, Hu Y, Meng T, et al. Immunofluorescence staining protocols for major autophagy proteins including LC3, P62, and ULK1 in mammalian cells in response to normoxia and hypoxia. *Methods Mol Biol (Clifton N.J.)* (2019) 1854:175–85. doi: 10.1007/7651_2018_124

21. Ma J, Hu S, Zang R, Su Y, Liang Y, Wang Y. MicroRNA-487a promotes proliferation of esophageal cancer cells by inhibiting p62 expression. *Eur Rev Med Pharmaco* (2019) 23(4):1502–12. doi: 10.26355/eurrev_201902_17108

22. Dranoff G. Cytokines in cancer pathogenesis and cancer therapy. *Nat Rev Cancer* (2004) 4(1):11–22. doi: 10.1038/nrc1252

23. Chen C, Wang Y, Huang C, Zhou Z, Zhao J, Zhang X, et al. IL-17 induces antitumor immunity by promoting beneficial neutrophil recruitment and activation in esophageal squamous cell carcinoma. *Oncoimmunology* (2017) 7(1):e1373234. doi: 10.1080/2162402X.2017.1373234

frontiers | Frontiers in Endocrinology

TYPE Original Research
PUBLISHED 06 April 2023
DOI 10.3389/fendo.2023.1147366

OPEN ACCESS

EDITED BY
Chenyu Sun,
AMITA Health, United States

REVIEWED BY
Qun Zhao,
Fourth Hospital of Hebei Medical University, China
Mubashir Ayaz Ahmed,
AMITA Health St Joseph Hospital, United States
Xiuzhi Jia,
Zhejiang University, China

*CORRESPONDENCE
Shijun Li
lishijun@dmu.edu.cn

SPECIALTY SECTION
This article was submitted to Cancer Endocrinology, a section of the journal Frontiers in Endocrinology

RECEIVED 18 January 2023
ACCEPTED 08 March 2023
PUBLISHED 06 April 2023

CITATION
Cao S, Xiao S, Zhang J and Li S (2023) Identification of the cell cycle characteristics of non-small cell lung cancer and its relationship with tumor immune microenvironment, cell death pathways, and metabolic reprogramming. *Front. Endocrinol.* 14:1147366. doi: 10.3389/fendo.2023.1147366

Identification of the cell cycle characteristics of non-small cell lung cancer and its relationship with tumor immune microenvironment, cell death pathways, and metabolic reprogramming

Shengji Cao[1], Sitong Xiao[2], Jingyang Zhang[1] and Shijun Li[1]*

[1]Department of Clinical Laboratory Medicine, First Affiliated Hospital of Dalian Medical University, Dalian, China, [2]Department of Clinical Laboratory Medicine, The Third People's Hospital of Yuhang District, Hangzhou, China

Background: The genes related to the cell cycle progression could be considered the key factors in human cancers. However, the genes involved in cell cycle regulation in non-small cell lung cancer (NSCLC) have not yet been reported. Therefore, it is necessary to evaluate the genes related to the cell cycle in all types of cancers, especially NSCLC.

Methods: This study constituted the first pan-cancer landscape of cell cycle signaling. Cluster analysis based on cell cycle signaling was conducted to identify the potential molecular heterogeneity of NSCLC. Further, the discrepancies in the tumor immune microenvironment, metabolic remodeling, and cell death among the three clusters were investigated. Immunohistochemistry was performed to validate the protein levels of the ZWINT gene and examine its relationship with the clinical characteristics. Bioinformatics analyses and experimental validation of the ZWINT gene were also conducted.

Results: First, pan-cancer analysis provided an overview of cell cycle signaling and highlighted its crucial role in cancer. A majority of cell cycle regulators play risk roles in lung adenocarcinoma (LUAD); however, some cell cycle genes play protective roles in lung squamous cell carcinoma (LUSC). Cluster analysis revealed three potential subtypes for patients with NSCLC. LUAD patients with high cell cycle activities were associated with worse prognosis; while, LUSC patients with high cell cycle activities were associated with a longer survival time. Moreover, the above three subtypes of NSCLC exhibited distinct immune microenvironments, metabolic remodeling, and cell death pathways. ZWINT, a member of the cell signaling pathway, was observed to be significantly associated with the prognosis of LUAD patients. A series of experiments verified the higher expression levels of ZWINT in NSCLC compared to those in paracancerous tissues. The activation of epithelial-mesenchymal transition (EMT) induced by ZWINT might be responsible for tumor progression.

Conclusion: This study revealed the regulatory function of the cell cycle genes in NSCLC, and the molecular classification based on cell cycle-associated genes could evaluate the different prognoses of patients with NSCLC. ZWINT expression was found to be significantly upregulated in NSCLC tissues, which might promote tumor progression *via* activation of the EMT pathway.

KEYWORDS

non-small cell lung cancer, cell cycle, pan-cancer analysis, tumor immune microenvironment, cell death pathways, metabolic reprogramming

1 Background

Lung cancer, a malignant tumor, is the most common type of cancer worldwide with the highest incidence and mortality (1). The histological types of lung cancer can be divided into small-cell lung cancer (SCLC) and non-small cell lung cancer (NSCLC) (2). Among them, the NSCLC accounts for about 80–85% of total lung cancer cases, and mainly includes lung adenocarcinoma (LUAD) and lung squamous cell carcinoma (LUSC) (3). Although there has been tremendous development in the clinical diagnosis and treatment of lung cancer, such as radiotherapy, chemotherapy, immunotherapy, molecular targeted therapy, etc., the 5-year survival rate of NSCLC is still poor because the lung cancer is often insidious in the early stage and there are delays in the diagnosis (1, 4). Therefore, it is necessary to develop and investigate specific neoplasm markers for improving the prediction of the clinical outcomes and chemotherapy sensitivity of patients with NSCLC.

In the past years, a series of related breakthroughs have found the relationship between the regulation mechanism of the cell cycle and the development of a tumor. The major cause of tumorigenesis is the unrestricted cell proliferation after the cell cycle disorder and therefore, the tumor could be regarded as a cell cycle disease (5–7). It is well known that the driving mechanism and the regulatory mechanism of the cell cycle play important roles during cell proliferation. When the regulatory mechanism of the cell cycle is damaged, there can be uncontrolled cell growth, which may lead to the transformation of tumor cells. As there is a close association between the cell cycle and the tumor, the cell cycle could be considered one of the primary cellular mechanisms in the occurrence and development of cancer (8). Several studies have reported that therapy targeting cell cycle could serve as a reasonable treatment option to delay tumor progression by inhibiting tumor cell proliferation and inducing its apoptosis (6, 9, 10). As the vital genes related to the cell cycle might act as markers for pre-cancerous lesions or early-stage cancers, doctors could choose the best treatment for cancer patients to prolong their survival (11). Hence, it is necessary to investigate the key molecular signatures participating in cell cycle regulation in cancer cells. Furthermore, the cell cycle-related genes have not been found to predict the clinical outcomes and chemotherapeutic strategies in NSCLC patients. Therefore, the development of an NSCLC risk stratification tool and exploring the key gene from the cell cycle-related genes are important.

In this study, the roles of cell cycle-related genes in NSCLC were investigated by obtaining samples from the Cancer Genome Atlas (TCGA) database. Moreover, the cell cycle-related genes were acquired from the MsigDb platform. We identified 93 cell cycle-related genes that were associated with the tumor stage of NSCLC. This study comprehensively highlighted the genome and transcriptome characteristics of 93 genes in human tumors for the first time. Based on the cell cycle scores and cell cycle-related gene expression, we separated patients with NSCLC into three distinct types and evaluated their association with prognosis, metabolic reprogramming, immune microenvironments, and cell death pathways. Finally, we identified the hub gene ZWINT using bioinformatics. The association between ZWINT expression and patient prognosis, its potential role in tumor immunity, the clinical features of pan cancer, and the important pathways in cancer were determined using R.

2 Materials and methods

2.1 Sample collection and acquisition of genes associated with the cell cycle

The TCGA-LUAD and TCGA-LUSC cohorts were obtained from the TCGA GDC website and recognized as NSCLC cohorts. The data filtering and polishing were conducted using Perl and R programming (12). The TCGA-LUAD cohort consisted of 539 tumor samples and 59 paracancerous samples, while the TCGA-LUSC cohort consisted of 502 tumor samples and 49 paracancerous samples. All these RNA-seq data were initially converted to log format and then the sva package was applied to complete the bulk rectification procedure. The clinical information about each patient was also collected and compiled. Finally, the cell cycle-related dataset was obtained and downloaded from the MsigDb platform and the "REACTOME CELL CYCLE" dataset was compiled (13, 14). A total of 693 genes were present in this dataset, all of which were considered to be related to the cell cycle.

2.2 Identification of the cell cycle genes associated with the development of NSCLC

The conversion of normal lung epithelial cells to NSCLC cells is considered a typical example of carcinogenesis. Therefore, a significant role played by genes in carcinogenesis has been a topic worthy of scientific investigation. The cell cycle genes associated with the development of NSCLC were identified by comparing the malignant and noncancerous tissues from the TCGA-LUAD and TCGA-LUSC cohorts. The cutoff values for differential expression analysis were set as follows: | logFC | > 1.5 and FDR < 0.05. Finally, the findings from the TCGA-LUAD and TCGA-LUSC cohorts were intersected to provide a list of differentially expressed genes.

The patients with NSCLC who acquire a tumor eventually progress from stage I to stage IV. Therefore, it is crucial to determine the cell cycle genes that are associated with the clinical stage of NSCLC patients. The GEPIA2 platform developed by Peking University was applied to facilitate the analysis (15, 16). The specific parameters used were as follows: "Expression DIY" toolbar, "Stage Plot" interface, and "LUAD + LUSC" dataset. Only the cell cycle genes with a P value of less than 0.05 were selected and further evaluated using bioinformatics.

2.3 Pan-cancer analysis

The pan-cancer cohort of TCGA was downloaded and integrated to analyze the involvement of the aforementioned cell cycle-related genes in diverse human cancers. The gene expression, prognostic value, mutation type, methylation level, and pathway regulation, among other factors, were reviewed by referring to the previously published pan-cancer analysis methods (17–19).

The differential expression analyses of cancer and paracancerous tissues at the pan-cancer level were conducted using R software packages, such as ggplot2, randomcoloR, ggpubr, GSVA, clusterProfiler, impute, and ComplexHeatmap, and the findings were represented as a heat map (20–22). The color of the dot on the heat map indicated whether the gene was up-regulated or down-regulated in the cancer tissue, and the size of the dot indicated the statistical P value. The greater the size of the dot, the greater the statistical significance of the finding.

The pan-cancer prognostic characteristics of the aforementioned cell cycle-related genes were studied in detail using the R packages survival and pheatmap, and a heat map was constructed. Red represents a dangerous gene, indicating that the greater the level of gene expression, the worse the prognosis of patients; blue shows a protective gene indicating that the higher the level of gene expression, the better the prognosis of patients. Gray suggests that the gene has no predictive association in patients with this form of malignancy.

A series of R packages, such as ggplot2, randomcoloR, tidyverse, magrittr, readxl, stringr, maftools, dplyr, reshape2, and RColorBrewer were used for single nucleotide variant (SNV) and copy number variant (CNV) analyses. The frequency of SNV mutations in each gene in a tumor is represented as a heat map, and the type of mutation of each SNV is represented as a waterfall map. Each hue in the CNV bar chart reflects a distinct type of tumor.

The pan-cancer methylation levels of the cell cycle genes were summarized using the R packages ggplot2, ChAMP, randomcoloR, ggpubr, GSVA, clusterProfiler, impute, and ComplexHeatmap. A red dot indicates a high amount of methylation of the gene in this type of tumor, whereas the blue dot indicates a low level of methylation. The size of the dot shows the P value; therefore, the bigger the dot, the greater the statistical significance.

A comprehensive analysis of the association between the cell cycle pathways and other traditional tumor pathways was conducted using clusterProfiler, limma, ggplot2, ggpubr, GSVA, and other R packages. Specifically, the relative score of each pathway was calculated using the GSVA package to indicate the relative activity of the pathway, and the correlation values between the cell cycle pathway and other pathways were examined by the correlation test, before being represented as a heat map.

2.4 Cluster analysis

First, univariate Cox regression analysis of the TCGA-LUAD cohort was conducted to determine the cell cycle-related genes with prognostic values, which were further used for conducting cluster analysis. For both the TCGA-LUAD and TCGA-LUSC cohorts, GSVA methods were used for calculating the cell cycle score of each sample (23, 24). We performed cluster analysis based on the expression levels of the samples using ward.D. Before classifying the tumor tissues into three subtypes based on the distinct cell cycle activities, we evaluated the mRNA expression levels in normal tissues. The survival and survminer programs were used to evaluate the prognosis of patients with different subtypes of NSCLC to highlight the clinical value of cluster analysis.

2.5 Analysis of tumor metabolic reprogramming, immune microenvironment, and cell death status

42 conventional metabolic pathways, 33 immune-related pathways, and 10 cell death pathways were classified using the MsigDb platform. The metabolic score, immunological score, and cell death score for each NSCLC sample were determined using the GSVA program. The Kruskal test was used to assess the pathway activity between the three subtypes of the cell cycle. Moreover, a comprehensive analysis of the differences in immune cell infiltration and gene expression at immune checkpoints was conducted to exhaustively describe the changes in the immune milieu across subtypes. The TIMER2.0 platform offers several immunological algorithms, including TIMER, CIBERSOFT, QUANTISEQ, EPIC, etc. (25, 26). The Kruskal test was used to assess the differences in the immune cell infiltration and gene expression at the immunological checkpoints across subtypes, and only the findings with P < 0.05 were represented.

2.6 Biological functional analysis of the ZWINT gene

The expression patterns of the ZWINT gene in both healthy and malignant tissues were obtained from Genotype-Tissue Expression (GTEx), Cancer Cell Line Encyclopedia (CCLE), and The Cancer Genome Atlas (TCGA) (27, 28). The information on ZWINT mRNA expression in normal tissues was obtained from GTEx, a dataset containing expression data of 31 healthy tissues, while the information on the expression distribution across various cancer cell lines was obtained from CCLE, a database containing information on more than 1100 cancer cell lines. TCGA provided information on the differential expression of genes between malignant and noncancerous tissues. The GTEx and TCGA databanks were accessed using the UCSC Xena platform.

Further, the linkages between ZWINT expression and clinical outcomes were obtained using the information on patient survival from the TCGA database. Disease-free interval (DFI), disease-specific survival (DSS), overall survival (OS), and progression-free interval (PFI) were used to evaluate the correlation between mRNA expression levels and patient survival rates (29). ZWINT expression and survival outcomes were analyzed using Kaplan-Meier (KM) and Cox analyses for patients with different types of cancer. KM curves and forest plots were created in R. Then, a correlation analysis of clinicopathological data such as tumor grade, tumor stage, gender, age, race, and tumor status was conducted using the "limma" and "ggpubr" packages in R (30). Both the "survminer" and "survival" packages in R were used to generate the survival curves. A P value of 0.05 was considered as the threshold of statistical significance.

The Tumor Immune Estimation Resource 2.0 online server is a useful resource for systematically analyzing the immune infiltrates across different cancer types. Initially, it was used to examine the differences in ZWINT expression between the tumor and normal tissues in all the TCGA cohorts. A correlation analysis between ZWINT expression and immune infiltration was conducted using several immunological deconvolution techniques. More importantly, the correlation between ZWINT expression and immune checkpoint levels was also evaluated in this study.

Biomarker Exploration of Solid Tumors website is a publicly free web-based platform for omics data. It was used to further explore the contribution of ZWINT in NSCLC. The GO and KEGG analyses for ZWINT were based on the TCGA-LUAD and TCGA-LUSC cohorts. Based on the median value of ZWINT expression, LUAD, and LUSC patients were stratified into high-ZWINT and low-ZWINT subgroups. Then, the mutation profiles between high-ZWINT and low-ZWINT subgroups were intensively studied. Besides, the predictive ability of ZWINT in the immunotherapy of NSCLC patients was also analyzed. Finally, the expression levels of the ZWINT gene in different clinical subgroups of NSCLC patients were comprehensively investigated.

To highlight the important roles of the ZWINT gene in tumor immune microenvironment, metabolic remodeling, and cell death, GSEA analyses were conducted in pan-cancer tissues following the previously described methods. Based on the expression levels of the ZWINT gene in pan-cancer tissues, it was ranked from high to low. The first 30% of the tumor samples were considered as ZWINT high expression subtype, and the last 30% of the tumor samples were regarded as ZWINT low expression subtype. Further, the tumor samples of different subtypes were analyzed by GSEA.

2.7 Clinical sample collection

We collected 30 NSCLC tissues and 30 paired paracancerous tissues from our hospital from 2021-08 to 2021-10. The tissues were immediately frozen in liquid nitrogen after surgically resecting specimens to extract total RNA. Moreover, 50 pairs of paraffin-embedded pathological specimens obtained from 2015-12 to 2016-12 were collected in this study. The essential information and clinically-relevant pathological information of patients with NSCLC are shown in Tables 1, 2, respectively. All the patients with NSCLC from whom the tissues were collected were pathologically confirmed to have NSCLC and were treated in the First Affiliated Hospital of Dalian Medical University. The informed consent was provided by the First Affiliated Hospital of Dalian Medical University. All the patients with NSCLC refused chemotherapy and radiation treatment before surgery. The Ethics Committee of the First Affiliated Hospital of Dalian Medical University approved this study.

TABLE 1 Basic information of the NSCLC patients.

Basic information	Gender		Age	
	Male	Female	≥60	<60
Number	26	24	30	20

TABLE 2 Clinically-relevant pathological information.

Pathological information	Histological type		Differentiation		Stage		Lymphatic metastasis	
	Squamous	Adenocarcinoma	High Middle	Minor	I + II	III + IV	Yes	No
Number	18	32	38	12	35	15	24	26

2.8 Isolation of the total RNA and validation of the expression level of the ZWINT gene by quantitative real-time PCR

Total RNA was extracted from the human NSCLC tissues by the RNAex Pro RNA reagent based on the manufacturer's instructions. Subsequently, the total RNA was reverse-transcribed using the Evo M-MLV RT Kit with gDNA Clean. The expression level of the ZWINT gene was calculated by RT-PCR using SYBR® Green Premix Pro Taq HS qPCR Kit. All the reagents above were procured from Accurate Biology. The ZWINT gene was normalized to β-actin. The ΔΔCt method was used for quantifying the level of RNA expression. The primer sequences for ZWINT and β-actin were as follows:

ZWINT, 5'-AGGAGGACACTGCTAAGGG-3'(Forward), 5'- AGGTGGCCTTCAGCTCTTTC-3' (Reverse); β-actin, 5'-CATGTACGTTGCTATCCAGGC-3' (Forward), 5'-CTCCTTAATGTCACGGACGAT -3' (Reverse).

2.9 Immunohistochemical staining

The protein expression of ZWINT was tested by immunohistochemical staining (IHC). The paraffin-embedded tissue slides were immune stained with anti-N-cadherin, anti-E-cadherin, vimentin, and ZWINT. After dewaxing, hydration, and epitope extraction, the sections were placed in 3% hydrogen peroxide for 15 min to inhibit endogenous peroxidase activity. Subsequently, the sections were incubated overnight with a solution containing the appropriate primary antibody. Then, 50 μL of secondary antibody was added in a sequence and incubated at room temperature for 20 min. IHC staining was carried out according to the manufacturer's protocol. The results were blindly assessed independently by two pathologists. Positive ZWINT-staining rate was considered on a scale of 0 to 4, with 1 indicating (0–25%), 2 (26–50%), 3 (51–75%), and 4 (76–100%). Staining intensity was rated as follows: 0 (no staining), 1 (weak staining), 2 (moderate staining), or 3 (strong staining). IHC score was calculated as a product of positive staining rate and intensity score. The patients were divided into high and low-expression groups, with a score of 2 or less considered as low expression, and a score of more than 2 considered as high expression.

3 Results

3.1 Identification of the cell cycle genes associated with the occurrence and development of NSCLC

A total of 148 genes involved in the cell cycle were determined to be differently expressed in LUAD and paracancerous tissues (Supplementary Table 1). 210 cell cycle-related genes were identified to be differently expressed in malignant and noncancerous LUSC tissues (Supplementary Table 2). The intersection of the LUAD and LUSC results revealed 143 potential cell cycle-related genes strongly linked with NSCLC (Supplementary Figure 1). There is a clinical progression of NSCLC as the tumor grows (StageI-StageII-StageIII-StageIV). Further, the cell cycle genes associated with the stage of NSCLC were identified. The findings from this study indicated that 93 out of 143 potential genes were linked with the tumor stage (Supplementary Table 3). Therefore, these 93 genes were retained and used for further analysis.

3.2 Pan-cancer characterization of the 93 cell cycle genes

To highlight the significance of the 93 genes in carcinogenesis and tumor development, a pan-cancer investigation was performed to exhaustively characterize their genomic and transcriptome properties in different human cancers. Except for NSCLC, practically all the genes showed highly up-regulated expression in the cancerous tissues of CESC, CHOL, GBM, LIHC, and UCEC (Figure 1A). However, a downregulated expression trend was observed in the cancer tissues of COAD and THCA (Figure 1A). This not only confirms the heterogeneity among tumors but also indicates that these genes may play different roles in different types of tumors. Importantly, our data indicated that a majority of these 93 genes perform deleterious functions in KIRC, SARC, PAAD, KIRP, LIHC, LUAD, LGG, MESO, ACC, KICH, PCPG, BRCA, PRAD, SKCM, and UVM (Figure 1B). In other words, as the expression of these genes increases, there is a clinical worsening in patients with these types of malignancies. For such cancer patients, gene-targeting techniques may provide a novel therapeutic option. However, these genes have a protective function in other types of cancer, including THYM, STAD, READ, COAD, DLBC, and LUSC (Figure 1B). Moreover, we also visualized their genetic characteristics. Figure 2A shows the CNVs. In individuals with distinct types of malignancies, several genes involved in the cell cycle exhibited considerably distinct genomic features, particularly CNV levels. The SNV mutations were more prevalent in patients with BLCA, BRCA, CESC, COAD, LUAD, LUSC, SKCM, STAD, and UCEC tumors (Figure 2B). It was evident that the degree of methylation of genes might impact the level of gene expression. Therefore, the methylation levels of these genes were examined in several tumor types. The data indicated that the degree of methylation in cancerous tissues is often lower than that in the surrounding tissues (Figure 3A). In addition, pathway enrichment analysis revealed that these cell cycle genes were significantly correlated with several classical tumor-related pathways, indicating that the cell cycle is intrinsically linked to tumor immune microenvironment, metabolic reprogramming, cell death, angiogenesis, and other biological phenomena (Figure 3B).

10.3389/fendo.2023.1147366

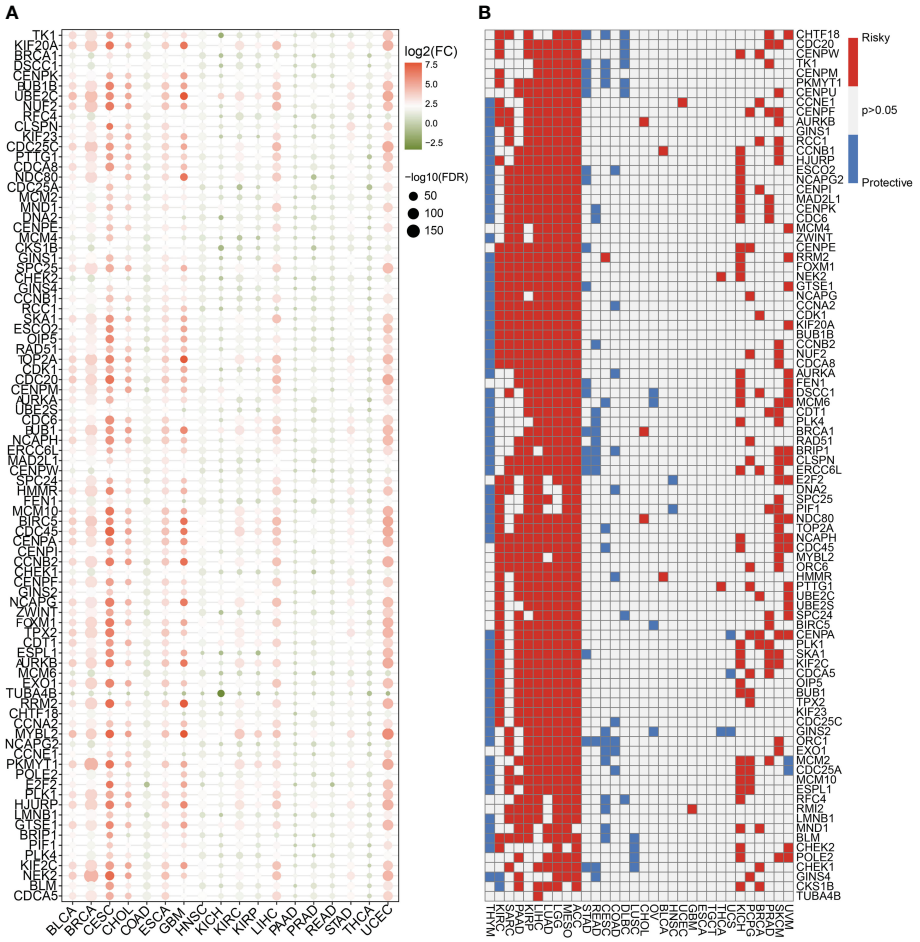

FIGURE 1
Expression traits and prognostic values of the cell cycle-related genes in pan cancer. **(A)** mRNA expression levels of the 93 cell cycle-related genes in other human tumors (P < 0.05). **(B)** Clinical outcomes of the cell cycle in pan cancer. White color (P > 0.05) indicates no statistical difference. Red color indicates the risk factor, while the blue color indicates the protective factor.

3.3 Cluster analysis of NSCLC patients based on the cell cycle gene expression characteristics and pathway activity

Previous pan-cancer research findings revealed that the cell cycle influences LUAD and LUSC differently or possibly contrary to each other (Figure 1B). To further elucidate the underlying molecular heterogeneity of NSCLC patients, a cluster analysis was performed followed by pattern characterization. First, a univariate COX regression analysis was conducted to identify 75 genes associated with prognosis. The identification of these prognostic genes can be useful in distinguishing clinically meaningful molecular subtypes more effectively (Supplementary Table 4). The clustering results are shown in Figures 4A, B. All the cancer patients, both from the TCGA-LUAD and TCGA-LUSC cohorts, were successfully classified into three subtypes (C1, C2, and C3). In the TCGA-LUAD cohort, the trend of pathway enrichment score was C1 > C2 > C3, but in the TCGA-LUSC cohort, the pathway enrichment score sequence was C2 > C1 > C3 (Figures 4C, D). Interestingly, in the TCGA-LUAD cohort, the survival times of patients followed the trend C3 > C2 > C1, but in the TCGA-LUSC cohort, the trend was C2 > C1 > C3 (Figures 4E, F). A comprehensive examination of metabolic reprogramming, immunological microenvironment, and cell death pathways was performed to completely identify the intrinsic molecular properties of several subtypes of the cell cycle (Figures 5, 6). The patients with LUAD and LUSC exhibited three fundamental metabolic abnormalities associated with metabolic reprogramming with a shift in their cell cycle activity, such as alanine aspartate and glutamate metabolism, alpha-linolenic acid metabolism, arachidonic acid metabolism, ether lipid metabolism, histidine metabolism, nitrogen metabolism, glyoxylate and dicarboxylate metabolism, and sulfur metabolism (Figures 5A, 6A). Innate immune response and adaptive immune response exhibited notable differences among cell cycle subtypes, such as antigen processing and presentation (Figures 5B, 6B). In addition, several subtypes of the cell cycle were followed by distinct cell death mechanisms, such as immunogenic cell death, necroptosis, phagocytosis, and PANoptosis (Figures 5C, 6C).

10.3389/fendo.2023.1147366

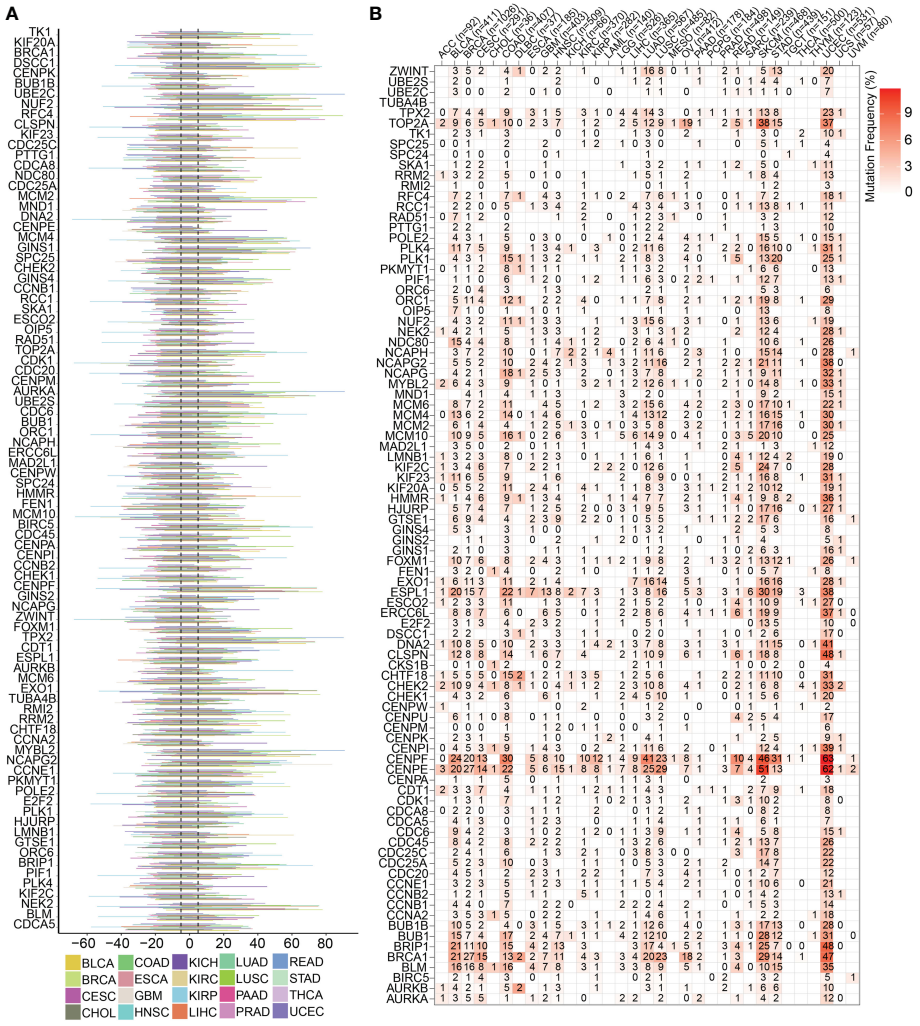

FIGURE 2
Genomics traits of cell cycle-related genes in pan cancer. **(A)** CNV outcomes of the 93 cell cycle-related genes in different types of cancers. The length line represents the wave frequency of the cell cycle-related genes in human malignant tumors. **(B)** Heatmap representing the SNV mutations for the 93 cell cycle-related genes.

3.4 Biological analysis of the ZWINT gene

As a traditional cell cycle-related gene, the ZWINT gene has been identified to regulate the onset and development of several types of cancers; however, its association with NSCLC remains unknown. Therefore, the expression of the ZWINT gene in pan cancer and the possible functions of NSCLC were examined. Combining the histology data from TCGA and GTEx established that ZWINT was significantly overexpressed in several types of human cancers, indicating its significant role in carcinogenesis (Supplementary Figures 2A, B). Comprehensive pan-cancer investigation based on the univariate COX regression analysis and KM analysis indicated the prognostic significance of the ZWINT gene (Supplementary Figures 3–7). Immune correlation research revealed a significant relationship between the ZWINT gene and infiltrating immune cells, such as B cells, CD4+ T cells, cancer-associated fibroblasts, CD8+ T cells, macrophages, neutrophils, and NK cells (Figure 7). Immune checkpoints are the primary limiting criteria for the activity of immunological cells. As shown in Supplementary Figure 8, we also studied the influence of the ZWINT gene on the expression levels of different types of immune checkpoints. Immunotherapy targeting immune checkpoints is an emerging research area in cancer treatment, and the study results indicated that the ZWINT gene can be used as a predictor of immunotherapy response to a certain extent (Supplementary Figure 9).

GO analysis revealed that the ZWINT gene was involved not only in controlling the cell cycle development in LUAD and LUSC but also in regulating processes such as cell division, chromosomal segregation, nucleoplasm, cell periphery, etc. (Figures 8A, B). However, there are still some gaps that need attention. The ZWINT gene has a stronger influence on the development and stability of cell membranes in LUAD and a greater influence on the extracellular matrix and some immunomodulatory responses in LUSC. KEGG analysis results further verified the influence of ZWINT on the advancement of the NSCLC cell cycle (Figures 8C, D). In addition, the genomic mutation data of

10.3389/fendo.2023.1147366

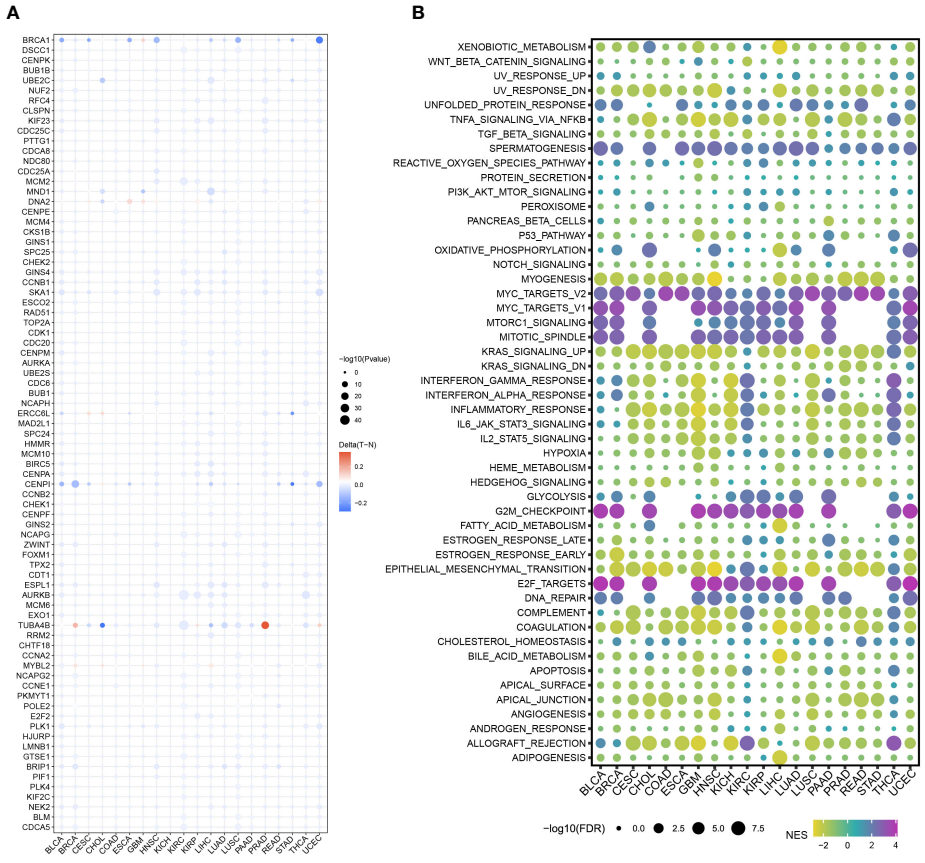

FIGURE 3
Methylation levels and pathway correlation of the cell cycle-related genes in pan cancer. **(A)** DNA methylation of the 93 cell cycle-related genes in different types of cancers (red to blue represents high to low). **(B)** 93 cell cycle-related genes were correlated with several classical tumor-related pathways (red to blue represents high to low).

NSCLC patients with varying ZWINT expression levels were also analyzed in this study. As shown in Figure 9, the ZWINT gene has a stronger impact on the SNV and CNV mutations in LUAD when compared to those in LUSC. NSCLC patients with different clinical traits demonstrated distinct expression levels of the ZWINT gene (Supplementary Figure 10). The male patients with LUAD had considerably higher levels of ZWINT gene expression than the female patients. The expression levels of the ZWINT gene were substantially higher in patients with LUSC younger than or equal to 65 years than in those older than 65 years. For both LUAD and LUSC patients, the expression of the ZWINT gene was significantly associated with the tumor stage. Above all, ZWINT expression was found to be significantly correlated with tumor immune-related pathways, metabolism-related pathways, and cell death-related pathways (Supplementary Figure 11). Specifically, ZWINT expression was negatively associated with the activities of the T cell receptor signaling pathway, B cell receptor signaling pathway, toll-like receptor signaling pathway, and cytokine-cytokine receptor interactions (Supplementary Figure 11A). A complex regulatory relationship was observed between the ZWINT gene and the classical metabolic pathways of the tumor. As shown in Supplementary Figure 11B, a significant positive correlation between the ZWINT gene and pyrimidine metabolism was observed in all types of tumor tissues. However, a different correlation was observed with other metabolic pathways due to tumor heterogeneity. In addition, ZWINT expression was positively related to several cell death pathways in patients with KIRC and THCA (Supplementary Figure 11C). ZWINT expression was negatively related to several cell death pathways in patients with CESC, ESCA, and GBM (Supplementary Figure 11C).

3.5 Expression validation of ZWINT gene in patients with NSCLC

We identified the expression of the ZWINT gene in 30 samples of NSCLC and nearby frozen tissues using RT-qPCR. Consistent with our previous hypothesis, the RT-qPCR data demonstrated that the expression of ZWINT in cancer tissues was much higher than that in the neighboring tissues (Figure 10A). The immunohistochemical results further elucidated the up-regulated expression of the ZWINT gene in cancer tissues from the perspective of protein levels (Figure 10B and Table 3). In addition, the immunohistochemistry studies demonstrated that the expression of E-cadherin was significantly down-regulated in cancerous tissues, while the expression of Vimentin and Slug protein was significantly up-regulated in cancerous tissues (Figure 10C). The protein expression levels of ZWINT in NSCLC were negatively linked with E-cadherin, strongly

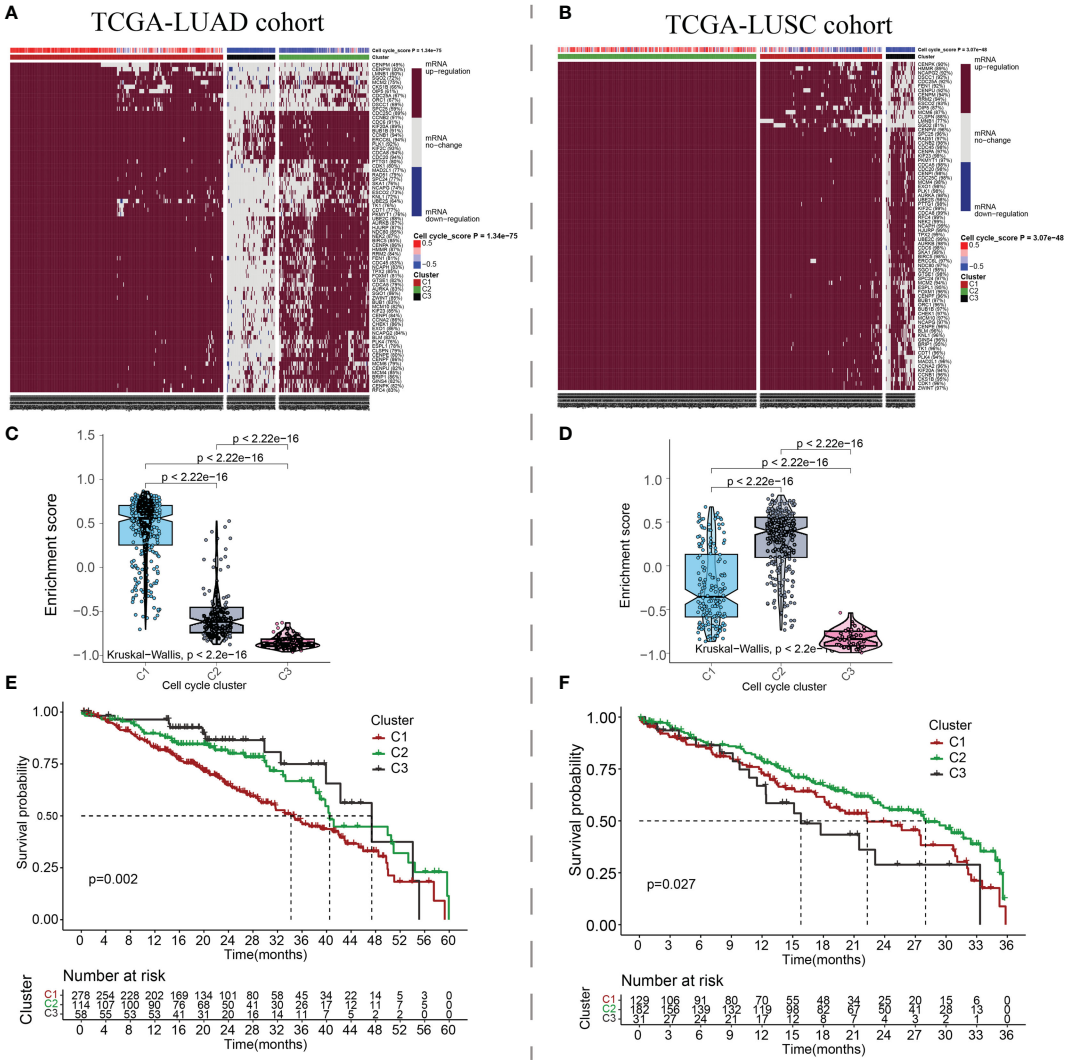

FIGURE 4
Cluster analysis based on the cell cycle-related genes. The patients with NSCLC in the TCGA-LUAD and TCGA-LUSC cohorts were successfully grouped into 3 clusters for LUAD **(A)** and LUSC **(B)**. Pathway enrichment scores followed the trend C1 > C2 > C3 in LUAD **(C)** and C2 > C1 > C3 in LUSC **(D)**. Three different clusters showed different survival curves. Cluster 1 has the worse survival rate in LUAD **(E)**. However, Cluster 1 has the worse survival rate in LUSC **(F)**. x indicates survival time and y indicates survival rate.

associated with Vimentin, and positively correlated with Slug protein (Table 4).

4 Discussion

Cell growth and differentiation are the essential phases of the cell cycle. The control of the cell fate through the cell cycle enables the development and self-renewal of mammalian cells. In other words, signaling pathways involved in the cell cycle regulate cell growth, proliferation, and differentiation. Each of the four phases of the cell cycle, namely, G1, S, G2, and M, occur sequentially and are rigorously controlled. The cell cycle checkpoint is the cell's feedback control mechanism that decides whether the cell can progress to the subsequent phase. When aberrant events (such as DNA damage) occur, cell cycle checkpoints are involved in halting cell transitions to the next stage, accruing repairs, and promoting the release of a series of repair-functioning proteins. According to tumor research, the formation and progression of tumors are closely connected to the aberrant composition of the control point in the G1/S phase. With the expansion of scientific research, it is generally accepted that cyclin-dependent kinase and cyclin are potential therapeutic targets of anti-tumor medicines. However, it is apparent that the cell cycle is an excellent and intricate network, in which each cell cycle regulator is closely connected, interacts with each other, regulates or inhibits the progression of the entire cell cycle, and ultimately leads to cancer. Therefore, there is an urgent need to use more cutting-edge analytical tools for investigating the possible intermolecular interactions and regulation of gene expression, which can enhance the understanding of the intrinsic characteristics of tumors. Moreover, it may provide a novel alternative therapeutic method.

In this study, 693 cell cycle regulators were identified, among which 93 were differentially expressed in NSCLC and surrounding tissues, and

10.3389/fendo.2023.1147366

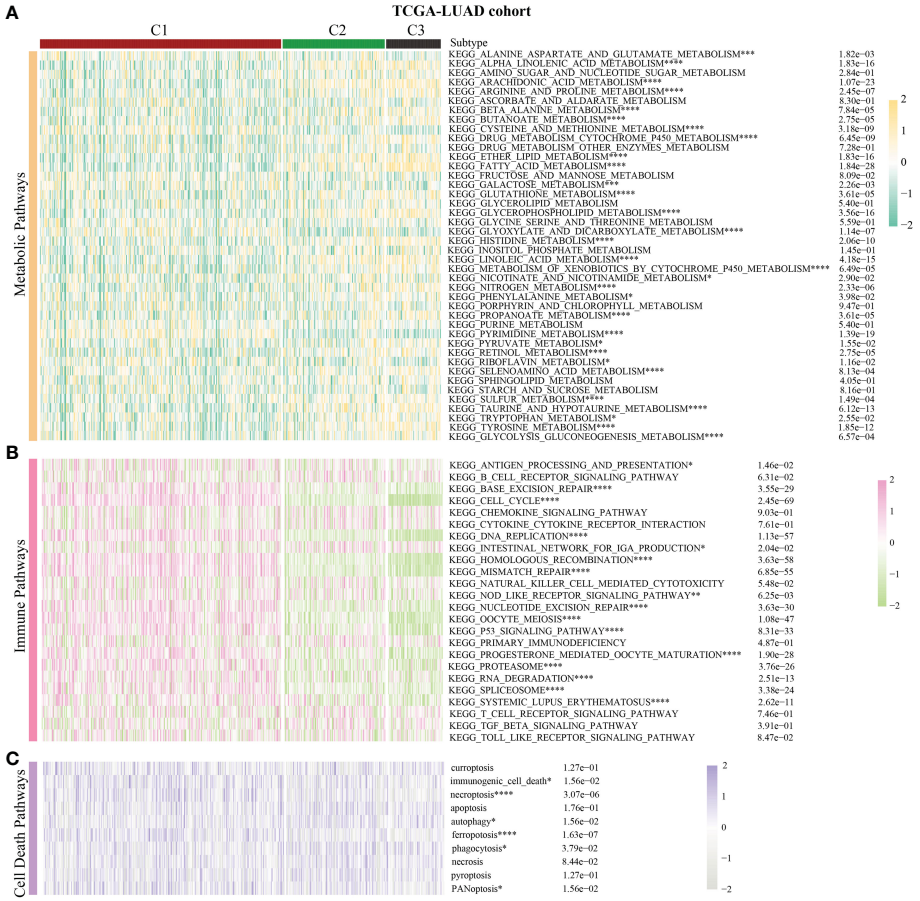

FIGURE 5
Correlation of the cell cycle-related gene scores with metabolic reprogramming, immunological microenvironment, and cell death pathways in LUAD. **(A)** Activity of well-recognized metabolic reprogramming in the three clusters for LUAD. **(B)** Activity of well-recognized immune pathways in the three clusters for LUAD. **(C)** Correlation between the cell cycle-related gene scores and cell death pathways for LUAD. * indicates $p < 0.05$; ** indicates $p < 0.01$; *** indicates $p < 0.001$; and **** indicates $p < 0.0001$.

were associated with the clinical stage of the tumor. With the rapid development of the bioinformatics field, people have gradually reached a consensus that differentially expressed genes between cancer and paracancerous tissues are often related to tumorigenesis, while genes related to the clinical stages are often involved in tumor progression. Therefore, the 93 cell cycle regulators identified in this study can be considered to be involved in controlling the incidence and progression of NSCLC to a certain extent, which is of tremendous research significance, and the further bioinformatics analysis and experimental verification in this study were also based on this.

The pan-cancer multi-group properties of these cell cycle regulators are systematically elucidated for the first time in this study, which is one of its novel contributions. The study findings implied that cell cycle signals may have contrasting regulatory effects on different subsets of NSCLC patients since the majority of genes play risk roles in LUAD but protective roles in LUSC. The phenomena have been documented for the first time in this study. Moreover, cell cycle signals are closely associated with other conventional tumor-associated signals, such as metabolic signals, immunological signals, cell death signals, etc. In addition to the consensus clustering of the transcriptome, we conducted a comprehensive analysis of the genomic characteristics of the regulators, such as CNV and SNV.

More importantly, cell cycle signal activity was used for the first time in this study for the effective classification of NSCLC patients into three subgroups. For patients with LUAD, the active cell cycle signal often led to unfavorable clinical results. However, for patients with LUSC, the longer their survival time, the more active the cell cycle signal. Consistent with our previous pan-cancer analysis findings, it was observed that there is evident molecular heterogeneity in patients with NSCLC, the reason for heterogeneity may be related to its pathological type, and cell cycle signaling, as the most fundamental process in cell survival, plays nearly opposite roles in LUAD and LUSC. In NSCLC patients with distinct cell cycle activity, the immunological microenvironment, metabolic reprogramming, and cell death mechanisms are often distinct. This further validates the connection between these complex networks and promotes the progression and development of malignancies.

ZWINT is a protein that interacts with ZW10 and is encoded by the ZWINT gene. This protein is essential for chromosomal mobility and spindle checkpoint regulation, as well as mitosis and cell proliferation (4, 31). It is generally accepted that mitotic

10.3389/fendo.2023.1147366

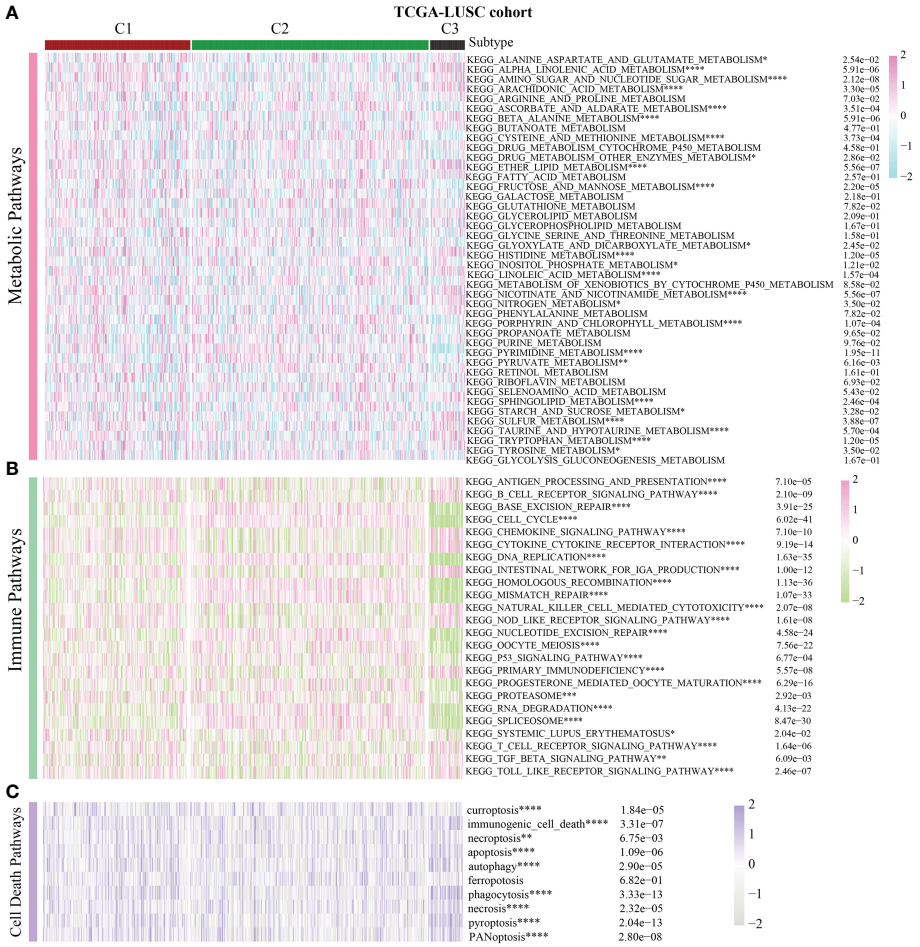

FIGURE 6
Correlation of the cell cycle-related gene scores with metabolic reprogramming, immunological microenvironment, and cell death pathways in LUSC. **(A)** Activity of well-recognized metabolic reprogramming in the three clusters for LUSC. **(B)** Activity of well-recognized immune pathways in the three clusters for LUSC. **(C)** Correlation between the cell cycle-related gene scores and cell death pathways for LUSC. * indicates $p < 0.05$; ** indicates $p < 0.01$; *** indicates $p < 0.001$; and **** indicates $p < 0.0001$.

abnormalities are characteristic of a majority of malignant tumors. Although the precise function of the molecular composition of the centromere and the interactions between various components of the centromere are unknown, there is growing evidence that ZWINT is frequently over-expressed in several tumors and associated with poor clinical prognosis and early recurrence (32). ZWINT has been demonstrated to diminish chromosomal stability during the development of cancer, indicating that it may function as an oncoprotein (33). The high expression of ZWINT is strongly associated with tumor recurrence, which is a possible risk factor for the high recurrence rate and poor survival rate in patients with liver cancer (34). Endo et al. revealed that the high expression of ZWINT is associated with the overall poor survival rate of LUAD, and ZWINT has a high sensitivity for early screening of lung cancer (35). Mou et al. have shown that ZWINT may affect the proliferation and migration of melanoma cells by regulating the expression of c-Myc (36). Kim et al. observed that ZWINT is abundantly expressed in pan-cancer cells and tissues and enhances pan-cancer cell proliferation and invasion through NF-kB signal transduction (37).

PCR and immunohistochemistry results indicated that the expression levels of the ZWINT gene were considerably higher in NSCLC cancer tissues than that in the surrounding tissues, and the ZWINT gene may contribute to disease progression by increasing the epithelial-mesenchymal transition (EMT). E-cadherin (cadherin), which is completely expressed on the membrane surface of epithelial cells, is the primary hallmark of EMT epithelioid cells, and a decline in the E-cadherin expression reduces the adhesion between cells (38). Vimentin and Slug are the primary markers of EMT interstitial-like cells (39). Slug overexpression may activate ERK2 in the nucleus, decrease E-cadherin production, and enhance the incidence of EMT (40, 41). In this study, ZWINT protein expression in NSCLC was negatively connected with E-cadherin and strongly correlated with Vimentin and Slug proteins. It is hypothesized that elevated ZWINT expression may upregulate the Vimentin and Slug proteins and downregulate the E-cadherin protein, thereby promoting the occurrence of EMT. This plays a significant role in the metastasis and development of NSCLC.

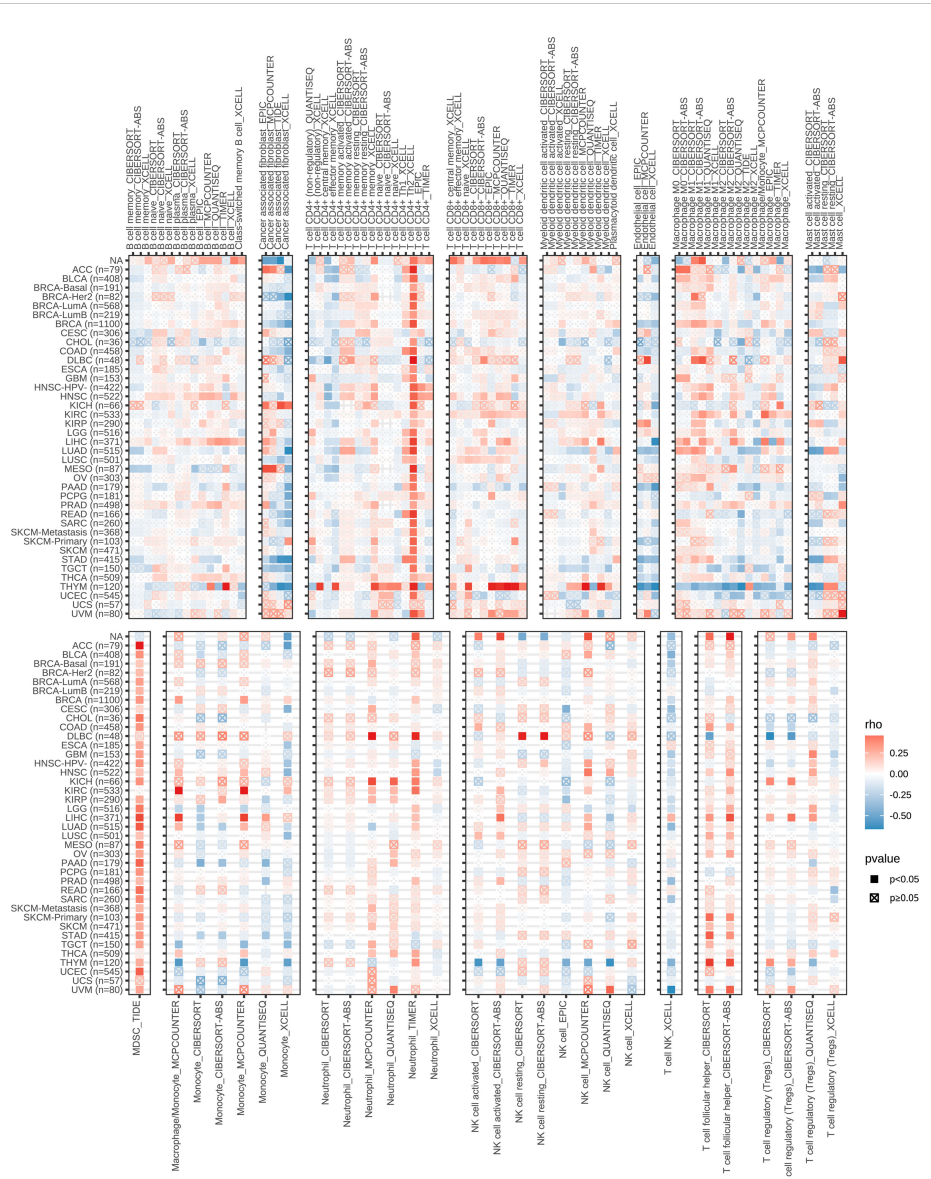

FIGURE 7
Correlation between the expression levels of ZWINT gene and immune cell infiltration in pan cancer. (Red to blue color represents high to low expression levels).

10.3389/fendo.2023.1147366

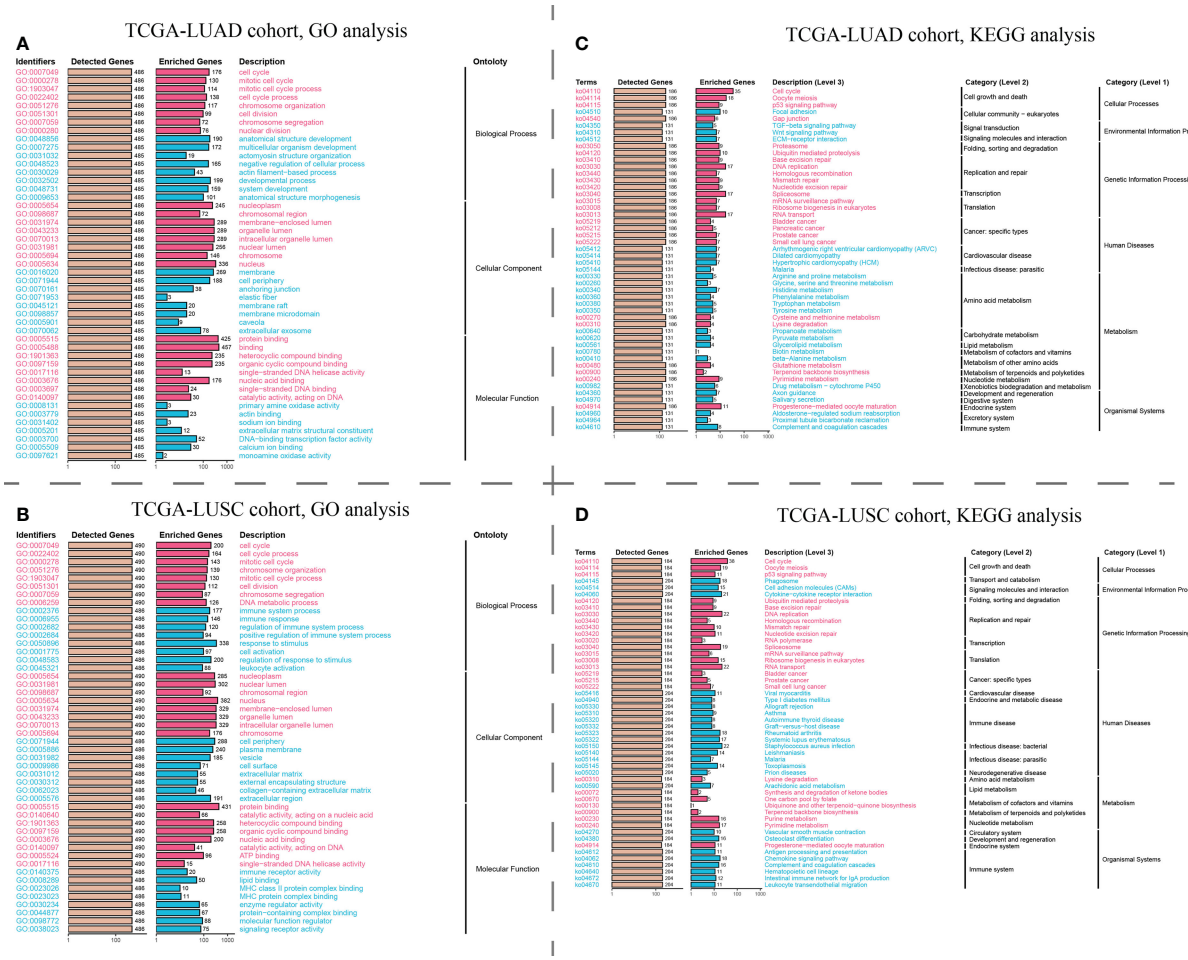

FIGURE 8
Pathway enrichment analysis of the hub ZWINT gene by GO and KEGG in LUAD and LUSU. **(A, B)** GO and KEGG analysis for investigating the relationship between the classic cancer pathways and the hub ZWINT gene in LUAD. **(C, D)** GO and KEGG analysis for evaluating the relationship between the classic cancer pathway and the hub ZWINT gene in LUSC.

10.3389/fendo.2023.1147366

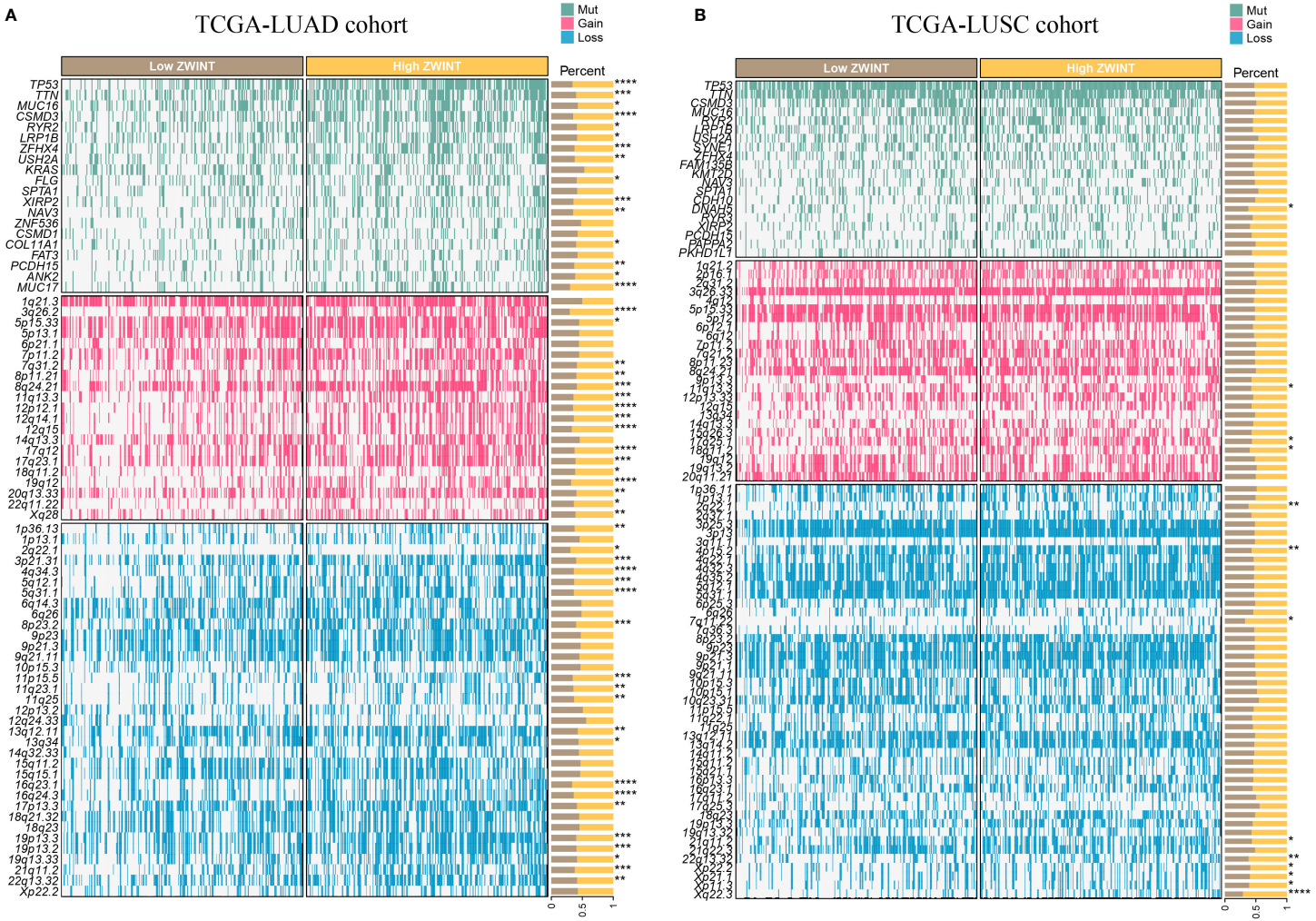

FIGURE 9
(A) Genomic mutation data of LUAD patients with varying ZWINT expression levels. **(B)** Genomic mutation data of LUSC patients with varying ZWINT expression levels. * indicates $p < 0.05$; ** indicates $p < 0.01$; *** indicates $p < 0.001$; and **** indicates $p < 0.0001$.

10.3389/fendo.2023.1147366

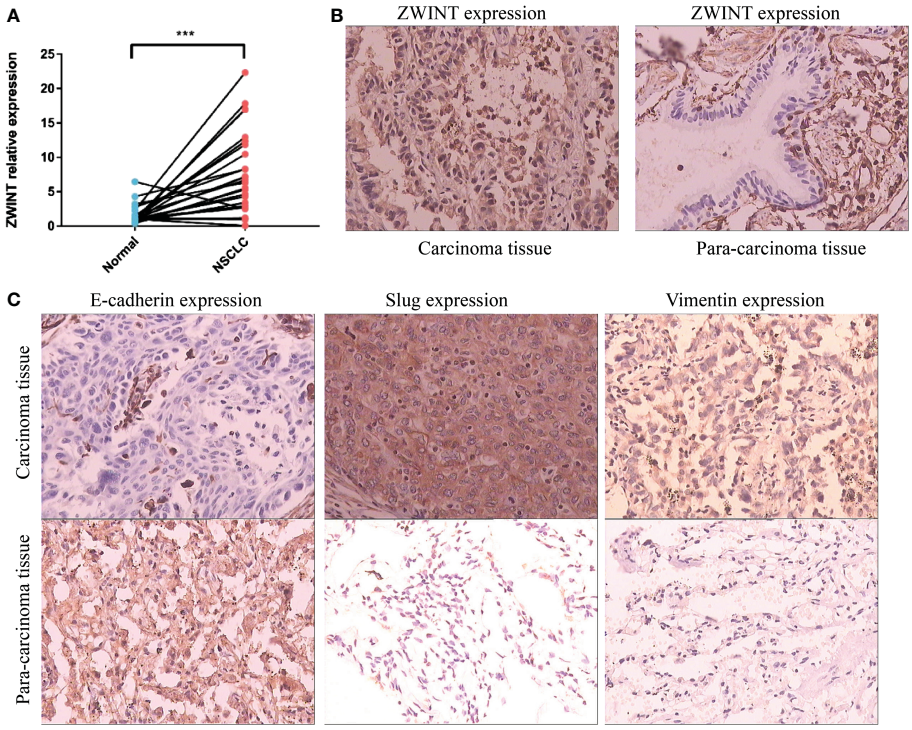

FIGURE 10
Expression validation of the ZWINT gene in NSCLC. **(A)** RT-qPCR analysis of 30 paired frozen cancerous and paracancerous tissues. **(B)** IHC experiments verified the expression levels of the ZWINT gene in cancerous and paracancerous tissues. **(C)** IHC experiments verified the expression levels of EMT pathway-associated markers in cancerous and paracancerous tissues. *** indicates $p < 0.001$.

TABLE 3 Protein expression of ZWINT in NSCLC and paracancer tissues (%).

Group	N	Protein expression levels of ZWINT		χ^2	p
		High(%)	Low(%)		
NSCLC	50	36(72%)	14(28%)	34.313	0.000
Para cancer	50	7(14%)	43(86%)		

Red value means that the p-value is less than 0.05, indicating statistical significance.

TABLE 4 Correlation between ZWINT and E-cadherin, Vimentin, and Slug protein expression (n).

ZWINT	E-cadherin		Vimentin		Slug	
	High	Low	High	Low	High	Low
High	13	22	23	13	26	10
Low	11	4	4	10	5	9
r	-0.332		0.318		0.338	
P	0.020		0.026		0.018	

Red values means that the p-value is less than 0.05, indicating statistical significance.

5 Conclusions

This study comprehensively characterized the pan-cancer cell cycle regulatory landscape for the first time. We successfully identified the molecular heterogeneity in patients with NSCLC based on the cell cycle activities. ZWINT has been proven to be significantly up-regulated in NSCLC tissues compared to paracancerous tissues, which might promote the progression of tumors through activation of the EMT pathway.

Data availability statement

The original contributions presented in the study are included in the article/Supplementary Material. Further inquiries can be directed to the corresponding author.

Ethics statement

The studies involving human participants were reviewed and approved by The Ethics Committee of the First Affiliated Hospital of Dalian Medical University. The patients/participants provided their written informed consent to participate in this study.

Author contributions

All the authors bear full responsibility for the content of this manuscript. All the authors were involved in the conception of this study, data gathering and analysis, manuscript drafting, and manuscript revision. All authors contributed to the article and approved the submitted version.

Acknowledgments

We thank Bullet Edits Limited for the linguistic editing of the manuscript.

Conflict of interest

The authors declare that the research was conducted in the absence of any commercial or financial relationships that could be construed as a potential conflict of interest.

Publisher's note

All claims expressed in this article are solely those of the authors and do not necessarily represent those of their affiliated organizations, or those of the publisher, the editors and the reviewers. Any product that may be evaluated in this article, or claim that may be made by its manufacturer, is not guaranteed or endorsed by the publisher.

Supplementary material

The Supplementary Material for this article can be found online at: https://www.frontiersin.org/articles/10.3389/fendo.2023.1147366/full#supplementary-material

SUPPLEMENTARY FIGURE 1
Venn diagram highlighting the shared differentially expressed cell cycle-related genes in both LUAD and LUSC cohorts.

SUPPLEMENTARY FIGURE 2
mRNA expression levels of ZWINT in different types of cancers **(A)** ZWINT expression traits in cancerous and normal samples based on the TCGA cohort. **(B)** ZWINT expression traits in cancerous and normal samples based on the TCGA and GTEx cohorts.

SUPPLEMENTARY FIGURE 3
Prognostic significance of ZWINT gene in pan cancer by univariate COX regression analysis.

SUPPLEMENTARY FIGURE 4
Overall survival of the ZWINT gene in pan cancer by KM analysis.

SUPPLEMENTARY FIGURE 5
Progression-free interval of ZWINT gene in pan cancer by KM analysis.

SUPPLEMENTARY FIGURE 6
Disease-specific survival of ZWINT gene in pan cancer by KM analysis.

SUPPLEMENTARY FIGURE 7
Disease-free interval of ZWINT gene in pan cancer by KM analysis.

SUPPLEMENTARY FIGURE 8
Relationship between the expression levels of ZWINT and immune checkpoints.

SUPPLEMENTARY FIGURE 9
Relationship between ZWINT and immunotherapy.

SUPPLEMENTARY FIGURE 10
Association of ZWINT expression with clinical characteristics of NSCLC patients.

SUPPLEMENTARY FIGURE 11
Association of ZWINT expression with **(A)** immune pathways, **(B)** metabolic pathways, and **(C)** cell death pathways in pan cancer.

References

1. Bray F, Ferlay J, Soerjomataram I, Siegel RL, Torre LA, Jemal A. Global cancer statistics 2018: GLOBOCAN estimates of incidence and mortality worldwide for 36 cancers in 185 countries. *CA Cancer J Clin* (2018) 68(6):394–424. doi: 10.3322/caac.21492

2. Torre LA, Siegel RL, Jemal A. Lung cancer statistics. *Adv Exp Med Biol* (2016) 893:1–19. doi: 10.1007/978-3-319-24223-1_1

3. Molina JR, Yang P, Cassivi SD, Schild SE, Adjei AA. Non-small cell lung cancer: Epidemiology, risk factors, treatment, and survivorship. *Mayo Clin Proc* (2008) 83 (5):584–94. doi: 10.1016/S0025-6196(11)60735-0

4. Chan GK, Jablonski SA, Starr DA, Goldberg ML, Yen TJ. Human Zw10 and ROD are mitotic checkpoint proteins that bind to kinetochores. *Nat Cell Biol* (2000) 2 (12):944–7. doi: 10.1038/35046598

5. Evan GI, Vousden KH. Proliferation, cell cycle and apoptosis in cancer. *Nature.* (2001) 411(6835):342–8. doi: 10.1038/35077213

6. Liu J, Peng Y, Wei W. Cell cycle on the crossroad of tumorigenesis and cancer therapy. *Trends Cell Biol* (2022) 32(1):30–44. doi: 10.1016/j.tcb.2021.07.001

7. Sherr CJ. Cancer cell cycles. *Science* (1996) 274(5293):1672–7. doi: 10.1126/science.274.5293.1672

8. Zangouei AS, Zangoue M, Taghehchian N, Zangooie A, Rahimi HR, Saburi E, et al. Cell cycle related long non-coding RNAs as the critical regulators of breast cancer progression and metastasis. *Biol Res* (2023) 56(1):1. doi: 10.1186/s40659-022-00411-4

9. Otto T, Sicinski P. Cell cycle proteins as promising targets in cancer therapy. *Nat Rev Cancer* (2017) 17(2):93–115. doi: 10.1038/nrc.2016.138

10. Hanahan D, Weinberg RA. Hallmarks of cancer: The next generation. *Cell* (2011) 144(5):646–74. doi: 10.1016/j.cell.2011.02.013

11. Loud JT, Murphy J. Cancer screening and early detection in the 21st century. *Semin Oncol Nurs* (2017) 33(2):121–8. doi: 10.1016/j.soncn.2017.02.002

12. Ren J, Zhang H, Wang J, Xu Y, Zhao L, Yuan Q. Transcriptome analysis of adipocytokines and their-related LncRNAs in lung adenocarcinoma revealing the association with prognosis, immune infiltration, and metabolic characteristics. *Adipocyte* (2022) 11(1):250–65. doi: 10.1080/21623945.2022.2064956

13. Liberzon A, Birger C, Thorvaldsdóttir H, Ghandi M, Mesirov JP, Tamayo P. The molecular signatures database (MSigDB) hallmark gene set collection. *Cell Syst* (2015) 1 (6):417–25. doi: 10.1016/j.cels.2015.12.004

14. Liberzon A, Subramanian A, Pinchback R, Thorvaldsdóttir H, Tamayo P, Mesirov JP. Molecular signatures database (MSigDB) 3. *0. Bioinf* (2011) 27 (12):1739–40. doi: 10.1093/bioinformatics/btr260

15. Tang Z, Li C, Kang B, Gao G, Li C, Zhang Z. GEPIA: A web server for cancer and normal gene expression profiling and interactive analyses. *Nucleic Acids Res* (2017) 45 (W1):W98–W102. doi: 10.1093/nar/gkx247

16. Yuan Q, Ren J, Wang Z, Ji L, Deng D, Shang D. Identification of the real hub gene and construction of a novel prognostic signature for pancreatic adenocarcinoma based on the weighted gene Co-expression network analysis and least absolute shrinkage and selection operator algorithms. *Front Genet* (2021) 12:692953. doi: 10.3389/fgene.2021.692953

17. Yuan Q, Zhang W, Shang W. Identification and validation of a prognostic risk-scoring model based on sphingolipid metabolism-associated cluster in colon adenocarcinoma. *Front Endocrinol (Lausanne)* (2022) 13:1045167. doi: 10.3389/fendo.2022.1045167

18. Yuan Q, Deng D, Pan C, Ren J, Wei T, Wu Z, et al. Integration of transcriptomics, proteomics, and metabolomics data to reveal HER2-associated metabolic heterogeneity in gastric cancer with response to immunotherapy and neoadjuvant chemotherapy. *Front Immunol* (2022) 13:951137. doi: 10.3389/fimmu.2022.951137

19. Chen X, Yuan Q, Liu J, Xia S, Shi X, Su Y, et al. Comprehensive characterization of extracellular matrix-related genes in PAAD identified a novel prognostic panel related to clinical outcomes and immune microenvironment: A silico analysis with *in vivo* and vitro validation. *Front Immunol* (2022) 13:985911. doi: 10.3389/fimmu.2022.985911

20. Hänzelmann S, Castelo R, Guinney J. GSVA: Gene set variation analysis for microarray and RNA-seq data. *BMC Bioinf* (2013) 14:7. doi: 10.1186/1471-2105-14-7

21. Yu G, Wang LG, Han Y, He QY. clusterProfiler: An r package for comparing biological themes among gene clusters. *OMICS* (2012) 16(5):284–7. doi: 10.1089/omi.2011.0118

22. Gu Z, Eils R, Schlesner M. Complex heatmaps reveal patterns and correlations in multidimensional genomic data. *Bioinformatics* (2016) 32(18):2847–9. doi: 10.1093/bioinformatics/btw313

23. Qi X, Che X, Li Q, Wang Q, Wu G. Potential application of pyroptosis in kidney renal clear cell carcinoma immunotherapy and targeted therapy. *Front Pharmacol* (2022) 13:918647. doi: 10.3389/fphar.2022.918647

24. Che X, Li J, Xu Y, Wang Q, Wu G. Analysis of genomes and transcriptomes of clear cell renal cell carcinomas identifies mutations and gene expression changes in the TGF-beta pathway. *Front Genet* (2022) 13:953322. doi: 10.3389/fgene.2022.953322

25. Li T, Fu J, Zeng Z, Cohen D, Li J, Chen Q, et al. TIMER2.0 for analysis of tumor-infiltrating immune cells. *Nucleic Acids Res* (2020) 48(W1):W509–14. doi: 10.1093/nar/gkaa407

26. Miao Y, Liu J, Liu X, Yuan Q, Li H, Zhang Y, et al. Machine learning identification of cuproptosis and necroptosis-associated molecular subtypes to aid in prognosis assessment and immunotherapy response prediction in low-grade glioma. *Front Genet* (2022) 13:951239. doi: 10.3389/fgene.2022.951239

27. Chen G, Luo D, Zhong N, Li D, Zheng J, Liao H, et al. GPC2 is a potential diagnostic, immunological, and prognostic biomarker in pan-cancer. *Front Immunol* (2022) 13:857308. doi: 10.3389/fimmu.2022.857308

28. Cui G, Wang C, Lin Z, Feng X, Wei M, Miao Z, et al. Prognostic and immunological role of ras-related protein Rap1b in pan-cancer. *Bioengineered* (2021) 12(1):4828–40. doi: 10.1080/21655979.2021.1955559

29. Chai D, Zhang L, Guan Y, Yuan J, Li M, Wang W. Prognostic value and immunological role of MORF4-related gene-binding protein in human cancers. *Front Cell Dev Biol* (2021) 9:703415. doi: 10.3389/fcell.2021.703415

30. Zhang L, Li M, Cui Z, Chai D, Guan Y, Chen C, et al. Systematic analysis of the role of SLC52A2 in multiple human cancers. *Cancer Cell Int* (2022) 22(1):8. doi: 10.1186/s12935-021-02432-7

31. Sharp DJ, Rogers GC, Scholey JM. Cytoplasmic dynein is required for poleward chromosome movement during mitosis in drosophila embryos. *Nat Cell Biol* (2000) 2 (12):922–30. doi: 10.1038/35046574

32. Wang HJ, Wang L, Lv J, Fu LQ, Wang Z, He XL, et al. Decreased expression of zwint-1 is associated with poor prognosis in hepatocellular carcinoma. *Int J Clin Exp Pathol* (2017) 10(10):10406–12.

33. Woo Seo D, Yeop You S, Chung WJ, Cho DH, Kim JS, Su Oh J. Zwint-1 is required for spindle assembly checkpoint function and kinetochore-microtubule attachment during oocyte meiosis. *Sci Rep* (2015) 5:15431. doi: 10.1038/srep15431

34. Ying H, Xu Z, Chen M, Zhou S, Liang X, Cai X. Overexpression of zwint predicts poor prognosis and promotes the proliferation of hepatocellular carcinoma by regulating cell-cycle-related proteins. *Onco Targets Ther* (2018) 11:689–702. doi: 10.2147/OTT.S152138

35. Endo H, Ikeda K, Urano T, Horie-Inoue K, Inoue S. Terf/TRIM17 stimulates degradation of kinetochore protein ZWINT and regulates cell proliferation. *J Biochem* (2012) 151(2):139–44. doi: 10.1093/jb/mvr128

36. Mou K, Zhang J, Mu X, Wang L, Liu W, Ge R. Zwint facilitates melanoma progression by promoting c-myc expression. *Exp Ther Med* (2021) 22(2):818. doi: 10.3892/etm.2021.10250

37. Kim JH, Youn Y, Lee JC, Kim J, Hwang JH. Involvement of the NF-κB signaling pathway in proliferation and invasion inhibited by zwint-1 deficiency in pancreatic cancer cells. *J Cancer* (2020) 11(19):5601–11. doi: 10.7150/jca.46173

38. Nieto MA. Epithelial plasticity: A common theme in embryonic and cancer cells. *Science* (2013) 342(6159):1234850. doi: 10.1126/science.1234850

39. Sinh ND, Endo K, Miyazawa K, Saitoh M. Ets1 and ESE1 reciprocally regulate expression of ZEB1/ZEB2, dependent on ERK1/2 activity, in breast cancer cells. *Cancer Sci* (2017) 108(5):952–60. doi: 10.1111/cas.13214

40. Serrano-Gomez SJ, Maziveyi M, Alahari SK. Regulation of epithelial-mesenchymal transition through epigenetic and post-translational modifications. *Mol Cancer* (2016) 15:18. doi: 10.1186/s12943-016-0502-x

41. Horiguchi K, Sakamoto K, Koinuma D, Semba K, Inoue A, Inoue S, et al. TGF-β drives epithelial-mesenchymal transition through δEF1-mediated downregulation of ESRP. *Oncogene* (2012) 31(26):3190–201. doi: 10.1038/onc.2011.493

frontiers | Frontiers in Endocrinology

TYPE Original Research
PUBLISHED 12 April 2023
DOI 10.3389/fendo.2023.1155307

OPEN ACCESS

EDITED BY
Ruiqin Han,
Institute of Basic Medical Sciences,
Chinese Academy of Medical Sciences,
China

REVIEWED BY
Monica Verrico,
Sapienza University of Rome, Italy
Bowen Chang,
Anhui Provincial Hospital, China

*CORRESPONDENCE
Hong Qiu
qiuhong@hust.edu.cn
Yan Luo
yanluo@hust.edu.cn

†These authors have contributed equally to this work

SPECIALTY SECTION
This article was submitted to Cancer Endocrinology, a section of the journal Frontiers in Endocrinology

RECEIVED 31 January 2023
ACCEPTED 28 March 2023
PUBLISHED 12 April 2023

CITATION
Xu L, Yang X, Xiang W, Hu P, Zhang X, Li Z, Li Y, Liu Y, Dai Y, Luo Y and Qiu H (2023) Development and validation of a contrast-enhanced CT-based radiomics nomogram for preoperative diagnosis in neuroendocrine carcinoma of digestive system.
Front. Endocrinol. 14:1155307.
doi: 10.3389/fendo.2023.1155307

Development and validation of a contrast-enhanced CT-based radiomics nomogram for preoperative diagnosis in neuroendocrine carcinoma of digestive system

Liang Xu[1], Xinyi Yang[1], Wenxuan Xiang[2], Pengbo Hu[1], Xiuyuan Zhang[1], Zhou Li[1], Yiming Li[1], Yongqing Liu[1], Yuhong Dai[1], Yan Luo[3*†] and Hong Qiu[1*†]

[1]Department of Oncology, Tongji Hospital, Tongji Medical College, Huazhong University of Science and Technology, Wuhan, China, [2]Department of Otolaryngology-Head and Neck Surgery, Tongji Hospital, Tongji Medical College, Huazhong University of Science and Technology, Wuhan, China, [3]Department of Radiology, Tongji Hospital, Tongji Medical College, Huazhong University of Science and Technology, Wuhan, China

Objectives: To develop and validate a contrast-enhanced CT-based radiomics nomogram for the diagnosis of neuroendocrine carcinoma of the digestive system.

Methods: The clinical data and contrast-enhanced CT images of 60 patients with pathologically confirmed neuroendocrine carcinoma of the digestive system and 60 patients with non-neuroendocrine carcinoma of the digestive system were retrospectively collected from August 2015 to December 2021 at Tongji Hospital, Tongji Medical College, Huazhong University of Science and Technology, and randomly divided into a training cohort (n=84) and a validation cohort (n=36). Clinical characteristics were analyzed by logistic regression and a clinical diagnosis model was developed. Radiomics signature were established by extracting radiomic features from contrast-enhanced CT images. Based on the radiomic signature and clinical characteristics, radiomic nomogram was developed. ROC curves and Delong's test were used to evaluate the diagnostic efficacy of the three models, calibration curves and application decision curves were used to analyze the accuracy and clinical application value of nomogram.

Results: Logistic regression results showed that TNM stage (stage IV) (OR 6.8, 95% CI 1.320-43.164, p=0. 028) was an independent factor affecting the diagnosis for NECs of the digestive system, and a clinical model was constructed based on TNM stage (stage IV). The AUCs of the clinical model, radiomics signature, and radiomics nomogram for the diagnosis of NECs of the digestive system in the training, validation cohorts and pooled patients were 0.643, 0.893, 0.913; 0.722, 0.867, 0.932 and 0.667, 0.887, 0.917 respectively. The AUCs of radiomics signature and radiomics nomogram were higher than clinical model, with statistically significant difference (Z=4.46, 6.85, both $p < 0.001$); the AUC difference between radiomics signature and radiomics nomogram was not

statistically significant (Z=1.63, p = 0.104). The results of the calibration curve showed favorable agreement between the predicted values of the nomogram and the pathological results, and the decision curve analysis indicated that the nomogram had favorable application in clinical practice.

Conclusions: The nomogram constructed based on contrast-enhanced CT radiomics and clinical characteristics was able to effectively diagnose neuroendocrine carcinoma of the digestive system.

KEYWORDS

radiomics, contrast-enhanced CT, neuroendocrine carcinoma, diagnosis model, digestive system

Introduction

Neuroendocrine neoplasms (NENs) are rare tumors arising from neuroendocrine cells and peptidergic neurons, which are characterized by secreting biogenic amines and various peptide hormones (1). They can develop in almost any organ of the body, mainly in the digestive and respiratory systems, such as the esophagus, gastroenteropancreas and lung tissues, and the biology of the disease is highly heterogeneous (2). Although relatively rare, the incidence of NENs has been increasing, with a more than 6-fold increase over a 40-year period, particularly in the digestive system (3). The latest 2019 WHO guidelines classified NENs into poorly differentiated and highly aggressive neuroendocrine cancers (NECs) and highly differentiated and inert neuroendocrine tumors (NETs) based on mitotic rate and Ki-67 index (4).

Due to the unspecific clinical symptoms of NECs of digestive system, it is prone to misdiagnose NECs as adenocarcinomas or squamous carcinomas before surgery in clinical practice. The low-differentiated digestive system NECs are highly malignant and aggressive, and most patients have distant metastasis at the time of diagnosis (5). For patients with combined distant metastasis, surgery does not benefit due to the rapidly progressive biology of NECs, and platinum-based chemotherapy is the primary recommended first-line treatment option. In the case of locally advanced non-NECs such as adenocarcinomas or squamous carcinomas of the digestive system, surgery is still an important treatment modality. In addition, the prognosis of NECs is also significantly worse compared to non-NECs. If the tumor can be diagnosed preoperatively, it will be beneficial to select a more suitable treatment modality and judge the prognosis. Currently, NECs in the digestive system are clearly diagnosed by postoperative pathological findings, and there is still a lack of effective and definitive methods for preoperative diagnosis. Therefore, exploring an effective new method for preoperative diagnosis is crucial for clinical practice.

Contrast-enhanced CT is one of the most common and important imaging examinations for diagnosing tumor of the digestive system. Medical images contain a large amount of invisible data, and it is the value of radiomics to reveal these invisible disease features. Radiomics has been defined as the use of mathematical algorithms to transform the underlying pathophysiological information contained in medical images into quantitative, high-dimensional image features and to explore the correlation of these image features with clinical outcomes or biological properties (6, 7). When radiomics is applied to cancer research, it is possible to characterize the imaging of tumor patients non-invasively, quantify the heterogeneity between tissues, describe the microenvironment of the tumor, assess the effectiveness of treatment, and predict survival after obtaining radiological images by CT, MRI, and other examination methods (8, 9).

In recent years, radiomics has been gradually and widely used in the diagnosis of cancers (10), identification of molecular typing of tumors (11), prediction of survival status of patients (12), and the use of imaging genomics to analyze the relationship between imaging features and genomic features to dissect tumor heterogeneity (13). Radiomics studies targeting NETs are also increasing, and radiomics can be applied in the diagnosis of pancreatic NETs (14), predicting the grading of pancreatic NETs (15), determining the prognosis of NETs (16), and assessing the effects of drug therapy for NETs (17). However, there are few radiomics studies for NECs, *Wang* et al. (18) identified gastric NECs from gastric adenocarcinoma with CT radiomics. To our knowledge, there are no radiomics studies for other digestive system NECs such as esophageal, intestinal and pancreatic. Therefore, we aim to conduct a study to extract tumor radiomics features based on contrast-enhanced CT images and construct a nomogram in combination with clinicopathological characteristics to diagnose NECs of the digestive system before surgery.

Materials and methods

Patients

This retrospective study was approved by the Medical Ethics Review Committee of Tongji Hospital, Tongji Medical College, Huazhong University of Science and Technology, and written consent was waived. The inclusion criteria were as follows: patients with pathological diagnosis of esophageal or gastroenteropancreatic

NEC by surgery or biopsy; CT examination within 2 weeks before surgery or biopsy. The exclusion criteria were as follows: receiving the corresponding treatment before the contrast-enhanced CT examination; No contrast-enhanced CT examination or unavailability of contrast-enhanced CT image data; poor image quality affecting image segmentation and evaluation.

A total of 177 patients pathologically-diagnosed NECs of the digestive system from August 2015 to December 2021 were identified from the hospital database. According to the above inclusion and exclusion criteria, 60 patients with NEC of the digestive system were finally included, including 23 esophageal NECs, 22 gastric NECs, 6 intestinal NECs, and 9 pancreatic NECs. The same number of adenocarcinomas or squamous carcinomas of the digestive system at the same sites were systematically sampled and matched as a control group for NECs. Patients were randomized in a 7:3 ratio into a training cohort (n=84) and a validation cohort (n=36) (Supplementary Figure 1).

Image acquisition

All 120 patients underwent contrast-enhanced CT examination within 2 weeks before surgery or biopsy using a 64-slice MDCT system (Discovery C750 HD, GE Healthcare). Patients were trained to breathe and hold their breath before the scanning examination. The patient was advised to be in a supine position during the examination, and the patient was told to over-supine the neck and lower the shoulders as much as possible during the scan and avoid swallowing movements.

Contrast-enhanced CT scans were performed by injecting non-ionic iodinated contrast agent Iopromide (Ultravist, Bayer Healthcare, Wayne, NJ, iodine concentration of 370 mg/mL) at a flow rate of 3.0-3.5 mL/s *via* the anterior elbow vein. Contrast-enhanced chest CT was acquired 15 seconds after injection. Bolus tracking technique was used for contrast-enhanced abdominal CT and arterial phase was automatically triggered 5-8 seconds after the attenuation of abdominal aorta reached 150 HU. The main scanning parameters were as follows: tube voltage 100-120 kV, rotation time 0.5- 0.6 s, tube current 200-350 mA, and slice thickness 5 mm. The acquired raw data were reconstructed to a slice thickness of 1.25 mm and exported in DICOM format for analysis.

Image segmentation and radiomics feature extraction

On the picture archiving and communication system, two experienced radiologists reviewed the contrast-enhanced CT images and discussed together to determine the tumor location with reference to endoscopy and other findings. Arterial phase images of the contrast-enhanced CT were used for image segmentation and radiomics feature extraction. Segmentation was performed by two experienced oncologist and radiologist who were blind to clinical information according to the tumor location recorded by the two radiologists. The 3D Slicer image computing platform (version 5.0.3) software was used to manually segment the 3D volume of interest (VOI) of the entire tumor, and the cystic or necrotic areas were avoided during the segmentation.

A total of 107 features, including First order features, Shape features (3D), Shape features (2D), Gray level co-occurrence matrix (GLCM) features, Gray level size zone matrix (GLSZM) features, Gray level run length matrix (GLRLM) features, Neighbouring gray tone difference matrix (NGTDM) features and Gray level dependence matrix (GLDM) features were extracted using the "Slicer Radiomics" extension package of 3D Slicer software. To determine the intra- and inter-reader reproducibility of radiomics features, 20 randomly-selected cases were segmented by the oncologist after a period of 1 month and by radiologist with 5 years of experience.

Radiomics feature selection and radiomics signature development

Radiomics features extracted from the images were subjected to Z-score normalization. Intraclass correlation coefficients (ICC) were calculated and features with ICC > 0.75 in intra- and inter-reader reproducibility tests were considered reproducible and include in feature selection. In the R software (version 4.2.0, http://www.r-project.org), the least absolute shrinkage and selection operator (LASSO) logistic regression algorithm using the "glmnet" package was used to select features that were closely associated with the diagnosis of NECs of the digestive system. The features in the training cohort that were strongly correlated with the diagnosis of NECs of the digestive system were screened by a 10-fold cross-validation.

Based on the linear combination of the screened features and their correlation coefficients, radiomics score (Rad-score) was calculated. Receiver operating characteristic (ROC) curves were plotted to analyze the efficacy of radiomics signature for diagnosing NEC of the digestive system.

Clinical model and clinical-radiomics model development

Clinical characteristics including age, gender, TNM stage, preoperative CEA and preoperative CA199 were compared between NECs and non-NECs of the digestive system, and factors with statistical significance were further included into multivariable logistic regression analysis to establish a clinical model.

The clinical features associated with the diagnosis of NECs were combined with radiomics signature using multivariable logistic regression analysis to build a clinical-radiomics model, and a nomogram based on these clinical-radiomics model was also built. ROC curves were plotted to assess the discrimination of the models, and Delong's test was used to compare the area under the curve of different models. Calibration curves were used to estimate the accuracy of the nomogram, and decision curve analysis (DCA) was used to assess the clinical utility of the nomogram.

Statistical analysis

All statistical analyses were performed in R software. The χ^2 test was used for the comparison of categorical data, and the t-test was used for the comparison of quantitative data. The "Glm" package of the R software package was used for logistic regression analysis, the "Glmnet" package was used for LASSO regression algorithm analysis, and the "pROC" package was used for ROC curves plotting. The calibration curve and DCA were executed using the "Rms" and "rmda" packages, respectively. The differences were statistically significant at $p<0.05$.

Results

Patient characteristics and clinical model construction and validation

There were 84 patients in the training cohort, among which 42 were NECs and 42 were non-NECs; there were 36 patients in the validation cohort, among which 18 were NECs and 18 were non-NECs. In the training and validation cohorts, the differences in TNM stage between the NEC and non-NEC groups were statistically significant ($p<0.05$), while the differences in clinical characteristics such as age, gender, preoperative CEA and CA199 were not statistically significant (all $p>0.05$), as shown in Table 1. In the training cohort, logistic regression was performed on TNM stage, and the results showed that only TNM stage (stage IV) (OR 6.8, 95%CI 1.320-43.164, $p=0.028$) was an independent factor for the diagnosis of NECs, and the variables and coefficients of the clinical model are shown in Supplementary Table 1. The clinical model was constructed from TNM stage (stage IV).

The ROC curves of the clinical models in the training and validation cohorts were plotted (Figure 1). In the training cohort, the AUC of the clinical model for diagnosing NECs is 0.643 (95%CI 0.553-0.733), the sensitivity is 0.405, the specificity is 0.881. In the validation cohort, the AUC of the clinical model for diagnosing NECs is 0.722 (95%CI 0.592-0.853), the sensitivity is 0.500, the specificity is 0.944.

Radiomics signature construction and validation

A total of 107 radiomics features were extracted, and the consistency assessment showed that the ICC of all radiomics features was >0.75. The best radiomics features with six non-zero coefficients in the training cohort were determined by the LASSO regression algorithm (Figure 2) to be closely related to the diagnosis of NECs, and the best value of the LASSO adjustable parameter (λ) was 0.092. These six radiomics features and their corresponding coefficients were linearly combined to construct the radiomics signature with the following equation: Rad-score= 0.00885470+ (0.15453837 × LeastAxisLength) – (0.18987915 × SurfaceVolume Ratio) – (0.10557837 × Uniformity) + (0.15860176 × Inverse Variance) + (0.35593795 ×MCC) + (0.11645836 × Large DependenceLowGrayLevelEmphasis).

The ROC curves were plotted for the Radiomics signature (Figure 3). In the training cohort, the AUC of the radiomics signature for diagnosing NECs is 0.893 (95%CI 0.822-0.965), the

TABLE 1 Patient clinical characteristics in the training and validation cohorts.

Characteristics	Training cohort			Validation cohort		
	NEC	Non-NEC	*p*-value	NEC	Non-NEC	*p*-value
Age(year), mean ± SD	64.02 ± 9.02	56.24 ± 9.69	0.606	62.72 ± 11.21	56.83 ± 9.488	0.762
Sex			0.503			1.000
Female	27	24		3	3	
Male	15	18		15	15	
CEA*(ng/ml)			0.357			1.000
<5	27	35		10	12	
≥5	8	6		4	4	
CA199*(u/ml)			0.281			0.426
<37	29	32		12	10	
≥37	2	6		1	4	
TNM			0.012			0.014
I	3	6		1	1	
II	8	17		6	10	
III	14	14		2	6	
IV	17	5		9	1	

*represents the presence of missing values.

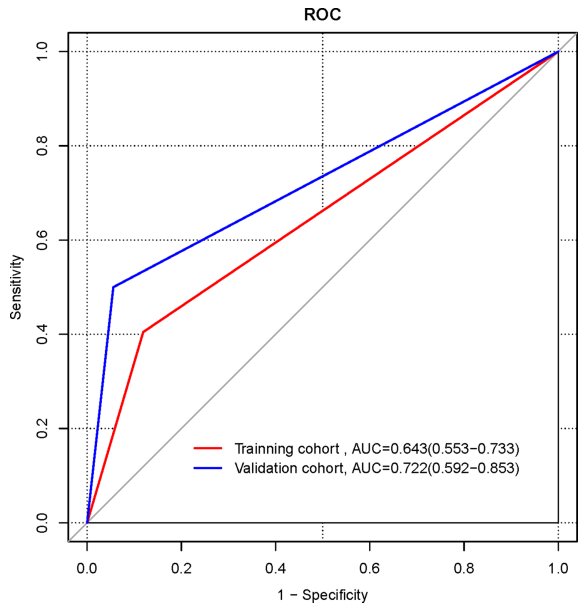

FIGURE 1
ROC curves of clinical model in the training and validation cohorts.

sensitivity is 0.833, the specificity is 0.833. In the validation cohort, the AUC of the radiomics signature for diagnosing NECs is 0.867 (95%CI 0.751-0.983), the sensitivity is 0.889, the specificity is 0.778.

Nomogram construction and validation

Logistic regression analysis showed that both radiomics signature (OR 56.869, 95% CI 11.354-471.239, p<0.001) and TNM stage (stage IV) (OR 5.03, 95% CI 1.741-16.937, p=0.005) were independent predictors for the diagnosis of NECs of the digestive system, and a combined clinical-radiomics diagnostic model containing these two predictors was constructed to generate a radiomics nomogram(Figure 4).

The ROC curves were plotted for the nomogram (Figure 5). In the training cohort, the AUC of the radiomics nomogram for diagnosing NECs is 0.913 (95%CI 0.849-0.976), the sensitivity is 0.833, the specificity is 0.833. In the validation cohort, the AUC of the radiomics nomogram for diagnosing NECs is 0.932 (95%CI 0.857-1.000), the sensitivity is 1.000, the specificity is 0.722.

The ROC curves were plotted for the clinical model, radiomics signature, and radiomics nomogram in the pooled population (Figure 6). The AUC of the clinical model for diagnosing NECs is 0.667 (95%CI 0.593-0.741), the sensitivity is 0.433, the specificity is 0.9. the AUC of the radiomics signature for diagnosing NECs is 0.887 (95% CI 0.828-0.946), the sensitivity is 0.867, the specificity is 0.783. the AUC of the radiomics nomogram for diagnosing NECs is 0.917 (95%CI 0.867-0.967), the sensitivity is 0.833, the specificity is 0.85. The diagnosis performance of three models in the training and validation cohort is shown in Supplementary Table 2.

Delong's test was used to compare the significance of the AUCs of the three different models. The results showed that the AUC of the radiomics signature and the radiomics nomogram were higher than those of the clinical model, and the differences were statistically significant (Z=4.46, 6.85, both p<0.001); the difference in the AUC of the radiomics signature and the radiomics nomogram were not statistically significant (Z=1.63, p =0.104).

Calibration curves were developed to verify the discriminative efficacy of the nomogram, and the mean absolute error of the calibration curves for the training cohort was 0.017 (Figure 7A); the mean absolute error of the calibration curves for the validation cohort was 0.06 (Figure 7B). The calibration curve was close to the ideal curve, which indicated that the prediction of the constructed nomogram for the diagnosis of NECs of the digestive system fitted well with the actual results.

DCA was used to verify the value of the nomogram for clinical applications, and the results showed that in the training cohort, DCA in the 4%-99% threshold range was more effective in diagnosing NECs using radiomics signature or radiomics

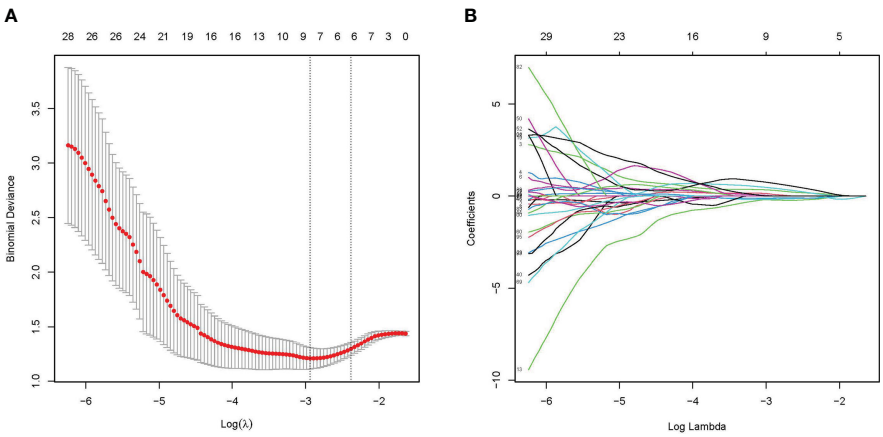

FIGURE 2
Radiomics feature selected by LASSO regression algorithm. **(A)** Plotting of multinomial deviance versus log(λ). **(B)** LASSO coefficient profiles of the radiomics features.

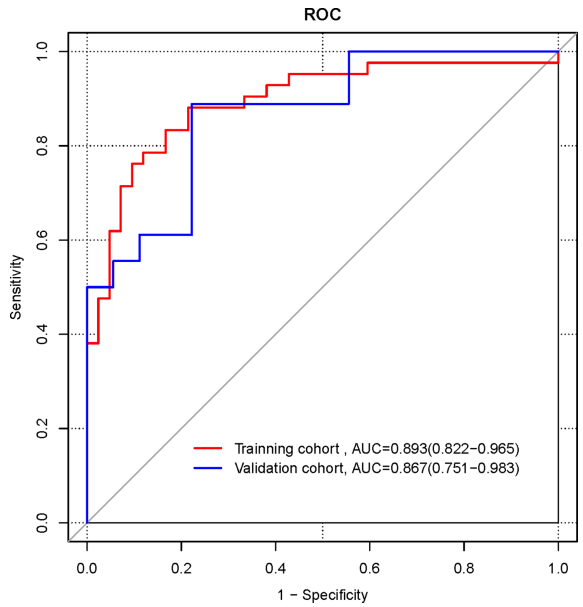

FIGURE 3
ROC curves of radiomics signature in the training and validation cohorts.

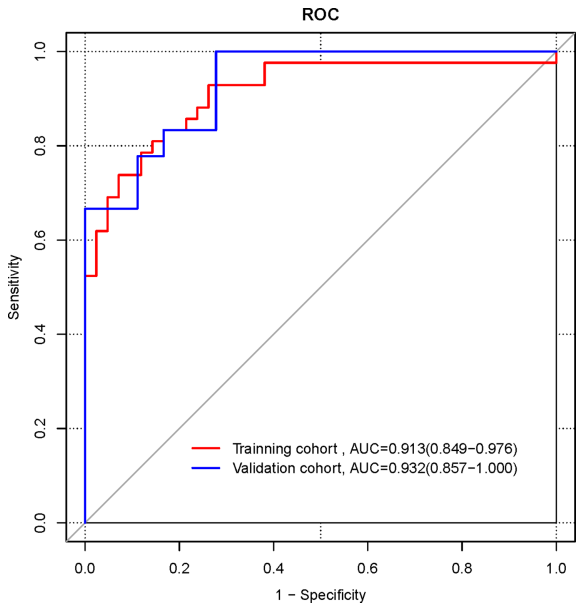

FIGURE 5
ROC curves of radiomics nomogram in the training and validation cohorts.

nomogram than using clinical model (Figure 8A). In the validation cohort, DCA in the 1%-35%, 37%-39%, and 69%-99% threshold range was more effective in diagnosing NECs using radiomics signature than using clinical model, DCA in the 1%-99% threshold range was more effective in diagnosing NECs using radiomics nomogram than using clinical model (Figure 8B). This suggested that radiomics signature or radiomics nomogram had great clinical application.

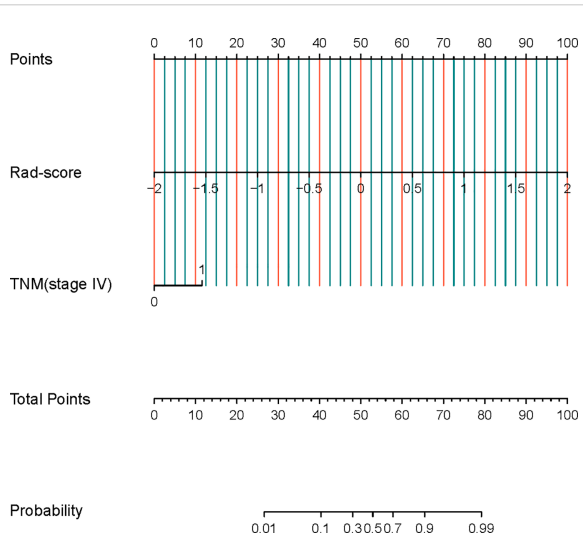

FIGURE 4
Radiomics nomogram constructed based on clinical model and radiomics signature.

Discussion

In this study, we developed and validated a new radiomics nomogram for preoperative diagnosis of NECs and non-NECs in the digestive system. The radiomics nomogram, which combines radiomic signature and TNM stage (stage IV), could be an effective method diagnosing NECs of the digestive system.

Due to the significant differences in treatment and prognosis between NECs and non-NECs, preoperative diagnosis is significant for the treatment options and prognosis of patients. At present, there is still a lack of effective methods. CT examination is an important examination for the diagnosis of cancer, which can not only detect cancer lesions but is also essential for the clinical staging of cancer (19), and contrast-enhanced CT will be more obvious. Contrast-enhanced CT is largely able to reflect the status of microcirculation inside the cancer, which could understand the differences between different cancers and judge the nature of the cancer (20, 21). The internal blood supply is overly adequate in most NECs (22), which means that it is possible to detect differences between NECs and non-NECs by contrast-enhanced CT, and contrast-enhanced CT is potentially an effective tool for diagnosing NECs.

Radiomics has a good application in the diagnosis of cancer by extracting information from the inner data of CT and MRI images, and the image features reflect the underlying pathophysiological changes to a certain extent, which can reflect the internal heterogeneity of cancers noninvasively and at low cost (23, 24). Radiomics analysis has also shown good clinical value in NETs.

Clinical characteristics of age, gender, TNM stage, preoperative CEA and preoperative CA199 were included in this study to explore the role of clinical characteristics in the diagnosis for NECs of the digestive system. The results showed that TNM stage (stage IV) was an independent predictor for the diagnosis of NECs. Stage IV

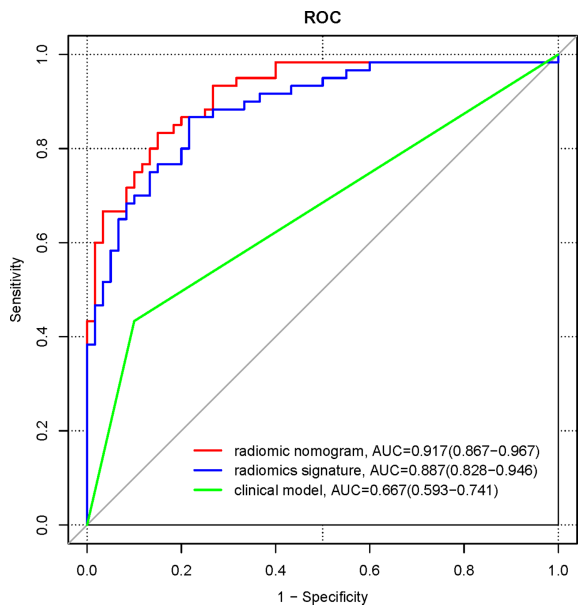

FIGURE 6
ROC curves for clinical model, radiomics signature, and radiomics nomogram in the pooled population.

indicated a higher possibility of diagnosis of NECs. This is consistent with the biological characteristics of NECs, which is highly malignant, with the majority having developed distant metastases at the time of diagnosis (5), and has mostly developed into stage IV at the time of diagnosis. However, we constructed clinical models with relatively low AUCs developed from TNM stage (stage IV) in the training cohort, validation cohort, and pooled population, 0.643, 0.722, and 0.691, respectively, suggesting the relatively limited predictive value of clinical model.

In this study, six radiomics features, including LeastAxisLength, SurfaceVolumeRatio, Uniformity, InverseVariance, MCC and LargeDependenceLowGrayLevelEmphasis were screened to obtain. Among them, 1 for First Order Features, 2 for Shape Features (3D), 2 for GLCM, and 1 for GLDM. The First Order Features are mainly based on histogram analysis and are used to depict the texture features associated with the gray frequency distribution within the Region of Interest (ROI) (25). In this study, Uniformity belongs to the First Order Features, which describes the image consistency of the ROI. Shape Features (3D) include features describing the size of the ROI and the similarity to a sphere. In this study, LeastAxisLength and SurfaceVolumeRatio belong to Shape Features (3D), which describe the minimum axis length as well as the volume of the ROI. Previous studies have shown that GLCM features are closely related to clinicopathology and can be used to assess the gray-level spatial dependence of ROI as well as to reflect tumor heterogeneity (26). InverseVariance and MCC in this study belong to GLCM features and the texture features derived from them are correlated with the diagnosis of NECs. This is the same as the findings of *Karahaliou* et al. (27) and *Yang* et al. (28) in breast and liver cancers, that GLCM features are sensitive indicators of tumor heterogeneity, and the use of GLCM features can improve the accuracy of diagnosis. GLDM features can also reflect tumor heterogeneity to some extent (29). LargeDependenceLowGrayLevelEmphasis in this study belongs to GLDM features, which can quantify the image grayscale correlation of ROI.

The results of the radiomics nomogram show that the AUC of the ROC curves of the radiomics signature or the radiomics nomogram is higher than the AUC of the ROC curves of the clinical model, and the differences are statistically significant. This implies that contrast-enhanced CT and TNM stage (stage IV) can successfully identify patients with NECs of the digestive system, demonstrating the value of radiomics signature or radiomics nomogram to identify NECs of the digestive system. This can provide a reliable basis for treatment options on the one hand, and a valuable judgment on the prognosis of patients on the other hand. The difference in the AUC of the ROC curves of the radiomics nomogram and the radiomics signature is not statistically significant. This suggests that TNM stage (stage IV) has little role in improving the diagnostic efficacy of NECs of the digestive system and that radiomic signature is more prominent for the diagnostic value of NECs of the digestive system. In addition, the nomogram

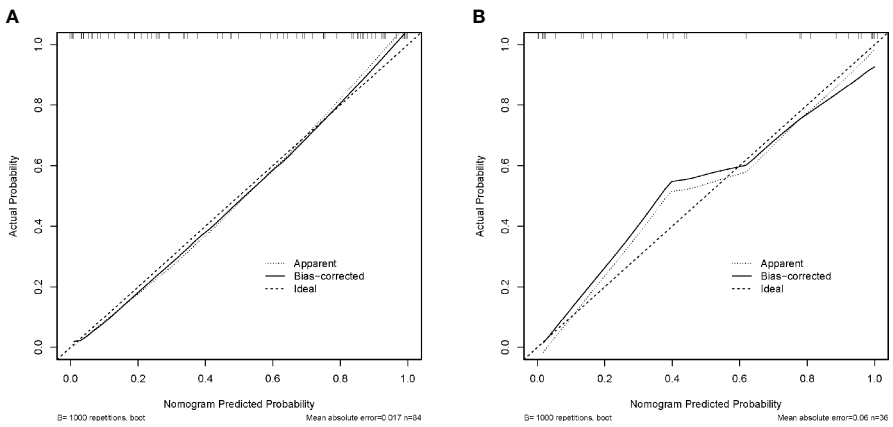

FIGURE 7
Calibration curves of the nomogram in the training **(A)** and validation **(B)** cohorts.

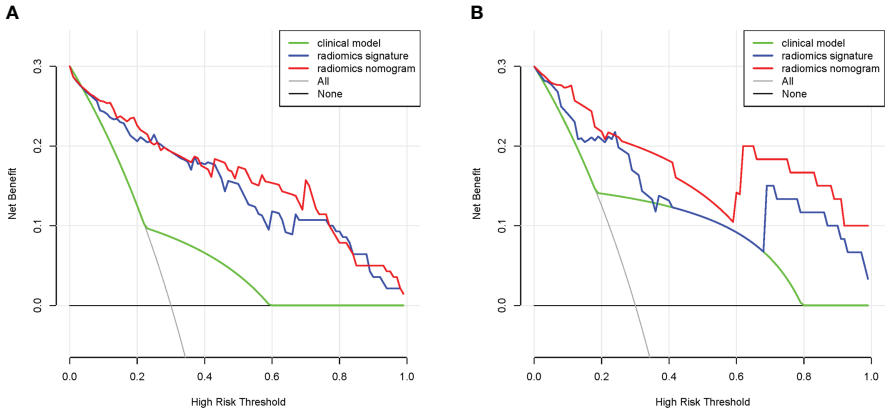

FIGURE 8
DCA of the nomogram in the training **(A)** and validation **(B)** cohorts.

developed in this study is easy to use and can be used as a tool for individualized preoperative diagnostic prediction of patients.

However, some limitations are inevitable in this study: first, this study was conducted on a malignancy of relatively rare incidence and was a single-center retrospective study with not particularly sufficient cases. Given the great clinical applicability of our findings for the diagnosis of NECs of the digestive system, the next step could be a large-sample multicenter study with more external validation of the constructed model. Second, there was sample selection bias in the retrospective study. Third, clinical characteristics such as age, gender, TNM stage, preoperative CEA and CA199 were included, and the study showed that only TNM stage (stage IV) was associated with the diagnosis for NECs of the digestive system, but the final diagnostic efficacy of the clinical model was still limited, and further exploration with a larger sample of clinical data may be needed in the future. Meanwhile, markers of neuroendocrine differentiation, such as chromogranin A (CgA), neuron-specific enolase (NSE) and synaptophysin (SYP) could be included in the future to allow a more comprehensive analysis of the diagnostic value of clinicopathological features for NECs of the digestive system (30). In addition, this study explored the diagnostic value of contrast-enhanced CT radiomics for NECs of the digestive system, and functional imaging examinations such as somatostatin receptor imaging and 18F-FDG-PET/CT (31) could be included in the future to more systematically assess the diagnostic value of preoperative radiomics for NECs of the digestive system.

In conclusion, we developed a radiomics nomogram that combined radiomics signature and clinical characteristics to effectively diagnose NECs of the digestive system. The nomogram was validated by multiple methods and showed great predictive ability. We expect that the radiomics nomogram can be used as a potential tool to diagnose these patients.

Data availability statement

The original contributions presented in the study are included in the article/Supplementary Material. Further inquiries can be directed to the corresponding authors.

Author contributions

All authors contributed to data analysis, drafting or revising the article, have agreed on the journal to which the article will be submitted, gave final approval of the version to be published, and agree to be accountable for all aspects of the work. All authors contributed to the article and approved the submitted version.

Funding

This study was supported by the National Natural Science Foundation of China (81372664).

Conflict of interest

The authors declare that the research was conducted in the absence of any commercial or financial relationships that could be construed as a potential conflict of interest.

Publisher's note

All claims expressed in this article are solely those of the authors and do not necessarily represent those of their affiliated organizations, or those of the publisher, the editors and the reviewers. Any product that may be evaluated in this article, or claim that may be made by its manufacturer, is not guaranteed or endorsed by the publisher.

Supplementary material

The Supplementary Material for this article can be found online at: https://www.frontiersin.org/articles/10.3389/fendo.2023.1155307/full#supplementary-material

References

1. Marotta V, Zatelli MC, Sciammarella C, Ambrosio MR, Bondanelli M, Colao A, et al. Chromogranin a as circulating marker for diagnosis and management of neuroendocrine neoplasms: more flaws than fame. *Endocr Relat Cancer* (2018) 25(1): R11–29. doi: 10.1001/jamaoncol.2019.4568

2. Chauhan A, Kohn E, Del Rivero J. Neuroendocrine tumors-less well known, often misunderstood, and rapidly growing in incidence. *JAMA Oncol* (2020) 6(1):21–2. doi: 10.1001/jamaoncol.2019.4568

3. Dasari A, Shen C, Halperin D, Zhao B, Zhou S, Xu Y, et al. Trends in the incidence, prevalence, and survival outcomes in patients with neuroendocrine tumors in the united states. *JAMA Oncol* (2017) 3(10):1335–42. doi: 10.1001/jamaoncol.2017.0589

4. Nagtegaal ID, Odze RD, Klimstra D, Paradis V, Rugge M, Schirmacher P, et al. WHO classification of tumours editorial board. the 2019 WHO classification of tumours of the digestive system. *Histopathology* (2020) 76(2):182–8. doi: 10.1111/his.13975

5. Garcia-Carbonero R, Sorbye H, Baudin E, Raymond E, Wiedenmann B, Niederle B, et al. Vienna Consensus conference participants. ENETS consensus guidelines for high-grade gastroenteropancreatic neuroendocrine tumors and neuroendocrine carcinomas. *Neuroendocrinology* (2016) 103(2):186–94. doi: 10.1159/000443172

6. Wang Q, Xu J, Wang A, Chen Y, Wang T, Chen D, et al. Systematic review of machine learning-based radiomics approach for predicting microsatellite instability status in colorectal cancer. *Radiol Med* (2023) 128(2):136–48. doi: 10.1007/s11547-023-01593-x

7. Lambin P, Leijenaar RTH, Deist TM, Peerlings J, Jong D, Timmeren J, et al. Radiomics: the bridge between medical imaging and personalized medicine. *Nat Rev Clin Oncol* (2017) 14:749–62. doi: 10.1038/nrclinonc.2017.141

8. Lin P, Lin YQ, Gao RZ, Wan WJ, He Y, Yang H. Integrative radiomics and transcriptomics analyses reveal subtype characterization of non-small cell lung cancer. *Eur Radiol* (2023). doi: 10.1007/s00330-023-09503-5

9. Khorrami M, Khunger M, Zagouras A, Patil P, Thawani R, Bera K, et al. Combination of peri- and intratumoral radiomic features on baseline CT scans predicts response to chemotherapy in lung adenocarcinoma. *Radiol Artif Intell* (2019) 1(2):180012. doi: 10.1148/ryai.2019180012

10. Hunter B, Chen M, Ratnakumar P, Alemu E, Logan A, Linton-Reid K, et al. A radiomics-based decision support tool improves lung cancer diagnosis in combination with the herder score in large lung nodules. *EBioMedicine* (2022) 86:104344. doi: 10.1016/j.ebiom.2022.104344

11. Su GH, Xiao Y, Jiang YZ, Shao ZM. Uncovering the molecular subtypes of triple-negative breast cancer with a noninvasive radiomic methodology. *Cell Rep Med* (2022) 3(12):100808. doi: 10.1016/j.xcrm.2022.100808

12. Cui Y, Li Z, Xiang M, Han D, Yin Y, Ma C. Machine learning models predict overall survival and progression free survival of non-surgical esophageal cancer patients with chemoradiotherapy based on CT image radiomics signatures. *Radiat Oncol* (2022) 17(1):212. doi: 10.1186/s13014-022-02186-0

13. Zhong ME, Duan X, Ni-Jia-Ti MY, Qi H, Xu D, Cai D, et al. CT-based radiogenomic analysis dissects intratumor heterogeneity and predicts prognosis of colorectal cancer: a multi-institutional retrospective study. *J Transl Med* (2022) 20 (1):574. doi: 10.1186/s12967-022-03788-8

14. Bian Y, Jiang H, Ma C, Wang L, Zheng J, Jin G, et al. CT-based radiomics score for distinguishing between grade 1 and grade 2 nonfunctioning pancreatic neuroendocrine tumors. *AJR Am J Roentgenol* (2020) 215(4):852–63. doi: 10.2214/AJR.19.22123

15. Liang W, Yang P, Huang R, Xu L, Wang J, Liu W, et al. A combined nomogram model to preoperatively predict histologic grade in pancreatic neuroendocrine tumors. *Clin Cancer Res* (2019) 25(2):584–94. doi: 10.1158/1078-0432.CCR-18-1305

16. An P, Zhang J, Li M, Duan P, He Z, Wang Z, et al. Clinical data-CT radiomics-based model for predicting prognosis of patients with gastrointestinal pancreatic neuroendocrine neoplasms (GP-NENs). *Comput Math Methods Med* (2022) 2022:4186305. doi: 10.1155/2022/4186305

17. Caruso D, Polici M, Rinzivillo M, Zerunian M, Nacci I, Marasco M, et al. CT-based radiomics for prediction of therapeutic response to everolimus in metastatic neuroendocrine tumors. *Radiol Med* (2022) 127(7):691–701. doi: 10.1007/s11547-022-01506-4

18. Wang R, Liu H, Liang P, Zhao H, Li L, Gao J. Radiomics analysis of CT imaging for differentiating gastric neuroendocrine carcinomas from gastric adenocarcinomas. *Eur J Radiol* (2021) 138:109662. doi: 10.1016/j.ejrad.2021.109662

19. Bicci E, Cozzi D, Cavigli E, Ruzga R, Bertelli E, Danti G, et al. Reproducibility of CT radiomic features in lung neuroendocrine tumours (NETs) patients: analysis in a heterogeneous population. *Radiol Med* (2023) 128(2):203–11 doi: 10.1007/s11547-023-01592-y

20. Mayer P, Fritz F, Koell M, Skornitzke S, Bergmann F, Gaida MM, et al. Assessment of tissue perfusion of pancreatic cancer as potential imaging biomarker by means of intravoxel incoherent motion MRI and CT perfusion: correlation with histological microvessel density as ground truth. *Cancer Imaging* (2021) 21(1):13. doi: 10.1186/s40644-021-00382-x

21. Gudmundsson E, Labby Z, Straus CM, Sensakovic WF, Li F, Rose B, et al. Dynamic contrast-enhanced CT for the assessment of tumour response in malignant pleural mesothelioma: a pilot study. *Eur Radiol* (2019) 29(2):682–8. doi: 10.1007/s00330-018-5533-9

22. Wang D, Zhang GB, Yan L, Wei XE, Zhang YZ, Li WB. CT and enhanced CT in diagnosis of gastrointestinal neuroendocrine carcinomas. *Abdom Imaging* (2012) 37 (5):738–45. doi: 10.1007/s00261-011-9836-4

23. Gillies RJ, Kinahan PE, Hricak H. Radiomics: images are more than pictures, they are data. *Radiology* (2016) 278(2):563–577. doi: 10.1148/radiol.2015151169

24. Huang Q, Deng B, Wang Y, Shen Y, Hu X, Feng C, et al. Reduced field-of-view DWI–derived clinical-radiomics model for the prediction of stage in cervical cancer. *Insights Imaging* (2023) 14(1):18. doi: 10.1186/s13244-022-01346-w

25. Chicklore S, Goh V, Siddique M, Roy A, Marsden PK, Cook GJ. Quantifying tumour heterogeneity in 18F-FDG PET/CT imaging by texture analysis. *Eur J Nucl Med Mol Imaging* (2013) 40(1):133–40. doi: 10.1007/s00259-012-2247-0

26. Li X, Guindani M, Ng C-S, Hobbs BP. Spatial Bayesian modeling of GLCM withapplication to malignant lesion characterization. *J Appl Statistics* (2018) 46(2):230–46. doi: 10.1080/02664763.2018.1473348

27. Karahaliou A, Vassiou K, Arikidis NS, Skiadopoulos S, Kanavou T, Costaridou L. Assessing heterogeneity of lesion enhancement kinetics in dynamic contrast-enhanced MRI for breast cancer diagnosis. *Br J Radiol* (2010) 83(988):296–309. doi: 10.1259/bjr/50743919

28. Yang WL, Zhu F, Chen WX. Texture analysis of contrast-enhanced magnetic resonance imaging predicts microvascular invasion in hepatocellular carcinoma. *Eur J Radiol* (2022) 156:110528. doi: 10.1016/j.ejrad.2022.110528

29. Fan TW, Malhi H, Varghese B, Cen S, Hwang D, Aron M, et al. Computed tomography-based texture analysis of bladder cancer: differentiating urothelial carcinoma from micropapillary carcinoma. *Abdom Radiol (NY)* (2019) 44(1):201–8. doi: 10.1007/s00261-018-1694-x

30. Beyer AL, Kaemmerer D, Sänger J, Lupp A. Co-Expression of adaptor protein FAM159B with different markers for neuroendocrine cells: An immunocytochemical and immunohistochemical study. *Int J Mol Sci* (2022) 23(21):13503. doi: 10.3390/ijms232113503

31. Sorbye H, Kong G, Grozinsky-Glasberg S. PRRT in high-grade gastroenteropancreatic neuroendocrine neoplasms (WHO G3). *Endocr Relat Cancer* (2020) 27(3):R67–77. doi: 10.1530/ERC-19-0400

frontiers | Frontiers in Endocrinology

TYPE Original Research
PUBLISHED 18 April 2023
DOI 10.3389/fendo.2023.1168245

OPEN ACCESS

EDITED BY
Peixin Dong,
Hokkaido University, Japan

REVIEWED BY
Yinde Huang,
The First Affiliated Hospital of China Medical University, China
Jiahao Ma,
Xinxiang University, China

*CORRESPONDENCE
Bin Li
libin@cicams.ac.cn

SPECIALTY SECTION
This article was submitted to Cancer Endocrinology, a section of the journal Frontiers in Endocrinology

RECEIVED 17 February 2023
ACCEPTED 04 April 2023
PUBLISHED 18 April 2023

CITATION
Wang K, Hou H, Zhang Y, Ao M, Luo H and Li B (2023) Ovarian cancer-associated immune exhaustion involves SPP1+ T cell and NKT cell, symbolizing more malignant progression.
Front. Endocrinol. 14:1168245.
doi: 10.3389/fendo.2023.1168245

Ovarian cancer-associated immune exhaustion involves SPP1+ T cell and NKT cell, symbolizing more malignant progression

Kunyu Wang, Hongyi Hou, Yanan Zhang, Miao Ao, Haixia Luo and Bin Li*

Department of Gynecology Oncology, National Cancer Center/National Clinical Research Center for Cancer/Cancer Hospital, Chinese Academy of Medical Sciences and Peking Union Medical College, Beijing, China

Background: Ovarian cancer (OC) is highly heterogeneous and has a poor prognosis. A better understanding of OC biology could provide more effective therapeutic paradigms for different OC subtypes.

Methods: To reveal the heterogeneity of T cell-associated subclusters in OC, we performed an in-depth analysis of single-cell transcriptional profiles and clinical information of patients with OC. Then, the above analysis results were verified by qPCR and flow cytometry examine.

Results: After screening by threshold, a total of 85,699 cells in 16 ovarian cancer tissue samples were clustered into 25 major cell groups. By performing further clustering of T cell-associated clusters, we annotated a total of 14 T cell subclusters. Then, four distinct single-cell landscapes of exhausted T (Tex) cells were screened, and SPP1 + Tex significantly correlated with NKT cell strength. A large amount of RNA sequencing expression data combining the CIBERSORTx tool were labeled with cell types from our single-cell data. Calculating the relative abundance of cell types revealed that a greater proportion of SPP1 + Tex cells was associated with poor prognosis in a cohort of 371 patients with OC. In addition, we showed that the poor prognosis of patients in the high SPP1 + Tex expression group might be related to the suppression of immune checkpoints. Finally, we verified *in vitro* that SPP1 expression was significantly higher in ovarian cancer cells than in normal ovarian cells. By flow cytometry, knockdown of SPP1 in ovarian cancer cells could promote tumorigenic apoptosis.

Conclusion: This is the first study to provide a more comprehensive understanding of the heterogeneity and clinical significance of Tex cells in OC, which will contribute to the development of more precise and effective therapies.

KEYWORDS

ovarian cancer, SPP1+ T cell, T cell exhaustion, single cell RNA sequencing, immune environment

1 Introduction

Ovarian cancer (OC) is one of the deadliest and most aggressive tumors in women, and its incidence has increased in recent years (1). Because the early specific signs and symptoms of OC are not obvious and develop rapidly, the vast majority of patients with OC are not diagnosed until the late stage (2). Patients with OC often have a poor prognosis, presumably because their heterogeneity limits reproducible prognostic classification (3). At present, surgery, chemotherapy and radiotherapy are the most common modalities used in the treatment of OC. However, the side effects of treatment in these patients are more severe and there is a serious decrease in the quality of life of the patients (4). Extensive heterogeneity in OC cells is a critical mechanism for overall survival and cancer progression (5). Therefore, it is of great significance to explore specific markers for the early diagnosis of OC to improve treatment and patient outcomes.

Emerging single-cell technologies provide powerful tools to explore heterogeneity and thereby aid in problem solving (6, 7). This technology has been increasingly used in the field of cancer and provides new mechanisms for understanding carcinogenesis and revealing therapeutic strategies (8–12). However, only a few studies have investigated OC at the single-cell level. A recent single-cell RNA sequencing (scRNA-seq) study investigated tumor heterogeneity at cellular resolution using OC samples (13). Another study examined how fallopian tube epithelial cell sources could accurately predict cancer behavior (14). These studies provide new insights into the carcinogenesis of OC, and their findings enhance our understanding of OC.

Tumors are characterized by significant heterogeneity that can lead to differential responses to the same therapy (15). Until now, there have been efforts to explore the heterogeneous characteristics of tumors. However, our understanding of tumor heterogeneity is still limited to tumor cells due to the limitations of technology. Recent studies have demonstrated that tumor-infiltrating immune and stromal cells exhibit heterogeneity (16). In addition, increasing evidence suggests that the tumor microenvironment (TME) plays an important role in targeting agents (17). Previous studies have highlighted CD8+ failure, immune checkpoints, and tumor-associated macrophages as key therapeutic targets (18, 19). These data enhance our understanding of TME heterogeneity.

To reveal the heterogeneity of T cell-associated subclusters in OC, we performed an in-depth analysis of single-cell transcriptional profiles and clinical information of patients with OC. We then explored the immune landscape of four different Tex and could clearly see a significant correlation between SPP1 + Tex and NKT cells. A large amount of RNA-seq expression data combining the CIBERSORTx tool and TCGA were labeled with cell types from our single-cell data. In calculating the abundance of immune cells for each patient, we found that the abundance of SPP1 + Tex cells was associated with poor prognosis. In addition, we showed that the poor prognosis of patients in the high SPP1 + Tex expression group might be related to the suppression of immune checkpoints. Finally, we performed *in vitro* experiments for validation. The expression level of SPP1 in ovarian cancer cells was significantly higher than that in normal ovarian cells, and the ability to promote apoptosis after knocking down SPP1 in ovarian cancer cells could be seen by flow cytometry. This is the first study to provide a more comprehensive understanding of the heterogeneity and clinical significance of Tex cells in OC, which will contribute to the development of more precise and effective therapies.

2 Materials and methods

2.1 Data collection

Three single-cell datasets (E-MTAB-8107, GSE154600, and GSE130000) were obtained from the Gene Expression Omnibus (http://www.ncbi.nlm.nih.gov/geo/) containing a total of 16 samples from patients with OC. RNA-seq data and accompanying clinical information from 371 OC samples were downloaded from the TCGA cohort for further correlation analysis (http://cancergenome.nih.gov/). This study used a publicly available dataset that received ethical approval from the original study.

2.2 Data filtering and correction

We used the "Seurat" and "SingleR" software packages for scRNA-seq data analysis. We filtered cells with unique feature counts > 2500 or < 200 and cells with mitochondrial counts > 5%. Then, the feature-expression measurements for each cell were normalized to the total expression using the default parameters of the Seurat "NormalizeData" function. Subsequently, all cell data were transferred to a combined Seurat object using the Harmony package. Variable genes were then scaled, and the principal component (PC) was analyzed. Using the "RunUMAP" (min. dist = 0.2, n. neighbors = 20) and "FindClusters" (resolution = 0.5) functions, significant PCs were selected for Umap and cluster analyses.

2.3 Cell annotation

To identify cell types, we performed two annotation modalities. Automated annotation (used for the first clustering to select T cell-related subsets): SingleR is an automated annotation method for scRNAseq data (20). Given a sample reference dataset (single cell or batch size) with known labels, it marks new units in the test dataset based on their similarity to the reference. Thus, for reference datasets, the burden of manually interpreting clusters and defining marker genes only needed to be done once, whereas biological knowledge could be spread to new datasets in an automated manner.

Manual annotation (used to cluster T cell-related subsets for the second time): We checked whether the well-studied marker genes were the top differentially expressed genes (DEGs) and annotated the most likely identity for each cell cluster. The remaining cell types were identified by manually searching the cell marker database (http://biocc.hrbmu.edu.cn/CellMarker/). The R package "estimate" was used for estimate analysis to classify and score cells as a whole: estimate score, immune score, and stromal score.

2.4 GSEA pathway and cell-to-cell communication analyses

We performed GSEA pathway and cell-to-cell communication analyses to explore the association between T cell-associated subsets. R package "ABGSEase" was used to perform biological pathway enrichment between the two groups, and the reference gene set was Hallmark, GO, and KEGG. Minimum gene set size minGSSize = 50, maximum gene set size maxGSSize = 100, and P-value truncated at P-value cutoff = 0.05 were set for the analysis. Cell–cell communication analysis uses the R package "CellChat", and the pathway selects the secreted signaling pathway. The reference human ligand–receptor database was CellChatDB. We examined the interactions between different cell types and filtering pathways with cell numbers less than 10.

2.5 Unsupervised consensus cluster analysis

Robust Tex cell infiltration-associated clusters can be found in TCGA cohort patients by consensus clustering techniques based on partitioning and expression of Tex cells in 4 with the help of the R package "ConsensuClusterPlus". The cumulative distribution function and consensus heat map were used to determine the optimal K-value. The method was repeated 1000 times to ensure the stability of the layering process.

2.6 Prognostic analysis

For the selected cells, univariate cox regression analysis was first performed to select prognostically relevant Tex cells ($P < 0.05$). Kaplan–Meier curves were used to assess the differences in survival between the high and low groups of such cells.

2.7 Immune infiltrate analysis

Immune infiltration analysis was performed using the CIBERSORTx algorithm (21), which quantifies the absolute content of 22 immune cells based on the patient's transcriptional profile information, as well as the absolute content of Tex cell infiltrates in 4 derived from a reference dataset of our own single-cell data.

2.8 DEG analysis

The main purpose of this analysis was to identify DEGs between the SPP1 + Tex high and low groups. DEG analysis was performed using the "limma" package in R software with thresholds set at log FoldChange ≥ 1 and adj PVal Filter (adj P) < 0.05. Subsequently, GSEA was performed for the SPP1 + Tex high and low groups to explore the significance of their biological functions. Finally, we analyzed the expression of immune checkpoints in the high and low SPP1 + Tex groups.

2.9 Cell culture

Human normal ovarian cells IOSE80 and ovarian cancer cells A2780 were purchased from American Type Culture Collection (ATCC, Rockville, MD, USA). Cells were cultured in RPMI-1640 medium containing 10% Fetal Bovine Serum (FBS) at 37° C and 5% CO2.

2.10 Quantitative real-time PCR (qRT-PCR)

Cells were treated with TRIzol reagent (Takara, Japan). We then extracted all RNA and reverse-transcribed it into cDNA. qRT-PCR was used to analyze the relative expression of SPP1, and data were normalized to GAPDH. Reverse transcription system: 500ng RNA, 2ul RT Master Mix, add RNase-free water to fix the volume to 10μl. qPCR system: 10μl 2xTB Green, 8ul ddH2O, 1μl cDNA, 1μl primer (22). The primer sequences are as follows: SPP1-F::5'-AGA CCC TGA CAT CCA GTA CCT G-3', SPP1-R: 5'-GTG GGT TTC AGC TAC CTG GT-3'. GAPDH-F: 5'-GGAGCGAGATCCCTCCAAAAT-3', GAPDH-R: 5'-GGCTGTTGTCATACTTCTCATGG-3'.

2.11 Apoptosis analysis

We analyzed cell apoptosis using flow cytometry after pre-cooling PBS washing and digestion with trypsin digestion solution containing no EDTA (Solarbio, Shanghai, China). Cells were harvested after centrifugation at 1000 rpm for 5 minutes, followed by 7-AAD (BD Biosciences, number 559, 925, USA) staining and annexin-APC (BD Biosciences, number 561, 012, USA) staining for 15 minutes.

2.12 Statistical analysis

The student's t-test was used for normally distributed continuous variables. The Mann–Whitney U test was used for continuous variables that were not normally distributed. Correlations between continuous variables were evaluated using Pearson's correlation analysis. Statistical significance was set at $P < 0.05$. R software version 4.1.0 (http://www.R-project.org) was used for data analysis and figure generation.

3 Results

Flowchart (Figure 1).

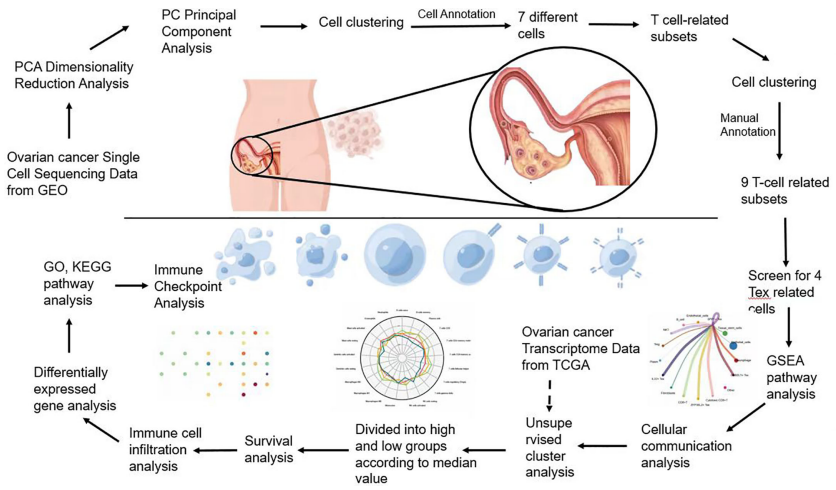

FIGURE 1
Flowchart.

3.1 Cell clustering of OC landscapes

First, we performed principal component analysis (PCA) on 16 samples to reduce dimensionality and selected the first 50 PCs for subsequent analysis (Figure 2A). Following data processing and screening, we obtained gene expression profiles for 85,699 cells from 16 OC samples and identified 25 cell clusters using Seurat (Figure 2B). Cell distributions are visualized by Umap plots for different samples (Figure 2C). Cells in clusters 0 and 20 were classified as T cells by defining the annotation of cell identity in each cluster by cross-referencing the DEGs in each cluster to canonical marker genes (Figure 2D). The heatmap visualizes the expression of genes in each cluster of cells, with yellow highlighted sections representing genes highly expressed in this cluster (Figure 2E). The expression levels of some signature genes in this cluster were visualized using violin plots (Supplementary Figure 1). In addition, we showed the infiltrative content of seven clusters of cells in each sample by histogram and found that epithelial cells accounted for the highest proportion in most samples (Figure 2F).

3.2 Cellular clustering of T cell subsets in OC

We calculated three scores for the three classes of cells using the package “estimate”. Immune cells had the highest immune score. tumor cells had the highest tumor purity score, and other cells had the highest stromal score (Supplementary Figure 2). This score also demonstrates the accuracy of the grouping.

First, we identified CD8+ T cell locations by determining the distribution of cell signature genes (Figure 3A) and proceeded with PCA dimensionality reduction of the T cell clusters (Figure 3B). Subsequently, Umap dimensionality reduction was performed to obtain 14 clusters of cells, and the cell distribution of different samples is shown (Figures 3C, D). Through bubble plots, we can visually observe the signature genes of each T cell subcluster (Figure 3E). The Umap plot shows the distribution of CD8A markers (Figure 3F). By determining the distribution of the Tex cell marker, clusters 5, 3, 4, and 1 were identified as CD8+ Tex cells based on this distribution (Supplementary Figure 3A). Clusters 8, 10, and 12 were identified as Treg cells based on the distribution of the two Treg cell markers (Supplementary Figure 3B). Finally, the results for T cell subsets were determined by manual annotation, with 14 cell clusters annotated as a total of nine Tex-related cell subsets (Figure 3G). Using the Umap plot, we determined the distribution of highly expressed genes in Tex cells (Supplementary Figure 3C). In addition, we determined the proportion of Tex cells in the samples using a histogram plot (Figure 3H). We found that the content of T cells in different samples was significantly different.

3.3 Pathway analysis of four Tex cells

By comparing the enriched pathways in four Tex cells using GSEA analysis, we found that SPP1 + cluster CD4+ αβ T cells were functionally active (Figure 4A). Comparing the SPP1 + Tex and ZFP36S2 + Tex cluster cells, we found that the positive regulation of cell adhesion was significantly activated (Figure 4B). GNB2L1 + Tex cluster cells showed activation of negative regulation of immune effector processes (Figure 4C). IL32 + Tex cluster cells showed significant activation of the lymphocyte-mediated immune function (Figure 4D). Cell communication analysis revealed a close connection between these cells (Figure 4E). In addition, we found that the signal emitted by SPP1 + Tex was very strong in NKT cells, in addition to a significant link with IL32 + Tex, GNB2L1 + Tex, and other cells (Figure 4F).

10.3389/fendo.2023.1168245

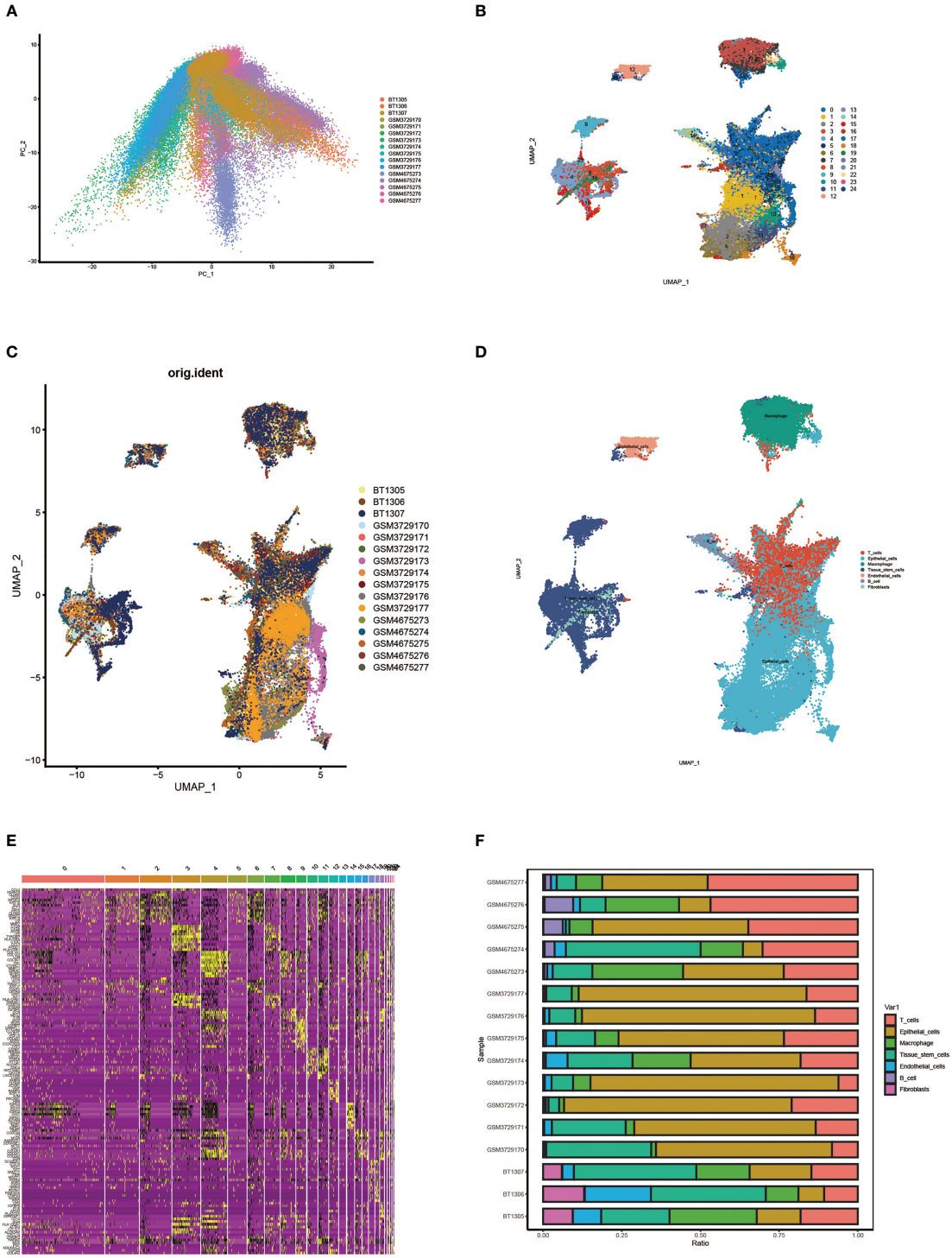

FIGURE 2
Single cell cluster analysis in patients with ovarian cancer. **(A)** Single cell data were subjected to PCA dimensionality reduction analysis and the first 50 PC principal components were selected for subsequent analysis. **(B)** Umap plots show 25 clusters of cells generated by clustering after dimension reduction. **(C)** Umap plot showing cell distribution for different samples. **(D)** Umap plots show the distribution of cells in each cluster after annotation. **(E)** Heat map of signature gene expression in different groups. **(F)** Histograms show the proportion of infiltrates per cluster of cells in each sample.

3.4 Identification of the role of Tex cell-related pathways

Subsequently, we visualized the cellular role of the sub-pathways of secretory cell communication. Cell communication diagram shows the signaling pathway networks of WNT, TGF-β, and SPP1. The results showed that endothelial cells expressed the WNT signaling pathway significantly, and the WNT-based pathway macrophage Tex cells had a strong effect on endothelial cells (Figure 5A). In addition, fibroblasts were more

10.3389/fendo.2023.1168245

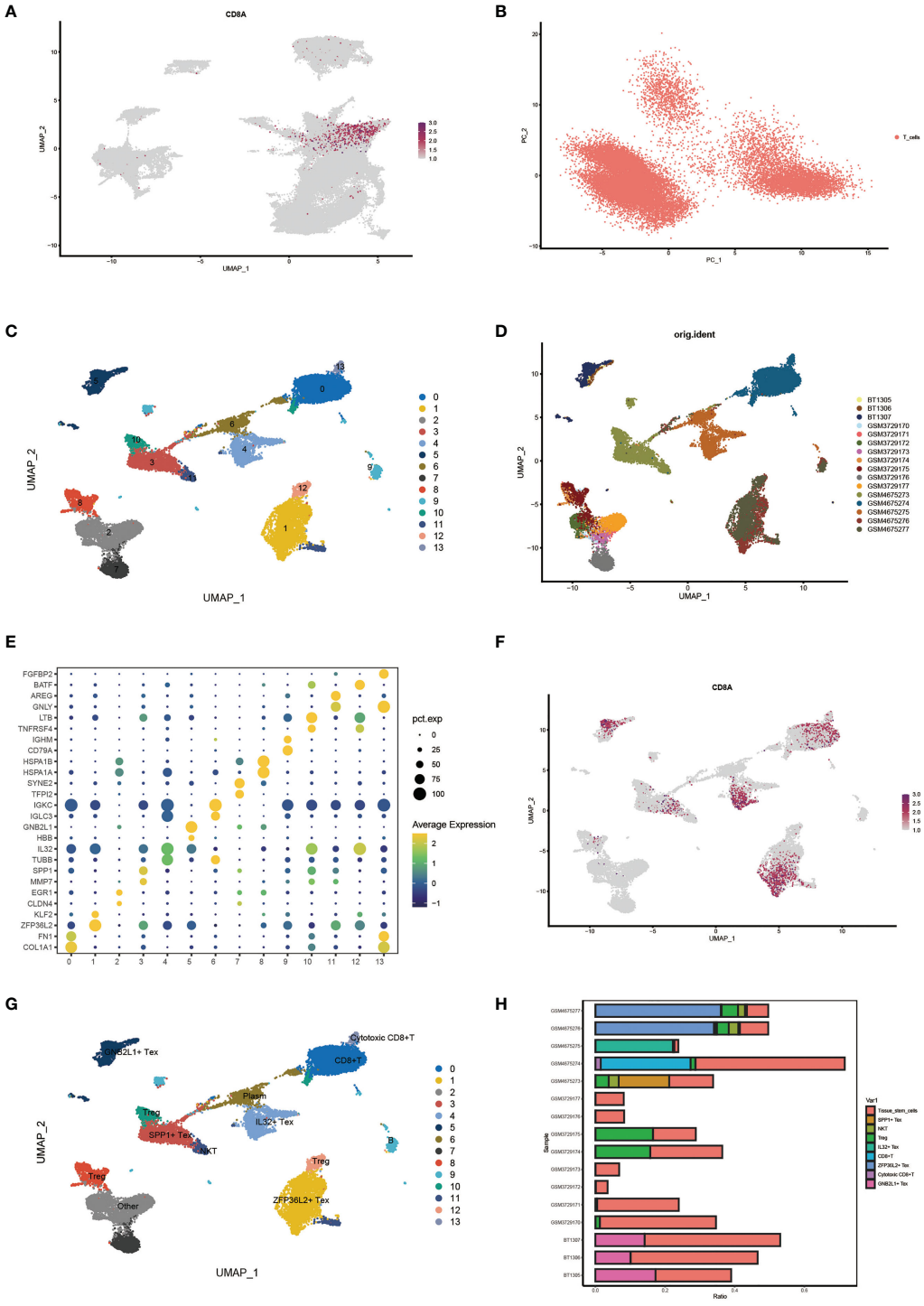

FIGURE 3
Identification of characteristic cell clusters. **(A)** View CD8 + T cell location by distribution of cell signature genes. **(B)** PCA Dimensionality Reduction Analysis of T Cell Clusters. **(C)** Umap shows 14 clusters of cells after dimension reduction. **(D)** Umap Plot of cell distribution by sample. **(E)** Bubble plots showing signature genes for each T cell subcluster. **(F)** Umap plot showing distribution of CD8marker. **(G)** Umap plots show results after annotation of T-cell clusters. **(H)** Histogram plot showing cell proportions for each sample.

potent based on the TGF-β pathway (Figure 5B). Based on the fact that SPP1 + Tex is highly active in the SPP1 signaling pathway, it was demonstrated that the main effect of SPP1 + Tex is from its marker SPP1 and that it may interact with fibroblasts (Figure 5C).

3.5 Identification of the prognostic role of Tex cells

Using single-cell data as reference data, Tex-related cell content was calculated from the OC dataset in TCGA using the

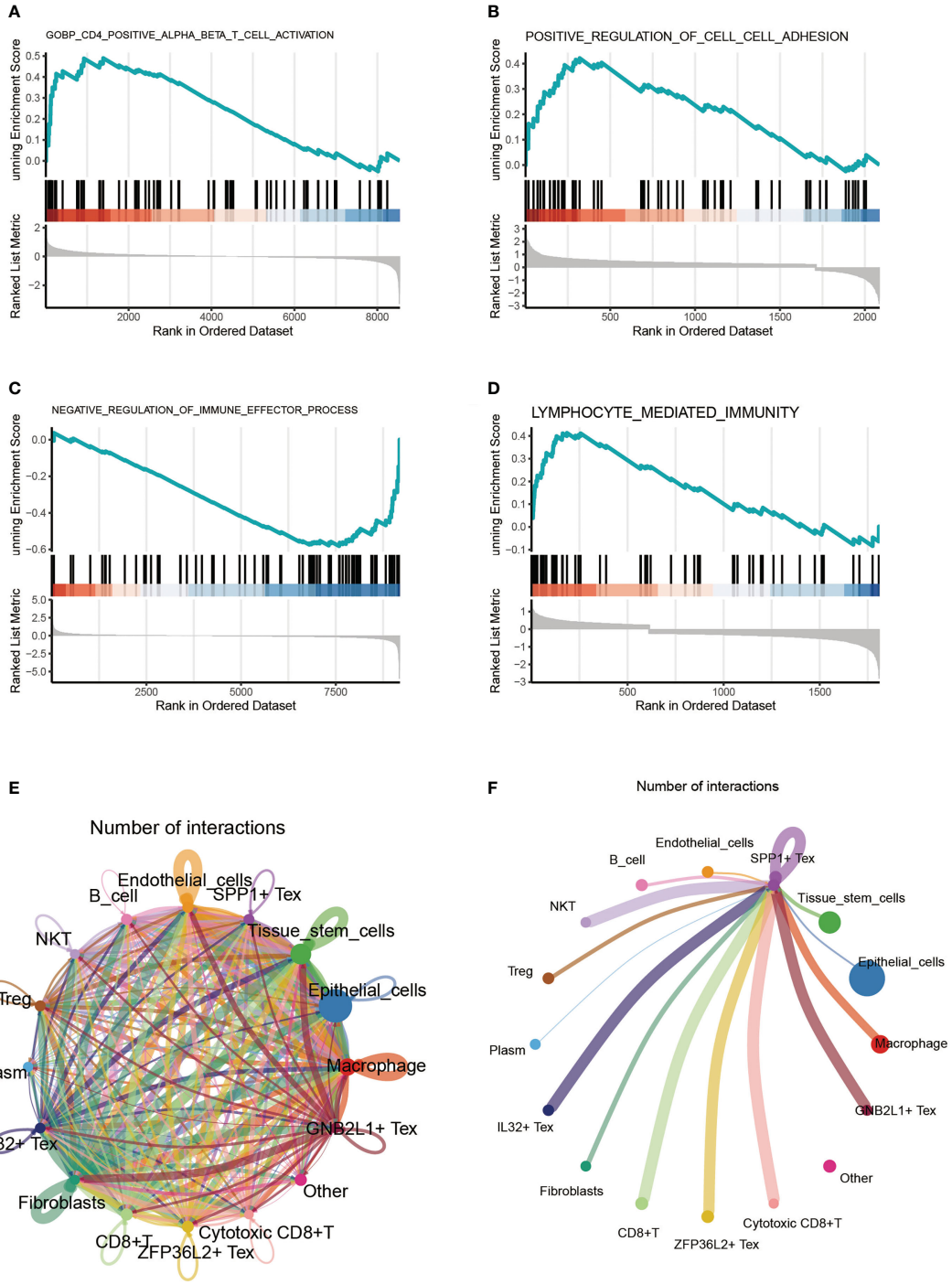

FIGURE 4
Cell-enriched pathway analysis. **(A-D)** GSEA analysis comparing enriched pathways in four Tex cells. **(E)** Shown the pathway analysis between cells. **(F)** Signaling pathway of SPP1 + Tex to other cells.

CIBERSORTx algorithm. A heat map showing the expression of four cells in the TCGA cohort was created (Figure 7A). Patients with OC were divided into two groups according to the median expression level. Many samples had expression values of 0 in ZFP36L2 + Tex cells, which may have affected the analytical results. hence, we did not perform subsequent analysis on them. Survival curves showed differences in survival between the high and low groups of the three Tex cells, with IL32 + Tex and GNB2L1 + Tex cells not being associated with survival (Figures 7B, C), whereas SPP1 + Tex cells showed a correlation with survival, and the high group had a poor prognosis (Figure 7D). In addition, univariate cox regression demonstrated that SPP1 + Tex cells are an unfavorable prognostic factor for OC (Figure 7E).

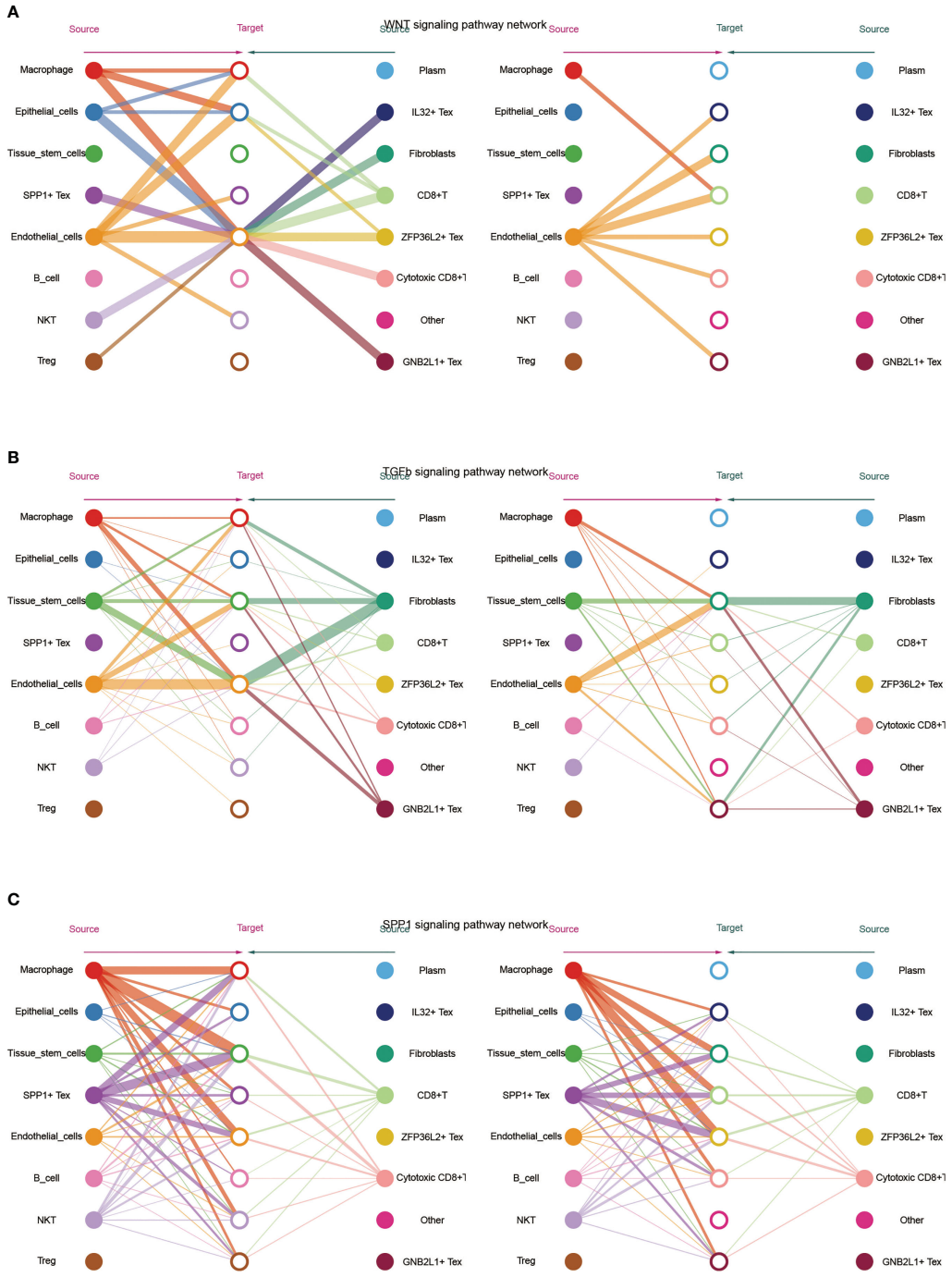

FIGURE 5
Network diagram showing **(A)** WNT, **(B)** TGF -β and **(C)** SPP1 related signaling pathways, respectively. The role of TGF-β-related pathways among all cells was shown by bubble plots, in which TGF-β 1 (TGF-β R1 + TGF-β R2) was generally more active among various types of cell communication (Figure 6A). In addition, analysis of the effect of related pathways between Tex cells showed that the effect of BMP4- and GDF5-related pathways differed between Tex cells, in which GNB2L1 + Tex actively interacted with stem cells, while SPP1 + Tex cells communicated mainly with stem cells through BMP4 (BMPR1B + ACVR2A) and GDF5 (BMPR1B + ACVR2A) (Figure 6B).

3.6 Identification of components of immune cell infiltration of Tex cells and their correlation

By performing immune cell infiltration analysis between the high and low groups of three Tex cells, we found significant differences in immune cell composition between the high and low groups. The results showed a significant difference between plasma cells and CD8 T cells in the high and low GNB2L1 + Tex cell groups (Figure 8A). There were significant differences in plasma cells, follicular helper T cells, and neutrophils between the high and low IL32 + Tex groups (Figure 8B).

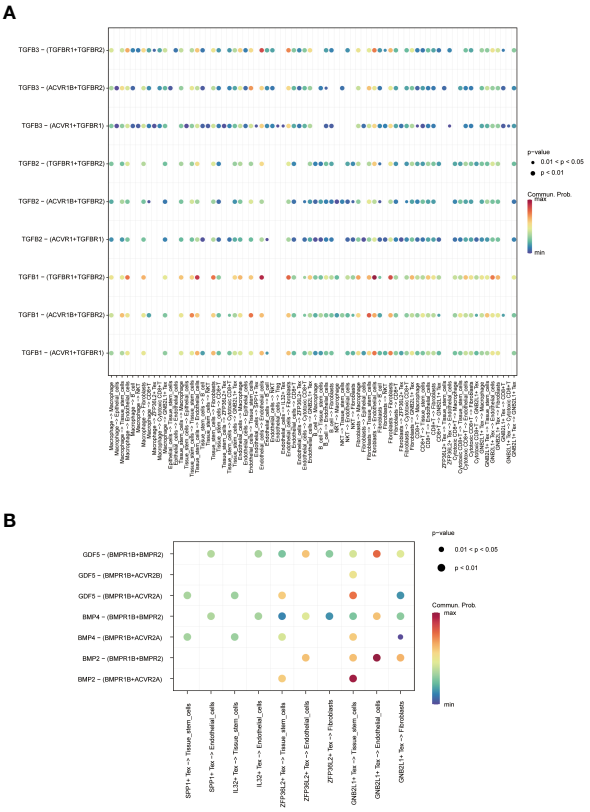

FIGURE 6
Analysis of cell-related pathways. **(A)** Bubble plots demonstrate the role of TGF-β related pathways across all cells. **(B)** Bubble plots demonstrate the role of Tex cell-associated pathways.

Plasma cells, CD8 T cells, follicular helper T cells, and NK cells were significantly different between the high and low SPP1 + Tex cell groups (Figure 8C). The proportion of helper infiltration of plasma cells, CD8 T cells, and T cell follicles in the low-expression group was significantly higher than that in the high-expression group, whereas the proportion of NK cell infiltration in the high-expression group was higher than that in the low-expression group. This result suggests that the difference in survival between the high and low SPP1 + Tex groups may be due to improved immune control.

Radar plots showed the correlation between the four Tex cells and other immune cells (Figure 8D). A significant negative correlation between SPP1 + Tex and IL32 + Tex cells, and a negative correlation was found between SPP1 + Tex and plasma cells, T cell follicular helper using correlation heat maps (Figure 8E). In addition, the correlation analysis of the 4 Tex cells also showed the strongest correlation between SPP1 + Tex and IL32 + Tex cells (Supplementary Figure 4).

3.7 Identification of differences between high and low SPP1 + Tex cell groups

By performing differential gene expression analysis between the SPP1 + Tex high and low groups, we drew a volcano plot for visualization (Figure 9A). GO analysis revealed that these DEGs were enriched in terms of extracellular matrix. therefore, SPP1 + Tex may be associated with extracellular matrix remodeling (Figure 9B). GSEA analysis, based on KEGG data, showed that DEGs were significantly enriched in chemokine signaling pathways, cytokine receptor interactions, ECM receptor interactions, and local adhesion signaling pathways (Figures 9C, D). In addition, the expression of immune checkpoints in the SPP1 + Tex high and low groups was analyzed, and the results showed significant differences in CD274, NRP1, NRP1.1, CD28, and CD44 between the high and low groups (Figure 9E). Interestingly, the number of patients in the high SPP1 + Tex expression group was larger than that in the low SPP1 + Tex expression group among these immune checkpoint inhibitors, corresponding to the worse outcome in the high-expression group.

3.8 *In vitro* validation

With the previous results, it can be seen that only SPP1 + Tex has prognostic value in KM analysis and COX analysis. Therefore, we mainly chose SPP1 as the subject of further study in our subsequent study. To validate the validity of our model and identify a potential biomarker, we performed *in vitro* experimental validation from selection of SPP1. It can be found by boxplots that SPP1 has a very high expression level in ovarian cancer patients (Figure 10A). The SPP1 gene was expressed at a significantly higher level in ovarian cancer cells A2780 than in normal ovarian cells IOSE80, which also demonstrated the accuracy of our experiment (Figure 10B). In addition, we knocked down the expression level of SPP1 gene in A2780 cells and quantified it again to verify our knockdown efficiency (Figure 10C). By flow cytometry, we analyzed the function of SPP1 in ovarian cancer. The results showed that knockdown of SPP1 significantly promoted apoptosis in ovarian cancer cells (Figure 10D). Therefore, SPP1 may be a potential therapeutic target for ovarian cancer.

4 Discussion

The past decade has witnessed a shift in the paradigm of cancer therapy with the advent of approaches to target or manipulate the immune system (“immunotherapy”) (23–25). Cancer cells are often immunogenic while in the organism, but the immune system is often unable to clear it. This is because cancer cells have mechanisms that prevent recognition by the immune system, including central tolerance, ignorance or failure to be activated in the periphery, extrinsic regulation of T cells (e.g., regulatory T cells, myeloid-derived suppressor cells, and suppressor cytokines), and intrinsic dysfunction of T cells, resulting in inappropriate or excessive antigenic stimulation (anergy and depletion) (26–28). Antibodies targeting inhibitory pathways, including CTLA-4 and PD-1, have paved the way for a new generation of cancer therapeutics (29–31).

T cell depletion is characterized by the overexpression of multiple inhibitory receptors, including PD-1 (CD279), cytotoxic T-

10.3389/fendo.2023.1168245

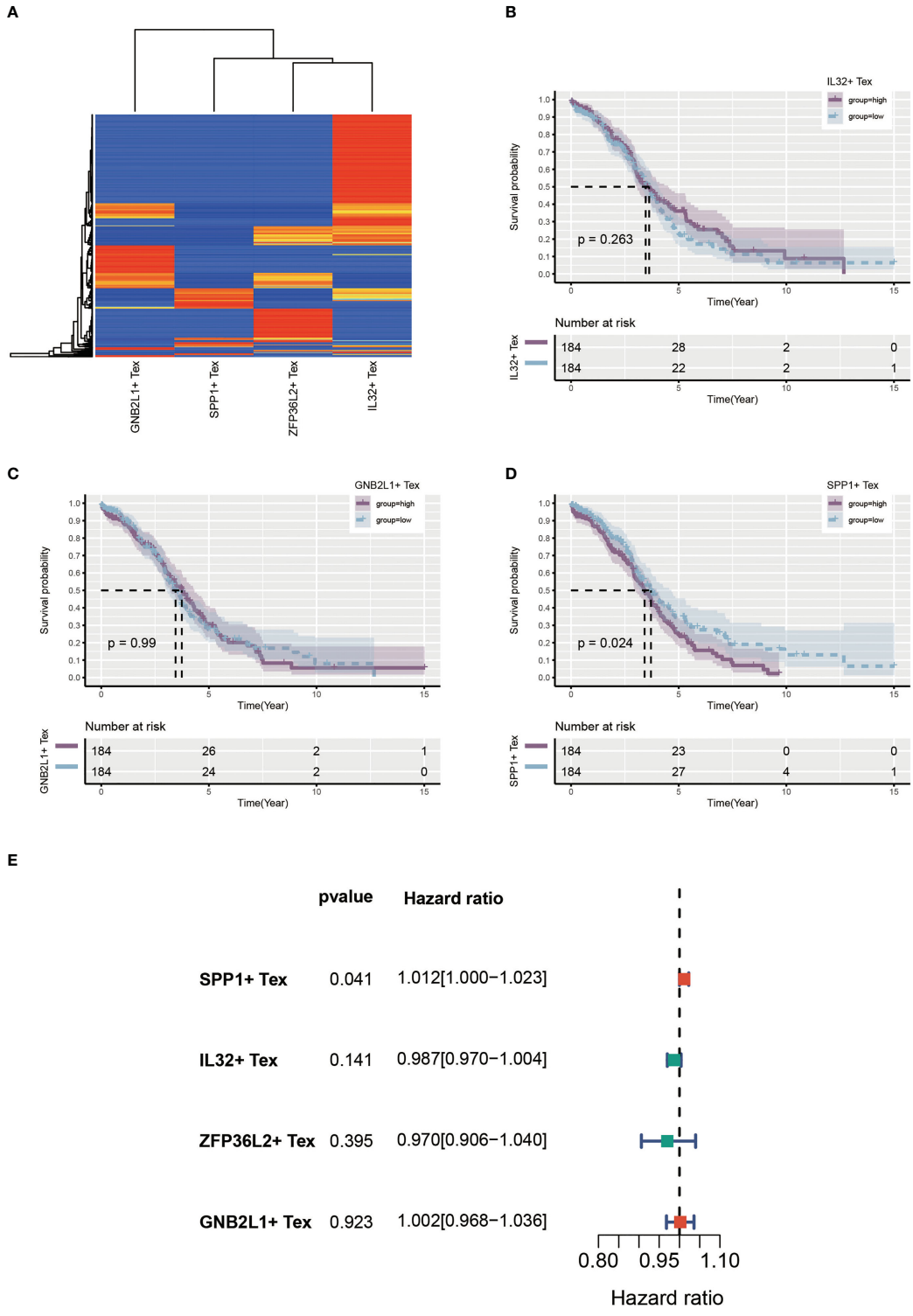

FIGURE 7
Identify Tex-related cellular features. **(A)** Heat map showing expression of four Tex-related cells in the TCGA cohort. **(B-D)** Survival curves showing survival differences between the three Tex cells in the high and low groups divided according to the median. **(E)** Forest plot showing the results of univariate cox regression.

lymphocyte antigen-4 (CTLA-4, CD152), lymphocyte activation gene 3 (Lag-3), T cell immunoglobulin domain and mucin domain 3 (Tim-3), CD244/2B4, CD160, T cell immune receptor-containing Ig and ITIM domains (TIGIT), and other receptors (32). Blocking the PD-1 pathway partially reverses failure and leads to reduced viral or tumor burden, which is a breakthrough (33, 34). These data suggest that Tex is not an ultimate dysfunction but can be revitalized and is important for the treatment of diseases, including cancer.

10.3389/fendo.2023.1168245

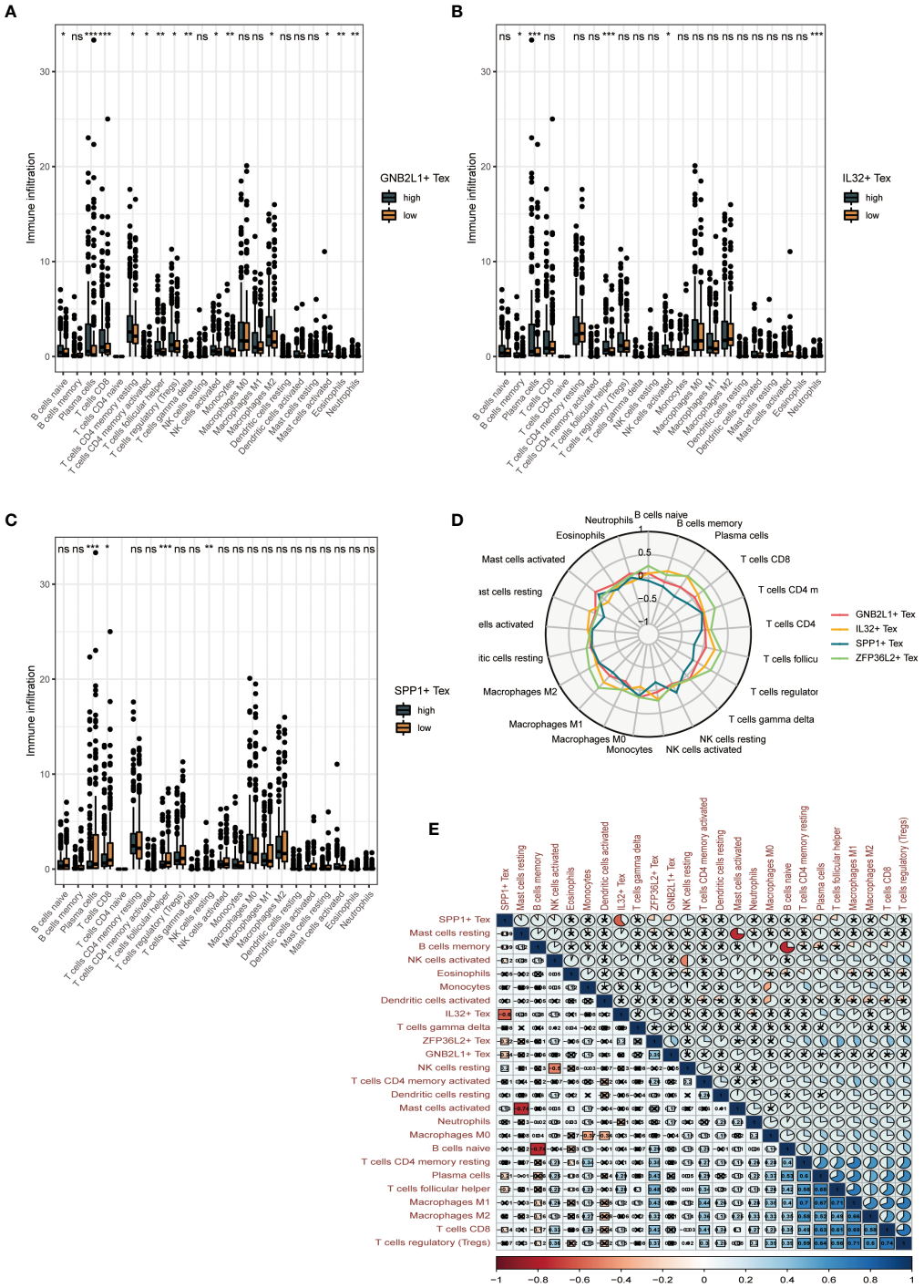

FIGURE 8
Clinical value of Tex cell clusters identified by our scRNA-seq analysis in patients from the TCGA OC cohort. **(A-C)** Difference in overall cellular infiltration between high and low groups according to median values for the 3 Tex cells. **(D)** Radar plots show the correlation of 4 cells with other immune cells. **(E)** Heat map showing correlation between all cells. * means <0.05,** means <0.01,*** means <0.001. ns means >0.05.

To reveal the heterogeneity of T cell-associated subclusters in OC, we performed an in-depth analysis of single-cell transcriptional profiles and clinical information of patients with OC. By performing further clustering of T cell-associated clusters, we annotated a total of 14 T cell subclusters. We then explored the immune landscape of four different Tex and could clearly see a significant correlation between SPP1 + Tex and NKT cells. A large amount of RNA-seq expression data combined with the CIBERSORTx tool and TCGA were labeled with cell types from our single-cell data. In all OC patients, we found that the higher the abundance of SPP1 + Tex cells, the worse prognosis of the patients.

We found a greater association between SPP1+ Tex and NKT cells by cell communication analysis. NKT cells are T cells with T-cell receptors that primarily recognize lipid antigens presented by CD1d. In cancer, NKT cells tend to play different roles, and type I NKT cells, which activate NK and CD8+ T cells by producing interferon-γ, are

10.3389/fendo.2023.1168245

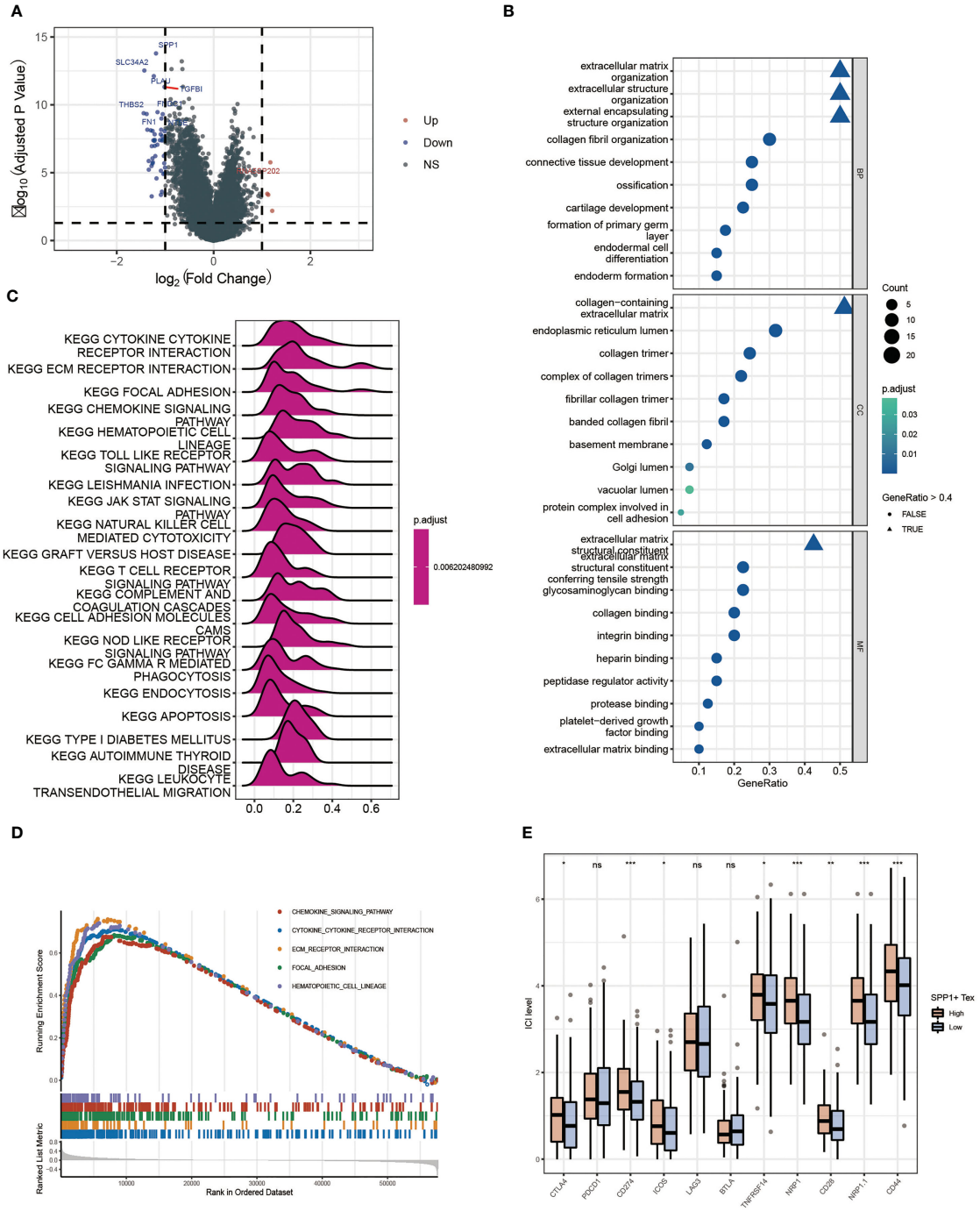

FIGURE 9
Differential enrichment analysis between high and low SPP1 + Tex groups. **(A)** Volcano plot of differentially expressed genes analysis between high and low groups. **(B)** GO enrichment analysis bubble plot. **(C)** Ridge plots for KEGG enrichment analysis. **(D)** Pathway plots for GSEA enrichment analysis. **(E)** Box plots show results of immune checkpoint analysis between SPP1 + Tex high and low groups. * means <0.05,** means <0.01, *** means <0.001. ns means >0.05.

mostly protective (35). In contrast, type II NKT cells, characterized by a more diverse T cell receptor recognizing CD1d-presented lipids, predominantly suppress tumor immunity (36). Moreover, type I and II NKT cells counter-regulate each other and form a novel immunomodulatory axis (35). Thus, manipulating this balance along the NKT regulatory axis may be critical for cancer immunotherapy.

In addition, we found that SPP1 + Tex significantly enhanced the regulation of cell adhesion compared to other Tex cells. Unlike most other tumor types that metastasize *via* the vasculature, OC metastasizes predominantly *via* the transcavitary route within the peritoneal cavity (37). In the peritoneal cavity, tumor-mesothelial adhesion is an important step in cancer dissemination (38).

10.3389/fendo.2023.1168245

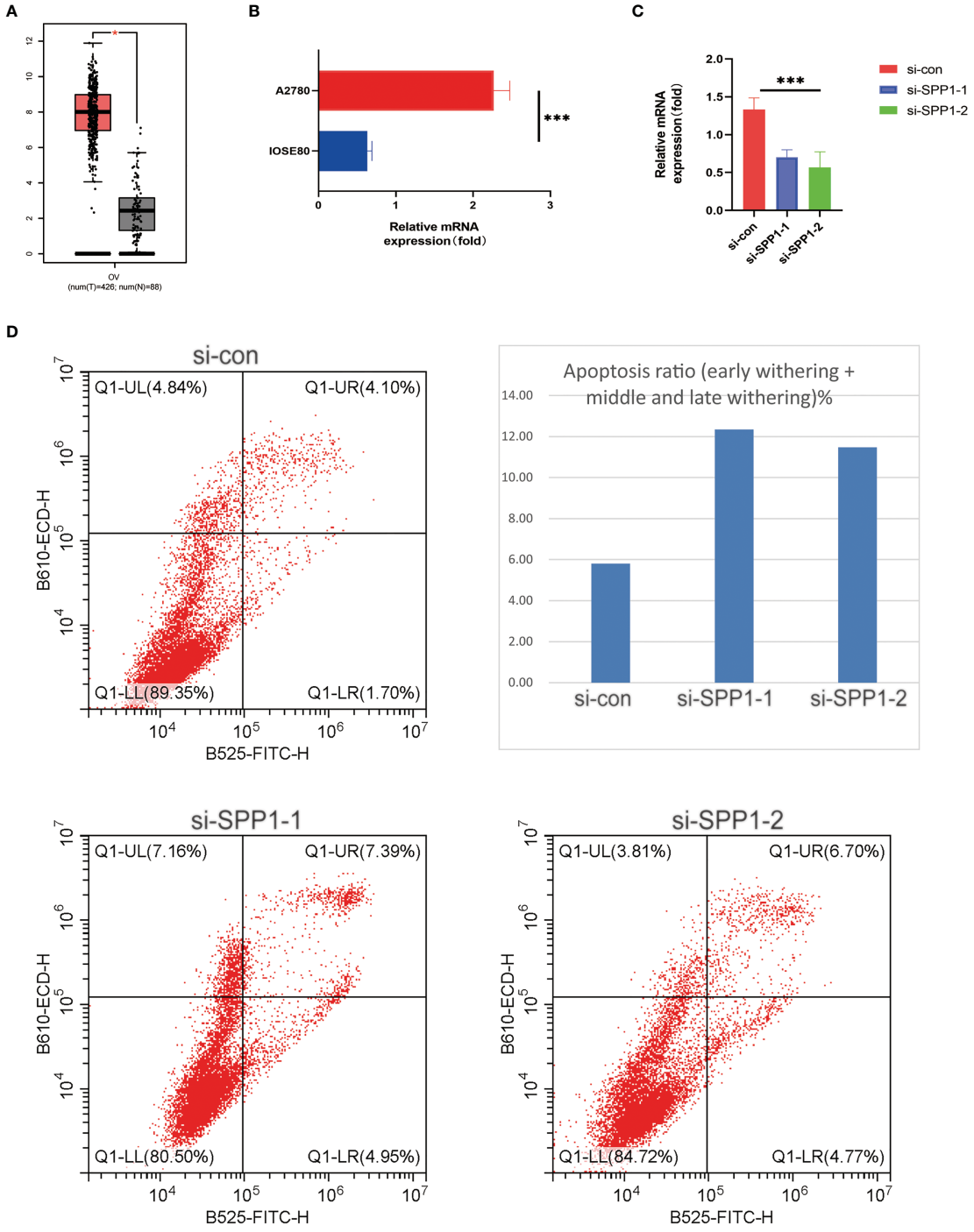

FIGURE 10
In vitro experiments validated SPP1 as a potential target. **(A)** Boxplot showing differential expression of SPP1 gene between ovarian cancer patients and normal patients. **(B)** Histogram showing expression levels of SPP1 gene in normal ovarian cells and ovarian cancer cells. **(C)** Histogram showing knockdown of SPP1 gene expression levels in ovarian cancer cells. **(D)** Flow cytometry scatter plot showed that SPP1 gene could affect apoptosis of ovarian cancer cells. *** means <0.001.

therefore, we reasoned that cell adhesion pathways could be potential pathways to inhibit OC.

Immunocyte infiltration analysis showed that the proportion of plasma cell, CD8 T cell, and follicular helper T cell infiltration in the low-expression group was significantly higher than that in the high-expression group. Plasma cell infiltration in OC has a significant impact on tumor progression and prognosis (39). Follicular helper T cells are specialized providers of T cells that contribute to B cells and the formation of germinal center responses, and numerous studies have demonstrated their important role in various malignancies (40, 41). Immune checkpoint inhibitor analysis revealed that the levels of immune checkpoint inhibitors were

significantly higher in the high SPP1 + Tex expression group than in the low SPP1 + Tex expression group. This corresponds to the outcome of poor prognosis in the high-expression group. Additionally, patients in the high SPP1 + Tex group may benefit more from anti-immune checkpoint inhibitors. In addition, we found that only SPP1 + Tex had better prognostic efficacy among the four previously studied Tex. Therefore, we selected SPP1 for further study in ovarian cancer. Finally, we verified *in vitro* that SPP1 expression was significantly higher in ovarian cancer cells than in normal ovarian cells. By flow cytometry, knockdown of SPP1 in ovarian cancer cells could promote tumorigenic apoptosis. SPP1 may be a potential therapeutic target for ovarian cancer.

Also, we must acknowledge the potential limitations of our analysis. First of all, our study is based on the analysis of public databases. Therefore, further multicenter, large sample, prospective studies that may follow are needed. Secondly, the screened gene SPP1 was only partially phenotypically experimented, and further exploration about the molecular mechanism needs to be followed up.

In addition, the cell type-specific marker expression patterns described in this study may contribute to a better understanding of the heterogeneity and biological characteristics of OC. The present work revealed markers for cells of different Tex subsets that may be better in diagnostics or other biological experiments. In conclusion, our study provides new insights into the heterogeneity of OC and may contribute to the development of new and efficient therapies for OC.

5 Conclusions

This is the first study to provide a more comprehensive understanding of the heterogeneity and clinical significance of Tex cells in OC, which will contribute to the development of more precise and effective therapies.

Data availability statement

The original contributions presented in the study are included in the article/Supplementary Material. Further inquiries can be directed to the corresponding author.

Author contributions

KW participated in literature research and writing, other authors participated in data analysis, and BL was responsible for the overall project design and adjustment. All authors contributed to the article and approved the submitted version.

Funding

This study is supported by National Natural Science Foundation of China (H1815/82272726).

Acknowledgments

We sincerely appreciate all the members who participated in data collection and analysis.

Conflict of interest

The authors declare that the research was conducted in the absence of any commercial or financial relationships that could be construed as a potential conflict of interest.

Publisher's note

Supplementary material

The Supplementary Material for this article can be found online at: https://www.frontiersin.org/articles/10.3389/fendo.2023.1168245/full#supplementary-material

References

1. Siegel RL, Miller KD, Jemal A. Cancer statistics, 2019. *CA: Cancer J Clin* (2019) 69 (1):7–34. doi: 10.3322/caac.21551

2. He C, Huang F, Zhang K, Wei J, Hu K, Liang M. Establishment and validation of an RNA binding protein-associated prognostic model for ovarian cancer. *J Ovarian Res* (2021) 14(1):1–11. doi: 10.1186/s13048-021-00777-1

3. Izar B, Tirosh I, Stover EH, Wakiro I, Cuoco MS, Alter I, et al. A single-cell landscape of high-grade serous ovarian cancer. *Nat Med* (2020) 26(8):1271–9. doi: 10.1038/s41591-020-0926-0

4. Elies A, Rivière S, Pouget N, Becette V, Dubot C, Donnadieu A, et al. The role of neoadjuvant chemotherapy in ovarian cancer. *Expert Rev Anticancer Ther* (2018) 18 (6):555–66. doi: 10.1080/14737140.2018.1458614

5. Zhao H, Gao Y, Miao J, Chen S, Li J, Li Z, et al. Single-cell RNA-seq highlights a specific carcinoembryonic cluster in ovarian cancer. *Cell Death Dis* (2021) 12(11):1–11. doi: 10.1038/s41419-021-04358-4

6. Lawson DA, Kessenbrock K, Davis RT, Pervolarakis N, Werb Z. Tumour heterogeneity and metastasis at single-cell resolution. *Nat Cell Biol* (2018) 20 (12):1349–60. doi: 10.1038/s41556-018-0236-7

7. Yuan X, Wang J, Huang Y, Shangguan D, Zhang P. Single-cell profiling to explore immunological heterogeneity of tumor microenvironment in breast cancer. *Front Immunol* (2021) 12:643692. doi: 10.3389/fimmu.2021.643692

8. Navin N, Hicks J. Future medical applications of single-cell sequencing in cancer. *Genome Med* (2011) 3(5):1–12. doi: 10.1186/gm247

9. Guo X, Zhang Y, Zheng L, Zheng C, Song J, Zhang Q, et al. Global characterization of T cells in non-small-cell lung cancer by single-cell sequencing. *Nat Med* (2018) 24(7):978–85. doi: 10.1038/s41591-018-0045-3

10. Savas P, Virassamy B, Ye C, Salim A, Mintoff CP, Caramia F, et al. Single-cell profiling of breast cancer T cells reveals a tissue-resident memory subset associated with improved prognosis. *Nat Med* (2018) 24(7):986–93. doi: 10.1038/s41591-018-0078-7

11. Ren X, Kang B, Zhang Z. Understanding tumor ecosystems by single-cell sequencing: promises and limitations. *Genome Biol* (2018) 19(1):1–14. doi: 10.1186/s13059-018-1593-z

12. Bartoschek M, Oskolkov N, Bocci M, Lövrot J, Larsson C, Sommarin M, et al. Spatially and functionally distinct subclasses of breast cancer-associated fibroblasts revealed by single cell RNA sequencing. *Nat Commun* (2018) 9(1):1–13. doi: 10.1038/s41467-018-07582-3

13. Shih AJ, Menzin A, Whyte J, Lovecchio J, Liew A, Khalili H, et al. Identification of grade and origin specific cell populations in serous epithelial ovarian cancer by single cell RNA-seq. *PloS One* (2018) 13(11):e0206785. doi: 10.1371/journal.pone.0206785

14. Liu Y, Wu J, Huang W, Weng S, Wang B, Chen Y, et al. Development and validation of a hypoxia-immune-based microenvironment gene signature for risk stratification in gastric cancer. *J Trans Med* (2020) 18(1):201. doi: 10.1186/s12967-020-02366-0

15. Nguyen HM, Vessella RL, Morrissey C, Brown LG, Coleman IM, Higano CS, et al. LuCaP prostate cancer patient-derived xenografts reflect the molecular heterogeneity of advanced disease and serve as models for evaluating cancer therapeutics. *Prostate* (2017) 77(6):654–71. doi: 10.1002/pros.23313

16. Zhang Y, Zhang Z. The history and advances in cancer immunotherapy: understanding the characteristics of tumor-infiltrating immune cells and their therapeutic implications. *Cell Mol Immunol* (2020) 17(8):807–21. doi: 10.1038/s41423-020-0488-6

17. Lai Y, Tang F, Huang Y, He C, Chen C, Zhao J, et al. The tumour microenvironment and metabolism in renal cell carcinoma targeted or immune therapy. *J Cell Physiol* (2021) 236(3):1616–27. doi: 10.1002/jcp.29969

18. Zhou J, Wang W, Li Q. Potential therapeutic targets in the tumor microenvironment of hepatocellular carcinoma: reversing the protumor effect of tumor-associated macrophages. *J Exp Clin Cancer Res* (2021) 40(1):1–12. doi: 10.1186/s13046-021-01873-2

19. Chamseddine AN, Assi T, Mir O, Chouaib S. Modulating tumor-associated macrophages to enhance the efficacy of immune checkpoint inhibitors: a TAM-pting approach. *Pharmacol Ther* (2022) 2021:107986. doi: 10.1016/j.pharmthera.2021.107986

20. Aran D, Looney AP, Liu L, Wu E, Fong V, Hsu A, et al. Reference-based analysis of lung single-cell sequencing reveals a transitional profibrotic macrophage. *Nat Immunol* (2019) 20(2):163–72. doi: 10.1038/s41590-018-0276-y

21. Steen CB, Liu CL, Alizadeh AA, Newman AM. Profiling cell type abundance and expression in bulk tissues with CIBERSORTx. *Methods Mol Biol*. (2020). 2117 135–57. doi: 10.1007/978-1-0716-0301-7_7

22. Shen J, Sun W, Liu J, Li J, Li Y, Gao Y. Metabolism-related signatures is correlated with poor prognosis and immune infiltration in hepatocellular carcinoma *via* multi-omics analysis and basic experiments. *Front Oncol* (2023) 13:1130094. doi: 10.3389/fonc.2023.1130094

23. Schuster M, Nechansky A, Kircheis R. Cancer immunotherapy. *Biotechnol Journal: Healthcare Nutr Technol* (2006) 1(2):138–47. doi: 10.1002/biot.200500044

24. Dillman RO. Cancer immunotherapy. *Cancer biotherapy radiopharmaceuticals* (2011) 26(1):1–64. doi: 10.1089/cbr.2010.0902

25. Mellman I, Coukos G, Dranoff G. Cancer immunotherapy comes of age. *Nature* (2011) 480(7378):480–9. doi: 10.1038/nature10673

26. Schreiber RD, Old LJ, Smyth MJ. Cancer immunoediting: integrating immunity's roles in cancer suppression and promotion. *Science* (2011) 331 (6024):1565–70. doi: 10.1126/science.1203486

27. Schietinger A, Greenberg PD. Tolerance and exhaustion: defining mechanisms of T cell dysfunction. *Trends Immunol* (2014) 35(2):51–60. doi: 10.1016/j.it.2013.10.001

28. Kim PS, Ahmed R. Features of responding T cells in cancer and chronic infection. *Curr Opin Immunol* (2010) 22(2):223–30. doi: 10.1016/j.coi.2010.02.005

29. Sharma P, Wagner K, Wolchok JD, Allison JP. Novel cancer immunotherapy agents with survival benefit: recent successes and next steps. *Nat Rev Cancer* (2011) 11 (11):805–12. doi: 10.1038/nrc3153

30. Page DB, Postow MA, Callahan MK, Allison JP, Wolchok JD. Immune modulation in cancer with antibodies. *Annu Rev Med* (2014) 65:185–202. doi: 10.1146/annurev-med-092012-112807

31. Callahan MK, Wolchok JD. At The bedside: CTLA-4-and PD-1-blocking antibodies in cancer immunotherapy. *J leukocyte Biol* (2013) 94(1):41–53. doi: 10.1189/jlb.1212631

32. Wherry EJ. T Cell exhaustion. *Nat Immunol* (2011) 12(6):492–9. doi: 10.1038/ni.2035

33. Barber DL, Wherry EJ, Masopust D, Zhu B, Allison JP, Sharpe AH, et al. Restoring function in exhausted CD8 T cells during chronic viral infection. *Nature* (2006) 439(7077):682–7. doi: 10.1038/nature04444

34. Hirano F, Kaneko K, Tamura H, Dong H, Wang S, Ichikawa M, et al. Blockade of B7-H1 and PD-1 by monoclonal antibodies potentiates cancer therapeutic immunity. *Cancer Res* (2005) 65(3):1089–96. doi: 10.1158/0008-5472.1089.65.3

35. Terabe M, Berzofsky JA. The role of NKT cells in tumor immunity. *Adv Cancer Res* (2008) 101:277–348. doi: 10.1016/S0065-230X(08)00408-9

36. Terabe M, Berzofsky JA. The immunoregulatory role of type I and type II NKT cells in cancer and other diseases. *Cancer Immunology Immunotherapy* (2014) 63 (3):199–213. doi: 10.1007/s00262-013-1509-4

37. ElMasri WM, Casagrande G, Hoskins E, Kimm D, Kohn EC. Cell adhesion in ovarian cancer. *Ovarian Cancer* (2009) 149:297–318. doi: 10.1007/978-0-387-98094-2_14

38. Hassan AA, Artemenko M, Tang MK, Wong AS. Selectins: an important family of glycan-binding cell adhesion molecules in ovarian cancer. *Cancers* (2020) 12 (8):2238. doi: 10.3390/cancers12082238

39. Lundgren S, Berntsson J, Nodin B, Micke P, Jirström K. Prognostic impact of tumour-associated b cells and plasma cells in epithelial ovarian cancer. *J Ovarian Res* (2016) 9(1):1–9. doi: 10.1186/s13048-016-0232-0

40. Gu-Trantien C, Loi S, Garaud S, Equeter C, Libin M, De Wind A, et al. CD4+ follicular helper T cell infiltration predicts breast cancer survival. *J Clin Invest* (2013) 123(7):2873–92. doi: 10.1172/JCI67428

41. Hetta HF, Elkady A, Yahia R, Meshall AK, Saad MM, Mekky MA, et al. T Follicular helper and T follicular regulatory cells in colorectal cancer: a complex interplay. *J Immunol Methods* (2020) 480:112753. doi: 10.1016/j.jim.2020.112753

frontiers | Frontiers in Endocrinology

TYPE Original Research
PUBLISHED 21 April 2023
DOI 10.3389/fendo.2023.1159235

OPEN ACCESS

EDITED BY
Chenyu Sun,
AMITA Health, United States

REVIEWED BY
Chen Chen,
Department of Hepatobilliary Surgery, Renmin Hospital of Wuhan University, China
Feng Chen,
Dalian Medical University, China

*CORRESPONDENCE
Kai Liu
liuk@jlu.edu.cn

†These authors contributed equally to this work

SPECIALTY SECTION
This article was submitted to Cancer Endocrinology, a section of the journal Frontiers in Endocrinology

RECEIVED 05 February 2023
ACCEPTED 06 April 2023
PUBLISHED 21 April 2023

CITATION
Zhou H, Chen J, Jin H and Liu K (2023) Genetic characteristics and clinical-specific survival prediction in elderly patients with gallbladder cancer: a genetic and population-based study.
Front. Endocrinol. 14:1159235.
doi: 10.3389/fendo.2023.1159235

Genetic characteristics and clinical-specific survival prediction in elderly patients with gallbladder cancer: a genetic and population-based study

Hao Zhou†, Junhong Chen†, Hengwei Jin and Kai Liu*

Department of Hepatobiliary and Pancreatic Surgery II, General Surgery Center, The First Hospital of Jilin University, Changchun, China

Background: Biliary system cancers are most commonly gallbladder cancers (GBC). Elderly patients (≥ 65) were reported to suffer from an unfavorable prognosis. In this study, we analyzed the RNA-seq and clinical data of elderly GBC patients to derive the genetic characteristics and the survival-related nomograms.

Methods: RNA-seq data from 14 GBC cases were collected from the Gene Expression Omnibus (GEO) database, grouped by age, and subjected to gene differential and enrichment analysis. In addition, a Weighted Gene Co-expression Network Analysis (WGCNA) was performed to determine the gene sets associated with age grouping further to characterize the gene profile of elderly GBC patients. The database of Surveillance, Epidemiology, and End Results (SEER) was searched for clinicopathological information regarding elderly GBC patients. Nomograms were constructed to predict the overall survival (OS) and cancer-specific survival (CSS) of elderly GBC patients. The predictive accuracy and capability of nomograms were evaluated through the concordance index (C-index), calibration curves, time-dependent operating characteristic curves (ROC), as well as area under the curve (AUC). Decision curve analysis (DCA) was performed to check out the clinical application value of nomograms.

Results: Among the 14 patients with GBC, four were elderly, while the remaining ten were young. Analysis of gene differential and enrichment indicated that elderly GBC patients exhibited higher expression levels of cell cycle-related genes and lower expression levels of energy metabolism-related genes. Furthermore, the WGCNA analysis indicated that elderly GBC patients demonstrated a decrease in the expression of genes related to mitochondrial respiratory enzymes and an increase in the expression of cell cycle-related genes. 2131 elderly GBC patients were randomly allocated into the training cohort (70%) and validation cohort (30%). Our nomograms showed robust discriminative ability with a C-index of 0.717/0.747 for OS/CSS in the training

cohort and 0.708/0.740 in the validation cohort. Additionally, calibration curves, AUCs, and DCA results suggested moderate predictive accuracy and superior clinical application value of our nomograms.

Conclusion: Discrepancies in cell cycle signaling and metabolic disorders, especially energy metabolism, were obviously observed between elderly and young GBC patients. In addition to being predictively accurate, the nomograms of elderly GBC patients also contributed to managing and strategizing clinical care.

KEYWORDS

energy metabolism, cell cycle, nomogram, elderly gallbladder cancer, OS, CSS

1 Introduction

Gallbladder cancer (GBC) is a kind of carcinoma mainly derived from gallbladder secretory cells; hence adenocarcinoma is the absolute dominant category. It is the predominant malignancy in the biliary duct system, making up more than 95% of cases (1). As reported by GLOBOCAN 2020, GBC ranks as the 25th most prevalent cancer and has a global mortality rate of 0.9% (2). However, the mortality of GBC (average 0.09%) is far lower than that of other highly malignant tumors, like lung cancer (18%) or female breast cancer (15%), the prognosis of GBC remains unsatisfying, which is possibly associated with non-specific manifestations, absence of early diagnosis and highly invasiveness of tumor itself (1, 3, 4). Nearly 1 out of 5 patients with GBC got timely diagnosis and treatment in the US (5). Because of characteristics like the peculiar anatomic site and blood supply of gallbladder, patients' physical differences and heterogeneity of cancer cells, etc., GBC is not well responsive to traditional chemotherapy and radiotherapy; as a result, surgical resection remains the primary treatment approach for individuals diagnosed with GBC (6). Possibly due to GBC taking decades for full development, a majority of patients are old (≥ 65), and GBC is typically diagnosed at an average age of 72 in the US (5). The SEER database revealed that the incidence rates of GBC (per 100,000) were age-adjusted and varied by age group in 2015. The rates increased with age, from 0.2 for those aged 20-49 years, to 1.6 for those aged 50-64 years, to 4.3 for those aged 65-74 years, and to 8.1 for those aged over 75 years. The mortality rates (per 100,000) followed a similar pattern, rising from 0.1 for those aged 20-49 years, to 0.7 for those aged 50-64 years, to 2.1 for those aged 65-74 years, and to 4.9 for those aged over 75 years (7). This informed us that older people are a high-risk population for GBC and, in the meanwhile, for patients with GBC, the older they are, the poorer prognosis they may suffer. Therefore, it is crucial to exploit innovative biomarkers or robust models for predicting survival probability of elderly patients (≥ 65) with GBC to aid clinical management better.

Nomograms are digital graphical tools with the integration of several key variables, which are now commonly applied for event prediction, especially for prognosis prediction in cancers. Compared to the traditional TNM stage, it can include more tumor characteristics and has gained extensive usage in forecasting the outcomes of various cancer types (8–10). Several nomograms have been established for prognosis prediction, lymph node metastasis prediction, or distant metastasis prediction in GBC (11–16). Still, there are no nomograms that are exploited based on elderly patients with GBC. Owing to the specificity of the elderly patients, creating a new model for this group is necessary. The GEO database (https://www.ncbi.nlm.nih.gov/geo/) is a widely used gene sequencing database from which we retrieved 14 cases of GBC with age-specific characteristics. Therefore, this study investigated the genetic characteristics of elderly GBC patients based on the sequencing data from the GEO database. The SEER database (https://seer.cancer.gov/) is a reliable and thorough online resource for collecting cancer statistics from the US population. With the goal of assisting clinical decision-making and maximizing benefits, our aim was to pinpoint prognostic factors and construct a trustworthy nomogram for calculating the likelihood of survival in elderly GBC patients relying on the SEER database.

2 Materials and methods

2.1 RNA-seq data collection and analysis

The present study employed RNA-seq data from 14 GBC patients, sourced from two chips available in the GEO database, namely GSE62335 and GSE76633. In order to eliminate batch effects, all RNA-seq data were de-identified using the Combat method, and log2 normalization was performed, following the protocol of prior studies (17, 18). The young and elderly subgroups were defined by an age cutoff of 65 years, with 10 and 4 patients respectively. To identify differentially expressed genes between the two subgroups, limma was employed with the

screening criteria of |log2FC| > 1 and p-value < 0.05 (19). Gene Set Enrichment Analysis (GSEA) was then performed using the Gene Ontology (GO), Kyoto Encyclopedia of Genes and Genomes (KEGG), and ReactomePA pathway gene sets. Additionally, Gene Set Variation Analysis (GSVA) was performed with the KEGG gene set as the reference gene set (20). WGCNA was applied to the differential genes between the two subgroups to further explore gene sets associated with aging (21). The important gene sets were annotated with gene function and Protein-Protein Interaction (PPI) analysis, and the top 10 hub genes in the PPI network were identified using the cytoHub method. To assess immune cell infiltration in the tumor microenvironment of the 14 GBC patients, immune cell prediction algorithms of the TIMER2.0 platform were employed (22). Finally, drug sensitivity and immunotherapy sensitivity analyses were conducted using the oncoPredict R package and TIDE analysis, respectively (23). The TIDE analysis for evaluating immunotherapy sensitivity is based on the TIDE website (http://tide.dfci.harvard.edu). The TIDE value obtained from the analysis can be used to assess the efficacy of immunotherapy. Generally, a higher TIDE value indicates lower sensitivity to immunotherapy.

2.2 Cohorts formation and data collection

The primary patient cohort was acquired from the SEER database (site code C23.9), including all patients diagnosed with GBC between 2010 and 2017. Inapplicable patients were screened out. Exclusion principles were detailed as follows (1): young patients (< 65) (2), without a pathological diagnosis (3), unknown tumor grade (4), unknown TNM stage (5), unknown tumor size (6), unknown surgery information and (7) survival period of under one month or indeterminate duration of survival.

Following exclusion, the training and validation cohorts were assigned at random in a 7/3 split. The SEER database provided clinicopathological information, which encompassed age, race, marital status, tumor size, gender, tumor grade, AJCC TNM stage, surgery information, radiotherapy, chemotherapy, overall survival (OS), and cancer-specific survival (CSS). The workflow is demonstrated in Supplementary Figure.

2.3 Nomograms construction and validation

The training cohort was subjected to both univariate and multivariate Cox regression analyses to identify independent prognostic variables. The resulting significant variables from the latter were then utilized to create nomograms for predicting CSS and OS, respectively. To assess the effectiveness of the nomograms, various methods were utilized. Calibration curves were used to display the accuracy of the predictions made by the nomograms. Meanwhile, time-dependent receiver operating characteristic (ROC) curves and area under the curve (AUC) were employed to evaluate how well the nomograms were able to distinguish between different groups over time. In order to ensure the validity of the results, the nomograms were then tested in a validation cohort, and the analyses were reperformed accordingly.

2.4 Clinical associations

Decision curve analysis (DCA) was performed to assess the suitability of the nomograms for practical clinical use in contrast to the AJCC TNM stage. Nomograms were utilized to calculate the optimal cut-off value for the risk score via the ROC curve for each patient. After calculating the risk scores, patients in the training and validation cohorts were classified into high-risk and low-risk categories. To evaluate the survival differences, we utilized K-M survival curves to analyze both CSS and OS between these groups in both cohorts. Additionally, we investigated the impact of various surgery conditions on survival differences for both high-risk and low-risk patients.

2.5 Statistical analysis

To compare between groups, either chi-square tests or non-parametric U tests were employed. Frequency distribution (%), obtained through the chi-square test, was used to describe the remaining variable types. The survival disparities between the groups were examined using the Log-rank test and K-M curves. The statistical analysis was conducted using R software (version 3.6.2). R packages utilized in this study included "rms," "survival," "survminer," and "ggDCA." All statistical significance in this study was determined using a P-value of ≤ 0.05.

3 Results

3.1 Gene differential analysis and gene enrichment analysis of GBC

In this study, we enrolled a total of 14 patients with GBC and recorded their ages for further analysis. Through gene differential analysis, we identified 272 highly expressed genes and 150 lowly expressed genes in the elderly GBC group compared to the young GBC group (Figure 1). Further, using GSEA analysis based on the GO gene set, we observed an increased function of chromosomal and keratin-related genes and a decreased function of metabolism-related genes in elderly GBC patients (Figure 1). Similarly, GSEA analysis of differential genes based on the KEGG gene set showed an increased function of cell cycle-related genes and a decreased function of bile secretion-related genes in elderly GBC patients (Figure 1). Furthermore, the GSEA analysis based on the ReactomePA gene set showed an increased function of cell cycle-related genes and a decreased function of drug metabolism-related genes in elderly GBC patients (Figure 1). Finally, we performed GSVA analysis based on the KEGG gene set and found a decrease in metabolism-related pathways and an increase in cell cycle-related pathways in elderly GBC patients (Figure 1). By integrating the results of the above gene enrichment analyses, our study reveals a

significant decrease in the expression of genes related to aerobic and lipid metabolism and an increase in the expression of genes related to cell cycle and mitosis in elderly GBC patients.

3.2 WGCNA analysis, drug sensitivity analysis, and immune microenvironment analysis of GBC

In this study, we conducted WGCNA analysis on sequencing data from two groups of GBC patients, employing a soft threshold of 14 (Figure 2A). We partitioned 13,991 genes into 22 gene set modules and subjected them to correlation analysis (Figures 2B, C). Our analysis revealed that the aging traits of GBC patients were significantly correlated with two gene modules, namely MEgreen (0.61, p = 0.02) and MEbrown (0.59, p = 0.03) (Figure 2D). Gene function annotation of the MEgreen gene module suggested that genes within this module were primarily associated with foreign body stimulation and aerobic metabolism (Figure 2E). On the other hand, functional annotation of the MEbrown gene module revealed that this module was mainly associated with the cell cycle and mitosis (Figure 2F). These findings corroborated our gene enrichment analysis results, demonstrating a low expression of energy metabolism-related genes and a high expression of cell cycle-related genes in elderly GBC patients.

We further performed a PPI analysis of the MEgreen and MEbrown gene modules and identified their top 10 hub genes (Figures 3A). The key hub genes, identified with the MT (mitochondrial) prefix, indicate that the majority of these genes originate from the mitochondrial genome (Figure 3). The top10 hub genes of MEgreen included ND1, ND2, ND3, ND4, ND4L, CYTB, COX1, COX2, ATP6, and ATP8, and the expression of these genes was reduced in elderly GBC patients (Figure 3). Moreover, they exhibited a high correlation (Figure 3). The top10 hub genes of

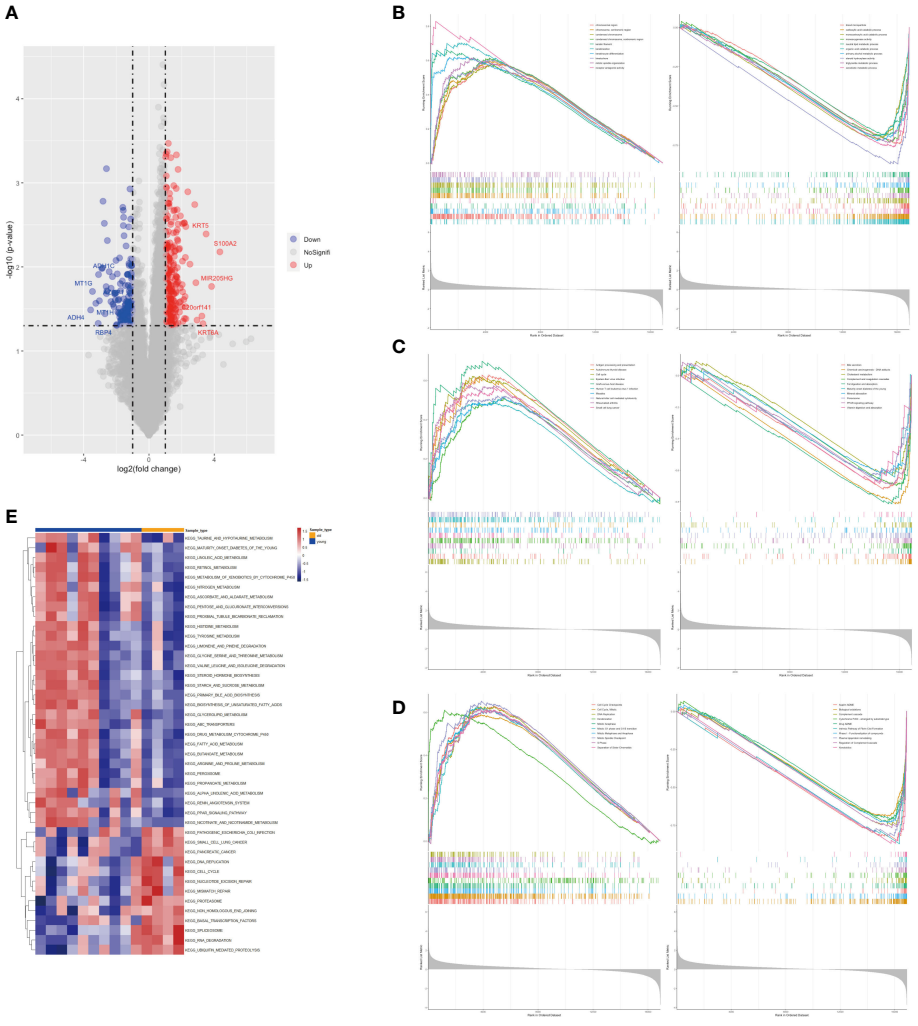

FIGURE 1
Gene differential analysis and gene enrichment analysis. **(A)** Volcano map of limma analysis. **(B)** GSEA enrichment analysis based on GO gene set. **(C)** GSEA enrichment analysis based on KEGG gene set. **(D)** GSEA enrichment analysis based on ReactomePA gene set. **(E)** GSVA pathway analysis based on KEGG gene set.

MEbrown were mainly AURKA, AURKB, CCNA2, CCNB1, CDK1, DLGAP5, KIF11, MELK, NCAPG, and TPX2, and these genes were elevatedly expressed in elderly GBC patients (Figure 3) and had a high correlation (Figure 3). These results indicated that elderly GBC patients had a high expression of cell cycle-related genes and a low expression of mitochondrial respiratory enzyme-related genes, reflecting the genetic characteristics of elderly GBC that promote metastasis and deterioration of GBC cells.

We also performed a drug sensitivity analysis for both groups, demonstrating that elderly GBC patients were less responsive to cisplatin and gemcitabine (Figure 3). Sensitivity analysis of immunotherapy revealed that elderly GBC patients displayed elevated expression of CD274 (PD-L1) and CTLA4, and demonstrated reduced responsiveness to immunotherapy, as indicated by a higher TIDE value (Figure 3). Finally, we employed a series of immunocyte prediction algorithms, which highlighted potential discrepancies in the tumor immune microenvironment between elderly and young GBC patients (Figure 4).

3.3 Clinicopathological characteristics of patients

8583 individuals with GBC between 2010 and 2017 were enrolled in the primary cohort. According to the exclusion criteria, 6452 inapplicable patients were screened out, including 2779 young patients (< 65), 866 patients without a pathological diagnosis, 1331 patients with unknown tumor grade, 436 patients with unknown TNM stage, 897 patients with unknown tumor size, 14 patients with unknown surgery information and 129 patients' survival period of under one month or indeterminate duration of survival. As a result, 2131 elderly patients with GBC were finally

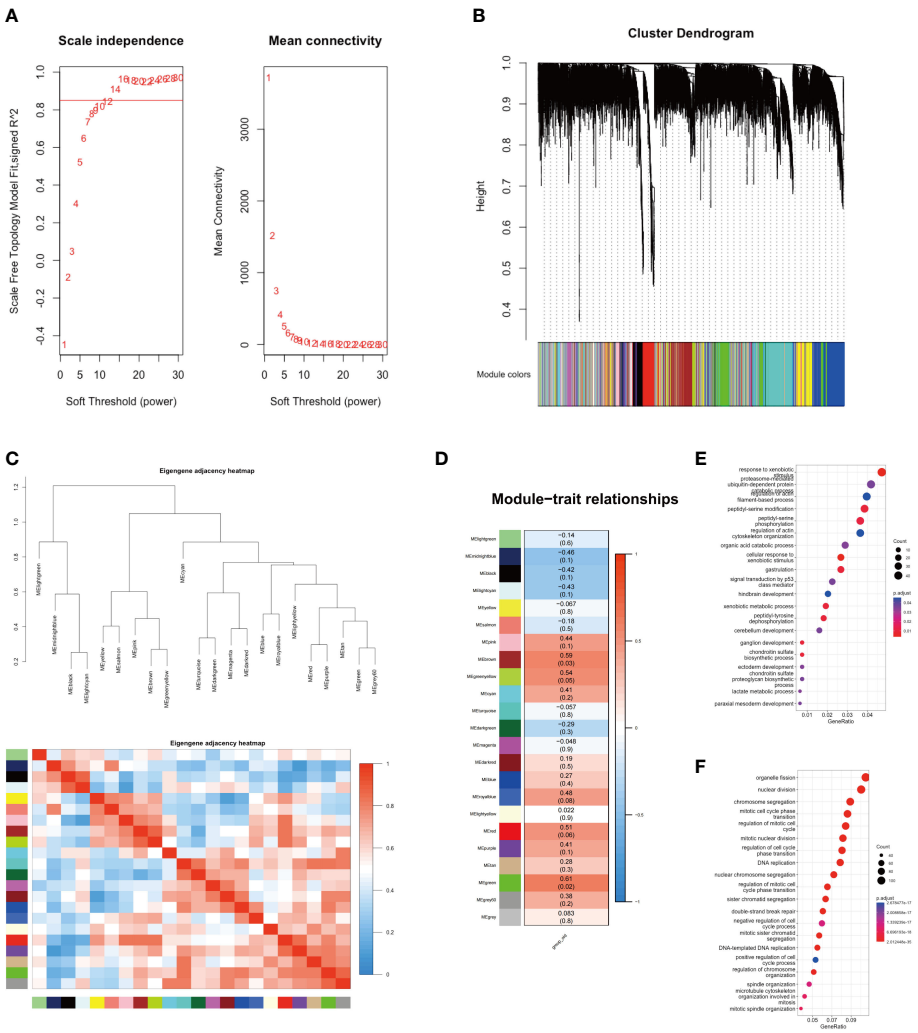

FIGURE 2
WGCNA analysis of two groups. **(A)** Scale independence and mean connectivity. **(B)** Cluster dendrogram of 22 modules. **(C)** Eigengene adjacency heatmap. **(D)** Module-trait relationships. **(E)** GO enrichment analysis of MEgreen gene module. **(F)** GO enrichment analysis of MEbrown gene module.

identified and randomly allocated to the training cohort (1492, 70%) and validation cohort (639, 30%). The clinicopathological characteristics of enrolled patients in both cohorts were summarized in Table 1. Females accounted for 67.95% of all patients, while males accounted for 32.05%. 55.89% of patients have aged over 74, and 44.11% of patients are aged between 65 and 74. Patients who didn't get married (51.99%) were approximately the same as patients who got married (48.01%). Most patients were white (77.48%). Tumor grades contained grade I (14.97%), grade II (44.91%), grade III (37.59%), and grade IV (2.53%). Patients were labeled as stage T1 (12.62%), stage T2 (47.82%), stage T3 (36.84%), and stage T4 (2.72%). Most patients were in the N0 stage (70.06%) and M0 stage (81.79%). Tumor size < 3 cm accounted for 49.37%, and tumor size ≥ 3 cm accounted for 50.63%. A majority of patients had local tumor excision/partial cholecystectomy surgery (82.40%), 11.78% of patients got radical cholecystectomy surgery, and only 5.82% of patients did not have surgery. A small part of patients (16.05%) got radiotherapy, and others (83.95%) did not. Also, the patients who had chemotherapy (34.58%) were less than those who did not (65.42%). There were no significant differences in these clinicopathological characteristics in both cohorts ($P > 0.05$).

3.4 Independent prognostic predictors from Cox regression analysis

Next, in the training cohort, univariate Cox regression analyses were conducted to determine risk factors associated with OS and CSS, respectively. Detailed information was integrated in Tables 2, 3. The results turned out to be that older age (> 74), higher tumor grade (grade II&III&IV), advanced TNM stage (T2&3&4, N1&2, and M1), and larger tumor size (≥ 3 cm) were significantly

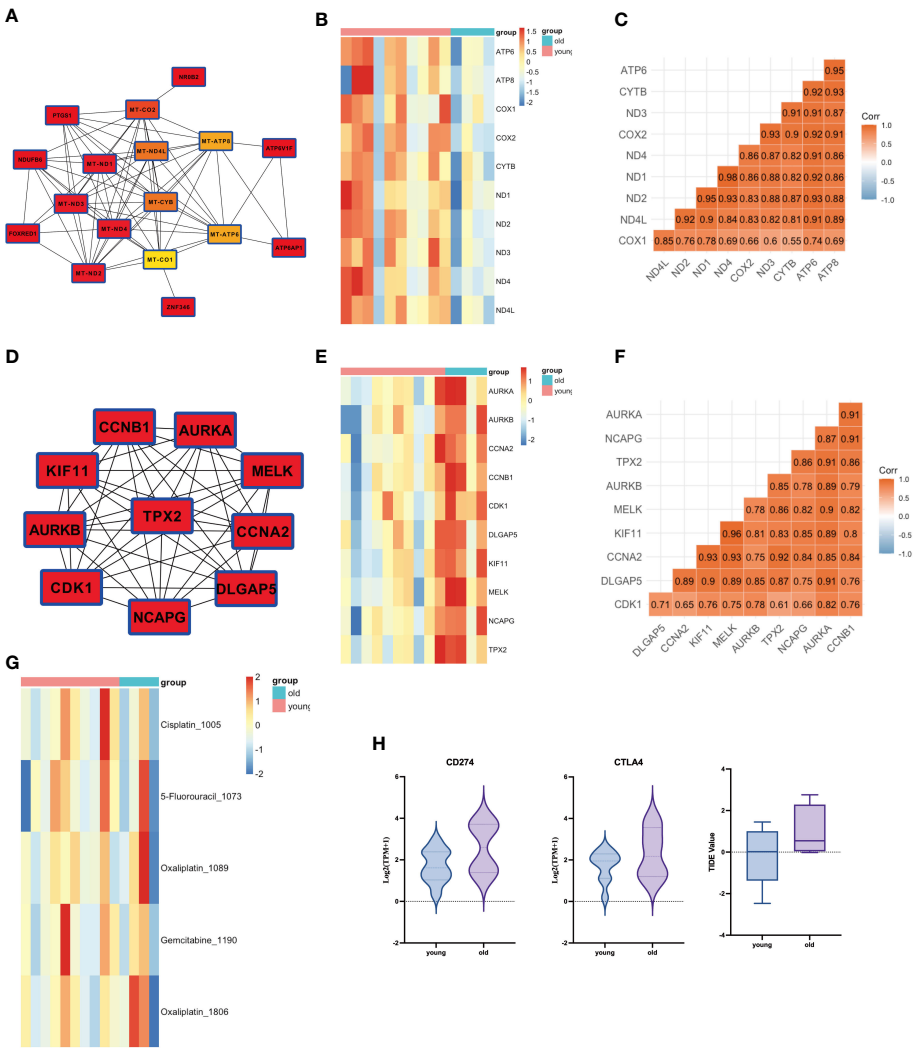

FIGURE 3
PPI analysis of WGCNA and drug sensitivity analysis. **(A)** Core network of the MEgreen gene module (MT: mitochondrial). **(B)** Gene expression of top 10 genes in MEgreen gene module. **(C)** Gene relation of top 10 genes in MEgreen gene module. **(D)** Core network of the MEbrown gene module. **(E)** Gene expression of top 10 genes in MEbrown gene module. **(F)** Gene relation of top 10 genes in MEbrown gene module. **(G)** Drug sensitivity analysis in common chemotherapy drugs. **(H)** Drug sensitivity analysis in immunotherapy.

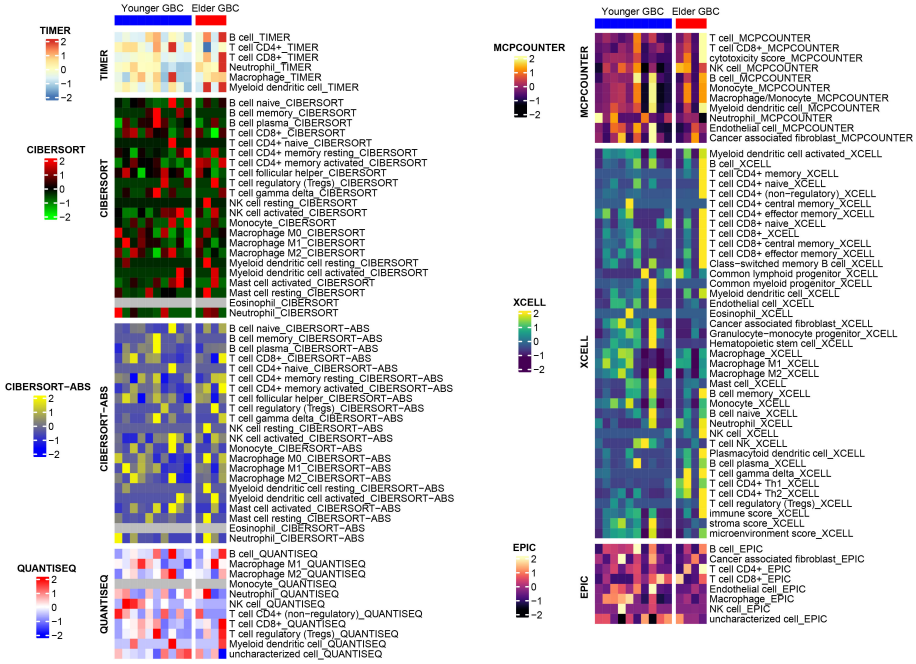

FIGURE 4
The discrepancies in immune cell infiltration between elderly and young GBC patients.

TABLE 1 Clinicopathological characteristics of elderly patients with GBC.

	All N = 2131	Training Cohort N = 1492	Validation Cohort N = 639	*P*-value
Sex				0.591
Male	683 (32.05%)	484 (32.44%)	199 (31.14%)	
Female	1448 (67.95%)	1008 (67.56%)	440 (68.86%)	
Age				0.952
65-74	940 (44.11%)	657 (44.03%)	283 (44.29%)	
> 74	1191 (55.89%)	835 (55.97%)	356 (55.71%)	
Marital status				0.523
No	1108 (51.99%)	783 (52.48%)	325 (50.86%)	
Married	1023 (48.01%)	709 (47.52%)	314 (49.14%)	
Race				0.745
White	1651 (77.48%)	1160 (77.75%)	491 (76.84%)	
Black	211 (9.90%)	149 (9.99%)	62 (9.70%)	
Other	269 (12.62%)	183 (12.27%)	86 (13.46%)	
Grade				0.497
I	319 (14.97%)	223 (14.95%)	96 (15.02%)	
II	957 (44.91%)	685 (45.91%)	272 (42.57%)	
III	801 (37.59%)	548 (36.73%)	253 (39.59%)	
IV	54 (2.53%)	36 (2.41%)	18 (2.82%)	

(Continued)

TABLE 1 Continued

	All N = 2131	Training Cohort N = 1492	Validation Cohort N = 639	*P*-value
T stage				0.817
T1	269 (12.62%)	185 (12.40%)	84 (13.15%)	
T2	1019 (47.82%)	709 (47.52%)	310 (48.51%)	
T3	785 (36.84%)	555 (37.20%)	230 (35.99%)	
T4	58 (2.72%)	43 (2.88%)	15 (2.35%)	
N stage				0.333
N0	1493 (70.06%)	1043 (69.91%)	450 (70.42%)	
N1	562 (26.37%)	401 (26.88%)	161 (25.20%)	
N2	76 (3.57%)	48 (3.22%)	28 (4.38%)	
M stage				0.402
M0	1743 (81.79%)	1213 (81.30%)	530 (82.94%)	
M1	388 (18.21%)	279 (18.70%)	109 (17.06%)	
Tumor size				0.773
< 3 cm	1052 (49.37%)	733 (49.13%)	319 (49.92%)	
≥ 3 cm	1079 (50.63%)	759 (50.87%)	320 (50.08%)	
Surgery				0.912
No	124 (5.82%)	88 (5.90%)	36 (5.63%)	
Local tumor excision/partial cholecystectomy	1756 (82.40%)	1226 (82.17%)	530 (82.94%)	
Radical cholecystectomy	251 (11.78%)	178 (11.93%)	73 (11.42%)	
Radiotherapy				0.694
No/Unknown	1789 (83.95%)	1249 (83.71%)	540 (84.51%)	
Yes	342 (16.05%)	243 (16.29%)	99 (15.49%)	
Chemotherapy				0.960
No/Unknown	1394 (65.42%)	977 (65.48%)	417 (65.26%)	
Yes	737 (34.58%)	515 (34.52%)	222 (34.74%)	

negatively correlated with OS. In contrast, married status and receiving surgery (local tumor excision/partial cholecystectomy surgery and radical cholecystectomy surgery) were positively correlated with OS. In terms of CSS, the risk factors mentioned above were still significantly associated with CSS, but age and marital status were. Receiving chemotherapy was mainly determined as a negative risk factor for CSS (HR = 1.267, 95% CI: 1.102-1.456). Results from subsequent multivariate Cox regression analyses further identified older age (> 74), married status, higher tumor grade (grade III&IV), advanced TNM stage (T2&3&4, N1, and M1), and receiving surgery (local tumor excision/partial cholecystectomy surgery and radical cholecystectomy surgery) as independent prognostic predictors for OS. Meanwhile, higher tumor grade (grade III&IV), advanced TNM stage (T2&3&4, N1, and M1), larger tumor size (≥ 3 cm), receiving surgery (local tumor excision/partial cholecystectomy surgery and radical cholecystectomy surgery), and receiving chemotherapy were determined as independent prognostic predictors for CSS.

3.5 Construction of nomograms to predict OS and CSS at 1-, 3-, and 5-year

Based on the results of Cox regression analysis, two distinct nomograms were created for predicting the OS and CSS at 1-, 3-, and 5-year, respectively (Figure 5). The nomograms revealed that certain demographic and clinical factors, such as age, marital status, tumor grade, surgery information, and TNM stage, played crucial roles in predicting OS. On the other hand, tumor grade, tumor size, surgery information, chemotherapy, and TNM stage were critical prognostic indicators for predicting CSS. In particular, T stage emerged as the most significant risk factor for both OS and CSS, as it had a considerable impact on the overall point score in the nomograms.

10.3389/fendo.2023.1159235

TABLE 2 Univariate and multivariate Cox regression analysis of OS in training cohort.

	Hazard ratio	Univariate 95% CI	*P*-value	Hazard ratio	Multivariate 95% CI	*P*-value
Sex						
Male						
Female	0.972	0.858-1.101	0.651			
Age						
65-74						
> 74	1.339	1.188-1.510	< 0.001	1.535	1.356-1.737	< 0.001
Marital status						
No						
Married	0.869	0.772-0.978	0.019	0.851	0.754-0.960	0.009
Race						
White						
Black	0.992	0.815-1.207	0.933			
Other	0.851	0.706-1.026	0.090			
Grade						
I						
II	1.312	1.083-1.589	0.005	1.166	0.961-1.414	0.120
III	2.194	1.808-2.661	< 0.001	1.540	1.264-1.878	< 0.001
IV	3.059	2.097-4.463	< 0.001	2.053	1.397-3.017	< 0.001
T stage						
T1						
T2	1.670	1.334-2.090	< 0.001	1.556	1.239-1.955	< 0.001
T3	4.306	3.434-5.401	< 0.001	3.340	2.625-4.250	< 0.001
T4	8.008	5.533-11.592	< 0.001	5.373	3.643-7.923	< 0.001
N stage						
N0						
N1	1.599	1.404-1.820	< 0.001	1.215	1.058-1.395	0.006
N2	1.964	1.428-2.702	< 0.001	0.991	0.712-1.381	0.959
M stage						
M0						
M1	3.119	2.703-3.598	< 0.001	2.167	1.847-2.542	< 0.001
Tumor size						
< 3 cm						
≥ 3 cm	1.659	1.473-1.868	< 0.001	1.113	0.979-1.265	0.101
Surgery						
No						
Local tumor excision/partial cholecystectomy	0.249	0.199-0.313	< 0.001	0.658	0.513-0.845	0.001
Radical cholecystectomy	0.292	0.223-0.384	< 0.001	0.481	0.363-0.638	< 0.001

(Continued)

10.3389/fendo.2023.1159235

TABLE 2 Continued

	Hazard ratio	Univariate 95% CI	*P*-value	Hazard ratio	Multivariate 95% CI	*P*-value
Radiotherapy						
No/Unknown						
Yes	0.927	0.794-1.084	0.344			
Chemotherapy						
No/Unknown						
Yes	1.069	0.946-1.209	0.283			

OS, overall survival; CI, confidential interval.

TABLE 3 Univariate and multivariate Cox regression analysis of CSS in training cohort.

	Hazard ratio	Univariate 95% CI	*P*-value	Hazard ratio	Multivariate 95% CI	*P*-value
Sex						
Male						
Female	0.909	0.788-1.049	0.193			
Age						
65-74						
> 74	1.135	0.988-1.302	0.073			
Marital status						
No						
Married	0.928	0.810-1.065	0.288			
Race						
White						
Black	0.954	0.756-1.204	0.692			
Other	0.834	0.670-1.038	0.104			
Grade						
I						
II	1.414	1.116-1.792	0.004	1.238	0.975-1.571	0.080
III	2.611	2.063-3.305	< 0.001	1.886	1.480-2.405	< 0.001
IV	4.244	2.825-6.376	< 0.001	2.676	1.765-4.058	< 0.001
T stage						
T1						
T2	1.708	1.287-2.265	< 0.001	1.653	1.241-2.203	0.001
T3	5.256	3.973-6.952	< 0.001	4.082	3.029-5.499	< 0.001
T4	10.345	6.809-15.718	< 0.001	7.635	4.913-11.866	< 0.001
N stage						
N0						

(Continued)

TABLE 3 Continued

	Hazard ratio	Univariate 95% CI	*P*-value	Hazard ratio	Multivariate 95% CI	*P*-value
N1	1.787	1.542-2.071	< 0.001	1.397	1.187-1.643	< 0.001
N2	2.285	1.614-3.236	< 0.001	1.034	0.720-1.486	0.855
M stage						
M0						
M1	3.792	3.242-4.435	< 0.001	2.640	2.209-3.155	< 0.001
Tumor size						
< 3 cm						
≥ 3 cm	1.891	1.645-2.174	< 0.001	1.222	1.051-1.421	0.009
Surgery						
No						
Local tumor excision/partial cholecystectomy	0.214	0.168-0.273	< 0.001	0.671	0.513-0.878	0.004
Radical cholecystectomy	0.297	0.222-0.398	< 0.001	0.547	0.405-0.739	< 0.001
Radiotherapy						
No/Unknown						
Yes	1.004	0.841-1.198	0.965			
Chemotherapy						
No/Unknown						
Yes	1.267	1.102-1.456	0.001	0.570	0.485-0.669	< 0.001

CSS, cancer-specific survival; CI, confidential interval.

3.6 Validation of nomograms and performance evaluation

The nomograms were subjected to internal validation in the validation cohort, where the concordance index (C-index) was calculated. In the training cohort, the C-index for OS was 0.717 (95% CI: 0.701-0.732), and for CSS, it was 0.747 (95% CI: 0.730-0.764). The C-index for the validation cohort was also calculated for both OS and CSS, which were found to be 0.708 (95% CI: 0.682-0.733) and 0.740 (95% CI: 0.715-0.766), respectively. The C-index values for the validation cohort were found to be moderate, indicating a reasonable degree of accuracy for the nomograms. To assess the predictive performance of our nomograms, we utilized two evaluation methods: calibration curves and time-dependent

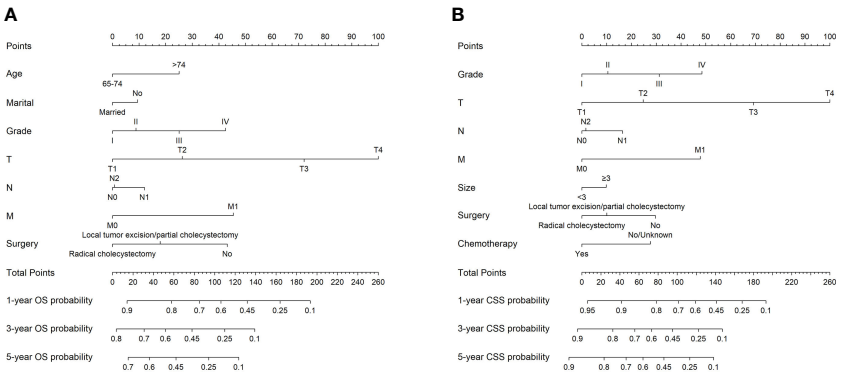

FIGURE 5
The nomograms to predict OS and CSS at 1-, 3-, and 5-year for elderly patients with GBC. **(A)** The nomogram to predict OS for elderly patients with GBC. **(B)** The nomogram to predict CSS for elderly patients with GBC.

10.3389/fendo.2023.1159235

ROC curves. The calibration curves, as depicted in Figure 6, demonstrated the accuracy of the predicted survival probabilities for both OS and CSS in both the training cohort and validation cohort. These curves exhibited a high degree of linearity, closely mirroring the actually observed survival probabilities. As such, our nomograms displayed robust predictive accuracy in both cohorts. Moreover, we also generated time-dependent ROC curves, as illustrated in Figure 7, to evaluate the discriminative ability of our nomograms. The AUCs for OS and CSS were calculated at 1-, 3-, and 5-year intervals for both the training and validation cohorts. The results revealed that our nomograms possessed excellent discrimination capabilities, with AUCs at 1-, 3-, and 5-year intervals ranging from 0.770 to 0.827 for OS and 0.784 to 0.816 for CSS across both cohorts. In summary, our nomograms demonstrated a high degree of accuracy in predicting survival probabilities, as evidenced by the calibration curves, and excellent discrimination capabilities, as indicated by the time-dependent ROC curves. These results support the robustness of our nomograms as a valuable tool for predicting survival outcomes.

3.7 Clinical application of nomograms

Figure 8 displays the outcomes of the DCA analysis, which showcases the superiority of our nomograms in terms of clinical benefits over the conventional TNM stage at 1-year in both the training and validation cohorts. However, the clinical benefits appeared to be out of advantage for our nomograms compared to the conventional TNM stage for 3-year and 5-year. This approved that our nomograms have better clinical application value to help clinicians assess early survival probability (1-year) both for OS and CSS compared to the conventional TNM stage. The nomograms were utilized to calculate the risk score and optimal cut-off value for each patient by means of the ROC curve. Patients were categorized into either a high-risk group, characterized by a total score greater than or equal to 96.00 for OS comparison and 88.91 for CSS comparison, or a low-risk group, with a total score less than the aforementioned cut-off values. The K-M survival curves demonstrated that patients who were classified as high-risk had a notably worse prognosis for both OS and CSS in both the training cohort and validation cohort, with all *P*-values being less than 0.0001 (Figure 9). For OS, the predicted survival probabilities at 1-, 3-, 5-year were 37.7%, 12.7%, and 7.1% for the high-risk group and 79.8%, 51.9%, and 42.8% for the low-risk group. For CSS, the predicted survival probabilities at 1-, 3-, 5-year were 48.1%, 21.9%, and 16.9% for the high-risk group and 87.3%, 66.8%, and 61.7% for the low-risk group. We found that the vast majority of patients underwent surgical treatment, both in the high- and low-risk groups. Moreover, survival probabilities (both OS and CSS) of patients who received surgery got significant improvements in contrast to that of patients who didn't receive surgery in the high-

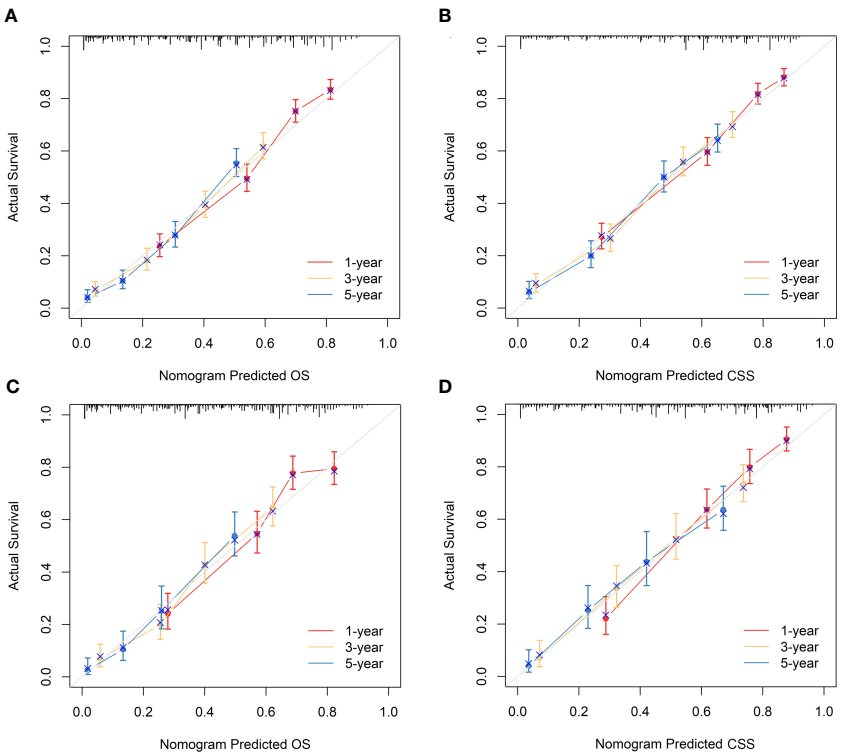

FIGURE 6
Calibration curves of the nomograms to predict OS and CSS at 1-, 3-, and 5-year for elderly patients with GBC. **(A)** Calibration curve of the nomogram to predict OS at 1-, 3-, and 5-year in the training cohort. **(B)** Calibration curve of the nomogram to predict CSS at 1-, 3-, and 5-year in the training cohort. **(C)** Calibration curve of the nomogram to predict OS at 1-, 3-, and 5-year in the validation cohort. **(D)** Calibration curve of the nomogram to predict CSS at 1-, 3-, and 5-year in the validation cohort. The horizontal axis of the nomogram represents the expected value, while the vertical axis represents the observed value.

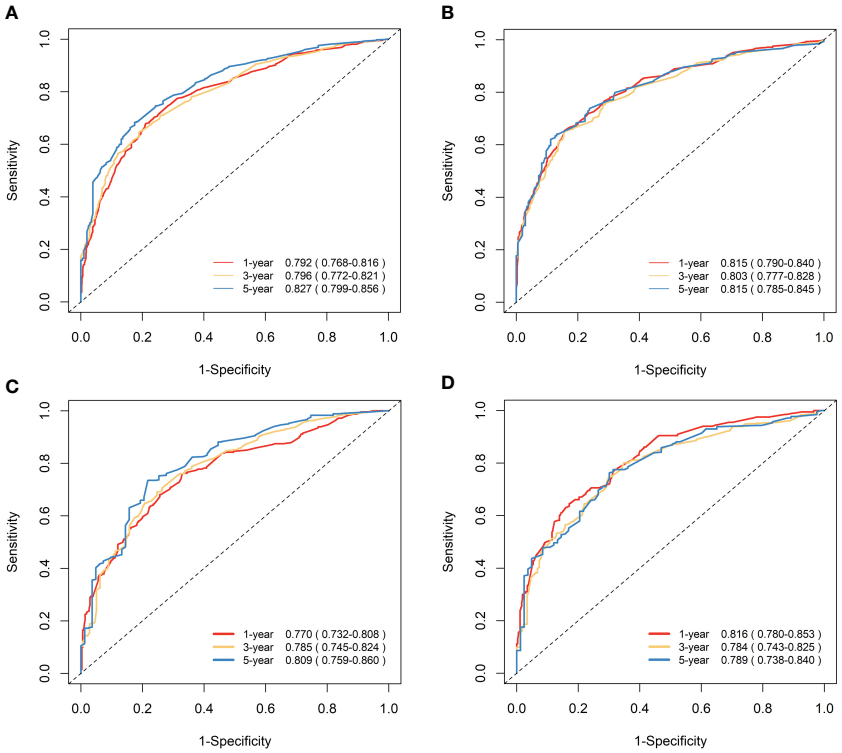

FIGURE 7
Time-dependent ROC curves to predict OS and CSS at 1-, 3-, and 5-year for elderly patients with GBC. **(A)** AUCs at 1-, 3-, and 5-year for OS prediction in the training cohort. **(B)** AUCs at 1-, 3-, and 5-year for CSS prediction in the training cohort. **(C)** AUCs at 1-, 3-, and 5-year for OS prediction in the validation cohort. **(D)** AUCs at 1-, 3-, and 5-year for CSS prediction in the validation cohort.

risk group ($P < 0.0001$, Figures 10A). It appeared to be that receiving radical cholecystectomy surgery contributes to slight OS improvement in the early five years, compared to receiving local tumor excision/partial cholecystectomy surgery (Figure 10). However, it revealed no apparent difference in CSS improvement between the local tumor excision/partial cholecystectomy surgery subgroup and the radical cholecystectomy surgery subgroup (Figure 10). In the low-risk group, patients who received surgery got significant CSS improvement in contrast to that of patients who didn't receive surgery. However, there were no significant survival improvements for both OS and CSS between the local tumor excision/partial cholecystectomy surgery subgroup and the radical cholecystectomy surgery subgroup (Figures 10C).

4 Discussion

In this study, we acquired GBC RNA-seq data from the GEO database and analyzed the genetic characteristics of elderly GBC patients. Our data set comprised 14 GBC patients, including four elderly and ten young patients. We performed genetic correlation analysis on age subgroups and discovered significant differences in the gene expression profiles of elderly and young GBC patients. Using WGCNA analysis, we identified a significant reduction in the expression of ND1, ND2, ND3, ND4, ND4L, CYTB, COX1, COX2, ATP6, and ATP8 genes, all of which are associated with mitochondrial respiratory enzyme functions in elderly GBC patients.

Additionally, pathway enrichment analysis results suggested that elderly GBC patients experience a significant decrease in aerobic metabolic processes, leading to reduced energy metabolism. Notably, few studies have investigated the metabolic aspects of GBC, making our findings particularly noteworthy. The reduced energy metabolic process observed in elderly GBC patients may hinder antitumor immune processes and drug metabolism, exacerbating the malignancy of aged GBC. Moreover, our study revealed an upregulation in the expression of cell cycle genes in elderly GBC patients, which could further contribute to their higher malignancy.

In addition, we successfully developed two nomograms to predict OS and CSS at 1-, 3-, and 5-year for elderly patients with GBC based on a large population from the SEER database. The predictive accuracy and capability of our nomograms were further verified in both the training cohort and validation cohort. Several independent prognostic predictors were identified and enrolled in our nomograms. Marital status, age, tumor grade, surgery information, T stage, N stage, and M stage were applied for OS prediction. Tumor grade, tumor size, chemotherapy, surgery information, T stage, N stage, and M stage were applied for CSS prediction.

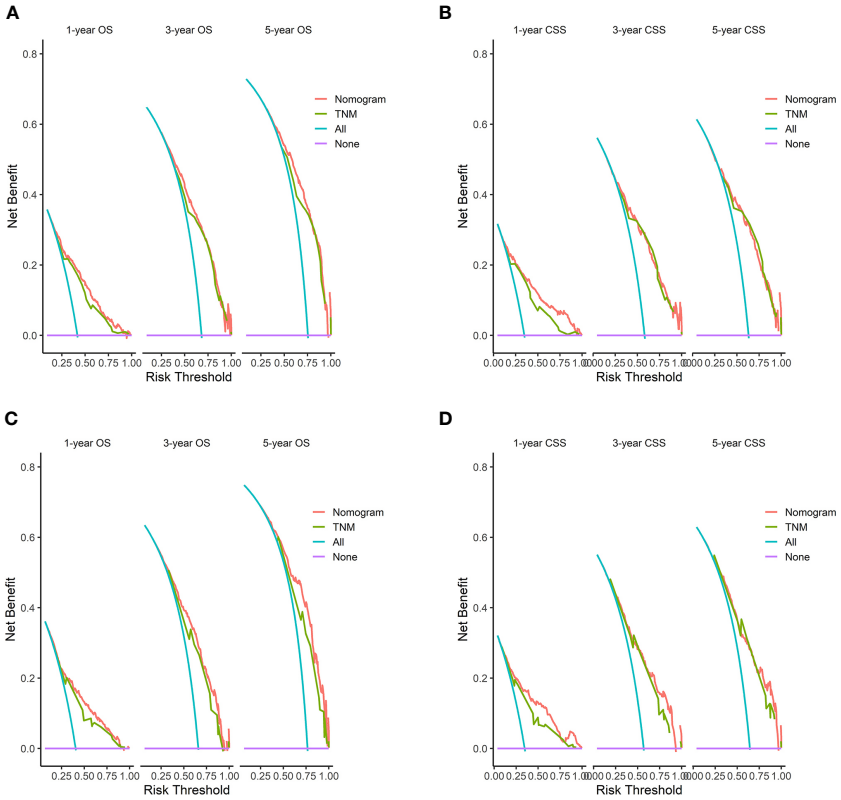

FIGURE 8
DCA of the nomograms to predict OS and CSS compared with TNM stage. **(A)** DCA of the nomogram to predict OS at 1-, 3-, and 5-year compared with TNM stage in the training cohort. **(B)** DCA of the nomogram to predict CSS at 1-, 3-, and 5-year compared with TNM stage in the training cohort. **(C)** DCA of the nomogram to predict OS at 1-, 3-, and 5-year compared with TNM stage in the validation cohort. **(D)** DCA of the nomogram to predict CSS at 1-, 3-, and 5-year compared with TNM stage in the validation cohort. When the threshold probability is between 20 and 100%, the net benefit of the model exceeds all deaths or none. DCA, decision curve analysis.

Good experience and emotional support from marriage may positively help patients to struggle with cancer. Marital status has been determined as a protective risk factor of OS for patients with GBC (24). Accordingly, our results also identified married status as a protective prognostic predictor of OS for elderly patients with GBC, but the marital status was inapplicable for CSS prediction. Age appears to be a common risk factor for prognosis in many cancer types (25–30), as well as in GBC (12). Generally, the older patients are, the poorer prognosis they may suffer. We came to the same conclusion that elderly patients aged over 74 (> 74) have a poorer prognosis (both OS and CSS) in contrast to elderly patients aged no more than 74 (≥ 65, ≤ 74). Tumor grade and TNM stage are essential evidence for clinicians to evaluate the clinical outcomes of patients. Higher tumor grade and more advanced TNM stage underline enhanced malignant potentials of cancer cells, naturally inferring worse clinical outcomes. In accordance with previous studies (12, 31), we verified that patients with higher tumor grades and more advanced TNM stage were calculated with higher risk scores and worse prognoses (both OS and CSS). Notably, results from DCA revealed the superior advantage of our nomograms to predict OS and CSS at 1-year compared to the traditional TNM stage for elderly patients with GBC. There is no common standard for tumor size grouping in GBC. In previous studies, the cut-off points include 2 cm and 5 cm (32), 1.4 cm and 6.3 cm (33), 1.9 cm and 4.8 cm (24), 4.5 cm (34), and 5 cm (35), etc. In this present study, we selected 3 cm as the cut-off point. Although the standards vary, the results all pointed out that tumor size is associated with the prognosis of patients with GBC (24, 32–35). Particularly, Zhang et al. (33) and Yan et al. (35) reported that larger tumor size is negatively associated with CSS of patients with GBC, which was consistent with our finding.

The clinical treatment of GBC is a comprehensive strategy, with the chief component being surgical resection (6, 36). Currently, a combination of PD-1/PD-L1-based immunotherapy and traditional cytotoxic drugs is rising to be an option for first-line treatments (37). Radiotherapy is set as a postoperative treatment for patients with GBC, especially for those with lymph node involvement and positive resection margins (38). In this present study, we determined that surgical section does improve survival probabilities (both OS and CSS) of elderly patients with GBC in contrast to patients without surgical resection in the high-risk group. Further, radical cholecystectomy surgical resection may contribute to slight OS improvement in the early five years compared with local tumor excision/partial cholecystectomy surgical resection. In the low-risk group, no significant survival improvements were observed for both OS and CSS between the local tumor excision/partial

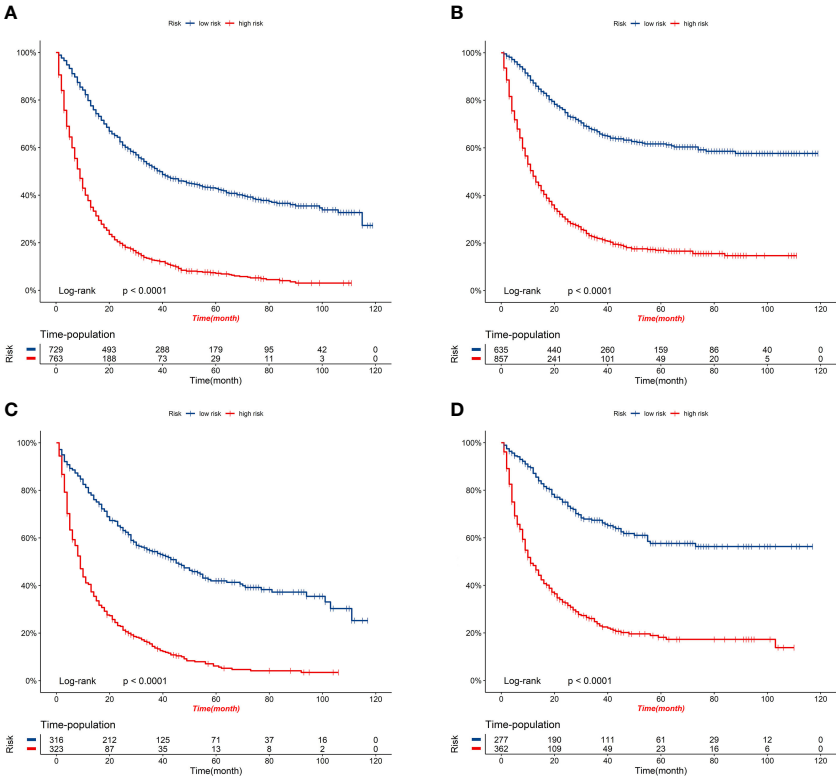

FIGURE 9
K-M survival curves of elderly patients with GBC in the high-risk and low-risk groups. **(A)** OS comparison of elderly patients with GBC based on risk score grouping in the training cohort. **(B)** CSS comparison of elderly patients with GBC based on risk score grouping in the training cohort. **(C)** OS comparison of elderly patients with GBC based on risk score grouping in the validation cohort. **(D)** CSS comparison of elderly patients with GBC based on risk score grouping in the validation cohort.

cholecystectomy surgery subgroup and the radical cholecystectomy surgery subgroup. In other words, radical cholecystectomy surgical resection may not achieve more satisfying clinical benefits as we expected in contrast to local tumor excision/partial cholecystectomy surgical resection for patients in the low-risk group. This finding may provide evidence for the choice of operation types, and it is possible to provide more rational treatment management for patients based on their risk stratification. However, to the best of our knowledge, our nomograms were the first to analyze the associations between survival benefits and surgery options based on risk score grouping in elderly patients with GBC. Receiving chemotherapy was determined to be a protective prognostic predictor for CSS prediction of elderly patients with GBC (HR = 0.57, 95% CI = 0.485-0.669), which was consistent with reported results (39, 40).

Radiotherapy can serve as a valuable supplementary therapy for particular groups of patients, particularly those at a higher risk of recurring cancer, such as individuals who have undergone an R1 resection or those who have tested positive for lymph nodes. A study conducted previously demonstrated that the implementation of adjuvant radiotherapy resulted in an increased survival rate among patients who had been diagnosed with gallbladder cancer and were also affected by regional lymph node metastasis (41). However, in our study, radiotherapy was not an influential factor in the prognosis of elderly patients with GBC. It could be because elderly patients often cannot tolerate having radiotherapy or cannot obtain more benefits because of the combination of multiple underlying diseases.

Despite the robust predictive accuracy and capability of our nomograms, there were still several limitations of this present study. Above all, relevant treatment information, blood test data, and essential clinical characteristics of patients with GBC were not provided in the SEER database, such as chemotherapy regimens, radiation dose, blood routine tests, liver function, tumor markers, smoke, alcohol consumption, etc. Recruitment of these factors may help to optimize the predictive accuracy of nomograms. Second, multi-omics data are recommended to improve nomograms to emphasize precision medicine. Besides, our data are all from the U.S. population, and their applicability to populations in other countries remains to be verified, and additional multicenter prospective studies are needed to validate our findings.

5 Conclusions

Discrepancies in cell cycle signaling and metabolic disorders, especially energy metabolism, were obviously

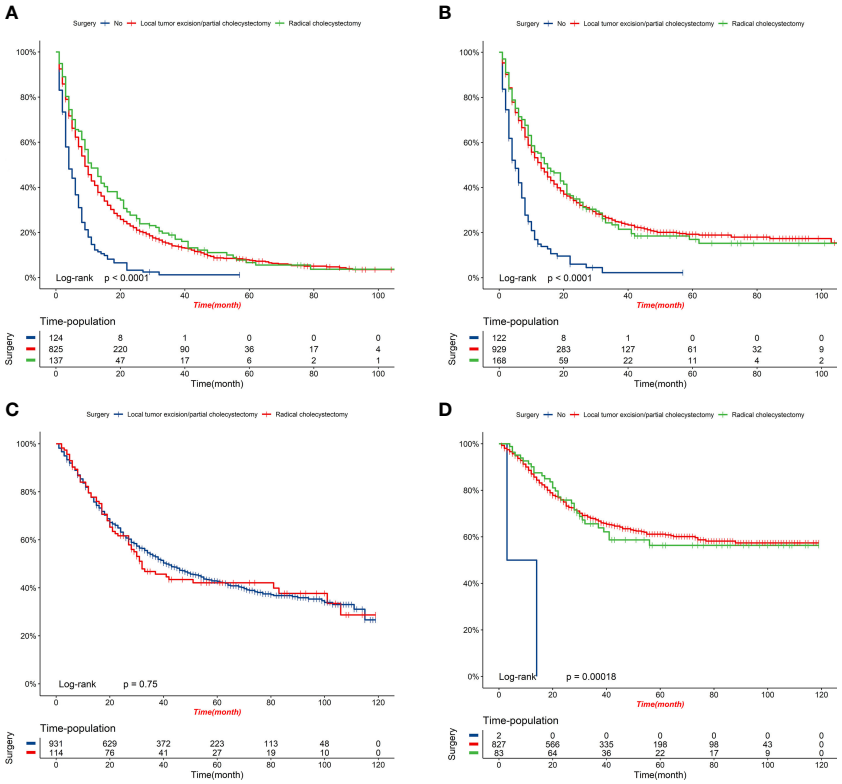

FIGURE 10
K-M survival curves of elderly patients with GBC under different surgery options. **(A)** OS comparison between patients under different surgery options in the high-risk group. **(B)** CSS comparison between patients under different surgery options in the high-risk group. **(C)** OS comparison between patients under different surgery options in the low-risk group. **(D)** CSS comparison between patients under different surgery options in the low-risk group.

observed between elderly and young GBC patients. In addition to being predictively accurate, the nomograms of elderly GBC patients also contributed to managing and strategizing clinical care.

Data availability statement

The original contributions presented in the study are included in the article/Supplementary Material. Further inquiries can be directed to the corresponding author.

Ethics statement

Ethical review and approval was not required for the study on human participants in accordance with the local legislation and institutional requirements. Written informed consent for participation was not required for this study in accordance with the national legislation and the institutional requirements.

Author contributions

All authors contributed to the article and approved the submitted version. In this study, all authors contributed significantly to the design, data collection, interpretation, and manuscript preparation and revision.

Funding

This research was funded by the Jilin Provincial Department of Education's Science and Technology Research Project (JJKH20201069KJ) and the Graduate Innovation Fund of Jilin University.

Conflict of interest

The authors declare that the research was conducted in the absence of any commercial or financial relationships that could be construed as a potential conflict of interest.

Publisher's note

Supplementary material

The Supplementary Material for this article can be found online at: https://www.frontiersin.org/articles/10.3389/fendo.2023.1159235/full#supplementary-material

SUPPLEMENTARY FIGURE
Workflow of the present study.

References

1. Hundal R, Shaffer EA. Gallbladder cancer: epidemiology and outcome. *Clin Epidemiol* (2014) 6:99–109. doi: 10.2147/clep.S37357

2. Sung H, Ferlay J, Siegel RL, Laversanne M, Soerjomataram I, Jemal A, et al. Global cancer statistics 2020: GLOBOCAN estimates of incidence and mortality worldwide for 36 cancers in 185 countries. *CA Cancer J Clin* (2021) 71(3):209–49. doi: 10.3322/caac.21660

3. Henley SJ, Weir HK, Jim MA, Watson M, Richardson LC. Gallbladder cancer incidence and mortality, united states 1999-2011. *Cancer Epidemiol Biomarkers Prev* (2015) 24(9):1319–26. doi: 10.1158/1055-9965.Epi-15-0199

4. Rawla P, Sunkara T, Thandra KC, Barsouk A. Epidemiology of gallbladder cancer. *Clin Exp Hepatol* (2019) 5(2):93–102. doi: 10.5114/ceh.2019.85166

5. SEER Cancer Statistics Review (CSR) 1975-2014. *Liver and bile duct* . Available at: https://seer.cancer.gov/csr/1975_2014/ (Accessed September 7, 2022).

6. Kakaei F, Beheshtirouy S, Nejatollahi SM, Zarrintan S, Mafi MR. Surgical treatment of gallbladder carcinoma: a critical review. *Updates Surg* (2015) 67(4):339–51. doi: 10.1007/s13304-015-0328-x

7. SEER*Explorer. *An interactive website for SEER cancer statistics [Internet] surveillance research program, national cancer institute* . Available at: https://seer.cancer.gov/explorer/ (Accessed September 7, 2022).

8. Shao CY, Yu Y, Li QF, Liu XL, Song HZ, Shen Y, et al. Development and validation of a clinical prognostic nomogram for esophageal adenocarcinoma patients. *Front Oncol* (2021) 11:736573. doi: 10.3389/fonc.2021.736573

9. Wang X, Wang H, Liu F, Jie L, Song Z. Establishment and verification of a nomogram for predicting survival in patients with triple-positive breast cancer. *Ann Transl Med* (2022) 10(16):884. doi: 10.21037/atm-22-3560

10. Ren C, Ma Y, Jin J, Ding J, Jiang Y, Wu Y, et al. Development and external validation of a dynamic nomogram to predict the survival for adenosquamous carcinoma of the pancreas. *Front Oncol* (2022) 12:927107. doi: 10.3389/fonc.2022.927107

11. Zheng C, Chen X, Zhang Z, Li A, Wang J, Cai T, et al. Nomogram based on intramuscular adipose tissue content for predicting the prognosis of patients with gallbladder cancer after radical resection. *Transl Cancer Res* (2022) 11(7):1898–908. doi: 10.21037/tcr-22-123

12. Xu X, He M, Wang H, Zhan M, Yang L. Development and validation of a prognostic nomogram for gallbladder cancer patients after surgery. *BMC Gastroenterol* (2022) 22(1):200. doi: 10.1186/s12876-022-02281-2

13. Wang J, Yang Y, Pan J, Qiu Y, Shen S, Wang W. Competing-risk nomogram for predicting survival in patients with advanced (stage III/IV) gallbladder cancer: A SEER population-based study. *Jpn J Clin Oncol* (2022) 52(4):353–61. doi: 10.1093/jjco/hyab212

14. Liu X, Liang X, Ruan L, Yan S. A clinical-radiomics nomogram for preoperative prediction of lymph node metastasis in gallbladder cancer. *Front Oncol* (2021) 11:633852. doi: 10.3389/fonc.2021.633852

15. Yang Z, Ren T, Liu S, Cai C, Gong W, Shu Y. Preoperative serum fibrinogen as a valuable predictor in the nomogram predicting overall survival of postoperative patients with gallbladder cancer. *J Gastrointest Oncol* (2021) 12(4):1661–72. doi: 10.21037/jgo-21-357

16. Cai YL, Lin YX, Jiang LS, Ye H, Li FY, Cheng NS. A novel nomogram predicting distant metastasis in T1 and T2 gallbladder cancer: A SEER-based study. *Int J Med Sci* (2020) 17(12):1704–12. doi: 10.7150/ijms.47073

17. Ren J, Zhang H, Wang J, Xu Y, Zhao L, Yuan Q. Transcriptome analysis of adipocytokines and their-related LncRNAs in lung adenocarcinoma revealing the association with prognosis, immune infiltration, and metabolic characteristics. *Adipocyte* (2022) 11(1):250–65. doi: 10.1080/21623945.2022.2064956

18. Yuan Q, Ren J, Chen X, Dong Y, Shang D. Contributions and prognostic performances of m7G RNA regulators in pancreatic adenocarcinoma. *Chin Med J (Engl)* (2022) 135(17):2101–3. doi: 10.1097/cm9.0000000000002179

19. Ritchie ME, Phipson B, Wu D, Hu Y, Law CW, Shi W, et al. Limma powers differential expression analyses for RNA-sequencing and microarray studies. *Nucleic Acids Res* (2015) 43(7):e47. doi: 10.1093/nar/gkv007

20. Hänzelmann S, Castelo R, Guinney J. GSVA: gene set variation analysis for microarray and RNA-seq data. *BMC Bioinf* (2013) 14:7. doi: 10.1186/1471-2105-14-7

21. Langfelder P, Horvath S. WGCNA: an r package for weighted correlation network analysis. *BMC Bioinf* (2008) 9:559. doi: 10.1186/1471-2105-9-559

22. Li T, Fu J, Zeng Z, Cohen D, Li J, Chen Q, et al. TIMER2.0 for analysis of tumor-infiltrating immune cells. *Nucleic Acids Res* (2020) 48(W1):W509–w14. doi: 10.1093/nar/gkaa407

23. Maeser D, Gruener RF, Huang RS. oncoPredict: an r package for predicting in vivo or cancer patient drug response and biomarkers from cell line screening data. *Brief Bioinform* (2021) 22(6). doi: 10.1093/bib/bbab260

24. Li P, Song L. Prognostic evaluation for patients over 45 years old with gallbladder adenocarcinoma resection: A SEER-based nomogram analysis. *BioMed Res Int* (2020) 2020:6370946. doi: 10.1155/2020/6370946

25. Tang LQ, Li CF, Li J, Chen WH, Chen QY, Yuan LX, et al. Establishment and validation of prognostic nomograms for endemic nasopharyngeal carcinoma. *J Natl Cancer Inst* (2016) 108(1). doi: 10.1093/jnci/djv291

26. Liang W, Zhang L, Jiang G, Wang Q, Liu L, Liu D, et al. Development and validation of a nomogram for predicting survival in patients with resected non-small-cell lung cancer. *J Clin Oncol* (2015) 33(8):861–9. doi: 10.1200/jco.2014.56.6661

27. Xu XS, Chen W, Miao RC, Zhou YY, Wang ZX, Zhang LQ, et al. Survival analysis of hepatocellular carcinoma: A comparison between young patients and aged patients. *Chin Med J (Engl)* (2015) 128(13):1793–800. doi: 10.4103/0366-6999.159356

28. Zhang Z, Zhanghuang C, Wang J, Tian X, Wu X, Li M, et al. Development and validation of nomograms to predict cancer-specific survival and overall survival in elderly patients with prostate cancer: A population-based study. *Front Oncol* (2022) 12:918780. doi: 10.3389/fonc.2022.918780

29. Zhang Z, Pu J, Zhang H. Development and validation of a simple-to-Use nomogram to predict early death in metastatic pancreatic adenocarcinoma. *Front Oncol* (2021) 11:729175. doi: 10.3389/fonc.2021.729175

30. Zhanghuang C, Wang J, Zhang Z, Jin L, Tan X, Mi T, et al. A web-based prediction model for cancer-specific survival of elderly patients with clear cell renal cell carcinoma: A population-based study. *Front Public Health* (2021) 9:833970. doi: 10.3389/fpubh.2021.833970

31. Lin Y, Chen H, Pan F. Prognostic nomograms to predict survival of patients with resectable gallbladder cancer: A surveillance, epidemiology, and end results (SEER)-based analysis. *Med Sci Monit* (2021) 27:e929106. doi: 10.12659/msm.929106

32. Wu D, Jin W, Zhang Y, An Y, Chen X, Chen W. Insights from the analysis of clinicopathological and prognostic factors in patients with gallbladder cancer. *Front Oncol* (2022) 12:889334. doi: 10.3389/fonc.2022.889334

33. Zhang Y, Zhou T, Han S, Chang J, Jiang W, Wang Z, et al. Development and external validation of a nomogram for predicting the effect of tumor size on cancer-specific survival of resected gallbladder cancer: a population-based study. *Int J Clin Oncol* (2021) 26(6):1120–9. doi: 10.1007/s10147-021-01891-2

34. Ma Z, Dong F, Li Z, Zheng Z, Zhou Z, Zhuang H, et al. A novel prognostic nomogram for gallbladder cancer after surgical resection: A single-center experience. *J Oncol* (2021) 2021:6619149. doi: 10.1155/2021/6619149

35. Yan Y, Lin J, Zhang M, Liu H, Zhou Q, Chen R, et al. A novel staging system to forecast the cancer-specific survival of patients with resected gallbladder cancer. *Front Oncol* (2020) 10:1281. doi: 10.3389/fonc.2020.01281

36. Gunasekaran G, Bekki Y, Lourdusamy V, Schwartz M. Surgical treatments of hepatobiliary cancers. *Hepatology* (2021) 73 Suppl 1:128–36. doi: 10.1002/hep.31325

37. Cowzer D, Harding JJ. Advanced bile duct cancers: A focused review on current and emerging systemic treatments. *Cancers (Basel)* (2022) 14(7). doi: 10.3390/cancers14071800

38. Keane FK, Zhu AX, Hong TS. Radiotherapy for biliary tract cancers. *Semin Radiat Oncol* (2018) 28(4):342–50. doi: 10.1016/j.semradonc.2018.06.003

39. Fang C, Li W, Wang Q, Wang R, Dong H, Chen J, et al. Risk factors and prognosis of liver metastasis in gallbladder cancer patients: A SEER-based study. *Front Surg* (2022) 9:899896. doi: 10.3389/fsurg.2022.899896

40. Hamad A, Aquina CT, Ansari A, Salahuddin A, Shen C, Cloyd JM, et al. Impact of delay in adjuvant therapy for gallbladder adenocarcinoma. *J Hepatobiliary Pancreat Sci* (2023) 30(2):212–20. doi: 10.1002/jhbp.1190

41. Mojica P, Smith D, Ellenhorn J. Adjuvant radiation therapy is associated with improved survival for gallbladder carcinoma with regional metastatic disease. *J Surg Oncol* (2007) 96(1):8–13. doi: 10.1002/jso.20831

frontiers | Frontiers in Endocrinology

TYPE Original Research
PUBLISHED 10 May 2023
DOI 10.3389/fendo.2023.1153909

OPEN ACCESS

EDITED BY
Chenyu Sun,
AMITA Health, United States

REVIEWED BY
Fenghua Xu,
Daping Hospital, China
Lei Liu,
Army Medical University, China

*CORRESPONDENCE
Changmiao Wang
wangchangmiaodl@sina.cn
Yougang Cui
cuiyougang@163.com
Jian Jiang
lyjiangjian@126.com

†These authors have contributed equally to this work

RECEIVED 30 January 2023
ACCEPTED 21 March 2023
PUBLISHED 10 May 2023

CITATION
Li N, Jia X, Wang Z, Wang K, Qu Z, Chi D, Sun Z, Jiang J, Cui Y and Wang C (2023) Characterization of anoikis-based molecular heterogeneity in pancreatic cancer and pancreatic neuroendocrine tumor and its association with tumor immune microenvironment and metabolic remodeling.
Front. Endocrinol. 14:1153909.
doi: 10.3389/fendo.2023.1153909

Characterization of anoikis-based molecular heterogeneity in pancreatic cancer and pancreatic neuroendocrine tumor and its association with tumor immune microenvironment and metabolic remodeling

Ning Li[1,2,3†], Xingqing Jia[4†], Zhong Wang[2†], Kaige Wang[3], Zumin Qu[5], Dong Chi[2], Zhubo Sun[2], Jian Jiang[1*], Yougang Cui[1,6*] and Changmiao Wang[1*]

[1]Department of General Surgery, First Affiliated Hospital of Dalian Medical University, Dalian, Liaoning, China, [2]Department of General Surgery, Wafangdian Central Hospital, Dalian, Liaoning, China, [3]Graduate School of Dalian Medical University, Dalian, Liaoning, China, [4]Department of Digestive, Jinan City People's Hospital, Jinan, Shandong, China, [5]Department of Pathology, Wafangdian Central Hospital, Dalian, Liaoning, China, [6]Department of General Surgery, The Affiliated Zhongshan Hospital of Dalian University, Dalian, Liaoning, China

Background: Accumulating evidence suggests that anoikis plays a crucial role in the onset and progression of pancreatic cancer (PC) and pancreatic neuroendocrine tumors (PNETs); nevertheless, the prognostic value and molecular characteristics of anoikis in cancers are yet to be determined.

Materials and methods: We gathered and collated the multi-omics data of several human malignancies using the TCGA pan-cancer cohorts. We thoroughly investigated the genomics and transcriptomics features of anoikis in pan-cancer. We then categorized a total of 930 patients with PC and 226 patients with PNETs into distinct clusters based on the anoikis scores computed through single-sample gene set enrichment analysis. We then delved deeper into the variations in drug sensitivity and immunological microenvironment between the various clusters. We constructed and validated a prognostic model founded on anoikis-related genes (ARGs). Finally, we conducted PCR experiments to explore and verify the expression levels of the model genes.

Results: Initially, we identified 40 differentially expressed anoikis-related genes (DE-ARGs) between pancreatic cancer (PC) and adjacent normal tissues based on the TCGA, GSE28735, and GSE62452 datasets. We systematically explored the pan-cancer landscape of DE-ARGs. Most DE-ARGs also displayed differential expression trends in various tumors, which were strongly linked to favorable or unfavorable prognoses of patients with cancer, especially PC. Cluster analysis successfully identified three anoikis-associated subtypes for PC patients and two

anoikis-associated subtypes for PNETs patients. The C1 subtype of PC patients showed a higher anoikis score, poorer prognosis, elevated expression of oncogenes, and lower level of immune cell infiltration, whereas the C2 subtype of PC patients had the exact opposite characteristics. We developed and validated a novel and accurate prognostic model for PC patients based on the expression traits of 13 DE-ARGs. In both training and test cohorts, the low-risk subpopulations had significantly longer overall survival than the high-risk subpopulations. Dysregulation of the tumor immune microenvironment could be responsible for the differences in clinical outcomes between low- and high-risk groups.

Conclusions: These findings provide fresh insights into the significance of anoikis in PC and PNETs. The identification of subtypes and construction of models have accelerated the progress of precision oncology.

KEYWORDS

pancreatic adenocarcinoma, pancreatic neuroendocrine tumors, anoikis, molecular characteristics, metabolic remodelling, tumor immune microenvironment

Introduction

Globally, pancreatic cancer (PC) is regarded as a lethal gastrointestinal malignancy with a mortality rate proportional to its occurrence (1, 2). Exposure to risk factors such obesity, diabetes, cigarette use, and alcohol intake is connected to the poor prognosis and steady incidence rates of PC patients; however, early-stage nonspecific symptoms also contribute to the diagnosis (3). In addition to pancreatic cancer, neuroendocrine tumors are also relatively common types of pancreatic tumors. The origin of pancreatic neuroendocrine tumors (PNETs) is concealed, and their biological activity is highly variable, being characterized by passive growth, invasive development, and even early metastasis; their biological characteristics may change as the disease progresses. As a result of the tumor's function in hormone release, PNETs may produce hormone-related symptoms or syndromes, and there are significant differences in prognosis between PNETs of different grades and stages. In modern medicine, surgery remains the therapeutic cornerstone of PC and PNETs, complemented by other, more all-encompassing treatments like radiation and chemotherapy (4). Despite extensive therapy, PC has a dismal 5-year survival rate of around 7% at present (4). The urgent need to establish the potential heterogeneity of PC and PNET patients is a necessary step in addressing this issue. This would enable physicians to generate more accurate prognoses on patient outcomes and swiftly execute tailored treatment programs.

Anoikis was initially identified in 1994, indicating that normal adhering cells would die of "homelessness" if they were suspended for an extended period of time (5). Anoikis is a kind of programmed cell death and is associated with "suicidal" cell activity (5). It is caused by separation from extracellular matrix (6). It is essential for maintaining the integrity of the body's tissues, and its primary role is to inhibit improper cell proliferation or attachment to abnormal extracellular matrix (7). Loss of nested apoptosis resistance is the basis of tumor spread, metastasis, and invasion, since it enables tumor cells to migrate to distant new tissues or lymph nodes through lymphatic or blood circulation and continue to grow (8). Loss of tumor cells and resistance to apoptosis play a significant role in the invasion and metastasis of pancreatic cancer.

In this study, we systemically summarized the pan-cancer landscape of anoikis for the first time. Based on the anoikis scores, 930 patients with PC were precisely stratified into three subtypes accompanied by distinct prognoses and tumor immune microenvironment. These three subtypes included anoikis-active, anoikis-normal, anoikis-inactive subpopulations. The patients in anoikis-active subtype had higher anoikis scores and worse prognoses, indicating the carcinogenic effects of anoikis in PC. 226 patients with PNETs were also stratified into S1 and S2 subtypes with distinct molecular characteristics. Finally, we also developed a novel anoikis-based prognostic model for patients with PC, which help promote the development of oncology precision.

Methods

Data collection and processing

A total of 794 anoikis-related genes (ARGs) were downloaded from the GeneCard website (https://www.genecards.org/). Among them, 501 ARGs with gene scores > 0.4 were preserved for further analysis (Table S1). Pan-cancer cohorts including gene expression profiles, mutation information, methylation levels, and clinical data were obtained from the Firehose (http://gdac.broadinstitute.org) and Xena Browser (https://xenabrowser.net/datapages/) platforms (9). A total of 930 PC and 171 para-cancerous tissues' transcriptomics data and their corresponding clinical data were acquired from the publicly free

platforms, including ArrayExpress (https://www.ebi.ac.uk/arrayexpress), The Cancer Genome Atlas (TCGA, https://portal.gdc.cancer.gov), International Cancer Genome Consortium (ICGC, https://dcc.icgc.org/), Gene Expression Omnibus (GEO, https://www.ncbi.nlm.nih.gov/geo/), and Genotype-Tissue Expression (GTEx) databases (10–14). Of note, patients without follow-up information were excluded in this study.

In addition to these, the transcriptomics data of 226 patients with PNETs were also collected and complied from the public websites. The ICGC-PAEN-AU cohort provided the data of 32 PNETs samples, GSE98894 cohort (15) provided the data of 113 PNETs samples, GSE73338 cohort (16) provided the data of 81 PNETs samples. A total of 171 normal pancreas samples consisting of 4 samples from TCGA platform and 167 samples from GTEx website were also collected as the control group. In order to eliminate the batch effects derived from the different platforms, a well-recognized bioinformatics algorithm, called ComBat, was utilized. The ComBat function was developed on the basis of the "sva" package in R (17).

The overall analysis strategies of this research are summarized as follows: a) To filter ARGs significantly associated with the occurrence of PC, the differentially expressed ARGs (DE-ARGs) were determined with the help of limma package in R. In the process of above analysis, three cohorts including GSE28735 (18, 19) (45 tumor samples vs 45 normal samples), GSE62452 (20) (69 tumor samples vs 61 normal samples), and TCGA+GTEx cohorts (178 tumor samples vs 171 normal samples) were utilized, and DE-ARGs were identified by taking the intersection of the results of above three cohorts. Subsequently, pan-cancer analysis highlighted the pivotal contributions of DE-ARGs in multiple human cancers. The specific analytic methods were similar to the previous studies (21, 22). b) The single sample gene set enrichment analysis (ssGSEA) was performed to evaluate the relative activities of 930 PC patients' anoikis signaling pathway. Cluster analysis was then carried out to classify 930 PC patients into three distinct subtypes with different anoikis activities. c) Considering the limitations for the clinical application of cluster results, a novel anoikis-related prognostic model (ARPM) was developed and validated. We separated 930 PC patients into two cohorts (i.e. training dataset and validation dataset). Among them, GSE57495 (23), GSE28735, GSE62452, E-MTAB-6134 (24), and TCGA-PC datasets including a total of 635 PC samples were compiled as a training cohort for future research, while 295 PC patients in the ICGC-CA and ICGC-AU datasets were defined as a validation cohort. d) 226 patients with PNETs were also performed cluster analysis to determine the possible heterogeneity.

Cluster analysis based on anoikis activities

Using single-sample gene set enrichment analysis (ssGSEA), enrichment scores for the anoikis pathway in patients with PC and PNETs were calculated. The "Gplots" and "pheatmap" R packages were used to display heatmaps incorporating DE-ARGs expression, anoikis scores, and clinical clusters for both PC and PNETs. Brown indicated that the expression of the gene was larger in tumor samples than in normal samples, while dark blue indicated the opposite. The status of mRNA expression in tumor tissues was categorized into 3 clusters: high expression of the ARGs, normal expression of the ARGs, and low expression of the ARGs. The violin plots were depicted to compare the anoikis enrichment scores between distinct clusters. Of note, those clusters with similar enrichment scores were further consolidated into one cluster. Higher scores indicated increased DE-ARG expression levels, whereas lower scores indicated the reverse. More importantly, we also evaluated the disparities in the distribution of immunological and metabolic pathways among diverse clusters.

Drug sensitivity analysis for PC patients

The R package "pRRophetic" was used to predict chemotherapy response in order to better comprehend the relationship between anoikis pathway gene expression and malignancy medication treatment. As one of the largest public repositories of information on cancer drug sensitivity, drug responses, and molecular targets, the "pRRophetic" package, which was based on the Cancer Genome Project (CGP) and contained 138 anticancer drugs against 727 cell lines, allowed for the identification of novel therapeutic targets to improve cancer treatment (25). Meanwhile, the semi-maximum inhibitory concentration (IC50) of the samples was calculated using the ridge regression approach. A smaller IC50 was usually related to a lower semi-inhibitory mass concentration of the drug in cancer cells, suggesting that the cancer cells were more vulnerable to the medication.

Associations of the anoikis scores with the classical cancer-related genes and tumor immune microenvironment in PC patients

The fundamental unit of genetic information is the gene. In general, two types of genes (i.e. oncogenes and tumor suppressor genes) in cells are intimately associated with the emergence and growth of tumors. Oncogenes are usually genes with the functions of promoting cell growth, activating cell cycle and inhibiting the level of apoptosis. Tumor suppressor genes negatively control cell development and cell cycle, induce apoptosis, and repair DNA damage. Considering the important role of oncogenes and tumor suppressor genes in tumorigenesis, we further analyzed the correlation between anoikis scores and these genes. Using the "pheatmap" and "gplots" packages in RStudio, we produced a heatmap showing the expression levels of various oncogenes and tumor suppressor genes in the three clusters in order to explore the likely regulatory mechanism of the anoikis pathway in PC.

The tumor immune microenvironments of three PC subtypes were then compared. We intensively examined the algorithms MCPCOUNTER, XCELL, CIBERSORT, EPIC, CIBERSORT-ABS, and TIMER for assessing cell immune responses or cellular components across the three subtypes of PC. Several algorithms were used to plot a heatmap to identify shifts in immune response. Immune checkpoint functioned as the major manager of immune

cell activity. Thus, we also investigated the expression features of immune checkpoint-related genes among various clusters.

In addition, the 29 well-recognized immune-associated gene sets were also quantified for assessing the scores of immune cells and immune-related functions using ssGSEA (26). The scores of immune cells and immune-related functions might partially represent the quantity of immune cell infiltration and the activation of immunological-related processes. Subsequently, the Spearman correlation analysis was employed to explore the correlation between ARG scores and immune scores. We created a scatter plot using the "ggscatterstats" package to show the relationships between the four immune-infiltrating components (macrophages, parainflammation, TIL, and Th1 cells) and the anoikis pathway scores. Finally, using Spearman's correlation coefficient, the R Studio tools "ggplot2" and "dplyr" were then applied to generate a heatmap illustrating the relationship between ARGs and immune cell infiltration (ICI).

Development and validation of a prognostic signature based on DE-ARGs

As a further step, we performed LASSO regression analysis on 40 DE-ARGs, with the minimal criteria determining the penalty parameter (λ). $Risk\ score = \sum_{k=1}^{n} expk * \beta k$. Using the median risk score, 930 individuals with PC from the training and validation cohorts were classified into high- and low-risk categories. The training cohort involved 635 PC patients from GSE57495, GSE28735, GSE62452, MTAB-6134, and TCGA-PC datasets, whereas, the validation cohort involved 295 PC patients from ICGC-CA and ICGC-AU datasets. For both training and validation cohorts, survival analyses using the KM technique were carried out to determine whether the signature could be used to forecast survival. ROC curves of 1-, 3-, 5-, and 7-years were also plotted to quantitatively evaluate the predictive ability of our prognostic model.

Immune cell infiltration and immune checkpoint gene expression differences between low-risk and high-risk subgroups

Based on the previous results of ICI assessment, the heatmaps were utilized to show the discrepancies in the tumor immune microenvironment between low- and high-risk subgroups. Each color represented different ICI prediction algorithms. The differential expression of common immune checkpoint genes (ICGs) in high-risk and low-risk categories was also examined, with only statistically significant results ($p< 0.05$) being displayed. The above analysis is performed in both the train and test cohorts.

Clinical significances of model genes in PC

We integrated the prognosis information, clinical stage, and expression of model genes to highlight their clinical significances. Both univariate Cox regression analysis and Kaplain-Meier analysis were employed to explore and validate their prognostic values. The GEPIA2 platform (http://gepia2.cancer-pku.cn/#analysis) was implemented to analyze their association with clinical stages. The BEST platform (https://rookieutopia.com/app_direct/BEST/#PageHomeAnalysisModuleSelection) was utilized to explore the expression traits of ARGs with clinical significances. Only DE-ARGs with prognostic significances and stage correlation were considered to be closely related to the occurrence and progression of PC.

Quantitative real-time PCR, immunohistochemistry and immunofluorescence

The MiaPaca-2 cell line was procured from BeNa Culture Collection, and Procell Life Science & Technology Co., Ltd. supplied the HPDE6-C7, CF-PAC1, Panc-1, and BxPC-3 cell lines. DMEM mixed with 10% FBS (Gibco, USA) was utilized to culture HPDE6-C7 (a human pancreatic ductal epithelium cell line), MiaPaca-2, and Panc-1 cell lines, while IMDM mixed with 10% FBS (Procell, China) was used for CF-PAC1, and BxPC-3 was cultured with 1640 mixed with 10% FBS (Procell, China). All the cell lines were incubated in a cell incubator maintained at a temperature of 37°C and with a CO2 concentration of 5%.

By using TRIzol extraction tool provided by Accurate Biotechnology, mRNAs associated with five different cell lines were isolated. These mRNAs were then reversed transcribed into cDNAs using the Reverse Transcription Reagent. The RT-PCR was executed by utilizing the qPCR Kit from Accurate Biotechnology. All reagents used in the experiment were provided by our laboratory. β-actin was selected as the control standard for the experiment, and the mRNA expression level analysis was calculated using the ΔΔCt method. The primer sequences were synthesized from Sango Biotech (Shanghai, China) shown as follows: HK2: 5'-TCCCCTCTCGCGTCTCC-3'(F), 5'- AGAGATACTGGTCAACCTTCTGC-3'(R); MMP11, 5'- GATCGACTTCGCCAGGTACT-3'(F), 5'- CCCCGATAGTCCAGGTCTCA-3'(R); CDH3, 5'- GACACCCATGTACCGTCCTC-3'(F), 5'- TCTCTCCCCTCCCCTCAATTA-3'(R); PDK4, 5'- CCAAGCCACATTGGAAGCAT-3'(F), 5'- TGAACACTCAAAGGCATCTTGG-3'(R); SERPINB5, 5'-ATGCCAAGGTCAAACTCTCCATTCC-3'(F), 5'- CAGCCCTAGATTTTCCAGACAAGCC-3'(R); SLC2A1, 5'- TGGCATCAACGCTGTCTTCT-3'(F), 5'- AGCCAATGGTGGCATACACA-3'(R); β-actin: 5'-CCTGGGCATGGAGTCCTGTG-3'(F), 5'-TCTTCATTGTGCTGGGTGCC-3'(R).

Ultimately, the HPA platform was employed to investigate the protein levels and cellular location of model genes in PC through immunohistochemistry and immunofluorescence techniques.

Results

Identification of DE-ARGs between tumor and normal tissues

The workflow of this study was displayed in Figure 1. In order to explore the ARGs closely associated with occurrence of PC, the

10.3389/fendo.2023.1153909

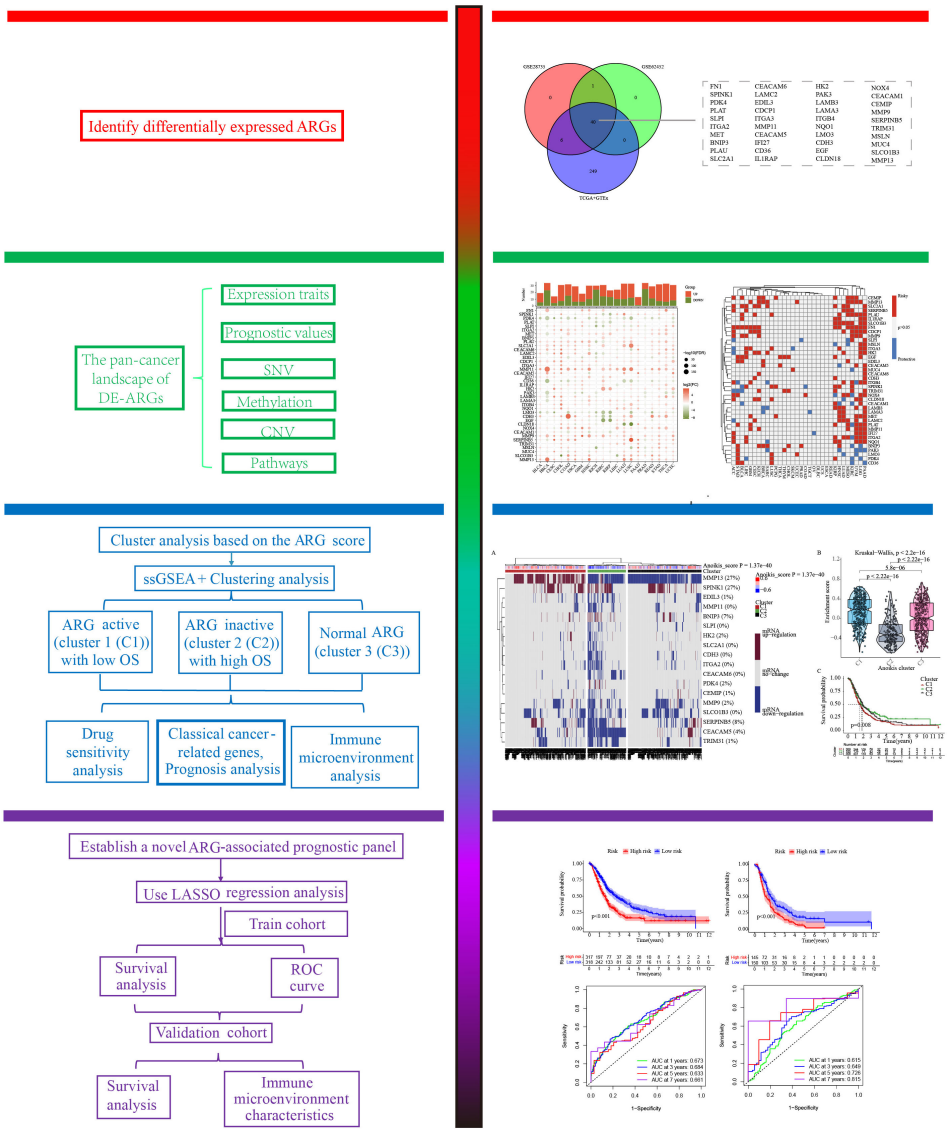

FIGURE 1
The study-flow of this research.

differential expression analyses of three public cohorts were carried out through the limma package in R. The results of GSE28735, GSE62452, and TCGA+GTEx cohorts identified 47, 41, and 295 DE-ARGs, respectively, which were further visualized *via* the heatmap package (Figures 2A–C). After taking the intersection of three cohorts, a total of 40 shared DE-ARGs were determined for further analysis (Figure 2D; Table S2).

Pan-cancer analysis characterization of the important roles of DE-ARGs

Up to now, the potential roles of DE-ARGs in the occurrence and progression of human multiple cancers remained unclear. Thus, we systematically summarized their pan-cancer characteristics through a series of complex bioinformatics algorithms. Interestingly, differentially expressed genes in pancreatic cancer and para-cancerous tissues showed a similar expression trend in other malignant tumors (Figure 3A). The expression levels of SLC2A1, MMP11, HK2, MMP7, and MMP13 in most tumors were significantly increased compared to corresponding para-cancerous tissues, suggesting their potential carcinogenesis. The expression levels of PDK4, LMO3 and PAK3 in most tumors were significantly decreased compared to corresponding para-cancerous tissues, suggesting their potentially protective roles. More importantly, nearly all the DE-ARGs exerted the pivotal parts in the clinical outcomes of patients with PAAD, LGG, UVM, and KIRC, which further highlighted their crucial contributions in the carcinogenesis (Figure 3B). Genomics data of pan-cancer revealed their CNV and SNV landscape, which might be responsible for their expression traits (Figures 3C–E). Specifically, SLCO1B3, PAK3, NOX4, MUC4, MMP9, MET, LAMB3, LAMA3, ITGB4, ITGA2, FN1, and EDIL3 genes exhibited obvious SNV traits. Furthermore, almost all of the DE-ARGs exhibited evident mutational patterns in patients diagnosed with SKCM and UCEC

10.3389/fendo.2023.1153909

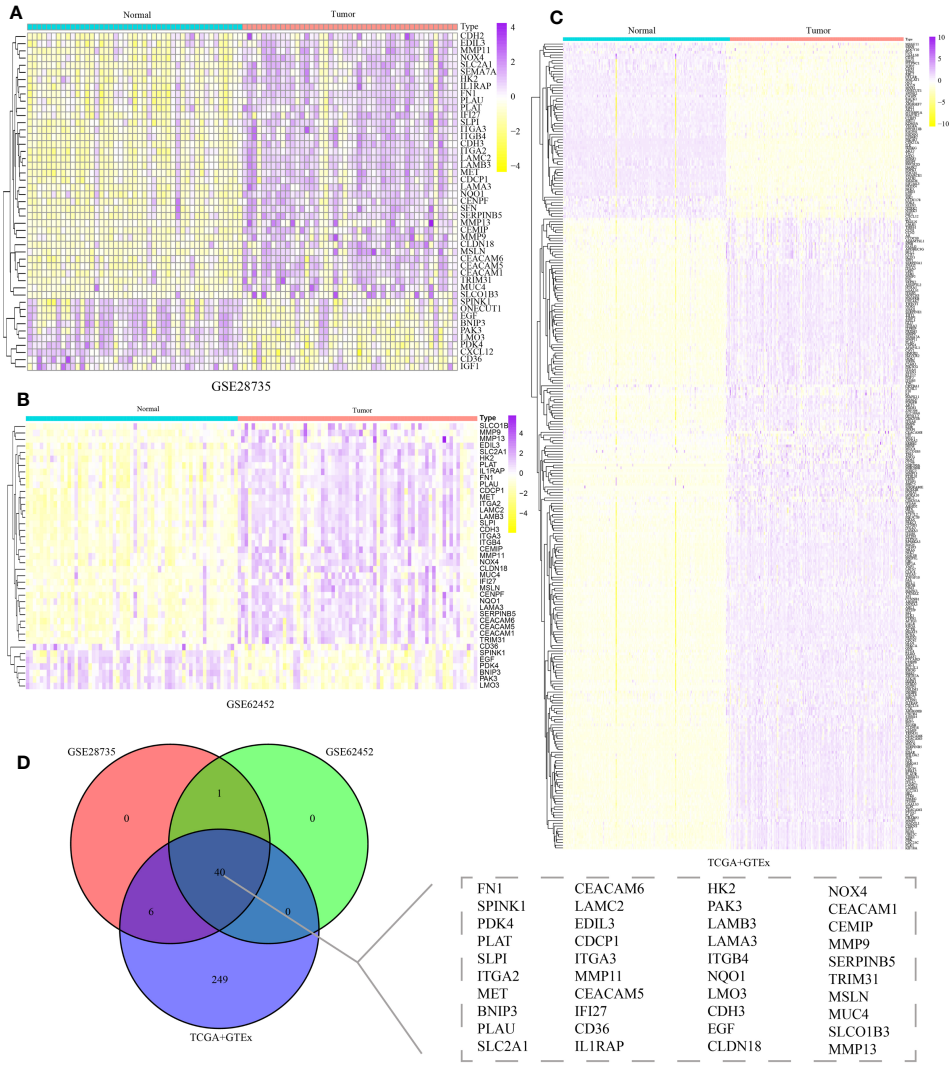

FIGURE 2
Identification of differentially expressed anoikis-related genes (DE-ARGs). Differential expression analysis of DE-ARGs in **(A)** GSE28735, **(B)** GSE62452, and **(C)** TCGA+GTEx cohorts. **(D)** Identification of 40 shared DE-ARGs.

(Figure 3C). Among the 40 DE-ARGs, the top three genes in the proportion of mutations were MUC4, LAMA3 and FN1, respectively (Figure 3D). Additionally, the methylation levels of DE-ARGs showed a significant difference in pan-cancer tissues and para-cancerous tissues (Figure 3F). CDH3, EDIL3, PDK4, and PLAT displayed relatively high methylation levels, while SLPI, CEACAM5, PAK3, TRIM31, and MMP13 displayed relatively low methylation levels (Figure 3F). Ultimately, the results of ssGSEA uncovered the significant correlation between DE-ARGs and several typical cancer-related pathways (Figure 3G). In particular, DE-ARGs were significantly correlated with the activities of typical cancer-related pathways.

Cluster analysis of 930 patients with PC based on the anoikis scores

Initially, ssGSEA was utilised to compute the anoikis scores of each PC patient. Subsequently, cluster analysis was conducted to classify 930 PC patients into three subtypes, namely C1, C2, and C3 (Figure 4A). The anoikis scores among the three subtypes demonstrated a significant difference, with C1 having the highest score, followed by C3, and C2 having the lowest score (Figure 4B). More significantly, subtype C1 demonstrated the poorest prognosis while subtype C2 exhibited the most favourable prognosis (Figure 4C). Additionally, the C1 subtype was observed to be accompanied by oncogene activation, whereas the C2 subtype was characterised by oncogene inhibition (Figure 4D). The aberrant expression of oncogenes may account for the variation in clinical outcomes among PC subtypes. Furthermore, our investigation revealed that immune and metabolic pathways were differentially activated in PC patients with distinct anoikis scores, which is of great significance (Figures 5A, B).

Tumor immune microenvironment analysis

As shown in Figure 6A, C2 subtype exhibited a higher proportion of immune cell infiltration, while C1 subtype demonstrated a lower

10.3389/fendo.2023.1153909

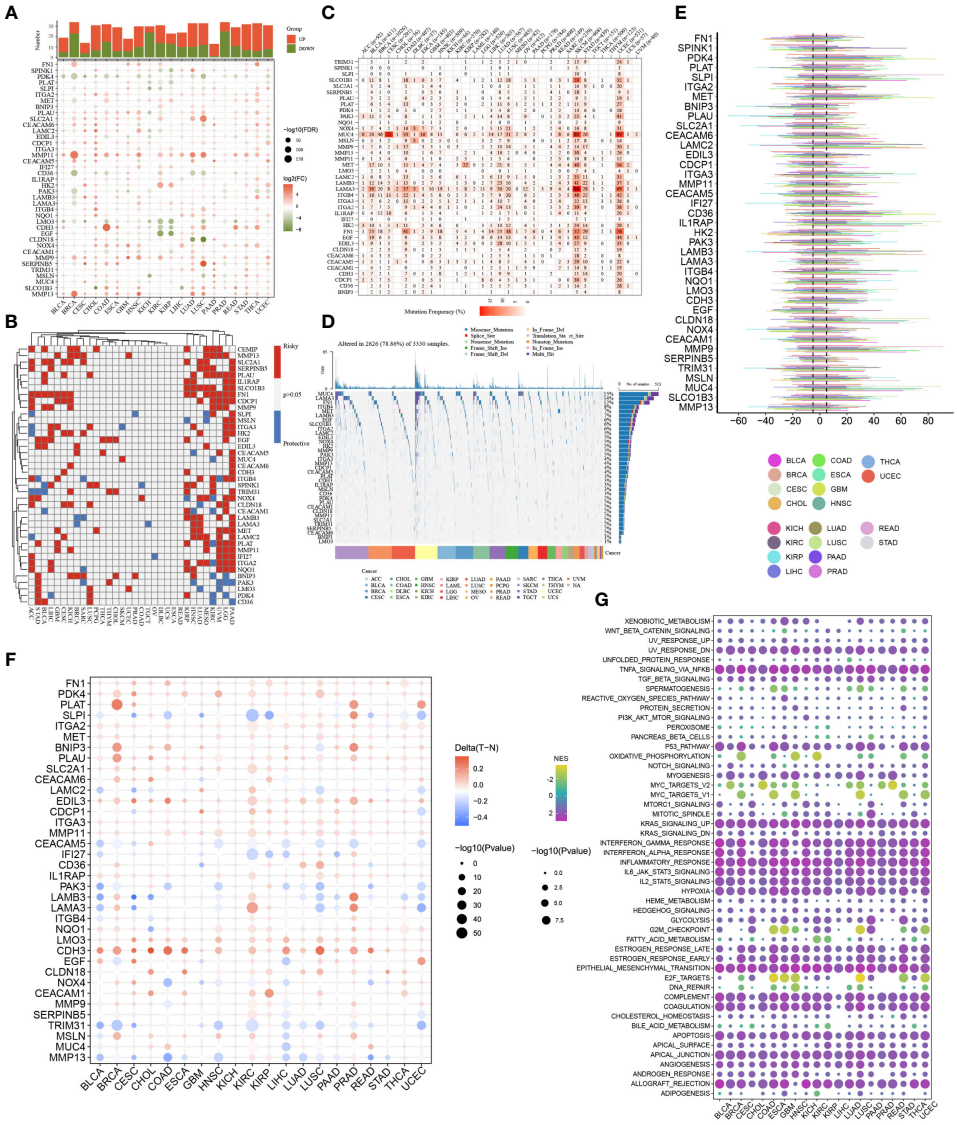

FIGURE 3
Pan-cancer overview of DE-ARGs. **(A)** mRNA expression traits of DE-ARGs in pan-cancer. **(B)** Prognostic values of DE-ARGs in pan-cancer. **(C, D)** SNV traits of DE-ARGs in pan-cancer. **(E)** CNV traits of DE-ARGs in pan-cancer. **(F)** Methylation levels of DE-ARGs in pan-cancer. **(G)** Pathway regulation ability of DE-ARGs in pan-cancer.

proportion of immune cell infiltration. It is widely acknowledged that immune cells play a crucial role in anti-tumor biological processes. A higher proportion of immune cells often indicate a stronger anticancer activity in the tumor microenvironment, although the regulatory role of ICGs cannot be ignored. Therefore, we conducted additional analysis on the expression distributions of ICGs among the three subtypes. The findings revealed that C1 subtype exhibited higher expression levels of ICGs, whereas C2 subtype demonstrated lower expression levels of ICGs (Figure 6B).

To examine the regulatory functions of anoikis in the tumor immune microenvironment, Spearman correlation analysis was conducted to explore the close relationship between anoikis scores and the immune microenvironment (Figure 6C). The findings revealed a positive correlation between anoikis scores and macrophage infiltration and parainflammation (Figures 6D, E), but a negative correlation with TIL and Th1 cell infiltration (Figures 6F, G). Ultimately, we also discovered that the majority of DE-ARGs exhibited significant correlations with immune cell infiltration and immune-related functions (Figure 6H). Specifically, MMP9, MMP13, MMP11, and CEMIP were positively associated with the tumor immune microenvironment, while SLPI, SLC2A1, SERPINB5, HK2, CEACAM6, and CEACAM5 were negatively associated with the tumor immune microenvironment.

Cluster analysis of 226 patients with PNETs based on the anoikis scores

According to the enrichment scores of each patient with PNETs, 226 samples were successfully classified into three clusters (Figure 7A). The enrichment scores of clusters C2 and C3 were significantly higher than that of cluster C1; however, there was no

10.3389/fendo.2023.1153909

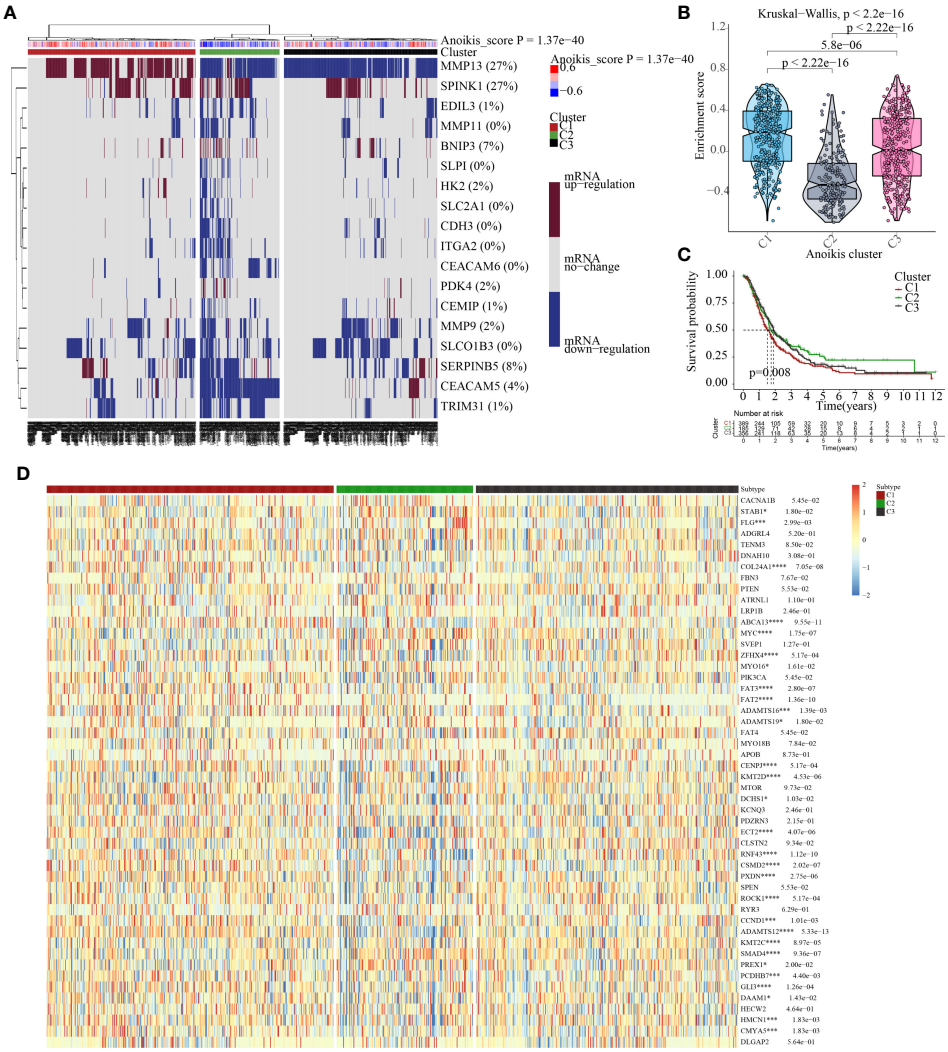

FIGURE 4
Cluster analysis help identify molecular heterogeneity of patents with PC. **(A)** Cluster analysis based on the anoikis scores obtained from the ssGSEA algorithms. **(B)** Distribution of anoikis enrichment scores among three subtypes (Score: C1 > C3 > C2). **(C)** Cluster-based survival analysis. The overall survival time is C2 > C3 > C1. **(D)** Expression traits of cancer-related genes among three subtypes. *p<0.05, ***p<0.001,****p<0.0001.

significant difference between clusters C2 and C3 (Figure 7B). Hence, C1 cluster was redefined as S1 subtype with low enrichment scores, while C2 and C3 clusters were merged and redefined as S2 subtype with high enrichment scores (Figure 7C). Further investigation was conducted to examine the differences in immune and metabolic characteristics between the two subtypes. Notably, there was no significant variation in the typical immune pathways between the S1 and S2 subtypes (Figure 8A). However, the activities of cysteine and methionine metabolism, propanoate metabolism, selenoamino acid metabolism, and sulfur metabolism were found to be significantly different between the S1 and S2 subtypes (Figure 8B).

Identification and verification of a novel ARG-based prognostic model

Taking into account the pathogenic impact of anoikis on PC, we postulated that DE-ARGs could facilitate the development of a new and robust prognostic model. The 40 DE-ARGs were inputted into a LASSO regression model in both the training and test datasets, resulting in the identification of 13 genes (Figures S1A, B). The risk score of prognostic model was computed as following: risk score = 0.19 0969310613421 * HK2 + 0.0519064867507077 * MMP11 + 0.04894081 94769506 * MMP9 + (-0.0210122866868812) * CEACAM5 + (-0.0168 359640064986) * MMP13 + 0.100798963932116 * BNIP3 + 0.0774100 41091489 * SLCO1B3 + (-0.0694892084881754) * EDIL3 + 0.059 818949860188 * CDH3 + (-0.00847433457654591) * PDK4 + 0.028246530675805 * SERPINB5 + (-0.052088581916376) * CEMIP + 0.0833490721065633 * SLC2A1. The patients in both the training and test cohorts were classified into high-risk and low-risk PC subgroups. In both cohorts, there was a significant survival advantage in the low-risk group compared to the high-risk group (P< 0.05) (Figures S2A, B). The risk scores were computed, and the median threshold of the risk score was set at 2.364683 to differentiate between high- and low-risk groups (Figures S2C, D). Survival scatter plots of the two cohorts demonstrated a negative association between

10.3389/fendo.2023.1153909

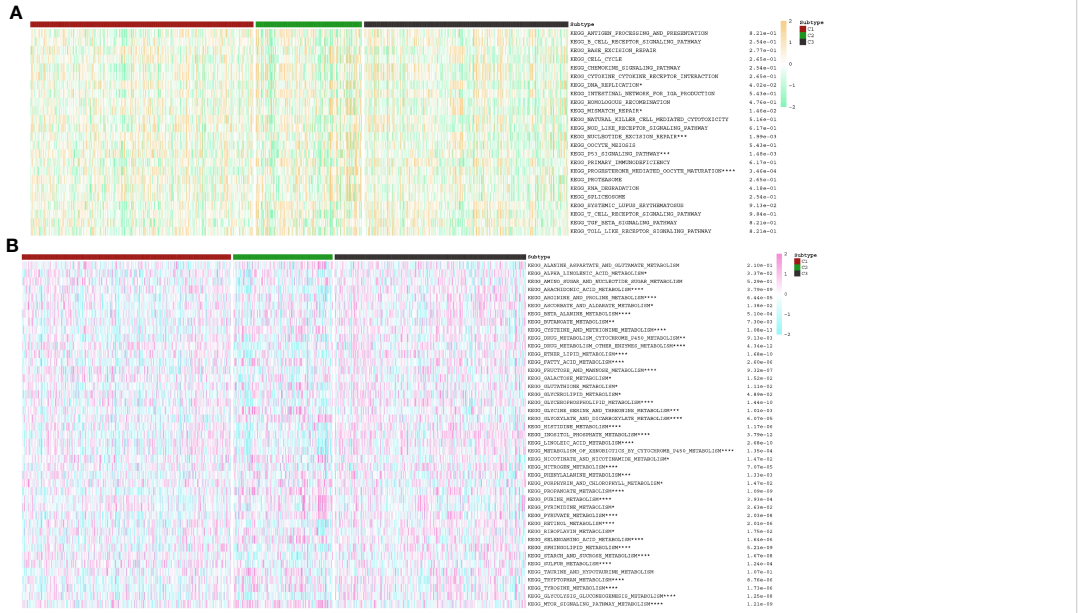

FIGURE 5
The discrepancies in the activities of **(A)** immune and **(B)** metabolism pathways among three PC clusters. *p<0.05, **p<0.01, ***p<0.001, ****p<0.0001.

survival time and the risk score, suggesting that patients in the high-risk group had poorer prognosis (Figures S2E, F). The time-dependent ROC curves for overall survival at 1, 3, 5, and 7 years in the training and test groups demonstrated excellent predictive performance using this model (Figures S2G, H). Ultimately, we also investigated the differences in ICI between the high- and low-risk subgroups. As shown in Figures 9A, B, low-risk PC patients exhibited a higher proportion of ICI than the high-risk subgroup, consistent with the finding that the low-risk subgroup had a significant survival advantage.

Clinical significances of model genes in PC

To emphasise the clinical significance of the 13 model genes in PC, we investigated the relationship between these genes and clinical outcomes, as well as clinical stages. The outcomes of univariate Cox regression analysis and KM survival analyses indicated that HK2, MMP11, MMP9, SLCO1B3, CDH3, PDK4, SERPINB5, and SLC2A1 were significantly associated with the survival time of PC patients (Figures 10A, B). In addition to PDK4, high expression levels of the other seven genes are unfavourable for the clinical outcomes of PC patients (Figures 10A, B). Moreover, HK2, MMP11, CDH3, PDK4, SERPINB5, and SLC2A1 expression were closely associated with tumour stages (Figure 10C).

After compiling a series of public PC cohorts, we also observed significant differences in the expression trends of HK2, MMP11, CDH3, PDK4, SERPINB5, and SLC2A1 between PC and para-cancerous tissues (Figure 11). It should be noted that HK2, MMP11, CDH3, SERPINB5, and SLC2A1 exhibited increased expression levels in PC tissues, while PDK4 showed decreased expression levels in PC compared to para-cancerous tissues (Figure 11). Furthermore, the qPCR results from cell lines confirmed the aforementioned expression trends of HK2, MMP11, CDH3, PDK4, SERPINB5, and SLC2A1 (Figure 12). More significantly, the IHC results were in line with the previous transcriptomics findings. The protein expression levels of HK2, CDH3, SERPINB5, and SLC2A1 were significantly higher in PC samples compared to para-cancerous samples. In contrast, the translational level of PDK4 was significantly lower in PC samples (Figure 13).

Discussion

The severity and progression of PC and PNETs pose a challenging clinical problem. Multi-omics has refined our understanding of the rudimentary genetics of PC and PNETs. Although multimodal therapy, including surgery, chemotherapy, radiation, targeted therapy, and immunotherapy, has extended the survival time of pancreatic tumor patients, treatment outcomes remain inadequate. Varied prognoses and clinical responses are observed among individuals with distinct subtypes of PC and PNETs. Prognostic models may accurately identify patients who would benefit from more aggressive treatment, such as extensive surgery, radiation therapy, neoadjuvant chemotherapy, or immunotherapy. Therefore, the development of molecular diagnostic biomarkers and therapeutic targets for PC and PNETs should be given priority.

Anoikis, a specialized kind of programmed cell death, plays a crucial role in body development, tissue homeostasis, disease manifestation, and tumor spread. In-depth research on anoikis has progressively identified the underlying molecular process. Anoikis triggers cell death, integrins sense and transduce extracellular matrix signals, and classical apoptotic pathways

10.3389/fendo.2023.1153909

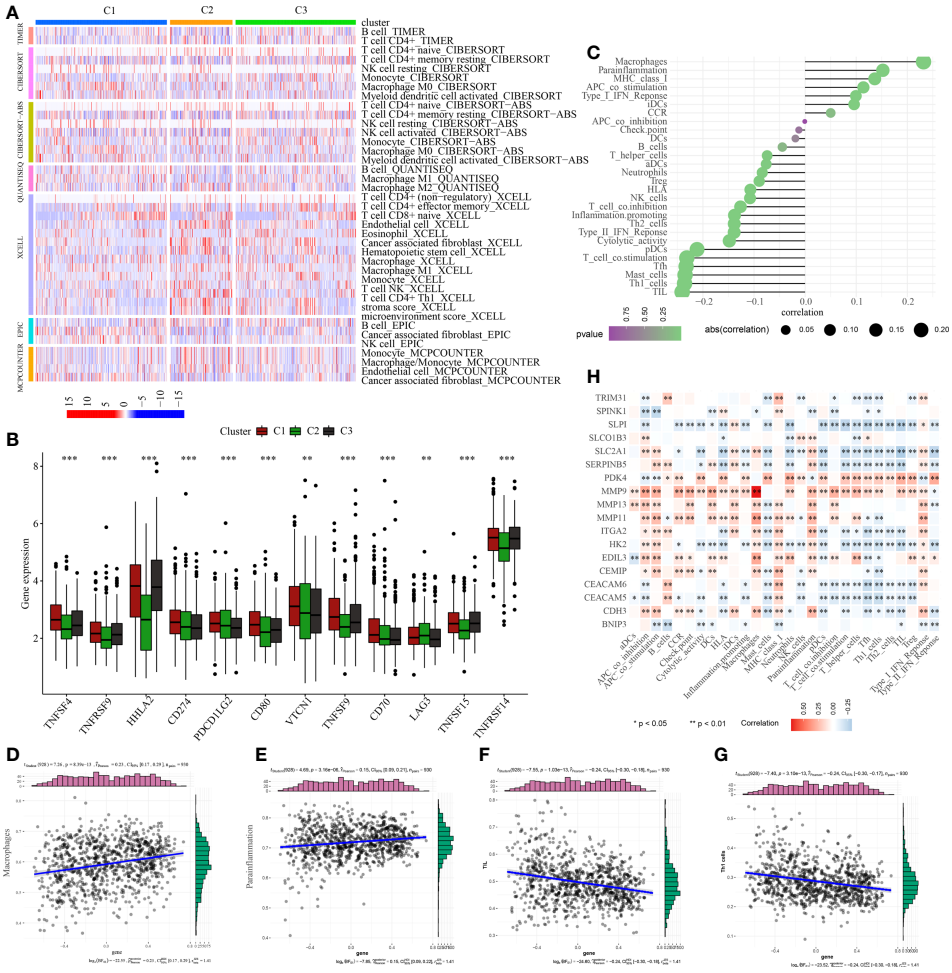

FIGURE 6
Analysis of tumor immune microenvironment. **(A)** Discrepancies in the immunocyte infiltration among three clusters. **(B)** Discrepancies in the immune checkpoint expression among three clusters. **(C)** Correlation among anoikis scores, immune cell infiltration and immune-related functions. Correlation between anoikis scores and **(D)** macrophages, **(E)** parainflammation, **(F)** TIL, and **(G)** Th1 cells. **(H)** Correlation among DE-ARGs expression and immune cell infiltration and immune-related functions. *p < 0.05; **p < 0.01; ***p < 0.001.

regulate cell adherence and survival. Bcl2 and its associated proteins play a significant role in the control of apoptosis, and several protein kinase signal molecules serve as regulatory hubs. Previous researches have highlighted the crucial role of anoikis in multiple human diseases, such as cancers.

Firstly, a pan-cancer analysis summarised and emphasised the essential role of ARGs in the onset and development of cancers. Significant differences in expression of certain ARGs were detected between cancers and para-cancerous tissues. These DE-ARGs were also closely associated with the clinical prognosis of patients with cancer, particularly PC. The aberrant expression patterns may be caused by genomic alterations. Therefore, we investigated the CNV and SNV patterns of DE-ARGs in pan-cancer, which further validated the above aberrant expression patterns. Additionally, we explored the methylation levels and pathway regulation relationship of DE-ARGs in pan-cancer. Most ARGs acted as high-methylation genes in PC. Furthermore, the tumour necrosis factor signalling, interferon signalling, inflammatory signalling, endothelial-to-mesenchymal transition signalling, and IL-6/JAK/STAT3 signalling pathways exhibited obvious correlations with the anoikis pathways in PC. Overall, this research was the first to systematically elaborate on the cancer landscape of anoikis, providing a foundation for future studies.

Bioinformatics technology helped to establish molecular classifiers associated with anoikis for patients with PC and PNETs. The classifier successfully stratified a total of 930 patients with PC into three clusters. Significant differences were observed in the activities of anoikis among different subtypes. Patients with high anoikis scores (C1 cluster) had worse clinical outcomes, while those with low anoikis scores (C2 cluster) had favorable prognoses. Moreover, the expression of most oncogenes varied among the three clusters. Specifically, CMYA5, HMCN1, GLI3, PCDHB7, ADAMTS12, CCND1, ROCK1, CSMD2, RNF43, ECT2, CENPJ, FAT3, ZFHX4, ABCA13, and COL24A1 exhibited significant overexpression trends in the C1 cluster.

To investigate the potential mechanisms underlying clinical outcome differences among patients with distinct anoikis scores, we conducted an intensive analysis of the components of the

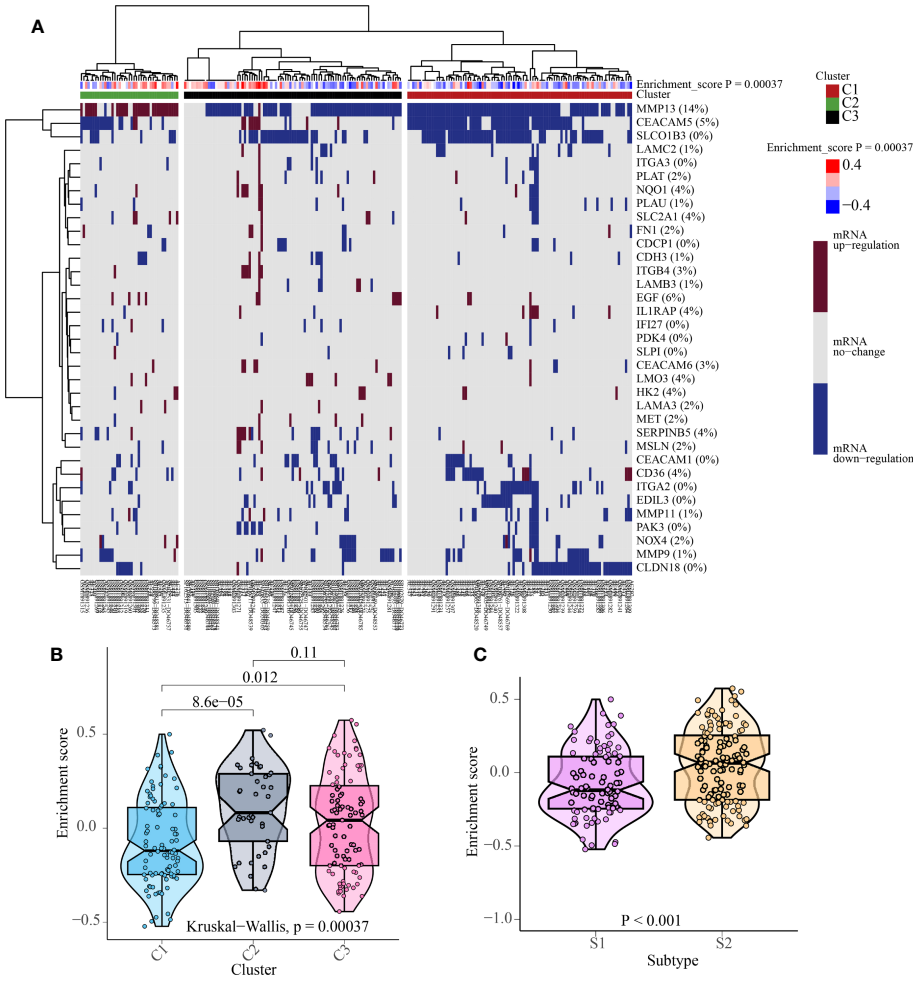

FIGURE 7
The cluster results of 226 patients with PNETs. **(A)** The unsupervised cluster of 226 patients with PNETs based on anoikis scores. **(B)** The enrichment scores of three clusters of PNETs. **(C)** The enrichment scores of two subtypes of PNETs.

immune microenvironment and expression of ICGs. Increasing evidence suggests that the immunocompetent cell response plays a crucial role in anti-tumour processes. The C2 subtype was associated with a higher proportion of many anti-tumour immune cells and lower expression levels of ICGs. Previous research has demonstrated a correlation between tumour-infiltrating B lymphocytes and favourable prognoses in cancer patients (27–29). The potential mechanisms underlying B-cell-mediated antitumor immunity may involve the secretion of effector cytokines, such as IFN-γ, by B cells, which can polarise T cells towards a Th1 or Th2 response or enhance T-cell responses through their antigen-presenting cell function (30). This distinctive ability of B cells to directly induce cytotoxicity in cancer is demonstrated by CpG-activated B cells, which can eliminate tumour cells through TRAIL/Apo-2L-dependent pathways (31). Similarly, the C2 subtype with favourable prognoses exhibited higher infiltration of B cells. It has been reported that NK cells recognized most tumor cells through two mechanisms: “missing-self recognition” and “stress-induced recognition” (32–34). After recognition, NK cells primarily exert anti-tumor effects through both direct and indirect pathways (35). Additionally, our findings revealed a higher proportion of NK cells in the C2 subtype. Overall, the dysregulation of the immune microenvironment among different anoikis subtypes may account for the differences in clinical outcomes.

In addition, we also explored the potential regulatory association between ARGs and ICI. Anoikis scores were positively correlated with macrophage levels and para-inflammation, and negatively correlated with TIL and Th1 levels, which were consistent with our previous cluster results. Patients with low anoikis scores (i.e. C2 subtype) had a higher infiltration level of TIL and CD4+T cells. This strong anti-tumor immune response might partly explain why the prognosis of these patients was relatively good. We then systematically investigated the correlation between each ARG and ICI. Interestingly, different genes possessed varying immunomodulatory properties. PDK4, MMP9, MMP13, MMP11, and EDIL3 were positively correlated with ICI and immune-related functions, while SLPI, SLC2A1, SERPINB5, HK2, CEACAM6, and CEACAM5 were negatively correlated with ICI and immune-related functions.

Subsequently, we classified a total of 226 PNET patients into three clusters; however, there was no significant difference between

10.3389/fendo.2023.1153909

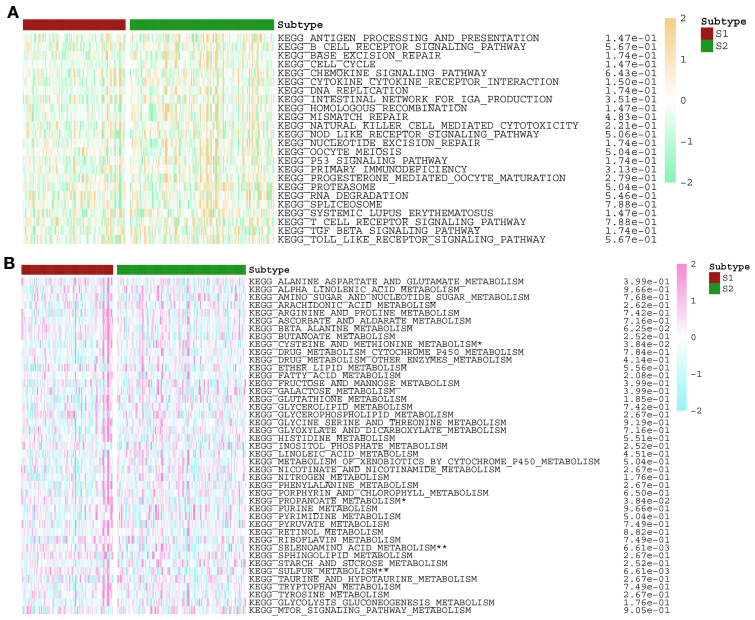

FIGURE 8
The activities of **(A)** immune and **(B)** metabolism pathways in S1 and S2 subtypes with PNETs. *p < 0.05, **p < 0.01.

C2 and C3 PNET patients. Therefore, we combined C2 and C3 PNET patients into one subtype. As we did not have follow-up information, we were unable to compare the survival time of patients with different PNET subtypes. While there were no significant differences in immune pathways among different PNET subtypes, differences in several metabolic pathways were notable.

Despite the fact that molecular typing is tremendously important for functional mining of anoikis, we must acknowledge that clustering is, to some extent, a black box. It cannot precisely predict the anoikis scores and clinical outcomes for individual patients. Therefore, we have developed a unique and robust prognostic model related to anoikis using the LASSO regression

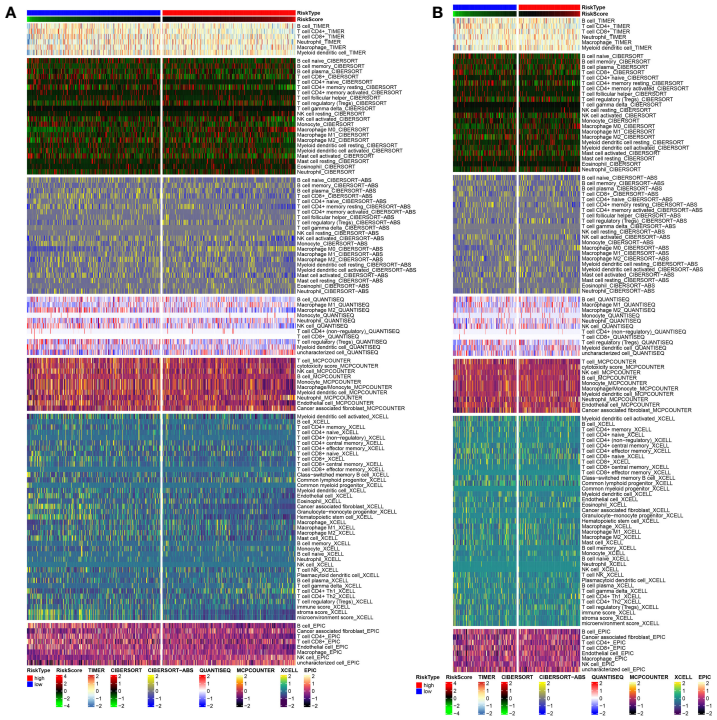

FIGURE 9
Tumor immune microenvironment analysis in **(A)** training and **(B)** test cohorts.

10.3389/fendo.2023.1153909

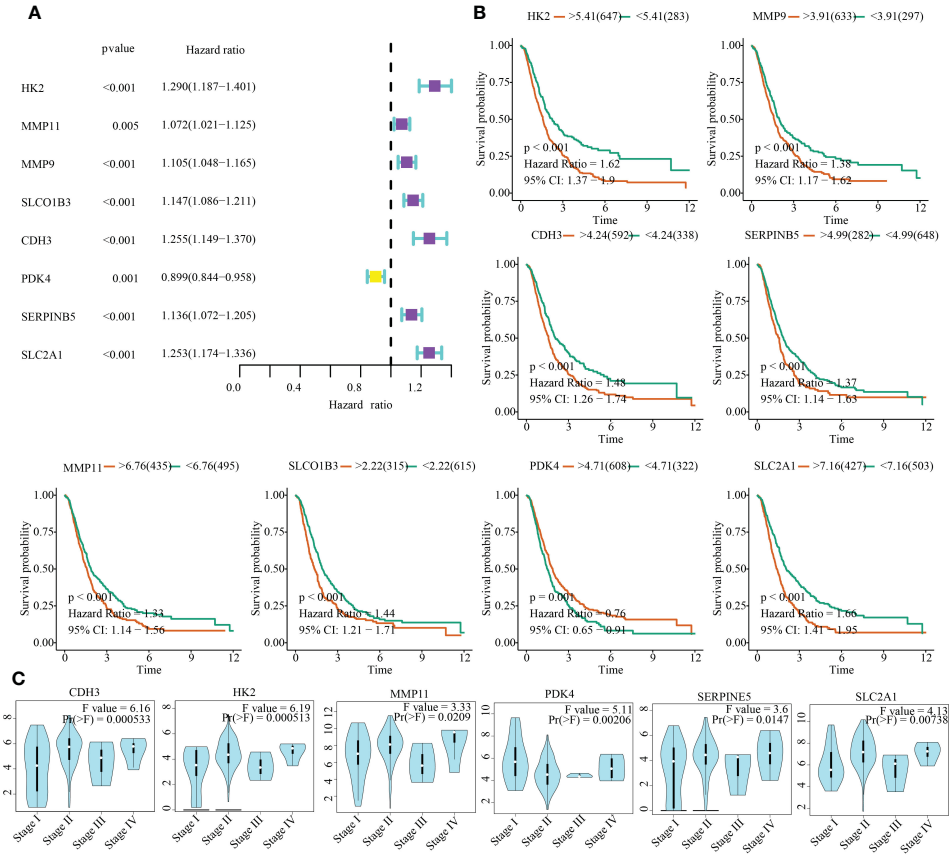

FIGURE 10
Clinical significances of model genes in PC. **(A)** Uninariate Cox regression analysis. **(B)** Kaplan-Meier survival analysis. **(C)** Correlation between clinical stage and gene expression.

technique. This model includes 13 genes associated with anoikis, including HK2, MMP11, MMP9, CEACAM5, MMP13, BNIP3, SLCO1B3, EDIL3, CDH3, PDK4, SERPINB5, CEMIP, and SLC2A1. There was a significant difference in survival outcomes between high-risk and low-risk pancreatic cancer patients in both the training and validation cohorts. More importantly, ROC curves further validated the prediction accuracy of the model and demonstrated its ability to predict the survival outcome of 930 patients with pancreatic cancer, which could have wide applications in the future and provide a reference value for individual patient intervention.

Hexokinase 2 (HK2) catalyzes the phosphorylation of glucose, a step required for glucose metabolism (36, 37). Anderson et al. have reported that HK2 had the potential to enhance tumor proliferation, growth, invasion, and metastasis *via* regulation of lactate metabolism in PC (38). In individuals with PC, HK2 also prevented cell apoptosis mediated by gemcitabine through voltage-dependent anion channel (39). Remodeling of the extracellular matrix (ECM) by matrix metalloproteinases (MMPs) was a crucial stage in the invasion and metastasis of solid malignant tumors as it enabled tumor cells to modify ECM components and release cytokines, thus promoting protease-dependent tumor progression (40). Cell adhesion, intracellular and intercellular signal transduction, cancer development, inflammation, angiogenesis, and metastasis are just a few of the activities of carcinoembryonic antigen-related cell adhesion molecules (CEACAMs) in complex biological processes. CEACAM5 is now considered a reliable clinical biomarker and a promising therapeutic target for melanoma, lung cancer, colorectal cancer, and pancreatic cancer (41).

However, there are some limitations associated with our research. Our signature was constructed using retrospective data from public datasets. To further establish the predictive significance of our prognostic signature, extensive prospective clinical research is necessary. Furthermore, as the signature was developed using bioinformatics research, additional fundamental research is required to validate our findings. Despite these limitations, our study still holds unique clinical significance. The pan-cancer comprehensive analysis of anoikis is particularly useful for the advancement of further fundamental research in the future. The molecular classifier and prognostic model based on anoikis score aid in identifying the inherent heterogeneity of pancreatic cancer patients, thus promoting the development of personalised intervention therapy for tumors.

Conclusion

This is the first study to systematically investigate anoikis in pan-cancer, categorize patients with PC and PNETs into unique

10.3389/fendo.2023.1153909

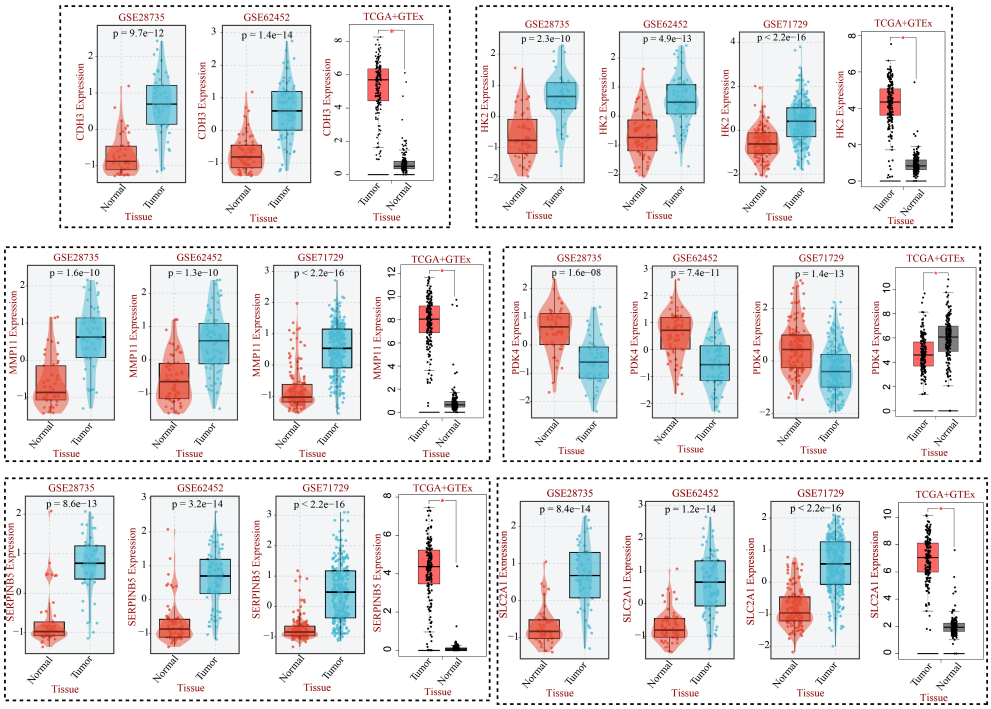

FIGURE 11
The transcriptomic levels of model genes in tumor and normal tissues. *p < 0.05.

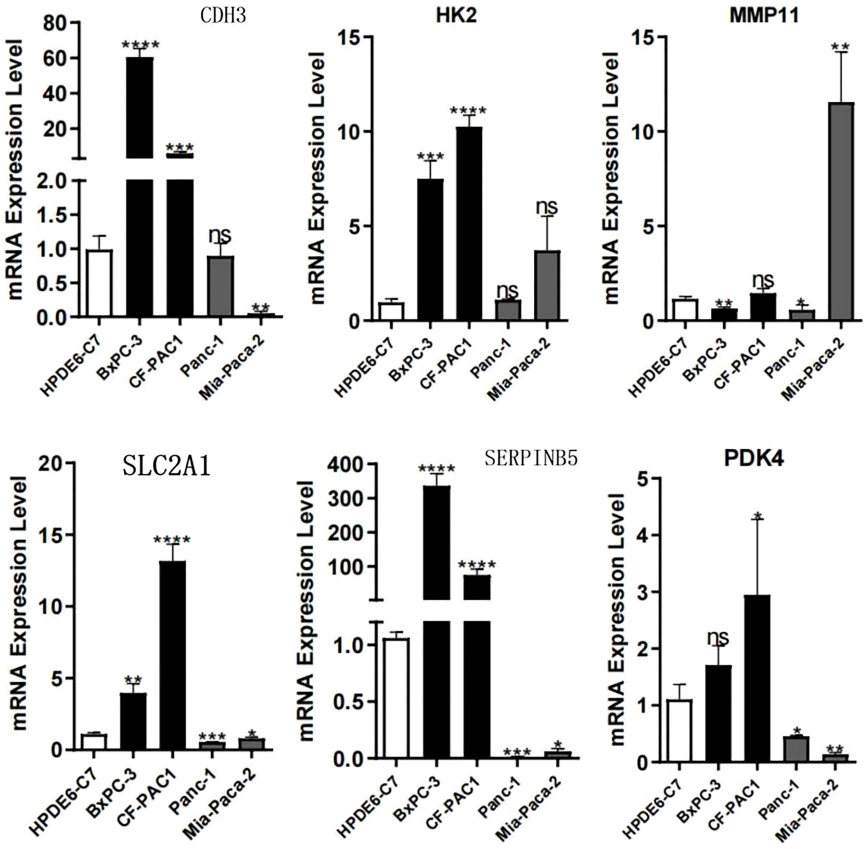

FIGURE 12
PCR experiments validated the expression levels of model genes. *p < 0.05; **p < 0.01; ***p < 0.001; ****p < 0.0001; ns, no significance.

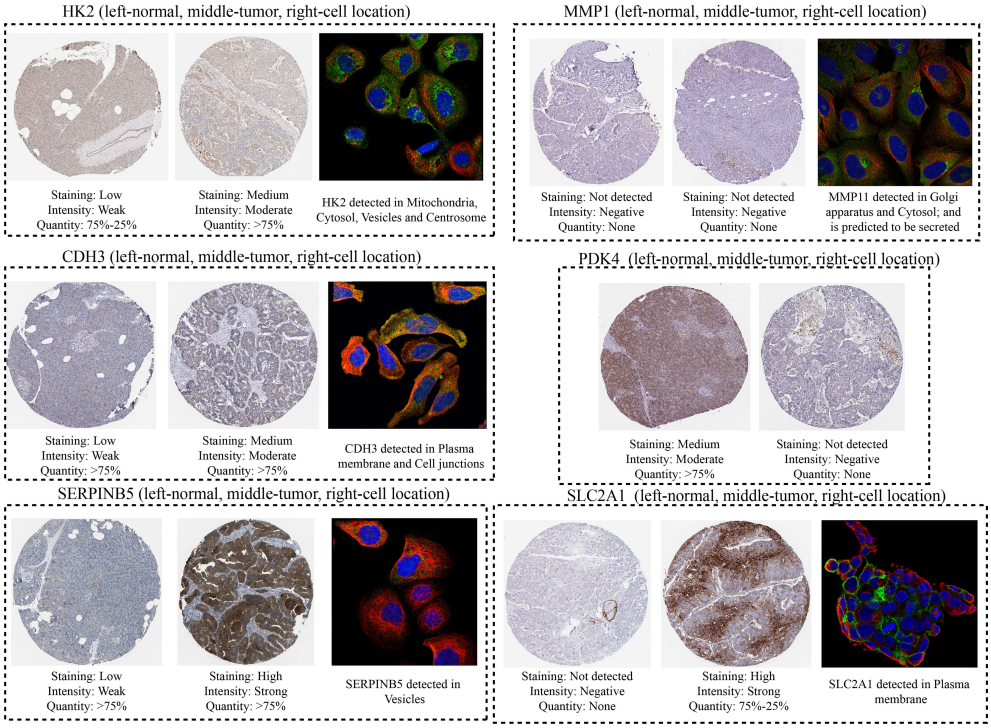

FIGURE 13
Immunocytochemistry and immunofluorescence results of model genes.

molecular subtypes according to their levels of anoikis, and create a dependable predictive model for PC based on anoikis. The functional status, tumor immune microenvironment, and clinical outcomes of patients with PC displayed considerable diversity. The survival rate of PC patients could be accurately anticipated by the risk model based on anoikis. Our findings hold the potential to enhance anoikis research and the targeted therapy of patients with pancreatic tumors.

Data availability statement

The original contributions presented in the study are included in the article/Supplementary Material. Further inquiries can be directed to the corresponding authors.

Author contributions

NL and ZW: The authors are responsible for the study design, data collection, data analysis, writing the manuscript, making the figures. XJ, KW, ZQ: The author is responsible for data collection, data analysis, revising the manuscript, making the figures. DC, ZS: The authors contribute to the study design, data collection, and writing the paper. JJ, YC, and CW: The authors supervised the project, designed this study, revised the manuscript. All authors contributed to the article and approved the submitted version.

Conflict of interest

The authors declare that the research was conducted in the absence of any commercial or financial relationships that could be construed as a potential conflict of interest.

Publisher's note

All claims expressed in this article are solely those of the authors and do not necessarily represent those of their affiliated organizations, or those of the publisher, the editors and the reviewers. Any product that may be evaluated in this article, or claim that may be made by its manufacturer, is not guaranteed or endorsed by the publisher.

Supplementary material

The Supplementary Material for this article can be found online at: https://www.frontiersin.org/articles/10.3389/fendo.2023.1153909/full#supplementary-material

SUPPLEMENTARY FIGURE 1
The processing of LASSO algorithms.

SUPPLEMENTARY FIGURE 2
Development and validation of the anoikis-based prognostic model. Survival curves of the anoikis-based prognostic model in **(A)** training and **(B)** test cohorts. Division of high-risk and low-risk groups in **(C)** training and **(D)** test cohorts. Distribution of survive time and risk scores in **(E)** training and **(F)** test cohorts. ROC curves of the anoikis-based prognostic model in **(G)** training and **(H)** test cohorts.

References

1. Yuan Q, Ren J, Li L, Li S, Xiang K, Shang D. Development and validation of a novel N6-methyladenosine (m6A)-related multi- long non-coding RNA (lncRNA) prognostic signature in pancreatic adenocarcinoma. *Bioengineered* (2021) 12(1):2432–48. doi: 10.1080/21655979.2021.1933868

2. Yuan H, Liu J, Zhao L, Wu P, Chen G, Chen Q, et al. Prognostic risk model and tumor immune environment modulation of m5C-related LncRNAs in pancreatic ductal adenocarcinoma. *Front Immunol* (2021) 12:800268. doi: 10.3389/fimmu.2021.800268

3. Yuan QH, Zhang LL, Xu Y, Chen X, Zhang B, Li LX, et al. Circulating leptin and adiponectin levels in patients with pancreatic cancer. *Chin Med J* (2021) 134(17):2134–6. doi: 10.1097/cm9.0000000000001509

4. Zhang X, Li X, Xie J, Zhu Q, Yuan Y. A novel immune-related prognostic signature predicting survival in patients with pancreatic adenocarcinoma. *J Oncol* (2022) 2022:8909631. doi: 10.1155/2022/8909631

5. Taddei ML, Giannoni E, Fiaschi T, Chiarugi P. Anoikis: an emerging hallmark in health and diseases. *J Pathol* (2012) 226(2):380–93. doi: 10.1002/path.3000

6. Chen S, Gu J, Zhang Q, Hu Y, Ge Y. Development of biomarker signatures associated with anoikis to predict prognosis in endometrial carcinoma patients. *J Oncol* (2021) 2021:3375297. doi: 10.1155/2021/3375297

7. Paoli P, Giannoni E, Chiarugi P. Anoikis molecular pathways and its role in cancer progression. *Biochim Biophys Acta* (2013) 1833(12):3481–98. doi: 10.1016/j.bbamcr.2013.06.026

8. Adeshakin FO, Adeshakin AO, Afolabi LO, Yan D, Zhang G, Wan X. Mechanisms for modulating anoikis resistance in cancer and the relevance of metabolic reprogramming. *Front Oncol* (2021) 11:626577. doi: 10.3389/fonc.2021.626577

9. Weinstein JN, Collisson EA, Mills GB, Shaw KR, Ozenberger BA, Ellrott K, et al. The cancer genome atlas pan-cancer analysis project. *Nat Genet* (2013) 45(10):1113–20. doi: 10.1038/ng.2764

10. Parkinson H, Kapushesky M, Shojatalab M, Abeygunawardena N, Coulson R, Farne A, et al. ArrayExpress–a public database of microarray experiments and gene expression profiles. *Nucleic Acids Res* (2007) 35(Database issue):D747–50. doi: 10.1093/nar/gkl995

11. Parkinson H, Kapushesky M, Kolesnikov N, Rustici G, Shojatalab M, Abeygunawardena N, et al. ArrayExpress update–from an archive of functional genomics experiments to the atlas of gene expression. *Nucleic Acids Res* (2009) 37 (Database issue):D868–72. doi: 10.1093/nar/gkn889

12. Parkinson H, Sarkans U, Kolesnikov N, Abeygunawardena N, Burdett T, Dylag M, et al. ArrayExpress update–an archive of microarray and high-throughput sequencing-based functional genomics experiments. *Nucleic Acids Res* (2011) 39 (Database issue):D1002–4. doi: 10.1093/nar/gkq1040

13. Zhang J, Bajari R, Andric D, Gerthoffert F, Lepsa A, Nahal-Bose H, et al. The international cancer genome consortium data portal. *Nat Biotechnol* (2019) 37(4):367–9. doi: 10.1038/s41587-019-0055-9

14. GTEx Consortium. The genotype-tissue expression (GTEx) project. *Nat Genet* (2013) 45(6):580–5. doi: 10.1038/ng.2653

15. Alvarez MJ, Subramaniam PS, Tang LH, Grunn A, Aburi M, Rieckhof G, et al. A precision oncology approach to the pharmacological targeting of mechanistic dependencies in neuroendocrine tumors. *Nat Genet* (2018) 50(7):979–89. doi: 10.1038/s41588-018-0138-4

16. Sadanandam A, Wullschleger S, Lyssiotis CA, Grötzinger C, Barbi S, Bersani S, et al. A cross-species analysis in pancreatic neuroendocrine tumors reveals molecular subtypes with distinctive clinical, metastatic, developmental, and metabolic characteristics. *Cancer discovery.* (2015) 5(12):1296–313. doi: 10.1158/2159-8290.Cd-15-0068

17. Leek JT, Johnson WE, Parker HS, Jaffe AE, Storey JD. The sva package for removing batch effects and other unwanted variation in high-throughput experiments. *Bioinformatics* (2012) 28(6):882–3. doi: 10.1093/bioinformatics/bts034

18. Zhang G, Schetter A, He P, Funamizu N, Gaedcke J, Ghadimi BM, et al. DPEP1 inhibits tumor cell invasiveness, enhances chemosensitivity and predicts clinical outcome in pancreatic ductal adenocarcinoma. *PloS One* (2012) 7(2):e31507. doi: 10.1371/journal.pone.0031507

19. Zhang G, He P, Tan H, Budhu A, Gaedcke J, Ghadimi BM, et al. Integration of metabolomics and transcriptomics revealed a fatty acid network exerting growth inhibitory effects in human pancreatic cancer. *Clin Cancer research: an Off J Am Assoc Cancer Res* (2013) 19(18):4983–93. doi: 10.1158/1078-0432.Ccr-13-0209

20. Yang S, He P, Wang J, Schetter A, Tang W, Funamizu N, et al. A novel MIF signaling pathway drives the malignant character of pancreatic cancer by targeting NR3C2. *Cancer Res* (2016) 76(13):3838–50. doi: 10.1158/0008-5472.Can-15-2841

21. Yuan Q, Deng D, Pan C, Ren J, Wei T, Wu Z, et al. Integration of transcriptomics, proteomics, and metabolomics data to reveal HER2-associated metabolic heterogeneity in gastric cancer with response to immunotherapy and neoadjuvant chemotherapy. *Front Immunol* (2022) 13:951137. doi: 10.3389/fimmu.2022.951137

22. Ren J, Zhang H, Wang J, Xu Y, Zhao L, Yuan Q, et al. Transcriptome analysis of adipocytokines and their-related LncRNAs in lung adenocarcinoma revealing the association with prognosis, immune infiltration, and metabolic characteristics. *Adipocyte.* (2022) 11(1):250–65. doi: 10.1080/21623945.2022.2064956

23. Chen DT, Davis-Yadley AH, Huang PY, Husain K, Centeno BA, Permuth-Wey J, et al. Prognostic fifteen-gene signature for early stage pancreatic ductal adenocarcinoma. *PloS One* (2015) 10(8):e0133562. doi: 10.1371/journal.pone.0133562

24. Puleo F, Nicolle R, Blum Y, Cros J, Marisa L, Demetter P, et al. Stratification of pancreatic ductal adenocarcinomas based on tumor and microenvironment features. *Gastroenterology.* (2018) 155(6):1999–2013.e3. doi: 10.1053/j.gastro.2018.08.033

25. Geeleher P, Cox N, Huang RS. pRRophetic: an r package for prediction of clinical chemotherapeutic response from tumor gene expression levels. *PloS One* (2014) 9(9):e107468. doi: 10.1371/journal.pone.0107468

26. Liu CQ, Xia QD, Sun JX, Xu JZ, Lu JL, Liu Z, et al. Identification and validation of a twelve immune infiltration-related lncRNA prognostic signature for bladder cancer. *Aging.* (2022) 14(3):1492–507. doi: 10.18632/aging.203889

27. Nielsen JS, Sahota RA, Milne K, Kost SE, Nesslinger NJ, Watson PH, et al. CD20 + tumor-infiltrating lymphocytes have an atypical CD27- memory phenotype and together with CD8+ T cells promote favorable prognosis in ovarian cancer. *Clin Cancer research: an Off J Am Assoc Cancer Res* (2012) 18(12):3281–92. doi: 10.1158/1078-0432.Ccr-12-0234

28. Al-Shibli KI, Donnem T, Al-Saad S, Persson M, Bremnes RM, Busund LT, et al. Prognostic effect of epithelial and stromal lymphocyte infiltration in non-small cell lung cancer. *Clin Cancer research: an Off J Am Assoc Cancer Res* (2008) 14(16):5220–7. doi: 10.1158/1078-0432.Ccr-08-0133

29. Nedergaard BS, Ladekarl M, Nyengaard JR, Nielsen K. A comparative study of the cellular immune response in patients with stage IB cervical squamous cell carcinoma. low numbers of several immune cell subtypes are strongly associated with relapse of disease within 5 years. *Gynecologic Oncol* (2008) 108(1):106–11. doi: 10.1016/j.ygyno.2007.08.089

30. Sarvaria A, Madrigal JA, Saudemont A. B cell regulation in cancer and anti-tumor immunity. *Cell Mol Immunol* (2017) 14(8):662–74. doi: 10.1038/cmi.2017.35

31. Kemp TJ, Moore JM, Griffith TS. Human b cells express functional TRAIL/Apo-2 ligand after CpG-containing oligodeoxynucleotide stimulation. *J Immunol* (2004) 173 (2):892–9. doi: 10.4049/jimmunol.173.2.892

32. Ljunggren HG, Kärre K. In search of the 'missing self': MHC molecules and NK cell recognition. *Immunol Today* (1990) 11(7):237–44. doi: 10.1016/0167-5699(90)90097-s

33. Bottino C, Dondero A, Bellora F, Moretta L, Locatelli F, Pistoia V, et al. Natural killer cells and neuroblastoma: tumor recognition, escape mechanisms, and possible novel immunotherapeutic approaches. *Front Immunol* (2014) 5:56. doi: 10.3389/fimmu.2014.00056

34. Fang F, Xiao W, Tian Z. NK cell-based immunotherapy for cancer. *Semin Immunol* (2017) 31:37–54. doi: 10.1016/j.smim.2017.07.009

35. Sungur CM, Murphy WJ. Positive and negative regulation by NK cells in cancer. *Crit Rev oncogenesis* (2014) 19(1-2):57–66. doi: 10.1615/critrevoncog.2014010805

36. Deeb SS, Malkki M, Laakso M. Human hexokinase II: sequence and homology to other hexokinases. *Biochem Biophys Res Commun* (1993) 197(1):68–74. doi: 10.1006/bbrc.1993.2442

37. Wilson JE. Isozymes of mammalian hexokinase: structure, subcellular localization and metabolic function. *J Exp Biol* (2003) 206(Pt 12):2049–57. doi: 10.1242/jeb.00241

38. Anderson M, Marayati R, Moffitt R, Yeh JJ. Hexokinase 2 promotes tumor growth and metastasis by regulating lactate production in pancreatic cancer. *Oncotarget.* (2017) 8(34):56081–94. doi: 10.18632/oncotarget.9760

39. Fan K, Fan Z, Cheng H, Huang Q, Yang C, Jin K, et al. Hexokinase 2 dimerization and interaction with voltage-dependent anion channel promoted resistance to cell apoptosis induced by gemcitabine in pancreatic cancer. *Cancer Med* (2019) 8(13):5903–15. doi: 10.1002/cam4.2463

40. Zhang X, Huang S, Guo J, Zhou L, You L, Zhang T, et al. Insights into the distinct roles of MMP-11 in tumor biology and future therapeutics (Review). *Int J Oncol* (2016) 48(5):1783–93. doi: 10.3892/ijo.2016.3400

41. Beauchemin N, Arabzadeh A. Carcinoembryonic antigen-related cell adhesion molecules (CEACAMs) in cancer progression and metastasis. *Cancer metastasis Rev* (2013) 32(3-4):643–71. doi: 10.1007/s10555-013-9444-6

frontiers | Frontiers in Endocrinology

TYPE Original Research
PUBLISHED 02 June 2023
DOI 10.3389/fendo.2023.1145722

OPEN ACCESS

EDITED BY
Chenyu Sun,
AMITA Health, United States

REVIEWED BY
Liu Yunfei,
Ludwig Maximilian University of Munich, Germany
Changjing Wang,
Hebei Medical University Third Affiliated Hospital, China

*CORRESPONDENCE
Qin Xie
xieqin1895@sina.com

†These authors have contributed equally to this work and share first authorship

RECEIVED 16 January 2023
ACCEPTED 23 May 2023
PUBLISHED 02 June 2023

CITATION
Xie Q, Liu T, Zhang X, Ding Y and Fan X (2023) Construction of a telomere-related gene signature to predict prognosis and immune landscape for glioma.
Front. Endocrinol. 14:1145722.
doi: 10.3389/fendo.2023.1145722

Construction of a telomere-related gene signature to predict prognosis and immune landscape for glioma

Qin Xie[1*†], Tingting Liu[2†], Xiaole Zhang[1], Yanli Ding[1] and Xiaoyan Fan[3]

[1]Department of Neurosurgery, Hangzhou Ninth People's Hospital, Hangzhou, Zhejiang, China, [2]Department of Endocrinology, Affiliated Haikou Hospital of Xiangya School of Central South University, Haikou, Hainan, China, [3]Intensive Care Unit, Hangzhou Ninth People's Hospital, Hangzhou, Zhejiang, China

Background: Glioma is one of the commonest malignant tumors of the brain. However, glioma present with a poor clinical prognosis. Therefore, specific detection markers and therapeutic targets need to be explored as a way to promote the survival rate of BC patients. Therefore, we need to search for quality immune checkpoints to support the efficacy of immunotherapy for glioma.

Methods: We first recognized differentially expressed telomere-related genes (TRGs) and accordingly developed a risk model by univariate and multivariate Cox analysis. The accuracy of the model is then verified. We evaluated the variations in immune function and looked at the expression levels of immune checkpoint genes. Finally, to assess the anti-tumor medications often used in the clinical treatment of glioma, we computed the half inhibitory concentration of pharmaceuticals.

Results: We finally identified nine TRGs and built a risk model. Through the validation of the model, we found good agreement between the predicted and observed values. Then, we found 633 differentially expressed genes between various risk groups to identify the various molecular pathways between different groups. The enrichment of CD4+ T cells, CD8+ T cells, fibroblasts, endothelial cells, macrophages M0, M1, and M2, mast cells, myeloid dendritic cells, and neutrophils was favorably correlated with the risk score, but the enrichment of B cells and NK cells was negatively correlated with the risk score. The expression of several immune checkpoint-related genes differed significantly across the risk groups. Finally, in order to create individualized treatment plans for diverse individuals, we searched for numerous chemotherapeutic medications for patients in various groups.

Conclusion: The findings of this research provide evidence that TRGs may predict a patient's prognosis for glioma, assist in identifying efficient targets for glioma immunotherapy, and provide a foundation for an efficient, customized approach to treating glioma patients.

KEYWORDS

glioma, signature, immunotherapy, checkpoint, clinical treatment

1 Introduction

According to the World Health Organization, glioma is one of the most prevalent malignant tumors of the brain and is categorized as grades 1, 2, 3, or 4; grades 1 and 2 are low grade glioma (LGG), while grades 3 and 4 are high grade glioma (glioblastoma multiforme, GBM) (1, 2). 30% of all primary brain and spinal cord tumors are glioma, which make up more than 80% of all malignant brain tumors and are clinically very likely to be fatal (3). Glioma currently have a poor clinical prognosis upon presentation. Despite advancements in chemotherapeutic agents, radiation, and surgical methods for resecting tumors, the overall survival of glioma patients is still not encouraging (4). After conventional surgery, radiation and chemotherapy, glioma patients have a median survival period of about 14 months and an estimated 5-year survival rate of about 9.8% (5). So far, immunotherapy for glioma is the more effective treatment modality. Immune checkpoint inhibitor therapy allows effector T cells to reactivate and exert cytotoxicity on tumor cells through a combination of specific antibodies and checkpoint molecules (10.3389/fimmu.2020.578877). Therefore, we need to search for quality immune checkpoints to support the efficacy of immunotherapy for glioma.

Telomere is a region at the end of a chromosome that is composed of two parts, the repetitive TTAGGG DNA sequence and the shieldin complex (6). Telomeres ensure the stability of chromosomes, providing security, and are significant for cell division and certain diseases (7). In addition, telomere abnormalities can lead to many diseases and are closely associated with the development of many mental health problems and cancer (7, 8). A study elucidated polymorphisms in telomere length-related genes and found that some telomeric loci were associated with a high risk of liver cancer (9). It has been shown that the length of the telomere-related genes (TRGs) is associated with the development of glioma (10). Malignant glioma usually exhibit telomerase activity, although normal brain tissue hardly ever does (11). Malignant glioma cells may be capable of unrestricted proliferation and apoptosis inhibition due to abnormal telomerase reactivation (11).

In the research, we screened and correlated TRGs with the aim of identifying immune checkpoints associated with glioma immunotherapy to improve the efficacy of clinical glioma and improve patient survival.

Abbreviations: TRGs, telomere-related genes; LGG, low grade glioma; GBM, glioblastoma multiforme; TRGs, telomere-related genes; DEGs, differentially expressed genes; KEGG, kyoto encyclopedia of genes and genomes; GO, gene ontology; TIDE, tumor immune dysfunction and exclusion; TMB, tumor mutation burden; ssGSEA, single-sample gene set enrichment analysis; IC50, half inhibitory concentration.

2 Materials and methods

2.1 Preparation of data

The TCGA-glioma and GEO-GSE74187 databases provided the RNA-seq data and clinical information for glioma (12). Data that was missing or had a survival time of less than 30 days was removed. TRGs were downloaded from TelNet (http://www.cancertelsys.org/telnet/; Table S1) (13).

2.2 Construction and validation of model

To find TRGs that were differently expressed between normal and glioma samples (|logFC| >= 1 and *P* value< 0.05), the R package limma and wilcox tests were used (14). Prognostic TRGs were identified using univariate Cox analysis (*P*< 0.001), and a risk model was created using multivariate Cox analysis. Each patient with glioma had their risk score calculated using a formula: $\sum_{i=1}^{k} \beta i Si$. To validate this model, the GEO-GSE74187 dataset was used as an external validation set. To compare the survival rates of various groups, a Kaplan-Meier analysis was used. To evaluate the accuracy of survival prediction, the receiver operating characteristic (ROC) curves and the area under curve (AUC) were used.

Based on clinical characteristics, we divided the patients into several groups and investigated the survival rates of various groups within various groupings. The model was tested using univariate and multivariate Cox analyses to ensure that it was an accurate predictor of prognosis. The consistency index (C-index) was used to calculate the model's accuracy. A nomogram was developed to predict the 1, 3, and 5-year survival rates of glioma patients using the model and clinical data. We found differentially expressed genes (DEGs) in different groups (|logFC > 1| and FDR< 0.05) and ran kyoto encyclopedia of genes and genomes (KEGG) and Gene Ontology (GO) enrichment analyses on these DEGs (*P*< 0.05) using clusterProfiler 4.0 (15).

2.3 Evaluation of immune landscape

The number of gene mutations was determined using mutational analysis, and scores for tumor immune dysfunction and exclusion (TIDE) and tumor mutation burden (TMB) were computed to forecast immunotherapy response (16, 17). Additionally, we computed survival variations between various TMB groups and other groups. Immune cell infiltration was calculated using the EPIC, TIMER, MCP-COUNTER, XCELL, QUANTISEQ, CIBERSORT, and CIBERSORT-ABS algorithms (18–24). To evaluate the variations in immune function and look into the expression levels of several immunological checkpoint genes, we used a single-sample gene set enrichment analysis (ssGSEA).

2.4 Identification of anti-tumor drugs

To assess the anti-tumor medications often used in the clinical treatment of glioma, we calculated the half inhibitory concentration (IC50) of pharmaceuticals and compared the IC50 across various groups using the "pRRophetic" R package (10.1371/journal.pone.0107468).

3 Result

3.1 Construction and validation of signature

Differential expression analysis revealed 22 differentially expressed TRGs (Figure 1A), univariate Cox analysis revealed 19 prognostic TRGs ($P< 0.001$; Figure 1B), and multivariate Cox analysis produced a signature with 9 prognostic TRGs (Figure 1C). The findings of the survival analysis ($P< 0.001$; Figure 1D) and the validation set from GSE74187 ($P = 0.011$; Figure 1E) both indicated that the high-risk group had a shorter survival time. The signature was used to forecast glioma patients' 1-, 3-, and 5-year survival rates, with the corresponding AUC values of 0.867, 0.909, and 0.867 (Figure 1F). Compared to other clinical

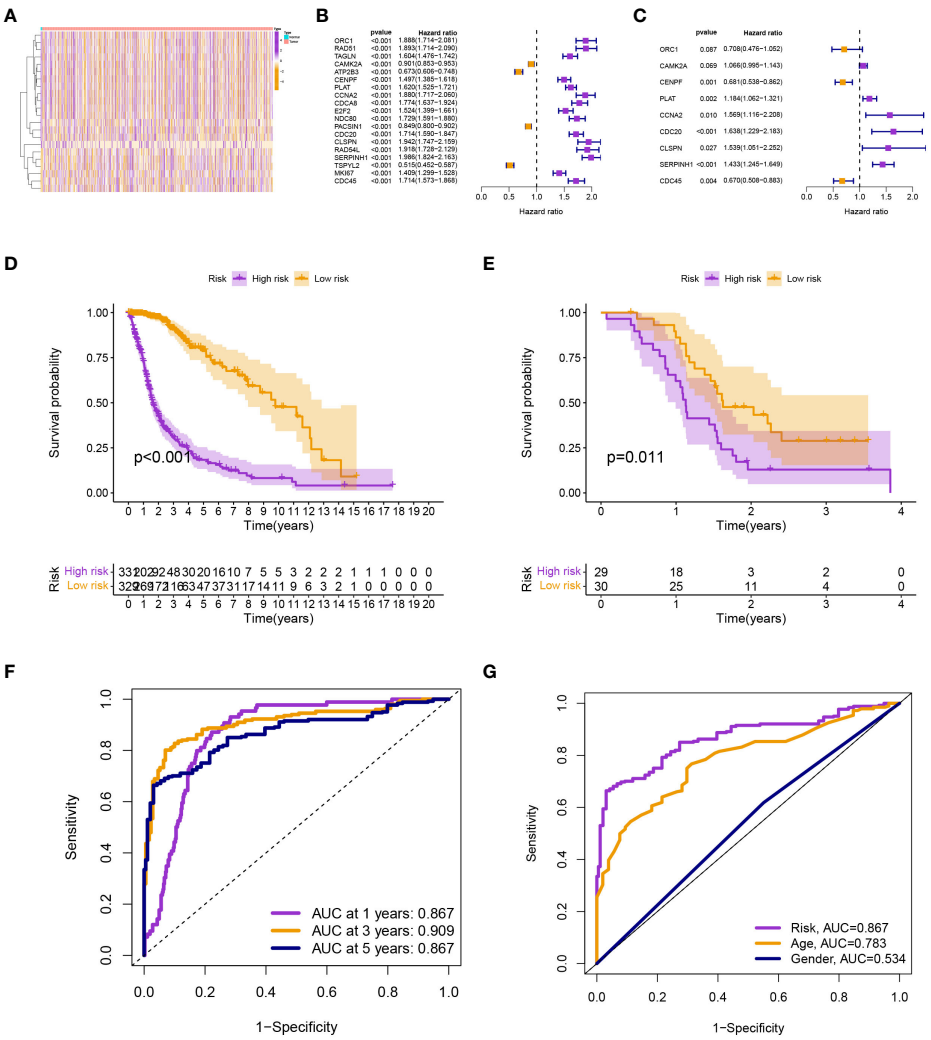

FIGURE 1
(A) Differential expression analysis. **(B)** and **(C)** Univariate and multivariate Cox analyses. **(D)** and **(E)** The survival analysis from TCGA-glioma and GSE74187. **(F)** The AUC values for the model. **(G)** The AUC of the model was also higher than other clinical features.

features, the model's AUC was greater, indicating that it is more trustworthy (Figure 1G).

Patients in the low-risk group had a longer survival time, according to the various clinical subgroups, suggesting that the model is applicable to patients with a range of clinical features (Figure 2A). In both univariate and multivariate Cox analyses, the risk score was shown to be an independent prognostic predictor ($P<$ 0.001; Figures 2B). The C-index showed that the model performed better in predicting the prognosis of glioma than did traditional clinical criteria (Figure 3A). The correlation plot showed that the observed 1, 3, and 5-year survival rates and the anticipated rates agreed strongly (Figure 3B). We developed a nomogram using the signature and clinical characteristics that might be used to precisely forecast the survival of glioma patients (Figure 3C).

3.2 Assessment of immunological landscape

We found 633 DEGs between various risk groups to analyze the various molecular pathways between different groups (Table S2). Figures 4A, B show the results of the GO and KEGG analyses, while Tables S3, S4 give more information. In comparison to the high-risk group, the frequency of gene mutations was much greater in the low-risk group (Figures 5A, B). Lower TIDE scores (P = 0.019; Figure 5C) and higher TMB scores ($P<$ 0.001; Figure 5D) in the high-risk group indicated that they were more likely to respond to immunotherapy. According to survival research, distinct TMB and risk groups had statistically different survival rates, suggesting that integrating TMB scores might improve the ability to predict the prognosis of glioma patients (Figures 5E, F).

The enrichment of CD4+ T cells, CD8+ T cells, fibroblasts, endothelial cells, macrophages M0, M1, and, M2, mast cells, myeloid dendritic cells, and neutrophils was favorably correlated with the risk score, but the enrichment of B cells and NK cells was negatively correlated with the risk score (Figure 6). The various risk groups showed statistically significant differences in all immunological activities (Figure 7A). The expression of several immune checkpoint-related genes, such as CTLA-4 ($P<$ 0.001), PDCD1 ($P<$ 0.001), LAG3 ($P<$ 0.001), and CD274 ($P<$ 0.001), differed significantly across the risk groups (Figure 7B).

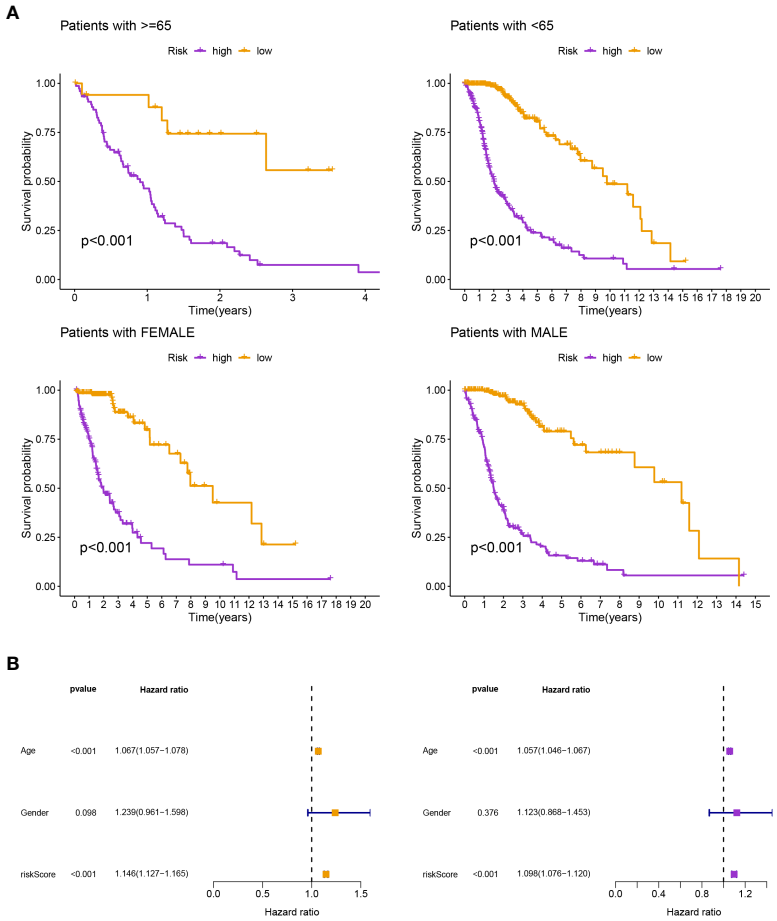

FIGURE 2
(A) According to the various clinical subgroups, patients in the low-risk group had a longer survival time. **(B)** It was discovered that the risk score was a standalone prognostic factor.

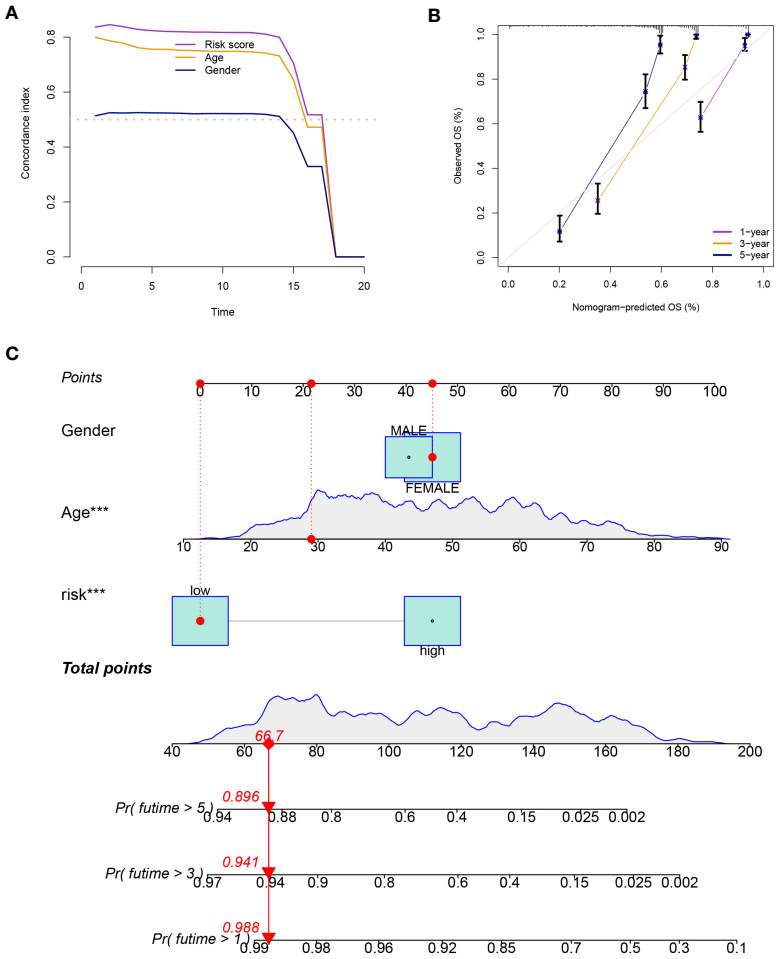

FIGURE 3
(A) The model performed better in predicting the prognosis of glioma than did traditional clinical criteria. **(B)** The observed survival rates demonstrated a strong agreement with the projected rates in the correlation plot. **(C)** A nomogram with signature and clinical characteristics.

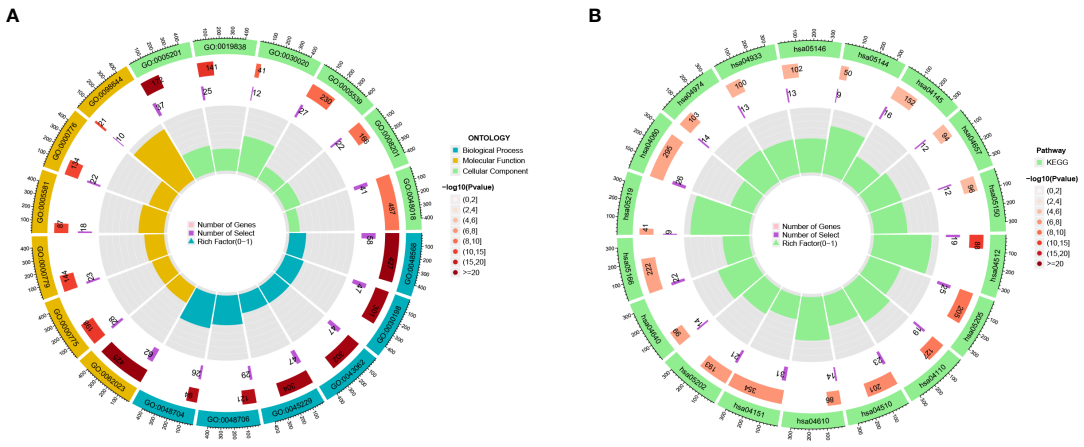

FIGURE 4
(A, B) The GO and KEGG analyses for 633 DEGs.

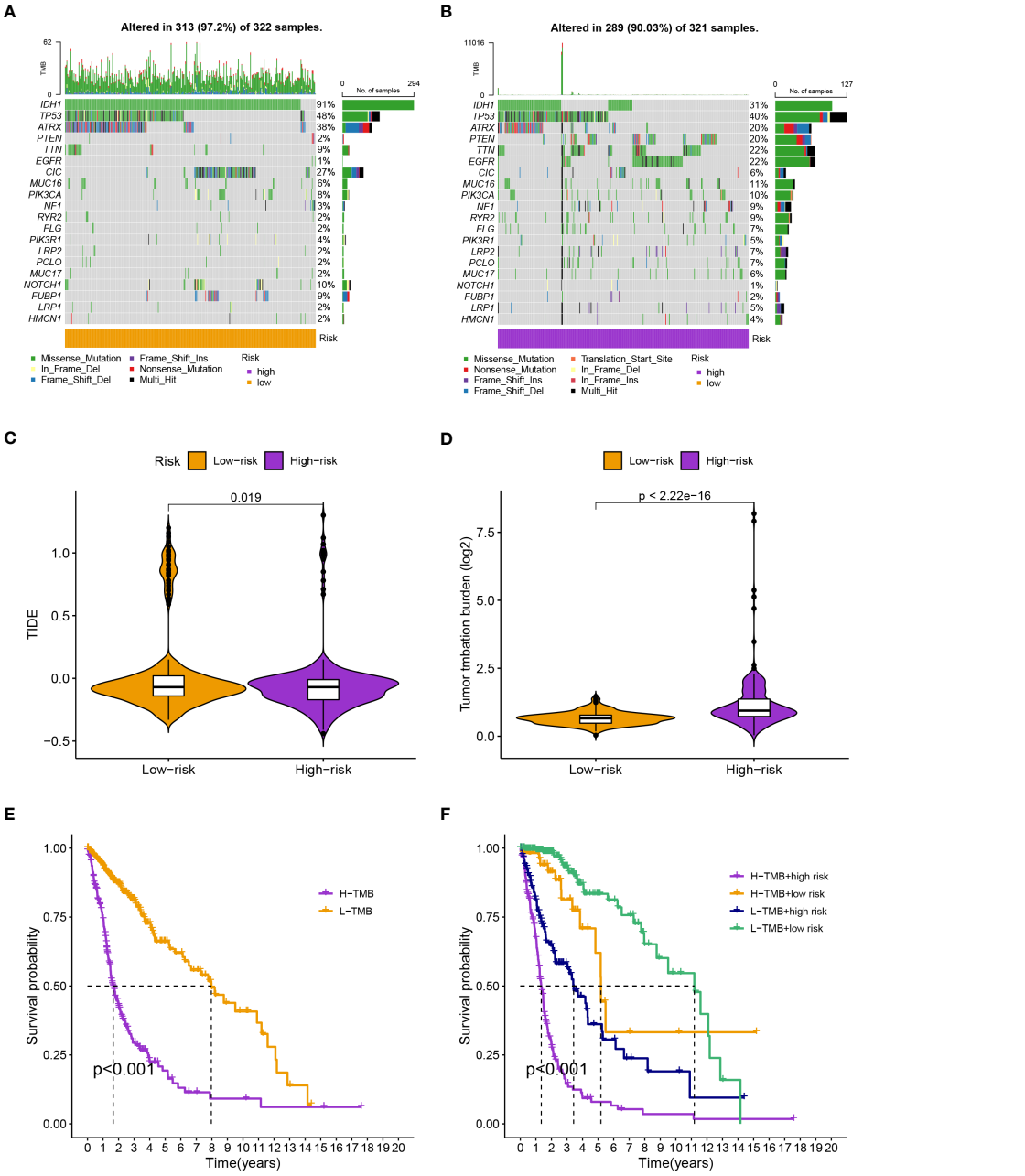

FIGURE 5
(A, B) The specific genes that have been altered differed substantially between groups. **(C)** and **(D)** The high-risk group have a lower TIDE score and a higher TMB score. **(E)** High-TMB groups had considerably reduced survival rates. **(F)** The four groups' survival rates varied greatly from one another.

3.3 Selection of anti-tumor drugs

Along with immunotherapy, we are looking for chemotherapeutic drugs for patients in different risk groups. Finally, in order to create individualized treatment plans for diverse individuals, we searched for numerous chemotherapeutic medications for patients in various groups ($P< 0.001$; Figure 8).

4 Discussion

With a low patient survival rate and a poor clinical prognosis, glioma has a high occurrence (25). The overall survival rate of glioma patients continues to be dismal despite the quick development of surgical resection methods, chemotherapy, and radiation (4). Therefore, to ensure that immunotherapy for glioblastoma is effective, we must discover superior immune checkpoints.

High-throughput sequencing data and computational biology are currently used extensively in the study of biomedicine (26, 27). Wang et al., for instance, identified biomarkers in several tumors using computational biology techniques like WGCNA, which gives us a methodologically sound foundation on which to examine the process of carcinogenesis (28–30). In the research, we first created a risk model linked to TRGs by discovering TRGs. After that, using

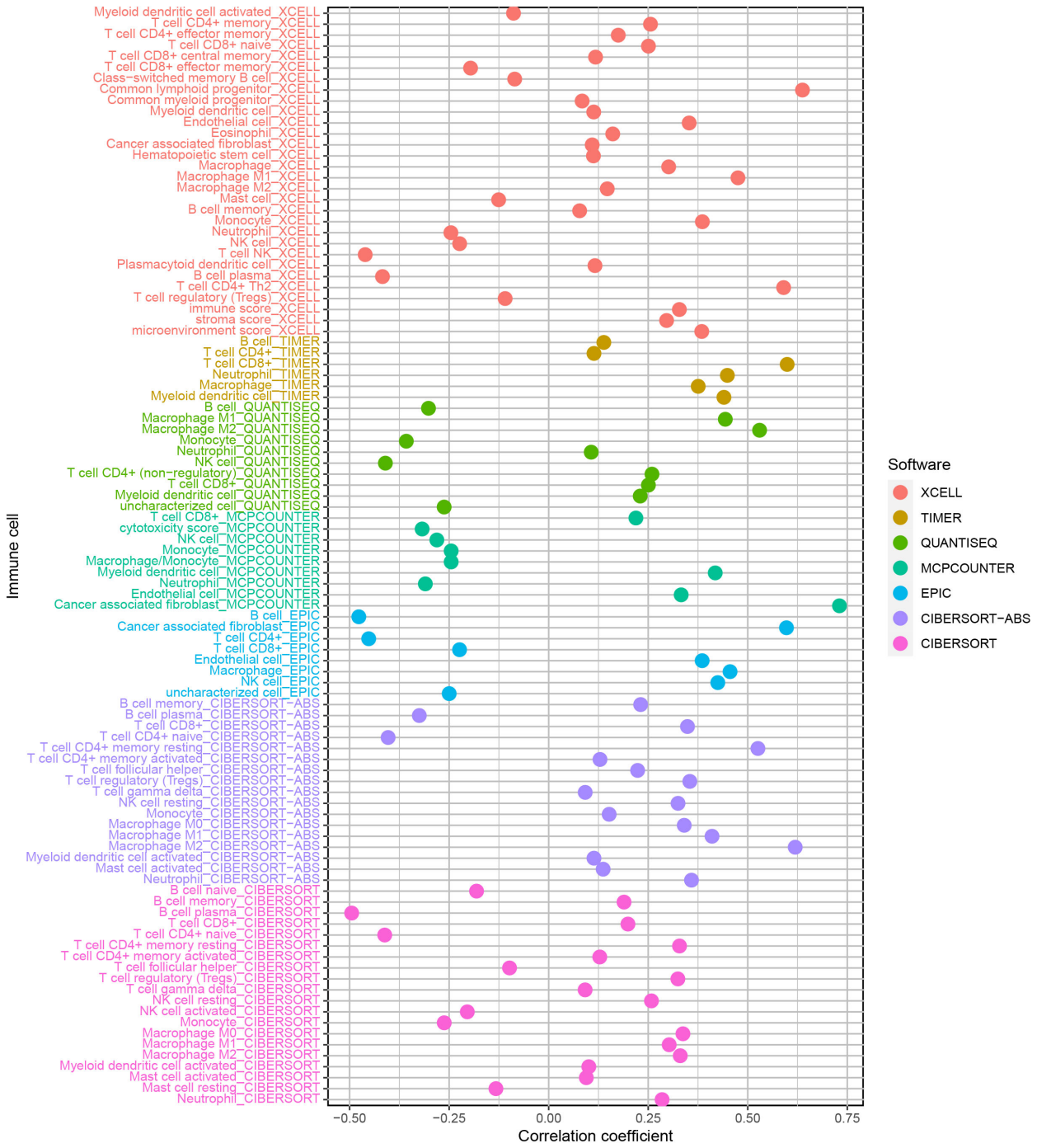

FIGURE 6
The enrichment of CD4+ T cells, CD8+ T cells, fibroblasts, endothelial cells, macrophages M0, M1 and, M2, mast cells, myeloid dendritic cells, and neutrophils was favorably correlated with the risk score, but the enrichment of B cells and NK cells was negatively related to the risk score.

this methodology to determine the risk score for glioma patients, we divided them into low- and high-risk groups. In order to confirm the validity of the model, we did univariate and multivariate Cox analyses on the patients in the high-risk group and discovered that they all had shorter survival rates than those in the low-risk group. As expected, the predictive accuracy of the risk model was high.

Then, we analyzed the immune infiltration in the high-risk and low-risk groups and found that the enrichment of CD4+ T cells, CD8+ T cells, fibroblasts, endothelial cells, macrophages M0, M1 and, M2, mast cells, myeloid dendritic cells, and neutrophils was favorably correlated with the risk score, but the enrichment of B cells and NK cells was negatively related to the risk score. CD8+ T cells are a common type of T cells, and the CD8+ T cell family establishes a neuronal-immune-cancer axis through midkine activation to enhance favorable conditions for the growth of low-grade glioma (31). In addition, in one study performed by Ge. et al,

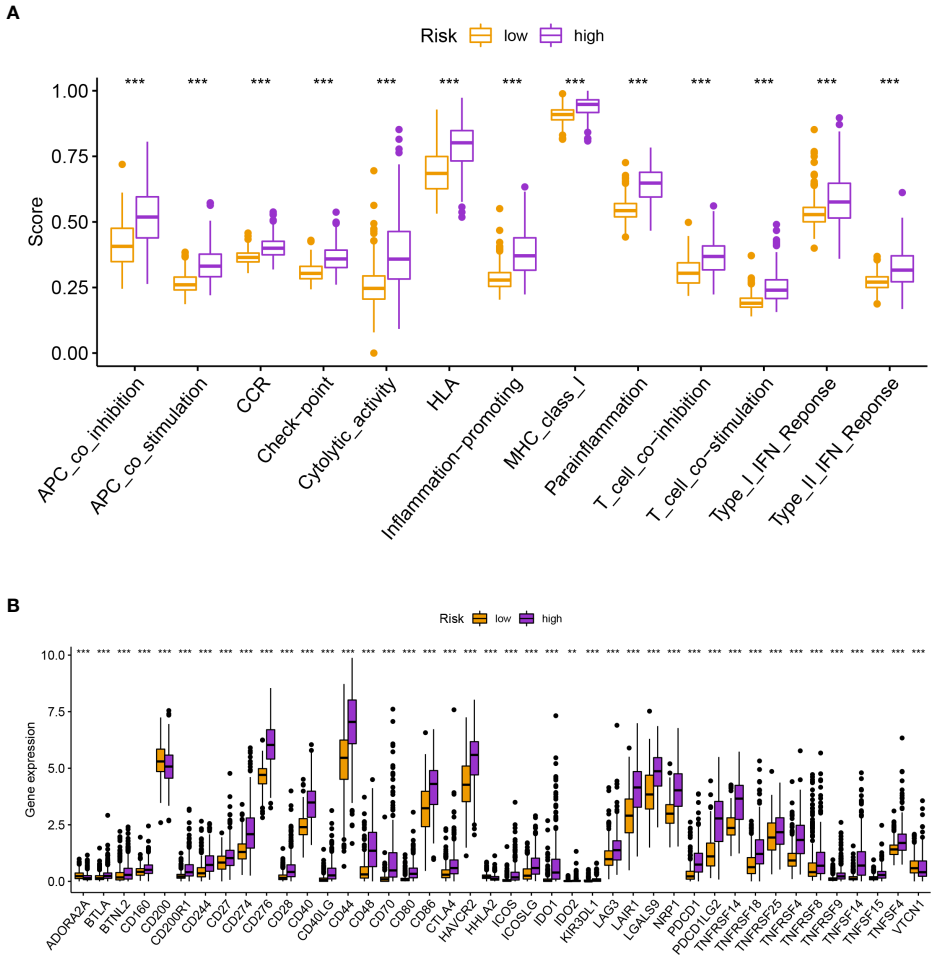

FIGURE 7
(A) The various risk groups showed statistically significant differences in all immunological activities. **(B)** The expression of immune checkpoint-related genes differed significantly across the risk groups. *** means P < 0.001.

related discussions elucidated that macrophages, neutrophils and fibroblasts can be regulated by TP53I13, altering tumor immune infiltration and thus promoting glioma development and metastasis (32). The potential of neutrophils as therapeutic targets in cancer biology has now been extensively studied. Neutrophils play a complex role in cancer, including their ability to exert pro- or anti-tumor activity (33). However, further studies are needed to investigate their exact roles and mechanisms of action to develop targeted therapeutic approaches. Furthermore, although the degree of neutrophil infiltration correlates with glioma grade, the underlying mechanisms are unknown (33).

In addition, in our study, we also found some significant TRGs such as CTLA-4, PDCD1, LAG3, and CD274 (PD-L1). A critical part of the tumor immune response pathway is played by CTLA-4 (34). Although it has been shown that CTLA-4 positively correlates with immune-related proteins in glioma, excessive CTLA-4 expression is associated with a worse prognosis for glioma patients (35). An immunoglobulin superfamily cell surface membrane protein, encoded by the PDCD1 gene, is responsible for programmed cell death. Activated monocytes, NK cells, T cells, and B cells are the main cell types that express it. Additionally, B or T cell receptor signaling can cause PDCD1 expression, and tumor necrosis factor stimulation can further increase it (36). LAG3, an inhibitory receptor that is predominantly located on activated immune cells and is frequently co-expressed with PD-1 on depleted T cells, has emerged as a crucial immunomodulator target (37). CD274 (PD-L1) is considered a major prognostic biomarker for immunotherapy of many cancers. CD274 (PD-L1) is not only associated with decreased cytotoxic T lymphocytes and increased Tregs in glioma lesions, but also has an intrinsic oncogenic effect through interaction with Ras (10.3389/fphar.2018.01503). It has been shown that LAG3 is realized to be highly expressed in glioma patients, but the sample size is small and further experimental validation is needed (38). In addition, in addition to immunotherapy, we have studied a large number of drugs for different groups of patients in order to develop individualized treatment plans.

Although we tried to avoid errors as much as possible to make our experiments credible, there are still some shortcomings that need to be improved. First, due to database limitations, we were unable to accurately compare the corresponding checkpoint inhibitor IC50. In addition, we did not conduct simultaneous *in vitro* experimental

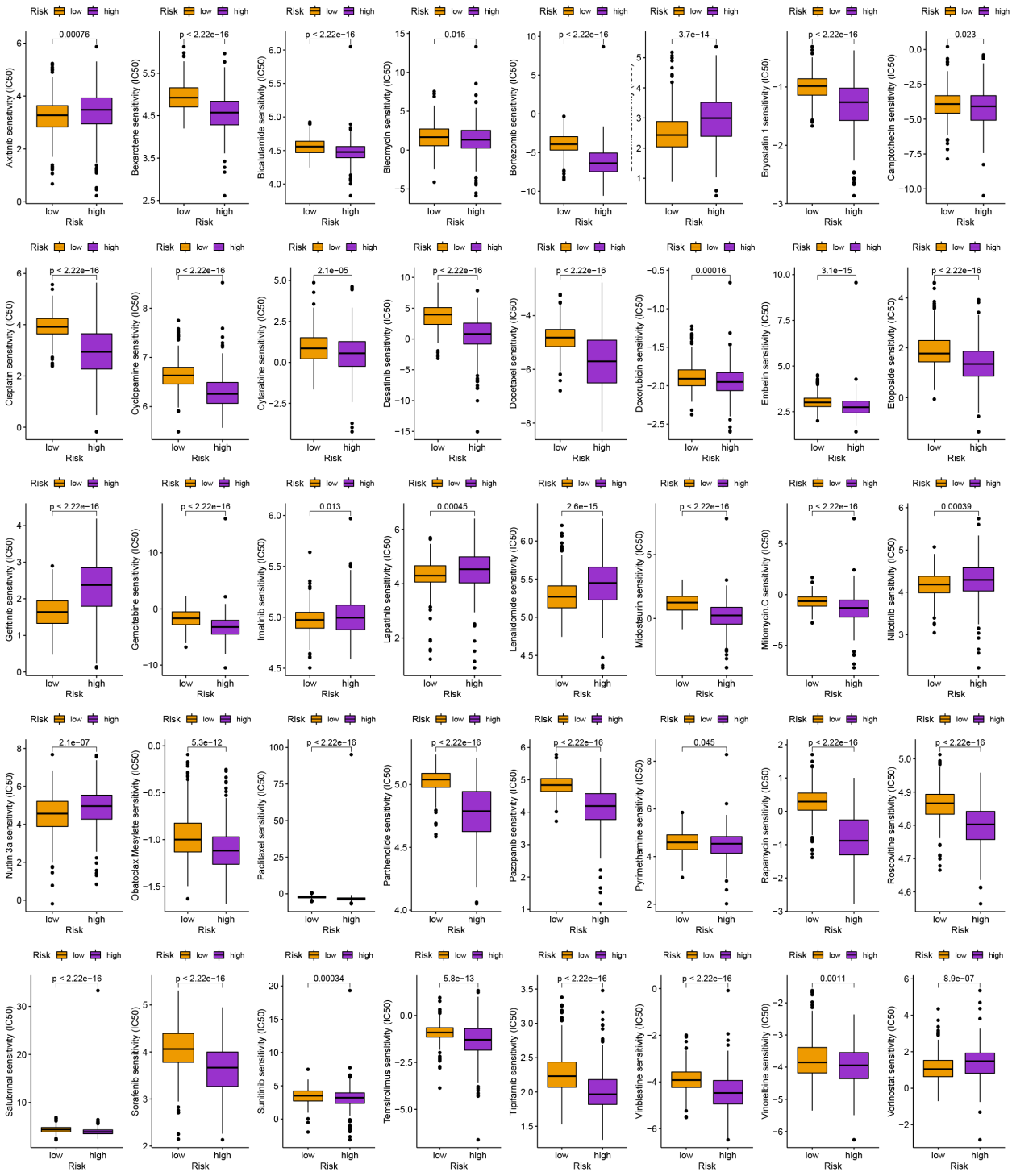

FIGURE 8
Identification of traditional chemotherapy medications.

validation, and further in-depth experiments are needed for this part. We believe that our risk model construction is reasonable and acceptable for further validation in future clinical trials based on the above analysis, validation, and previous relevant reports. Most importantly, the current data is limited and we need to collect more data from the clinic to expand the database for future studies.

Conclusion

The present study support that TRGs could predict the prognosis of glioma patients and help to find effective targets for glioma immunotherapy and can serve as a basis for effective individualized treatment of glioma patients.

Data availability statement

The datasets presented in this study can be found in online repositories. The names of the repository/repositories and accession number(s) can be found in the article/Supplementary Material.

Ethics statement

This study was reviewed and approved by the Ethics Committee of Hangzhou Ninth People's Hospital.

Author contributions

QX and TL designed the study. QX, TL, XZ, YD, and XF performed data analysis. QX and TL drafted and revised the manuscript. All authors read and approved the final manuscript.

Funding

This work was supported by the Health Science and Technology Program of Hangzhou (A20220002) and the Hainan Provincial Natural Science Foundation of China (No. 822RC860).

Conflict of interest

The authors declare that the research was conducted in the absence of any commercial or financial relationships that could be construed as a potential conflict of interest.

Publisher's note

Supplementary material

The Supplementary Material for this article can be found online at: https://www.frontiersin.org/articles/10.3389/fendo.2023.1145722/full#supplementary-material

SUPPLEMENTARY TABLE 1
The TRGs.

SUPPLEMENTARY TABLE 2
The 33 DEGs.

SUPPLEMENTARY TABLE 3
The GO enrichment analysis.

SUPPLEMENTARY TABLE 4
The KEGG enrichment analysis.

References

1. Sung H, Ferlay J, Siegel RL, Laversanne M, Soerjomataram I, Jemal A, et al. Global cancer statistics 2020: GLOBOCAN estimates of incidence and mortality worldwide for 36 cancers in 185 countries. *CA Cancer J Clin* (2021) 71(3):209–49. doi: 10.3322/caac.21660

2. Louis DN, Perry A, Reifenberger G, von Deimling A, Figarella-Branger D, Cavenee WK, et al. The 2016 world health organization classification of tumors of the central nervous system: a summary. *Acta Neuropathol* (2016) 131(6):803–20. doi: 10.1007/s00401-016-1545-1

3. Siegel RL, Miller KD, Fuchs HE, Jemal A. Cancer statistics, 2021. *CA Cancer J Clin* (2021) 71(1):7–33. doi: 10.3322/caac.21654

4. Ghotme KA, Barreto GE, Echeverria V, Gonzalez J, Bustos RH, Sanchez M, et al. Gliomas: new perspectives in diagnosis, treatment and prognosis. *Curr Top Med Chem* (2017) 17(12):1438–47. doi: 10.2174/1568026617666170103162639

5. Tran B, Rosenthal MA. Survival comparison between glioblastoma multiforme and other incurable cancers. *J Clin Neurosci* (2010) 17(4):417–21. doi: 10.1016/j.jocn.2009.09.004

6. Shay JW, Wright WE. Telomeres and telomerase: three decades of progress. *Nat Rev Genet* (2019) 20(5):299–309. doi: 10.1038/s41576-019-0099-1

7. Savage SA. Beginning at the ends: telomeres and human disease. *F1000Res* (2018) 7. doi: 10.12688/f1000research.14068.1

8. Li SC, Jia ZK, Yang JJ, Ning XH. Telomere-related gene risk model for prognosis and drug treatment efficiency prediction in kidney cancer. *Front Immunol* (2022) 13:975057. doi: 10.3389/fimmu.2022.975057

9. Huang P, Li R, Shen L, He W, Chen S, Dong Y, et al. Single nucleotide polymorphisms in telomere length-related genes are associated with hepatocellular carcinoma risk in the Chinese han population. *Ther Adv Med Oncol* (2020) 12:1758835920933029. doi: 10.1177/1758835920933029

10. Saunders CN, Kinnersley B, Culliford R, Cornish AJ, Law PJ, Houlston RS. Relationship between genetically determined telomere length and glioma risk. *Neuro Oncol* (2022) 24(2):171–81. doi: 10.1093/neuonc/noab208

11. Komata T, Kanzawa T, Kondo Y, Kondo S. Telomerase as a therapeutic target for malignant gliomas. *Oncogene* (2002) 21(4):656–63. doi: 10.1038/sj.onc.1205072

12. Yu X, Feng L, Liu D, Zhang L, Wu B, Jiang W, et al. Quantitative proteomics reveals the novel co-expression signatures in early brain development for prognosis of glioblastoma multiforme. *Oncotarget* (2016) 7(12):14161–71. doi: 10.18632/oncotarget.7416

13. Braun DM, Chung I, Kepper N, Deeg KI, Rippe K. TelNet - a database for human and yeast genes involved in telomere maintenance. *BMC Genet* (2018) 19(1):32. doi: 10.1186/s12863-018-0617-8

14. Ritchie ME, Phipson B, Wu D, Hu Y, Law CW, Shi W, et al. Limma powers differential expression analyses for RNA-sequencing and microarray studies. *Nucleic Acids Res* (2015) 43(7):e47. doi: 10.1093/nar/gkv007

15. Wu T, Hu E, Xu S, Chen M, Guo P, Dai Z, et al. clusterProfiler 4.0: a universal enrichment tool for interpreting omics data. *Innovation (Camb)* (2021) 2(3):100141. doi: 10.1016/j.xinn.2021.100141

16. Fu J, Li K, Zhang W, Wan C, Zhang J, Jiang P, et al. Large-Scale public data reuse to model immunotherapy response and resistance. *Genome Med* (2020) 12(1):21. doi: 10.1186/s13073-020-0721-z

17. Krøigård AB, Thomassen M, Lænkholm AV, Kruse TA, Larsen MJ. Evaluation of nine somatic variant callers for detection of somatic mutations in exome and targeted deep sequencing data. *PloS One* (2016) 11(3):e0151664. doi: 10.1371/journal.pone.0151664

18. Newman AM, Liu CL, Green MR, Gentles AJ, Feng W, Xu Y, et al. Robust enumeration of cell subsets from tissue expression profiles. *Nat Methods* (2015) 12(5):453–7. doi: 10.1038/nmeth.3337

19. Li T, Fan J, Wang B, Traugh N, Chen Q, Liu JS, et al. TIMER: a web server for comprehensive analysis of tumor-infiltrating immune cells. *Cancer Res* (2017) 77(21):e108–e10. doi: 10.1158/0008-5472.Can-17-0307

20. Dienstmann R, Villacampa G, Sveen A, Mason MJ, Niedzwiecki D, Nesbakken A, et al. Relative contribution of clinicopathological variables, genomic markers,

transcriptomic subtyping and microenvironment features for outcome prediction in stage II/III colorectal cancer. *Ann Oncol* (2019) 30(10):1622–29. doi: 10.1093/annonc/mdz287

21. Aran D, Hu Z, Butte AJ. xCell: digitally portraying the tissue cellular heterogeneity landscape. *Genome Biol* (2017) 18(1):220. doi: 10.1186/s13059-017-1349-1

22. Finotello F, Mayer C, Plattner C, Laschober G, Rieder D, Hackl H, et al. Molecular and pharmacological modulators of the tumor immune contexture revealed by deconvolution of RNA-seq data. *Genome Med* (2019) 11(1):34. doi: 10.1186/s13073-019-0638-6

23. Tamminga M, Hiltermann TJN, Schuuring E, Timens W, Fehrmann RS, Groen HJ. Immune microenvironment composition in non-small cell lung cancer and its association with survival. *Clin Transl Immunol* (2020) 9(6):e1142. doi: 10.1002/cti2.1142

24. Racle J, de Jonge K, Baumgaertner P, Speiser DE, Gfeller D. Simultaneous enumeration of cancer and immune cell types from bulk tumor gene expression data. *Elife* (2017) 6. doi: 10.7554/eLife.26476

25. Xu S, Tang L, Li X, Fan F, Liu Z. Immunotherapy for glioma: current management and future application. *Cancer Lett* (2020) 476:1–12. doi: 10.1016/j.canlet.2020.02.002

26. Zhao Z, Zhang D, Yang F, Xu M, Zhao S, Pan T, et al. Evolutionarily conservative and non-conservative regulatory networks during primate interneuron development revealed by single-cell RNA and ATAC sequencing. *Cell Res* (2022) 32 (5):425–36. doi: 10.1038/s41422-022-00635-9

27. Xu D, Zhi Y, Liu X, Guan L, Yu J, Zhang D, et al. WDR62-deficiency causes autism-like behaviors independent of microcephaly in mice. *Neurosci Bull* (2022). doi: 10.1007/s12264-022-00997-5

28. Wang Y, Yan K, Wang J, Lin J, Bi J. M2 macrophage Co-expression factors correlate with immune phenotype and predict prognosis of bladder cancer. *Front Oncol* (2021) 11:609334. doi: 10.3389/fonc.2021.609334

29. Wang Y, Yan K, Lin J, Li J, Bi J. Macrophage M2 Co-expression factors correlate with the immune microenvironment and predict outcome of renal clear cell carcinoma. *Front Genet* (2021) 12:615655. doi: 10.3389/fgene.2021.615655

30. Wang Y, Yan K, Wang L, Bi J. Genome instability-related long non-coding RNA in clear renal cell carcinoma determined using computational biology. *BMC Cancer* (2021) 21(1):727. doi: 10.1186/s12885-021-08356-9

31. Guo X, Pan Y, Xiong M, Sanapala S, Anastasaki C, Cobb O, et al. Midkine activation of CD8(+) T cells establishes a neuron-immune-cancer axis responsible for low-grade glioma growth. *Nat Commun* (2020) 11(1):2177. doi: 10.1038/s41467-020-15770-3

32. Ge X, Xu M, Cheng T, Hu N, Sun P, Lu B, et al. TP53I13 promotes metastasis in glioma via macrophages, neutrophils, and fibroblasts and is a potential prognostic biomarker. *Front Immunol* (2022) 13:974346. doi: 10.3389/fimmu.2022.974346

33. Lin YJ, Wei KC, Chen PY, Lim M, Hwang TL. Roles of neutrophils in glioma and brain metastases. *Front Immunol* (2021) 12:701383. doi: 10.3389/fimmu.2021.701383

34. Huang J, Liu F, Liu Z, Tang H, Wu H, Gong Q, et al. Immune checkpoint in glioblastoma: promising and challenging. *Front Pharmacol* (2017) 8:242. doi: 10.3389/fphar.2017.00242

35. Liu F, Huang J, Liu X, Cheng Q, Luo C, Liu Z. CTLA-4 correlates with immune and clinical characteristics of glioma. *Cancer Cell Int* (2020) 20:7. doi: 10.1186/s12935-019-1085-6

36. Miao Y, Wang J, Li Q, Quan W, Wang Y, Li C, et al. Prognostic value and immunological role of PDCD1 gene in pan-cancer. *Int Immunopharmacol* (2020) 89(Pt B):107080. doi: 10.1016/j.intimp.2020.107080

37. Puhr HC, Ilhan-Mutlu A. New emerging targets in cancer immunotherapy: the role of LAG3. *ESMO Open* (2019) 4(2):e000482. doi: 10.1136/esmoopen-2018-000482

38. Mair MJ, Kiesel B, Feldmann K, Widhalm G, Dieckmann K, Wöhrer A, et al. LAG-3 expression in the inflammatory microenvironment of glioma. *J Neurooncol* (2021) 152(3):533–39. doi: 10.1007/s11060-021-03721-x

frontiers | Frontiers in Endocrinology

TYPE Original Research
PUBLISHED 03 July 2023
DOI 10.3389/fendo.2023.1153802

OPEN ACCESS

EDITED BY
Ruiqin Han,
Chinese Academy of Medical Sciences, China

REVIEWED BY
Wencai Liu,
The First Affiliated Hospital of Nanchang University, China
Wenhui Chen,
First Affiliated Hospital of Jinan University, China
Jinxiang Wang,
Sun Yat-sen University, China
Xiaozhu Liu,
Second Affiliated Hospital of Chongqing Medical University, China

*CORRESPONDENCE
Yewei Zhang
zhangyewei@njmu.edu.cn

†These authors have contributed equally to this work

RECEIVED 30 January 2023
ACCEPTED 02 May 2023
PUBLISHED 03 July 2023

CITATION
Shi Y, Wang Y, Zhang W, Niu K, Mao X, Feng K and Zhang Y (2023) N6-methyladenosine with immune infiltration and PD-L1 in hepatocellular carcinoma: novel perspective to personalized diagnosis and treatment.
Front. Endocrinol. 14:1153802.
doi: 10.3389/fendo.2023.1153802

N6-methyladenosine with immune infiltration and PD-L1 in hepatocellular carcinoma: novel perspective to personalized diagnosis and treatment

Yanlong Shi†, Yizhu Wang†, Wenning Zhang†, Kaiyi Niu†, Xinyu Mao, Kun Feng and Yewei Zhang*

Hepatopancreatobiliary Center, The Second Affiliated Hospital of Nanjing Medical University, Nanjing, Jiangsu, China

Background: Increasing evidence elucidated N6-methyladenosine (m6A) dysregulation participated in regulating RNA maturation, stability, and translation. This study aimed to demystify the crosstalk between m6A regulators and the immune microenvironment, providing a potential therapeutic target for patients with hepatocellular carcinoma (HCC).

Methods: Totals of 371 HCC and 50 normal patients were included in this study. GSE121248 and GSE40367 datasets were used to validate the expression of HNRNPC. The R package "ConsensusClusterPlus" was performed to screen consensus clustering types based on the expression of m6A regulators in HCC. The R package "pheatmap", "immunedeconv", "survival", "survminer" and "RMS" were applied to investigate the expression, immunity, overall survival, and clinical application in different clusters and expression groups. Comprehensive analysis of HNRNPC in pan-cancer was conducted by TIMER2 database. Besides, HNRNPC mRNA and protein expression were verified by qRT-PCR and immunohistochemistry analysis.

Results: Most of m6A regulators were over-expressed excerpt for ZC3H13 in HCC. Three independent clusters were screened based on m6A regulators expression, and the cluster 2 had a favorable prognosis in HCC. Then, the cluster 2 was positively expression in macrophage, hematopoietic stem cell, endothelial cell, and stroma score, while negatively in T cell $CD4^+$ memory and mast cell. We identified HNRNPC was an independent prognostic factor in HCC, and nomogram performed superior application value for clinical decision making. Moreover, PD-L1 was significantly up-regulated in HCC tissues, cluster 1, and cluster 3, and we found PD-L1 expression was positively correlated with HNRNPC. Patients with HCC in high-expression groups was associated with tumor-promoting cells. Besides, HNRNPC was correlated with prognosis, TMB, and immune checkpoints in cancers. Particularly, the experiments confirmed that HNRNPC was positively expression in HCC cells and tissues.

Conclusion: The m6A regulators play irreplaceable roles in prognosis and immune infiltration in HCC, and the relationship of HNRNPC and PD-L1 possesses a promising direction for therapeutic targets of immunotherapy response. Exploration of m6A regulators pattern could be build the prognostic stratification of individual patients and move toward to personalized treatment.

KEYWORDS

N6-methyladenosine, hnRNPC, PD-L1, hepatocellular carcinoma, prognosis, immune infiltration, immunotherapy

Introduction

Liver cancer is the sixth most common cancer in humans and the fourth leading cause of cancer-related death worldwide (1). Hepatocellular carcinoma (HCC) is characterized by rapid progression and poor prognosis, accounting for 90% of primary liver cancer (2). HCC can be attributed to adverse factors, mainly including hepatitis B virus, alcohol, and aflatoxin (3). Moreover, most HCC patients suffer from recurrence and metastasis due to tumor heterogeneity, resulting in a poor prognosis (4). Immunotherapy, a promising therapeutic strategy, refers to artificially enhancing or inhibiting body's immune function to treat diseases (5). Although immunotherapy has fewer toxic side effects than chemotherapy, the blocking of the immune checkpoints by immune microenvironment is still the leading cause of poor prognosis in HCC patients (6). Furthermore, the expression of PD-L1 is regulated by adverse of factors, resulting in different meanings of PD-L1 positivity1. Hence, it is essential to further understand the molecular mechanisms of immunotherapy of HCC and improve the therapeutic effect.

N6-methyladenosine (m6A) modification, the most abundant internal modification of RNA in eukaryotic cells, is attracting wide attention from researchers (7). m6A methylation is regulated by regulatory factors: writer, reader and eraser, which contribute to physiological and pathological occurrence (8). It affects almost every aspect of RNA metabolism, playing a crucial role in regulating RNA maturation, stability, and translation (9). It was reported that IGF2BP1, a crucial m6A-dependent manner, might be a novel drug candidate for cancer therapeutics by modulating tumor immune microenvironment in m6A regulation (10). Increasing evidence reported that m6A dysregulation participated in various cancers, including HCC (11, 12). For example, methyltransferase-like 3 (*METTL3*), the critical component of m6A RNA methyltransferase, was obviously up-regulated in HCC, and knockdown of *METTL3* could weaken lung metastasis (11). Moreover, an important study elaborated on the vital role of m6A in both primitive and adaptive immune responses, suggesting the potential role of m6A in tumor immunity (13). The combination of m6A regulators and programmed cell death protein 1 (*PD-1)* inhibitors was required to maintain of cell and tissue homeostasis, and had a synergistic effect to enhance the efficacy of cancer immunotherapy (14). Although progress has been made in the modification of m6A in HCC, its mechanism in tumor immunotherapy remains unclear. Therefore, demystifying the crosstalk between m6A regulators and the immune microenvironment could be a potential therapeutic target for HCC patients.

In this study, we comprehensively assessed the roles of m6A regulators based on molecular subtypes in HCC, and identified and validated a key m6A regulator *HNRNPC* in different datasets and basic experiments. Moreover, we systematically undertook the relationship of *HNRNPC* and *PD-L1* in expression, prognosis, and immune microenvironment.

Abbreviations: COAD, Colon Adenocarcinoma; DFS, Disease free survival; HCC, Hepatocellular carcinoma; LGG, Lower Grade Glioma; LUSC, Lung Squamous Cell Carcinoma; m6A, N6-methyladenosine; OS, Overall survival; PCPG, Pheochromocytoma and Paraganglioma; PFS, Progression free survival; READ, Rectum Adenocarcinoma; STAD, Stomach Adenocarcinoma; SKCM, Skin Cutaneous Melanoma; TCGA, The Cancer Genome Atlas; THCA, Thyroid Carcinoma; THYM, Thymoma; Tregs, T cell regulatory; UCEC, Uterine Corpus Endometrial Carcinoma.

Materials and methods

Data acquisition

The RNA-seq data and relevant information were obtained from The Cancer Genome Atlas (TCGA) database (https://portal.gdc.cancer.gov/), with 371 HCC and 50 normal tissues. Pan-cancer analysis included totals of 33 types tumors and adjacent normal tissues in TIMER2 database. GSE121248 and GSE40367 datasets were used to validate the expression of HNRNPC (https://www.ncbi.nlm.nih.gov/geo/) (15, 16).

Analysis and evaluation of m6A regulators consensus clustering

The R package "ConsensusClusterPlus" was used for consensus analysis for HCC, and the parameter was set as clusterAlg = "hc", innerLinkage='ward.D2' (17). The cluster heatmap was analyzed by R package "pheatmap". The gene expression heatmap retained genes with variance above 0.1. In correlation analysis, the circles represent genes related to m6A, the lines represent the interrelationships between genes, and the different colors of the

circles represent different clustering categories. Among them, red and blue represent positive and negative correlation respectively. The prognosis of various clusters was determined by Kaplan-Meier survival curve in HCC, following HR with 95% confidence interval. The R package "immunedeconv" was applied to immune infiltration cells and score between cluster 1 and cluster 2 (18). Then, we extracted the expression values of immune checkpoint-related genes from RNA-seq data to observe the expression of immune checkpoint-related genes in different clusters.

Identification, validation, development of key m6A regulators

The key m6A regulator was identified by Venn diagram. The boxplot of gene expression was plotted using R package "Boxplot". The R package "survival" and "survminer" was performed to compare the survival differences between the two or more groups, and the timeROC analysis was used to compare the prediction accuracy. The Kaplan-Meier plot database was conducted to investigate overall survival (OS), progression free survival (PFS), and disease free survival (DFS) in HCC. The univariate and multivariate cox regression estimated the independent prognostic value, then presented it by R package "forestplot". Based on the results of multivariate Cox regression, the R package "RMS" developed the nomogram to predict survival probability. The proportion of immune infiltration cells was calculated by CIBERSORT algorithm.

Cell culture

The hepatic normal cell (LO2) and HCC cell line (HepG2) were donated from School of Basic Medicine, Anhui Medical University. All cells were cultured with DMEM containing 10% fetal bovine serum (VivaCell, Shanghai, China), and culture conditions were as follows: 5% CO_2, 37°C.

Quantitative real-time polymerase chain reaction

Experimental procedures were performed as in previous studies (19). The SYBR Green qPCR Mix (Takara) was used to quantitative *HNRNPC* expression in different groups compared to *GADPH* expression. The results were calculated as $2^{-\Delta\Delta Ct}$ method. All primer sequences were as follows: *HNRNPC*:5'-aattgtgggctgctctgttc-3'; 3'-aacctggccagcaatcattc-5', *GADPH*: 5'-CTCACCGGATGCACCAATGTT-3'; 3'-CGCGTTGCTCACAATGTTCAT-5'.

Analysis of immunohistochemistry

The detailed procedure of Immunohistochemistry in a previous study has been described (20). *HNRNPC* protein expression was detected by immunohistochemistry in normal and HCC tissues. In the HPA database, we detected the image of *HNRNPC* expression in "tissue" and "pathology" modules (21). All results were re-judged by two pathologists. Regents as follows: *HNRNPC*: Atlas Antibodies Cat#AMAb91010, RRID : AB_2665761, dilution 1:1500.

Statistical analysis

The version 3.8.1 was used for all R packages. The Spearman analysis was applied to the correlation among m6A regulators. The significance of two groups was determined by the Wilcox test, and the significance of three groups or more was determined by the Kruskal-Wallis test. The log rank test was used for survival differences. The expression of *HNRNPC* was analyzed by Student's t-test in tissues and cell lines. $P<0.05$ was defined as a statistical difference.

Results

Differences in the expression of m6A regulators between HCC and normal tissues

Totals of 20 m6A regulators across 33 cancer types were obtained from previous study (17) (Supplement Table 1). To understand the role of m6A regulators in HCC, we investigated the expression of m6A regulators between 371 HCC and 50 normal tissues in the TCGA database. It was found that the majority of m6A regulators was up-regulated in HCC except *ZC3H13*, including *METTL3*, *METTL4*, *WTAP*, *VIRMA*, *RMB15B*, *YTHDC1*, *YTHDC2*, *YTHDF3*, *YTHDF1*, *YTDHF2*, *HNRNPC*, *IGF2BP1*, *IGF2BP2*, *IGF2BP3*, *RBMX*, *HNRNPA2B1*, *FTO*, and *ALKBHS* (Figures 1A, B). A correlation analysis indicated a positive correlation among writers, readers, and erasers of m6A (Figure 1C). These findings suggest that m6A regulators might act as a vital role in mediating the development and progression of HCC.

Identification and evaluation of HCC subtypes based on m6A regulators

Based on the expression of m6A regulators, we applied to consensus clustering analysis in HCC. In Figure 2A, the optimal matrix value shows a good distribution in different parts. From the relative change in area under cumulative distribution function curves, the delta area of 3~4 was steepest from k=2 to 6 (Figure 2B). Therefore, the k value of 3 was conducted to follow-up analysis. The baseline characteristics of the three clusters and associations are presented in Table 1. Then, the expression difference in three clusters was shown by heatmap analysis. We found that the cluster 1 and cluster 3 were up-regulated in m6A regulators of HCC, but down-regulated in cluster 2 (Figure 2C).

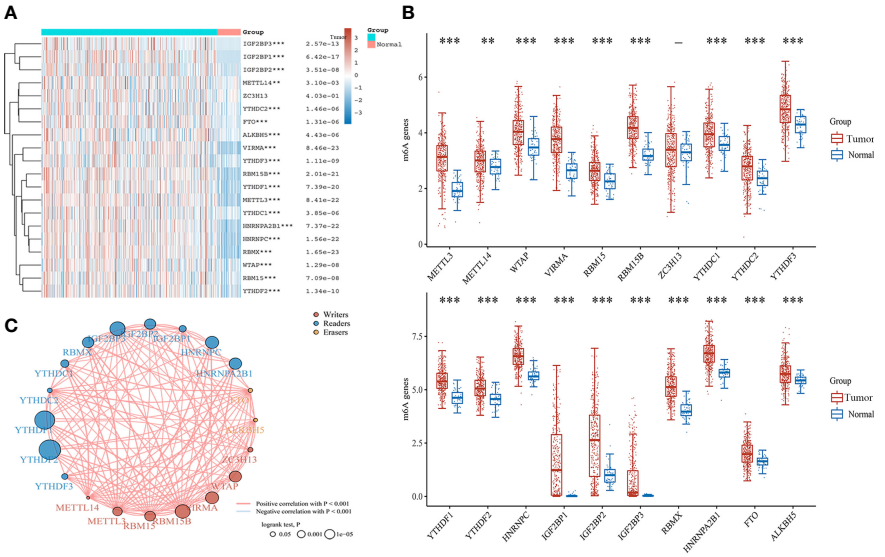

FIGURE 1
The expression and correlation of m6A regulators in HCC. **(A)** Heatmap of m6A regulators between HCC and normal tissues. **(B)** The expression of m6A regulators in HCC and normal tissues by Box plot analysis. **(C)** The correlation of m6A regulators in HCC by Spearman analysis. ***P*<0.01, ****P*<0.001.

Moreover, Kaplan–Meier curves suggested that patients with cluster 2 had favorable overall survival ($P < 0.05$) (Figure 2D), progression-free survival ($P < 0.05$) (Figure 2E), and disease free survival ($P < 0.05$) (Figure 2F) than cluster 1 and cluster 3. These results revealed an obvious distinction among cluster 1, cluster 2, and cluster 3 of patients with HCC.

Relationship of m6A subtypes with immune microenvironment and PD-L1 expression in HCC

To determine the association between cluster subtypes and immune microenvironment, we first explored the difference in

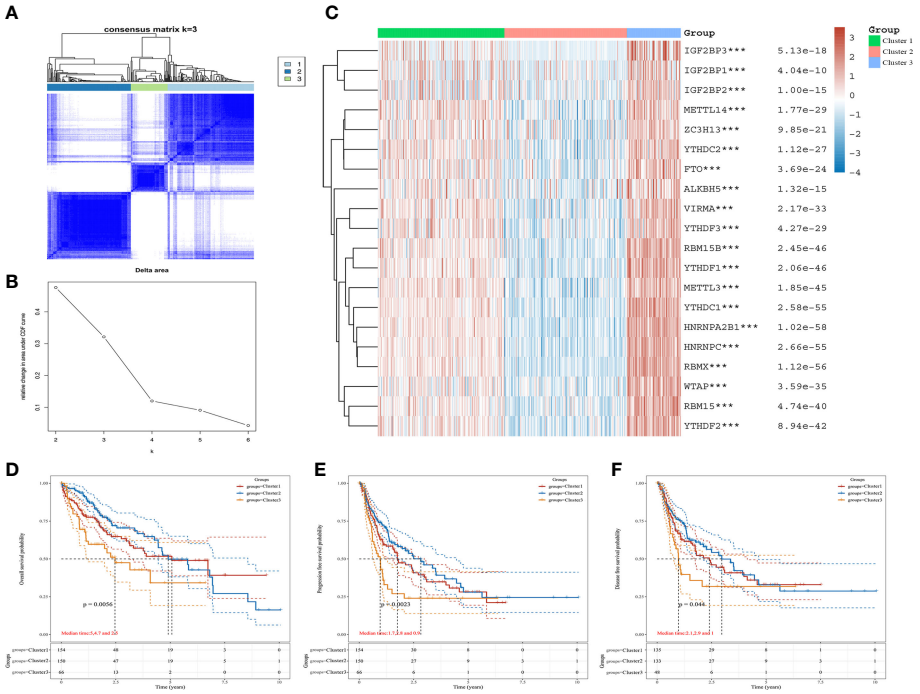

FIGURE 2
The expression and prognosis of m6A regulators of HCC in different clusters. **(A)** The optimal consensus clustering matrix k=3. **(B)** The relative change in area under cumulative distribution function curves. **(C)** The expression of m6A regulators in three clusters of HCC by heatmap. **(D–F)** The prognostic value for three clusters of HCC patients by Kaplan–Meier curves. **(D)** Overall survival. **(E)** Disease-free survival. **(F)** Progression free survival. ****P*<0.001.

TABLE 1 Clinical characteristics of three clusters of patients with HCC.

Characteristics		Cluster 1 (n=155)	Cluster 2 (n=150)	Cluster 3 (n=66)	*P*_value
Status	Alive	101 (65.2%)	103	37	0.201
	Dead	54 (34.8%)	47	29	
Age	Mean (SD)	61.3 (12.6)	59.8 (13.3)	54.2 (14.9)	0.004
Gender	FEMALE	52	44	25	0.443
	MALE	103	106	41	
Race	AMERICAN INDIAN	1	1		0.266
	ASIAN	66	60	32	
	BLACK	11	3	3	
	WHITE	75	78	31	
	Not known	2	8		
Grade	G1	23	28	4	0.006
	G2	73	80	24	
	G3	51	38	33	
	G4	4	4	4	
	Not known	4		1	
T stage	T1	80	82	19	0.056
	T2	37	36	21	
	T3	16	13	16	
	T3a	12	11	6	
	T3b	3	2	1	
	T4	6	5	3	
	Not known	1	1		
N stage	N0	108	97	47	0.288
	N1	1	1	2	
	NX	46	52	16	
	Not known			1	
M stage	M0	111	108	47	0.936
	MX	44	39	18	
	M1		3	1	
pTNM_stage	I	73	79	19	0.028
	II	34	35	17	
	IIIA	27	20	18	
	IIIB	5	2	1	
	IIIC	3	2	4	
	III		1	2	
	IV		4	1	
	Not known	13	7	4	

immune cell infiltration levels in three clusters using by XCELL algorithm. The cluster 2 was positively expressed in macrophage, hematopoietic stem cell, endothelial cell, microenvironment score, and stroma score, while negative in T cell CD4+ memory and mast cell (Figure 3A). The three clusters were lower expression in B cell naive. The corresponding proportion of immune infiltration cells is presented in Figure 3B. Then, the connection of immune checkpoints and cluster subtypes was assessed by heatmap of gene expression in HCC, and the results showed a significant difference in the expression of immune checkpoints and cluster subtypes (Figure 3C). Then, we selected *PD-L1* for further study. Compared with normal tissues and cluster 2, the expression of *PD-L1* was significantly up-regulated in HCC tissues and the other two clusters (Figures 3D, E). Moreover,we further analyzed the correlation between m6A regulators and *PD-L1* expression. *PD-L1* expression was positively correlated with m6A regulators, mainly including *FTO*, *HNRNPA2B1*, *HNRNPC*, *RBM15*, *WTAP*, *YTHDC1*, and *YTHDF2*, while negatively in *IGF2BP1* (Figure 3F).

The m6A regulator *HNRNPC* was over-expressed in HCC

To further investigate the potential effects of m6A regulators in HCC, we conducted an intersection analysis to screen key m6A regulators among up-regulated expression of HCC, positively correlated with the expression of *PD-L1*, and associated with worse prognosis. We identified 11 relevant genes (Figure 4A). However, only *HNRNPC* expression was correlated with tumor stages (Figure 4B). These results indicated that *HNRNPC* might play a vital role in HCC progression and metastasis. In Figure 4C, we first validated the expression of *HNRNPC* between HCC and normal tissues in GSE121248 database. The result showed *HNRNPC* expression was over-expressed in HCC. Subsequently, compared with hepatic hemangioma tissues, *HNRNPC* expression was also significantly increased in HCC with metastasis tissues, and metastatic HCC tissues respectively based on GSE40367 database (Figures 4D, E). Moreover, our experiment demonstrated the expression of *HNRNPC* was up-regulated in HCC cell lines by qRT-PCR analysis (Figure 4F). Notably, the protein expression of *HNRNPC* was detected by HPA database. *HNRNPC* protein was positively expressed in HCC tissues compared to normal tissues, and was mainly located in nuclear (Figure 4G).

HNRNPC independent prognostic value in HCC

The Kaplan-Meier plotter showed the low expression group had a better prognosis (Figure 5A). In Figure 5B, HCC patients in low expression group had a longer survival than high expression group. Then we further explored the relationship between *HNRNPC* expression and overall survival. Subsequently, the AUC values of *HNRNPC* expression in 1-, 3-, and 5-year were 0.676, 0.613, and

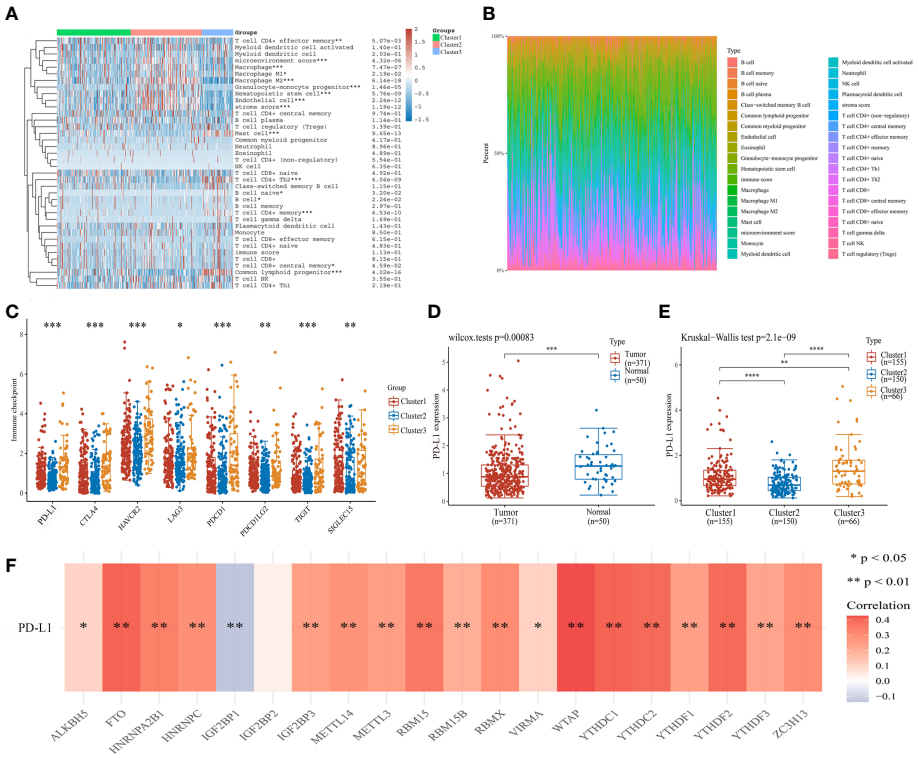

FIGURE 3
Association of cluster subtypes with immune microenvironment and *PD-L1* expression in HCC. **(A)** The relationship between m6A subtypes and immune cell infiltration level in HCC by heatmap analysis. **(B)** Proportion of immune infiltration cells in different cluster groups. **(C)** The relationship between cluster subtypes and immune checkpoint expression in HCC. **(D)** *PD-L1* expression in HCC and normal tissues. **(E)** The difference of *PD-L1* expression in cluster 1, cluster 2, and cluster 3. **(F)** The correlation of m6A regulators and *PD-L1* expression. **P*<0.05, ***P*<0.01, ****P*<0.001, and *****P*<0.0001.

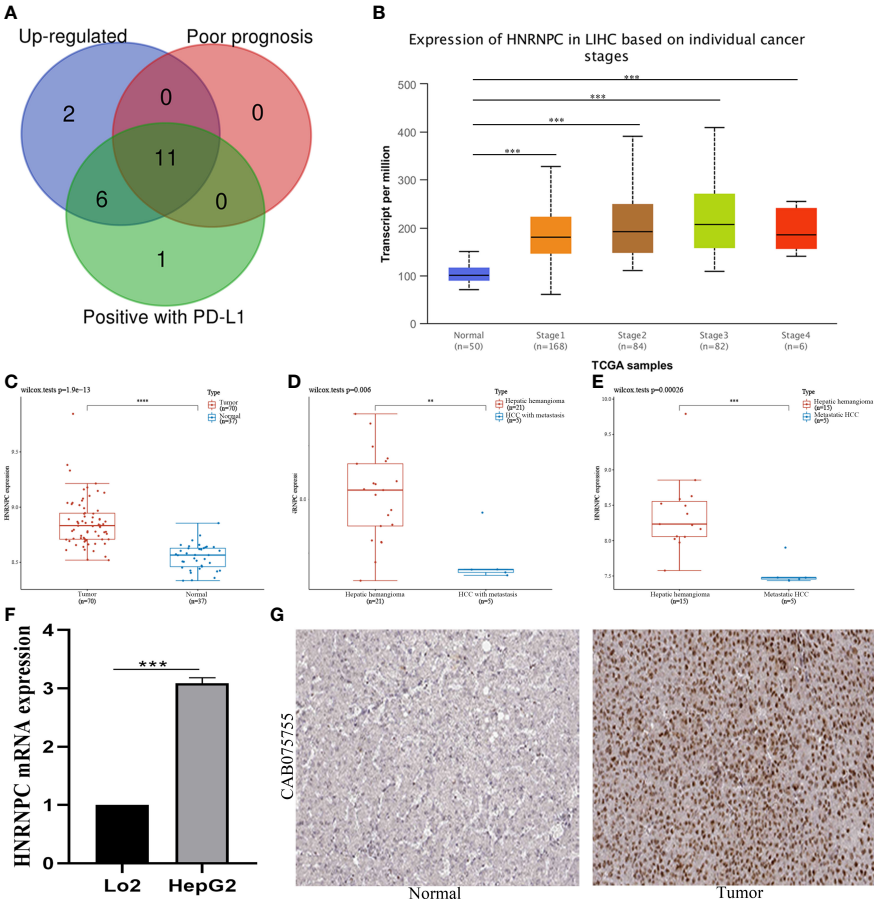

FIGURE 4
Identification and validation of *HNRNPC* expression in HCC. **(A)** Screening of 11 hub genes among up-regulated genes, genes of poor prognosis, and genes with *PD-L1* positively by venn graph. **(B)** Expression of *HNRNPC* in HCC based on individual cancer stages. **(C)** *HNRNPC* expression in 70 HCC tissues and 37 normal tissues in GSE121248 database. **(D)** *HNRNPC* expression in 21 hepatic hemangioma tissues and 5 HCC with metastatic tissues in GSE40367 database. **(E)** *HNRNPC* expression in 15 hepatic hemangioma tissues and 5 metastatic HCC in GSE40367 database. **(F)** *HNRNPC* expression in HCC cell lines by qRT-PCR analysis. **(G)** *HNRNPC* protein expression in HCC and normal tissues by HPA database. ***P*<0.01, ****P*<0.001, and *****P*<0.0001.

0.637 for forecasting survival (Figure 5C). Moreover, forest plots of univariate and multivariate Cox analysis suggested *HNRNPC* expression (*P*=0.001, HR=1.715; P=0.049, HR=1.705), and pTNM –stage (*P*<0.001, HR=1.376; P=0.006, HR=1.530) was associated with OS (Figures 5D, E). Besides, to evaluate the predictive efficiency of *HNRNPC* expression, we established the nomogram to predict 1-, 2-, and 3-years survival probability, with the value of C-index as 0.743(0.687–1) (Figure 5F). The calibration curve of nomogram performed a superior application for clinical decision making (Figure 5G). These results revealed that *HNRNPC* could serve as a novel independent prognostic biomarker for HCC patients.

Analysis of the correlation between *HNRNPC* expression and PD-L1, and immune infiltrating cells

We explored the relationship between immune infiltration cells and *HNRNPC* low- and high-expression groups by CIBERSORT algorithm. Patients in high-expression groups were increased in mast cell, T cell CD4+ Th2, class-switched memory B cell, B cell naive, T cell CD4+ memory, and common lymphoid progenitor, but decreased in microenvironment score, macrophage M2, granulocyte-monocyte progenitor, hematopoietic stem cell, and stroma score (Figure 6A). Moreover, the proportional abundance of immune infiltrating cells was visualized by heatmap in *HNRNPC* low- and high-expression groups (Figure 6B). To definite the role of immunity in *HNRNPC* expression, we conducted a correlation analysis between *HNRNPC* expression and *PD-L1* expression in HCC. *HNRNPC* was positively correlated with *PD-L1* expression in HCC (*P*=1.31e-08, Spearman=0.29) (Figure 6C). The Oncoplot showed the somatic landscape of HCC, altered in 270 (75.42%) of 358 samples (Figure 6D). *TP53* mutation is most common, followed by *TTN* and *CTNNB1* mutations. The mutation pattern of *HNRNPC* was Nonsense_Mutation and Missense_Mutation, accounting for 1%. In Figure 6E, We further exhibit the variation distribution of variant classifications, types and SNV class, so as to provide novel theories into immunotherapy for different risk groups.

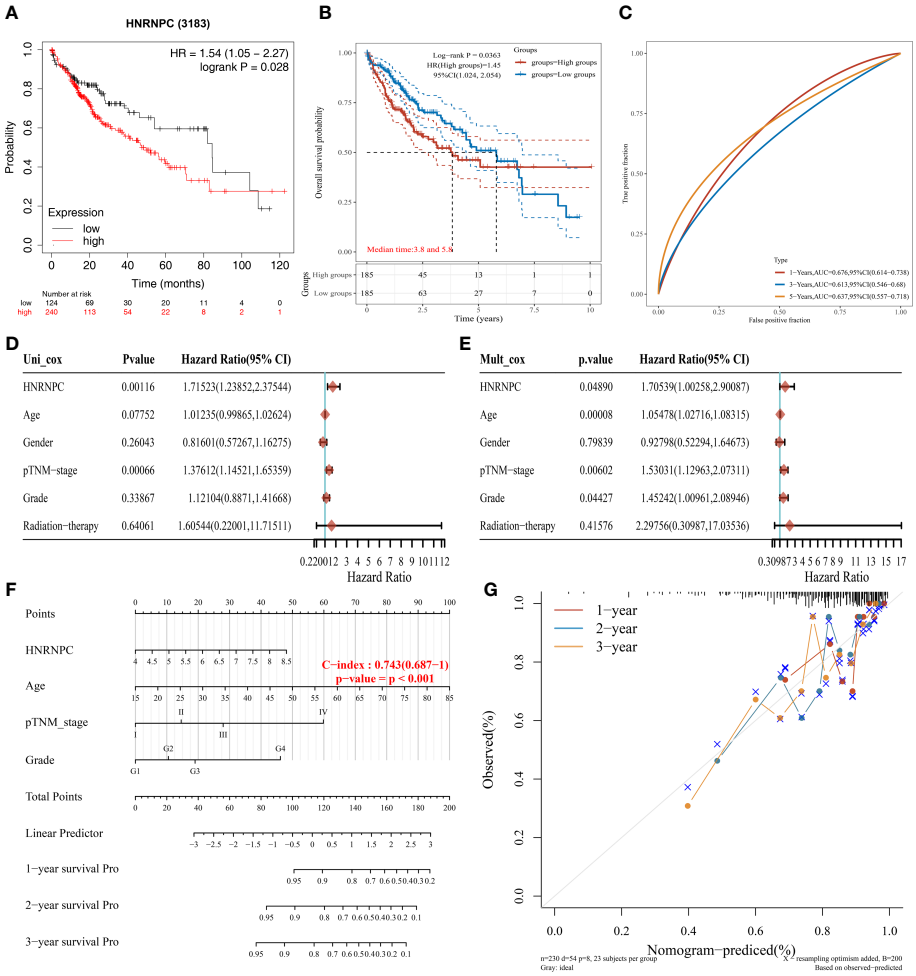

FIGURE 5
Independent prognostic value of *HNRNPC* in *HCC*. **(A)** The prognosis of HCC patients with low and high *HNRNPC* expression by Kaplan-Meier plotter database. **(B)** The overall survival probability of *HNRNPC* in HCC patients of TCGA database. **(C)** The AUC value of *HNRNPC* in 1-, 3-, and 5-years. **(D)** The univariate Cox regression between *HNRNPC* expression and clinicopathological characteristics. **(E)** The multivariate Cox regression between *HNRNPC* expression and clinicopathological characteristics. **(F)** Evaluation of overall survival in 1-, 2-, and 3-years for HCC patients by nomogram. **(G)** Calibration curve of the nomogram model.

Comprehensive analysis of *HNRNPC* in pan-cancer

To reveal the potential role of m6A regulator *HNRNPC*, we further analyzed *HNRNPC* expression, prognosis, TMB, immune checkpoints, and immune infiltration cells in pan-cancer. The up-regulation in *HNRNPC* expression was shown among 17 types cancers (Figure 7A). Importantly, we noticed that *HNRNPC* was down-regulated in Kidney chromophobe compared with normal tissues. Then, the forest suggested that *HNRNPC* had a poor prognosis in Adrenocortical Carcinoma (ACC), Head and Neck Squamous Cell Carcinoma (HNSC), Kidney Renal Papillary Cell Carcinoma (KIRP), LIHC, Lung Adenocarcinoma (LUAD), Pancreatic Adenocarcinoma (PAAD), and Sarcoma (Figure 7B). TMB has been considered as a quantifiable and profound immune response biomarker to forecast immunotherapy effects (22). The expression level of *HNRNPC* was associated with TMB in several cancers, including STAD, LUAD, Lung Squamous Cell Carcinoma (LUSC), Skin Cutaneous Melanoma (SKCM), Thyroid Carcinoma (THCA), Thymoma (THYM) (Figure 7C). Moreover, we estimated the relationship between the *HNRNPC* expression and immune checkpoints, and the results identified that the expression of HNRNPC was positively associated with most immune checkpoints in BLCA, LIHC, PAAD, PCPG, STAD, UVM, while negatively correlated with immune modulators in BRCA, GBM, LUSC, TGCT and THYM (Figure 7D). In addition, we observed T cell regulatory (Tregs), CD8+ T cell, NK cell activated, CD4+ T cell, Macrophage M1, and B cell memory were linked with the *HNRNPC* expression (Figure 7E).

Discussion

The emergence of immunotherapy, aiming to eradicate malignant cells and reinforce human immune system, is a revolutionary innovation for cancer treatment (23). Recently, with

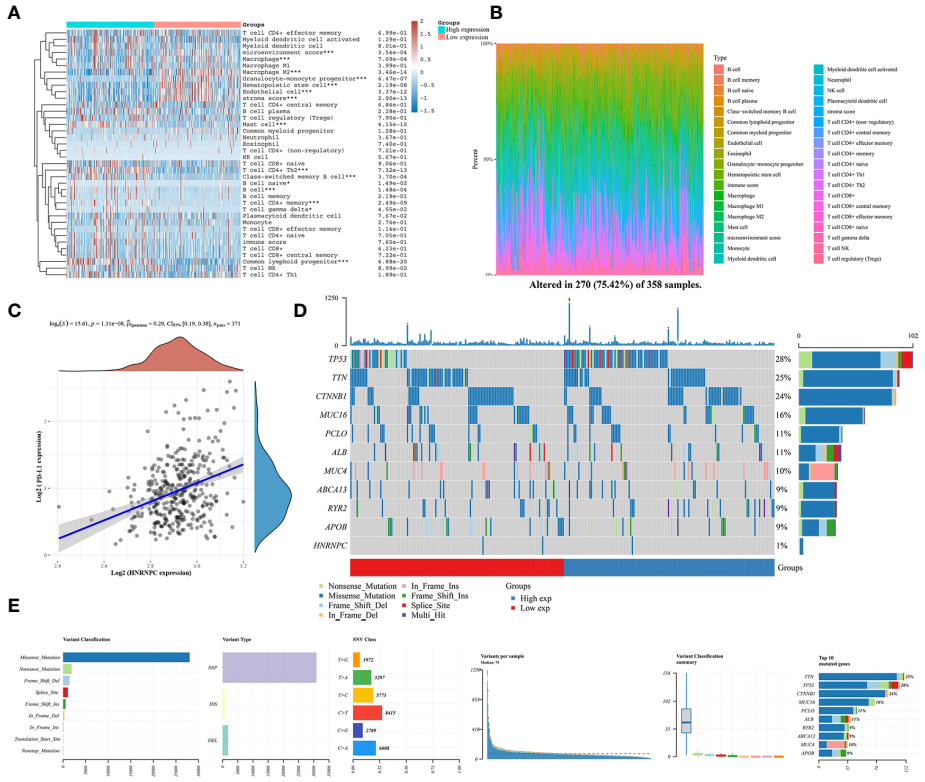

FIGURE 6
The relationship between immune microenvironment and HNRNPC expression groups and HNRNPC somatic landscape in HCC. **(A)** Analysis of immune cell infiltration level and low and high HNRNPC expression in HCC by heatmap analysis. **(B)** Proportion of immune infiltration cells in low and high HNRNPC expression groups. **(C)** The correlation of HNRNPC expression and PD-L1. **(D)** Lollipop charts of the mutated HNRNPC gene. **(E)** The variation distribution of variant classifications, types and SNV class in HCC. *P<0.05, ***P<0.001.

RNA modification coming into scientific arena, m6A modification, as a critical process in transcript expression, has collected enormous interest. Amounts studies have illustrated that the aberrant expression of m6A regulators is involved in cancer formation and progression, thus providing a new direction for immunotherapy (24). For example, m6A modification affects the *IL-7/STAT* pathway by regulating the mRNA of *SOCS* family genes to influence T cells (25). Moreover, the downregulation of *METTL14* was involved in tumor metastasis, and it performed an adverse prognostic factor for survival without recurrence in HCC patients (26). However, the relationship of m6A regulator and *PD-L1* is not fully elaborated.

Herein, we identified different m6A regulators subtypes by consensus clustering based on the differential expression of 20 m6A regulators in HCC. Then, we performed the relationship between three independent clusters and different clinicopathological characteristics, prognosis, immune microenvironment, and *PD-L1* in HCC. The cluster 2 was down-regulated expression in HCC, suggesting that patients with cluster 2 had a favorable prognosis by Kaplan-Meier curves analysis. An adequate characterization and validation determined *HNRNPC* as a prognosis biomarker and immune infiltration-related m6A regulator in HCC by public databases, qRT-PCR and immunohistochemistry analysis. Moreover, the pan-cancer analysis further demonstrated the comprehensive landscapes of *HNRNPC* in different cancers.

HNRNPC, a key m6A regulator belonging to the hnRNP family, regulates multiple functions in RNA splicing, RNA expression, RNA stabilization, and RNA translation (27–29). Increasing evidence suggested that up-regulation *HNRNPC* expression was associated with the occurrence and progression of tumors, such as breast cancer (30), gastric cancer (31), and glioblastoma (32). *HNRNPC* expression was correlated with tumor stage, lymph node metastasis, and poor prognosis in oral squamous cell carcinoma (33). Moreover, HNRNPC impairs vascular endothelial function and promotes the occurrence of vascular complications in type 2 diabetes (34). In our study, we found that *HNRNPC* was up-regulated in HCC tissues compared to normal tissues, and this result was validated by GSE121248 and GSE40367 datasets. Importantly, the qRT-PCR and immunohistochemistry analysis suggested the expression level of *HNRNPC* was over-expressed in HCC cells, and *HNRNPC* protein was positively expressed in HCC tissues. The Kaplan-Meier plotter showed the low expression group had a better prognosis. Furthermore, the univariate and multivariate Cox analysis indicated *HNRNPC* expression was an independent prognostic factor. Besides, based on *HNRNPC* expression and clinical features, we established the nomogram to

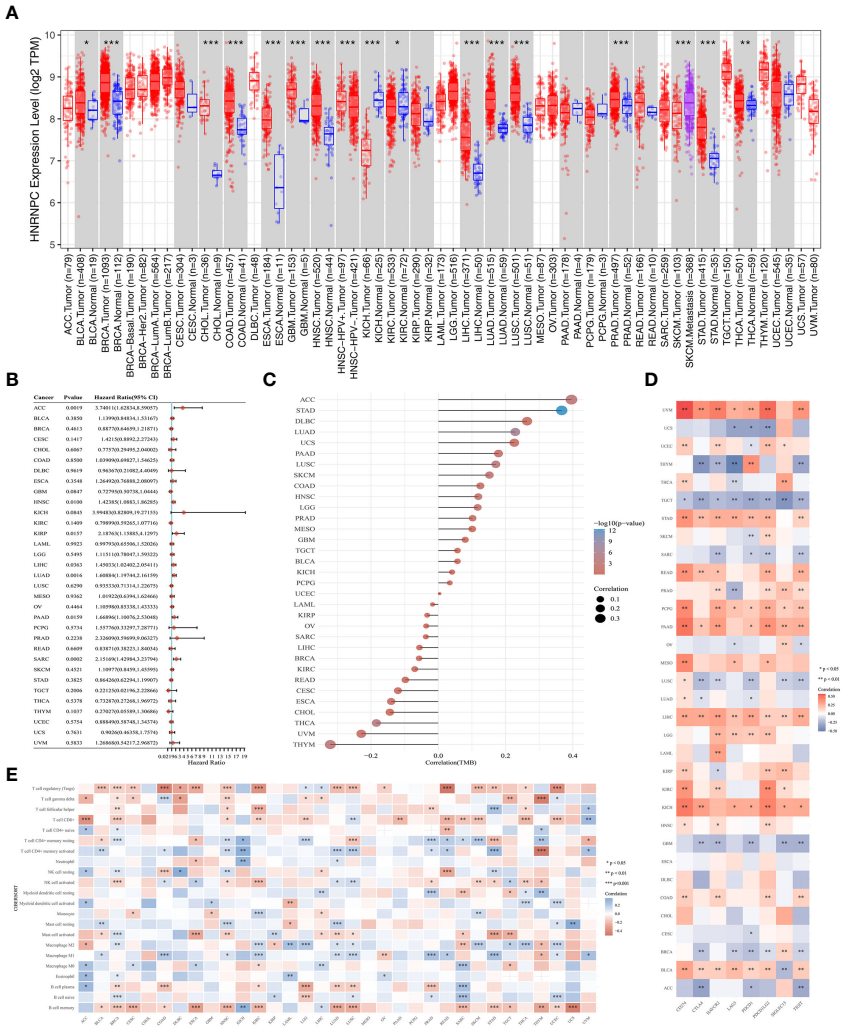

FIGURE 7
Comprehensive analysis of key m6A regulator HNRNPC in pan-cancer. **(A)** The expression of HNRNPC was up-regulated in various cancers. **(B)** The prognosis of HNRNPC in pan-cancer by forest plot. **(C)** The association between tumor mutation load and HNRNPC expression. **(D)** The correlation of HNRNPC expression with immune checkpoints in pan-cancer. **(E)** The correlation of HNRNPC expression with immune infiltrating cells in pan-cancer. *P<0.05, **P<0.01, and ***P<0.001.

evaluate the predictive efficiency, and the results performed a superior application for clinical decision making. However, the underlying function and mechanism need to exploit in HCC in detail.

The combination of m6A regulators and immune inhibitors have an active influenced on cancer immunotherapy efficacy. In this study, patients with HCC were classified into three clusters based on m6A regulators. Various differences in immune infiltration cells among three clusters with HCC were identified by the XCELL algorithm. For example, the infiltration levels with anti-tumor cells like T cell CD4+ effector memory, endothelial cell, and macrophage M2 were significantly up-regulated in cluster 2. Meanwhile, tumor-promoting cells like mast cell, T cell CD4+ Th2, T cell CD4+ memory, and T cell CD8+ central memory were higher in HCC patients with cluster 1 and cluster 3. The expression of Treg cells and NK cells was no difference in different clusters and expression groups. However, Li et al. reported that HNRNPC regulated the activation of Treg cells by activating the immune microenvironment, which may be a potential therapeutic target for prostate cancer (35). In pancreatic cancer, HNRNPC induced DNA damage repair and cancer-associated fibroblast activation through the RhoA/ROCK2-YAP/TAZ signaling pathway (36). Moreover, we also investigated the relationship between *HNRNPC* expression and immune infiltration cells based on *HNRNPC* low- and high-expression groups. Interesting, the results of infiltration levels in patients with low *HNRNPC* expression were consistent with cluster 2. These findings are in accordance with the role T cell CD4+ effector memory (37) and endothelial cell (38) act in regulating anti-tumor responses. Furthermore, previous studies reported mast cell promoted tumor growth and invasion in the tumor microenvironment, leading to poor overall clinical prognosis (39). Our results confirmed that m6A regulators in low-expression group could enhance tumor immune microenvironment to kill tumors. Notably, this study is the first to reveal the correlation between *HNRNPC* and *PD-L1* in HCC,

resulting be a potential biomarker for prognosis, and offering novel theory for immunotherapy response and therapeutic target related to *PD-L1*.

TMB could be consider a potential immunotherapy parameter that can determine patients responsiveness to immune checkpoint blockers (40). The higher mutation rate in patients with HCC provides novel insights into immunotherapy in different risk groups. Moreover, the immune microenvironment of HCC mainly involved the upregulation of *PD-L1* and *PD-L2* in Kupffer cells, hepatic sinus endothelium and leukocyte (41). It was reported that inflammatory responses with overexpression of *PD-1* and *PD-L1* were detected in 25% of HCC patients (6). Tumor cells can use *PD-L1* to bind to the *PD-1* of T cells, evading recognition and allowing them to continue to spread throughout the body (42). We found that *PD-L1* expression was significantly up-regulated in HCC tissues and other two clusters, and there was a closely relationship between *PD-L1* and m6A regulators. Moreover, *HNRNPC* expression was positively correlated with *PD-L1* expression in HCC. The combination of anti-*PD-L1* and other therapy strategies is gradually improving the prognosis of advanced cancers in HCC, maintaining its ability to recognize and kill tumor cells (43). Besides, comprehensive analysis indicated that the key m6A regulator, *HNRNPC*, is not only a novel prognostic biomarker in multiple cancers, but also regulates tumor immune microenvironment and immune checkpoints, providing a vital opportunity for developing immune targets.

This study has some potential limitations that deserves to be noticed. Firstly, m6A regulators were obtained from previous study, some m6A regulators may have not been included in this study. Secondly, although the TCGA cohort was used to clustering and grouping, further validation is still needed in multi-center and prospective cohorts in the future. Besides, it is necessary to explore the biological function and mechanism between m6A key regulator *HNRNPC* and *PD-L1* in HCC *in vivo* and vitro.

Conclusion

An extraordinary analysis was undertaken, referring to the expression and the relationship with prognosis, immune microenvironment, and *PD-L1* of m6A regulators in HCC based on different clusters and expression groups. The key m6A regulator *HNRNPC* could be a prognostic biomarker, which discloses the association between *HNRNPC* and immune microenvironment in HCC. Further exploration should focus on the potential mechanisms by which *HNRNPC* modulates the immunotherapy and offer a novel theory for therapeutic targets related to PD-L1 in HCC.

Data availability statement

The datasets presented in this study can be found in online repositories. The names of the repository/repositories and accession number(s) can be found in the article/Supplementary Material.

Author contributions

YS, YW, and WZ conceived and designed the study, revised the manuscript. YS,YW, and KN wrote the manuscript. WZ and XM extracted and analyzed the data alone. KF and KN performed the experiments. YZ edited the manuscript and funded this study. All the authors read and approved the final manuscript.

Funding

This study was supported by the Major Project of the National Natural Science Foundation of China (62227803), the National Natural Science Foundation of China (62141109), the Foreword Leading Technology Fundamental Research Project of Jiangsu (BK20212012), Jiangsu Province Social Development Project (BE2022812).

Conflict of interest

The authors declare that the research was conducted in the absence of any commercial or financial relationships that could be construed as a potential conflict of interest.

Publisher's note

Supplementary material

The Supplementary Material for this article can be found online at: https://www.frontiersin.org/articles/10.3389/fendo.2023.1153802/full#supplementary-material

References

1. Kulik L, El-Serag HB. Epidemiology and management of hepatocellular carcinoma. *Gastroenterology* (2019) 156(2):477–491.e1. doi: 10.1053/j.gastro.2018.08.065

2. Li X, Ramadori P, Pfister D, Seehawer M, Zender L, Heikenwalder M. The immunological and metabolic landscape in primary and metastatic liver cancer. *Nat Rev Cancer* (2021) 21(9):541–57. doi: 10.1038/s41568-021-00383-9

3. Mancebo A, Varela M, González-Diéguez ML, Navascués CA, Cadahía V, Mesa-Álvarez A, et al. Incidence and risk factors associated with hepatocellular carcinoma surveillance failure. *J Gastroenterol Hepatol* (2018) 33(8):1524–9. doi: 10.1111/jgh.14108

4. Yu Z, Ou Q, Chen F, Bi J, Li W, Ma J, et al. Evaluation of the prognostic value of paraoxonase 1 in the recurrence and metastasis of hepatocellular carcinoma and establishment of a liver-specific predictive model of survival. *J Trans Med* (2018) 16 (1):327. doi: 10.1186/s12967-018-1707-0

5. Rudra D, Kumar H. Advances and challenges in CAR-T cell-mediated immunotherapy. *Int Rev Immunol* (2022) 41(6):565–6. doi: 10.1080/08830185.2022.2111107

6. Sangro B, Sarobe P, Hervás-Stubbs S, Melero I. Advances in immunotherapy for hepatocellular carcinoma. *Nat Rev Gastroenterol hepatol* (2021) 18(8):525–43. doi: 10.1038/s41575-021-00438-0

7. Niu Y, Zhao X, Wu YS, Li MM, Wang XJ, Yang YG. N6-methyl-adenosine (m6A) in RNA: an old modification with a novel epigenetic function. *Genom Proteomics Bioinf* (2013) 11(1):8–17. doi: 10.1016/j.gpb.2012.12.002

8. Liu J, Harada BT, He C. Regulation of gene expression by N(6)-methyladenosine in cancer. *Trends Cell Biol* (2019) 29(6):487–99. doi: 10.1016/j.tcb.2019.02.008

9. Zhu ZM, Huo FC, Pei DS. Function and evolution of RNA N6-methyladenosine modification. *Int J Biol Sci* (2020) 16(11):1929–40. doi: 10.7150/ijbs.45231

10. Liu Y, Guo Q, Yang H, Zhang XW, Feng N, Wang JK, et al. Allosteric regulation of IGF2BP1 as a novel strategy for the activation of tumor immune microenvironment. *ACS Cent science.* (2022) 8(8):1102–15. doi: 10.1021/acscentsci.2c00107

11. Chen M, Wei L, Law CT, Tsang FH, Shen J, Cheng CL, et al. RNA N6-methyladenosine methyltransferase-like 3 promotes liver cancer progression through YTHDF2-dependent posttranscriptional silencing of SOCS2. *Hepatol (Baltimore Md)* (2018) 67(6):2254–70. doi: 10.1002/hep.29683

12. Liu GM, Zeng HD, Zhang CY, Xu JW. Identification of METTL3 as an adverse prognostic biomarker in hepatocellular carcinoma. *Digest Dis Sci* (2021) 66(4):1110–26. doi: 10.1007/s10620-020-06260-z

13. Paramasivam A, Vijayashree Priyadharsini J. Novel insights into m6A modification in circular RNA and implications for immunity. *Cell Mol Immunol* (2020) 17(6):668–9. doi: 10.1038/s41423-020-0387-x

14. Huang H, Weng H, Chen J. m(6)A modification in coding and non-coding RNAs: roles and therapeutic implications in cancer. *Cancer Cell* (2020) 37(3):270–88. doi: 10.1016/j.ccell.2020.02.004

15. Wang SM, Ooi LL, Hui KM. Identification and validation of a novel gene signature associated with the recurrence of human hepatocellular carcinoma. *Clin Cancer Res* (2007) 13(21):6275–83. doi: 10.1158/1078-0432.Ccr-06-2236

16. Roessler S, Lin G, Forgues M, Budhu A, Hoover S, Simpson RM, et al. Integrative genomic and transcriptomic characterization of matched primary and metastatic liver and colorectal carcinoma. *Int J Biol Sci* (2015) 11(1):88–98. doi: 10.7150/ijbs.10583

17. Li Y, Xiao J, Bai J, Tian Y, Qu Y, Chen X, et al. Molecular characterization and clinical relevance of m(6)A regulators across 33 cancer types. *Mol cancer.* (2019) 18 (1):137. doi: 10.1186/s12943-019-1066-3

18. Sturm G, Finotello F, Petitprez F, Zhang JD, Baumbach J, Fridman WH, et al. Comprehensive evaluation of transcriptome-based cell-type quantification methods for immuno-oncology. *Bioinf (Oxford England)* (2019) 35(14):i436–45. doi: 10.1093/bioinformatics/btz363

19. Shi Y, Wang J, Huang G, Zhu J, Jian H, Xia G, et al. A novel epithelial-mesenchymal transition gene signature for the immune status and prognosis of hepatocellular carcinoma. *Hepatol Int* (2022) 16(4):906–17. doi: 10.1007/s12072-022-10354-3

20. Shi Y, Ge C, Fang D, Wei W, Li L, Wei Q, et al. NCAPG facilitates colorectal cancer cell proliferation, migration, invasion and epithelial-mesenchymal transition by activating the wnt/β-catenin signaling pathway. *Cancer Cell Int* (2022) 22(1):119. doi: 10.1186/s12935-022-02538-6

21. Thul PJ, Lindskog C. The human protein atlas: a spatial map of the human proteome. *Protein Sci* (2018) 27(1):233–44. doi: 10.1002/pro.3307

22. Greillier L, Tomasini P, Barlesi F. The clinical utility of tumor mutational burden in non-small cell lung cancer. *Trans Lung Cancer Res* (2018) 7(6):639–46. doi: 10.21037/tlcr.2018.10.08

23. Zhang Y, Zhang Z. The history and advances in cancer immunotherapy: understanding the characteristics of tumor-infiltrating immune cells and their therapeutic implications. *Cell Mol Immunol* (2020) 17(8):807–21. doi: 10.1038/s41423-020-0488-6

24. Chen M, Wong CM. The emerging roles of N6-methyladenosine (m6A) deregulation in liver carcinogenesis. *Mol Cancer* (2020) 19(1):44. doi: 10.1186/s12943-020-01172-y

25. Li HB, Tong J, Zhu S, Batista PJ, Duffy EE, Zhao J, et al. m(6)A mRNA methylation controls T cell homeostasis by targeting the IL-7/STAT5/SOCS pathways. *Nature* (2017) 548(7667):338–42. doi: 10.1038/nature23450

26. Qin S, Mao Y, Chen X, Xiao J, Qin Y, Zhao L. The functional roles, cross-talk and clinical implications of m6A modification and circRNA in hepatocellular carcinoma. *Int J Biol Sci* (2021) 17(12):3059–79. doi: 10.7150/ijbs.62767

27. Fischl H, Neve J, Wang Z, Patel R, Louey A, Tian B, et al. hnRNPC regulates cancer-specific alternative cleavage and polyadenylation profiles. *Nucleic Acids Res* (2019) 47(14):7580–91. doi: 10.1093/nar/gkz461

28. Zarnack K, König J, Tajnik M, Martincorena I, Eustermann S, Stévant I, et al. Direct competition between hnRNP c and U2AF65 protects the transcriptome from the exonization of alu elements. *Cell* (2013) 152(3):453–66. doi: 10.1016/j.cell.2012.12.023

29. Liu N, Dai Q, Zheng G, He C, Parisien M, Pan T. N(6)-methyladenosine-dependent RNA structural switches regulate RNA-protein interactions. *Nature* (2015) 518(7540):560–4. doi: 10.1038/nature14234

30. Wu Y, Zhao W, Liu Y, Tan X, Li X, Zou Q, et al. Function of HNRNPC in breast cancer cells by controlling the dsRNA-induced interferon response. *EMBO J* (2018) 37 (23):e99017. doi: 10.15252/embj.201899017

31. Huang H, Han Y, Zhang C, Wu J, Feng J, Qu L, et al. HNRNPC as a candidate biomarker for chemoresistance in gastric cancer. *Tumour Biol* (2016) 37(3):3527–34. doi: 10.1007/s13277-015-4144-1

32. Park YM, Hwang SJ, Masuda K, Choi KM, Jeong MR, Nam DH, et al. Heterogeneous nuclear ribonucleoprotein C1/C2 controls the metastatic potential of glioblastoma by regulating PDCD4. *Mol Cell Biol* (2012) 32(20):4237–44. doi: 10.1128/mcb.00443-12

33. Huang GZ, Wu QQ, Zheng ZN, Shao TR, Chen YC, Zeng WS, et al. M6A-related bioinformatics analysis reveals that HNRNPC facilitates progression of OSCC *via* EMT. *Aging* (2020) 12(12):11667–84. doi: 10.18632/aging.103333

34. Cai Y, Chen T, Wang M, Deng L, Li C, Fu S, et al. N6-methylation of RNA-bound adenosine regulator HNRNPC promotes vascular endothelial dysfunction in type 2 diabetes mellitus by activating the PSEN1-mediated notch pathway. *Diabetes Res Clin practice* (2023) 197:110261. doi: 10.1016/j.diabres.2023.110261

35. Cheng Y, Li L, Wei X, Xu F, Huang X, Qi F, et al. HNRNPC suppresses tumor immune microenvironment by activating treg cells promoting the progression of prostate cancer. *Cancer Sci* (2023) 114(5):1830–45. doi: 10.1111/cas.15745

36. Xia N, Yang N, Shan Q, Wang Z, Liu X, Chen Y, et al. HNRNPC regulates RhoA to induce DNA damage repair and cancer-associated fibroblast activation causing radiation resistance in pancreatic cancer. *J Cell Mol Med* (2022) 26(8):2322–36. doi: 10.1111/jcmm.17254

37. Tian Y, Babor M, Lane J, Schulten V, Patil VS, Seumois G, et al. Unique phenotypes and clonal expansions of human CD4 effector memory T cells re-expressing CD45RA. *Nat Commun* (2017) 8(1):1473. doi: 10.1038/s41467-017-01728-5

38. Rohlenova K, Veys K, Miranda-Santos I, De Bock K, Carmeliet P. Endothelial cell metabolism in health and disease. *Trends Cell Biol* (2018) 28(3):224–36. doi: 10.1016/j.tcb.2017.10.010

39. DeNardo DG, Ruffell B. Macrophages as regulators of tumour immunity and immunotherapy. *Nat Rev Immunol* (2019) 19(6):369–82. doi: 10.1038/s41577-019-0127-6

40. Chan TA, Yarchoan M, Jaffee E, Swanton C, Quezada SA, Stenzinger A, et al. Development of tumor mutation burden as an immunotherapy biomarker: utility for the oncology clinic. *Ann Oncol* (2019) 30(1):44–56. doi: 10.1093/annonc/mdy495

41. Kassel R, Cruise MW, Iezzoni JC, Taylor NA, Pruett TL, Hahn YS. Chronically inflamed livers up-regulate expression of inhibitory B7 family members. *Hepatol (Baltimore Md)* (2009) 50(5):1625–37. doi: 10.1002/hep.23173

42. Kudo M. Limited impact of anti-PD-1/PD-L1 monotherapy for hepatocellular carcinoma. *Liver Cancer* (2020) 9(6):629–39. doi: 10.1159/000512170

43. Helmy DO, Khattab F, Hegazy AE, Sabry RM. Immunohistochemical expression of immune check point protein PDL-1 in hepatocellular carcinoma denotes its prognostic significance and association with survival. *J Immunoassay Immunochem* (2022) 24:1–16. doi: 10.1080/15321819.2022.2137810

Frontiers in Endocrinology

Explores the endocrine system to find new therapies for key health issues

The second most-cited endocrinology and metabolism journal, which advances our understanding of the endocrine system. It uncovers new therapies for prevalent health issues such as obesity, diabetes, reproduction, and aging.

Discover the latest Research Topics

See more →

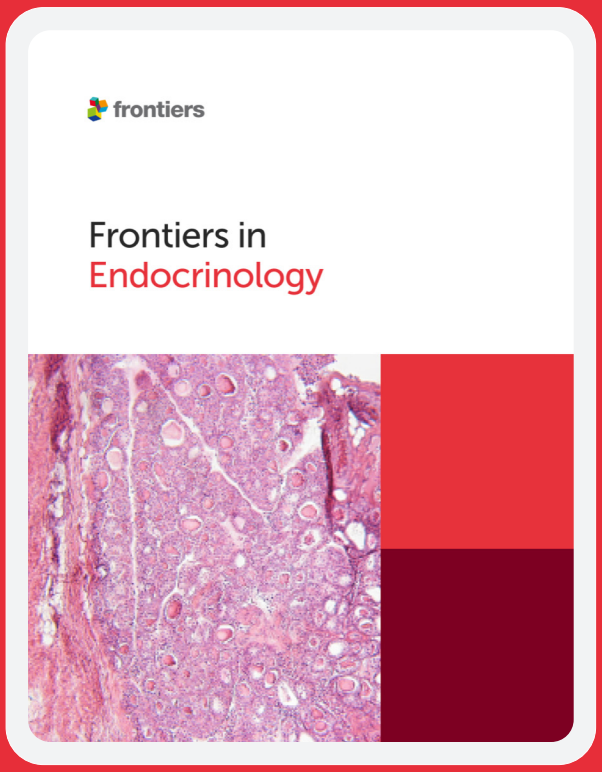

Frontiers

Avenue du Tribunal-Fédéral 34
1005 Lausanne, Switzerland
frontiersin.org

Contact us

+41 (0)21 510 17 00
frontiersin.org/about/contact